ORNL-5237

cy 1

Mechanical Properties Test Data for Structural Materials Quarterly Progress Report for Period Ending October 31, 1976

[redacted]

OAK RIDGE NATIONAL LABORATORY
CENTRAL RESEARCH LIBRARY
DOCUMENT COLLECTION
LIBRARY LOAN COPY
DO NOT TRANSFER TO ANOTHER PERSON
If you wish someone else to see this document, send in name with document and the library will arrange a loan.
UCN-7969
(3 3-67)

OAK RIDGE NATIONAL LABORATORY
OPERATED BY UNION CARBIDE CORPORATION FOR THE ENERGY RESEARCH AND DEVELOPMENT ADMINISTRATION

Printed in the United States of America. Available from
the Energy Research and Development Administration,
Technical Information Center
P.O. Box 62, Oak Ridge, Tennessee 37830
Price: Printed Copy $11.00 ; Microfiche $3.00

This report was prepared as an account of work sponsored by the United States Government. Neither the United States nor the Energy Research and Development Administration/United States Nuclear Regulatory Commission, nor any of their employees, nor any of their contractors, subcontractors, or their employees, makes any warranty, express or implied, or assumes any legal liability or responsibility for the accuracy, completeness or usefulness of any information, apparatus, product or process disclosed, or represents that its use would not infringe privately owned rights.

ORNL-5237
Distribution
Categoty UC-79b, -h, -k

Contract No. W-7405-eng-26

METALS AND CERAMICS DIVISION

MECHANICAL PROPERTIES TEST DATA FOR STRUCTURAL MATERIALS QUARTERLY PROGRESS REPORT FOR PERIOD ENDING OCTOBER 31, 1976

EG&G Idaho, Inc.

Argonne National Laboratory

Oak Ridge National Laboratory

Naval Research Laboratory

Hanford Engineering Development Laboratory

Westinghouse Advanced Reactors Division

University of Cincinnati

University of California at Los Angeles

General Electric Company

Compiled by M. R. Hill

Date Published: December 1976

OAK RIDGE NATIONAL LABORATORY
Oak Ridge, Tennessee 37830
operated by
UNION CARBIDE CORPORATION
for the
ENERGY RESEARCH AND DEVELOPMENT ADMINISTRATION

FOREWORD

This is the thirteenth in a series of progress reports, the purpose of which is to record and distribute quarterly the collected results of all structural materials mechanical properties test programs sponsored by the Reactor Development and Demonstration and the Nuclear Research and Applications Divisions of the Energy Research and Development Administration.

To be useful as resource documents, the reports in this series must be published and distributed in a timely manner to those in the reactor design and materials technology community who have a need of mechanical property test data for nuclear reactor and power plant applications. A test and material index is included to increase the effectiveness of the report.

Reports previously issued in this series are as follows: ORNL-4936, period ending October 31, 1973; ORNL-4948, period ending January 31, 1974; ORNL-4963, period ending April 30, 1974; ORNL-4998, period ending July 31, 1974; ORNL-5103, period ending October 31, 1974; ORNL-5104, period ending January 31, 1975; ORNL-5105, period ending April 30, 1975; ORNL-5106, period ending July 31, 1975; ORNL-5107, period ending October 31, 1975; ORNL-5112, period ending January 31, 1976; ORNL-5150, period ending April 30, 1976; and ORNL-5200, for period ending July 31, 1976. The next quarterly report will be for the period ending January 31, 1977, and contributions are due at ORNL by February 15, 1977.

W. R. Martin
Metals and Ceramics Division
Oak Ridge National Laboratory

CONTENTS

SUMMARY xiii

1. EG&G IDAHO, INC. 1

1.1 INTRODUCTION 1

1.2 MECHANICAL PROPERTY PROGRAM OF ALLOY 718 1

1.2.1 Creep-Rupture Tests 2

1.2.2 Cyclic Stress-Strain Tests 2

1.2.3 Fatigue Tests 2

1.3 REFERENCES 6

2. ARGONNE NATIONAL LABORATORY 13

2.1 INTRODUCTION 13

2.2 FRACTURE AND FATIGUE STUDIES ON STAINLESS STEELS . . . 13

2.2.1 Effect of Notches on Elevated-temperature Low-cycle Fatigue Behavior of Type 304 Stainless Steel 13

2.2.1.1 Introduction 13

2.2.1.2 Scope 14

2.2.1.3 Experimental Program 14

2.2.1.4 Results 16

2.2.1.5 Future Work 23

2.2.2 Elevated-temperature Low-cycle Fatigue Behavior of Different Heats of Type 304 Stainless Steel 23

2.2.2.1 Material Characterization and Experimental Procedure 24

2.2.2.2 Results and Discussion 31

2.2.3 Observations of Crack Initiation in Low-cycle Fatigue Specimens of Type 304 Stainless Steel 38

2.3 SODIUM EFFECTS ON LMFBR MATERIALS 43

2.3.1 Effect of Sodium Environment on the Uniaxial Creep-rupture Properties of Type 316 Stainless Steel 43

2.3.2 Representation of Tensile Behavior of Type 304 Stainless Steel in a Sodium Environment . . 52

2.3.3 Influence of Sodium Environment on the Low-Cycle Fatigue Behavior of Austenitic Stainless Steel 69

2.4 REFERENCES 85

3. OAK RIDGE NATIONAL LABORATORY 89

3.1 INTRODUCTION 89

3.2 MECHANICAL PROPERTIES AND BEHAVIOR FOR STRUCTURAL MATERIALS 89

3.2.1 Mechanical Property Characterization of Type 304 Stainless Steel Reference Heat — Influence of Strain Rate and Test Temperature on Ductility of Types 304 and 316 Stainless Steel 89

3.2.1.1 Three-Dimensional Plots 90

3.2.1.2 Choice of Ductility Indices for Strain Limits 99

3.2.1.3 Summary and Conclusions 102

3.2.2 Mechanical Property Characterization of Type 316 Stainless Steel Reference Heat 105

3.2.2.1 Product Form Characterization 106

3.2.2.2 Creep and Creep Properties of the 16-mm Plate of Reference Heat 133

3.2.3 Heat-to-Heat Variation of Mechanical Properties of Austenitic Stainless Steels of Types 304 and 316 — Time to Rupture and Minimum Creep Rate Modeling for Types 304 and 316 Stainless Steel 134

3.2.4 Elastic Properties of Engineering Construction Materials 139

3.2.4.1 Program Progress 140

3.2.4.2 Dynamic Elastic Constants of Inconel 617 143

3.2.5 Inconel Alloy 718 Mechanical Property Program 147

3.3 MECHANICAL AND METALLURGICAL BEHAVIOR OF WELDMENTS FOR LMFBR 150

3.3.1 Status of Testing on 16-8-2 Submerged-Arc Welds 150

3.3.2 Mechanical Properties of Welds in LMFBR Primary Piping Materials 156

3.3.3 Novel Measurement of Ultrasound Velocity in Type 308 Stainless Steel Weld Metal 157

3.3.4 Measurement of Ultrasound Velocity in Type 308 Stainless Steel Weld Metal 159

3.3.5 Model for Residual Stress in Welded Steel Pipe and its Correlation with Ultrasonic Rayleigh Waves 160

3.4 MECHANICAL PROPERTIES OF STEAM GENERATOR MATERIALS MATERIALS 163

3.4.1 Creep and Rupture Behavior of 2 1/4 Cr-1 Mo Steel 163

3.4.2 Heat-to-Heat Variation of 2 1/4 Cr-1 Mo Steel 178

3.4.3 Thermal Aging Effects on 2 1/4 Cr-1 Mo Steel 194

3.4.4 Effect of Sodium on the Mechanical Properties 2 1/4 Cr-1 Mo Steel 197

3.4.5 Fatigue Behavior of 2 1/4 Cr-1 Mo Steel 199

3.4.5.1 Specimen Geometry Effects 199

3.4.5.2 Subcritical Crack Growth Studies . . . 204

3.4.6 Creep and Tensile Properties of Transition Weld Joint Materials 211

3.4.6.1 Tensile Properties of Transverse Weldments 211

3.4.6.2 Creep and Rupture Behavior of Inconel 82 Weld Metal 212

3.5 HIGH-TEMPERATURE DESIGN 213

3.6 MECHANICAL PROPERTIES OF HTGR STEAM GENERATOR AND PRIMARY CIRCUIT MATERIALS 213

3.6.1 Tensile Testing 214

3.6.2 Environmental Creep Testing 214

3.6.3 Environmental Fatigue and Creep-Fatigue Interaction 219

3.7 FATIGUE STUDIES IN SUPPORT OF THE ISX 222

3.8 REFERENCES 226

4. NAVAL RESEARCH LABORATORY 233

4.1 INTRODUCTION 233

4.2 SIGNIFICANCE OF WELDING VARIABLES, LONG TERM AGING, AND TENSION HOLD TIMES ON FATIGUE CRACK GROWTH IN TYPE 316 STAINLESS STEEL WELDS 233

4.2.1 Background 233

4.2.2 Materials 234

4.2.3 Specimen Design and Evaluation 234

4.2.4 Experimental Test Matrix 238

4.2.5 Results and Discussion 238

4.2.5.1 Effect of Thermal Aging 238

4.2.5.2 Effect of Fatigue Cycling Rate With Load-Hold Time 241

4.2.5.3 Effect of Welding Materials — Flux Lot 241

4.2.5.4 Effect of Welding Materials — Filler Lot 241

4.2.5.5 Effect of Welding Materials — Filler and Flux Lots 241

4.2.6 Weld Deposit vs ASME Code Section XI Design Curve 246

4.2.7 Conclusions 246

4.3 CHARPY-V NOTCH DUCTILITY OF SELECTED ALLOY 718 PLATE, WELD DEPOSIT, AND FORGING MATERIALS 248

4.3.1 Background 248

4.3.2 Materials 248

4.3.3 Results 250

4.4 REFERENCES 252

5. HANFORD ENGINEERING DEVELOPMENT LABORATORY 253

5.1 INTRODUCTION 253

5.2 LMFBR STRUCTURAL MATERIALS 253

5.2.1 Effect of a Liquid Sodium Environment Upon Fatigue-Crack Growth in a Pressure Vessel Steel 253

5.2.1.1 Objective 253

5.2.1.2 Accomplishments and Status 253

5.2.1.3 Expected Achievements During Next Reporting Period 256

5.2.2 The Effect of Heat Treatment on the Fracture Toughness Response of Inconel 718 at 75°F and 800°F 258

5.2.2.1 Objective 258

5.2.2.2 Accomplishments and Status 258

5.2.2.3 Expected Achievements in the Next Reporting Period 263

5.2.3 Creep-Rupture Behavior of Inconel 600 After Thermal Exposure 263

5.2.3.1 Objective 263

5.2.3.2 Accomplishments and Status 263

5.2.3.3 Expected Accomplishments 268

5.2.4 Elevated Temperature High Strain Rate Tensile Properties of Alloy 600 268

5.2.4.1 Objective 268

5.2.4.2 Accomplishments and Status 268

5.2.4.3 Expected Accomplishments 287

5.3 MATERIALS INFORMATION DOCUMENTATION 287

5.3.1 Objective 287

5.3.2 Accomplishments and Status 287

5.3.3 Expected Achievements in the Next Reporting Period 288

5.4 REFERENCES 289

6. WESTINGHOUSE ADVANCED REACTORS DIVISION 291

6.1 INTRODUCTION 291

6.2 BASIC SPECIMEN TESTING 292

6.2.1 Type 304 Stainless Steel Testing 292

6.2.1.1 BTW-2 Transverse Weld in B-Type Model at 19 ksi (131 MPa) and 1100°F (593°C) 292

6.2.1.2 BAW-2 Axial Weld in B-Type Model at 22 ksi (151.7 MPa) and 1100°F (593°C) 292

6.2.1.3 C-4 B-Type Model with Central Hole 18 ksi (124.1 MPa) and 1100°F (593°C) 293

6.2.2 Type 316 Stainless Steel Tests 293

6.2.2.1 6A1 Type A Model at 32.5 ksi (224.1 MPa) and 1100°F (593°C) 293

6.2.2.2 6D2 Notches Bar at 28 ksi (193 MPa) and 1100°F (593°C). 294

6.2.2.3 6D3 Notched Bar at 25 ksi (172.4 MPa) and 1100°F (593°C) 294

6.3 TUBULAR SPECIMEN TESTING 294

6.3.1 Type 304 SS Testing and Analysis 294

6.3.2 Type 316 SS Heat Treatment 295

6.4 SODIUM EFFECTS ON MECHANICAL PROPERTIES OF STRUCTURAL MATERIALS 295

6.4.1 Type 316 Stainless Steel 297

6.5 REFERENCES 303

7. UNIVERSITIES 307

7.1 UNIVERSITY OF CINCINNATI 307

7.1.1 Introduction 307

7.1.2 Experimental Program 307

7.1.2.1 Activation Energy for Creep of AISI 310 Stainless Steel and Inconel 718 Calculated from Hot-Hardness Data 308

7.1.2.2 A Study on Subgrain/Cell Development During Creep Deformation 313

7.1.2.3 Fatigue Crack Characteristics as a Function of the Fatigue Life of AISI 304 Stainless Steel Tested at 649°C 317

7.1.2.4 Stress-Temperature Effects on Substructures 319

7.1.3 References 330

7.2 UNIVERSITY OF CALIFORNIA, LOS ANGELES 331

7.2.1 Mechanical Properties Evaluation of Carburized Type 304 Stainless Steel 331

7.2.2 Creep Studies in Stainless Steels 337

7.2.2.1 Introduction 337

7.2.2.2 Results 341

7.2.2.3 Discussion 342

7.2.3 Microstructures and Mechanical Properties of Cr-Mo Steels 343

7.3 References 351

8. GENERAL ELECTRIC COMPANY 353

8.1 INTRODUCTION 353

8.2 MECHANICAL PROPERTIES OF STAINLESS STEEL IN CARBURIZING SODIUM 354

8.2.1 Fatigue Crack Growth Studies 354

8.2.1.1 Background 354

8.2.1.2 Current Progress 356

8.2.2 Creep Investigation 359

8.3 DECARBURIZATION KINETICS AND DESIGN METHODS VERIFICATION TESTING 364

8.3.1 Background 364

8.3.2 Decarburization Kinetics of 2 1/4 Cr-1 Mo 365

8.3.2.1 Current Progress 365

8.3.2.2 Future Work 368

8.3.3 Mechanical Properties of 2 1/4 Cr-1 Mo Steel in Decarburizing Sodium 369

8.4 FRACTURE TOUGHNESS OF LMFBR STEAM GENERATOR MATERIALS 370

8.4.1 Background 370

8.4.2 Current Progress 371

8.5 References 381

SUMMARY

1. EG&G IDAHO, INC.

Mechanical property tests of Alloy 718 given the 1227 K (1750°F) solution anneal plus duplex age are being conducted. Current tests include creep-rupture at 1005 K (1350°F) and 1033 K (1400°F), cyclic stress-strain, and the beginning of high cycle fatigue with mean stress and notch effects.

2. ARGONNE NATIONAL LABORATORY

The initial results of an investigation into the effects of geometric stress concentrations on the elevated-temperature low-cycle fatigue behavior of Type 304 stainless steel are presented. Notched axially loaded specimens with theoretical elastic stress concentration factors of 1.5-4.0 were tested at 593°C (1100°F), and the results are compared with data from unnotched specimens over the life range of 10^2-10^5 cycles. Comparisons with curves derived from an equation given in the ASME Code Case for components in elevated-temperature service are also included.

The low-cycle fatigue results of three heats of Type 304 stainless steel have been obtained at 593°C and compared with those generated for the reference heat (9T2796) of steel. The continuous-cycling low-cycle fatigue behavior of the three heats of stainless steel, which exhibit different microstructural features, is approximately the same as that of the reference heat, but the three heats show improved fatigue strength under tensile hold-time conditions. The differences in creep-fatigue behavior are discussed on the basis of the microstructural features observed in the various heats of steel.

Observations of surface damage in Type 304 stainless steel fatigue specimens tested at 593°C and interrupted after a significant portion of total life have been made by means of plastic replica techniques. The microstructural observations of surface damage are consistent with the crack-initiation life determined from fatigue-striation spacing measurements made on the fracture surface.

Uniaxial creep-rupture tests have been conducted on Type 316 stainless steel specimens in the solution-annealed condition and after exposure to flowing sodium of controlled nonmetallic-element concentrations. In general, the data obtained at 700, 650, and 600°C show that, for the sodium-purity conditions established in the present investigation, the exposure of this stainless steel to a sodium environment results in a decrease in minimum creep rate when compared with material in the solution-annealed condition.

An analysis of the tensile behavior of Type 304 stainless steel was conducted for specimens in the solution-annealed condition and after exposure to a sodium environment. The Voce equation was used to describe tensile-flow curves for plastic strains >0.005 at all temperatures and strain rates of our experimental investigation. The results showed that the tensile-flow behavior of the sodium-exposed specimens was characterized by a higher strain-hardening rate, which decreased rapidly with an increase in flow stress. For sodium-exposed specimens, the values of the saturation stress for uniform elongation predicted from the Voce model were higher than for specimens in the solution-annealed condition at strain rates of $\lesssim 5 \times 10^{-5}\ s^{-1}$ and lower for strain rates $>5 \times 10^{-5}\ s^{-1}$.

Low-cycle fatigue tests have been conducted on Types 304 and 316 stainless steel in sodium at 550°C. The data obtained in sodium on annealed and preexposed material (5000 h in 550°C sodium with controlled nonmetallic-impurity concentrations) are compared with air data from the literature. The fatigue lifetime of annealed Type 316 stainless steel tested in sodium is a factor of three to four greater than that in air, whereas the fatigue lifetime of annealed Type 304 stainless steel does not differ substantially from that in air. In sodium, cyclic stress associated with preexposed Type 316 stainless steel is substantially lower than that of the annealed material, whereas the cyclic stress does not differ substantially for Type 304 stainless steel in the two conditions. Data obtained on the two steels in the thermally aged condition (1500 h at 600°C) agree well with data obtained earlier on the respective steels after preexposure to sodium for 1500 h. Similar behavior is observed at temperatures of 700°C. Low-cycle fatigue tests are being conducted at low strain rates, viz., $4 \times 10^{-5}\ s^{-1}$, to investigate the creep-fatigue behavior of austenitic stainless steels in a sodium environment. The initial tests, which have been conducted on annealed Type 316 stainless steel at 600°C, show a factor of four decrease in cycles to failure when compared with results obtained at a strain rate of $4 \times 10^{-3}\ s^{-1}$. Analysis of the fracture surfaces of Type 304 stainless steel specimens by scanning-electron microscopy indicates that the fracture mode was predominently transgranular for all tests at a strain rate of $4 \times 10^{-3}\ s^{-1}$.

3. OAK RIDGE NATIONAL LABORATORY

Three-dimensional plots of total elongation, reduction of area and uniform elongation as functions of test temperature have been completed for high-strain-rate and nominal-strain-rate data of type 304 stainless steel. Isothermal plots of various ductility indices were made and used to illustrate the strain rate and temperature conditions for change in fracture mode from trans- to intergranular. The strain to onset of tertiary creep and tensile uniform elongation were used to identify the boundaries showing changes in instability mode from strain rate independent to strain rate dependent.

The product of minimum creep rate and time to rupture was suggested as a possible index for defining strain limits.

Microstructure, grain size, hardness, and tensile property determinations of three plates, four pipes, and three bars of the reference heat of type 316 stainless steel were completed. Tensile properties were compared with *Nuclear Systems Materials Handbook* minimum value curves. Results were also compared with certified mechanical property data supplied by the vendor.

Time to rupture and minimum creep rate models containing an elevated-temperature ultimate tensile strength term have been presented to predict the creep behavior of new heats of types 304 and 316 stainless steel. Excellent comparisons are shown between the long-term creep data obtained from National Research Institute of Metals (Tokyo) and the predicted values from models containing ultimate tensile strength.

Dynamic elastic constants (E, G, and ν) were established for Inconel 617 (Heat XX00A3US) in the solution annealed condition from room temperature to 899°C (1650°F). Cubic polynomials are presented for the individual constants, and estimates of the properties at 28°C (50°F) increments are tabulated. A program on elastic properties was planned for the coming year. Capacitor strain-gage equipment was procured for evaluation and comparison with weldable resistance strain gages for determining static constants.

In support of the program already in progress at E, G, and G Idaho, Inc., mechanical property studies on Inconel alloy 718 were recently initiated. Creep-rupture tests are being carried out at 593, 649, 704, and 760°C (1100, 1200, 1300, and 1400°F) on specimens supplied by E, G, and G. Rupture results obtained to date are presented. Specimens of three additional heats have been prepared for creep-rupture evaluation, limited tensile and stress relaxation tests, and determination of effects of long-term aging.

The tensile, creep-rupture, and impact properties of a submerged-arc 16-8-2 weld are presented. Long-time creep-rupture tests and aging studies are in progress.

A summary is presented of important creep data for types 316 and 16-8-2 welds from a report entitled *Mechanical Properties of LMFBR Primary Piping Materials*, ORNL/TM-5594 (October 1976).

A method for determining the velocity of sound as a function of direction in metal has been developed. The probe is moved by an immersed goniometric device about three cylindrical specimens. A cube is used for standardization. Measurements made on an electroslag type 308 stainless steel weld demonstrate anisotropic sound velocity that can be used to calculate elements of the dynamic elastic modulus matrix.

Rayleigh wave ultrasound velocity was shown to be a promising measure of residual stress in an austenitic stainless steel pipe weld.

Our studies have demonstrated the effect of stress, temperature, and heat treatment on the characteristic behavior of annealed 2 1/4 Cr-1 Mo steel during creep and creep rupture. We have explained the observed behavior in terms of the solid solution and precipitation strengthening effects that occur in this material. Such knowledge should prove useful in the extrapolation of creep behavior to stresses where significant creep does not occur in reasonable times and is not readily measured. Extrapolations of this type are required to determine design properties.

When all available mechanical property data for a given material are examined, large variations are usually observed. In a program to determine the reasons for such heat-to-heat variation, 12 heats of 2 1/4 Cr-1 Mo steel are being tested. We determined their tensile properties over the range 25 to 566°C.

Specimens from four tubing heats and a 25.4-mm-thick (1-in.) plate are being thermally aged at 454, 510, and 566°C for times up to 20,000 hr. We have completed tensile tests on specimens from the four tubing heats for material aged for 1000 and 2500 hr. The results show a decrease in strength with aging time, the relative effect being greater as the temperature is increased.

Our initial creep-rupture tests on the 2 1/4 Cr-1 Mo steel decarburized in sodium for 26,500 hr at 566°C (1050°F) were completed. The results show a substantial decrease in the creep-rupture strength.

Effects of specimen geometry on experimental fatigue data were investigated. Though no difference was observed in test data at room temperature, fatigue life at 538°C (1000°F) from uniform-gage specimens was lower than but more than half that from hourglass specimens. Data from two hourglass specimens with the same R/D ratio of 6 but of different minimum diameters were consistent.

Subcritical fatigue crack growth studies of 2 1/4 Cr-1 Mo steel in air are discussed. The following areas are covered: (1) temperature effects below room temperature; (2) frequency effects at 371, 510, and 593°C (700, 950, and 1100°F); (3) effect of carbon content; (4) effect of aging.

Creep-rupture studies on the mechanical properties of Inconel 82 weld metal continued. Further tests were completed at 454, 510, and 566°C (850, 950, and 1050°F); creep-rupture curves are now complete at these temperatures to several thousand hours. Tests have been started at 621, 677, and 732°C (1150, 1250, and 1350°F).

No significant differences have as yet been found between stress-rupture data of Hastelloy X from HTGR-helium environmental tests compared with air tests at 649, 760, and 871°C (1200, 1400, and 1600°F) up to a

rupture life of 6500 hr. Similar results have also been found for 2 1/4 Cr-1 Mo steel at 593°C (1100°F) up to a rupture life of 9600 hr.

Creep-fatigue testing of 2 1/4 Cr-1 Mo steel has continued, and recent data are presented. An environmental fatigue-test chamber is being installed to characterize the fatigue behavior of HTGR materials in simulated primary coolant helium environments, and progress in integrating this chamber into an existing facility is reported.

Fatigue-related problems of the ISX are discussed and a supporting test program is described. Results of load-controlled fatigue tests on chromium-copper CDA182 are given. This work is in support of ORNL fusion research.

4. NAVAL RESEARCH LABORATORY

The effects of welding variables, long term thermal conditioning (aging), and tension hold times on fatigue crack growth rate were explored for AISI Type 316 submerged arc weld deposits. Three welds representing statistical variations in filler lot and flux lot were examined using single-edge-notched (SEN) specimens cycling in air using a zero-tension-zero load cycle. Cycling rates were 1 and 10 cycles per minute which, respectively, provided 54 and zero tension hold times. Weld comparisons were based on crack growth rate per cycle (da/dN) versus stress intensity factor range (ΔK).

No appreciable effect of 500°F (260°C) — 2500 hour thermal conditioning on fatigue crack growth behavior was observed. However, fatigue crack growth rate was found to be reduced by a tension hold time, as compared to continuous cycling, at values of ΔK over 40 ksi $\sqrt{\text{in.}}$ The results revealed that a factor of ten difference in fatigue resistance is possible between random filler lot and flux lot combinations. Moreover, fatigue crack growth rates determined for two of the three welds were much more rapid than that described by the ASME Code, Section XI, design curve for low alloy steel.

A comparison of Charpy-V notch ductility of two plates (VAR and ESR), one weld deposit (GTA), and one forging (VAR) has been made at 75, 800, and 1160°F (24, 427, and 627°C). The plates and weld deposit were heat treated according to INEL-developed heat treatment specifications; the forging received a standard commercial heat treatment.

Forging determinations indicated better notch toughness than the VAR plate but somewhat lower notch toughness than the ESR plate. Weld deposit notch ductility was much lower than that anticipated over the entire range investigated. A detailed investigation of heat treatment variable effects indicated that the mode of cooling from the solution anneal temperature, i.e., step cooling at 100°F (56°C) per hour ±25°F (14°C) versus continuous cooling at the same rate, is very critical to

weld notch ductility properties. In contrast, step cooling versus continuous cooling produced only small (or negligible) differences in plate properties.

5. HANFORD ENGINEERING DEVELOPMENT LABORATORY

The fatigue crack growth rate of 2 1/4 Cr-1 Mo steel at 427°C (800°F) was less in sodium than in air and not greatly affected by frequency in the range 0.67 to 6.7 Hz (40–400 cpm). The INEL heat treatment nearly doubled the fracture toughness of Inconel 718 with only slight decrease in strength compared with conventional heat treatment. The effect of aging up to 10,000 hr at the test temperature is given for the creep of Inconel 600 at 538, 649, and 760°C (1000, 1200, and 1400°F). Tensile properties of alloy 600 are presented for the temperature range 22 to 760°C (72–1400°F) and the strain rate range 3×10^{-5} to 1.0/sec. An update package for the *Nuclear Systems Materials Handbook* is ready for distribution, and another is nearing publication. A volume on "Materials and Processes: Selection and Control" has been redrafted and is in review.

6. WESTINGHOUSE ADVANCED REACTORS DIVISION

Creep tests were continued on 304 SS plate specimens to evaluate axial weld and transverse weld behavior and to study creep crack growth from a plate specimen containing a central hole in the gauge section. Notched bar 316 SS tests also continued at 25 and 28 ksi stress levels.

Additional heat treatment studies were performed to determine an optimum annealing procedure for the 316 SS tubular specimens.

Low cycle fatigue results for solution annealed Type 316 stainless steel, tested in flowing sodium at 593°C, were obtained for samples sodium pre-exposed at 593°C for 2000 and 5000 hours, as well as as-fabricated material. The fatigue life for the as-fabricated material was greatest in all cases, with the difference increasing as the total strain range decreased. In addition, the fatigue life decreased as the sodium pre-exposure time increased. At 593°C, all conditions of the Type 316 stainless steel material describe the same plastic strain range vs. cycles to failure curve, with a transition in the fatigue life occuring at approximately 20,000 cycles.

Creep-rupture tests of solution annealed Type 316 stainless steel in flowing sodium at 593°C show that sodium pre-exposure at 593°C for 2000 and 5000 hours significantly increases the rupture life and ductility of the material. At the same time, the rupture life for the material pre-exposed 5000 hours is less than that for the material pre-exposed 2000 hours.

7. UNIVERSITIES

UNIVERSITY OF CINCINNATI

Hot-hardness tests were performed on AISI 310 stainless steel and Inconel 718 at temperatures of R.T. ∿ 1200°C and 900–1200°C, respectively. Compared to AISI 330 stainless steel, both AISI 310 stainless steel and Inconel 718 are lower in hardness values at all temperatures investigated, however, their hardness curves have the similar characteristics as AISI 330 stainless steel. The activation energy for creep calculated from the hot-hardness data is 85 kcal/mole for AISI 310 stainless steel and 64 kcal/mole for Inconel 718.

As an effort to investigate the mechanisms of subgrain/cell formation during creep deformation, a series of creep tests were conducted on AISI 330 stainless steel at 652°C with an applied stress of 35 ksi for various strains (times), including three stress-rupture tests. These tests were reproducible with less than 1 percent deviation in the total strain and are considered to be suitable for the detailed microstructure studies. Preliminary TEM and SEM observations on one of the ruptured specimens revealed an ill-defined cellular structure containing precipitates and a transgranular fracture surface, respectively.

Fatigue crack characteristics were investigated on AISI 304 stainless steel fatigue-tested at 649°C to different fractions of the fatigue life and to failure. The striation density was determined from SEM micrographs of the fractured surface, and the number of cycles for crack propagation and the number of cycles to initiate a crack of one grain diameter length were calculated. Optical microscopy on the specimens tested to various fractions of the fatigue life revealed a crack at various stages of crack initiation and propagation periods. The crack lengths determined from the optical microscope agreed with the values obtained from the SEM technique. Finally, the microhardness values obtained from the interrupted specimens show good agreement with the stress amplitude measurements and the substructure development.

As a continuation of the creep-substructure study on AISI 330 stainless steel, stress-rupture tests have been completed on three more specimens since the last progress report was submitted, and one long term test is presently in progress at 600°C with an applied stress of 20 ksi. Preliminary analyses of the creep data compiled up to the present time show the following:

$$\Delta H_c = 100 \text{ kcal/mole}$$

$$n = 7.4 \text{ at } 701°C$$

$$n = 7.1 \text{ at } 800°C$$

These numbers should be considered as tentative because of the limited number of datum points used for the calculation. However, it is interesting to note that the activation energy for creep, 100 kcal/mole, is in reasonable agreement with the value obtained from the hot-hardness data on the same material, i.e. 93 kcal/mole as reported in the last progress report. Finally, a limited study on the cracking behavior of this material has been initiated.

UNIVERSITY OF CALIFORNIA, LOS ANGELES

Constant-load crack-growth rates of type 304 stainless steel over the range 650–800°C (1202–1472°F) were measured and correlated with the stress intensity factor by $da/dt = CK^{0.34}$ with an activation energy of 166.5 kJ/mole (39.8 kcal/mole). Transmission electron micrographs show the development of dislocation structure during creep of both annealed and cold-worked type 304 stainless steel during creep at 704°C (1300°F) and 172 MPa (25.0 ksi). The tensile properties of normalized-and-tempered 2 1/4 Cr-1 Mo steel at 454°C showed a complex variation with aging time (2880–8640 hr), aging temperature [454–566°C (850–1050°F)], and carbon content (0.009–0.12%).

8. GENERAL ELECTRIC COMPANY

Programs designed to study the effects of high temperature sodium environments on the mechanical properties of stainless steels and 2¼Cr-1Mo steel are continuing. The results of programs evaluating the effects of heat treatment, welding, and melting practice on the mechanical behavior of 2¼Cr-1Mo steel are also reported.

Fatigue crack propagation rates of Type 316 stainless steel are being determined at 510°C (950°F) in air and in carburizing sodium under a variety of loading conditions. Preliminary results for annealed base metal are reported for both environments, including hold time test results. Hold time results, in air, are lower (slower growth) than for tests with no hold at peak load; possibly a consequence of crack tip blunting. High stress ratio (R = 0.4) results in air are in agreement with R = 0.05 results. GTA welds (with 16-8-2 filler metal) have been pre-exposed, and testing in air and sodium has been initiated. A crevice exposure specimen, with crevices of different spacings, has been exposed in carburizing sodium for 1000 hours, and analysis is proceeding. These results will be related to test specimen crack opening displacements and crack growth rates in terms of a carburization process zone size expected at the crack tip.

Fracture toughness properties of 2¼Cr-1Mo steel are being determined through the use of J-Integral test methods. Room temperature and elevated temperature (to 510°C [950°F]) results are reported for various relevant heat treated and potentially embrittling conditions, as well as

for SMAW weld metal and HAZ locations. Tension test results show that the weld is stronger than the base material, even after a 12 hour post weld heat treatment (PWHT) at 727°C (1340°F). Fracture toughness results for base material tested at 24°C (75°F) after a temper embrittling treatment reveal that the toughness is still above the ASME Code K_{IR} curve. Preliminary HAZ tests at 24°C (75°F) indicate that this material condition may also be above the K_{IR} curve, for this temperature. Fracture toughness results at elevated temperatures continue to give concern because they fall below the assumed shelf of the Code K_{IR} curve. Testing emphasis is being directed in this area.

The rupture strength of carburized stainless steel is found to be dependent on the stress/strain history of the material. The rupture strength is determined by a balance between creep ductility and the rate of deformation. Under conditions of equivalent strain history, the rupture strength of the uncarburized condition may be limiting, and, in this instance, base metal data would serve as a conservative estimate for design.

Progress in the mechanical properties investigation of decarburized 2¼Cr-1Mo steel was limited this reporting period by the non-availability of a suitable sodium-filling source. Loop 6R, previously used for carburization studies, has been modified for capsule filling. The requirement for a source of clean (<10ppm Oxygen) and low carbon activity sodium has been met through hot trapping techniques.

1. EG&G IDAHO, INC.

D. D. Keiser

1.1 INTRODUCTION

EG&G Idaho, Inc. is conducting mechanical properties investigations under a program sponsored by ERDA Division of Reactor Development and Demonstration. Program IA-009, Alloy 718 Mechanical Property Program, has as its primary objective the acquisition of the necessary mechanical property data to permit safe, efficient use of this material in LMFBR service. The specific immediate application is for selected structural components of the Clinch River Breeder Reactor Project (CRBRP). Other reactor service applications which require high levels of mechanical properties at temperatures up to 922 K (1200 °F) are also expected to make use of this material.

To provide an adequate data base for CRBRP design needs and to qualify for ASME Code approval, additional data is being generated to complement existing data in the literature. All current tests are being conducted on material given the 1227 K (1750 °F) conventional heat treatment.* The additional data required will include: (1) tensile properties from room temperature to 1033 K (1400 °F), (2) physical properties from room temperature to 977 K (1300 °F) to include density, thermal expansion, heat capacity, and thermal conductivity, (3) creep-rupture properties between 811 K (1000 °F) and 1033 K (1400 °F), (4) low cycle fatigue (to 10^6 cycles) from room temperature to 977 K (1300 °F), (5) high cycle fatigue (to 10^9 cycles) from room temperature to 977 K (1300 °F), (6) relaxation properties at 922 K (1200 °F), (7) creep-fatigue interaction at 922 K (1200 °F), and (8) long term aging effects from 866 K (1100 °F) to 1033 K (1400 °F) at times up to 30,000 hours.

1.2 MECHANICAL PROPERTY PROGRAM OF ALLOY 718

G. E. Korth and G. R. Smolik

* 1227 K (1750 °F) SA 1 h, AC, duplex age 991 K (1325 °F) 8 h, FC to 894 K (1150 °F) and age an additional 8 h.

1.2.1 Creep-Rupture Tests

Test specimens prepared from 12.7 mm (1/2 inch) thick plate of heat 2180-4-9478 were tested in air at 1005 K (1350 °F) and 1033 K (1400 °F). The specimens were cut from the plate such that the material was loaded parallel to the major rolling direction. Results from current tests are listed in Table 1.1.

1.2.2 Cyclic Stress-Strain Tests

To determine cyclic stress-strain behavior of Alloy 718, several tests were conducted using the multiple-step technique (incrementally increasing the strain range of a strain controlled fatigue test and connecting the hysteresis loop tips from each increment after the stress has stabilized). Figure 1.1 illustrates the cyclic stress-strain behavior of one heat of Alloy 718 at four different temperatures. Also plotted for comparison are some data points from some constant amplitude fatigue tests from the same heat. These data points are plotted as $\Delta\sigma/2$ vs $\Delta\varepsilon_t/2$ at $N_f/2$. In Figure 1.2 the cyclic stress-strain behavior is shown for four different heats of plate material at one temperature. One monotonic test is also shown for one heat for comparison. From Figure 1.2 it is readily apparent that Alloy 718 undergoes cyclic softening. From the limited tests of Heat 6 at 700 K (800 °F), it appears that the proportional limit of the monotonic test is approximately equal to the 0.2% offset yield strength of the cyclic test. Some cyclic tests exhibited some degree of relatively rapid cyclic softening after entering the inelastic regime which is illustrated in Figures 1.1 and 1.2 as a dip in the stress-strain curve.

1.2.3 Fatigue Tests

As testing moved into the high cycle regime ($N_f > 10^5$), notch sensitivity was observed and considerable problems have been encountered with specimens failing outside the gage area. The least bit of notch effect from machining marks or specimen geometry or fretting from gripping resulted in premature failure at those points. Modifications in both specimen design and gripping were necessary to conduct valid tests.

Table 1.1 Creep-Rupture Tests of Alloy 718 Plate[a]

Specimen Ident.	Stress MPa (ksi)	Test Temperature K (F)	Elong in 50.8 mm	Reduction In Area,%	Min Creep Rate, h^{-1}	Onset of Tertiary Creep, h	Time to Rupture, h
6-19-16	483 (70.0)	1005 (1350)	8[b]	22	---	---	31
6-19-18	412 (59.7)	1005 (1350)	19	35	4.1×10^{-3}	12	40
6-19-17	381 (55.2)	1005 (1350)	16	39	8.2×10^{-4}	57	134
6-19-19	205 (29.7)	1005 (1350)	23	60	---	---	1384
6-19-15	137 (19.9)	1033 (1400)	21[b]	61	---	---	1714

[a] Heat 2180-4-9478 12.7 mm (1/2 inch) thick plate; heat treatment: 1227 K (1750 °F) solution anneal for 1 h, air cool, aged at 991 K (1325 °F) for 8 h, furnace cooled to 894 K (1150 °F) and aged an additional 8 h.

[b] Failure occurred near the end of the reduced section.

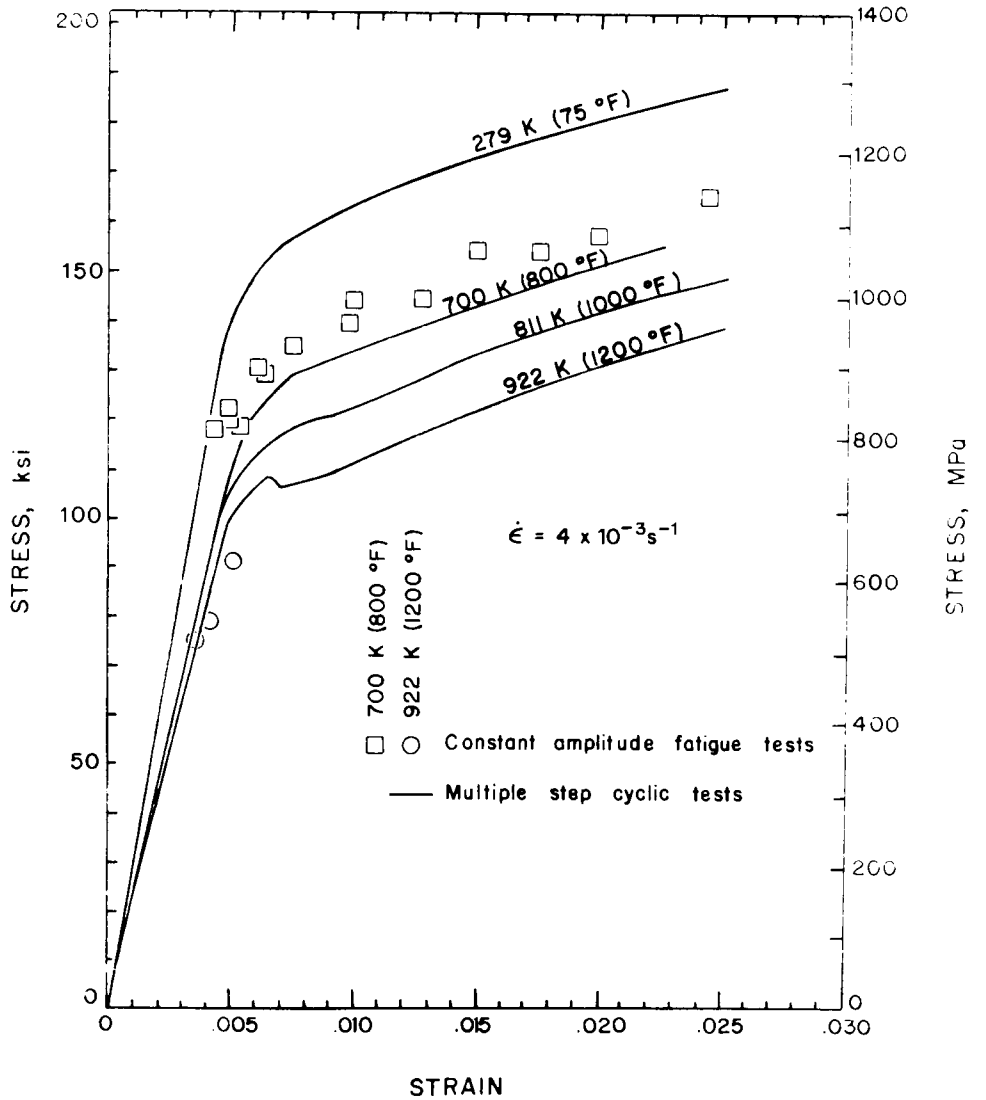

Figure 1.1 Cyclic Stress-strain curves for Alloy 718 at four different temperatures of Heat 6 (2180-4-9478)

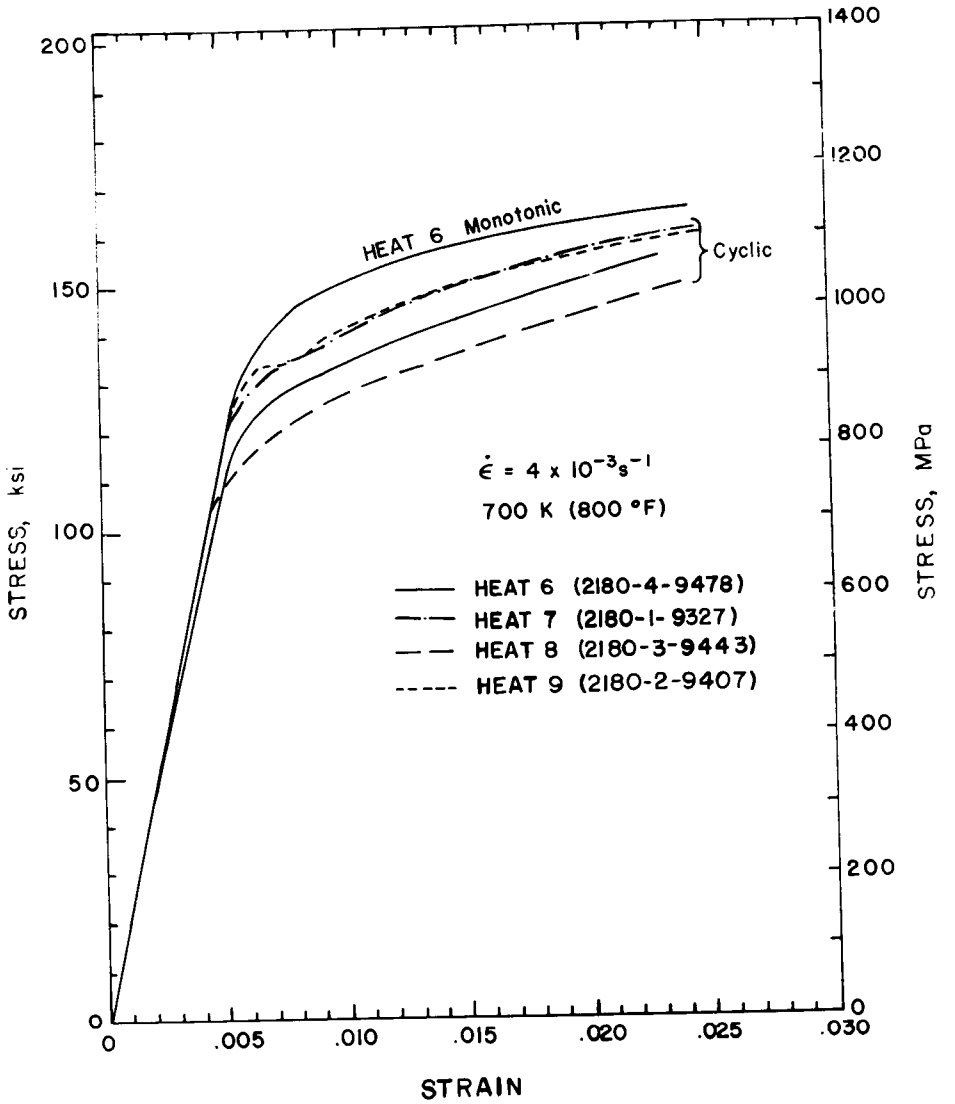

Figure 1.2 Cyclic Stress-strain of four heats compared to monotonic stress-strain of one heat of Alloy 718 at 700 K (800 °F) given the 1227 K (1750 °F) conventional heat treatment.

Figure 1.3 shows tests conducted to date at room temperature and includes many of the tests where failure occurred in the grip area. Also illustrated in Figure 1.3 is the comparison between strain controlled and load controlled tests and the effect of maximum mean stress and notch effects on a limited basis. A maximum mean stress test is defined as a test where the mean stress is such that the peak tensile stress is equal to the proportional limit of a monotonic tensile test. The strain controlled and mean stress data have been reported previously[1] and the current tests are tabulated in Table 1.2. Fatigue data at 700 K (800 °F) for strain controlled, load controlled, mean stress, and notch effects are compared in Figure 1.4. Table 1.3 lists the current data except the strain controlled tests which have been reported previously.[1] Included in Table 1.3 are additional mean stress data at less than maximum levels which was not plotted on Figure 1.4 for the sake of clarity. Additional test results will be forthcoming in the load controlled high cycle fatigue area with notch and mean stress effects since current tests are in progress in this area.

1.3 REFERENCES

1. "Mechanical Properties Test Data for Structural Materials Quarterly Progress Report for Period Ending July 31, 1976," ORNL-5200, p. 2-15.

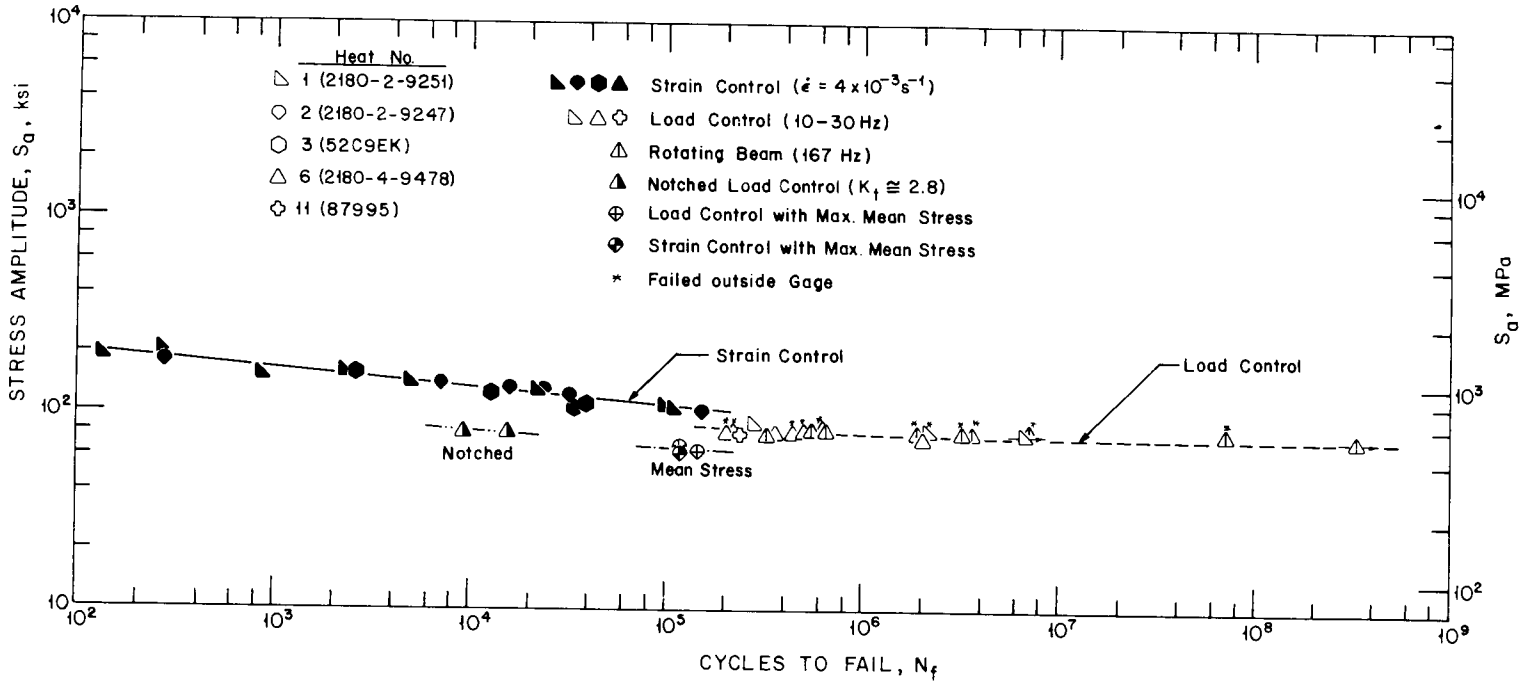

Figure 1.3 Fatigue of Alloy 718 at room temperature given the 1227 K (1750 °F) conventional heat treatment.

Table 1.2 Load Controlled Fatigue of Alloy 718 Tested at Room Temperature

Specimen No.[a]	Type Loading	Testing Frequency Hz	Stress Amplitude MPa	(ksi)	Cycles to Fail N_f	Remarks
214-39	Axial	10	620	(90.0)	283,500	Good test
619-33	Rot. Beam	167	577	(83.7)	554,000	Good test
619-47	Rot. Beam	167	565	(82.0)	666,000	Good test
619-32	Rot. Beam	167	560	(81.2)	7,257,000	Failed outside gage
11-1	Axial	30	552	(90.0)	237,000	Good test
615-9	Axial	30	552	(80.0)	203,000	Failed outside gage
614-3	Axial	30	552	(80.0)	239,000	Failed outside gage
615-1	Axial	30	552	(80.0)	229,000	Failed outside gage
615-2	Axial	30	552	(80.0)	247,000	Failed outside gage
623-83	Axial	30	552	(80.0)	357,000	Failed outside gage
623-97	Axial	30	552	(80.0)	457,000	Failed outside gage
615-10	Axial	30	552	(80.0)	509,000	Failed outside gage
615-5	Axial	30	552	(80.0)	627,000	Failed outside gage
616-25	Axial	30	552	(80.0)	649,000	Failed outside gage
619-36	Rot. Beam	167	552	(80.0)	1,940,000	Failed outside gage
114-44	Axial	10	552	(80.0)	2,283,000	Failed outside gage
619-34	Rot. Beam	167	552	(80.0)	3,230,000	Failed outside gage
619-31	Rot. Beam	167	552	(80.0)	3,360,000	Failed outside gage

Table 1.2 (Cont.)

115-16	Axial	20	552	(80.0)	6,836,300	Machine malfunction caused failure
619-37	Rot. Beam	167	552	(80.0)	72,400,000	Failed outside gage
619-49	Rot. Beam	167	545	(79.0)	328,000	Good test
619-39	Rot. Beam	167	525	(76.2)	344,750,000	Did not fail
623-92	Axial	30	517	(75.0)	2,041,000	Good test
616-3	Axial	10	552	(80.0)	9,300	Notched ($K_t \cong 2.8$)
616-5	Axial	10	552	(80.0)	15,860	Notched ($K_t \cong 2.8$)

[a] Specimen No. 1XX-XX = Heat 1 (2180-2-9251)
2XX-XX = Heat 2 (2180-2-9247)
6XX-XX = Heat 6 (2180-4-9478)
11-1 = Heat 11 (87995)

All specimens given the 1227 K (1712 °F) conventional heat treatment

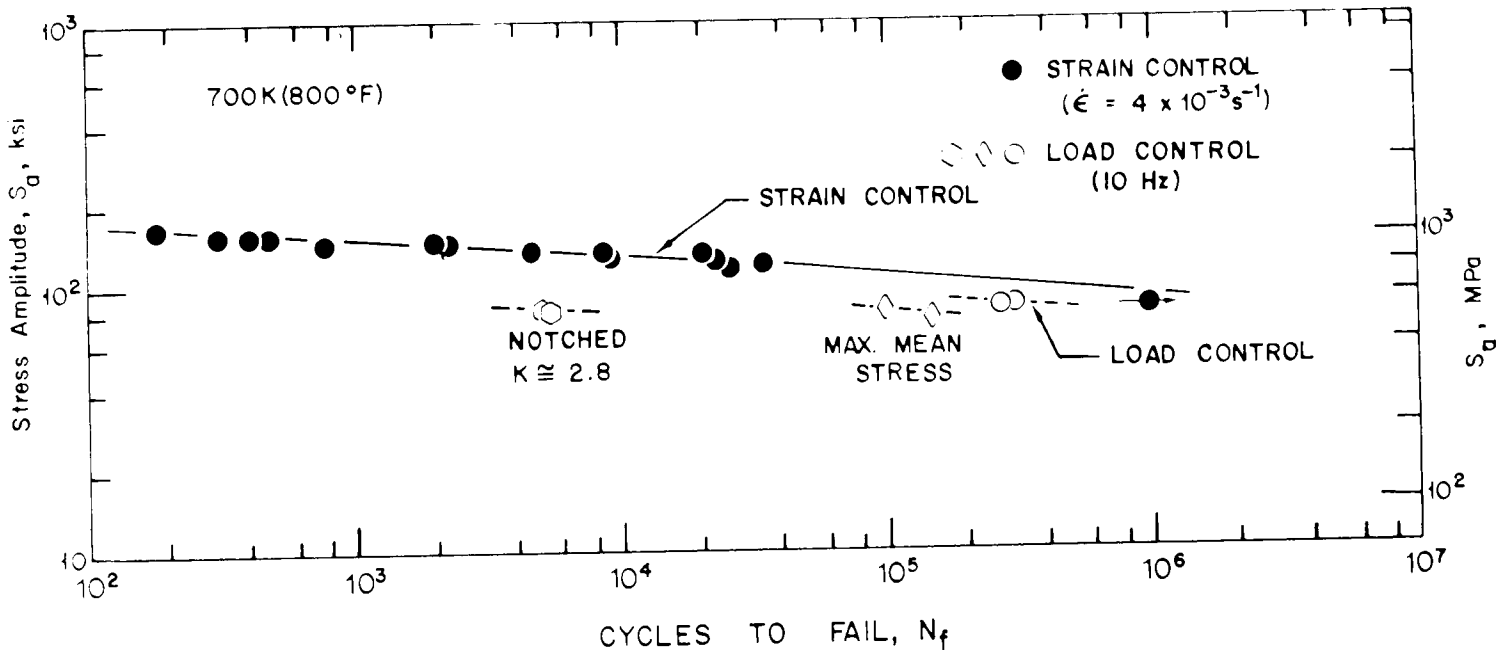

Figure 1.4 Fatigue Behavior of Alloy 718 at 700 K (800 °F) of Heat 6 (2180-4-9478) given the 1227 K (1750 °F) conventional heat treatment.

Table 1.3 Load Controlled Fatigue of Alloy 718 Tested[a] at 700 K (800 °F)

Specimen No.[b]	Stress Amplitude MPa	(ksi)	Mean Stress MPa	(ksi)	Cycles to Fail, N_f
623-93	586	(85.0)	0	(0)	312,900
623-81	552	(80.0)	0	(0)	278,660
623-89[c]	552	(80.0)	276	(40.0)	99,660
623-75	552	(80.0)	241	(35.0)	171,130
623-91	552	(80.0)	138	(20.0)	421,950
623-95[c]	517	(75.0)	310	(45.0)	153,260
623-96	517	(75.0)	241	(35.0)	279,790
623-82	517	(75.0)	172	(25.0)	352,970
623-102	517	(75.0)	103	(15.0)	772,530
616-16[d]	552	(80.0)	0	(0)	5,390
616-11[d]	552	(80.0)	0	(0)	5,530

[a] Tested in axial push-pull loading mode with 10 Hz sine waveform.

[b] 12.7 mm (.050 inch) plate Heat 6 (2180-4-9478) given the 1227 K (1750 °F) conventional heat treatment.

[c] Maximum mean stress tests (peak stress = proportional limit)

[d] Notched specimens ($K_t \cong 2.8$)

2. ARGONNE NATIONAL LABORATORY

R. W. Weeks

2.1 INTRODUCTION

Argonne National Laboratory (ANL) is conducting extensive programs to provide elevated-temperature, low-cycle fatigue data on Types 304 and 316 stainless steel and to study the effects of sodium environment on the elevated-temperature mechanical properties of these materials. Both programs are in support of LMFBR component design. In the present report, results on notch effects, heat-to-heat variations, and surface-damage and crack-initiation observations are described for the elevated-temperature low-cycle fatigue of Type 304 stainless steel. In addition, the effects of sodium preexposure on the creep-rupture life to Type 316 stainless steel and tensile behavior of Type 304 stainless steel are reported, and low-cycle fatigue data on both materials tested in flowing sodium after various pretest heat treatments are presented.

2.2 FRACTURE AND FATIGUE STUDIES ON STAINLESS STEELS -- D. R. Diercks, P. S. Maiya, S. Majumdar, and D. T. Raske

2.2.1 Effect of Notches on Elevated-temperature Low-cycle Fatigue Behavior of Type 304 Stainless Steel -- D. T. Raske and P. S. Maiya

2.2.1.1 Introduction

The present report describes the initial results of an investigation into the effects of geometric stress concentrations on the elevated-temperature low-cycle fatigue behavior of Type 304 stainless steel. The primary objective of this study is to develop a systematic means that will enable designers to predict the creep-fatigue behavior of structural components which contain discontinuities. Although several earlier studies have addressed this problem,[1-3] none have resulted in specific conclusions or recommendations to guide the design of these components, which operate in the creep-fatigue regime.

2.2.1.2 Scope

The present report summarizes the results of fatigue tests on notched specimens at 593°C (1100°F) in air. Notch sizes, applied loads, and loading frequencies were varied to provide an adequate data base for subsequent phases of the present investigation. Data for unnotched specimens generated at a strain rate of 4×10^{-3} s^{-1} over the fatigue life range of $\sim 10^2$-10^5 cycles are used for comparison.

2.2.1.3 Experimental Program

The chemical composition of the Type 304 stainless steel used (Heat 9T2976) is provided in Ref. 4. Prior to testing, the specimens were solution annealed and then aged at 593°C (1100°F) for 1000 h.

Axially loaded specimens with circumferential notches were employed (Fig. 2.1). The notch geometry was such that the theoretical elastic stress-concentration factors, K_t, were 1.5, 2.0, 3.0, and 4.0.[5] To minimize residual stresses, the notches were machined with successively lighter tool cuts. The final 0.025 mm of material at the notch root was removed by mechanical polishing. The resultant finish at the notch root was $\sim$0.025 μm (8 μm) surface roughness. A 50X optical comparator was used to determine the final notch dimensions.

Tests were conducted in a closed-loop hydraulic system that operates in the load-control mode. The specimens were subjected to fully reversed axial loadings using a triangular waveform. Specimen heating was accomplished by an induction coil that operated at 455 KHz. The coil was designed to provide a flat temperature profile over a distance of $\sim$6 mm on either side of the notch. With this coil arrangement, the temperature at the notch root was within 5°C of the controlled surface temperature.

Groups of specimens with constant values of K_t were tested in the life range of $\sim 10^2$-10^5 cycles. Cyclic frequencies that correspond to notch-root-material strain rates of 4×10^{-3} s^{-1} were employed. Neuber's rule[6] was used to estimate these frequencies prior to testing. This rule, or equation, is given as

$$K_t = (K_\sigma K_\varepsilon)^{1/2}, \qquad (1)$$

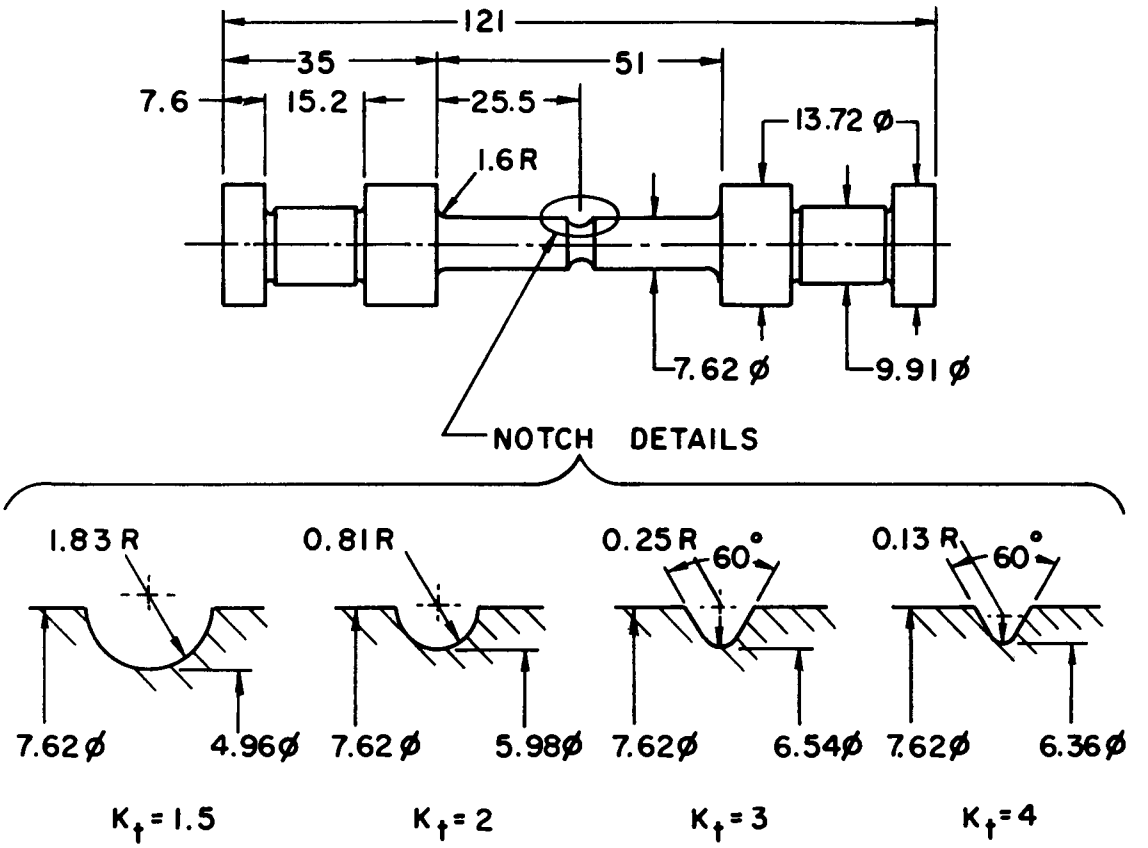

Fig. 2.1. Notched Specimens. Neg. No. MSD-63467.

where K_σ is the stress-concentration factor (the stress range at the notch root, $\Delta\sigma$, divided by the nominal stress range over the net area, Δs) and K_ε is the strain-concentration factor (the strain range at the notch root, $\Delta\varepsilon$, divided by the nominal strain range over the net area, Δe). Values of the notch root stress and strain were obtained by the usual assumption that both smooth and notched samples will have equal fatigue lives if the same stress and strain ranges are present at the location of crack initiation. This procedure is shown schematically in Fig. 2.2.

The cyclic stress-strain curve used in conjunction with Neuber's rule was obtained from continuous-cycling fatigue data on material from the same heat and with the same heat treatment as in the present study. A linear regression analysis was performed on the logarithms of the stable stress and plastic strain amplitudes from 31 fatigue tests at 593°C with a strain rate of 4×10^{-3} s^{-1}. The results were of the form

$$\Delta\sigma/2 = K(\Delta\varepsilon_p/2)^{n'}, \tag{2}$$

where K is the strength coefficient, $\Delta\varepsilon_p$ is the plastic strain range, and n' is the cyclic strain-hardening exponent. Values of K and n' were computed to be 2211.2 MPa (320.7 ksi) and 0.387, respectively. The cyclic stress-strain curve shown in Fig. 2.3 was then calculated using the relation[7]

$$\Delta\varepsilon/2 = \Delta\varepsilon_e/2 + \Delta\varepsilon_p/2 = \Delta\sigma/2E + (\Delta\sigma/2K)^{1/n'}, \tag{3}$$

where $\Delta\varepsilon_e$ is the elastic strain range and the elastic modulus, E, has a value of 149.62×10^6 MPa (21.7×10^3 ksi).

2.2.1.4 Results

The results of this phase of the investigation are listed in Table 2.1. Included are the controlled nominal stress ranges, cyclic frequencies and lives, and the nominal strain ranges determined from the cyclic stress-strain curve. The local strain and stress ranges were determined by the method shown in Fig. 2.2 using the unnotched

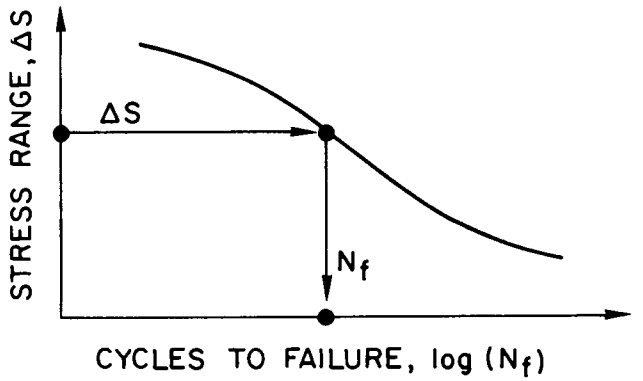

(a) NOTCHED SPECIMEN STRESS-LIFE CURVE

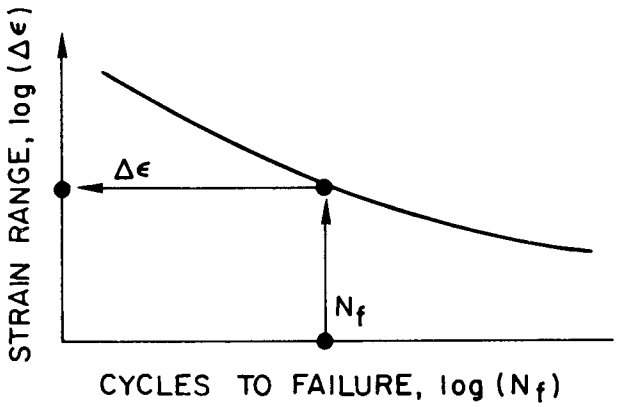

(b) UNNOTCHED SPECIMEN STRAIN-LIFE CURVE

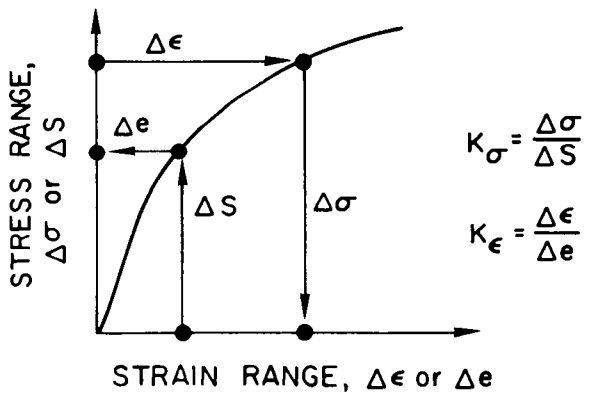

(c) UNNOTCHED SPECIMEN CYCLIC STRESS-STRAIN CURVE

Fig. 2.2. Curves Used to Determine K Values in Neuber's Equation. Neg. No. MSD-63466.

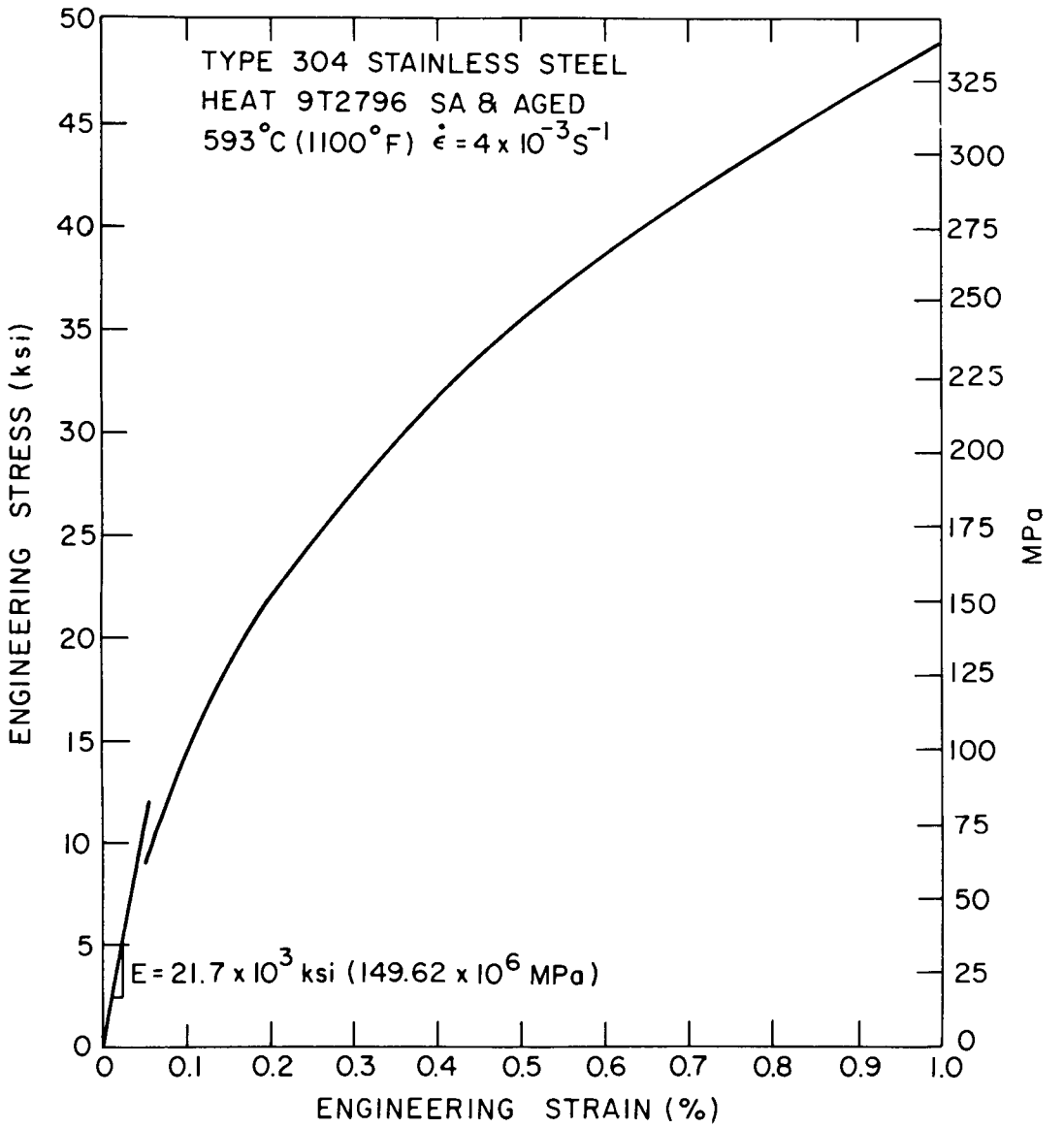

Fig. 2.3. Cyclic Stress-Strain Curve. Neg. No. MSD-63463.

Table 2.1. Results for Notched Specimens--Type 304 Stainless Steel, 593°C (1100°F)

Specimen Number	Nominal Stress Range (Δs), MPa (ksi)	Cycles to Failure (N_f)	Cyclic Frequency Hz	Nominal Strain Range (Δe), %	Local Strain Range ($\Delta \varepsilon$), %	Local Strain Rate ($\dot{\varepsilon}$), $\times 10^{-3}$ s^{-1}	Local Stress Range ($\Delta \sigma$), MPa (ksi)	Stress Concentration (K_σ)	Strain Concentration (K_ε)
				$K_t = 1.5$					
N-14	526.1 (76.3)	1 180	0.1	1.17	1.60	3.2	608.1 (88.2)	1.16	1.37
N-15	459.2 (66.6)	1 456	0.133	0.88	1.44	3.8	579.2 (84.0)	1.26	1.64
N-13	309.6 (44.9)	6 324	0.268	0.42	0.76	4.1	426.1 (61.8)	1.38	1.81
N-12	255.8 (37.1)	>406 000[a]	0.4	0.30	-	-	-	-	-
				$K_t = 2$					
N-11	553.6 (80.3)	228	0.08	1.30	4.00	6.4	~913 (132.4)	1.65	3.08
N-8	437.1 (63.4)	1 205	0.1	0.80	1.60	3.2	608.1 (88.2)	1.39	2.00
N-7	361.3 (52.4)	2 685	0.2	0.55	1.09	4.4	508.8 (73.8)	1.41	1.98
N-10	311.6 (45.2)	4 725	0.267	0.42	0.85	4.5	450.9 (65.4)	1.45	2.02
N-9	277.8 (40.3)	15 752	0.4	0.34	0.55	4.4	359.9 (52.2)	1.29	1.62
				$K_t = 3$					
N-5	446.1 (64.7)	397	0.1	0.83	2.90	5.8	~806 (117)	1.81	3.49
N-2	357.8 (51.9)	2 126	0.2	0.55	1.20	4.8	532.3 (77.2)	1.49	2.18
N-1	248.2 (36.0)	9 708	0.4	0.28	0.65	5.2	393.0 (57.0)	1.58	2.32
N-6	232.4 (33.7)	48 216	0.4	0.25	0.41	3.3	306.1 (44.4)	1.32	1.64
N-4	197.2 (28.6)	>553 000[a]	0.4	0.20	-	-	-	-	-
				$K_t = 4$					
N-18	406.1 (58.9)	744	0.1	0.69	2.04	4.1	675.7 (98.0)	1.66	2.96
N-17	345.4 (50.1)	1 635	0.1	0.51	1.37	2.7	566.7 (82.2)	1.64	2.68
N-19	271.6 (39.4)	3 789	0.1	0.32	0.93	1.9	471.6 (68.4)	1.74	2.91
N-20	208.2 (30.2)	21 271	0.4	0.21	0.50	4.0	342.0 (49.6)	1.64	2.38

[a]Specimen did not fail.

specimen strain-life curve shown in Fig. 2.4 and the cyclic stress-strain curve. Values of the average local strain rate were calculated from the cyclic frequency and local strain range.

The unnotched specimen curve shown in Fig. 2.4 is the result of the multivariable regression analysis described in a previous report.[8] The curves shown in this figure for the notched specimens are plotted in terms of the nominal strain range, Δe. Arrows on two data points in this figure are for specimens that did not fail. The dashed curves in Fig. 2.4 are based on the equation for elastic analysis when inelastic strains are present given in the ASME Code Case 1592-7.[9] These curves are derived from the unnotched specimen curve of Fig. 2.4 and the cyclic stress-strain curve using the Code Case equation. Ignoring the thermal strain term and assuming the theoretical elastic strain-concentration factor equals K_t, this equation is written as

$$\varepsilon_T = K_t e_e + K_t^2 e_p, \tag{4}$$

where ε_T (or $\Delta\varepsilon_T$ in terms of strain range) is the derived maximum strain, e_e is the net section elastic strain (exclusive of strain concentration), and e_p is the net section plastic strain (exclusive of strain concentration). As shown, the Code Case equation results in conservative fatigue-life estimates, especially for specimens with stress-concentration factors of 3.0 and 4.0 at long life.

Values for the stress- and strain-concentration factors from Table 2.1 are plotted as a function of cyclic life in Fig. 2.5. The trends of these curves, especially for the stress-concentration factor, are different than those observed from tests on notched specimens at room temperature.[10-12] At room temperature, the stress-concentration factor usually increases from a value of approximately one for short lives to a peak value for intermediate lives and then decreases as the life increases. The peak value has been shown to correspond with loadings that cause the onset of local yielding in the material at the notch root.[11] Reported changes in the strain-concentration factor with life are not as consistent as for the stress-concentration factor;

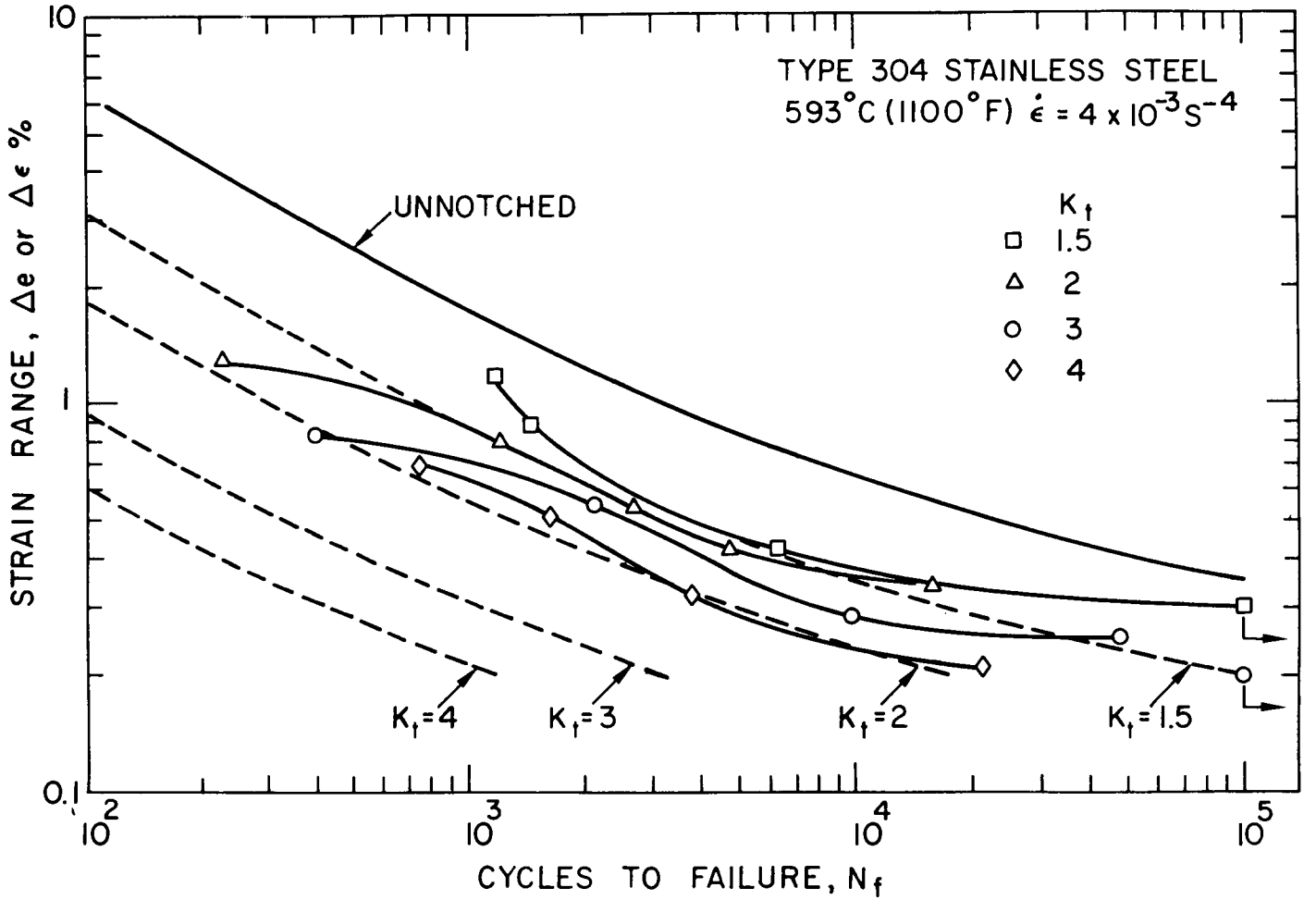

Fig. 2.4. Strain-life Curves for Type 304 Stainless Steel. Neg. No. MSD-63464.

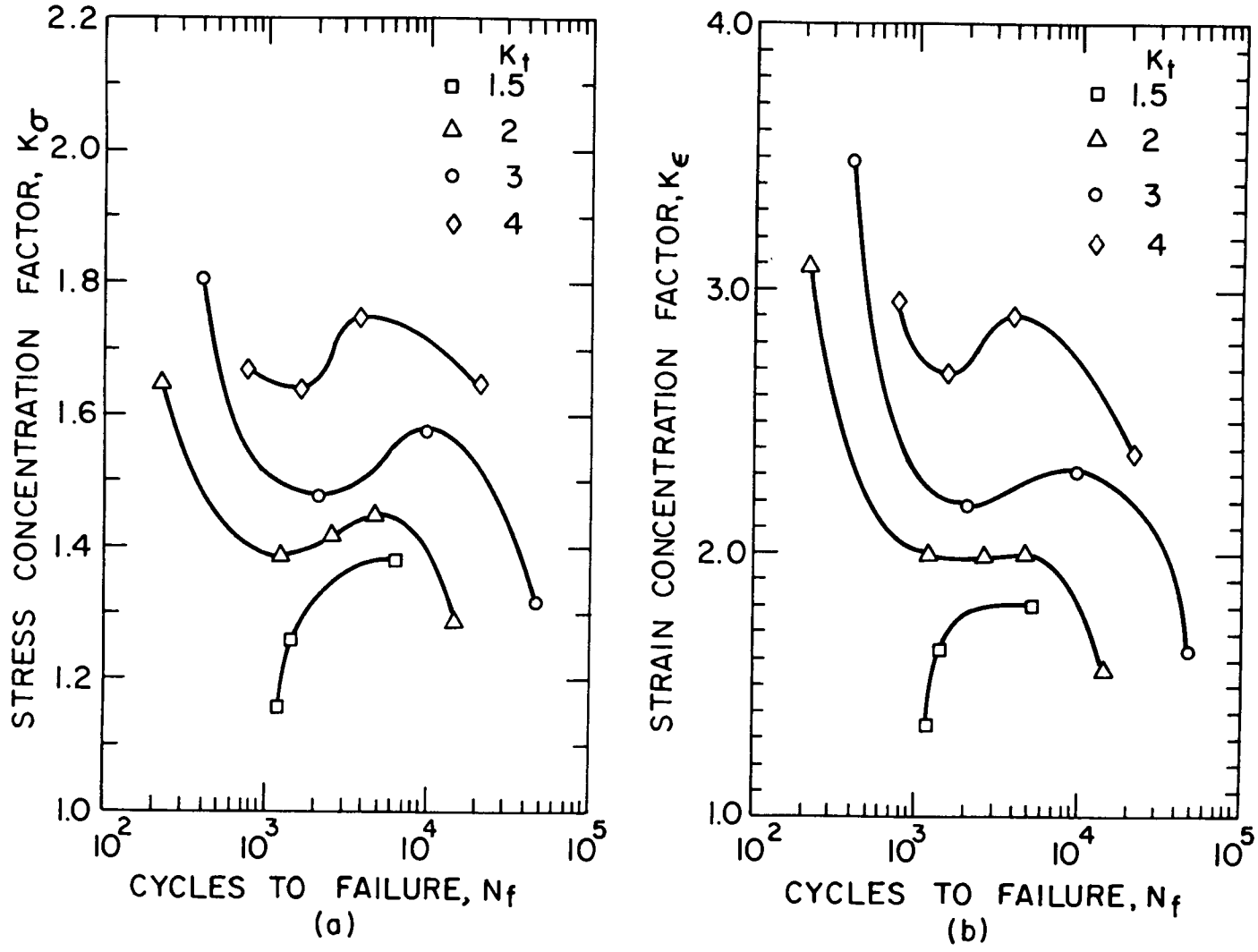

Fig. 2.5. Variation of Stress- and Strain-concentration Factors with Fatigue Life. Neg. No. MSD-63465.

thus, trend comparisons with the results of the present study are not possible.

2.2.1.5 Future Work

In addition to analysis of the data discussed in the present report, future work in this investigation will be directed toward studies of strain rate, temperature, and hold-time effects.

The effect of strain rate will be studies by testing specimens with stress-concentration factors of 2.0 and 4.0 under the same conditions of temperature and local strain range as described in the present report, but with a local strain rate of 4×10^{-5} s^{-1}. Temperature effects will be investigated with tests conducted at 482°C (900°F). Creep-fatigue tests with tensile hold times of 1, 10, and 60 min at 593°C (1100°F) are also planned.

2.2.2 Elevated-temperature Low-cycle Fatigue Behavior of Different Heats of Type 304 Stainless Steel -- P. S. Maiya and S. Majumdar

The majority of the elevated-temperature low-cycle fatigue tests have been performed on material obtained from a single heat of Type 304 stainless steel (9T2796), which was produced as a reference heat for all LMFBR test programs. One of the areas of concern is the effect of heat-to-heat variations on the creep-fatigue behavior of Type 304 stainless steel. The ANL data generated on the reference heat are used as a basis for comparison. The different heats of Type 304 stainless steel tested meet the required ASTM specifications insofar as chemical composition is concerned. However, variations in high-temperature creep-fatigue properties can occur depending upon the thermomechanical treatment, small chemical composition variations, and other microstructural variables such as grain size and distribution and morphology of second phases.

Three heats of material were selected and supplied by Oak Ridge National Laboratory and are designated 346544, 346845, and X22807.*

*For convenience, only the last three digits of the heat number will be used to identify the heat.

Hourglass-shape specimens (6.35-mm minimum diameter) were fabricated from a 25.4-mm-thick plate of Type 304 stainless steel. The longitudinal axis of most of the specimens was parallel to the direction of rolling, and a few specimens of each heat had the longitudinal axis perpendicular to the direction of rolling. The present report describes the low-cycle fatigue properties determined for hourglass specimens obtained from these heats of material.

2.2.2.1 Material Characterization and Experimental Procedure

The chemical compositions[13] of the various heats of material of interest in the present study are summarized in Table 2.2. All hourglass specimens were solution annealed in evacuated quartz tubes backfilled with argon and aged for 1000 h at 593°C. The grain size of the reference heat is larger (∿150 μm) than that of the other three heats of steel, which have approximately the same grain size (∿85 μm).[13] Two of the heats (807 and 544) contain a considerable amount stringlet phase.

The specimens obtained from the aged steel were electrolytically etched[14] in CH_3OH + 5% HCl for 2 min at a current density of ∿450 mA/cm^2 to delineate grain-boundary precipitates and phases, such as the stringlets, in the matrix. This procedure permitted retention of the carbides and other phases and examination by means of scanning-electron microscopy and energy-dispersive X-ray analysis. Typical scanning-electron micrographs of the second-phase distribution at grain boundaries and in the matrix of Heats 807, 544, and 845 are shown in Fig. 2.6. In these heats, precipitates (light areas) form a continuous phase along the grain boundaries. In addition, a fine distribution of precipitates in the matrix of two of the heats (845 and 807) is discernible. The characteristic X-ray spectra of some selected areas in Fig. 2.6 obtained using the energy-dispersive spectrometer are shown in Fig. 2.7. Qualitatively, the spectra reveal the following. The grain-boundary precipitates (regions B and E of Fig. 2.6) are rich in Cr when compared with those in the matrix (region A) and are believed to be carbides. The matrix of Heats 845 and 807 contains a dispersion of second-phase particles (e.g., regions F, G, and H) of different compositions. For

Table 2.2. Chemical Analysis (wt%) of Various Heats of Type 304 Stainless Steel

Elements	Heat Numbers			
	9T2796	346544	346845	X22807[a]
C	0.047	0.063	0.057	0.029
N	0.031	0.019	0.024	0.021
P	0.029	0.023	0.023	0.024
B	–	0.0002	0.0002	0.0005
O	0.011	0.0081	0.0092	0.01
H	0.0006	0.0006	0.0013	0.0012
S	0.012	0.006	0.006	0.023
Mn	1.22	0.99	0.92	1.26
Si	0.47	0.47	0.53	0.5
Mo	0.10	0.2	0.10	0.2
Ti	0.003	0.017	0.008	0.002
Cu	0.10	0.12	0.11	0.11
Co	0.05	0.05	0.07	0.03
Pb	0.01	0.01	0.01	0.01
Sn	0.02	0.01	0.01	0.01
Ta	<0.0005	0.0006	<0.0005	<0.0005
Nb	0.008	0.005	0.01	0.0015
V	0.037	0.025	0.05	0.012
W	0.022	0.026	0.007	0.02
Cr	18.5	18.4	18.4	18.8
Ni	9.58	9.12	9.28	9.67
Fe	Balance	Balance	Balance	Balance

[a]Type 304L stainless steel.

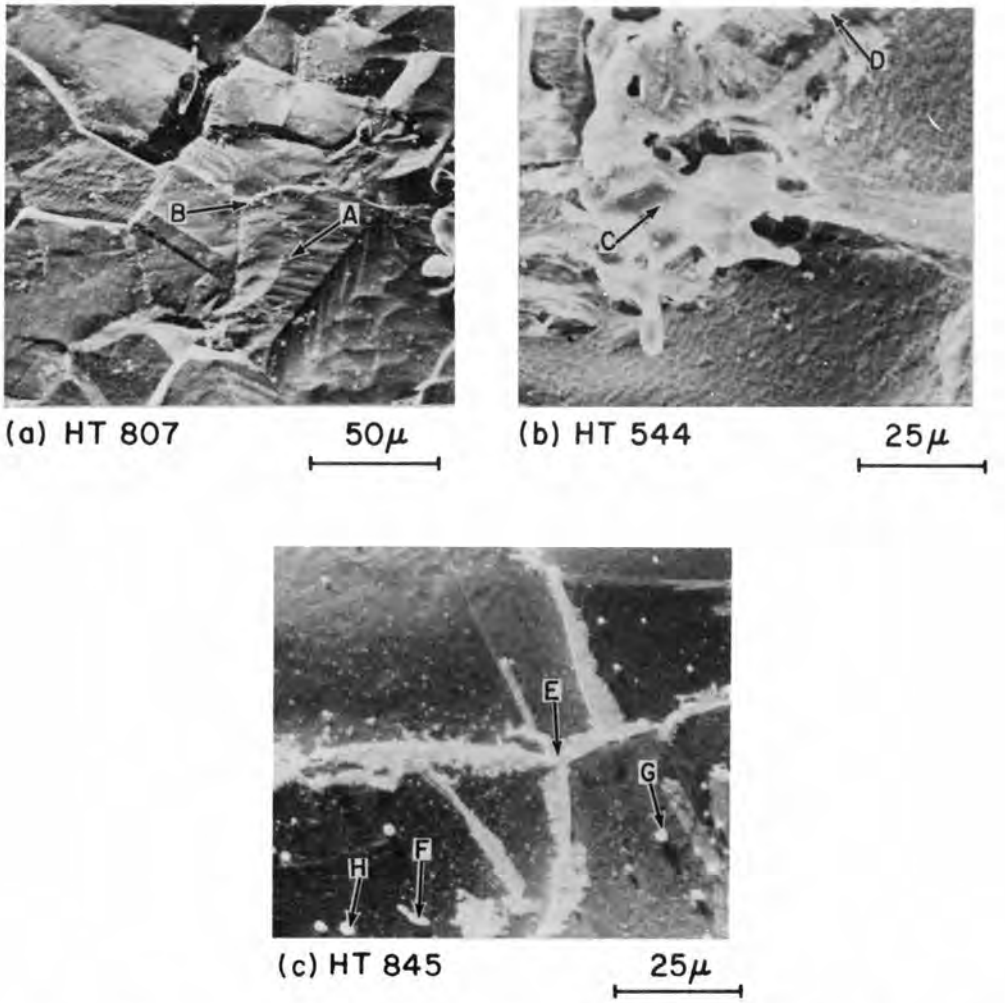

Fig. 2.6. Scanning-electron Micrographs of Three Heats of Type 304 Stainless Steel. Specimens have been solution annealed and aged. Areas (A-H) selected for X-ray analysis are indicated. Light areas show the presence of second phases. Neg. No. MSD-62859.

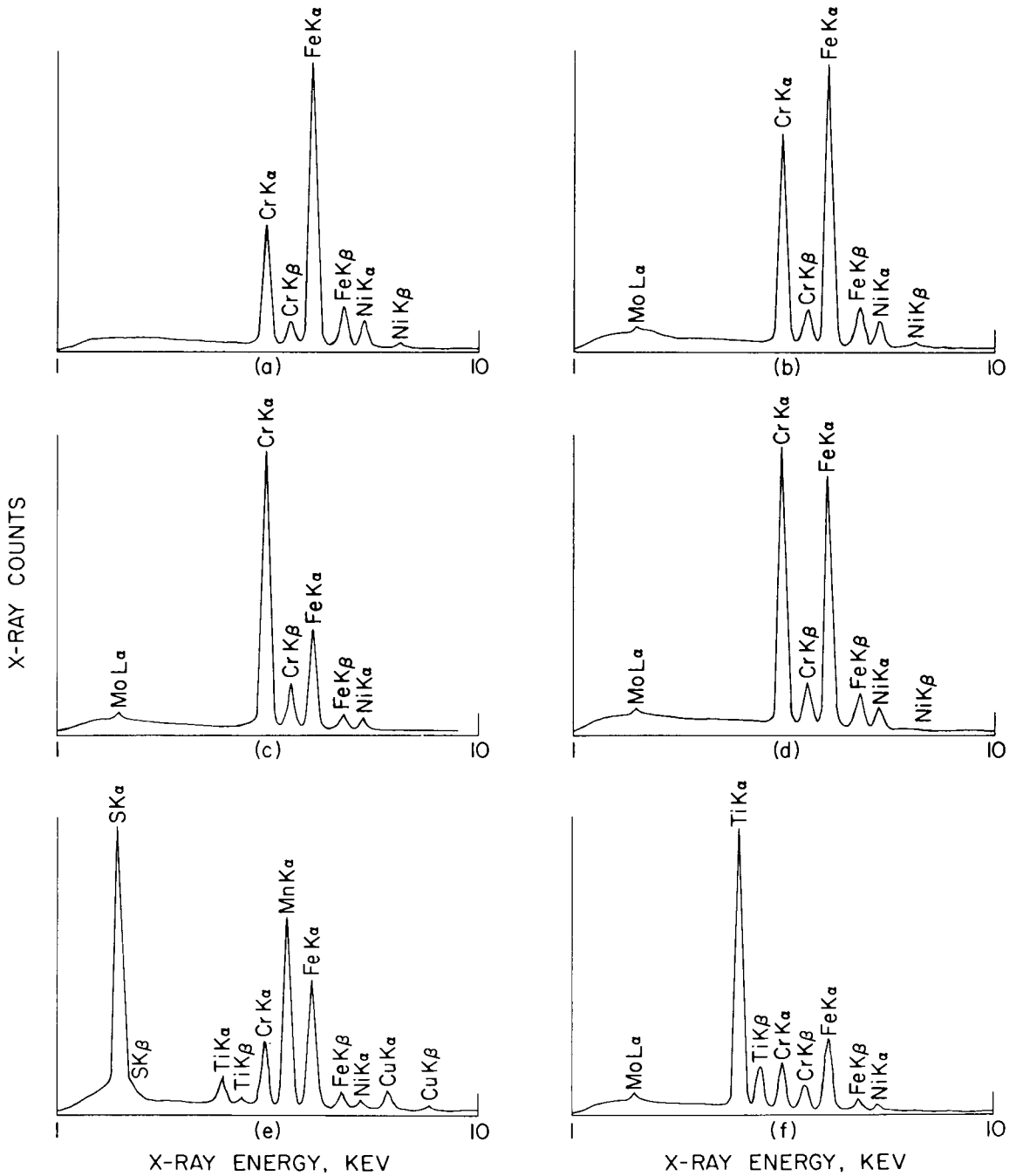

Fig. 2.7. Characteristic X-ray Spectra of Type 304 Stainless Steel Specimens. (a) Heat 807 (area A), (b) Heat 807 (area B), (c) Heat 544 (areas C and D), (d) Heat 845 (area E), (e) Heat 845 (area F), and (f) Heat 845 (areas G and H). ANL Neg. No. 306-75-240A.

example, region F is rich in Mn and regions G and H are Ti rich. The morphology of the Mn- and Ti-rich phases appears to be different. The stringlets observed in Heats 807 and 544 are of similar composition. An example of the stringlet phase is shown in Fig. 6b, where it is observed to be Cr rich (region C). The stringlets present in one of the heats (807 were additionally examined by Auger electron spectroscopy.[15] Figure 2.8a shows the absorbed-current image of an area of stringlets in Heat 807, and Fig. 2.8b-e shows the Auger images of Cr, Fe, Ni, and C. The results clearly demonstrate that Cr and C are associated and enriched in the dark region shown in Fig. 2.8a. The complete spectra obtained from a surface region of average composition and Cr-rich regions of the surface, which contain stringlets, are shown in Fig. 2.9a and b. From these results, it is clear that the stringlets are devoid of O and contain primarily Cr associated with small amounts of Fe, Ni, and C. Quantitative estimates were also obtained from these Cr-rich regions. The calculations show that the Cr-rich region is $\sim$73% Cr, 24% Fe, and 2.5% Ni. The composition of this phase lies in the α region of the Cr-Fe-Ni ternary diagram.[16] The purpose of this microstructural characterization is to establish the sensitivity or insensitivity of creep-fatigue behavior to the presence of second phases.

The fatigue tests were performed in air in servo-controlled, hydraulically actuated fatigue machines in the axial-strain-control mode at strain rates between 4×10^{-3} and 4×10^{-6} s^{-1} with zero hold time and at strain rates of 4×10^{-3} and 4×10^{-5} s^{-1} with tensile and/or compressive hold times imposed in each cycle. The total strain range in the tests varied from 0.75 to 2.0%, and the hold-times per cycle varied from 1 to 60 min. The test temperature was 593°C. The above cyclic-loading variables were chosen to determine whether significant variation in high-temperature low-cycle fatigue properties exists from one heat of steel to another and, if differences in properties prevail, attempt to correlate (at least qualitatively) the observed property variations and microstructural features described above.

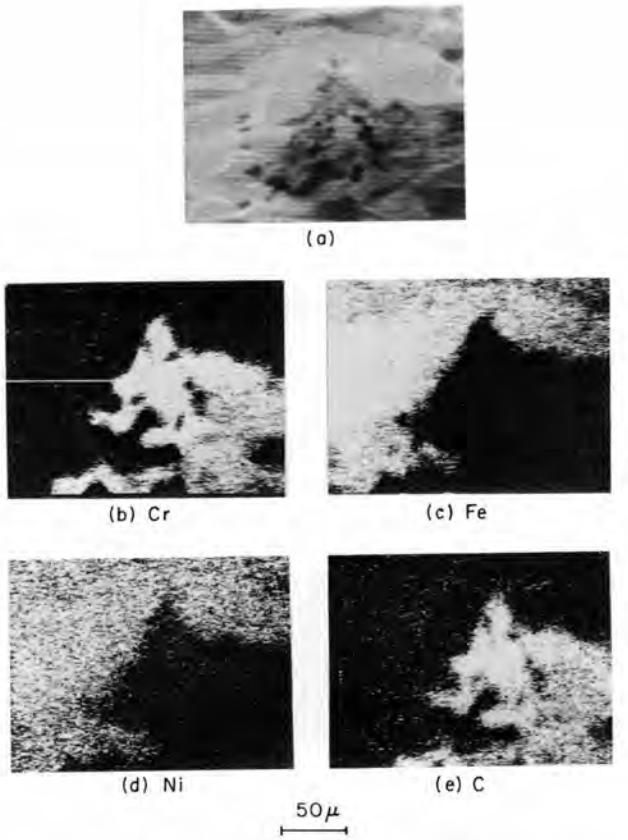

Fig. 2.8. Images of Type 304 Stainless Steel Specimen (Heat 807). (a) Absorbed-current image; (b-e) Auger images. Light areas in (b-e) indicate the presence of Cr, Fe, Ni, and C, respectively. Neg. No. MSD-62858.

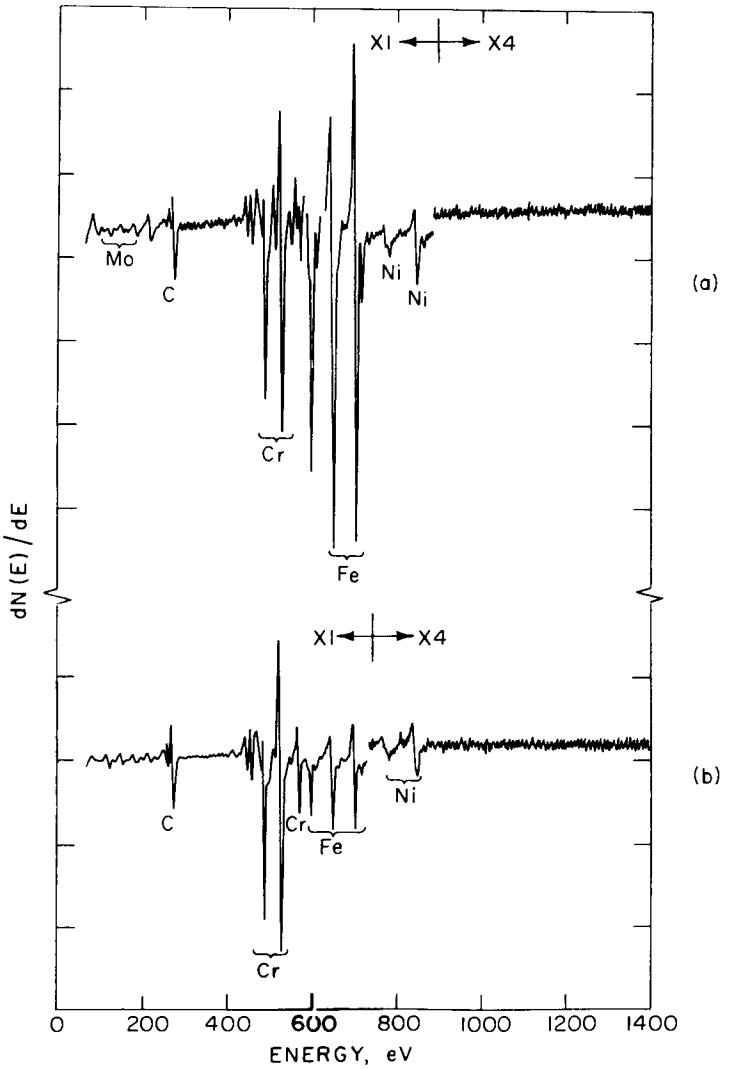

Fig. 2.9. Auger Electron Spectra (a) Showing Average Composition of the Surface and (b) Obtained from a Cr-rich Stringlet Region. Heat 807. Neg. No. MSD-62310.

2.2.2.2 Results and Discussion

The total ($\Delta\varepsilon_t$) and plastic ($\Delta\varepsilon_p$) strain ranges, saturation stress range ($\Delta\sigma_s$), obtained at approximately half the fatigue life, and number of cycles to failure (N_f) for the four heats of stainless steel (796, 544, 845, and 807) under continuous cycling at different strain rates ($\dot{\varepsilon}_t$) are listed in Table 2.3 for comparison. More extensive data are available[17] for the reference heat (796), but, for the purpose of comparing the fatigue behavior, only a few representative data for this heat have been tabulated. An examination of the data shows that the fatigue behavior of all four heats of steel is essentially the same, although one heat (845) exhibits a slight but consistent trend toward improved fatigue resistance. This trend becomes clearer when the hold-time data of the four heats are compared (Table 2.4).

The tensile hold-time data for Heat 845 and the limited data for Heats 544 and 807 show that these three heats are superior in creep-fatigue strength to the reference heat. The improvement is most marked under long tensile-hold-time conditions. For example, with tensile hold times of 10-60 min, Heat 845 shows an improvement in fatigue life of a factor of 2.5-3 when compared with the behavior of the reference heat. In all cases, tensile hold time produces more damage than compressive or symmetric hold times. The results also suggest that fatigue life is not sensitive to the presence of stringlets (irrespective of whether the stringlets lie in the direction of the longitudinal axis of the hourglass specimens or in the transverse direction). Reference should be made to a similar heat-to-heat variation study by Brinkman and Korth[18] of five other heats of Type 304 stainless steel. Under tensile hold-time conditions, four of these heats exhibited approximately similar fatigue behavior, and the fifth heat showed better fatigue strength.

In the present investigation, some insight into the reasons for the observed fatigue behavior in the different heats of stainless steel can be obtained by consideration of microstructural features of the fractured surfaces. The scanning-electron micrographs (Fig. 2.10) of the fracture surfaces of all four heats of Type 304 stainless steel

Table 2.3. Continuous-cycling Low-cycle Fatigue Behavior of Various Heats of Type 304 Stainless Steel at 593°C

Specimen Number	Heat Number	$\Delta\varepsilon_t$, %	$\Delta\varepsilon_p$, %	$\dot{\varepsilon}_t$ s^{-1}	$\Delta\sigma_s$, MPa	N_f
T-238	796	1.02	0.70	4×10^{-3}	486.4	3938
845-2	845	1.0	0.65	4×10^{-3}	517.0	4376
544-1	544	1.0	0.66	4×10^{-3}	511.6	3870
807-5	807	1.0	0.69	4×10^{-3}	465.6	4022
807-2A[a]	807	1.0	0.71	4×10^{-3}	447.6	4328
T-267	796	1.0	0.69	4×10^{-5}	460.5	1105
845-4	845	1.0	0.68	4×10^{-5}	489.8	1707
845-1A[a]	845	1.0	0.67	4×10^{-5}	509.5	1761
544-3	544	1.0	0.66	4×10^{-5}	509.5	1658
544-1A[a]	544	1.0	0.66	4×10^{-5}	519.8	1480
807-3	807	1.02	0.69	4×10^{-5}	504.5	1637
807-1A[a]	807	1.0	0.68	4×10^{-5}	501.4	1630
T-345	796	2.01	1.66	4×10^{-5}	546.0	275
845-8	845	2.03	1.65	4×10^{-5}	589.3	350
T-277	796	2.04	1.62	4×10^{-3}	643.7	700
845-10	834	1.99	1.56	4×10^{-3}	656.2	1010
T-197	796	2.04	1.62	4×10^{-4}	644.4	380
845-7	845	1.99	1.57	4×10^{-4}	635.6	681
T-348	796	1.0	0.67	4×10^{-4}	506.0	2595
845-6	845	1.01	0.67	4×10^{-4}	520.2	2935
T-218	796	2.0	1.67	4×10^{-6}	508.0	204
845-11	845	1.98	1.66	4×10^{-6}	490.5	251
845-9	845	0.59	0.34	4×10^{-3}	391.7	18605
845-13	845	2.01	1.60	1×10^{-4}	617.4	470
845-12	845	1.99	1.69	1×10^{-5}	456.5	262

[a]The longitudinal axis of the specimen if perpendicular to the direction of rolling. In all the other specimens, the longitudinal axis is parallel to the direction of rolling.

Table 2.4. Hold-time Low-cycle Fatigue Behavior of Various Heats of Type 304 Stainless Steel at 593°C

Specimen Number	Heat Number	$\Delta\varepsilon_t$, %	$\Delta\varepsilon_p$, %	$\dot{\varepsilon}_t$, s^{-1}	Hold Times,[a] min	$\Delta\sigma_{s_{max}}$,[b] MPa	N_f[c]
AA-10	796	1.0	0.70	4×10^{-3}	1T	482.9	1664
T-275	796	1.0	0.69	4×10^{-3}	1T	499.6	1560
T-285	796	1.0	0.69	4×10^{-3}	1T	514.4	1593
T-308	796	1.0	0.70	4×10^{-3}	1T	481.5	1528
845-3	845	1.0	0.69	4×10^{-3}	1T	499.2	3034
544-2	544	1.0	0.70	4×10^{-3}	1T	496.1	2712
807-2	807	0.99	0.72	4×10^{-3}	1T	436.6	2755
T-70	796	0.99	0.72	4×10^{-5}	60T	471.5	305
845-5	845	1.00	0.78	4×10^{-5}	60T	390.8	767
544-4	544	1.02	0.72	4×10^{-5}	60T	509.2	751
807-4	807	1.01	0.79	4×10^{-5}	60T	396.9	874
T-371	796	1.0	0.72	4×10^{-3}	10T	465.8	706
845-14	845	0.99	0.72	4×10^{-3}	10T	459.3	1826
AA-14	796	1.01	0.70	4×10^{-3}	1C	474.8	3344
845-24	845	1.03	0.72	4×10^{-3}	1C	495.0	2747
T-376	796	1.01	0.71	4×10^{-3}	2C	487.0	2993
845-17	845	0.99	0.69	4×10^{-3}	2C	488.6	2659
T-378	796	1.02	0.71	4×10^{-3}	4C	511.9	2453
845-18	834	1.0	0.71	4×10^{-3}	4C	484.2	2997
544-5	544	1.02	0.72	4×10^{-3}	4C	476.6	2366
807-11	807	1.02	0.75	4×10^{-3}	4C	432.6	2602
AA-17	796	1.02	0.73	4×10^{-3}	1S	487.2	2207
845-19	845	0.99	0.69	4×10^{-3}	1S	490.0	2880
T-377	796	1.03	0.74	4×10^{-3}	2S	490.0	2177
845-20	845	0.99	0.71	4×10^{-3}	2S	476.2	2348
845-25	845	1.03	0.72	4×10^{-3}	5T	496.3	2222
845-15	845	1.00	0.72	4×10^{-3}	10C	454.8	2624

[a]T = tension, C = compression, and S = symmetric.

[b]Maximum stress range.

[c]The satisfactory reproducibility of the low-cycle fatigue test results is shown by the first four tests performed on Heat 796 with 1-min tensile hold time.

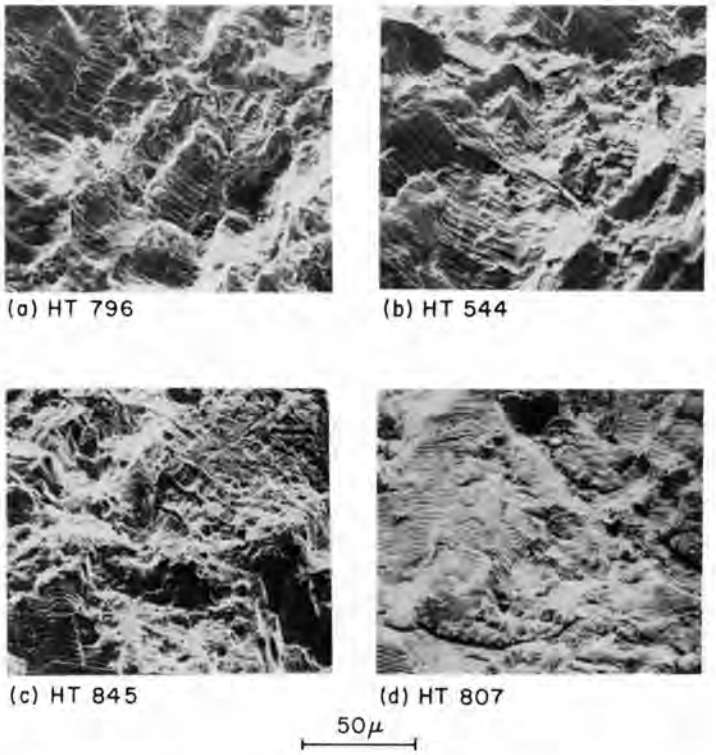

Fig. 2.10. Scanning-electron Micrographs of Fracture Surfaces of Type 304 Stainless Steel Specimens; Strain Rate = 4×10^{-5} s^{-1}, Zero Hold Time, $\Delta\varepsilon_t$ = 1%, and Temperature = 593°C. Neg. No. MSD-62328.

after fatigue testing at a total strain range of 1% and strain rate of 4×10^{-5} s^{-1} with zero hold time show fatigue striations associated with the transgranular fracture mode. No distinction in the appearance of the microstructures can be made. However, under the same cyclic-loading conditions and with a tensile hold time of 60 min imposed during each cycle, a series of scanning-electron micrographs of the fracture surfaces of the four heats shows some differences (Fig. 2.11). The reference heat exhibits well-defined intergranular fracture, but the other three heats, in addition, show some striated grains. The fracture surfaces of specimens tested at a strain rate of 4×10^{-3} s^{-1} and total strain range of 1% with a 1-min tensile hold time also show that these three heats (807, 544, and 845) have more striated regions than the reference heat. This indicates that the three heats of steel are more

resistant to intergranular fracture than the reference heat, which is consistent with the observed fatigue results. The above discussion is additionally substantiated by microstructural observations made on the pretest specimens.

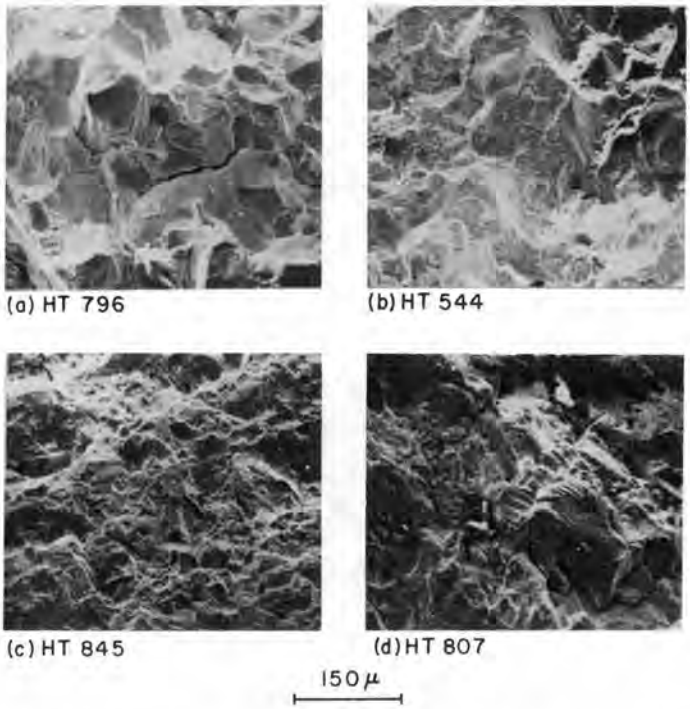

Fig. 2.11. Scanning-electron Micrographs of Fracture Surfaces of Type 304 Stainless Steel; Strain Rate = 4×10^{-5} s^{-1}, 60-min Tensile Hold Time, $\Delta\varepsilon_t$ = 1%, and Temperature = 593°C. Neg. No. MSD-62329.

As described earlier, the reference heat has a larger grain size than that of the other heats. It is known that, in high-temperature creep and fatigue studies,[19] the tendency toward intergranular fracture increases with an increase in grain size. This may be associated with stress concentrations that occur at the grain-boundary triple junctions as a result of grain-boundary sliding.[20] In specimens with large grain size, the stress concentrations can be substantial and the relaxation of stress concentration is less easily achieved. Consequently, a small grain size results in improved creep-fatigue resistance. Thus,

the observed differences in low-cycle hold-time fatigue properties can be partially attributed to the variation in grain size, and supporting evidence comes from two preliminary low-cycle fatigue tests performed on one heat of steel (544) with an enlarged grain size. Two fatigue specimens with an initial grain size of 84 μm were solution annealed at 1092°C for 35 and 168 h, respectively, followed by aging at 593°C for 1000 h. The resultant average grain (intercept) diameters are 107 and 295 μm, respectively.* These specimens, when tested at a strain rate of 4×10^{-5} s^{-1}, total strain range of 1%, and tensile hold time of 60 min, have fatigue lives of 550 and 378 cycles, the specimen with the larger grain size having the shorter life. Therefore, by changing the initial grain size from 84 to 295 μm, the fatigue life for the above cyclic-loading conditions decreases from 751 (Table 2.4) to 378 cycles.

The observed difference in creep-fatigue behavior may also originate from variation in grain-boundary precipitate morphology observed in different heats of steel. An examination of the scanning-electron micrographs of the specimens in the pretest condition shows that the precipitate distribution at the grain boundaries is less continuous in the reference heat than in the other three heats (Figs. 2.6 and 2.12). It has been observed[21] in austenitic steel that sliding is less promoted at grain boundaries that contain $M_{23}C_6$ carbides spaced at certain intervals than at grain boundaries in carbide-free alloys. In addition, it has been documented[22] that intergranular crack initiation occurs at the interface between grain-boundary precipitates and adjacent grains. Furthermore, it appears[20] that reducing the particle spacing at the grain boundaries (in the limiting case, particles form a continuous phase) results in an increased resistance to grain-boundary sliding. These considerations imply that the reference heat of steel should be weaker under tensile hold-time conditions because grain-boundary sliding can occur more easily in this heat when compared with

---

*It should be noted that in these experiments a change in grain size may also be associated with a change in grain-boundary composition and structure.

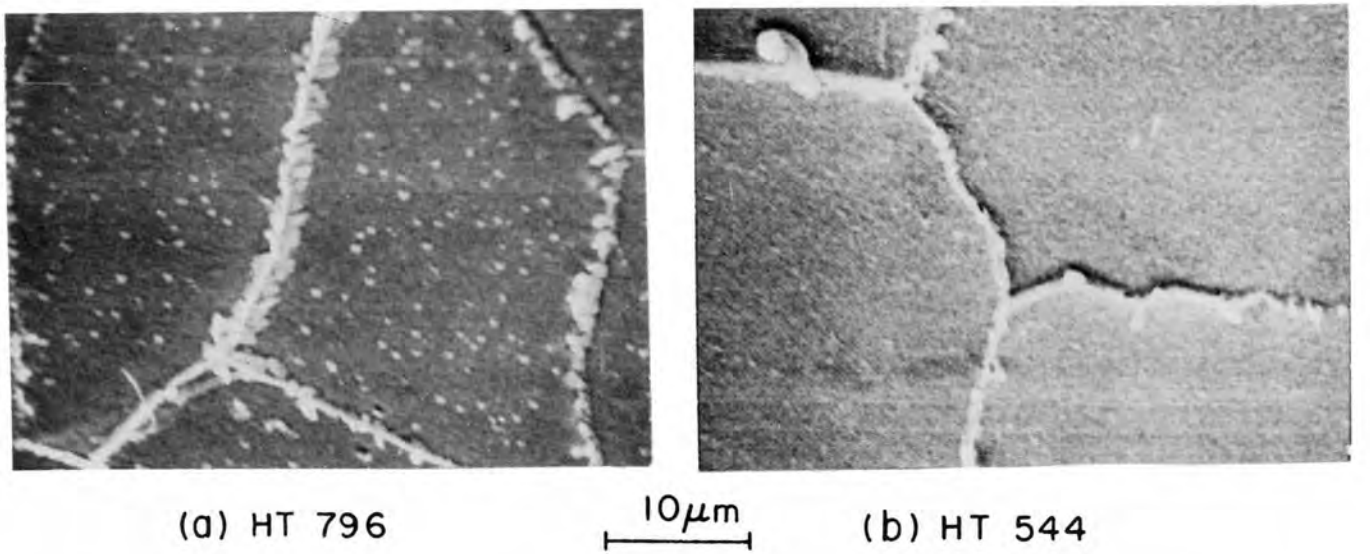

Fig. 2.12. Scanning-electron Micrographs of Type 304 Stainless Steel. Solution annealed and aged. Grain boundaries contain Cr-rich carbides (light areas). Neg. No. MSD-62320.

the other three heats. Thus, the observed differences in low-cycle hold-time fatigue behavior of various heats of steel can be accounted for in part by the variation in grain-boundary precipitate morphology.

The damage-rate parameters used in creep-fatigue life prediction for the reference heat[8,23,24] are affected by microstructural variables such as grain size and precipitate distribution and morphology at the grain boundaries. Because of the smaller grain size and continuous nature of precipitate morphology at the grain boundaries, the three heats of steel (807, 544, and 845) should have a higher value for the creep-fatigue interaction parameter k than the reference heat. Also, the transition in the plots of the damage-rate parameters versus plastic strain rate for the three heats of steel should occur at a much lower plastic strain rate than in the reference heat. Using the damage-rate parameters determined for the reference heat and accounting for the effects of microstructure on these damage-rate parameters (which are also consistent with the available creep-rupture and tensile data[4,25]), it has become possible to predict satisfactorily the fatigue life of the three heats of steel.

2.2.3 Observations of Crack Initiation in Low-cycle Fatigue Specimens of Type 304 Stainless Steel -- P. S. Maiya

The procedure for obtaining crack-initiation life data in strain-controlled, fully reversed low-cycle fatigue tests is based on the plots of ln a versus N (a is the crack length after N strain cycles).[26] The information on crack growth is obtained, assuming each striation is caused by one cycle, from fatigue-striation spacing measurements made on the fracture surfaces of fatigue specimens. Using this procedure, it is observed[13,27] in Type 304 stainless steel at 593°C that, for a total strain range $\Delta\varepsilon_t$ of 1.0%, the life to crack initiation is ∿60% or greater of total life and, for a total strain range of 0.5%, the major portion of life (90% or greater) consists of crack initiation. The crack-initiation life is defined as the period in the fatigue sequence required to generate a crack of specified length, usually of the order of one or two grain diameters. Thus, the crack-initiation life includes both the number of cycles to crack nucleation (which occurs early in

life under low-cycle fatigue conditions) and the cycles to propagate a crack of specified length. The purpose of the present study is to describe some observations of surface damage in specimens after the fatigue tests were interrupted following a significant portion of total life N_f and to determine whether the observations are consistent at least qualitatively with the crack-initiation life N_0 determined in earlier studies.[13,27]

The total fatigue life of smooth hourglass-shape specimens of Type 304 stainless steel at a strain rate $\dot{\varepsilon}_t$ of 4×10^{-3} s^{-1}, strain ranges between 0.5 and 2.0%, and a temperature of 593°C is given by[27]

$$N_f = 0.012(\Delta\varepsilon_p)^{-2.47} + 3.91(\Delta\varepsilon_p)^{-1.1}, \tag{5}$$

where $\Delta\varepsilon_p$ is the plastic strain range, the first term on the right-hand side of Eq. (5) is the crack-initiation life N_0, and the second term is the crack-propagation life N_p. For a chosen plastic strain range in the experiments, it is thus possible to interrupt the test at a life approximately close to N_0 and examine the surface damage around the circumference of the hourglass-shape specimens by means of plastic-replica techniques. The technique used in the present study is the same as that described by Henry.[28] After interrupting the test, the specimen is cooled, removed from the fatigue machine, and mounted in a specimen jig that enables a known rotation of the specimen about the longitudinal axis to permit replication. Thus, the assembly facilitates replication of approximately the entire surface region (at the minimum cross section) of the hourglass-shape specimen. The plastic replicas are shadowed with gold (∿100 Å in thickness) and examined by optical microscopy. The experimental variables for the fatigue tests are listed in Table 2.5.

Figures 2.13 and 2.14 show optical micrographs of shadowed plastic replicas of Type 304 stainless steel taken at intervals of 45° all around the circumference of the minimum cross section of the hourglass-shape specimens. These micrographs reveal a number of microcracks and slip-band damage that occur after ∿80% of the total life. The dark areas indicate the presence of oxide. Figures 2.13a and b reveal more

Table 2.5. Interrupted Low-cycle Fatigue Tests for Type 304 Stainless Steel at 593°C in Air; Strain Rate = $4.0 \times 10^{-3}\ s^{-1}$

Specimen Number	Total Strain Range, %	Plastic Strain Range, %	N_0 [a]	N_p [a]	Percent of Life at Interruption of Test
T382	0.5	0.285	24 158	2510	∿85
T383	0.5	0.283	24 691	2534	∿95
T385	1.0	0.691	2 698	944	∿70

[a]Calculated from Eq. (5).

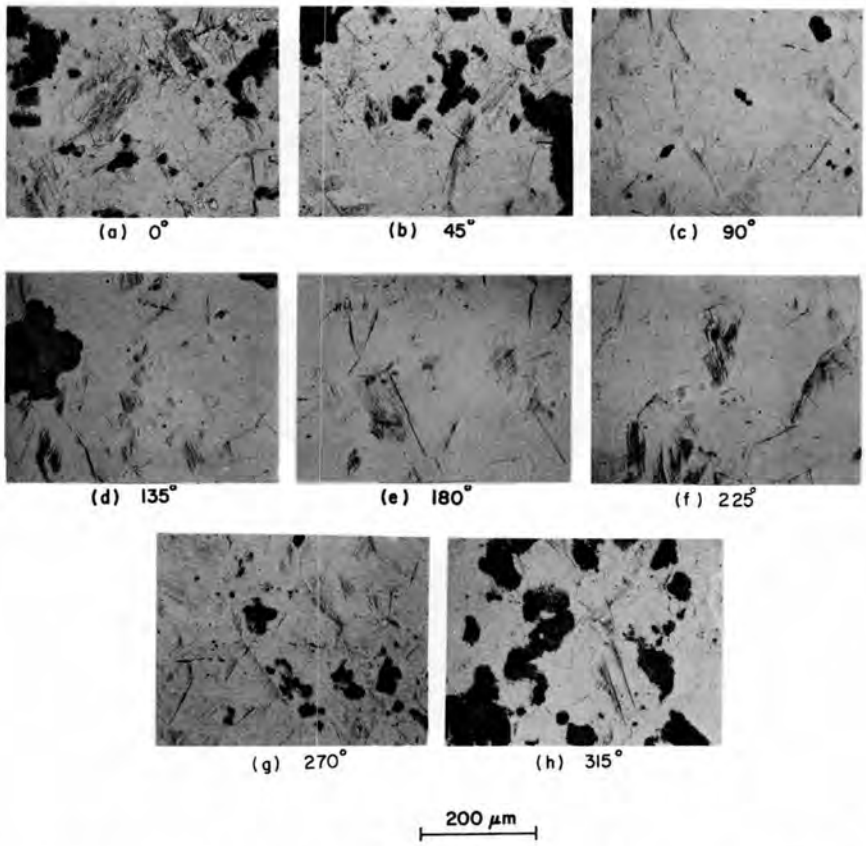

Fig. 2.13. Optical Micrographs of Shadowed Plastic Replicas of a Type 304 Stainless Steel Fatigue Specimen Interrupted at N = 23352 cycles. $\Delta\varepsilon_t = 0.5\%$, $\dot{\varepsilon}_t = 4 \times 10^{-3}\ s^{-1}$, and temperature = 593°C. ANL Neg. No. 306-75-238.

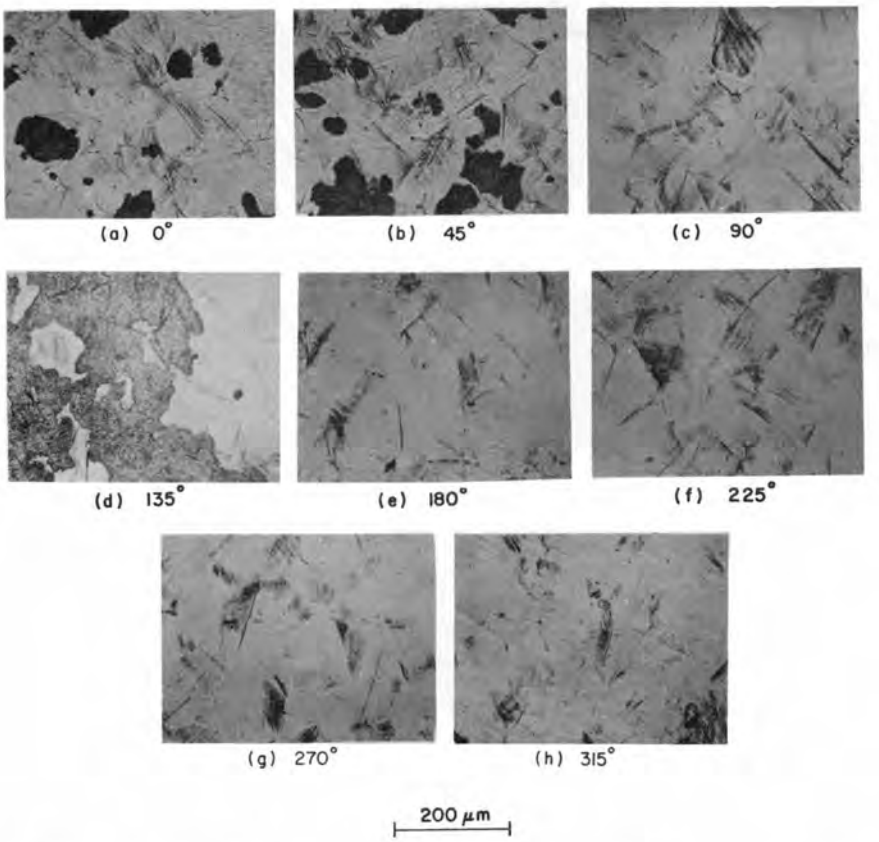

Fig. 2.14. Optical Micrographs of Shadowed Plastic Replicas of a Type 304 Stainless Steel Fatigue Specimen Interrupted at N = 26500 cycles. $\Delta\varepsilon_t = 0.5\%$, $\dot{\varepsilon}_t = 4 \times 10^{-3}\ s^{-1}$, and temperature = 593°C. ANL Neg. No. 306-75-237.

surface damage than in the other regions of this specimen and suggest the possibility that the microcracks in these regions join to form a major crack, which subsequently propagates to failure. Interferometric examination of the replicas indicates that the cracks are ≤ 4 μm in depth. The surface damage of the specimen tested at a total strain range of 1% and interrupted after ∿70% of the total life is shown in Fig. 2.15. Obviously, no large cracks of the type shown in Fig. 2.15 are visible in Figs. 2.13 and 2.14. A cursory examination of Fig. 2.15 indicates that in regions d and f well-defined cracks exist.

In the absence of a clear-cut definition of what constitutes a crack, the observations made on the surface damage should be regarded as qualitative. They are not inconsistent with the crack-initiation life determined from fatigue-striation spacing measurements in earlier studies.[13,27] Finally, the replica technique has been shown to be useful for investigating the progression of damage associated with continued cycling in elevated-temperature low-cycle fatigue studies and providing a better physical basis for understanding fatigue damage.

2.3 SODIUM EFFECTS ON LMFBR MATERIALS -- T. F. Kassner

2.3.1 Effect of Sodium Environment on the Uniaxial Creep-rupture Properties of Type 316 Stainless Steel -- K. Natesan and O. K. Chopra

The effect of carburization on the creep-rupture properties of Type 316 stainless steel, after exposure to well-characterized sodium at temperatures between 550 and 700°C, is being determined. The mechanical-property changes in the carburized material will be correlated with the sodium purity, which will be helpful in establishing better design and performance criteria for components that operate in a sodium environment.

Uniaxial creep-rupture data have been obtained on Type 316 stainless steel in the solution-annealed condition and after exposure to a flowing sodium environment at temperatures of 700, 650, and 600°C. The specimens were exposed to sodium for times between 120 and 5012 h

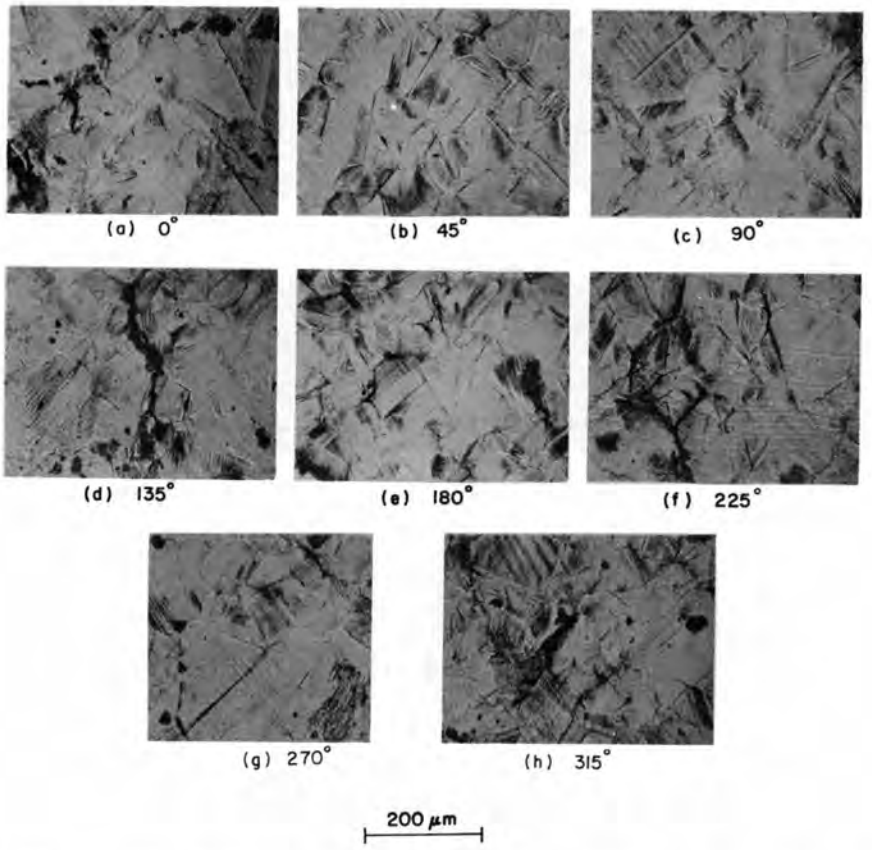

Fig. 2.15. Optical Micrographs of Shadowed Plastic Replicas of a Type 304 Stainless Steel Fatigue Specimen Interrupted at N = 2700 cycles. $\Delta\varepsilon_t$ = 1.0%, $\dot{\varepsilon}_t = 4 \times 10^{-3}\ s^{-1}$, and temperature = 593°C. ANL Neg. No. 306-75-239.

to produce carbon penetration depths of ∿0.01, 0.02, and 0.038 cm. The specimens were subsequently used in uniaxial creep-rupture tests in a static argon environment to obtain creep curves and creep-rupture times. The creep strain in the specimens was measured by a linear-variable-differential transducer, in which displacements of 5×10^{-4}cm could be accurately determined. From each creep curve, strain values ε_1 and ε_2 and times t_1 and t_2, which correspond to the beginning and end of the secondary creep stage, respectively, were determined. At rupture, elongation ε_r and rupture time t_r were determined. The minimum creep rate $\dot{\varepsilon}_m$, that is, the slope of the linear portion of the ε-t curve between t_1 and t_2, was also obtained from the creep-rupture curve. These quantities are listed in Tables 2.6-2.8 for specimens tested in the solution-annealed condition and after exposure to a flowing sodium environment. The average carbon concentrations in the mechanical test specimens are being determined from combustion analysis of the specimens subsequent to creep testing.

Figure 2.16 shows the variation of minimum creep rate with applied stress at 700, 650, and 600°C for specimens tested in the solution-annealed condition and after exposure to a flowing sodium environment for different times. In general, the data show that, for the range of carburization attained in the present investigation, the exposure of the steel to the sodium environment results in a slight decrease in minimum creep rate when compared with material in the solution-annealed condition.

Relationships are being developed between rupture life and minimum creep rate of time for onset of tertiary creep. These correlations, if developed, can be used to evaluate the desired creep quantities from standard stress-rupture tests. Figure 2.17 shows a plot of ln t_r versus ln $\dot{\varepsilon}_m$ for specimens tested in the solution-annealed condition and after exposure to flowing sodium at 700, 650, and 600°C. In general, the results indicate no significant difference in the creep behavior for annealed and sodium-exposed materials. Figure 2.18 shows a plot of ln t_2 versus ln t_r for specimens tested in the solution-annealed condition and after exposure to flowing

Table 2.6. Uniaxial Creep Behavior of Type 316 Stainless Steel in the Solution-annealed Condition

Test Temperature, °C	Applied Stress, MPa	t_1, h	ε_1, %	t_2, h	ε_2, %	t_r, h	ε_r, %	$\dot{\varepsilon}_m$, %/h
700	55.8	20.8	2.5	113.3	9.5	361.4	75.5	0.076
	62.5	12	3.3	140	8.7	423	66.9	0.042
	69.4	5.8	2.4	82.5	14.4	188.2	64.8	0.16
	83.3	5.3	2.8	38.5	13.7	115.8	69.6	0.33
	104.2	0.3	0.5	5.3	7.0	20.8	71.3	1.30
	111.1	0.8	2.4	13.0	16.7	27.3	55.4	1.17
	125	1.2	4.0	5.4	14.6	14.1	64.9	2.52
	138.9	0.05	1.5	0.7	11.4	1.9	40.7	15.2
650	111.1	25.5	2.5	178.5	16	355.5	59.3	0.09
	173.6	3.8	8.9	12.3	20.8	23	58.2	1.40
	208.3	3.6	10.3	7.8	17.6	17.5	57.4	1.74
	243	0.27	7.8	1.23	20	2.4	64	20.3
600	138.9	64	3.2	348	10	850	55.2	0.024
	208.3	7.9	7.4	33.2	22.9	51.9	47.6	0.61
	243	2.4	4.7	22	27.3	32.2	50.7	1.15
	277.7	0.66	3.4	6.04	21.3	9.3	42.5	3.31

Table 2.7. Uniaxial Creep Behavior of Type 316 Stainless Steel upon Exposure to a Sodium Environment at 700°C

Sodium-exposure Temperature, °C	Time, h	Carbon Penetration Depth, μm	Test Temperature, °C	Applied Stress, MPa	t_1, h	ε_1, %	t_2, h	ε_2, %	t_r, h	ε_r, %	$\dot{\varepsilon}_m$, %/h
700	120	∿100	700	59	18.4	1.3	644.7	18.3	937.5	71.9	0.027
				69.4	0.1	0.3	298	14	857.4	52.8	0.047
				83.3	0.1	0.3	137	14	297.8	61.7	0.10
				104.2	0.1	0.3	29.3	7	110.6	50	0.23
				138.9	0.5	1.7	6.3	14	15.4	65.7	2.12
			650	138.9	3.6	2.8	37.1	16.8	80.4	62.8	0.42
			600	138.9	25	2	417.5	15.3	838.2	62.3	0.034
700	504	∿200	700	83.3	1.0	0.2	99	10.4	248.3	58.6	0.10
				104.2	0.9	2.2	9.2	12.7	23.4	62.2	1.27
			650	138.9	0.1	0.3	50.3	16.5	104.4	58.5	0.32
			600	138.9	225	4.0	1217.5	11.4	1865.0	55.1	0.0075
700	1512	∿375	700	62.5	10	2	209	18.7	405.1	62.3	0.084
				104.2	0.1	0.2	14.2	12	36.2	56.7	0.84
				138.9	0.12	2.5	1.6	16.3	3.4	54.8	9.32
			650	138.9	2.3	3.7	15.1	15.2	30.7	45.4	0.90
			600	138.9	36	3.5	378	17.5	721.7	62.7	0.041

Table 2.8. Uniaxial Creep Behavior of Type 316 Stainless Steel upon Exposure to a Sodium Environment at 650 and 600°C

Sodium-exposure Temperature, °C	Time, h	Carbon Penetration Depth, μm	Test Temperature, °C	Applied Stress, MPa	t_1, h	ε_1, %	t_2, h	ε_2, %	t_r, h	ε_r, %	$\dot{\varepsilon}_m$, %/h
650	312	100	650	104.1	16	1	180	7.4	518.6	58.7	0.039
				138.9	2.3	2.3	38.3	19.3	69.1	53.5	0.47
				166.6	1.4	1.2	42	24.7	62.5	51.5	0.58
				173.6	2.3	4	19.8	20	37.6	53.5	0.91
				187.5	0.65	2.3	14.2	18.7	23.6	49.2	1.21
				208.3	0.3	1.3	7.1	24	9.8	50.8	3.34
			700	138.9	0.23	3.7	6.1	19.8	10.7	60.6	2.74
			600	138.9	43.3	2.4	583.3	14.2	1304.5	52	0.022
650	1512	200	650	104.1	8.3	1.3	186.7	15.8	363.3	60.5	0.081
				138.9	2.9	2.7	31.8	16.3	62.6	63.3	0.47
				173.6	2.1	4	18.8	19.0	34.7	56.3	0.90
				208.3	0.8	4.7	3.1	14.3	6.5	48.7	4.2
			700	138.9	0.4	2.1	4.5	17.4	8.8	58.4	3.73
			600	138.9	115	4	530	11.6	1392.6	50.1	0.014
650	5012	375	650	93.7	3	0.3	309	8.5	1007.5	57.1	0.027
				138.9	2.5	1.7	60	15.7	122.5	59	0.24
				173.6	0.89	5.0	5.1	16.2	10.2	52.2	2.66
			700	138.9	0.3	2.3	2.5	14.4	5.8	54	5.5
			600	138.9	33.3	1.8	516.7	12.4	122.5	59	0.24
600	1512	100	600	138.9	100	4.7	655	19.5	1192	57.9	0.027
				173.6	-	-	260	15.8	457	37.5	0.06
				208.3	56.4	10	234.3	27.9	310.4	42.6	0.10
			650	138.9	17	1.4	352	18.6	602	48.4	0.051

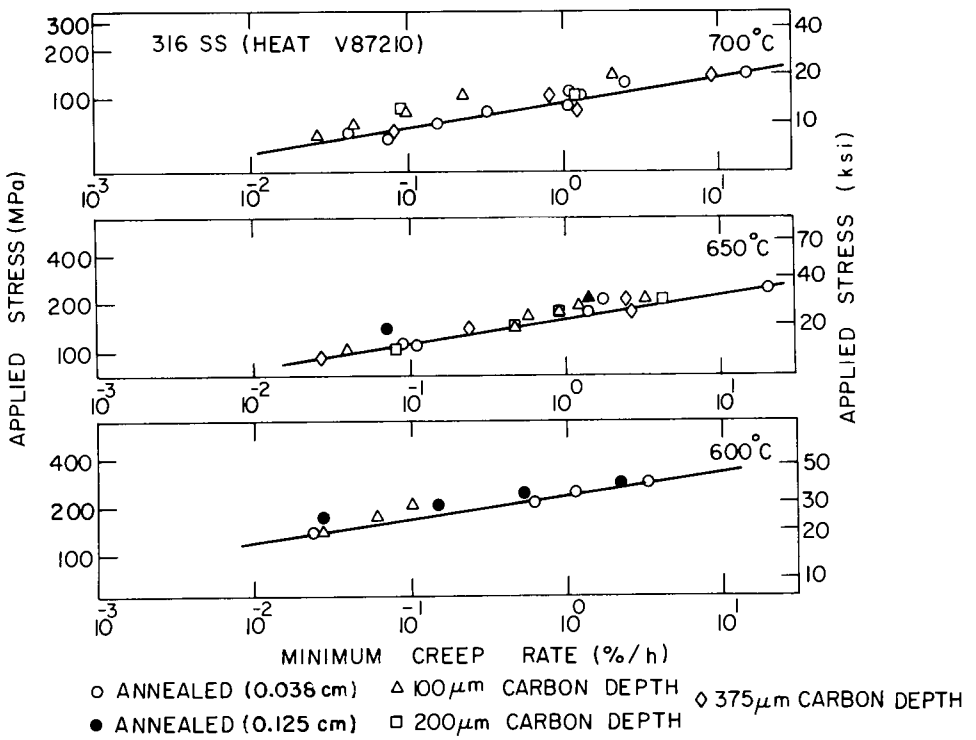

Fig. 2.16. Variations in Minimum Creep Rate with Applied Stress at 700, 650, and 600°C for Type 316 Stainless Steel Specimens in Solution-annealed and Sodium-exposed Conditions. Neg. No. MSD-63486.

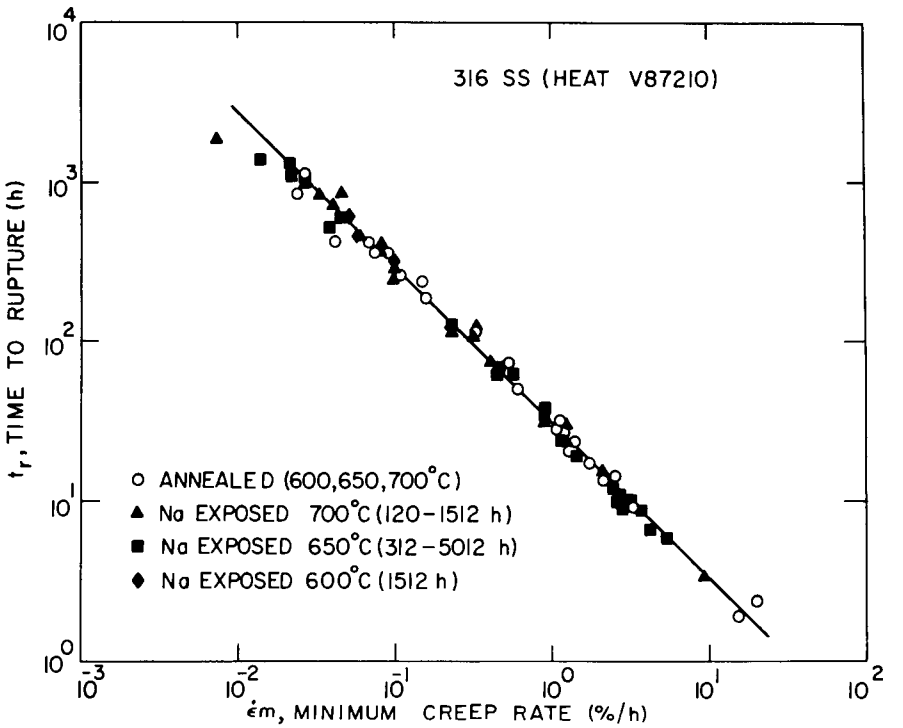

Fig. 2.17. Plot of Rupture Life vs Minimum Creep Rate for Specimens in Solution-annealed and Sodium-exposed Conditions. Neg. No. MSD-63478.

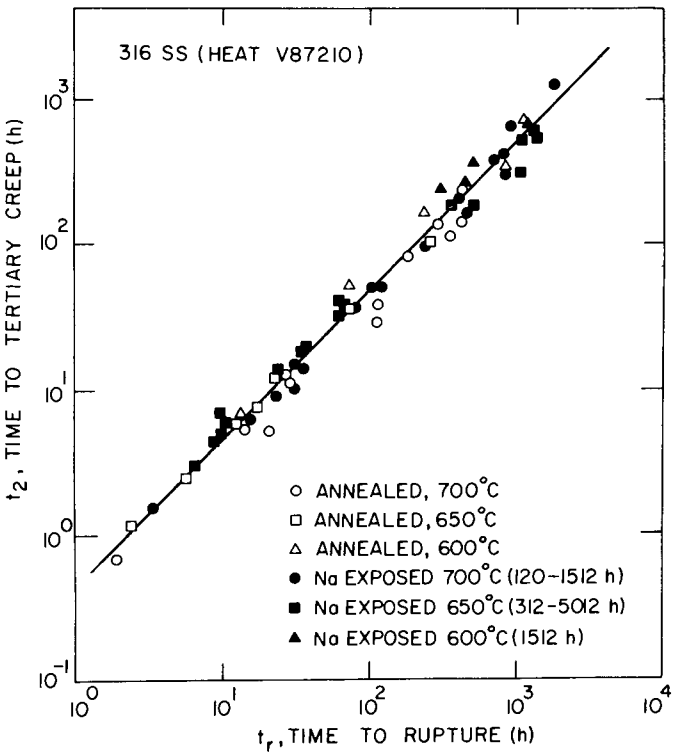

Fig. 2.18. Plot of Rupture Life vs Time to Tertiary Creep for Specimens in Solution-annealed and Sodium-exposed Conditions. Neg. No. MSD-63479.

sodium at 700, 650, and 600°C. The results show that the time to initiation of tertiary creep is a fixed fraction of the time to rupture for the annealed and carburized conditions in the temperature range 600-700°C.

The information generated from the creep tests will be correlated with sodium-purity conditions and microstructural changes in the creep-tested samples.

2.3.2 Representation of Tensile Behavior of Type 304 Stainless Steel in a Sodium Environment -- O. K. Chopra and K. Natesan

The effect of carburization on the tensile properties of Type 304 stainless steel is being determined after exposure of the material to well-characterized sodium at temperatures between 550 and 700°C. Since the composition and microstructure of the material can have a strong influence on the strain-hardening behavior and plastic strain accumulation during high-temperature deformation, the degree of carburization that results from the sodium environment must be correlated with the mechanical-property changes in the material. In the present report, the Voce expression is used to describe the tensile-flow behavior of Type 304 stainless steel in the solution-annealed condition and after exposure to flowing sodium for different times and temperatures. The combined tensile and creep-rupture data were analyzed to evaluate the effect of plastic strain rate on the strain-hardening behavior of the steel.

The experimental procedure that describes the specimen preparation and sodium-exposure and tensile-test conditions is presented elsewhere.[29-31] Load-elongation data from the tensile tests were converted to true stress-true strain curves by a computer program that made use of a constant-volume approximation. These curves were compared with the Voce equation[32]

$$\frac{\sigma - \sigma_s}{\sigma_o - \sigma_s} = \exp\left(-\frac{\varepsilon_p}{\varepsilon_c}\right), \tag{6}$$

where σ is the true stress, ε_p is the true axial plastic strain, and

σ_o, σ_s, and ε_c are constants that depend on temperature, strain rate, and material history. The true stress-true strain data were fitted by the equation in the plastic strain range of 0.005 to the end of uniform strain. The latter condition is not obvious from the true stress-true strain curves in all cases. The point at which necking instabilities develop was considered to be the strain where the true strain-hardening rate equals the true stress. A computer fit of the data using a variable-metric minimization program was employed to evaluate the constants σ_o, σ_s, and ε_c in Eq. (6). The values are listed in Tables 2.9 and 2.10 for the specimens in the solution-annealed and sodium-exposed conditions, respectively.

It can be observed from Table 2.9 that the values of the constants σ_o, σ_s, and ε_c decrease as the strain rate decreases for all the temperatures and increase with a decrease in temperature for corresponding strain rates. These trends suggest that the constants are interrelated. Figure 2.19 shows a logarithmic plot of ε_c versus σ_s, in which the parameters are normalized by the temperature-dependent shear modulus μ. The linear dependence observed for all temperatures and strain rates follows a power-law relation of the form

$$\varepsilon_c = \alpha \left(\frac{\sigma_s}{\mu} \right)^{\beta}. \tag{7}$$

The values of the constants α and β were obtained by a least-squares analysis and are listed in Table 2.11. A distinct difference is observed between the values of σ_s and ε_c obtained for the sodium-exposed and solution-annealed conditions. For example, at any given value of σ_s/μ, the constant ε_c is lower for the sodium-exposed material. This difference is observed after a short-time exposure to sodium. Longer exposure periods and larger carbon penetration depths do not result in any additional variations.

A straight-line relationship between the constants σ_o and σ_s, both normalized by the shear modulus, was obtained from the expression

$$\frac{(\sigma_s - \sigma_o)}{\mu} = a \left(\frac{\sigma_s}{\mu} \right)^{b}. \tag{8}$$

Table 2.9. Values of Constants in Voce Equation for Solution-annealed Type 304 Stainless Steel

Temperature, °C	Strain Rate, s^{-1}	σ_o, MPa (ksi)	σ_s, MPa (ksi)	ε_c
700	1.90×10^{-3}	117.4 (17.02)	352.0 (51.04)	0.094
	9.52×10^{-4}	91.2 (13.22)	302.3 (43.83)	0.074
	3.81×10^{-4}	92.8 (13.46)	260.1 (37.71)	0.044
	3.81×10^{-4}	81.8 (11.86)	269.2 (39.03)	0.064
	9.52×10^{-5}	87.7 (12.72)	225.6 (32.72)	0.052
	3.81×10^{-5}	98.8 (14.33)	198.5 (28.79)	0.039
	7.62×10^{-6}	83.0 (12.03)	154.9 (22.46)	0.014
650	1.90×10^{-3}	113.7 (16.49)	479.4 (69.51)	0.150
	9.52×10^{-4}	103.5 (15.01)	420.1 (60.91)	0.127
	3.81×10^{-4}	86.1 (12.48)	407.9 (59.15)	0.111
	9.52×10^{-5}	92.7 (13.45)	314.9 (45.66)	0.081
	3.81×10^{-5}	94.0 (13.64)	285.0 (41.32)	0.060
	3.81×10^{-6}	80.1 (11.61)	184.3 (26.73)	0.016
600	9.52×10^{-4}	105.8 (15.34)	581.3 (84.29)	0.195
	3.81×10^{-4}	95.9 (13.91)	625.6 (90.79)	0.193
	9.52×10^{-5}	98.9 (14.34)	478.0 (69.31)	0.142
	3.81×10^{-5}	102.6 (14.88)	425.3 (61.67)	0.099
	7.62×10^{-6}	93.4 (13.54)	284.3 (41.23)	0.054
550	9.52×10^{-4}	107.2 (15.55)	759.7 (110.17)	0.283
	3.81×10^{-4}	100.1 (14.51)	573.1 (83.11)	0.169
	9.52×10^{-5}	112.3 (16.29)	670.4 (97.21)	0.220
	3.81×10^{-5}	109.6 (15.90)	661.7 (95.95)	0.203
	7.62×10^{-6}	101.9 (14.78)	499.4 (72.42)	0.138

Table 2.10. Values of Constants in Voce Equation for Sodium-exposed Type 304 Stainless Steel

Temperature, °C	Sodium-exposure Time, h	Carbon Penetration Depth, μm	Surface Carbon Concentration, wt%	Average Carbon Concentration, wt%	Strain Rate, s^{-1}	σ_o, MPa (ksi)	σ_s, MPa (ksi)	ε_c
700	120	∿100			3.81×10^{-4}	92.3 (13.38)	247.7 (35.92)	0.043
					3.81×10^{-4}	101.1 (14.66)	248.0 (35.96)	0.043
	504	∿200	0.046	0.043-0.046	3.81×10^{-4}	86.1 (12.49)	238.7 (34.62)	0.042
	1512	∿375			3.81×10^{-4}	86.3 (12.51)	250.9 (36.38)	0.044
650	312	100	0.095	0.078	3.81×10^{-4}	102.8 (14.91)	350.3 (50.79)	0.061
					3.81×10^{-4}	105.0 (15.22)	354.8 (51.44)	0.061
	1512	200	0.25 ± 0.02	0.122 ± 0.01	3.81×10^{-4}	103.6 (15.02)	343.6 (49.83)	0.056
					3.81×10^{-5}	95.6 (13.86)	281.9 (40.87)	0.050
	5012	375	0.25 ± 0.02	0.195 ± 0.01	3.81×10^{-4}	90.5 (13.12)	349.6 (50.69)	0.083
					3.81×10^{-5}	103.8 (15.05)	280.7 (40.70)	0.043
600	1512	100	0.30 ± 0.02	0.145 ± 0.01	3.81×10^{-4}	131.6 (19.08)	514.3 (74.58)	0.104
					3.81×10^{-5}	102.0 (14.79)	451.7 (65.50)	0.105
	5012	200	0.30 ± 0.02	-	3.81×10^{-4}	104.9 (15.21)	477.1 (69.18)	0.130
					3.81×10^{-5}	108.9 (15.79)	406.2 (58.90)	0.090

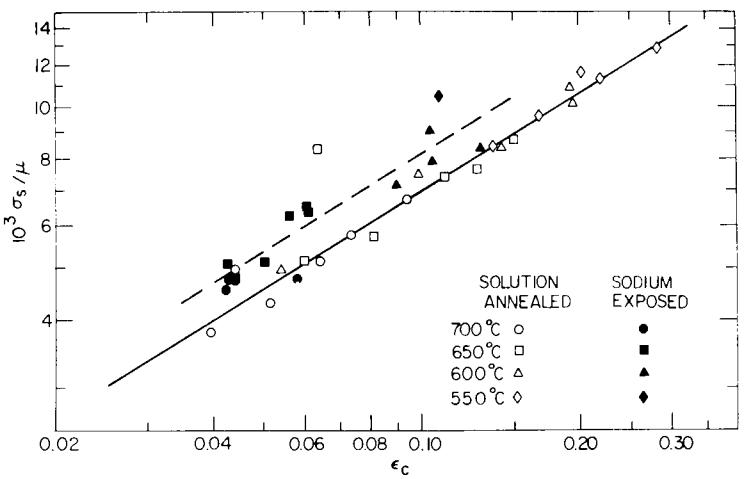

Fig. 2.19. Dependence of Voce Constant ε_c on Saturation Stress σ_s. Neg. No. 63508.

Table 2.11. Values of Parameters in the Equations That Describe the Tensile-flow Curves

Equation Number	Temperature, °C	Parameter	Value	
			Annealed	Na Exposed
(7)	550-700	α	272.4	206.8
		β	1.60	1.60
(8)	550-700	a	3.98	3.98
		b	1.34	1.34

As shown in Fig. 2.20, the data from solution-annealed and sodium-exposed specimens follow a single relationship. The values of the constants a and b are independent of temperature, strain rate, and material history and are listed in Table 2.11.

The parameter σ_s in the Voce equation represents a constant saturation stress at large plastic strains dueing a tensile test. Consequently, the deformation behavior of the material corresponds to that of steady-state creep. The usefulness of σ_s in the prediction of the creep rates was examined by a comparison of the strain-rate dependence of σ_s with the creep-rupture data.[31] The tensile strain and minimum creep rates are plotted as a function of normalized stress in Figs. 2.21 and 2.22 for the solution-annealed and sodium-exposed conditions, respectively. The straight-line behavior observed in the figures indicates that the combined data can be expressed adequately by a single relationship of the form

$$\dot{\varepsilon} = A \left(\frac{\sigma_s}{\mu}\right)^n , \qquad (9)$$

where $\dot{\varepsilon}$ is the creep rate and A and n are temperature-dependent constants. The values of the constants are listed in Table 2.12. As observed in Fig. 2.22, for the sodium-exposed material σ_s is higher than for specimens in the solution-annealed condition at strain rates $\lesssim 5 \times 10^{-5}$ s^{-1} and lower at strain rates above this value.

Equations (6-9) can be used to establish the true stress-true strain curves for any strain rate and temperature. Examples of the computed curves are shown in Fig. 2.23 for the solution-annealed and sodium-exposed conditions. The computed curves, shown as dashed lines, represent the tensile-flow behavior quite well in the range of uniform strain.

The strain-hardening rate of the solution-annealed and sodium-exposed material is compared in Figs. 2.24a and 24b for strain rates of 3.81×10^{-4} and 3.81×10^{-5} s^{-1}, respectively. The strain-hardening coefficient θ is plotted as a function of flow stress, for which both variables are normalized by the shear modulus. In general, the strain-hardening rates are higher for the sodium-exposed

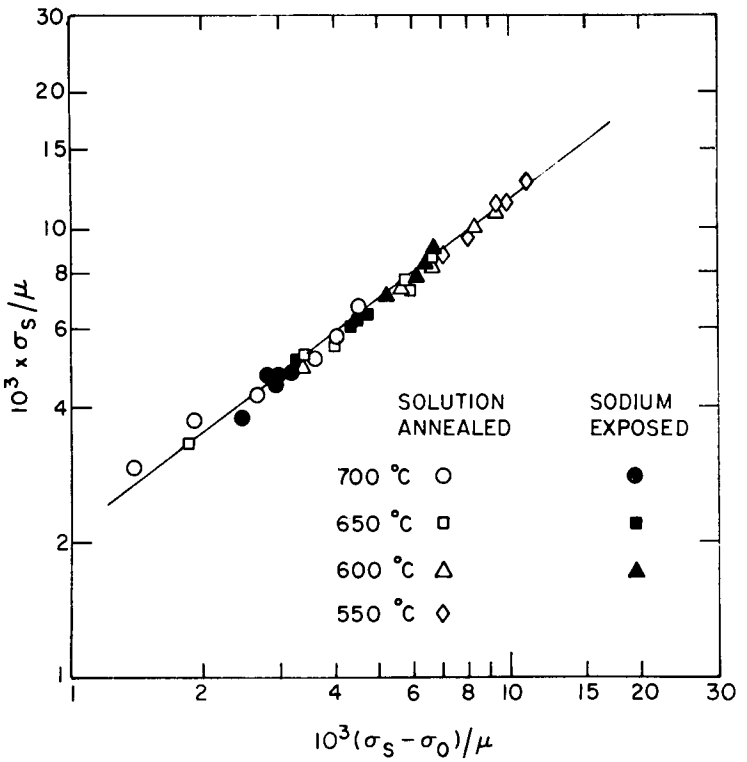

Fig. 2.20. Interdependence of Voce Constants σ_o and σ_s. Neg. No. MSD-63504.

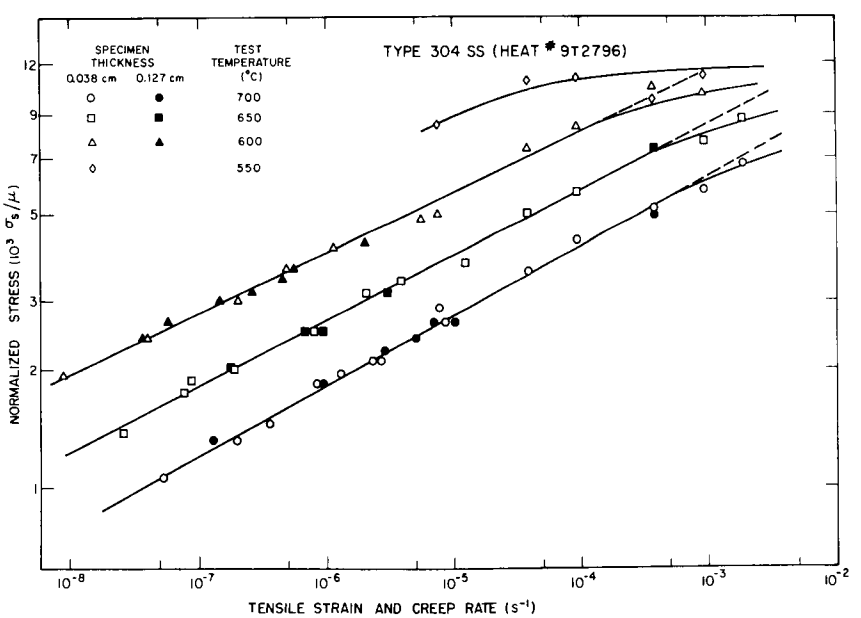

Fig. 2.21. Comparison of Saturation Stress Predicted from the Voce Equation with Creep Data for Solution-annealed Material. Neg. No. MSD-63509.

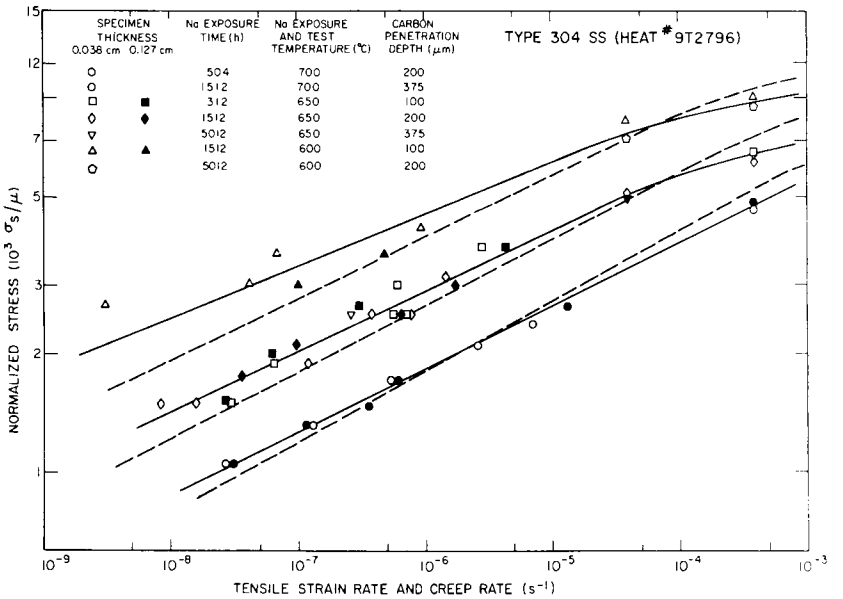

Fig. 2.22. Comparison of Saturation Stress Predicted from the Voce Equation with Creep Data for Sodium-exposed Materials. Neg. No. MSD-63503.

Table 2.12. Values of Constants in Equation (9) That Describe the Combined Tensile and Creep Data

Temperature, °C	Solution Annealed		Sodium Exposed	
	A,[a] s^{-1}	n	A, s^{-1}	n
600	5.42×10^{9}	6.4	6.49×10^{11}	7.6
650	1.77×10^{9}	5.9	3.75×10^{10}	6.5
700	2.17×10^{9}	5.6	1.36×10^{11}	6.2

[a]An average value of 2.4×10^{9} s^{-1} was used in computing the plots shown in Fig. 2.21.

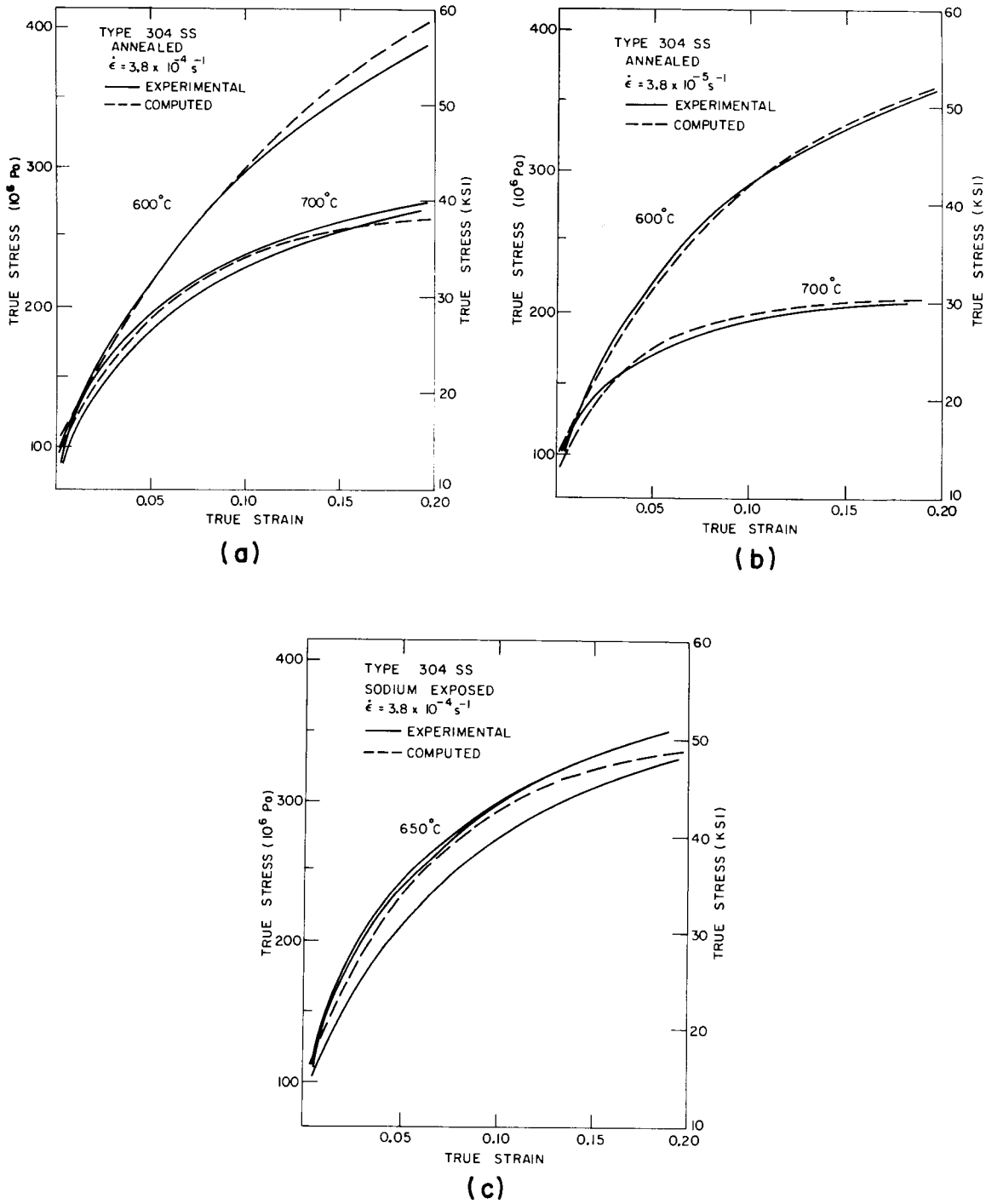

Fig. 2.23. Comparison of Experimental True Stress-True Strain Tensile Curves (Solid Lines) with Curves Predicted by the Voce Model (Dashed Lines). (a) and (b) solution-annealed condition and (c) sodium-exposed condition. Neg. Nos. MSD-63511, 63510, and 63502.

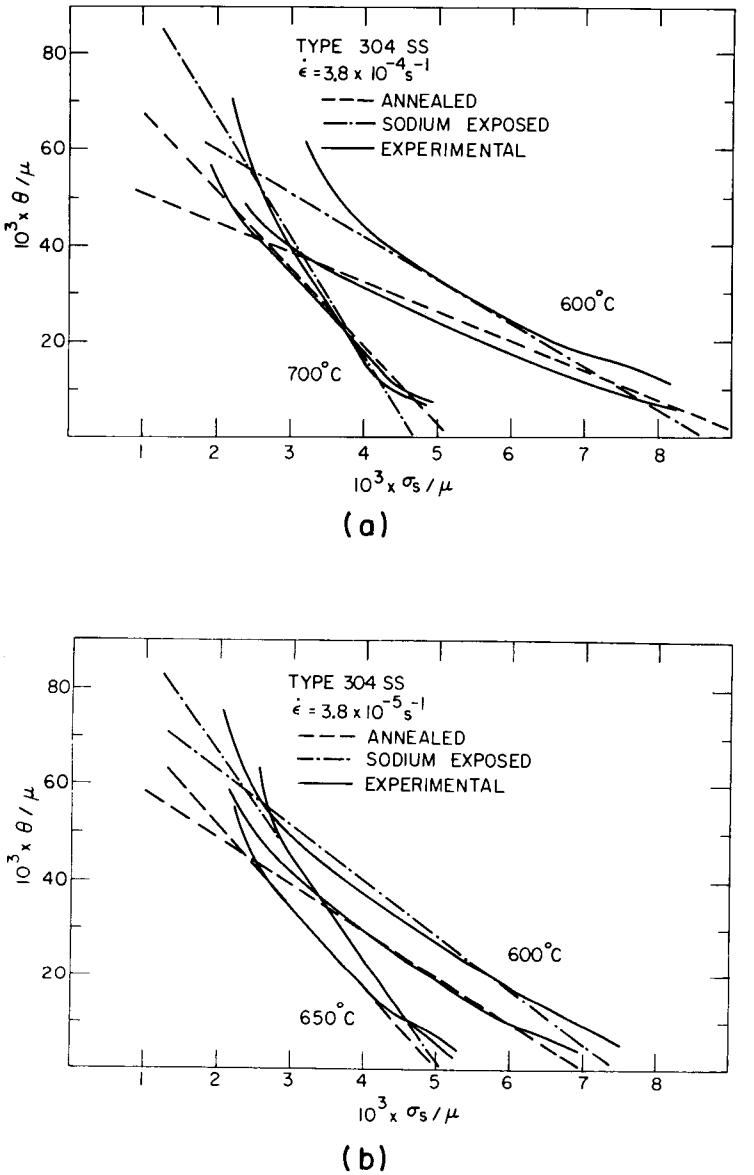

Fig. 2.24. Variation in Strain-hardening Rate θ with Flow Stress σ, both Normalized by the Temperature-dependent Shear Modulus μ. (a) $\dot{\varepsilon} = 3.81 \times 10^{-4}\ s^{-1}$ and (b) $\dot{\varepsilon} = 3.81 \times 10^{-5}\ s^{-1}$. Neg. Nos. MSD-63505 and 63507.

material. However, the decrease in the strain-hardening rate with an increase in flow stress is faster in the sodium-exposed specimens; particularly at the higher strain rate and temperature. This behavior leads to a lower saturation stress σ_s (the value of flow stress at zero strain-hardening rate) in the sodium-exposed specimens at a strain rate of 3.81×10^{-4} s^{-1}.

Scanning-electron micrographs of the fracture surfaces of the solution-annealed and sodium-exposed specimens tested at various strain rates are shown in Figs. 2.25-27 for test temperatures of 600, 650, and 700°C, respectively. These micrographs indicate a transition in the fracture mode from a completely dimpled fracture to a partial intergranular fracture as the strain rate decreases. This transition occurs at higher values of strain rate at the lower temperatures. For example, in the solution-annealed specimens tested at 600°C, the fracture surface shows a dimpled structure at a strain rate of 3.81×10^{-4} s^{-1} (Fig. 2.25a), whereas some intergranular fracture surfaces are observed at a strain rate of 3.81×10^{-5} s^{-1} (Fig. 2.25b). In the creep range, i.e., a creep rate of 2×10^{-7} s^{-1}, the fracture is mostly intergranular. A similar dimple-structure fracture mode is observed in the solution-annealed specimens at higher temperatures, with the exception of 700°C, at which the ductile fracture mode consists of large cavities and voids instead of a regular dimpled structure.

The influence of sodium exposure on the fracture mode is the inhibition of the intergranular fracture observed at lower strain rates. As observed in Figs. 2.25f and 2.26f, the extent of intergranular fracture is considerably less in the sodium-exposed specimens. Also, the exposed grain-boundary surfaces show some evidence of plastic flow before fracture.

The values of uniform elongation predicted from the Voce equation are shown as a function of normalized saturation stress in Fig. 2.28 for the solution-annealed and sodium-exposed conditions. The criterion for the onset of plastic instability used in these computations was the strain at which the flow stress equals the rate of strain hardening.

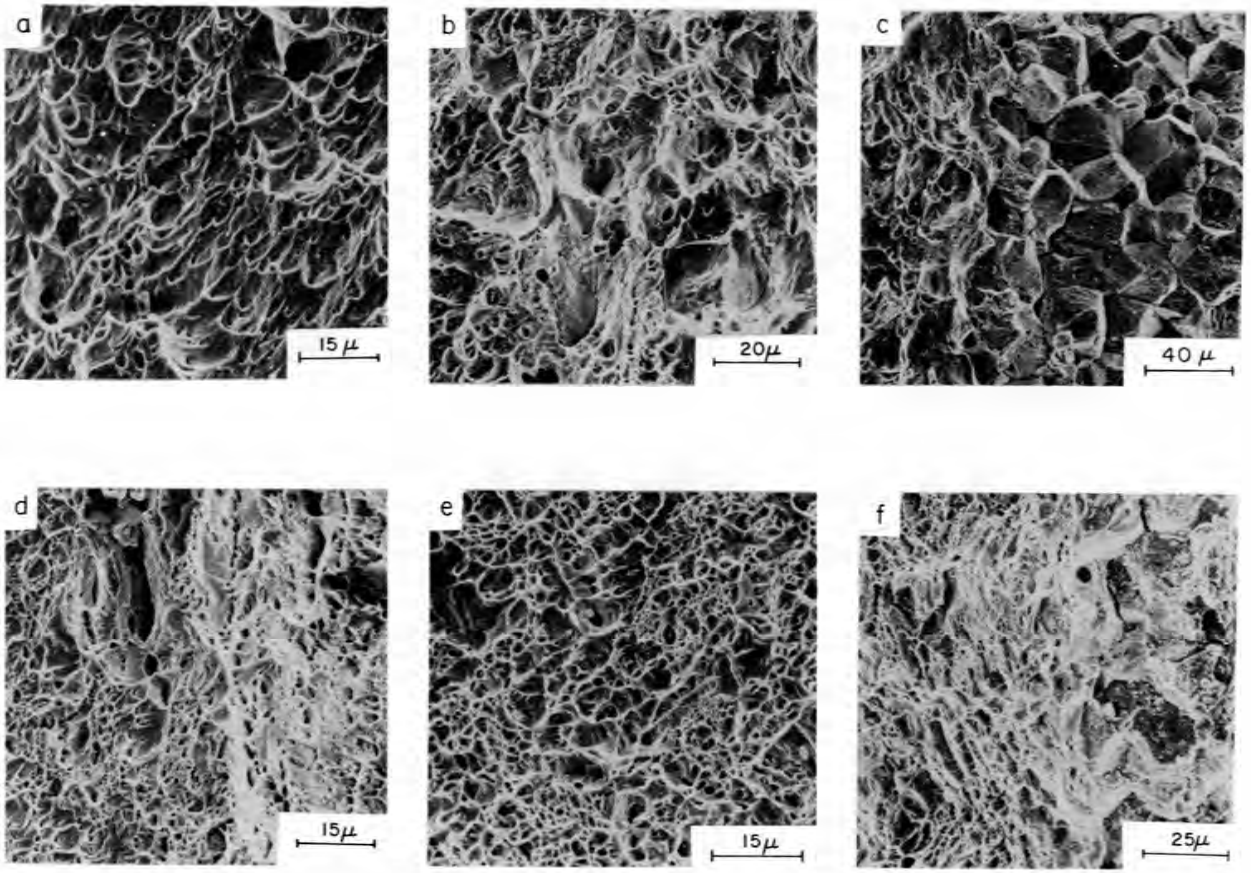

Fig. 2.25. Scanning-electron Micrographs of Fracture Surfaces of Type 304 Stainless Steel Tested at 600°C. (a)-(c) solution-annealed condition and (d)-(f) exposed to sodium for 5012 h at 600°C. (a) and (d) $\dot{\varepsilon} = 3.81 \times 10^{-4}\ s^{-1}$, (b) and (e) $\dot{\varepsilon} = 3.81 \times 10^{-8}\ s^{-1}$, (c) $\dot{\varepsilon} = 2.00 \times 10^{-7}\ s^{-1}$, and (f) $\dot{\varepsilon} = 4.10 \times 10^{-8}\ s^{-1}$. ANL Neg. No. 306-76-197.

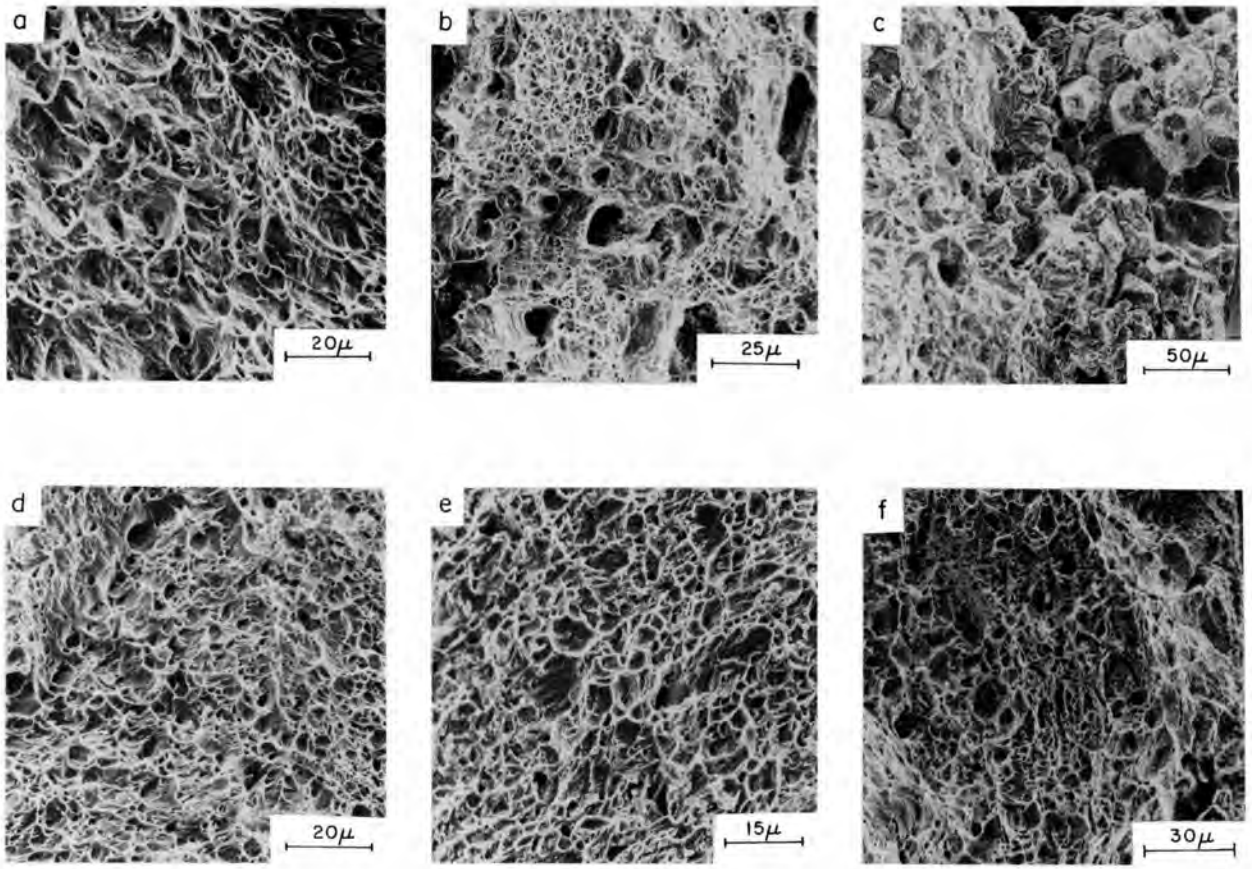

Fig. 2.26. Scanning-electron Micrographs of Fracture Surfaces of Type 304 Stainless Steel Tested at 650°C. (a)-(c) solution-annealed condition and (d)-(f) exposed to sodium for 1512 h at 650°C. (a) and (d) $\dot{\varepsilon} = 3.81 \times 10^{-4}\ s^{-1}$, (b) and (e) $\dot{\varepsilon} = 3.81 \times 10^{-5}\ s^{-1}$, (c) $\dot{\varepsilon} = 2.50 \times 10^{-7}\ s^{-1}$, and (f) $\dot{\varepsilon} = 6.35 \times 10^{-8}\ s^{-1}$. ANL Neg. No. 306-76-195.

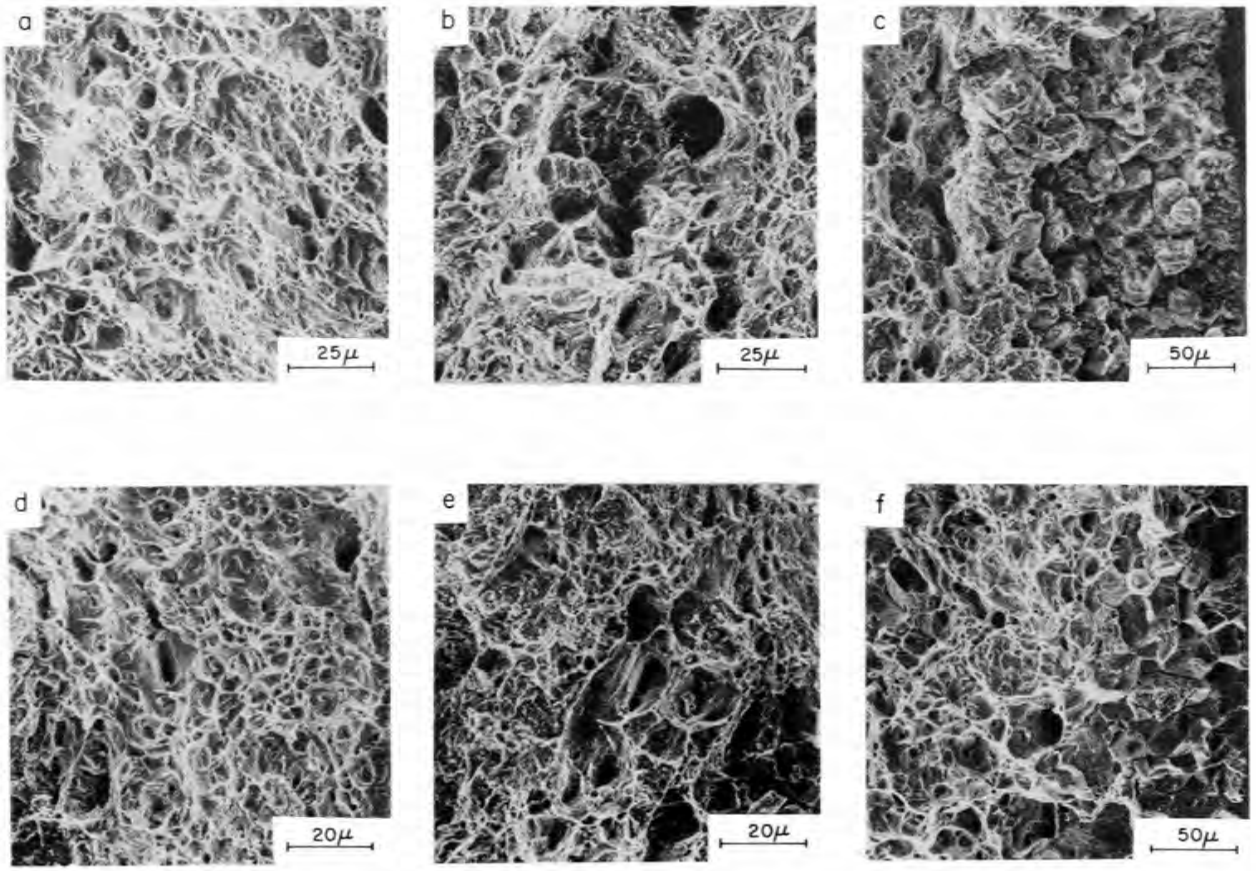

Fig. 2.27. Scanning-electron Micrographs of Fracture Surfaces of Type 304 Stainless Steel Tested at 700°C. (a)-(c) solution-annealed condition and (d)-(f) exposed to sodium for 1512 h at 700°C. (a) and (d) $\dot{\varepsilon} = 3.81 \times 10^{-4}\ s^{-1}$, (b) and (e) $\dot{\varepsilon} = 3.81 \times 10^{-5}\ s^{-1}$, (c) $\dot{\varepsilon} = 8.30 \times 10^{-7}\ s^{-1}$, and (f) $\dot{\varepsilon} = 6.95 \times 10^{-6}\ s^{-1}$. ANL Neg. No. 306-76-196.

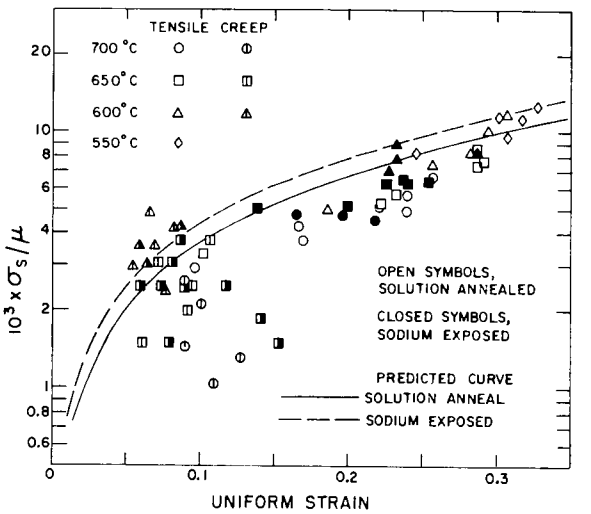

Fig. 2.28. Comparison of Uniform Elongation Predicted from the Voce Equation with Experimental Tensile and Creep Data. Neg. No. MSD-63506.

The tensile data points shown in Fig. 2.28 correspond to this condition in the experimental curves. The creep data represent the plastic strain at the point of inflection in the creep curve, i.e., the midpoint of the secondary-creep stage. The predicted values of uniform strain compare well with the values obtained from the tensile tests. However, in the creep regime the model underestimates uniform strains. In fact, the experimental data do not corroborate the trend predicted by the model in that the inflection strain increases as the stress decreases. Since the predicted uniform strain is approximately proportional to $\varepsilon_c \ln(\sigma_s/\mu)$, this discrepancy probably arises from the value of ε_c assumed in the Voce model. Equations (6-9) indicate that ε_c decreases and the initial strain-hardening rate increases as σ_s decreases. Although this behavior is consistent with the observed tensile results, i.e., Figs. 2.19 and 2.24, a judicious extrapolation of Eq. (7) into the creep regime requires additional tensile data at much lower strain rates.

2.3.3 Influence of Sodium Environment on the Low-Cycle Fatigue Behavior of Austenitic Stainless Steel -- D. L. Smith and G. J. Zeman

The effects of high-temperature sodium environment on the low-cycle fatigue behavior of AISI Types 304 and 316 stainless steel are being investigated. The experimental program has been formulated to determine both the effect of testing in a sodium environment and the effect of long-term sodium exposure on the fatigue properties of the two steels. The fatigue tests are performed in sodium of controlled purity, viz., ∿1 ppm oxygen and 0.3 ppm carbon, with a fully reversed triangular waveform and zero mean strain. Preexposure of the steels for periods up to 5000 h has been conducted in sodium of similar purity.

In the present report period a series of fatigue tests at 550°C has been completed on the two steels. These tests were conducted at a strain rate $\dot{\varepsilon}$ of 4×10^{-3} s^{-1} on annealed material and material that had been exposed to sodium for 5000 h at 550°C. Results from this series of fatigue tests are shown in Figs. 2.29-34. Figure 2.29 is a plot of fatigue lifetime as a function of total strain range for annealed Types 304 and 316 stainless steel tested in sodium. The 566°C

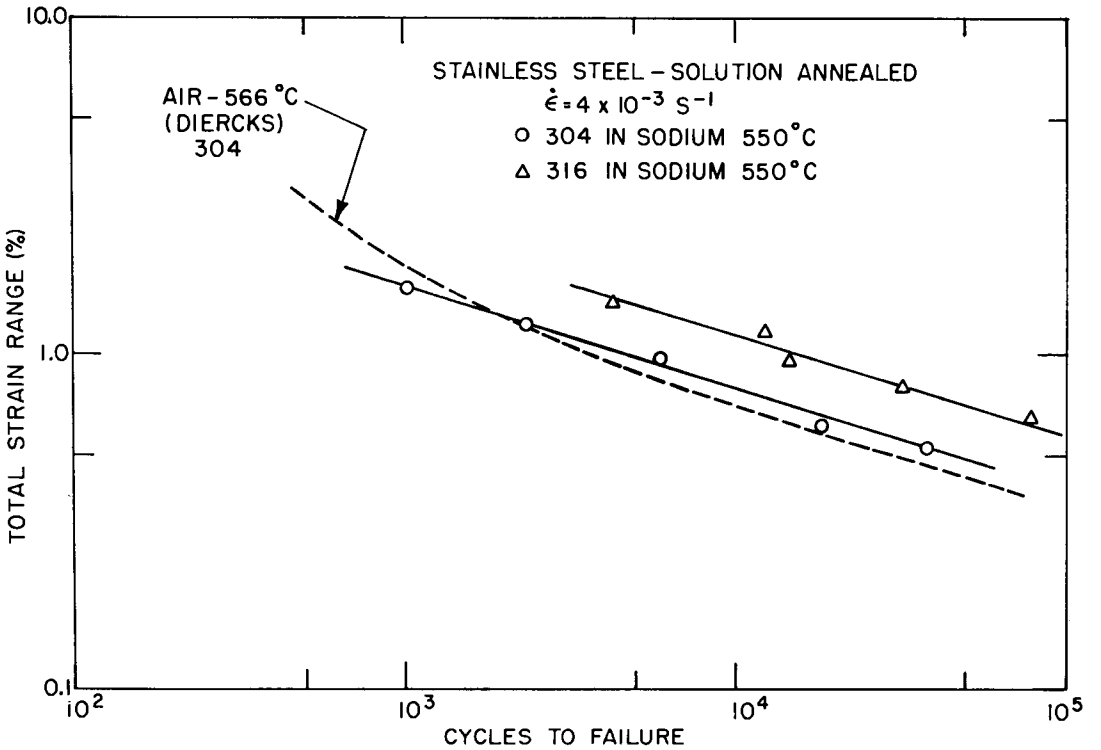

Fig. 2.29. Total Strain Range vs Cycles to Failure for Types 304 and 316 Stainless Steel Tested in Sodium and Air.[8] Neg. No. MSD-63497.

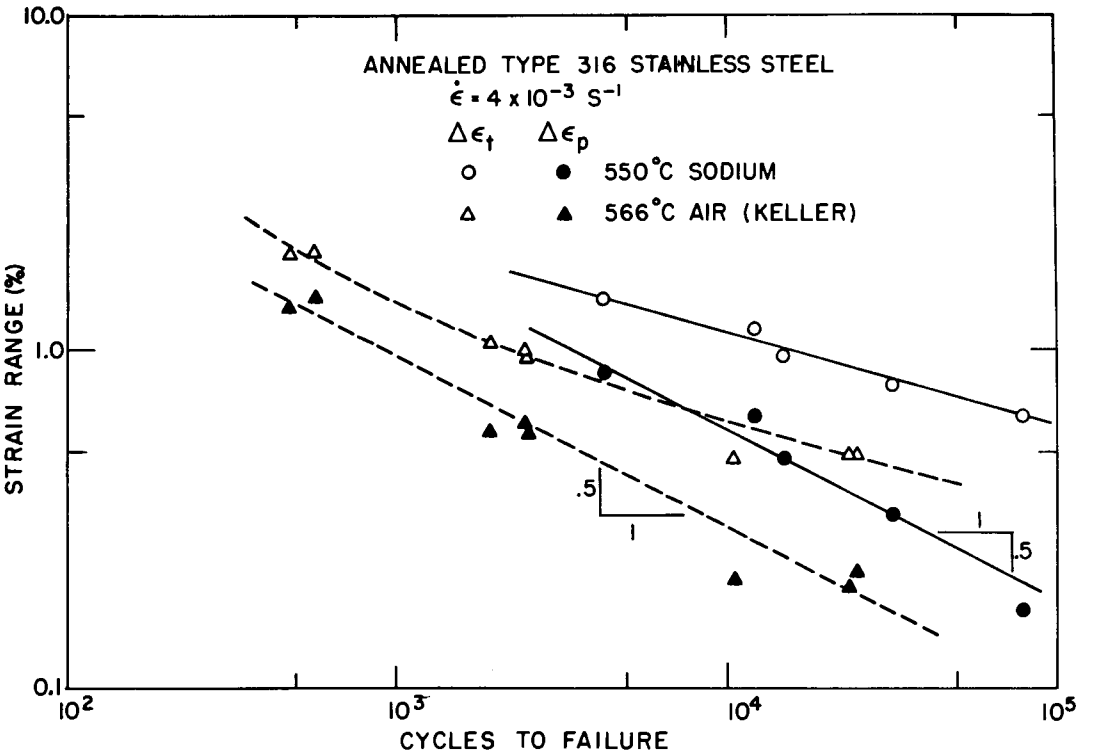

Fig. 2.30. Total and Plastic Strain Range vs Cycles to Failure for Annealed Type 316 Stainless Steel Tested in Sodium and Air.[33] Neg. No. MSD-63489.

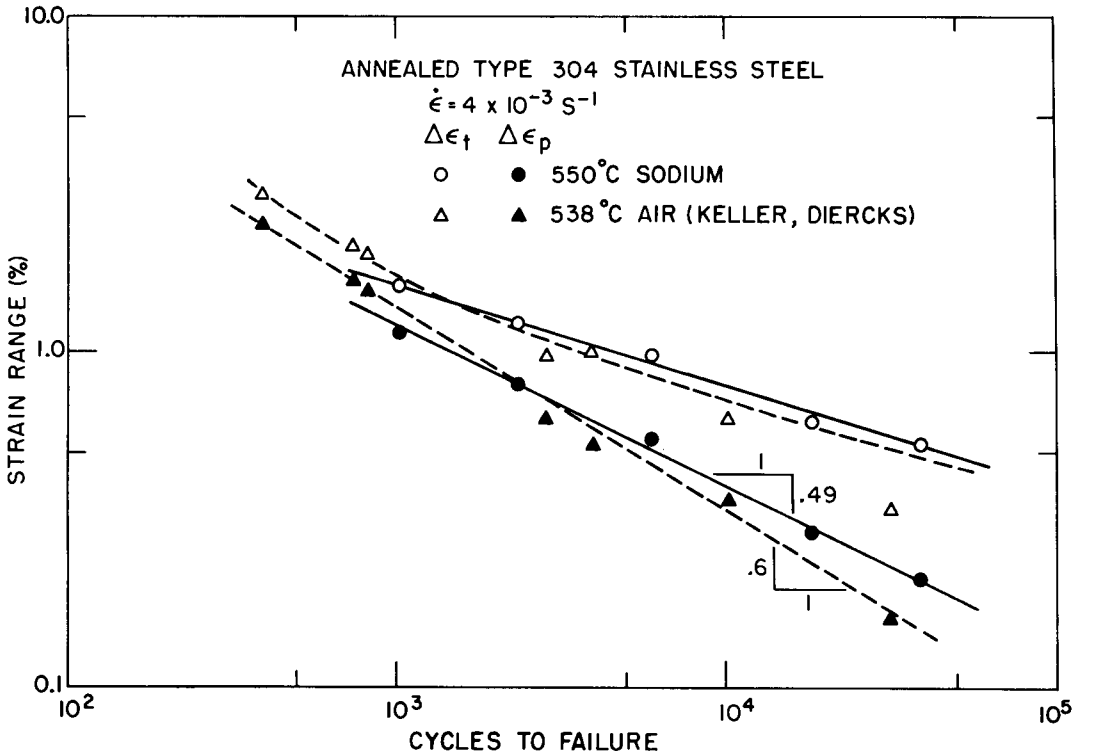

Fig. 2.31. Total and Plastic Strain Range vs Cycles to Failure for Annealed Type 304 Stainless Steel Tested in Sodium and Air.[8,34] Neg. No. MSD-63494.

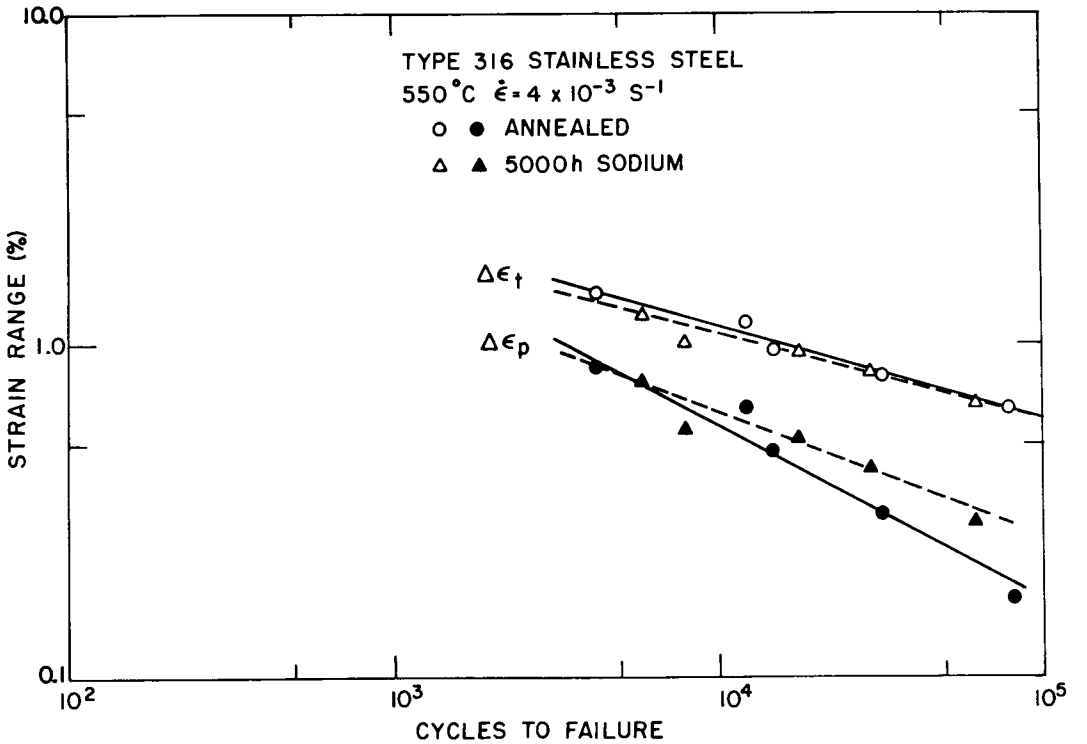

Fig. 2.32. Fatigue Data Obtained in Sodium on Type 316 Stainless Steel in the Annealed and Sodium-exposed Conditions. Neg. No. MSD-63491.

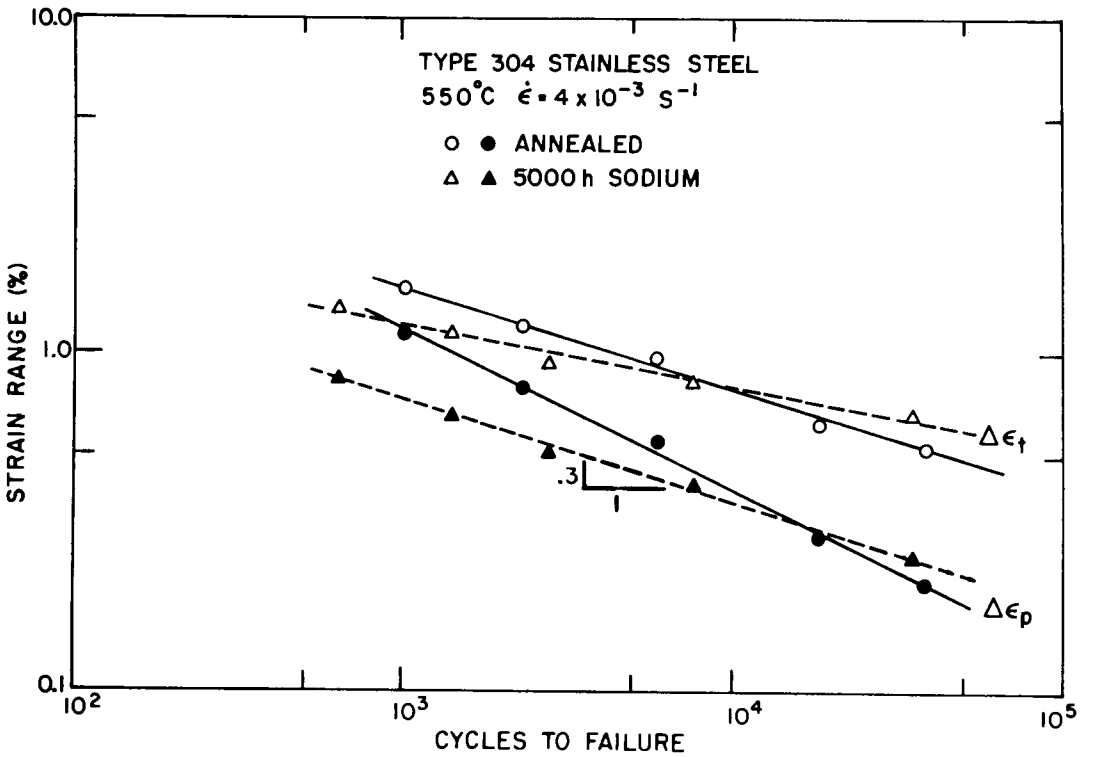

Fig. 2.33. Fatigue Data Obtained in Sodium on Type 304 Stainless Steel in the Annealed and Sodium-exposed Conditions. Neg. No. MSD-63487.

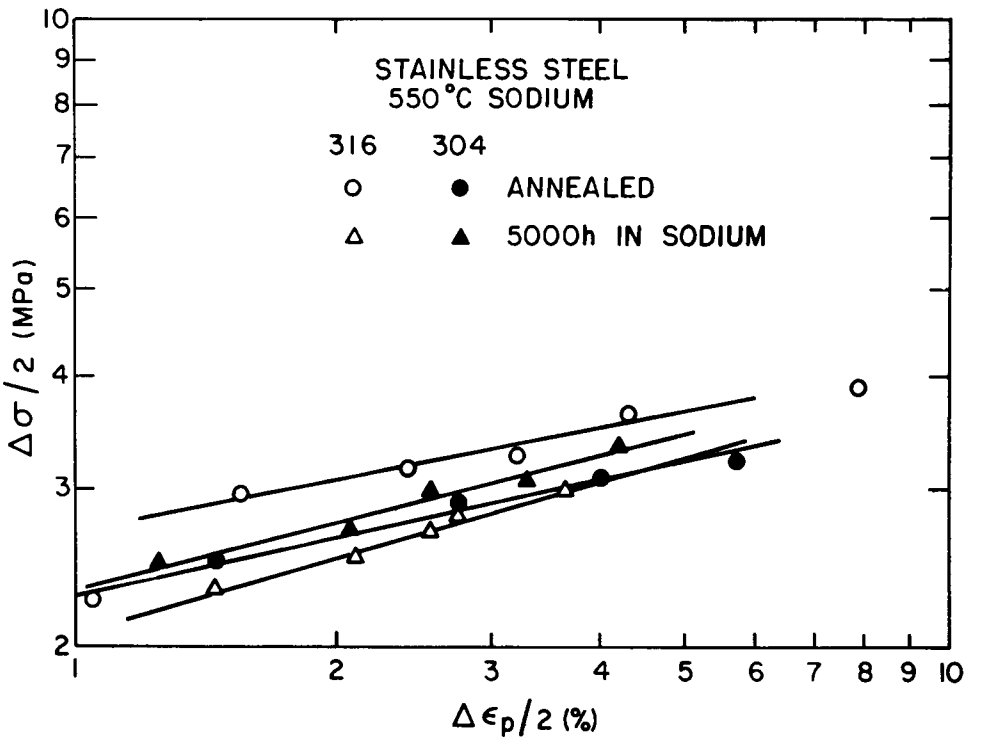

Fig. 2.34. Cyclic Stress-Strain Response for Types 304 and 316 Stainless Steel Tested in Sodium at 550°C in the Annealed and Sodium-exposed Conditions. Neg. No. MSD-63493.

curve proposed by Diercks[8] from a correlation of available air data is included for a reference. The fatigue life of Type 304 stainless steel in sodium deviates from the air curve by <50% for the strain ranges investigated. This result is in agreement with earlier data obtained at 600 and 700°C,[35] which indicate little effect of the test environment on fatigue life for a strain rate of 4×10^{-3} s^{-1}. In contrast, the fatigue life of Type 316 stainless steel at 550°C is a factor of 3-4 greater when tested in sodium than when tested in air. A similar enhancement was also observed at the higher temperatures.[35,36]

Figure 2.30 shows both the total ($\Delta\varepsilon_t$) and plastic ($\Delta\varepsilon_p$) strain-range data for Type 316 stainless steel tested at 550°C in sodium. Included for comparison are available data from the literature for annealed material tested in air at 566°C.[33] The well-known Coffin-Manson expression[37,38]

$$\Delta\varepsilon_p \cdot N_f^{\alpha} = C, \tag{10}$$

where C and α are constants, has been widely used to relate the plastic strain range $\Delta\varepsilon_p$ and cycles to failure N_f. A value of $\alpha = 0.5$ has been shown to be representative of a variety of materials tested at room temperature or tested in inert atmospheres at elevated temperatures (for example, Ref. 39). Even though the fatigue life of Type 316 stainless steel is enhanced by testing in sodium, Fig. 2.30 shows that a value of 0.5 for α satisfactorily represents the data for both environments at a strain rate of 4×10^{-3} s^{-1}. Similar data shown in Fig. 2.31 for Type 304 stainless steel indicate that $\alpha = 0.5$ adequately represents the fatigue data in sodium; however, the air data[34] are better represented by a value for α of $\sim$0.60. Although the fatigue life as a function of total strain range is similar for the annealed material tested in the two environments, substantial differences in the plastic strain range-lifetime response are observed.

Figures 2.32 and 2.33 show the fatigue data for the two steels after 5000 h exposure to sodium. For the conditions tested, the sodium exposure did not significantly affect the fatigue life relative to the total strain range for Type 316 stainless steel. However, the fatigue

life response plotted as a function of plastic strain range is considerably different for the annealed and sodium-exposed conditions. The slope of the plastic strain-range curve is better represented by a value of $\alpha = 0.38$ for the sodium-exposed material. As indicated in Fig. 2.33 the fatigue-life response for Type 304 stainless steel at 550°C is different for the annealed and sodium-exposed conditions. The curve for total strain range indicates a shorter fatigue life for the sodium-exposed material at strain ranges above $\Delta\varepsilon_t = 0.8\%$ and a longer fatigue life at strain ranges below this value. A value of $\alpha = 0.30$ is obtained for the sodium-exposed material. The decrease in slope (α) of the plastic strain-range curve is more pronounced for Type 304 than for Type 316 stainless steel at this particular temperature, strain rate, and sodium exposure. Also, the lower values of α observed for the sodium-exposed material contrast with the larger slopes observed when testing at elevated temperatures in an oxidizing environment.[39]

The cyclic stress-strain response for the two steels is shown in Fig. 2.34 for the annealed and sodium-exposed conditions. The cyclic stress ($\Delta\sigma$) associated with the preexposed Type 316 stainless steel is substantially lower than that of the annealed material. In contrast, the cyclic stress for Type 304 stainless steel is slightly enhanced by the 5000-h sodium exposure. When expressed in terms of the simplified cyclic stress-strain parameters given by

$$\frac{\Delta\sigma}{2} = K\left(\frac{\Delta\varepsilon_p}{2}\right)^{n'} , \tag{11}$$

where K is the strength coefficient and n' is the cyclic strain-hardening exponent, the sodium exposure tends to slightly increase the strain-hardening exponent for both materials. This effect is more pronounced for Type 316 stainless steel.

Thermally aged specimens have also been tested in sodium in an attempt to distinguish the effects produced only by the aging phenomenon from those caused by the sodium environment for the sodium-exposed samples. Figure 2.35 shows the results obtained on Type 316

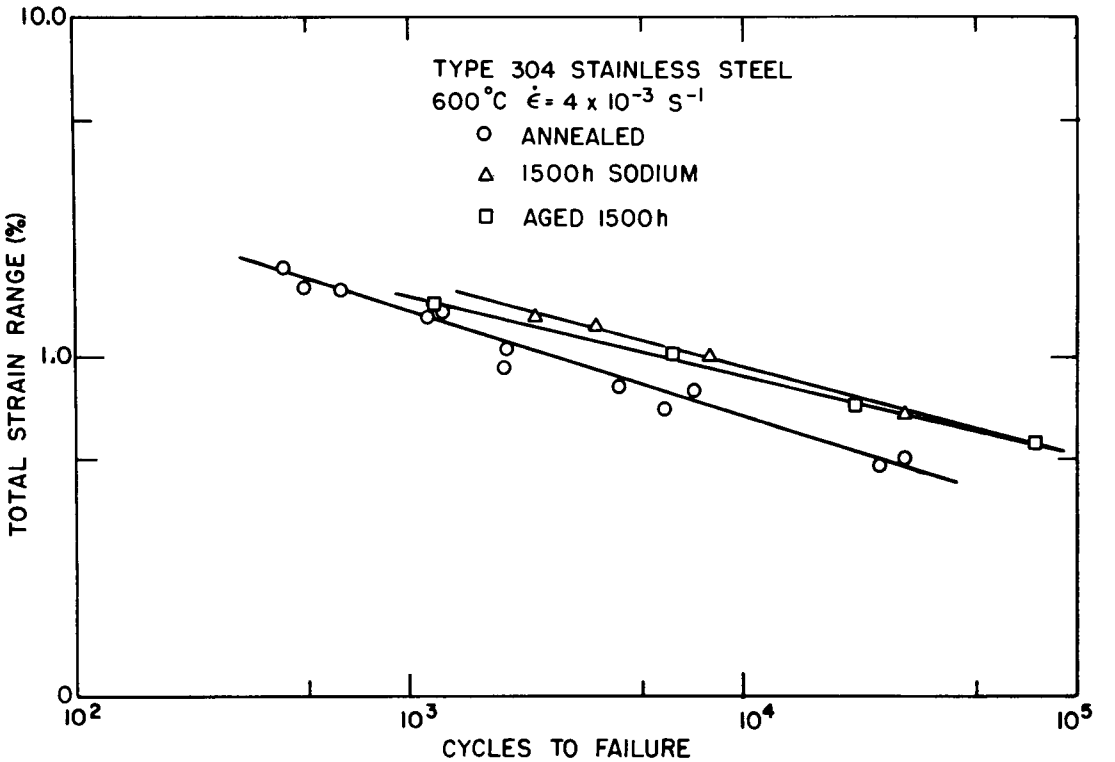

Fig. 2.35. Fatigue Data Obtained in Sodium at 600°C on Type 316 Stainless Steel in the Annealed, Thermally Aged, and Sodium-exposed Conditions. Neg. No. MSD-63492.

stainless steel that was thermally aged for 1500 h at 600°C and then tested in sodium at a strain rate of 4×10^{-3} s^{-1}. Also shown for comparison are the data obtained previously for annealed and sodium-exposed material.[35] The fatigue lifetime as a function of total strain range is not significantly affected by the various pretreatments. The plastic strain-range curves for the aged and sodium-exposed material are similar and indicate an ∿50% increase in lifetime when compared with the curve for annealed material. This effect is also reflected in the cyclic stress-strain response, for which similar results are obtained for the aged and sodium-exposed material.

The low-cycle fatigue behavior of thermally aged (1500 h at 700°C) Type 304 stainless steel tested in sodium is shown in Fig. 2.36. Data obtained on annealed and sodium-exposed (1500 h at 700°C) material are shown for comparison. The fatigue life of the aged material as a function of total strain range is approximately a factor of two greater than that for the annealed condition. Data for the sodium-exposed material lie between the other two curves. No significant change in carbon concentration of the steel occurred for the 700°C exposures. As indicated in the figure, the slopes of the plastic strain-range curves are similar. The cyclic stress-strain response for the aged material is in good agreement with the curve reported previously for the sodium-exposed material.[35]

A series of tests has been initiated to investigate the creep-fatigue interaction for specimens tested in a sodium environment. The initial tests, which have been conducted on annealed Type 316 stainless steel at 600°C, were performed under continuous cycling at a strain rate of 4×10^{-5} s^{-1}. Similar to the previous high strain-rate tests, axial strain-control loading was used with a fully reversed triangular waveform and zero mean strain. The results of two tests are shown in Fig. 2.37. Also shown for comparison are the high strain-rate results ($\dot{\varepsilon} = 4 \times 10^{-3}$ s^{-1}) obtained previously for annealed material.[35] The cycles to failure at the low strain rate are reduced by a factor of approximately four for the strain ranges investigated. Similar low strain-rate tests on Type 304 stainless steel at 600°C are in progress.

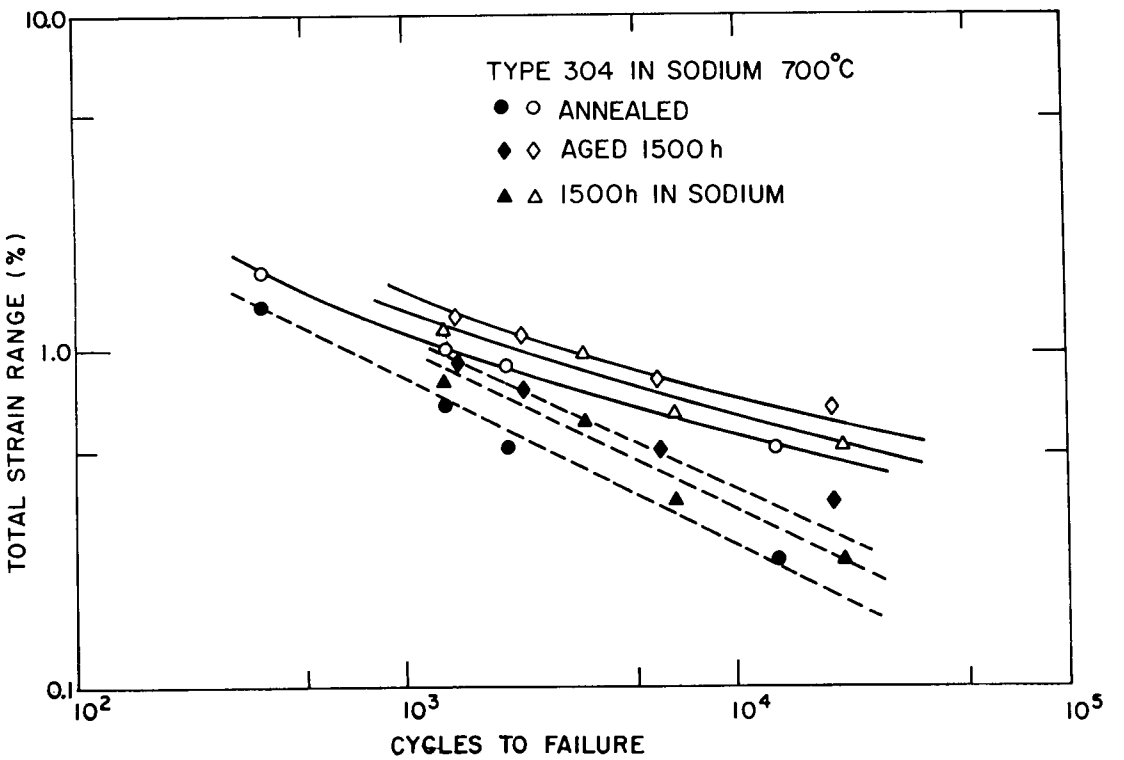

Fig. 2.36. Fatigue Data Obtained in Sodium at 700°C on Type 304 Stainless Steel in the Annealed, Thermally Aged, and Sodium-exposed Conditions. Neg. No. MSD-63488.

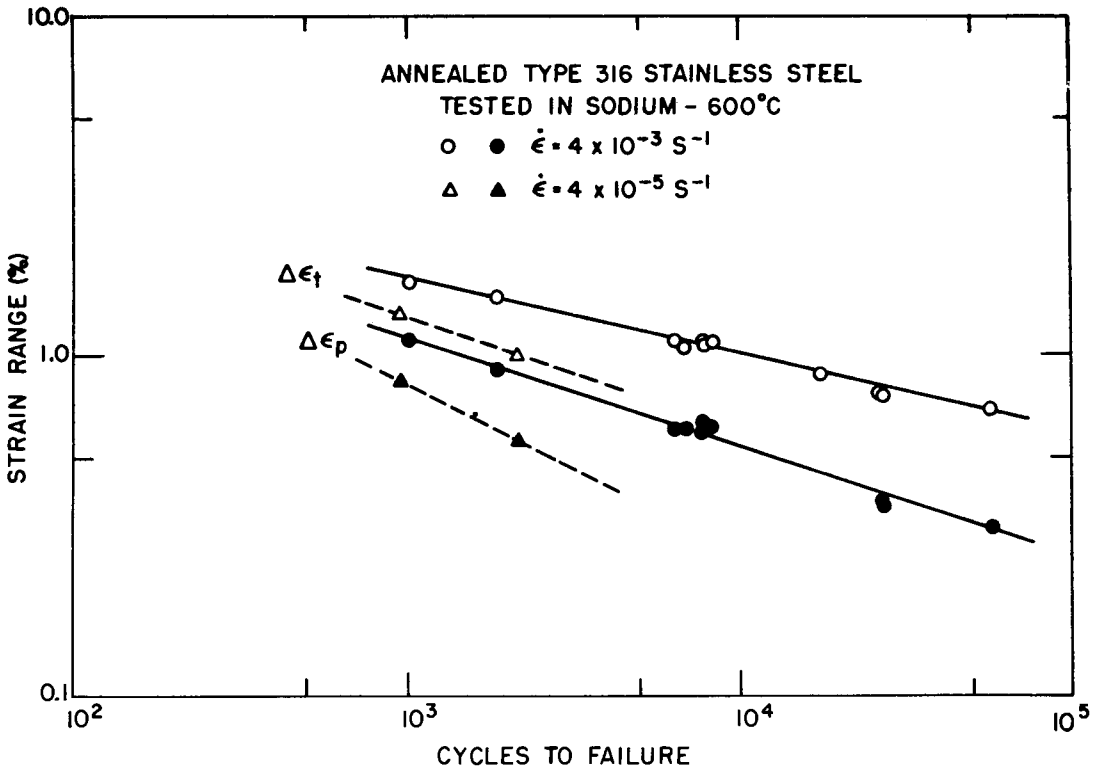

Fig. 2.37. Low-cycle Fatigue Data Obtained in Sodium at Two Strain Rates on Annealed Type 316 Stainless Steel. Neg. No. MSD-63490.

Optical and scanning-electron microscopy are being used for post-test analysis of the cracking mode, fracture surface, and microstructure of the fatigue specimens. The fracture surfaces of the Type 304 stainless steel specimens tested in sodium at a strain rate of 4×10^{-3} s^{-1} have been examined with the scanning-electron microscope. Figure 2.38 shows a typical fracture surface for preexposed material (5000 h at 600°C) after testing in sodium at 600°C. The fracture mode was transgranular as evidenced by the striated surface. The fracture mode was predominantly transgranular for annealed and sodium-exposed Type 304 stainless steel at the three temperatures investigated, viz., 550, 600, and 700°C. A transition from transgranular to intergranular cracking, which tends to occur at higher temperatures and lower strain rates,[40] has not been observed in the present series of tests. Analysis of the fracture mode of specimens from low strain-rate tests is in progress.

As described above and in previous reports,[35,36] the fatigue life of annealed Type 304 stainless steel tested in sodium is similar to that in air, whereas the fatigue life of annealed Type 316 stainless steel is substantially greater in sodium than in air. Also, the fatigue life of Type 316 stainless steel is relatively unaffected by sodium preexposure, whereas significant differences in the fatigue life of annealed and sodium-exposed Type 304 stainless steel have been observed. Attempts are being made to explain these differences in fatigue behavior of the two steels relative to the test environment and pretreatment. Figure 2.39 shows the microstructures from interior regions of specimens after fatigue tests at 700°C. The microstructures in Fig. 2.39a and b are of annealed Types 304 and 316 stainless steel respectively, and those in Fig. 2.39 c and d are of sodium-preexposed material (1500 h at 700°C). Although the carbide precipitation is more pronounced in the preexposed material, considerable precipitation in the grain boundaries and twin boundaries as well as within the grains is observed in all cases shown. The precipitation in the annealed materials apparently occurs during the test period (∿20 h) at 700°C. The additional carbide precipitation

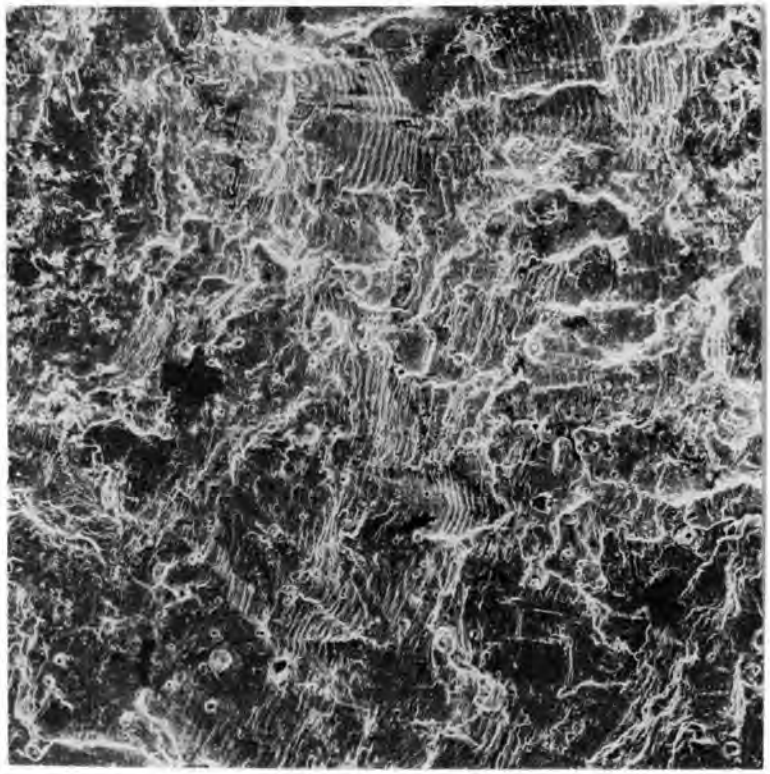

Fig. 2.38. Fracture Surface of Sodium-exposed (5000 h at 600°C) Type 304 Stainless Steel Fatigue Specimen after Testing in Sodium at 600°C ($\Delta\varepsilon_t \sim 1\%$). Scanning-electron microscope, 200X. Neg. No. MSD-63495.

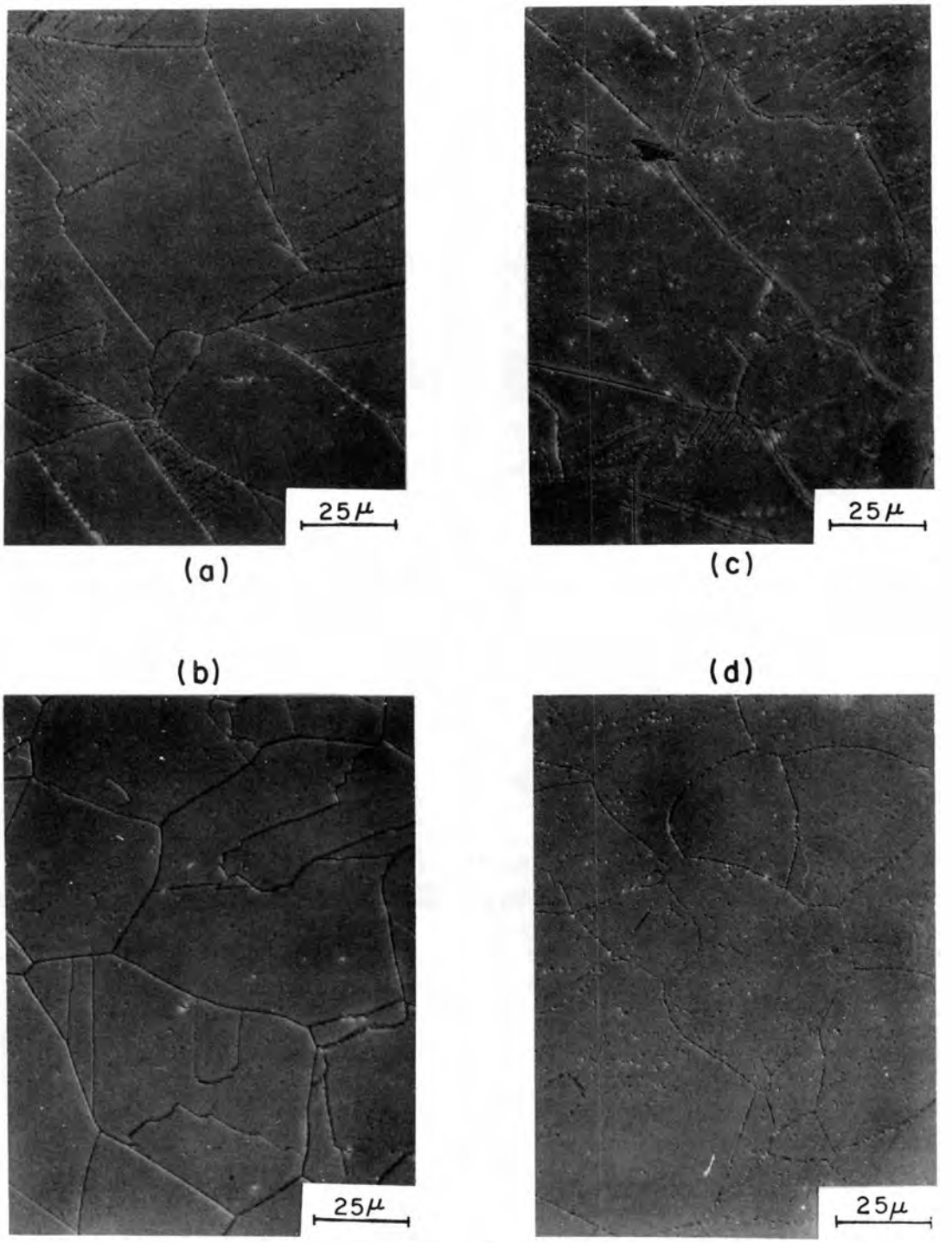

Fig. 2.39. Microstructures of Interior Region of Types 304 and 316 Stainless Steel Specimens after Fatigue Testing in Sodium at 700°C with a Total Strain Range of ∿1.0%. (a) Type 304--annealed, (b) Type 316--annealed, (c) Type 304--preexposed to sodium for 1500 h at 700°C, and (d) Type 316--preexposed to sodium for 1500 h at 700°C. Neg. No. MSD-63496.

at grain-boundaries of the preexposed material does not lead to a change in fracture mode from that of the annealed material for the conditions investigated. The small amount of softening observed in the cyclic stress-strain response[35] for preexposed material is tentatively attributed to coarsening of the carbides.

2.4 REFERENCES

1. A. T. Price and W. J. Elder, "High Strain Fatigue and Crack Propagation in Type 316 Steel," *J. Iron and Steel Institute* 204: 594-598 (1966).

2. R. A. T. Dawson, W. J. Elder, G. J. Hill, and A. T. Price, "High-Strain Fatigue of Austenitic Steels," in *Thermal and High-Strain Fatigue*, Inst. of Metals and Inst. of Metallurgists, London, 1967, pp. 239-269.

3. A. Coles, G. J. Hill, R. A. T. Dawson, and S. J. Watson, "The High-Strain Fatigue Properties of Low-Alloy Creep-Resisting Steels," in *Thermal and High-Strain Fatigue*, Inst. of Metals and Inst. of Metallurgists, London, 1967, pp. 270-294.

4. V. K. Sikka, H. E. McCoy, Jr., M. K. Booker, and C. R. Brinkman, "Heat-to-heat Variation in Creep Properties of Types 304 and 316 Stainless Steels," *J. Pressure Vessel Technol.* 97(J-4): 243-251 (1975).

5. R. E. Peterson, *Stress Concentration Design Factors*, John Wiley and Sons, New York, 1953.

6. H. Neuber, "Theory of Stress Concentration for Shear Strained Prismatical Bodies with Arbitrary Non Linear Stress Strain Law," *J. Applied Mechanics* 28: 544-550 (December 1961).

7. D. T. Raske and Jo Dean Morrow, "Mechanics of Materials in Low Cycle Fatigue Testing," in *Manual on Low Cycle Fatigue Testing*, ASTM STP 465, American Society for Testing and Materials, December 1969, pp. 1-25.

8. *Mechanical Properties Test Data for Structural Materials Quarterly Progress Report for Period Ending April 30, 1976*, Oak Ridge National Laboratory, ORNL-5150, pp. 3-40.

9. *Cases of ASME Boiler and Pressure Vessel Code, Case 1592-7*, American Society of Mechanical Engineers, New York, 1975, p. 389.

10. B. M. Wundt, *Effect of Notches on Low-cycle Fatigue -- A Literature Survey*, ASTM STP 490, American Society for Testing and Materials, 1972.

11. D. T. Raske, "Fatigue Failure Predictions for Plates with Holes and Edge Notches," *J. Testing and Eval.* 1: 394-404 (September 1973).

12. K. Iida, Y. Urabe, and Y. Ando, "Low Cycle Fatigue Strength Reduction Factor for a Mild Steel," lecture presented at the general meeting of the Japan Society of Naval Architecture, November 1971.

13. *Mechanical Properties Test Data for Structural Materials Quarterly Progress Report for Period Ending January 31, 1975,* Oak Ridge National Laboratory, ORNL-5104, pp. 13-30.

14. P. S. Maiya and D. E. Busch, "Grain-boundary Penetration of Type 316 Stainless Steel Exposed to Cesium or Cesium and Tellurium," *Met. Trans.* 6A: 409 (1975).

15. Work performed as a collaborative effort with A. Joshi, Physical Electronics Industries, Inc., Eden Prairie, Minnesota.

16. *Metals Handbook,* Vol. 8, American Society for Metals, Metals Park, Ohio, 1973, p. 425.

17. R. W. Weeks, D. R. Diercks, and C. F. Cheng, *ANL Low-Cycle Fatigue Studies--Program, Results, and Analysis,* Argonne National Laboratory, ANL-8009 (1973).

18. C. R. Brinkman and G. E. Korth, "Heat-to-heat Variations in the Fatigue and Creep-fatigue Behavior of AISI Type 304 Stainless Steel at 593°C," *J. Nucl. Mater.* 48: 293 (1973).

19. M. Gell and G. R. Leverant, *Mechanisms of High-Temperature Fatigue,* ASTM STP 520, American Society for Testing and Materials, 1973, p. 37.

20. R. Raj, "Crack Initiation in Grain Boundaries Under Conditions of Steady-State and Cyclic Creep," *J. Eng. Mater. and Technol.* 98: 139 (1976).

21. J. H. Driver, "The Effect of Boundary Precipitates on the High-Temperature Fatigue Strength of Austenitic Stainless Steels," *Metal Science J.* 5: 47 (1971).

22. J. H. Driver and R. W. K. Honeycombe, "Elevated-Temperature Fatigue of a Nb-stabilized Austenitic Stainless Steel," *J. Iron and Steel Institute* 209: 729 (1971).

23. S. Majumdar and P. S. Maiya, "A Unified and Mechanistic Approach to Creep-fatigue Damage," in *Proc. Second International Conf. on Mechanical Behavior of Materials,* Aug. 16-20, 1976, Boston, Massachusetts, American Society for Metals, Metals Park, Ohio, 1976, p. 924; also Argonne National Laboratory, ANL-76-58 (1976).

24. *Mechanical Properties Test Data for Structural Materials Quarterly Progress Report for Period Ending July 31, 1976*, Oak Ridge National Laboratory, ORNL-5200, pp. 31-43.

25. V. K. Sikka, Oak Ridge National Laboratory, private communication (1976).

26. P. S. Maiya and D. E. Busch, "Effect of Surface Roughness on Low-cycle Fatigue Behavior of Type 304 Stainless Steel," *Met. Trans.* 6A: 1761-1766 (1975).

27. P. S. Maiya, "Considerations of Crack Initiation and Crack Propagation in Low-cycle Fatigue," *Scripta Met.* 9: 1141-1146 (1975).

28. F. Henry, *A. Technique for Monitoring Time Dependent Surface Damage*, General Electric Company Report No. 71-C-338, November 1971.

29. *Mechanical Properties Test Data for Structural Materials Quarterly Progress Report for Period Ending July 31, 1975*, Oak Ridge National Laboratory, ORNL-5106, pp. 24-35.

30. K. Natesan, D. L. Smith, T. F. Kassner, and O. K. Chopra, "Influence of Sodium Environment on the Tensile Behavior of Austenitic Stainless Ste-ls," in *Symp. on Structural Materials for Service at Elevated Temperatures in Nuclear Power Generation*, ASME Winter Annual Meeting, November 30-December 5, 1975, Houston, Texas, American Society of Mechanical Engineers, New York, 1975, pp. 302-315.

31. *Mechanical Properties Test Data for Structural Materials Quarterly Progress Report for Period Ending January 31, 1976*, Oak Ridge National Laboratory, ORNL-5112, pp. 21-35.

32. E. Voce, "The Relationship Between Stress and Strain for Homogeneous Deformation," *J. Inst. of Metals* 79: 537 (1962).

33. D. L. Keller, *Progress on LMFBR Cladding, Structural, and Component Materials Studies During July 1971 through June 1972*, Final Report, Battelle-Columbus Laboratories, BMI-1928, 1972.

34. D. L. Keller, *Progress on LMFBR Cladding, Structural, and Component Materials Studies During July 1970 through June 1971*, Final Report, Battelle-Columbus Laboratories, BMI-1914, 1971.

35. D. L. Smith, G. J. Zeman, K. Natesan, and T. F. Kassner, "Influence of Sodium on the Low-cycle Fatigue Behavior of Types 304 and 316 Stainless Steel," in *Proc. Intl. Conf. Liquid Metal Technology in Energy Production*, Champion, Pennsylvania, May 3-6, 1976, to be published.

36. D. L. Smith, K. Natesan, T. F. Kassner, and G. J. Zeman, "Effects of Sodium on the Low-cycle Fatigue Behavior of Austenitic Stainless Steel," in *Structural Materials for Service at Elevated Temperatures in Nuclear Power Generation*, ASME MPC-1, American Society of Mechanical Engineers, New York, 1975, pp. 290-301.

37. S. S. Manson, *Behavior of Materials Under Conditions of Thermal Stress*, NASA TN-2933, U. of Michigan Press, Ann Arbor, 1952.

38. L. F. Coffin, Jr., *The Problem of Thermal Stress Fatigue in Austenitic Steels at Elevated Temperatures*, Knolls Atomic Power Laboratory, KAPL-1070, 1954.

39. L. F. Coffin, Jr., "Fatigue at High Temperatures," in *Fatigue at Elevated Temperatures*, ASTM STP-520, American Society for Testing and Materials, 1973, p. 5.

40. J. T. Berling and T. Slot, "Effect of Temperature and Strain Rate on Low-Cycle Fatigue Resistance of AISI 304, 316, and 348 Stainless Steel," in *Fatigue at High Temperature*, ASTM STP-459, American Society for Testing and Materials, 1969, p. 3.

3. OAK RIDGE NATIONAL LABORATORY

W. R. Martin

3.1 INTRODUCTION

The ORNL mechanical properties effort comprises several programs. The program Mechanical Properties and Behavior for Structural Materials deals with materials of general applicability to the LMFBR program. Other programs are concerned with the mechanical properties of weldments in LMFBR components, the specific materials of interest for LMFBR steam generators, collection and correlation of mechanical data needed for design on high-temperature LMFBR systems, and materials for the primary circuit and steam generators of HTGR systems.

3.2 MECHANICAL PROPERTIES AND BEHAVIOR FOR STRUCTURAL MATERIALS* — C. R. Brinkman

The objective of this program is to collect mechanical property data and material behavior for LMFBR structural and component materials. Included in the scope of this effort are the following: (1) basic tensile, creep, creep-rupture, and relaxation base-line data that are directly applicable to design criteria and methods for types 304 and 316 stainless steel reference heats and cyclic stress-strain tests performed with emphasis on loading and aging history effects, (2) variations in properties for several heats of types 304 and 316 stainless steel determined to allow establishment of minimum and average values of specific properties and the equation parameters required for design purposes. This work will include determination of property variation of samples from different mill products within a given heat of stainless steel.

3.2.1 Mechanical Property Characterization of Type 304 Stainless Steel Reference Heat — Influence of Strain Rate and Test Temperature on Ductility of Types 304 and 316 Stainless Steel — V. K. Sikka, R. W. Swindeman, C. R. Brinkman and R. L. Stephenson†

*Progress on work performed under 189a, OH050.
†Computer Sciences Division.

3.2.1.1 Three-Dimensional Plots

Effort on developing three-dimensional ductility plots continued during the last quarter. Various ductility indices are plotted as functions of strain rate and test temperature. Both separate and combined plots are being developed for the following tensile and creep ductility indices:

1. total elongation — for creep test total elongation refers to the sum of loading strain and elongation during creep;
2. reduction of area;
3. uniform elongation for tensile tests and strain to onset of tertiary creep for the creep tests. For the combined tensile and creep plot, loading strain is added to the tertiary creep strain. However, for separate plots, tertiary creep strain is plotted with and without adding loading strains.

As a first approximation minimum creep rate is considered as the overall strain rate for creep ductility indices. Data used for type 304 stainless steel are on 25- and 51-mm (1- and 2-in.) plate of the reference heat (9T2796). The high-strain-rate and additional creep data from Steichen's[1,2] and Blackburn's[3] work on heat 55697 are also included.

Figures 3.1 through 3.3 show three-dimensional plots of total elongation, reduction of area, and uniform elongation as functions of log strain rate and test temperature. Each figure shows a high-strain-rate view and a low-strain-rate view. The tensile strain rate varies over eight orders of magnitude, and the test temperature ranges from 50 to 800°C (122-1472°F). These plots show the following:

1. On the high-strain-rate end — Figs. 3.1 through 3.3 — total elongation, reduction of area, and uniform elongation all show high values, which are essentially independent of test temperature.

2. In the tensile strain rate range all three ductility indices show temperature dependence, with a loss in ductility occurring at temperatures above 400°C ($\geq 0.40T_m$), where T_m is the absolute melting point (1673 K). The ductility loss initiation temperature decreases with decreasing strain rate. This is more clearly illustrated in two-dimensional plots for the 25- and 51-mm plates of the reference heat

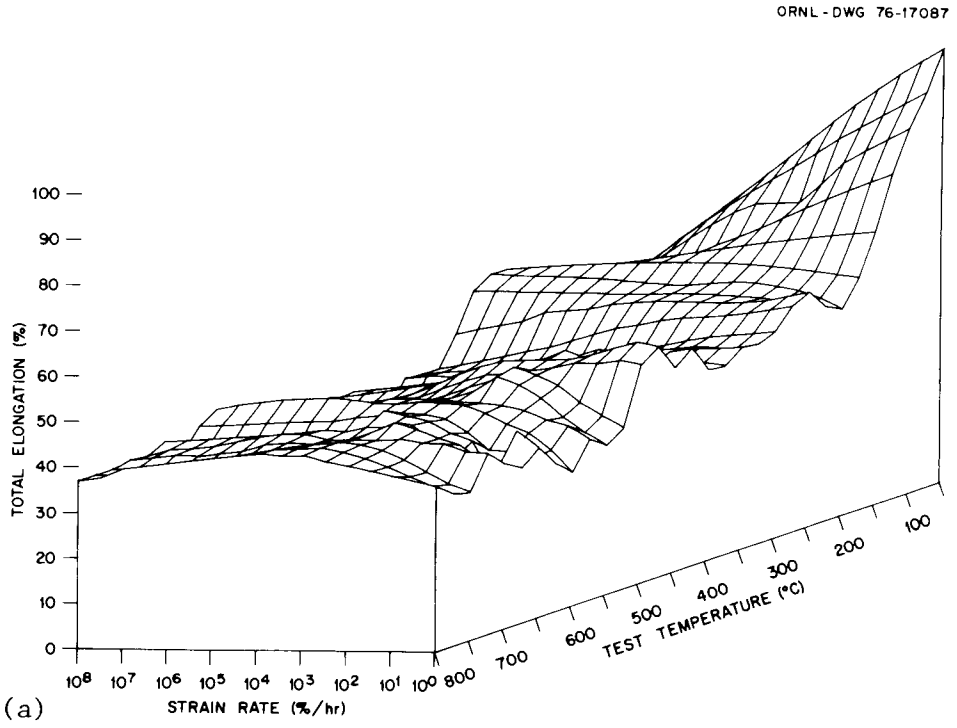

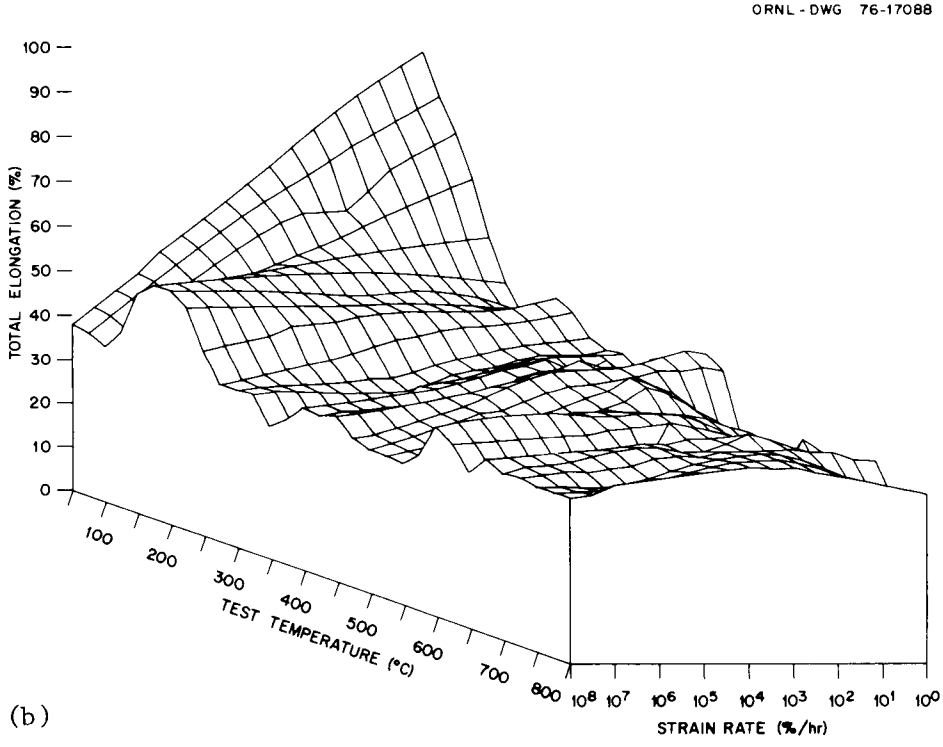

Fig. 3.1. Three-Dimensional Plots of Total Elongation as a Function of Log Strain Rate and Test Temperature for Tensile Data on Type 304 Stainless Steel. (a) Low-strain-rate. (b) High-strain-rate view.

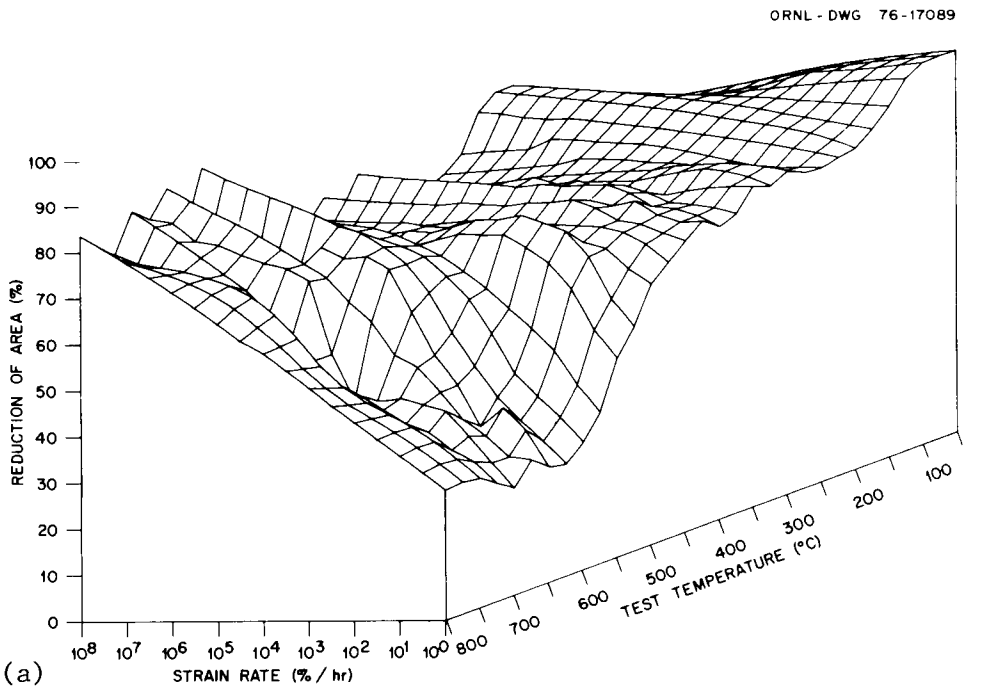

(a)

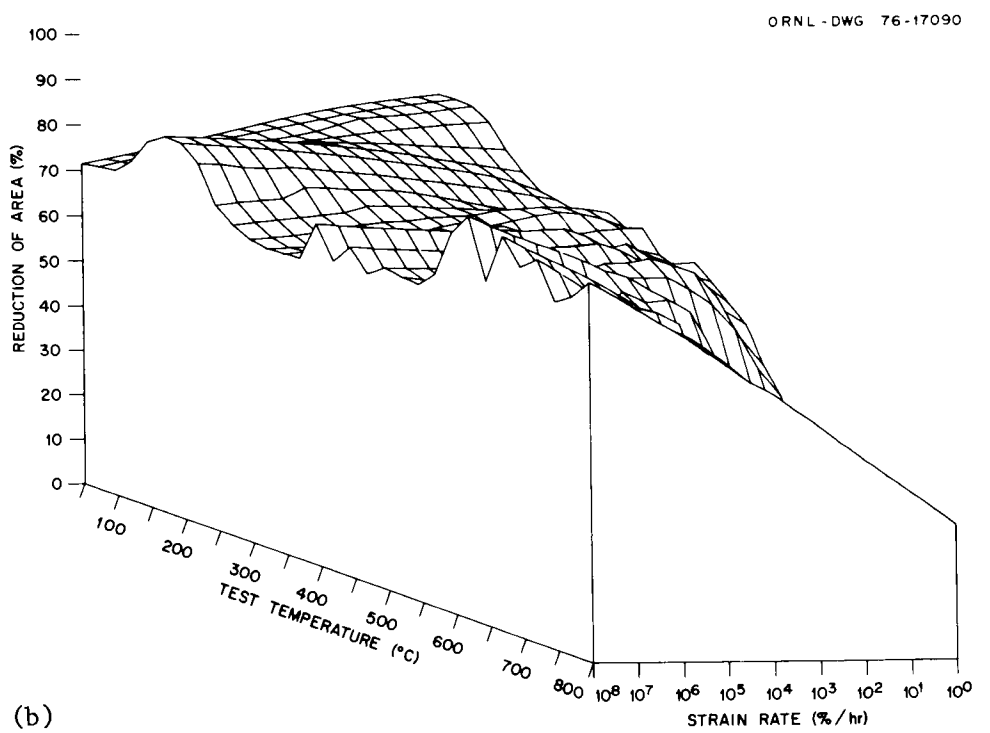

(b)

Fig. 3.2. Three-Dimensional Plots of Reduction of Area as a Function of Log Strain Rate and Test Temperature for Tensile Data on Type 304 Stainless Steel. (a) Low-strain-rate view. (b) High-strain-rate view.

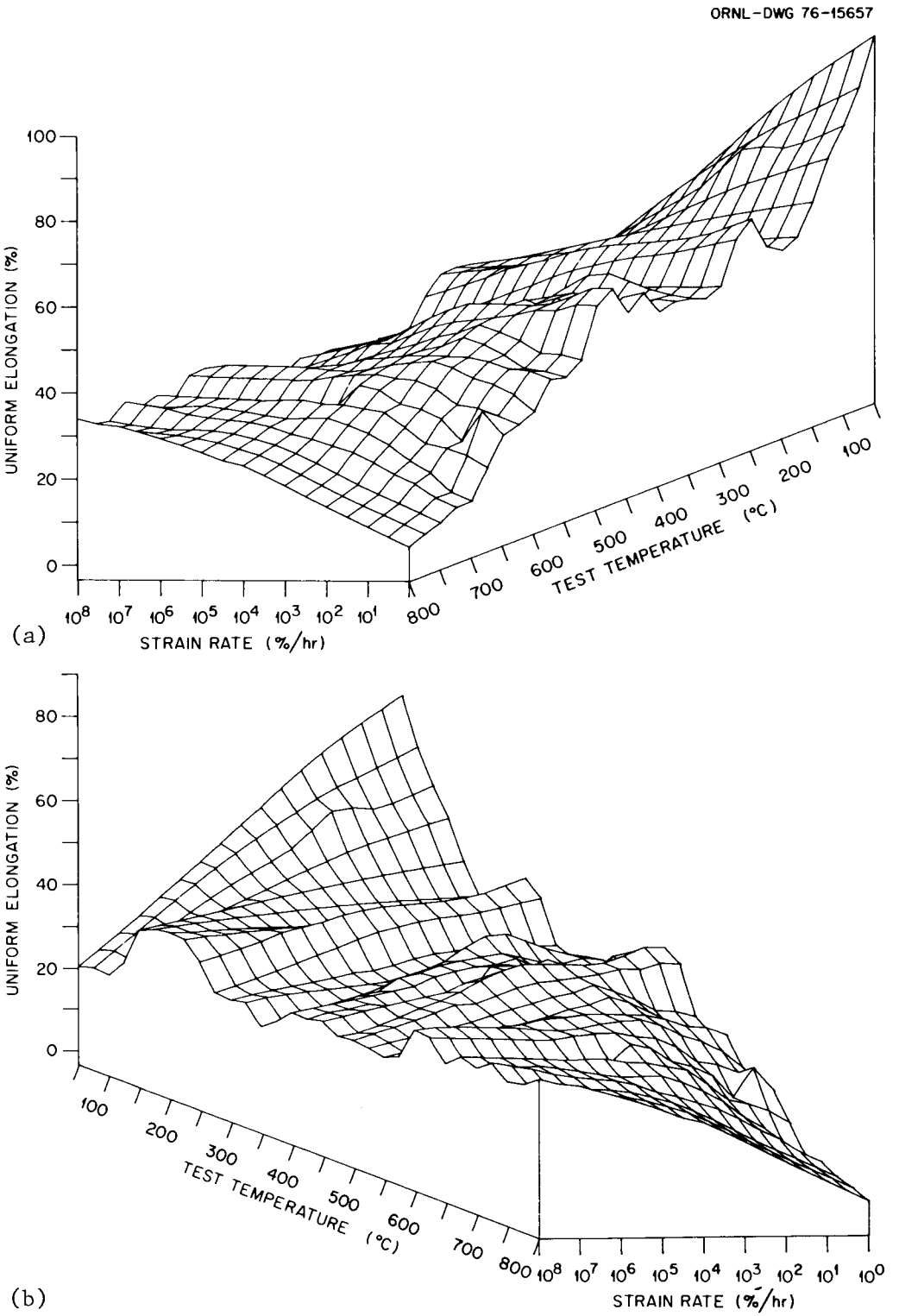

Fig. 3.3. Three-Dimensional Plots of Uniform Elongation as a Function of Log Strain Rate and Test Temperature for Tensile Data on Type 304 Stainless Steel. (a) Low-strain-rate view. (b) High-strain-rate view.

of type 304 stainless steel in Figs. 3.4 and 3.5. The decreasing strain rate lowered not only the ductility loss initiation temperature, but also the ductility value. Isothermal plots showing the strain-rate dependence of various ductility indices for the reference heat of type 304 stainless steel are shown in Figs. 3.6 through 3.8. These figures include both the tensile and creep data. The tertiary creep strain value in Fig. 3.8 includes loading strain.

Figures 3.6, 3.7, and 3.8 show that, except at room temperature, all ductility indices are independent of strain rate for test temperatures up to 427°C ($0.42T_m$). At room temperature, all indices showed a decrease in ductility with increasing strain rate, and this is associated with the increasing amount of martensite formed with increasing strain rates.[4] The ductility indices measured at failure (total elongation and reduction of area) show distinct breaks at strain rate values that decrease with increasing temperature. These break points when joined (Figs. 3.6 and 3.7) give the boundary line for change in fracture mode from transgranular to intergranular. Different fracture mode regions are identified in the figures. The region of intergranular fracture with limited recovery shows a decrease in ductility with increasing strain rate, because intergranular cracks once nucleated will propagate without any means of relaxing stresses at the tip of the crack. However, at temperatures where stresses at the crack tip can be relaxed by recovery and recrystallization, a large number of cracks can form without propagating, and thereby not only higher but essentially strain-rate-independent ductility values result.

Figure 3.8 shows that strain to onset of tertiary creep and/or tensile test uniform elongation also shows break points at various strain rates. At strain rates below the break point the tensile and creep instability strain values decrease with decreasing strain rate. The line joining the strain-rate break points describes the boundary below which the instability initiation strain decreases with decreasing strain rate. Regions of instability with and without recovery are marked in Fig. 3.8. For comparison, we have also included in Fig. 3.8 the line for fracture mode change from Figs. 3.6 and 3.7. Note that the instability mode change

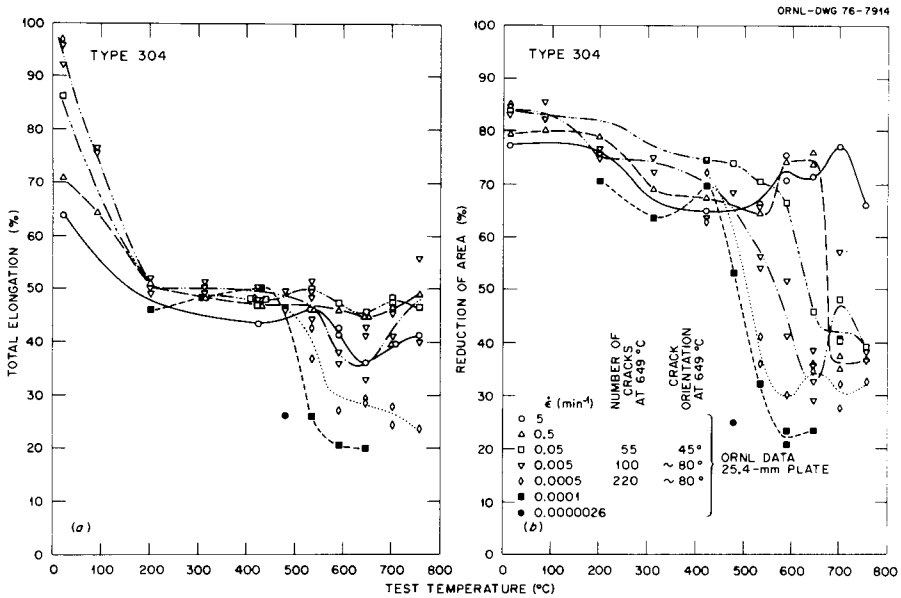

Fig. 3.4. Tensile Total Elongation and Reduction of Area as Functions of Test Temperature for 25-mm (1-in.) Plate of the Reference Heat of Type 304 Stainless Steel.

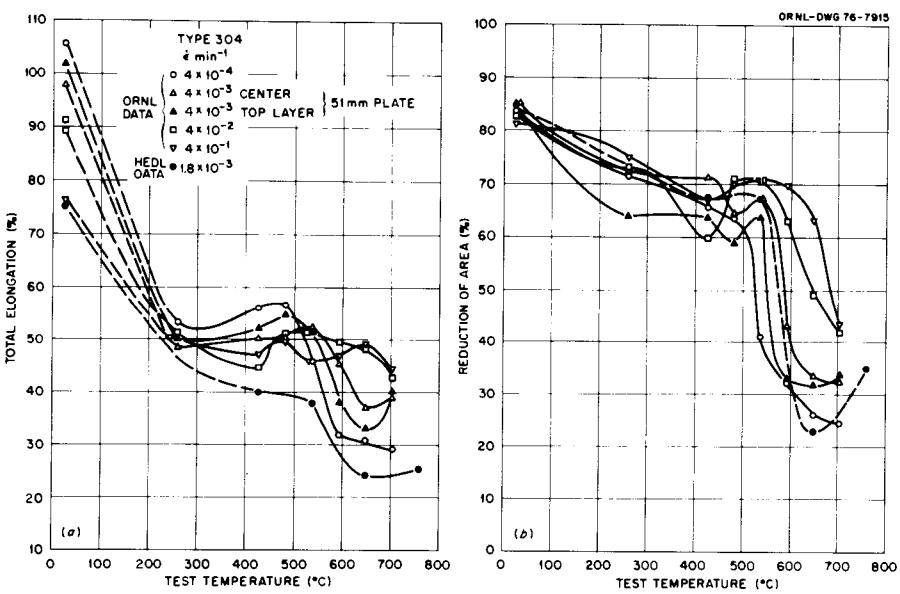

Fig. 3.5. Tensile Total Elongation and Reduction of Area as Functions of Test Temperature for 51-mm (2-in.) Plate of the Reference Heat of Type 304 Stainless Steel.

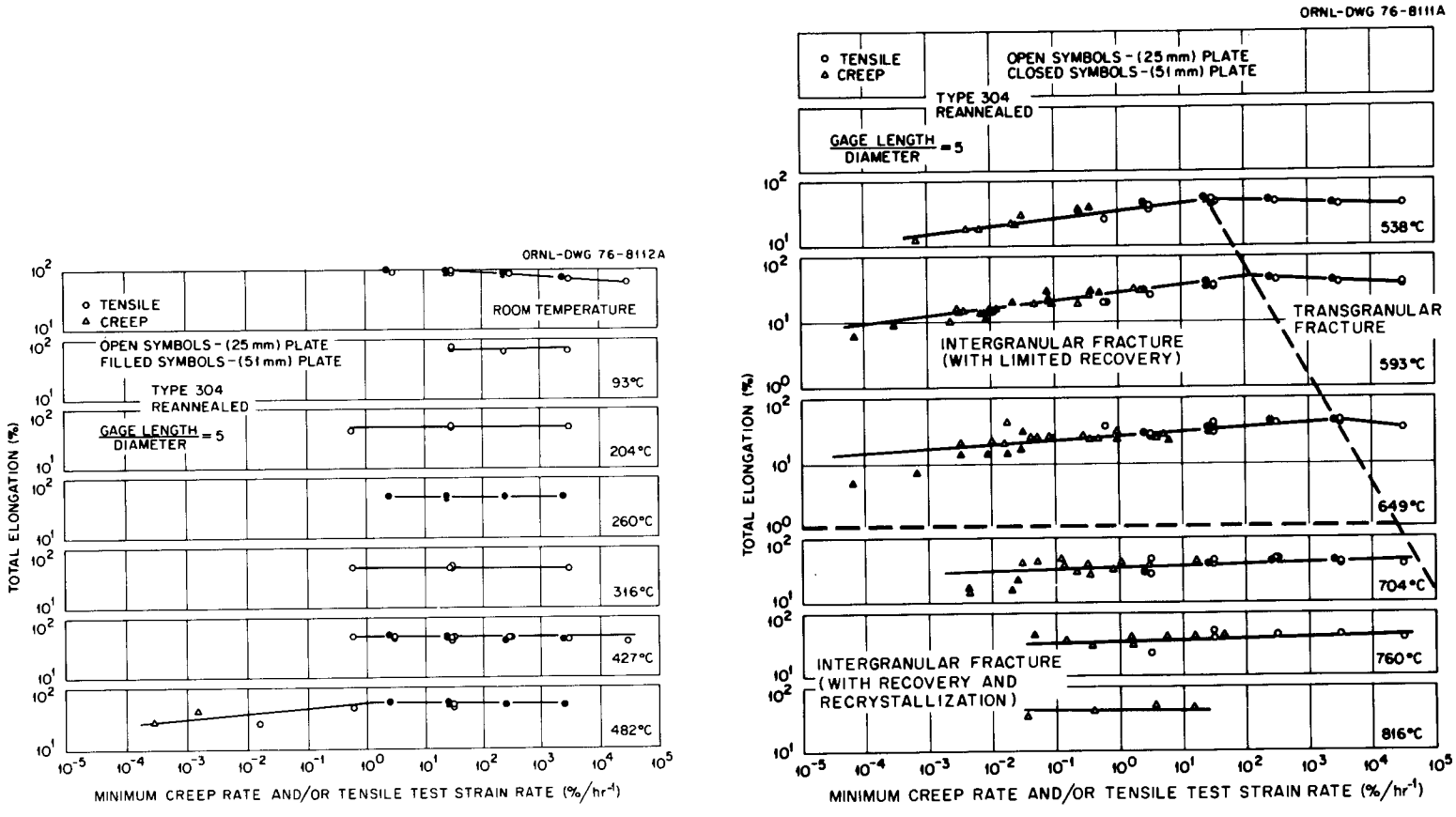

Fig. 3.6. Creep and Tensile Total Elongation as a Function of Minimum Creep Rate and/or Tensile Test Strain Rate for 25- and 51-mm (1- and 2-in) Plates of the Reference Heat of Type 304 Stainless Steel. Note the identification of various fracture modes at the higher temperatures.

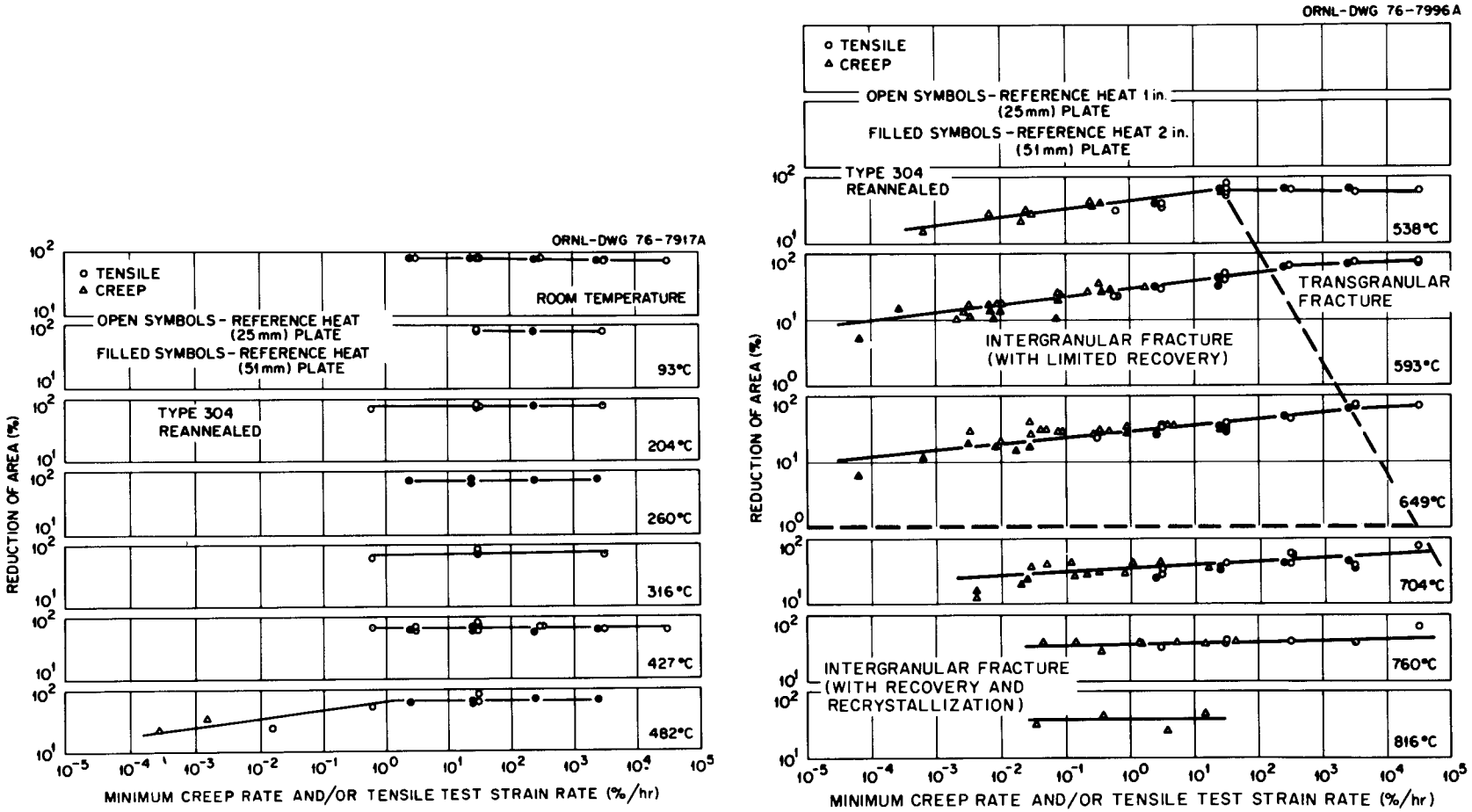

Fig. 3.7. Plots of Creep and Tensile Reduction of Area as a Function of Minimum Creep Rate and/or Tensile Test Strain Rate for 25- and 51-mm (1- and 2-in.) Plates of the Reference Heat of Type 304 Stainless Steel. Note the identification of various fracture modes at the higher temperatures.

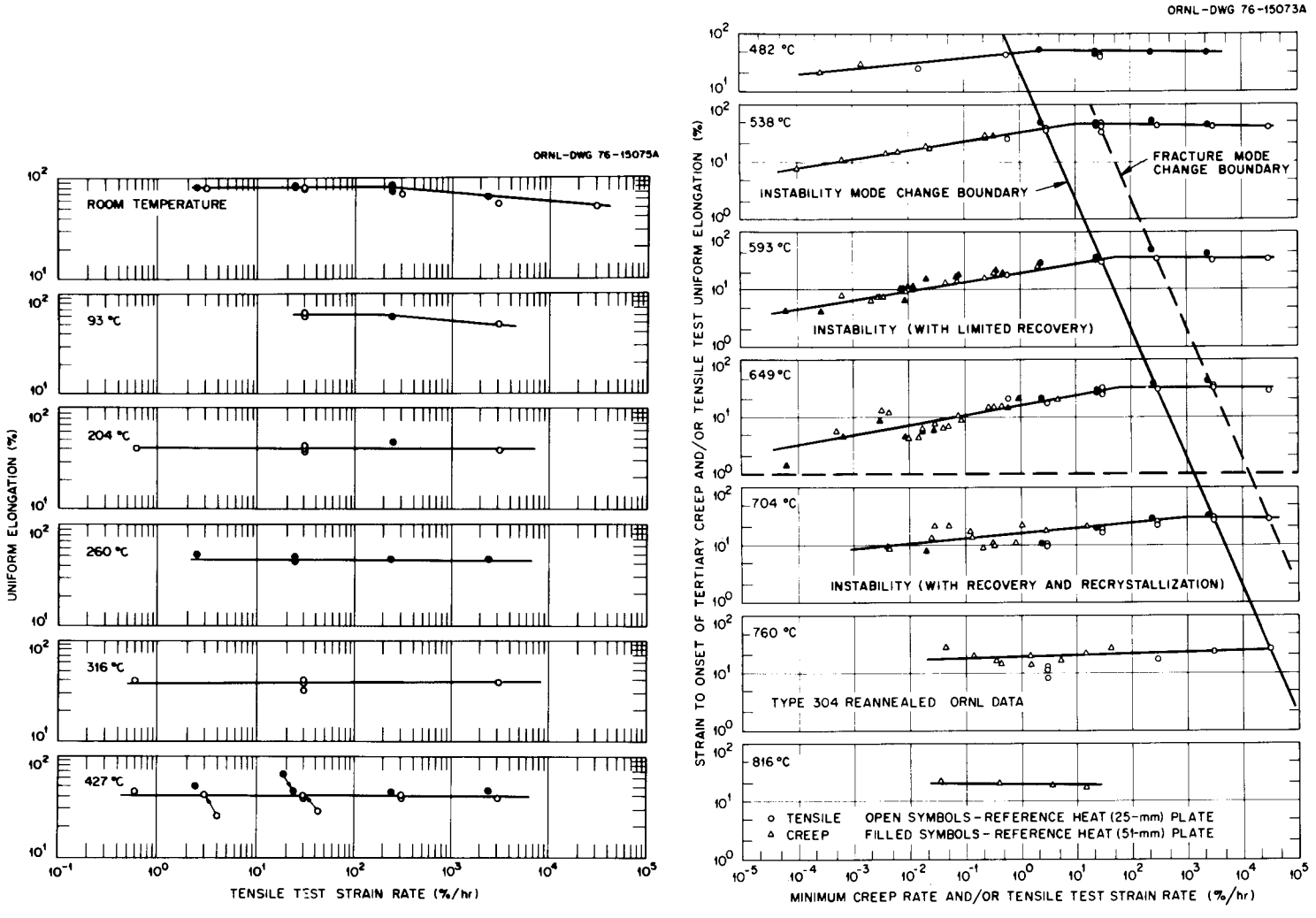

Fig. 3.8. Strain to Onset of Tertiary Creep and/or Tensile Uniform Elongation as a Function of Minimum Creep Rate and/or Tensile Strain Rate. Note the identification of various instability regions in the creep range.

boundary line goes through an order of magnitude lower strain rates than observed for change in fracture mode. Reasons and the significance of such differences between the two boundaries are not clear at present. However, crack density data listed in Fig. 3.4(b) agree well with the regions marked in Figs. 3.6 and 3.8.

3.2.1.2 Choice of Ductility Indices for Strain Limits

To properly choose ductility indices for defining strain limits, we have examined strain-rate and temperature dependence of the following ductility indices:

TE = total elongation,

RA = reduction of area,

e_{ss} = strain to onset of tertiary creep (excludes loading strain),

$e = \dot{e}_m t_r$, where $\dot{e}_m$ is minimum creep rate and t_r is time to rupture.

All four indices for 25- and 51-mm plate of the reference heat of type 304 stainless steel are plotted as functions of minimum creep rate in Figs. 3.9 and 3.10 for various test temperatures. The important observations from these plots are as follows:

1. Total elongation and reduction of area have the same magnitude and similar strain-rate dependence for all test temperatures.

2. Strain to onset of tertiary creep and $e = \dot{e}_m t_r$ have the same magnitude and a similar strain-rate dependence for test temperatures of 482, 538, and 593°C (900, 1000, and 1100°F).

3. At test temperatures of 649°C and higher, the value of e starts showing slightly higher values than e_{ss}. The higher value of e as compared with e_{ss} arises from increased time spent during the tertiary stage. The tertiary creep stage, which consists of accelerated creep, occurs as a result of nucleation and growth of intergranular cracks and/or metallurgical changes. At test temperatures of 649°C and higher, recovery and recrystallization are possible, and these processes delay the growth and interlinkage of intergranular cracks by relieving stresses at the tips of cracks. Therefore, long tertiary creep stages are expected and observed in creep tests at 649°C (1200°F) and higher.

4. The differences between TE, RA and e_{ss}, e decreases with

ORNL-DWG 76-17071

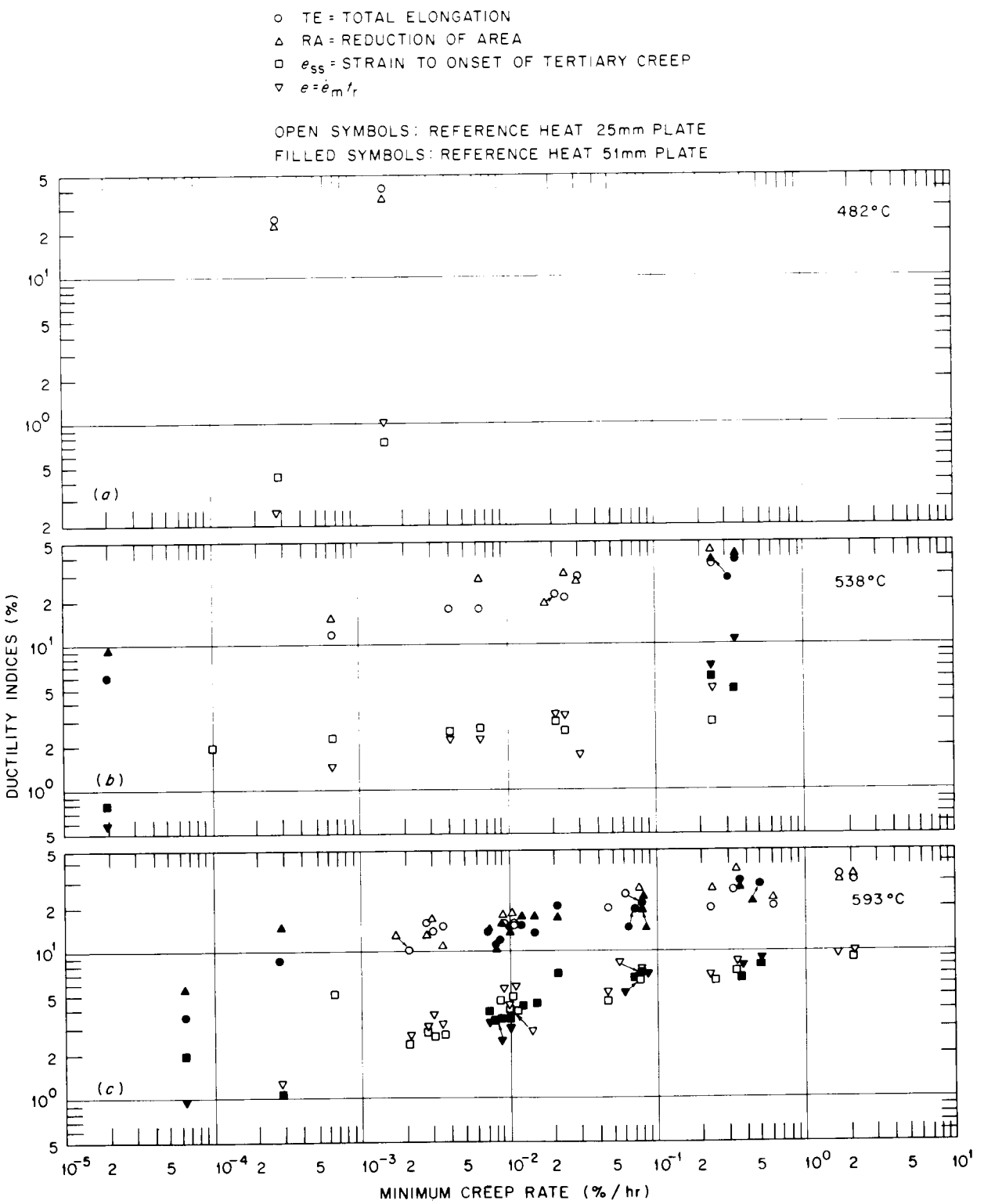

Fig. 3.9. Creep Ductility Indices as Functions of Minimum Creep Rate for 25- and 51-mm (1- and 2-in) Plate of the Reference Heat of Type 304 Stainless Steel. (a) 482°C (900°F). (b) 538°C (1000°F). (c) 593°C (1100°F).

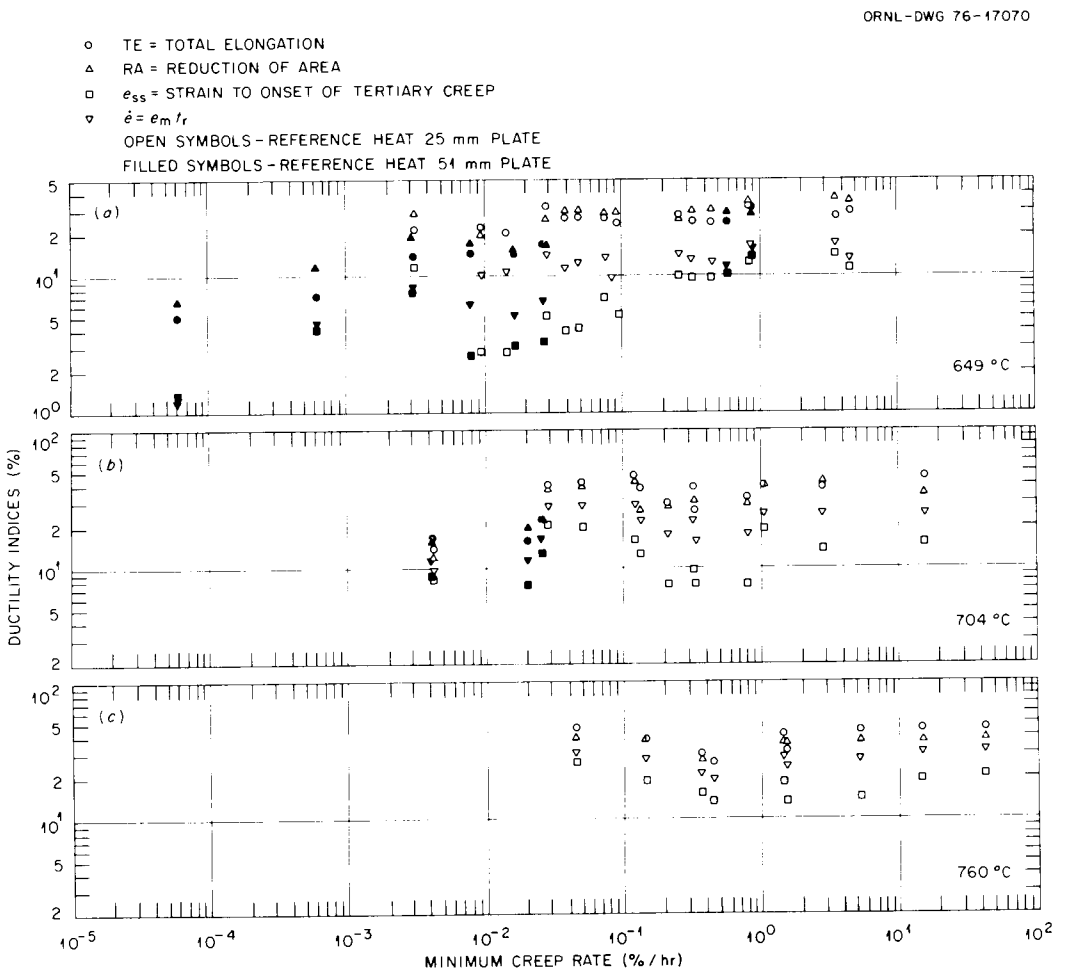

Fig. 3.10. Creep Ductility Indices as Functions of Minimum Creep Rate for 25- and 51-mm (1- and 2-in.) Plate of the Reference Heat of Type 304 Stainless Steel. (a) 649°C (1200°F). (b) 704°C (1300°F). (c) 760°C (1400°F).

increasing test temperature. The larger differences at lower temperature exist by the nature of stresses required at these temperatures to reach steady-state creep in reasonable test duration. For the similar creep rates plasticity on loading decreases with increasing test temperature.

5. Results in Fig. 3.9 show that since e_{ss} and e have similar magnitudes and strain-rate dependences, e can be used as a possible index for defining strain limits. The additional reason for selecting e is the vast amount of minimum creep rate and time to rupture data available in the literature, while a large number of creep curves are

required if e_{ss} is to be used for strain limits. Furthermore, since e and e_{ss} have similar magnitudes, e can be considered as a measure of the instability point.

6. The similarity in behavior of TE and RA suggest that either of the indices could be used for setting a failure limit. However, Dieter[5] points out that reduction of area is not a true material property, but only an indicator of the fracture tendency in a certain mode of testing. The total elongation, on the other hand, is sensitive to the ratio d/l, where d and l are the diameter and gage length of the specimen. Low-stress creep tests show almost no necking, and therefore specimen dimension effects on creep total elongation become negligible. Therefore, TE should be a possible index for a failure limit.

Figure 3.11 shows that the discussion presented above also applies to Blackburn[3] data on heat 55697 of type 304 stainless steel. Figure 3.12 shows the excellent agreement between e values calculated from long-term (65,000-hr) AR-2 creep data[6] and the ORNL trend line observed for e_{ss} values from creep curves and e values calculated from $\dot{e}_m$ and t_r.

Plots in Fig. 3.13 shows that the discussion presented above in favor of e as an index for strain limits also holds true for the Blackburn[3] data on type 316 stainless steel.

3.2.1.3 Summary and Conclusions

1. Three-dimensional plots of total elongation, reduction of area, and uniform elongation as functions of log strain rate and test temperature were completed for the high-strain-rate and nominal-strain-rate data on type 304 stainless steel.

2. The three-dimensional plots provide an overall strain rate and temperature dependence of various ductility indices. However, several two-dimensional plots were needed to examine the details in some parts of the three-dimensional plots.

3. The isothermal plots of total elongation and reduction of area for both creep and tensile data were used to identify boundaries showing changes in fracture mode from transgranular to intergranular. The isothermal plots of tertiary creep strain and tensile uniform elongation

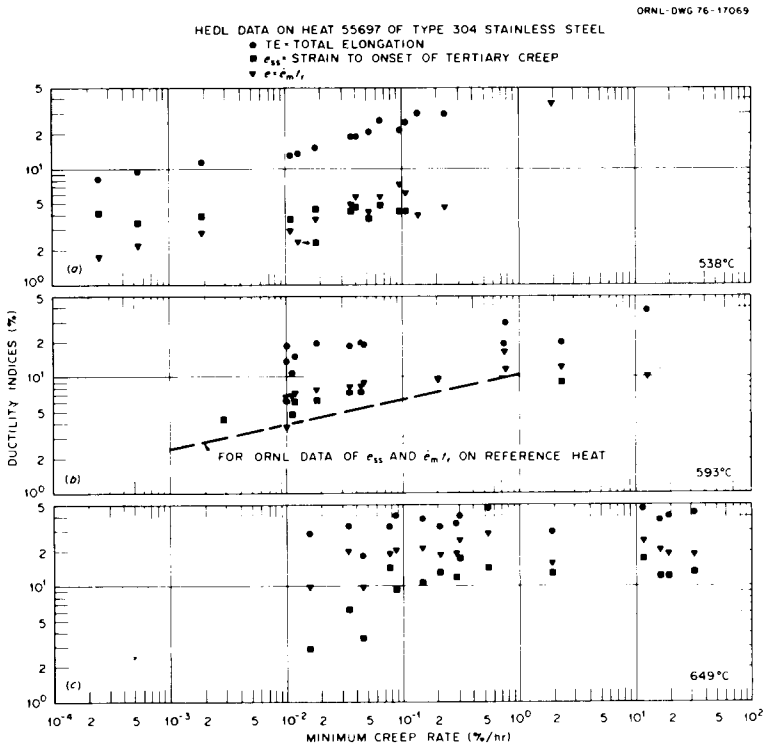

Fig. 3.11. Creep Ductility Indices as Functions of Minimum Creep Rate for Blackburn Data on Heat 55697 of Type 304 Stainless Steel. (a) 538°C (1000°F). (b) 593°C (1100°F). (c) 649°C (1200°F).

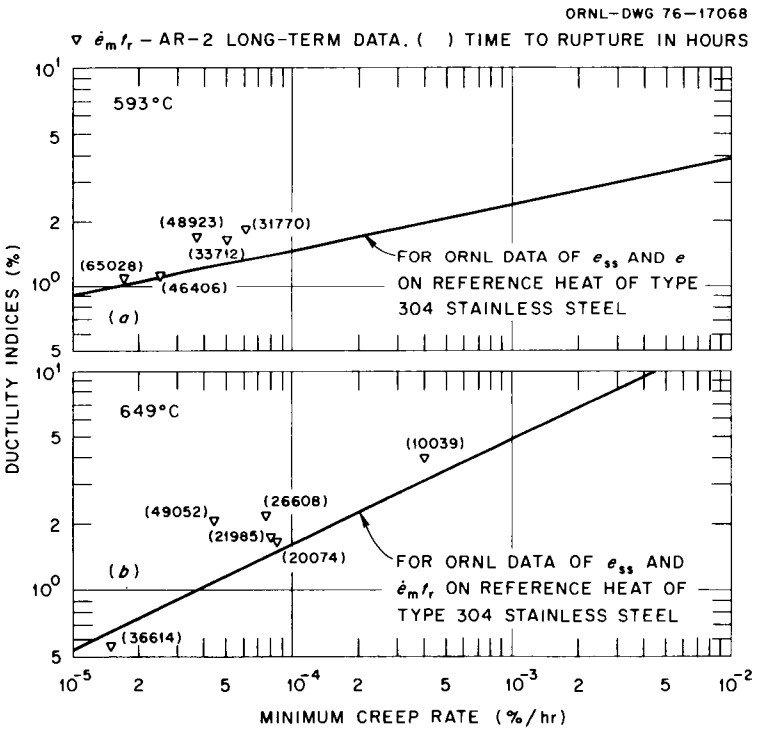

Fig. 3.12. Comparison Between the ORNL Trend for the Reference Heat and the Longest Term AR-2 Data on Type 304 Stainless Steel. (a) 593°C (1100°F). (b) 649°C (1200°F).

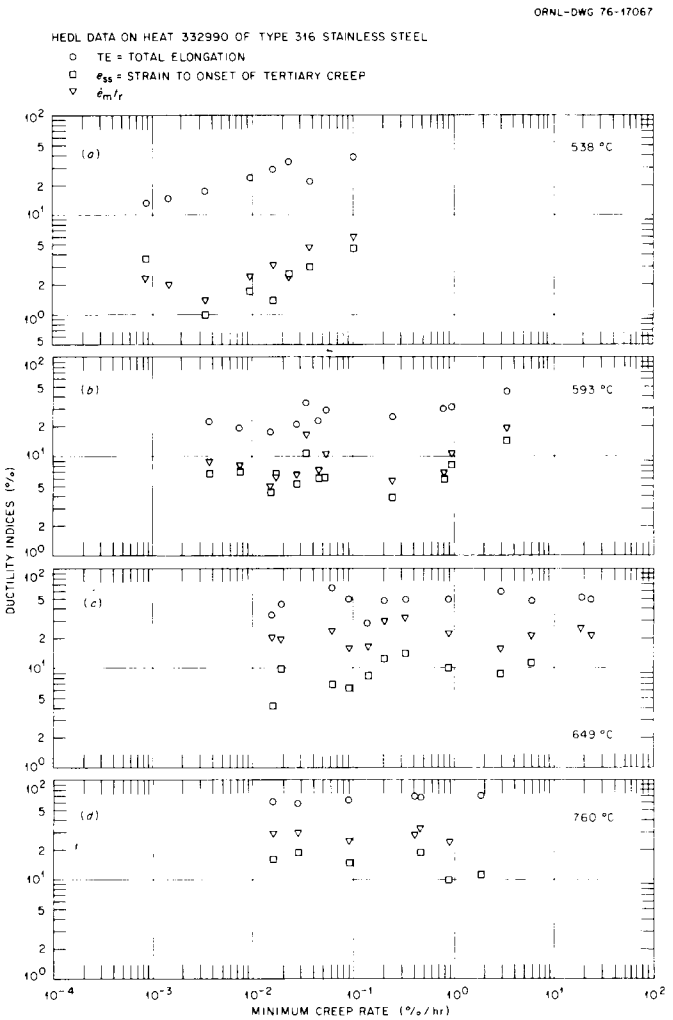

Fig. 3.13. Creep Ductility Indices as Functions of Minimum Creep Rate for Blackburn Data on Heat 332290 of Type 316 Stainless Steel. (a) 538°C (1000°F). (b) 593°C (1100°F). (c) 649°C (1200°F). (d) 760°C (1400°F).

were used to identify boundaries showing changes in instability mode from strain rate independent to strain rate dependent.

4. The magnitude and strain-rate dependence of tertiary creep strain and the strain e obtained from the product of minimum creep rate and time to rupture indicated that the latter could be used for strain limits.

5. The use of e for strain limits was further supported by the availability of a large amount of minimum creep rate and time to rupture data in the literature, as opposed to only limited availability and access to actual creep curves if strain to onset of tertiary creep is considered for strain limits.

3.2.2 Mechanical Property Characterization of Type 316 Stainless Steel Reference Heat — V. K. Sikka, R. H. Baldwin, and E. B. Patton

The reference heat of type 316 stainless steel was air melted in a 200-ton electric furnace at Republic Steel's No. 4 melt shop of the Steel Division, Canton, Ohio. The heat was made in February 1974 and was intended to meet the ORNL-MC-316 specification.[7] The ladle analysis in Table 3.1 shows that the chemical analysis of the reference heat was in close agreement with ORNL-MC-316, RDT, and *Nuclear Systems Materials Handbook*[8] (NSMH) specifications. Various product forms were made from this heat, and here we describe the work being carried out at ORNL on mechanical property characterization of these products.

Table 3.1. Comparison of Ladle Chemical Analysis for the Reference Heat (8092297) of Type 316 Stainless Steel with ORNL, RDT, and *Nuclear Systems Material Handbook* Specifications

Chemical Element	Content, wt %			
	RDT Standards	NSMH	ORNL-MC-316	Ladle Analyses
C	0.04–0.10	0.08 max	0.050–0.080	0.057
Mn	2 max	2.00 max	1.50–2.00	1.86
P	0.030 max	0.045 max[a]	0.02–0.03	0.024
S	0.030 max	0.030 max	0.010–0.025	0.019
Si	0.75 max	1.00 max[b]	0.030–0.60	0.58
Ni	11.00–14.00	10.00–14.00[c]	13.25–13.75	13.48
Cr	16.00–18.00	16.00–18.00	16.5–17.5	17.25
Mo	2.0–3.0	2.00–3.00	2.20–2.50	2.34
Co	None	None	0.10 max	0.02
Cu	None	None	0.20 max	0.10
N	None	None	0.05 max	0.03
Nb + Ta	d	None	0.020 max	e
B	None	None	0.003 max	0.0005
Ti	None	None	0.020 max	0.02
Pb				0.003
Sn				0.004
Al			Not required	

[a]0.030 max for seamless pipe (SA 376).

[b]0.75 max for seamless pipe (SA 376).

[c]11.00–14.00 for seamless pipe (SA 376).

[d]The Nb + Ta content shall be not less than ten times the carbon content and not more than 1.00%.

[e]Not detectable at level of 0.01 wt %.

3.2.2.1 Product Form Characterization

The product forms being studied include, plate, pipe, and bar of various sizes, listed in Table 3.2. They were fabricated as follows:

Plate Product — The 16-mm-thick plates were produced from 635- by 685-mm ingots. These ingots were bloomed to 457- by 102-mm blooms. Each bloom was cut into three sections and each section was hot rolled to plate approximately 100- by 200-mm long. the 25- and 51-mm-thick plates were processed similarily except that the ingot size was 508 by 1041 mm and it was bloomed to 863- by 127-mm slabs. All plates were solution annealed at 1065 ± 30°C (1950 ± 50°F) before shipping.

Pipe Products — All pipes except 406- and 711-mm-diam pipe were produced at the Ellwood City works of U.S. Steel. Seamless pipe was produced by the Mannesman process, in which the round, after being heated to temperature, is squeezed between rotating rolls while being rotated at high speed and drawn through the mill over a piercing point located between the rolls. After piercing the pipe is reduced by either plug rolling and reeling or bar rolling and sizing. The 406- and 711- by 10-mm-wall pipes were produced at Rollmet by roll extrusion, a reduction process at room temperature that involves intermediate annealing. The 406-mm pipe was produced by external roll extrusion in which the die ring works from the outside, increasing the length and decreasing the thickness while maintaining constant inside diameter. The 711-mm-diam by 10-mm-wall pipe was produced by internal roll extrusion, in which solid rollers inserted within the forged ring apply pressure on the internal surfaces, while a tight-fitting external die ring maintains the outside diameter within very close tolerances. All pipe was solution annealed at 1065 ± 30°C (1950 ± 50°F).

Bar Products — All bars were produced from 635- by 689-mm ingots, bloomed to 229 by 197 mm, cut into multiples, and hot-rolled through a series of intermediate breakdowns to slightly above final product diameter. All bars were solution annealed at 1065 ± 30°C (1950 ± 50°F) and subsequently straightened, turned, and ground to final size. The bars being investigated are 25, 51, and 64 mm (1, 2, and 2.5 in.) in diameter.

Table 3.2. Product Form, Size, and Grain Sizes of Various Products of Reference Heat (8092297) of Type 316 Stainless Steel

Product Form	Size mm(in.)	Grain Size, ASTM (μm)							
		As-Received Condition				Reannealed Condition			
		Longitudinal		Transverse		Longitudinal		Transverse	
		With Twins	Without Twins	With Twins	Without Twins	With Twins	Without Twins	With Twins	Without Twins
Plate	16 (5/8)	6.2 (37)	5.3 (50)	6.4 (34)	5.4 (48)	5.5 (46)	3.6 (90)	5.8 (41)	5.0 (56)
Plate	25 (1)	6.2 (36)	4.2 (74)	6.1 (38)	4.2 (74)	6.3 (35)	4.2 (74)	5.5 (47)	4.2 (74)
Plate	51 (2)	5.3 (50)	4.2 (74)	4.8 (59)	4.0 (79)	5.3 (50)	4.2 (74)	4.8 (59)	3.8 (85)
Pipe[a]	114 OD × 13 wall (4 1/2 × 1/2)			not measurable 6.3 (35) not measurable	5.0 (56)			not measurable 6.1 (38) 5.1 (53)	4.2 (74) 2.5 (130)
Pipe[a]	219 OD × 13 wall (8 5/8 × 1/2)			6.0 (39) 6.6 (32) 6.6 (32)	4.0 (78) 4.8 (59) 4.4 (68)			6.3 (35) 6.0 (40) 6.2 (37)	4.8 (59) 4.8 (59) 4.2 (73)
Pipe[a]	406 OD × 10 wall (16 × 0.4)			6.1 (38) 6.1 (38) 6.1 (38)	4.8 (59) 3.8 (85) 4.2 (73)			6.1 (38) 5.3 (50) 6.2 (37)	4.0 (78) 3.5 (93) 4.4 (68)
Pipe[a]	711 OD × 10 wall (28 × 0.4)			6.5 (36) 5.1 (53) 5.3 (51)	4.0 (78) 3.5 (93) 3.5 (93)			5.4 (48) 5.5 (45) 5.0 (56)	3.7 (85) 3.5 (93) 2.9 (115)
Bar	25 (1)	6.2 (37)	4.2 (73)	6.0 (40)	4.2 (73)	6.3 (35)	3.7 (86)	6.2 (37)	4.4 (68)
Bar[a]	51 (2)	5.5 (46)	3.1 (108)	6.1 (38) 5.7 (44)	4.4 (68) 3.5 (93)	5.4 (48)	3.5 (92)	5.9 (41) 4.8 (58)	4.0 (79) 3.2 (102)
Bar[a]	64 (2.5)	5.7 (44)	4.0 (78)	5.7 (44) 6.0 (40)	4.0 (78) 3.5 (93)	5.9 (41)	3.5 (92)	5.6 (45) 5.9 (41)	4.0 (78) 3.7 (85)

[a]The three lines of entries for each pipe size are, in order, for the inner edge, the midwall, and the outer edge. The second transverse values for the larger bars are for the outer edge.

3.2.2.1.1 Chemical Analysis. The vendor analyses along with the ORNL check analyses on several products are summarized in Table 3.3. For comparison the ORNL-MC-316 specification and ladle analysis are also included. The chemical analysis of all ten products is essentially the same.

3.2.2.1.2 Microstructure. Optical microstructure is shown in Figs. 3.14 through 3.23 for various product forms of the reference heat in both as-received and reannealed conditions. Grain sizes were measured[9] from these micrographs and are summarized in Table 3.2. Grain sizes for pipe product were measured at the inner surface, midwall, and outer surface. The grain size at the outer surface was generally larger than at the other two locations for both as-received and reannealed conditions. The outer surface of the 51- and 64-mm bars also showed coarser grain size in both mill- and laboratory-annealed conditions. In general, none of the products showed unusual or excessive grain growth on reannealing for 0.5 hr at 1065°C (1950°F).

3.2.2.1.3 Hardness Studies. Previous studies[10–13] on product form characterization of type 304 stainless steel indicated that the bars were subjected to greater hardness variation across the section than other products. Therefore, bar products of the reference heat of type 316 stainless steel were also subjected to careful hardness traverses. These are shown in Fig. 3.24. The 51- and 64-mm-diam bars showed hardness gradients in the as-received condition. The 25-mm-diam bar did not, but it showed a large variation in hardness, indicating a highly inhomogenous product. Reannealing for 0.5 hr at 1065°C removed hardness gradients and variations and lowered the average values.

3.2.2.1.4 Tensile Properties. The tensile test matrix for product form characterization of the reference heat is as follows:

1. For each product form and condition one specimen will be tested at a strain rate of 0.004/min at each test temperature.

2. For as-received material, the tests will be at room temperature and 93, 204, 316, 427, 538, and 649°C.

Table 3.3. Summary of Chemical Analysis for Variance Product Forms of Reference Heat (8092297) of Type 316 Stainless Steel

Chemical Element	ORNL-MC-316 Specification	Ladle Analysis	Concentration, wt %												
			Vendor Analysis for Various Product Forms and Size in mm										ORNL Check Analysis		
			Plates			Pipe				Bar			Plate	Pipe	
			16	25[a]	51[b]	13 × 114[c]	13 × 219[d]	10 × 406[d]	10 × 711[e]	25	51	64	16	10 × 406	10 × 711
C	0.050–0.080	0.057	0.060	0.059–0.060	0.062–0.065	0.061–0.065	0.061–0.68	0.01–0.065	0.065–0.07	0.060	0.051	0.054	0.0645	0.064	0.066
Mn	1.50–2.00	1.86	1.88	1.84–1.86	1.82–1.85	1.86	1.85–1.87	1.75–1.81	1.77–1.84	1.85	1.87	1.86		1.75	1.6
P	0.02–0.03	0.024	0.023	0.024	0.022–0.024	0.023–0.024	0.026–0.027	0.04–0.20	0.015–0.02	0.024	0.030	0.024	0.022	0.020	0.022
S	0.01–0.025	0.019	0.020	0.018	0.018–0.020	0.018	0.018	0.010–0.013	0.012–0.014	0.019	0.018	0.019	0.0188	0.018	0.019
Si	0.30–0.60	0.58	0.62	0.57–0.58	0.57–0.58	0.57–0.59	0.56–0.58	0.58–0.60	0.55–0.58	0.58	0.53	0.60	0.51	0.65	0.62
Cu	0.20 max.	0.10	0.08	0.10	0.08	0.10	0.10–0.11	0.05–0.14	0.05–0.13	0.09	0.09	0.08	0.12	0.04	0.03
Ni	13.25–13.75	13.48	13.40	13.40–13.45	13.30–13.40	13.50–13.60	13.48–13.50	12.80–12.95	12.65–12.80	13.70	13.45	13.50	13.86	13.50	13.3
Cr	16.5–17.5	17.25	17.30	17.15	16.90–17.15	17.10–17.20	17.07–17.20	17–50	17.18–17.40	17.10	17.28	17.19	16.46	17.50	16.8
Mo	2.20–2.50	2.34	2.34	2.34	2.29–2.34	2.34	2.32–2.35	2.34–2.41	2.18–2.37	2.35	2.32	2.34	2.44	2.38	2.38
Ti	0.020 max.	0.02	<0.01	<0.01	<0.01	0.020	0.01–0.02	<0.01–0.01	<0.01–0.01	0.01	0.02	0.02	<0.01	<0.01	<0.01
Co	0.10 max.	0.02	0.02	0.02	0.01	<0.01	<0.01			0.02	0.02	0.02	0.01		
N	0.05 max.	0.03	0.034	0.031–0.033	0.031–0.033	0.031–0.032	0.031–0.032			0.032	0.030	0.03	0.0305	0.05	0.03
B	0.003 max.	0.0005	0.0005	0.0005–0.0006	0.0005–0.0006	0.0005	0.0004–0.0005		<0.01–<0.001	0.0005	0.0005	0.0005	0.0005	0.0003	0.0015
Nb + Ta	0.020 max.	<0.01	<0.01	<0.01	<0.01	<0.01	<0.01	<0.05–<0.01	<0.05–<0.01	<0.01	<0.01	<0.01	0.10[f]	<0.05	<0.05
Ae	Not Required					0.015–0.017	0.014–0.017	<0.01–<0.001		0.023			<0.02		
Pb		0.003											<0.02		
Sn		0.004											<0.02		
O													0.0043		
H													0.0007		
W													0.0020		

[a]Range for three lots of plates (individual analyses available in ORNL/TM-5196).

[b]Range for four lots of plates (individual analyses available in ORNL/TM-5196).

[c]Range for six analyses on three different lots (individual analyses available in ORNL/TM-5196).

[d]Range for four analyses on two different lots (individual analyses available in ORNL/TM-5196).

[e]Range for three analyses on three different lots (individual analyses available in ORNL/TM-5196).

[f]For Ta; 0.0004% Nb.

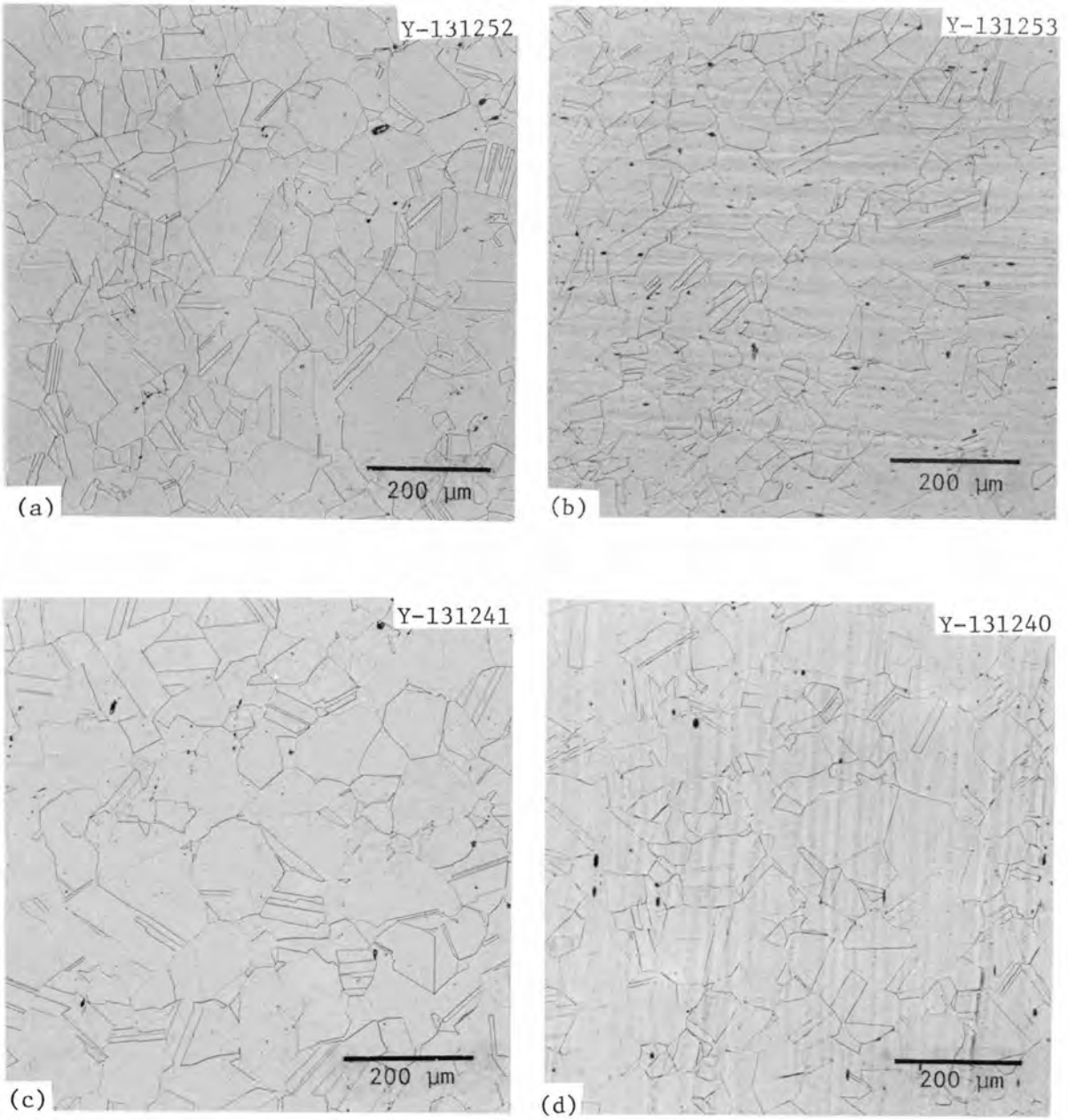

Fig. 3.14. Optical Microstructure of 16-mm Plate of the Reference Heat (8092297) of Type 316 Stainless Steel. (a), (b) Longitudinal and transverse sections, as received. (c), (d) Longitudinal and transverse sections, reannealed. Scales are 0.0079 in. Plate is 5/8 in.

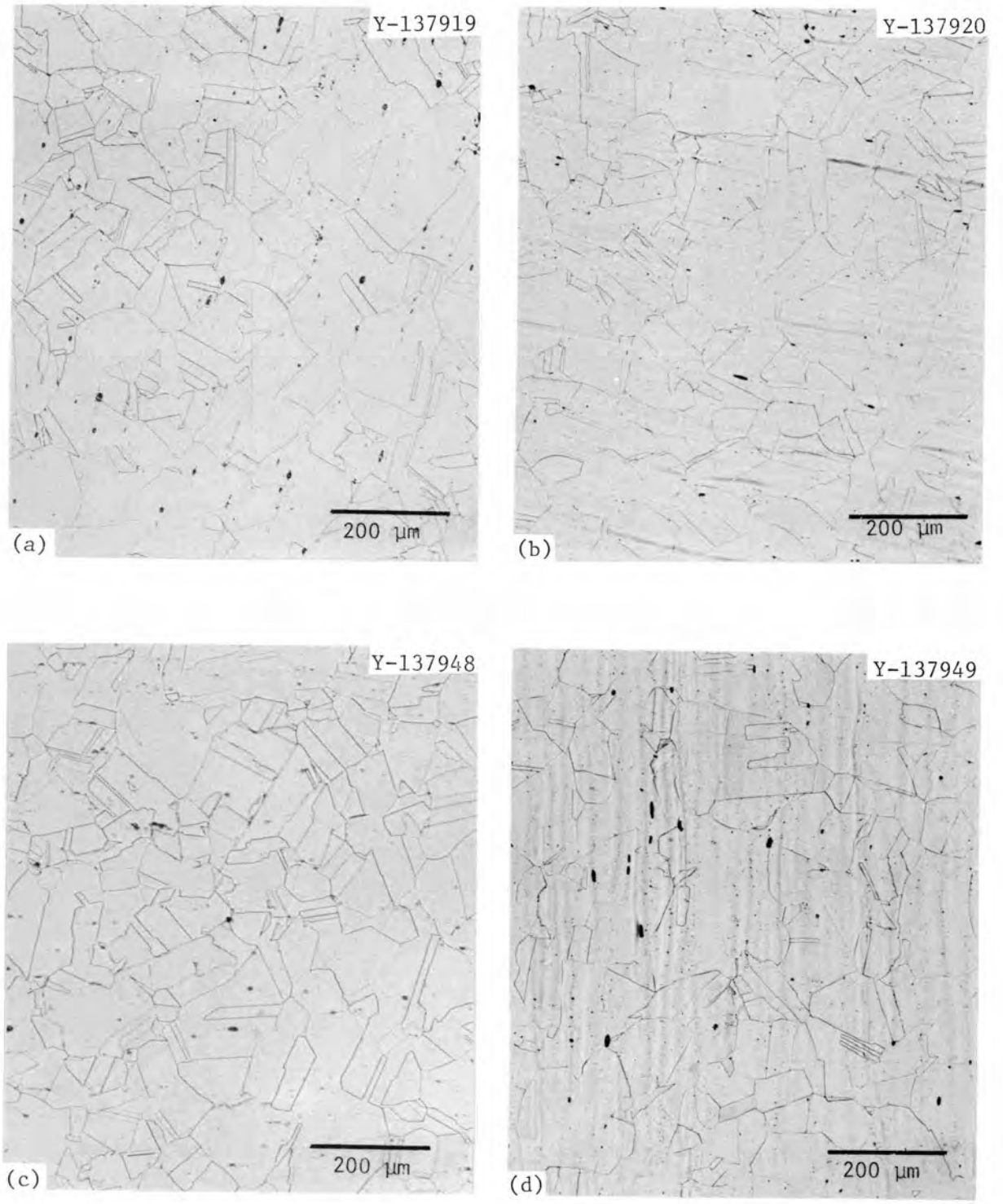

Fig. 3.15. Optical Microstructure of 25-mm Plate of the Reference Heat (8092297) of Type 316 Stainless Steel. (a), (b) Longitudinal and transverse sections, as received. (c), (d) Longitudinal and transverse sections, reannealed. Scales are 0.0079 in. Plate is 1 in.

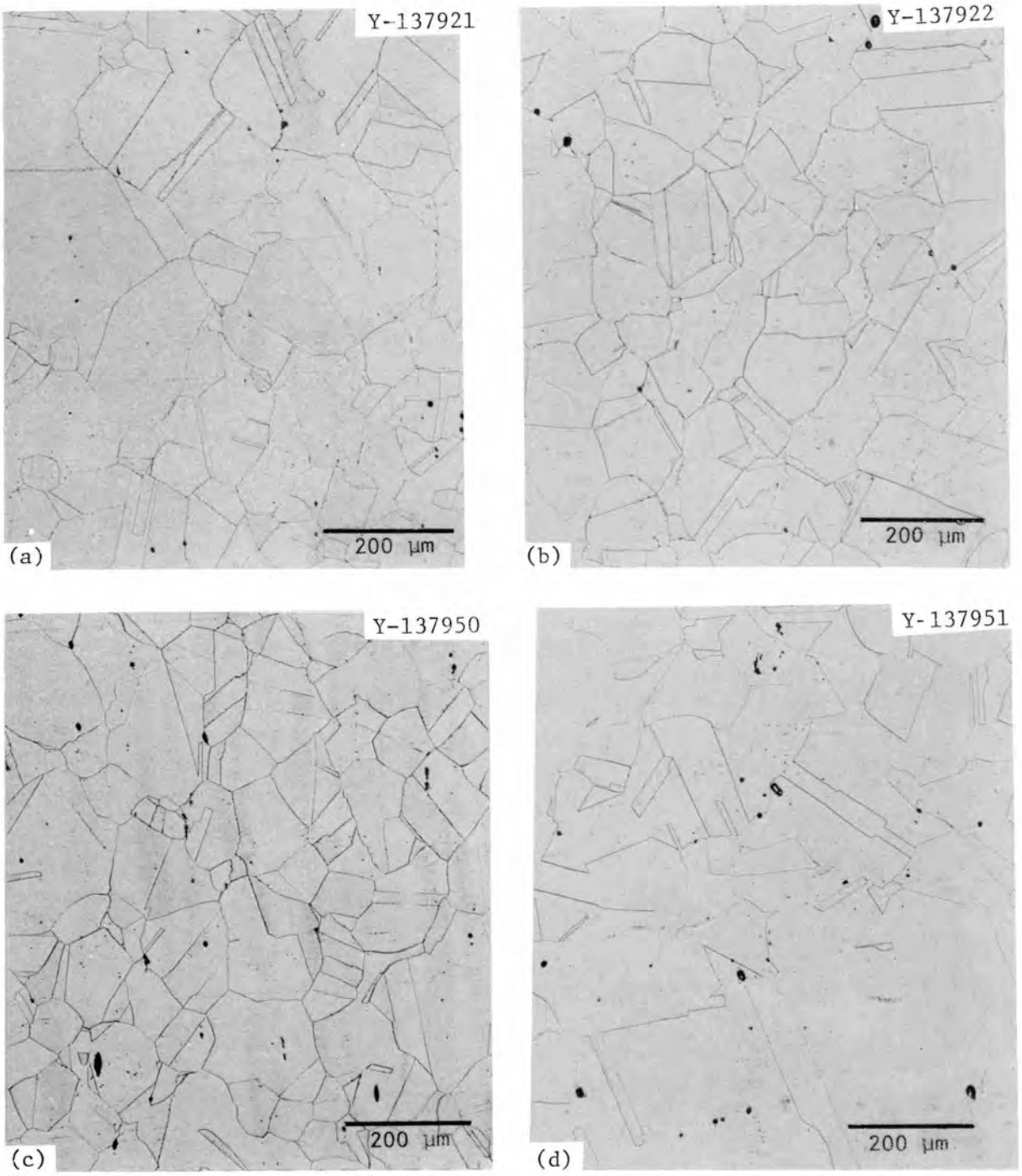

Fig. 3.16. Optical Microstructure of 51-mm Plate of the Reference Heat (8092297) of Type 316 Stainless Steel. (a), (b) Longitudinal and transverse sections, as received. (c), (d) Longitudinal and transverse sections, reannealed. Scales are 0.0079 in. Plate is 2 in.

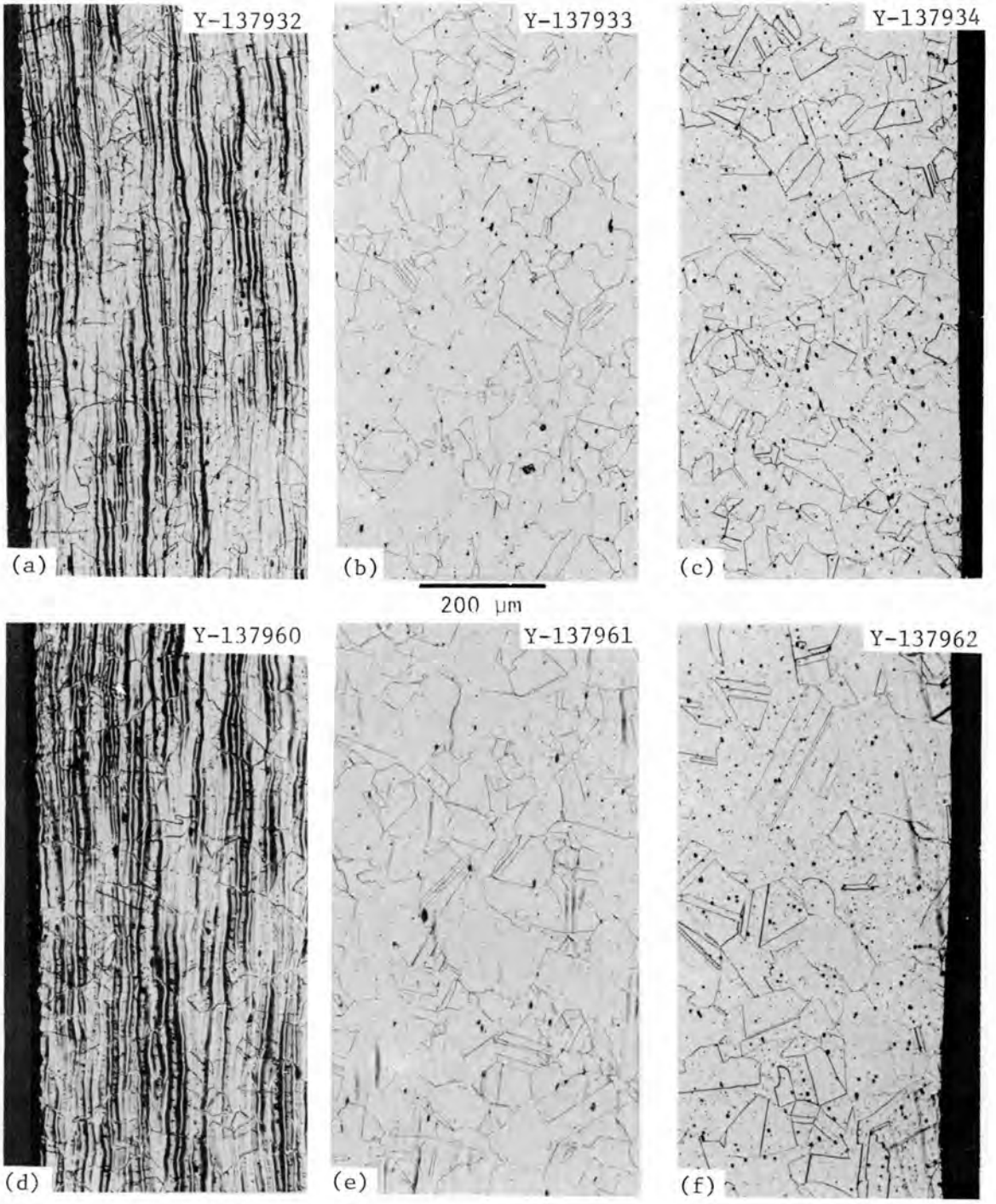

Fig. 3.17. Optical Microstructure of 13 by 114-mm Pipe of the Reference Heat (8092297) of Type 316 Stainless Steel. (a) Inner surface, (b) midwall, and (c) outer surface, as received. (d) Inner surface, (e) midwall, and (f) outer surface, reannealed. Scale is 0.0079 in. Pipe is 1/2 by 4 1/2 in.

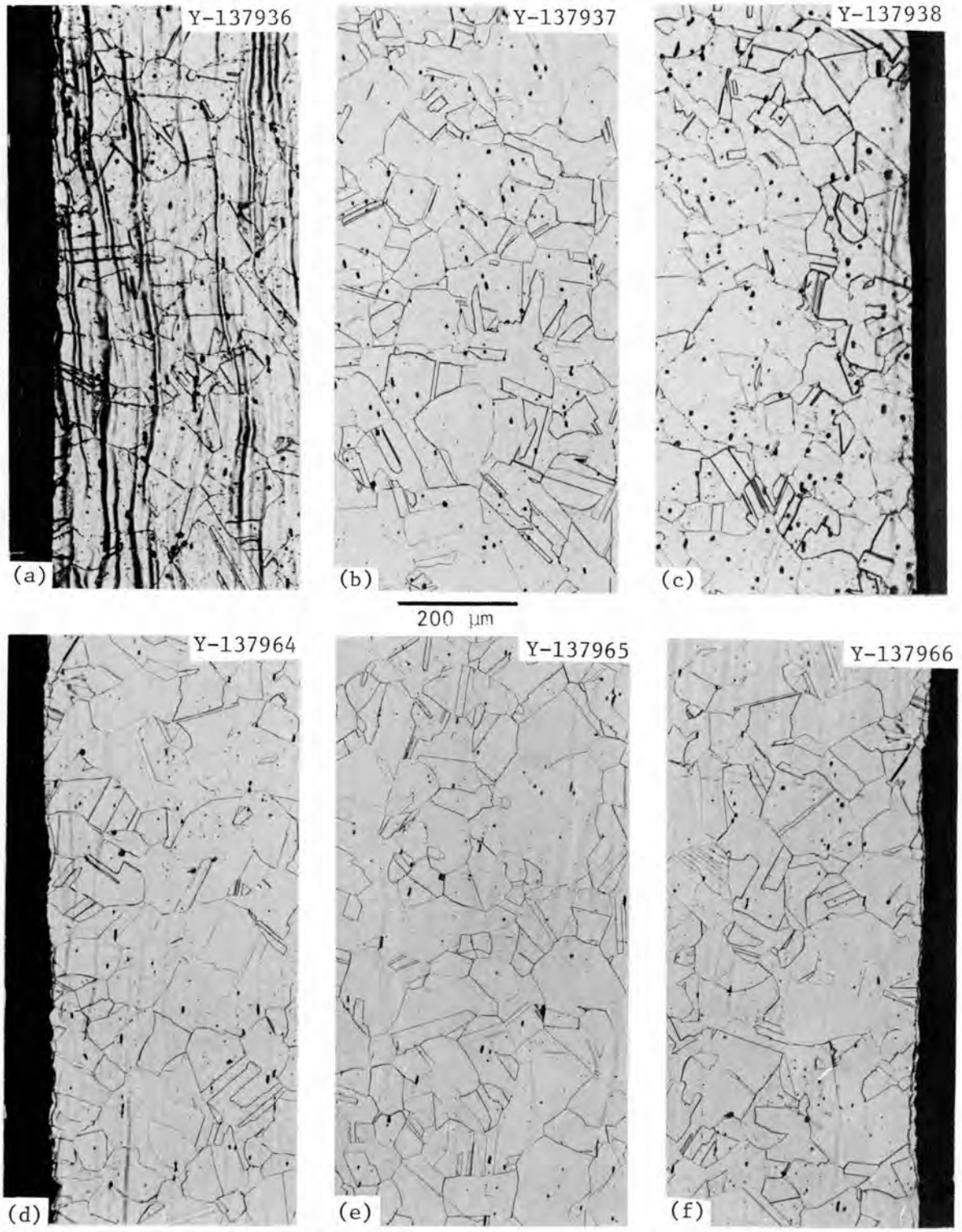

Fig. 3.18. Optical Microstructure of 13 by 219-mm Pipe of the Reference Heat (8092297) of Type 316 Stainless Steel. (a) Inner surface, (b) midwall, and (c) outer surface, as received. (d) Inner surface, (e) midwall, and (f) outer surface, reannealed. Scale is 0.0079 in. Pipe is 1/2 by 8 5/8 in.

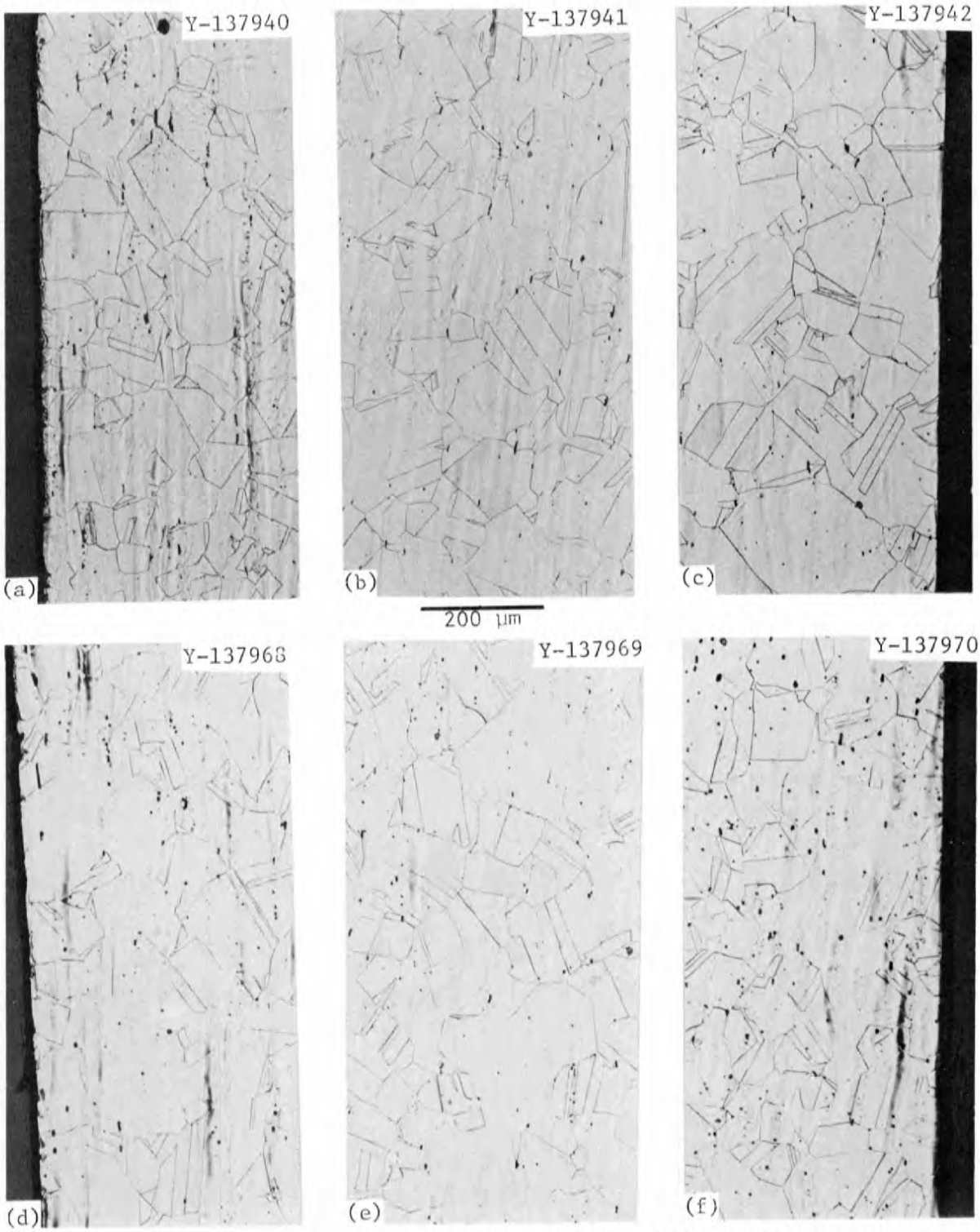

Fig. 3.19. Optical Microstructure of 10 by 406-mm Pipe of the Reference Heat (8092297) of Type 316 Stainless Steel. (a) Inner surface, (b) midwall, and (c) outer surface, as received. (d) Inner surface, (e) midwall, and (f) outer surface, reannealed. Scale is 0.0079 in. Pipe is 0.4 by 16 in.

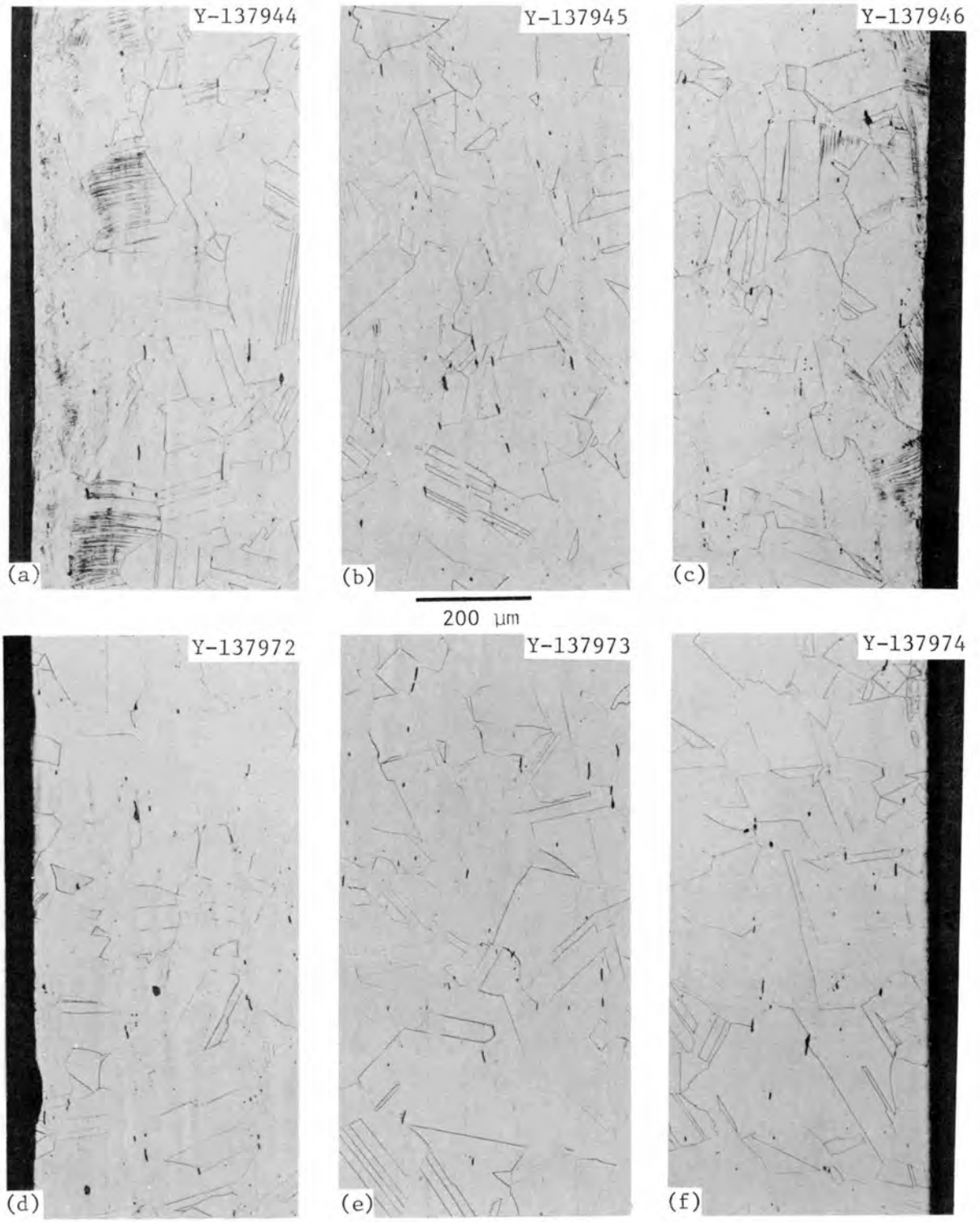

Fig. 3.20. Optical Microstructure of 10 by 711-mm Pipe of the Reference Heat (8092297) of Type 316 Stainless Steel. (a) Inner surface, (b) midwall, and (c) outer surface, as received. (d) Inner surface, (e) midwall, and (f) outer surface, reannealed. Scale is 0.0079 in. Pipe is 0.4 by 28 in.

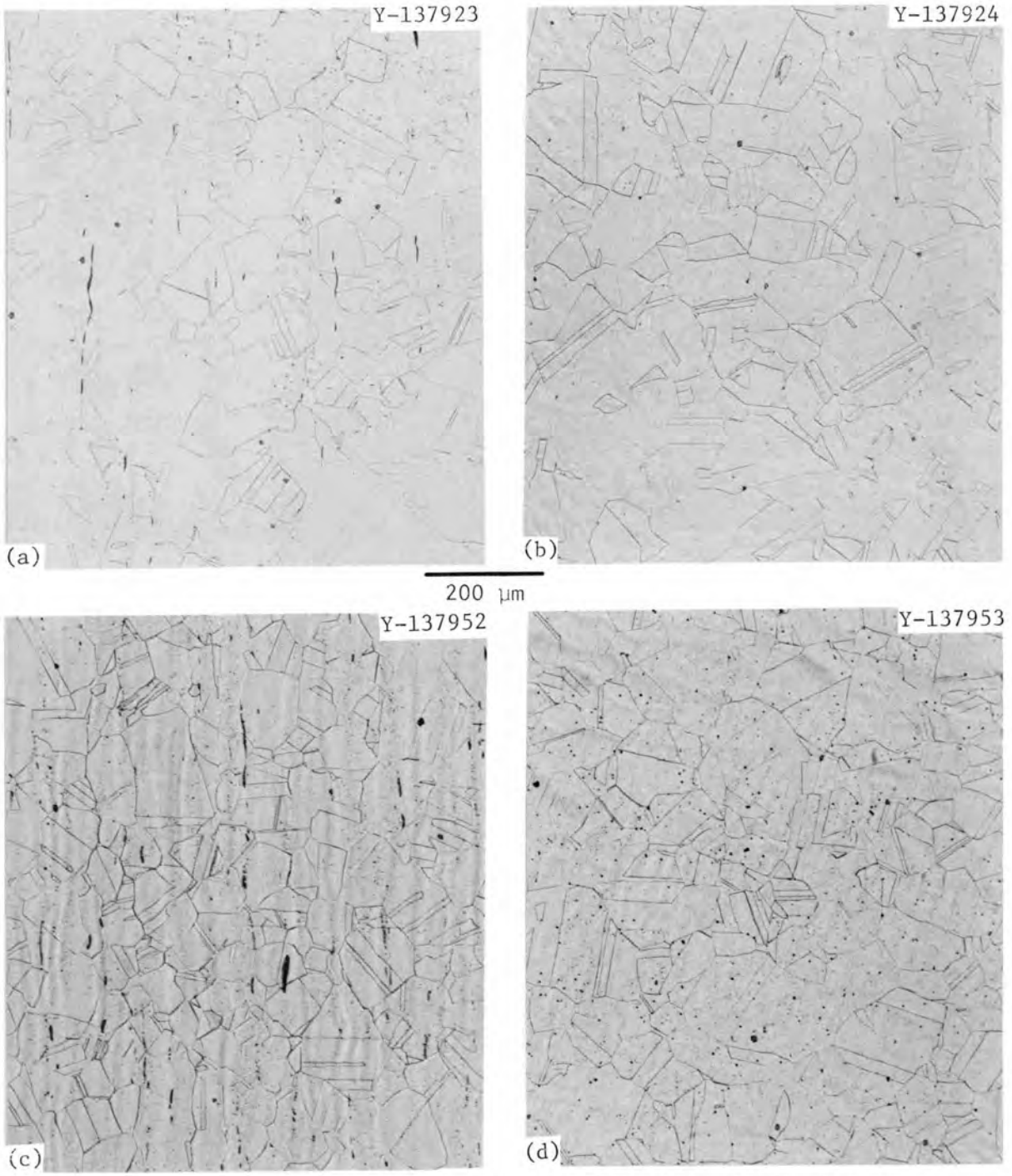

Fig. 3.21. Optical Microstructure of 25-mm bar of the Reference Heat (8092297) of Type 316 Stainless Steel. (a), (b) Longitudinal and transverse sections, as received. (c), (d) Longitudinal and transverse sections, reannealed. Scale is 0.0079 in. Bar is 1 in.

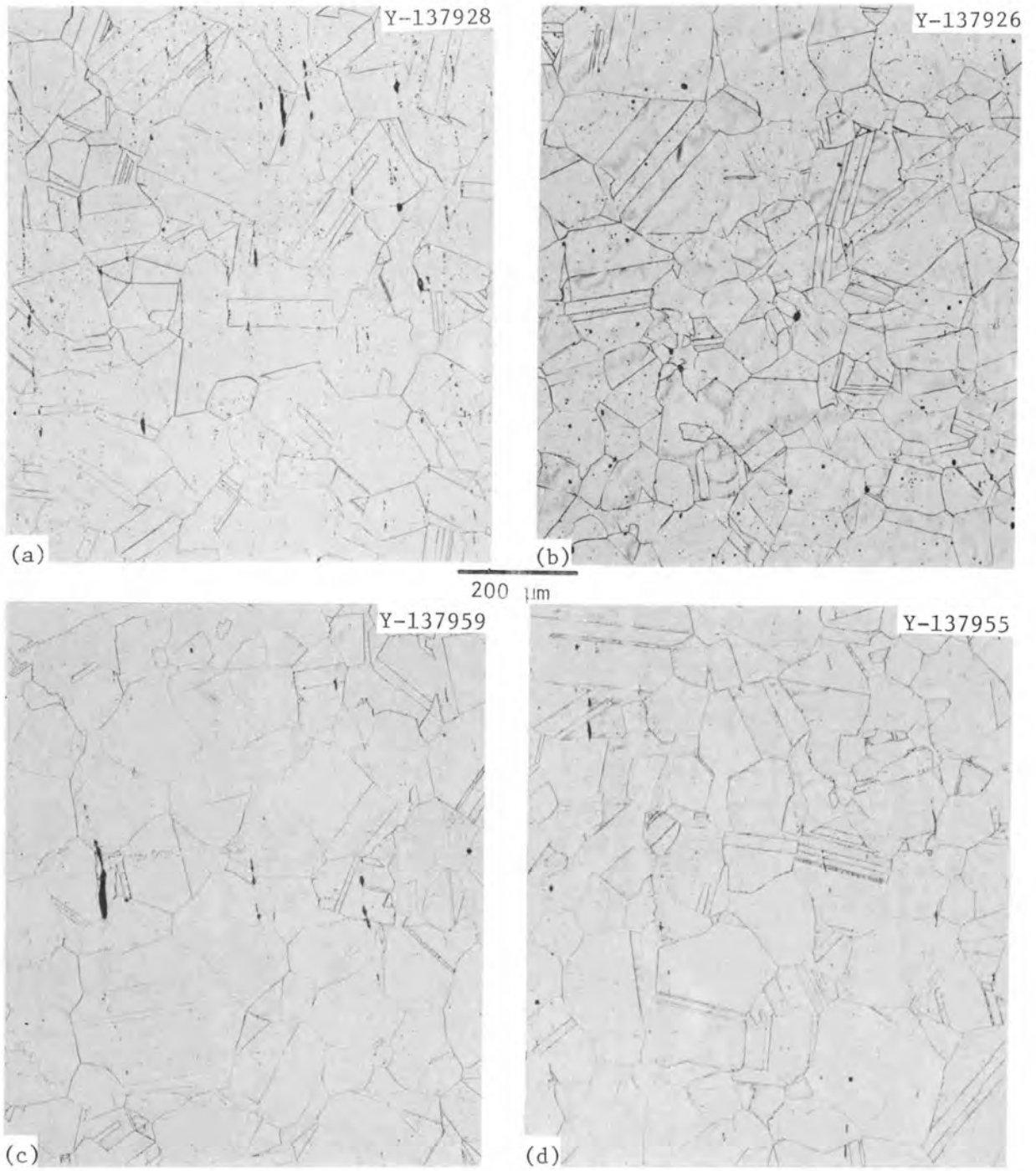

Fig. 3.22. Optical Microstructure of 51-mm bar of the Reference Heat (8092297) of Type 316 Stainless Steel. (a), (b) Longitudinal and transverse sections, as received. (c), (d) Longitudinal and transverse sections, reannealed. Scale is 0.0079 in. Bar is 2 in.

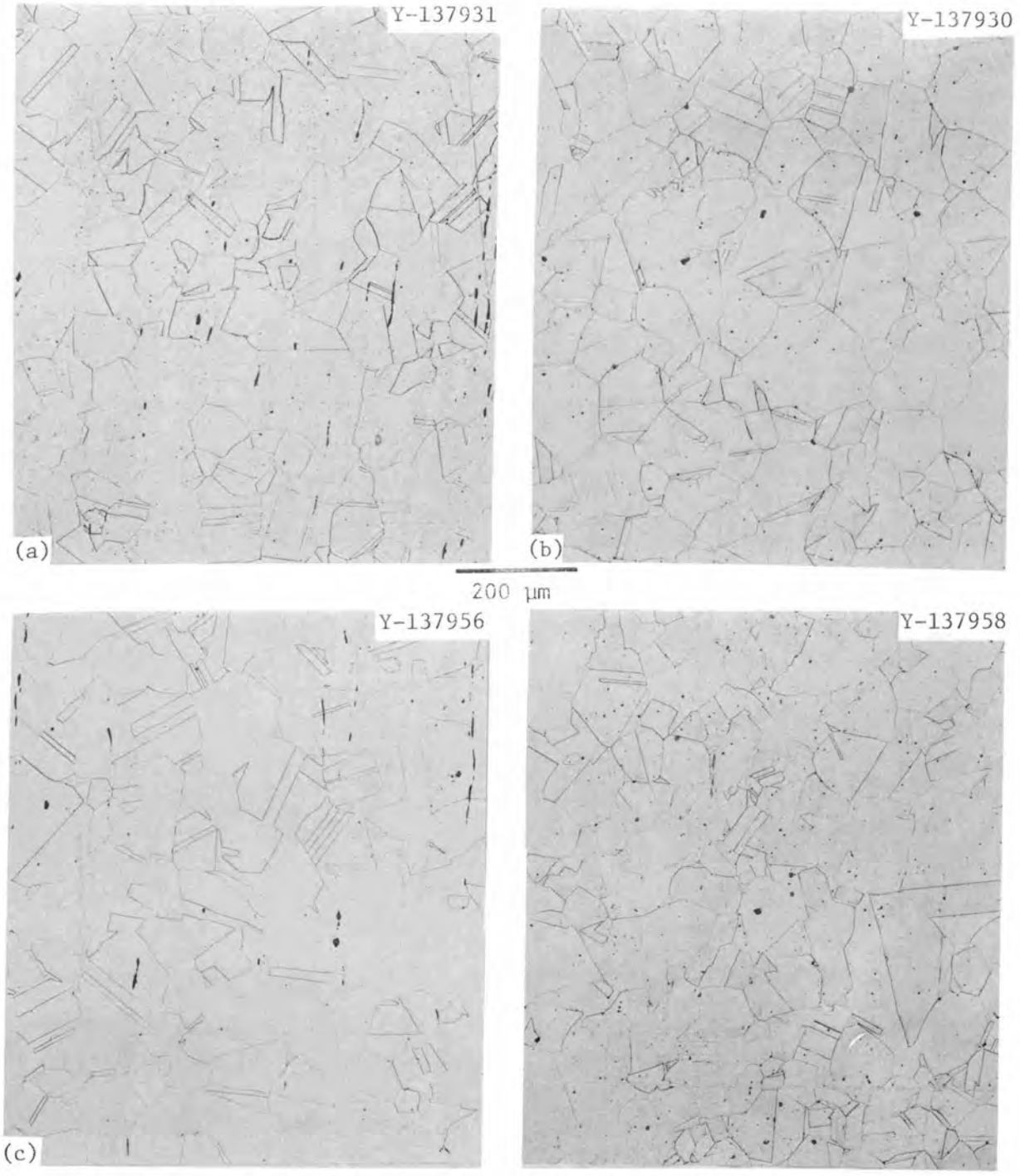

Fig. 3.23. Optical Microstructure of 64-mm bar of the Reference Heat (8092297) of Type 316 Stainless Steel. (a), (b) Longitudinal and transverse sections, as received. (c), (d) Longitudinal and transverse sections, reannealed. Scale is 0.0079 in. Bar is 2.5 in.

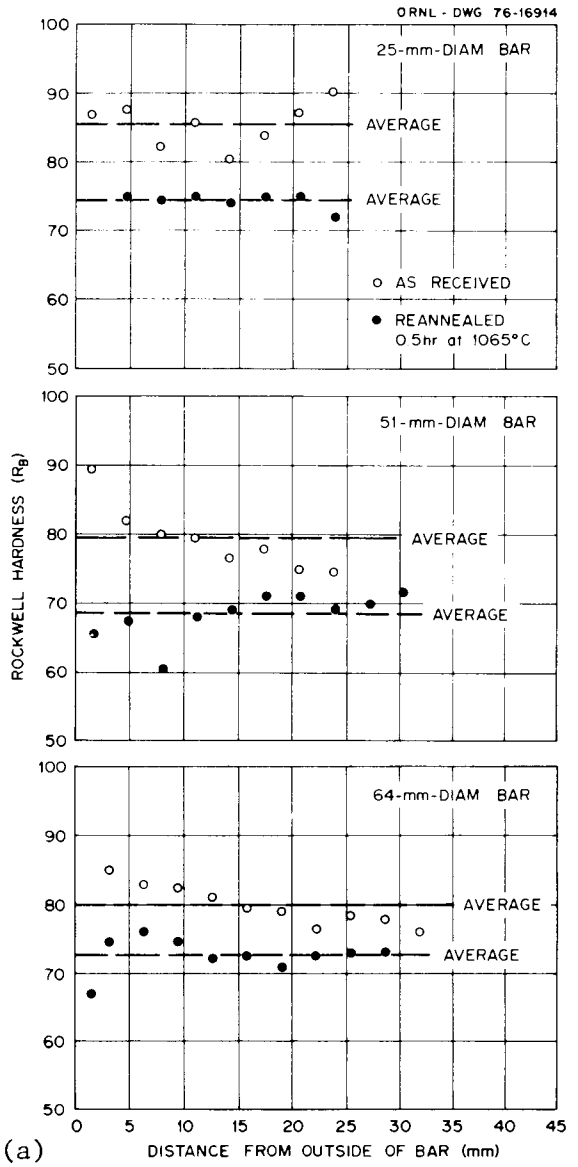

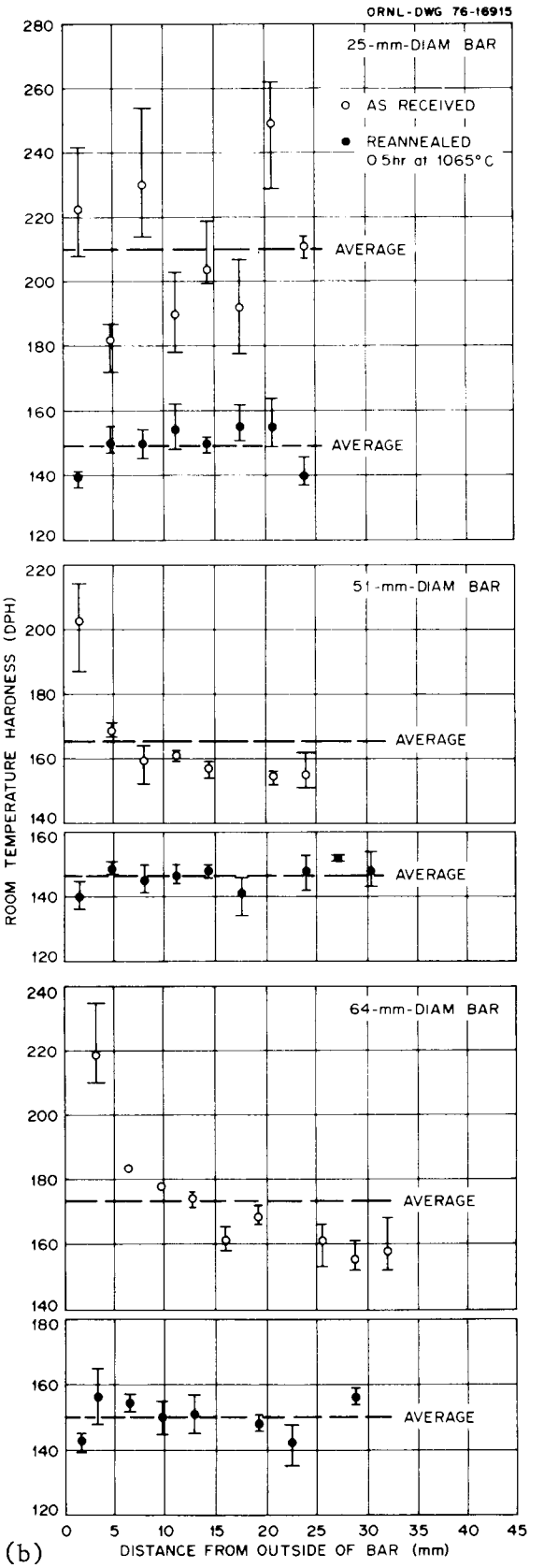

Fig. 3.24. Hardness Profiles for Bars of the Reference Heat (8092297) of Type 316 Stainless Steel. (a) Rockwell hardness number. (b) Microhardness. To convert: 1 mm = 0.03937 in.

3. For material reannealed 0.5 hr at 1065°C, the tests will be at room temperature and 204, 427, 593, and 649°C (400, 800, 1100, and 1200°F). All tests on as-received material have been completed. Only room-temperature tests were completed on various products in the reannealed condition. Tensile data on various products in the as-received condition are summarized in Table 3.4. Plots of 0.2% yield stress, ultimate tensile strength, uniform and total elongation, and reduction of area as functions of test temperature are presented in Figs. 3.25 through 3.29. For the sake of clarity, properties for plate and pipe products are compared in (a) and for 16-mm plate and bar products in (b) of those figures. *Nuclear Systems Materials Handbook*[8] minimum value curves for various properties are also included in these plots.

0.2% Yield Strength — All product forms except 10 × 711-mm pipe met the room-temperature minimum specified value of 207 MPa (30 ksi). Bars of all sizes showed higher yield strength values than plate and pipe. This observation is consistent with the previously published results.[12,14] As compared with plate and pipe, bar showed more variation in the data. Figure 3.25(a) also shows that meeting the room-temperature minimum value does not assure that the elevated-temperature data will lie above the Handbook minimum curve. Such an observation points out that the ratio method of defining minimum value curves may not be adequate for elevated-temperature applications.

Ultimate Tensile Strength — Room-temperature ultimate tensile strength values for all product forms were above the minimum specified value of 517 MPa (75 ksi). Unlike yield strength data, there was no significant difference between the ultimate tensile strength data on various product forms for the whole temperature range. Ultimate tensile strength for all product forms was above the Handbook minimum curve for all test temperatures except 649°C (1200°F). Strain-rate sensitivity of ultimate tensile strength at 649°C is the possible reason for the observed values to fall below the minimum curve. Ultimate tensile strength values for all products showed a slight increase in the temperature range from 300 to 500°C (570–930°F), and this is associated with possible dynamic strain aging effects.

Table 3.4. Tensile Properties of Various Product Forms of the Reference Heat (8092297) of Type 316 Stainless Steel Tested at a Strain Rate of 0.04/min

Test	Test Temperature (°C)	Test Temperature (°F)	Stress, MPa (ksi): Proportional Limit	Stress: Yield 0.02%	Stress: Yield 0.2%	Stress: Ultimate Tensile	Elongation, %: Uniform	Elongation: Total, in 1 in.	Elongation: Total, in 2 in.	Reduction of Area (%)	Work to Plastic Instability $\left(\frac{MJ}{m^3}\right)$	Work to Plastic Instability $\left(\frac{ft\text{-}lb}{in.^3}\right)$
						25-mm (1-in.) Plate						
16819	25	77	105(15.2)	169(24.5)	216(31.3)	572(82.9)	57.0	80.4	65.9	78.8	290	3496
16820	93	200	79(11.4)	130(18.8)	174(25.3)	513(74.4)	40.4	62.0	55.0	79.9	180	2169
16821	204	400	67(9.76)	97(14.1)	135(19.5)	483(70.1)	36.3	51.4	42.7	73.6	144	1734
16822	316	600	68(9.8)	91(13.2)	119(17.2)	496(71.9)	44.2	43.7	48.2	67.9	182	219
16823	427	800	42(6.1)	86(12.4)	115(16.6)	496(72.0)	45.9	58.0	51.6	69.5	156	2197
16824	538	1000	52(7.5)	78(11.3)	103(15.0)	458(66.4)	36.5	56.7	48.6	66.3	132	1590
16825	649	1200	59(8.6)	77(11.2)	102(14.8)	316(45.8)	27.1	51.0	43.4	41.9	75	910
						51-mm (2-in.) Plate						
16826	25	77	99(14.3)	182(26.4)	242(35.1)	556(80.7)	63.1	82.8	80.2	78.8	314	3791
16827	93	200	99(14.3)	151(21.9)	207(30.0)	494(71.7)	38.8	60.2	47.8	79.8	168	2026
16828	204	400	73(10.6)	126(18.3)	171(24.8)	464(67.3)	36.0	51.4	42.0	69.0	141	1703
16829	316	600	90(13.1)	121(17.6)	159(23.1)	463(67.1)	38.6	38.7	44.4	64.8	147	1781
16830	427	800	59(8.56)	113(16.4)	153(22.2)	478(69.3)	38.5	36.6	42.1	70.0	150	1815
16831	538	1000	65(9.41)	101(14.6)	141(20.5)	458(66.5)	38.7	54.3	48.5	65.8	144	1744
16832	649	1200	74(10.8)	101(14.7)	137(19.9)	305(44.3)	23.5	32.2	28.1	41.6	66	795
						13 × 114-mm (1/2 × 4 1/2-in.) Pipe						
16854	25	77	127(18.4)	183(26.5)	235(34.1)	573(83.1)	56.0	78.8	65.8	79.6	286	3459
16855	93	200	79(11.4)	143(20.7)	195(28.3)	515(74.8)	39.3	60.5	47.5	78.2	178	2155
16856	204	400	85(12.3)	123(17.9)	169(24.5)	488(70.7)	34.4	51.8	41.6	72.5		
16857	316	600	68(9.8)	110(15.9)	155(22.5)	509(73.9)	41.3	50.5	44.8	65.9	176	2132
16858	427	800	56(8.1)	101(14.6)	141(20.5)	500(72.5)	39.3	49.2	40.0	64.0	164	1986
16859	538	1000	50(7.3)	90(13.1)	128(18.6)	478(69.3)	38.5	51.0	45.3	64.1	152	1842
16860	649	1200	68(9.8)	91(13.2)	125(18.2)	307(44.6)	21.8	35.8	33.9	28.1	61	743
						13 × 219-mm (1/2 × 8 5/8-in.) Pipe						
16861	25	77	134(19.4)	186(27.0)	241(35.0)	568(82.5)	58.7	80.4	68.2	79.5	297	3588
16862	93	200	80(11.6)	152(22.1)	201(29.1)	504(73.2)	40.2	58.6	48.0	79.0	175	2115
16864	316	600	54(7.8)	112(16.2)	152(22.1)	490(71.1)	39.1	52.8	46.2	67.3	160	1928
16865	427	800	65(9.4)	107(15.5)	145(21.1)	497(72.1)	39.1	54.2	46.1	67.7	159	1922
16866	538	1000	62(9.0)	91(13.2)	128(18.6)	458(66.4)	40.5	53.4	48.0	64.7	154	1859
16867	649	1200	57(8.2)	88(12.7)	123(17.8)	304(44.1)	23.2	38.0	32.7	34.9	64	774
						10 × 406-mm (0.4 × 16 in.) Pipe						
17354	25	77	117(17.0)	185(26.8)	212(30.8)	564(81.8)	64.4	75.3	77.5	79.4	323	3900
17355	93	200	99(14.3)	162(23.5)	179(26.0)	499(72.4)	41.6	63.7	50.6	79.5	178	2146
17356	204	400	87(12.6)	126(18.2)	141(20.5)	474(68.8)	37.0	54.6	43.7	74.6	144	1740
17357	316	600	74(10.7)	113(16.4)	128(18.5)	488(70.8)	42.2	53.6	45.9	67.8	168	2026
17358	427	800	72(10.5)	103(14.9)	115(16.7)	488(70.7)	43.2	44.1	46.2	66.9	169	2047
17359	538	1000	68(9.9)	93(13.5)	106(15.3)	454(65.9)	40.6	53.6	45.4	68.7	149	1798
17360	649	1200	76(11.0)	91(13.2)	101(14.6)	301(43.7)	26.1	46.8	38.3	37.6	71	853
						10 × 711-mm (0.4 × 28-in.) Pipe						
17361	25	77	126(18.3)	183(26.5)	205(29.7)	556(80.7)	58.0	66.2	69.1	79.2	288	3479
17362	93	200	83(12.1)	146(21.1)	176(25.5)	502(72.8)	41.6	62.6	50.5	78.8	180	2176
17363	204	400	84(12.2)	121(17.5)	140(20.3)	476(69.0)	37.7	52.2	43.8	74.3	147	1777
17364	316	600	65(9.4)	104(15.1)	123(17.8)	484(70.2)	43.4	41.7	47.4	69.1	170	2051
17365	315	598	77(11.1)	114(16.5)	125(18.1)	482(69.9)	44.5	47.3	49.2	66.2	176	2123
17366	538	1000	64(9.3)	90(13.0)	104(15.1)	451(65.4)	41.2	53.4	49.2	62.7	150	1808
17367	649	1200	58(8.4)	80(11.6)	98(14.2)	300(43.5)	24.2	42.0	35.3	38.7	64	776
						25-mm (1-in.) Bar						
16833	25	77	110(15.9)	196(28.5)	270(39.2)	574(83.3)	56.0	83.1	68.9	79.0	292	3532
16834	93	200	87(12.6)	183(26.5)	245(35.5)	513(74.4)	37.1	58.7	46.4	78.5	171	2064
16835	204	400	101(14.6)	162(23.5)	204(29.6)	486(70.5)	34.7	50.6	42.8	74.7	156	1887
16836	316	600	90(13.0)	135(19.6)	179(25.9)	483(70.1)	37.5	52.0	44.3	69.9	154	1864
16837	427	800	101(14.7)	146(21.2)	176(25.6)	497(72.1)	40.4	54.8	46.5	69.7	170	2053
16839	649	1200	85(12.3)	122(17.7)	150(21.8)	312(45.3)	23.6	49.8	42.1	43.2	68	826
						51-mm (2-in.) Bar						
16840	25	77	73(10.6)	163(23.6)	274(39.7)	571(82.8)	58.3	81.8	68.4	79.1	300	3625
16841	93	200	73(10.6)	233(23.2)	233(33.8)	511(74.2)	37.9	60.1	48.4	78.9	172	2080
16842	204	400	112(16.3)	154(22.3)	194(28.2)	482(70.0)	34.0	49.0	40.6	75.8	140	1695
16843	316	600	93(13.5)	131(19.0)	174(25.2)	479(69.5)	37.0	50.9	44.1	69.8	151	1810
16844	427	800	87(12.6)	134(19.5)	174(25.2)	494(71.7)	36.7	52.5	46.4	68.7	150	1813
16845	538	1000	93(13.5)	120(17.4)	155(22.5)	464(67.4)	37.5	52.0	45.7	67.1	143	1731
16846	649	1200	83(12.1)	108(15.7)	148(21.4)	307(44.5)	24.1	48.8	41.4	41.5	68	826
						64-mm (2.5-in.) Bar						
16847	25	77	59(8.6)	225(32.7)	324(47.0)	580(84.2)	55.9	77.9	65.4	80.1	299	3617
16848	93	200	76(11.0)	141(20.5)	196(28.5)	499(72.4)	39.0	61.7	49.1	80.9	163	1965
16849	204	400	85(12.3)	123(17.9)	160(23.2)	470(68.1)	35.0	53.8	44.4	76.5		
16850	316	600	126(18.3)	181(26.3)	225(32.6)	498(72.3)	39.3	39.8	45.1	72.2	171	2068
16851	427	800	141(20.5)	190(27.5)	229(33.2)	506(73.4)	36.6	49.2	43.2	68.3	162	1959
16852	538	1000	90(13.0)	140(20.3)	176(25.6)	467(67.7)	38.4	50.4	43.5	68.2	151	1826
16853	649	1200	99(14.4)	141(20.4)	181(26.3)	309(44.9)	21.1	45.3	38.4	36.4	62	753

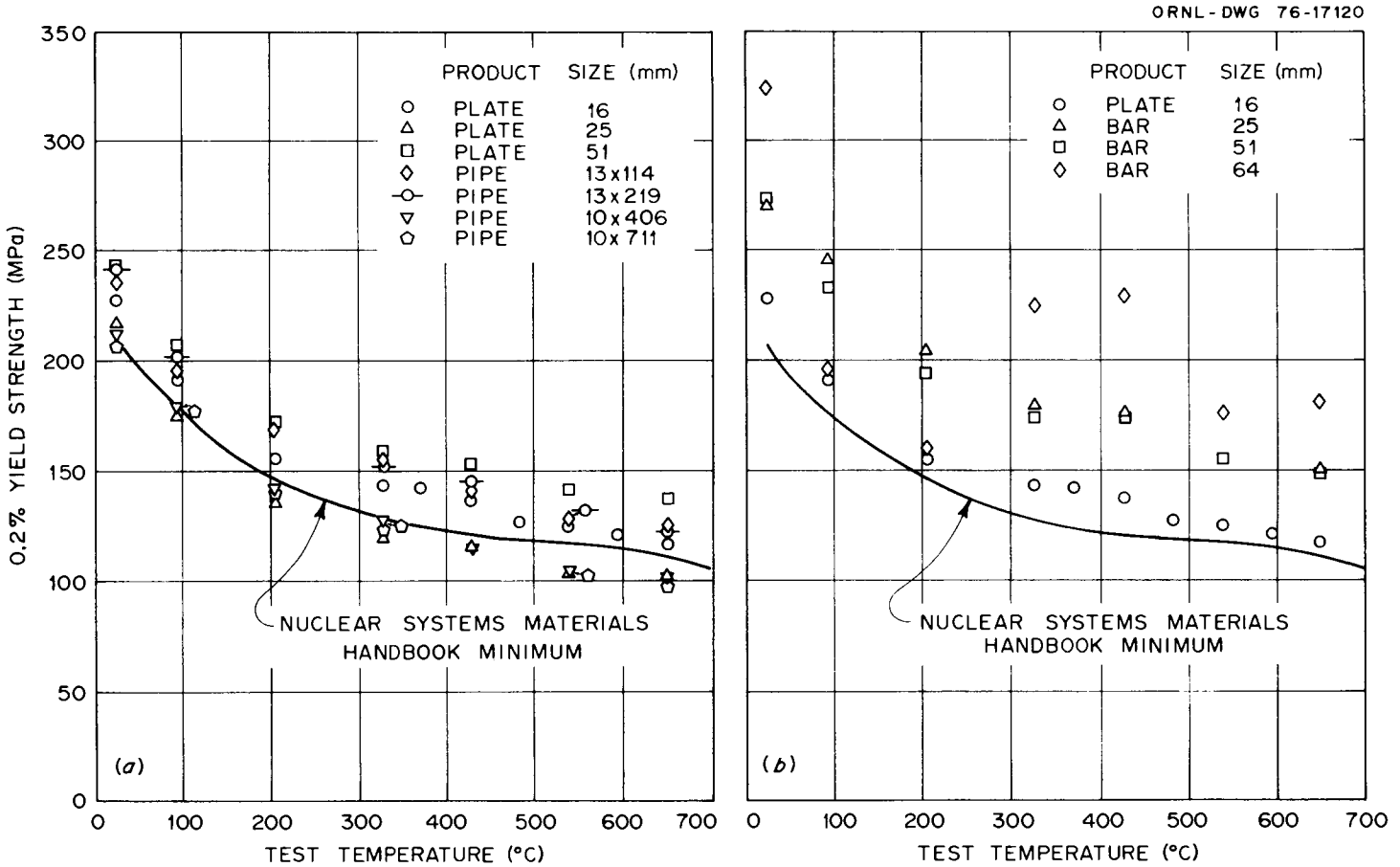

Fig. 3.25. The 0.2% Yield Strength as a Function of Test Temperature for Various Products of the Reference Heat (8092297) of Type 316 Stainless Steel in the As-Received Condition at a Strain Rate of 0.004/min. (a) Plate and pipe. (b) 16-mm Plate and bar.

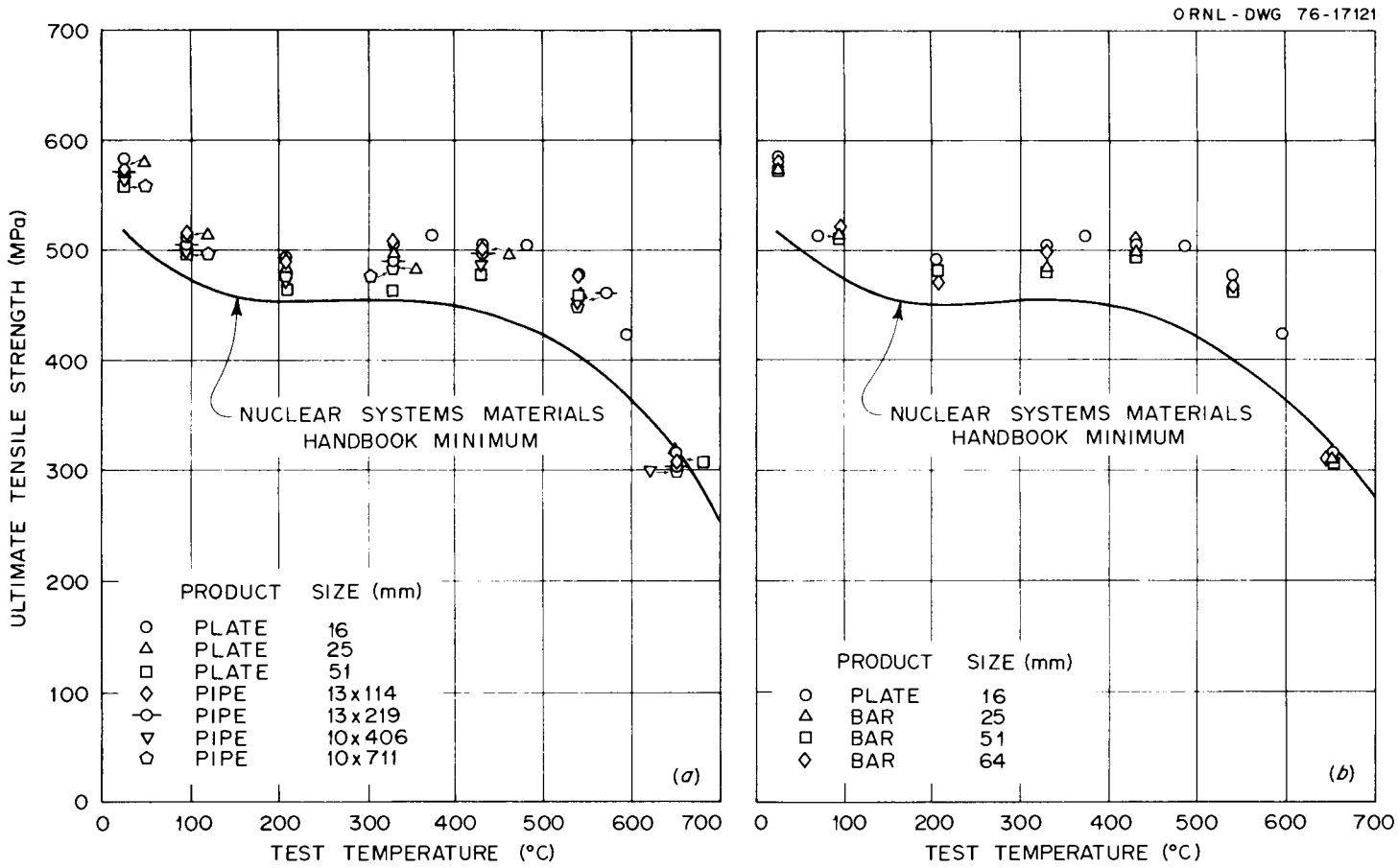

Fig. 3.26. The Ultimate Tensile Strength as a Function of Test Temperature for Various Products of the Reference Heat (8092297) of Type 316 Stainless Steel in the As-Received Condition at a Strain Rate of 0.004/min. (a) Plate and pipe. (b) 16-mm Plate and bar.

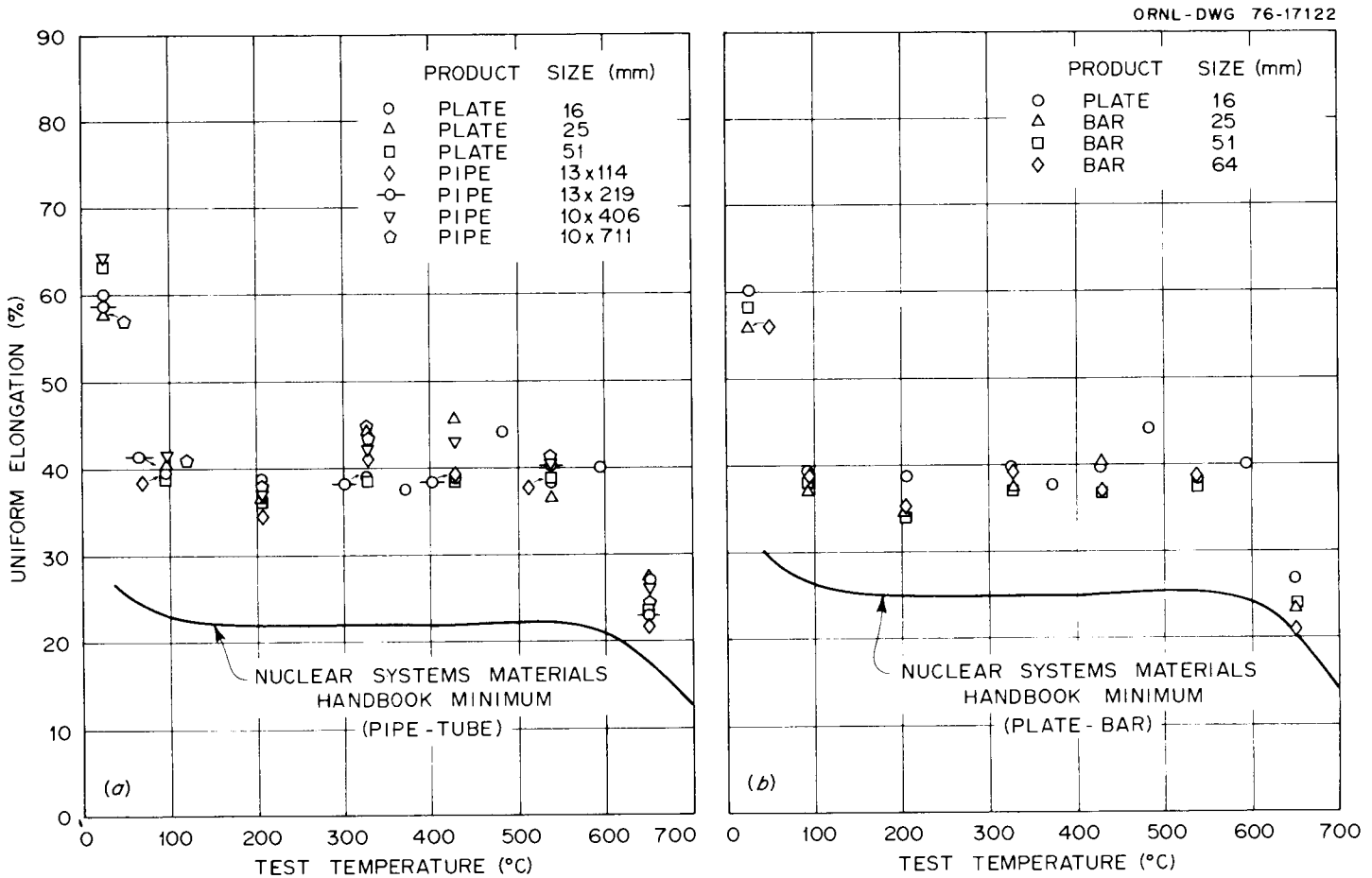

Fig. 3.27. The Uniform Elongation as a Function of Test Temperature for Various Products of the Reference Heat (8092297) of Type 316 Stainless Steel in the As-Received Condition at a Strain Rate of 0.004/min. (a) Plate and Pipe. (b) 16-mm Plate and bar.

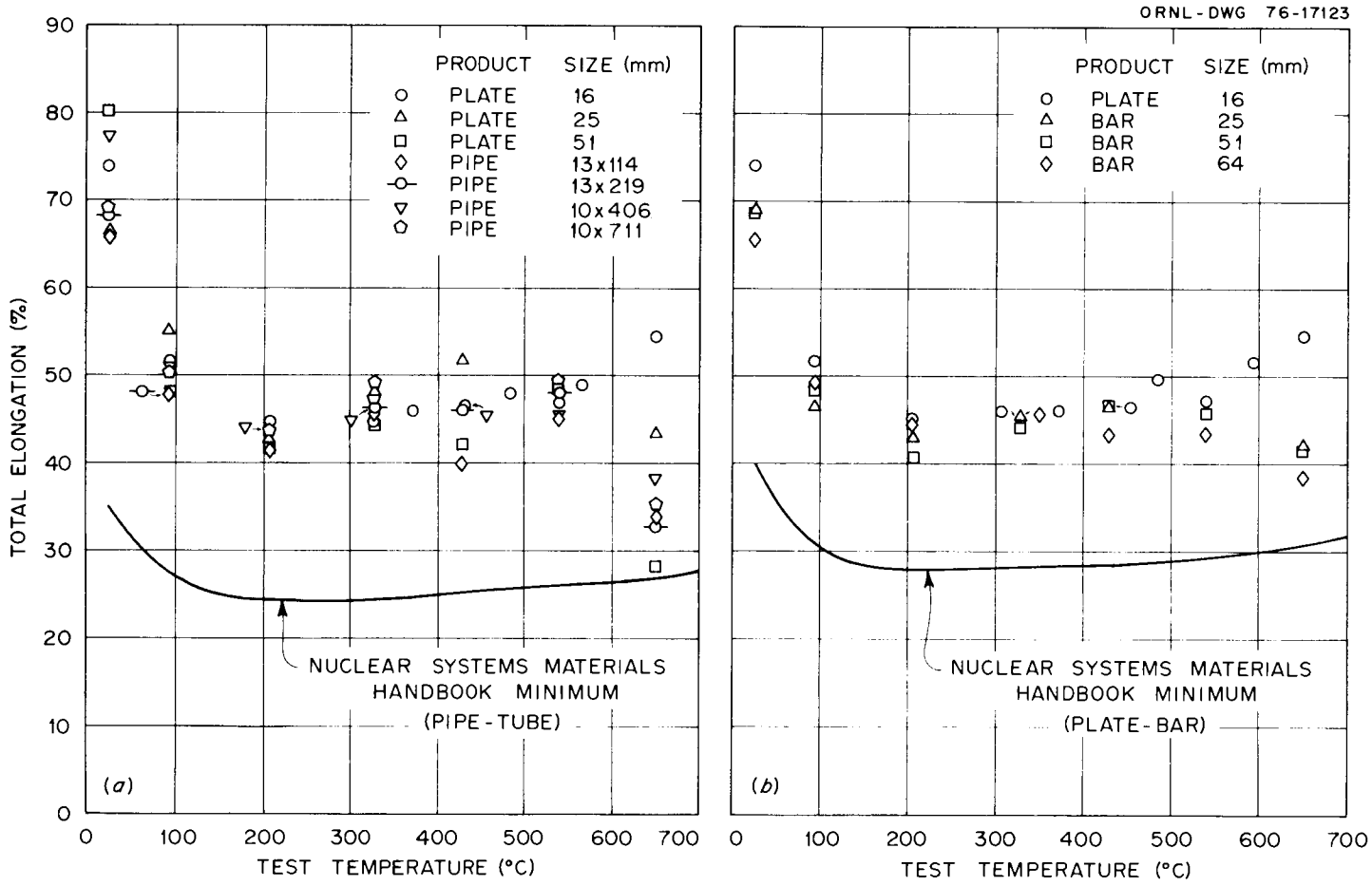

Fig. 3.28. The Total Elongation as a Function of Test Temperature for Various Products of the Reference Heat (8092297) of Type 316 Stainless Steel in the As-Received Condition at a Strain Rate of 0.004/min. (a) Plate and pipe. (b) 16-mm Plate and bar.

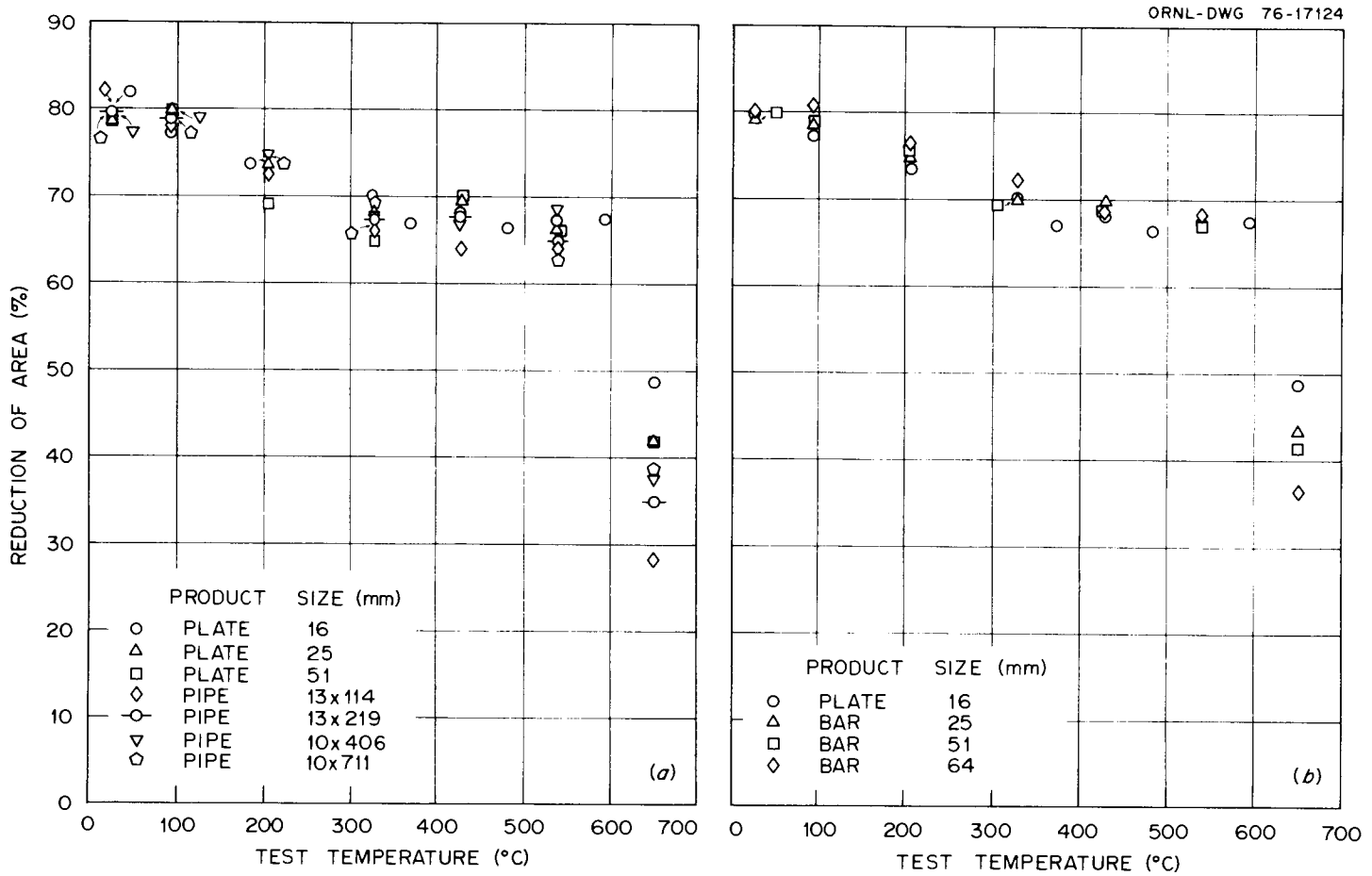

Fig. 3.29. The Reduction of Area as a Function of Test Temperature for Various Products of the Reference Heat (8092297) of Type 316 Stainless Steel in the As-Received Condition at a Strain Rate of 0.004/min. (a) Plate and pipe. (b) 16-mm Plate and bar.

Uniform Elongation — Uniform elongation data for all product forms were above the Handbook minimum for the whole temperature range of this investigation. Dynamic strain aging over the range 300 to 500°C resulted in increased values of uniform elongation for all product forms. The Handbook includes separate minimum value curves for pipe-tube and plate-bar products. The present data on various products show no real differences in values for the different products and that if desired the plate should be combined with pipe and tube rather than with bar. Furthermore, the minimum value curve should be higher for plate-pipe-tube product forms as compared with plate-bar, which is contrary to the values reported in the Handbook.

Total Elongation — Total elongation values for all product forms were above the Handbook minimum curves. The comments made for uniform elongation on separate minimum curves for plate-pipe-tube and bar also hold true for total elongation.

One feature missing from the Handbook minimum value curves is the experimentally observed sharp drop in total elongation at 649°C (1200°F). Such a drop is associated with tensile ductility minimum conditions, which are discussed elsewhere.[15]

Reduction of Area — Reduction of area values for various product forms are plotted in Fig. 3.29. The Handbook does not contain any minimum value curve for this property. However, it is interesting to note that reductions of area for all product forms were essentially the same, and all showed a sharp drop at 649°C. Such a drop is again associated with the ductility minimum conditions, which are discussed elsewhere.[15]

Work to Plastic Instability — The area under the stress-strain curve up to the ultimate tensile strength point is a measure of toughness of the material. Values of this quantity were computed for various product forms of the reference heat and are displayed as a function of test temperature in Fig. 3.30. These plots show that the toughness of all products decreases sharply at a test temperature of 649°C. This is the same temperature at which creep effects become important and fracture becomes intergranular.[15] The dynamic strain-aging effects were also reflected in toughness values.

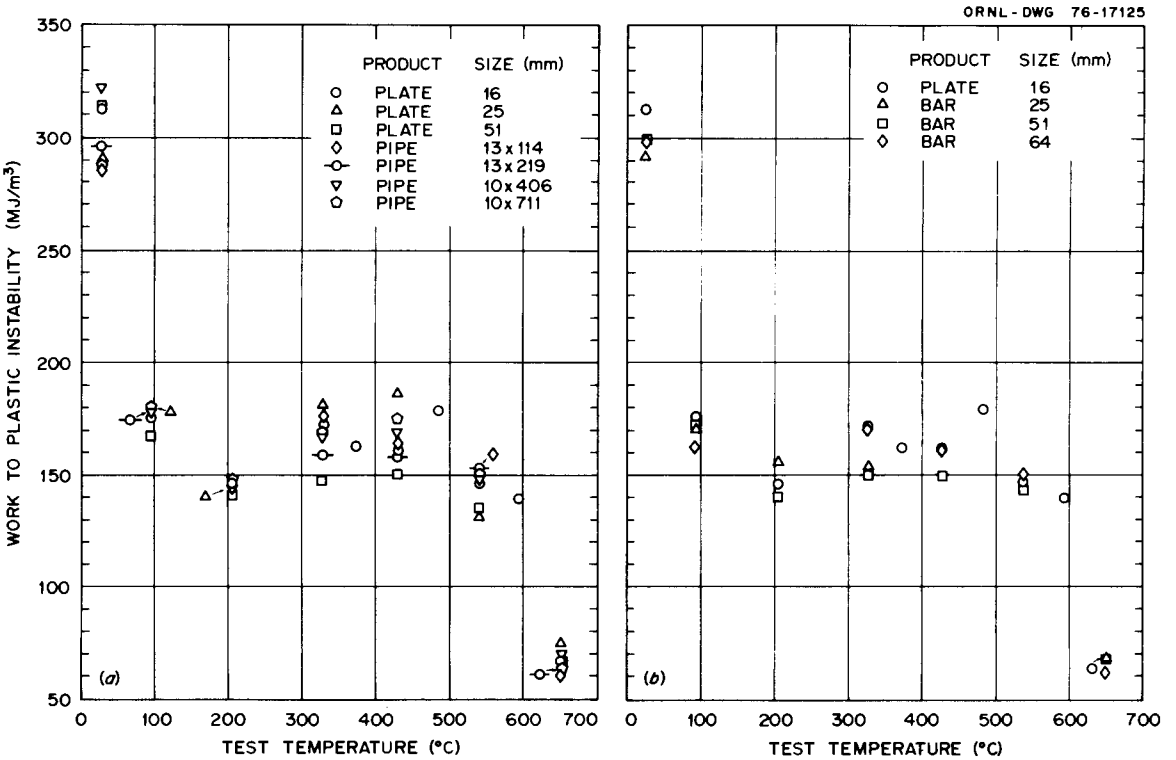

Fig. 3.30. Work to Plastic Instability as a Function of Test Temperature for Various Products of the Reference Heat (8092297) of Type 316 Stainless Steel in the As-Received Condition at a Strain Rate of 0.004/min. (a) Plate and pipe. (b) 16-mm plate and bar.

3.2.2.1.5 Comparison of 0.2% Yield Strength Data with Data on Older Heats. The 0.2% yield strength data on pipe and bar products are compared with the range of data on older heats[16] in Fig. 3.31. The literature data were fitted to a third degree polynomial in temperature. The dotted lines in these plots are for the expected ±2SEE (Standard Error of Estimate). Superimposed in Fig. 3.31(a) are our data on as-received pipe of four different sizes. Data on all pipe made from the reference heat fall in between the expected and lower bound curves. Figure 3.31(b) shows that yield strength values of bar products of the reference heat are close to or above the expected value curves for the older heats. Considering the expected ±2SEE method of defining the range of properties, the ORNL reference heat can be classified to fall within the range of the older heats. However, when compared with the Handbook minimum value curve, the 10 by 406 and 10 by 711-mm pipes of the reference

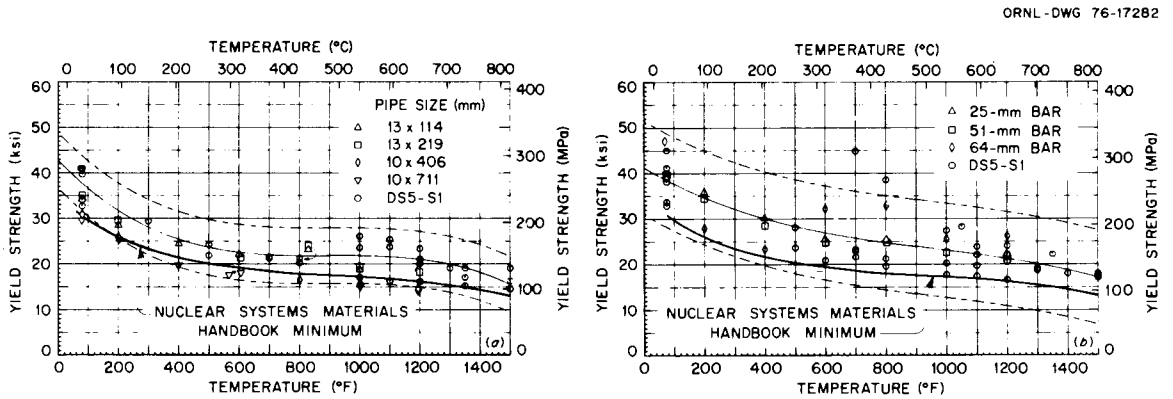

Fig. 3.31. Comparison of 0.2% Yield Strength Data on the Reference Heat of Type 316 Stainless Steel with the Range of Older Literature Data. (a) Pipe of four sizes. (b) Bar of three sizes. The solid line is a polynomial fit to the literature data; the dashed lines represent twice the standard error of estimate of the polynomial.

heat will have to be considered different or weaker than the older heats. Thus, it appears that the real answer to whether the ORNL reference heat, melted recently, is comparable with older heats depends on the method of defining the minimum values.

3.2.2.1.6 Comparison of 0.2% Yield and Ultimate Tensile Strengths with Certified Mechanical Property Data. Certified room-temperature mechanical property data were supplied by the vendor on each product form of the reference heat. Figure 3.32 compares the certified data with ASTM minimum values and our values of 0.2% yield and ultimate tensile strength. The ORNL values were obtained at a strain rate of 0.004/min for material in both as-received and reannealed conditions.

Yield Strength — Figure 3.32(a) shows a significant difference between the certified data supplied by the vendor and the ORNL data. The plate and pipe product data supplied by the vendor were significantly higher than the data obtained at ORNL. However, the reverse was true for the bar product. The differences between the two data sources became even greater for reannealed plate and pipe products. Again the reverse was true for the bar products.

Ultimate Tensile Strength — Figure 3.32(b) shows that only minimal differences existed for this property between the data supplied by the

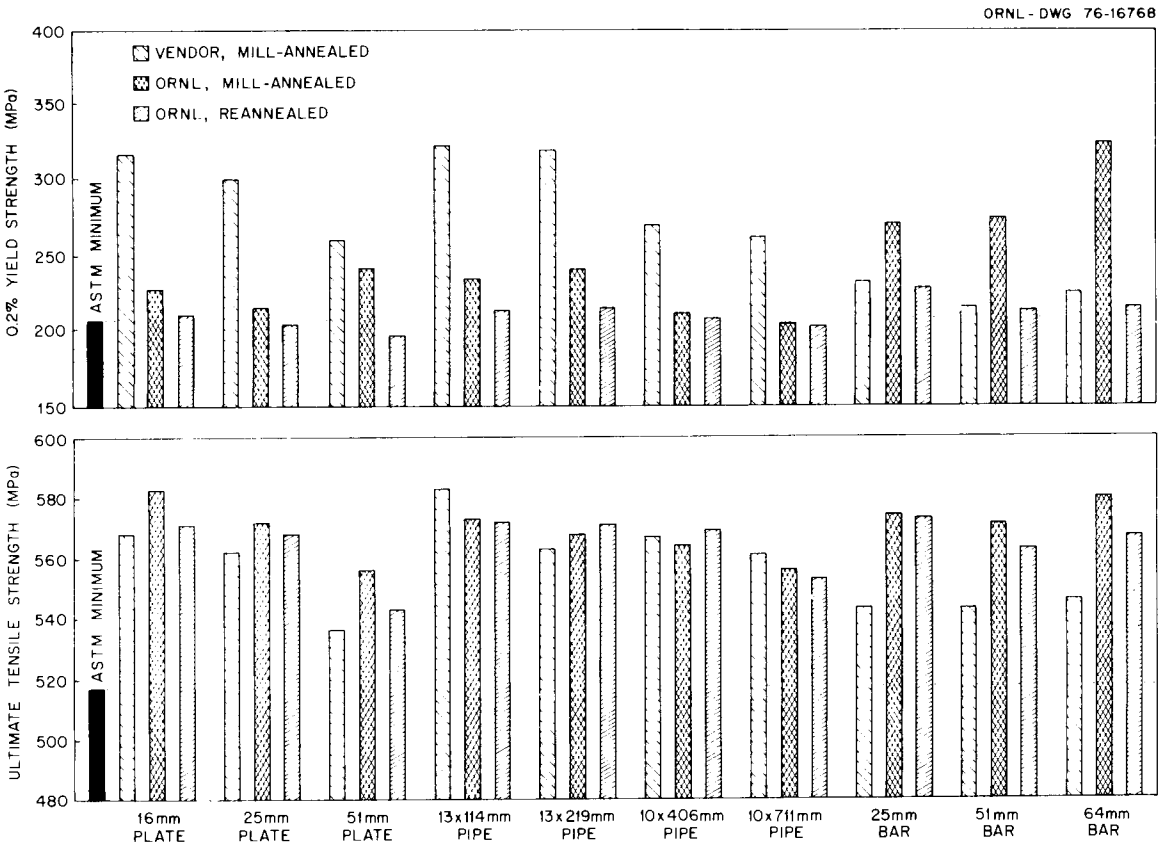

Fig. 3.32. Comparison of 0.2% Yield and Ultimate Tensile Strength Data with Certified Room-Temperature Properties Supplied by Vendors on Various Products of the Reference Heat (8092297) of Type 316 Stainless Steel.

vendor and that produced at ORNL. Such a result is expected because ultimate tensile strength values are relatively insensitive to residual stresses introduced by straightening and finishing.

Previous work[4] showed that 0.2% yield strength controls the time-independent design stresses for test temperatures below 600°C. Therefore, the difference observed between the two data sets raises some questions about the significance of the certified mechanical property data supplied by the vendor. The differences observed between the two data sets have further implications, if the vendor-certified room-temperature values of a given product were used in conjunction with yield strength ratios[17] to generate a yield strength versus temperature plot.

The vendor of the reference heat, Republic Steel, was contacted[18] to establish possible reasons for differences observed between the ORNL

data and certified data supplied by the vendor. The following possible explanations were offered for the differences for various products:

Bar Products — The vendor took specimens from bars after annealing. However, after taking specimens the bars were straightened and ground to size before shipping. Thus, the higher values observed by ORNL data are a result of residual cold work introduced in the bar by straightening and grinding. If the vendor's explanation is correct, ORNL reannealed data should agree with the certified value. Figure 3.32 shows that indeed ORNL reannealed data showed excellent agreement with the vendor data for all three bar products.

Pipe Products — The vendor data on all pipe products were higher than the values obtained at ORNL. The vendor suggested that transverse test bars from the pipe products were taken by cutting rings from various pipes and straightening the rings into flat plate. The ring straightening process introduced a large amount of cold work and gave quite high yield strength value. As the pipe size increases, straightening should produce lesser degree of cold work and thus lower yield strength for pipes of increasing size. Figure 3.32 confirms that the vendor yield strength values decreased with increasing pipe diameter. The ORNL test bars were 6 mm (1/4 in.) in diameter and were taken from the length of the pipe. This method of making test bars did not require any pipe ring straightening operation similar to that performed by the vendor. Therefore, ORNL specimens should show lower yield strength values than the vendor data, which is also illustrated in Fig. 3.32.

Plate Products — The vendor data on all plate products were higher than the ORNL data. However, the vendor at the present time could not give us any suitable explanation about the differences in specimen selection, preparation, or testing procedure to rationalize the observed differences.

3.2.2.1.7 Summary and Conclusions.

1. Optical microstructure and grain size measurements were completed on three plate, four pipe, and three bar products of reference heat in both as-received and reannealed conditions. Some grain size differences

were observed between the outer surface and the center of pipe and the 51- and 64-mm (2- and 2.5-in.) bar. However, reannealing for 0.5 hr at 1065°C (1900°F) did not result in excessive grain growth of any products.

2. Rockwell and microhardness profiles were completed on 25-, 51-, and 64-mm (1-, 2-, and 2.5-in.) bars. The 51- and 64-mm bars showed steep gradients from the outer edge to the center of the bar. Such gradients were not observed in the 25-mm bar, but hardness data showed large variations.

3. Tensile data were completed on all products in the mill-annealed condition at room temperature, 93, 204, 316, 427, 538, and 649°C (200, 400 600, 800, 1000, and 1200°F) at a strain rate of 0.004/min.

4. The 0.2% yield strength data showed maximum differences between the various products. Plate and pipe were weaker than bar. The room-temperature yield strength value for 10 by 711-mm (0.4 × 28 in.) pipe was slightly below the ASTM minimum specified value of 207 MPa (30 ksi). Results also showed that meeting the room-temperature specified value did not assure the elevated-temperature values to fall above the *Nuclear Systems Materials Handbook* minimum curve.

5. Ultimate tensile strength, uniform and total elongation, and reduction of area were not significantly different between the various products.

6. Total elongation and reduction of area showed drops at a test temperature of 649°C. However, the Handbook minimum curve does not include such a drop.

7. Yield strength data on bar and pipe showed that the ORNL reference heat is comparable with older heats.

8. Certified 0.2% yield strength data supplied by the vendor showed significant differences when compared with the ORNL data.

3.2.2.2 Creep and Creep Properties of the 16-mm Plate of Reference Heat

Several creep tests on 16-mm (5/8-in.) plate of the reference heat of type 316 stainless steel (8092297) continued. The test times and creep strains of these tests have been updated and summarized in Table 3.5. All tests are progressing smoothly and will be continued during the next quarter.

Table 3.5. Summary of Creep Tests on Type 316 Stainless Steel Reference Heat 8092297 16-mm-Thick (5/8-in.) Plate[a]

Test	Temperature (°C)	Temperature (°F)	Stress (MPa)	Stress (ksi)	Time in Test[b] (hr)	Strain (%) Loading	Strain (%) Creep	Comments
16019	538	1000	97	14	8386.8	0.071	0.080	
15891	538	1000	110	16	3000.0	0.126	0.055	Discontinued
17119	538	1000	138	20	3544.8	0.414	0.176	
15791	538	1000	179	26	1800.0	2.20	0.275	Discontinued
17178	538	1000	276	40	2905	7.41	2.99	
17135	538	1000	276	40	289.2	8.03	0.595	Discontinued
16100	565	1050	69	10	1626.0	0.070	0.014	Discontinued
16357	565	1050	69	10	5937.8	0.059	0.060	
16384	565	1050	172	25	5844.1	2.25	0.948	
16265	565	1050	207	30	1908.7	3.83	2.80	Discontinued
16739	565	1050	207	30	4498.7	3.91	2.23	
16099	565	1050	276	40	750.3	8.63	14.0	Ruptured
15607	593[c]	1100	207	30	831.1	3.93	34.3	Ruptured
16279	593	1100	207	30	3246.0	3.91	17.8	Ruptured
16365	649	1200	69	10	5747.0	0.053	6.16	
15842	649	1200	97	14	9660.4	0.139	27.9	
15594	649	1200	124	18	1983.0	0.540	16.8	Discontinued
15538	649	1200	138	20	1884.2	0.790	44.4	Ruptured
15460	649	1200	207	30	110.2	4.27	40.2	Ruptured
17349	704	1300	69	10	2197.7	0.058	8.00	
15889	704	1300	83	12	234.0	0.0303	12.6	Ruptured
15593	760	1400	97	14	100.0	0.083	90.6	Ruptured

[a]All tests are being performed for plate in the as-received (mill-annealed) condition.

[b]Unless otherwise noted, tests are in progress.

[c]Shorter rupture time and high creep strain as compared with test 16279 indicate temperature controller malfunctioning.

3.2.3 Heat-to-Heat Variation of Mechanical Properties of Austenitic Stainless Steels of Types 304 and 316 — Time to Rupture and Minimum Creep Rate Modeling for Types 304 and 316 Stainless Steel — V. K. Sikka and M. K. Booker

Our efforts are continuing to develop time to rupture, t_r, and minimum creep rate, $\dot{e}_m$, models and a creep equation to estimate the behavior of an individual heat of type 304 or 316 stainless steel. Previous work[19,20] showed that the best models to estimate the creep behavior of an individual heat must contain the ultimate tensile strength, S_u, at the creep test temperature. These models and the creep equation were presented[20] during the last quarter for type 304 stainless steel. The purpose of this section is to present the progress made in developing the model for type 316 stainless steel. Furthermore, these models will

be checked against the recently obtained[21] long-term creep data from the National Research Institute of Metals (NRIM),[21] Tokyo.

For type 316 stainless steel 132 t_r and 102 $\dot{e}_m$ data points were available[3,16] with specified elevated-temperature S_u values. Assuming that those tests were run in accordance with ASTM specifications, we expect the strain rate to be 6.67×10^{-4}/sec. These data, when subjected to systematic analysis similar to that used[22] for type 304 stainless steel showed that the optimum models (with and without S_u) were not extremely different in a statistical sense. These models were:

$$\log t_r = -7.801 - 3.047 \log S - 0.009098S + 17{,}565/T \ , \tag{1}$$

$$\log t_r = -5.138 - 2.181 \log S + 13{,}768/T - 3771S/TS_u \ , \tag{2}$$

where S and S_u were in MPa and T was in K. The values of R^2 and SEE for the models in Eqs. (1) and (2) are included in Table 3.6. However, for $\dot{e}_m$ data, where heat-to-heat variations were almost twice as large as those observed for t_r, the following relations were found in terms of S, T and S, T, and S_u:

$$\log \dot{e}_m = 9.6223 + 4.592 \log S + 0.00725S - 21{,}120/T \ , \tag{3}$$

$$\log \dot{e}_m = -3.534 + 2.0734 \log S - 45.064S_u/T + 0.0183S_u \log S \ , \tag{4}$$

where S and S_u are in MPa and T in K. These equations were derived from 102 data points, and values of R^2 and SEE for them are included in Table 3.6. The table shows that R^2 improved from 91.4 to 94% and SEE in $\log \dot{e}_m$ from 0.47 to 0.37 for the model with S_u, Eq. (4). Therefore, S_u can be used to estimate the creep behavior of an individual heat of type 316 stainless steel. Figure 3.33 compares the predicted and experimental values of t_r and $\dot{e}_m$ from the models both with and without S_u [Eqs. (1) through (4)]. The capability of Eq. (4) in estimating the minimum creep behavior of individual heats based on their elevated-temperature ultimate tensile strengths is illustrated in Fig. 3.34 for

ORNL data at a fixed stress and temperature on seven heats of type 316 stainless steel. The improvement in predicting $\dot{e}_m$ of an individual heat from Eqs. (3) and (4) is illustrated in Fig. 3.35 for Blackburn[3] data.

Table 3.6. Summary of the Coefficient of Determination (R^2) and Standard Error of Estimate (SEE) for Literature Data on Type 316 Stainless Steel

Model	Equation	Data Points	Property	R^2 (%)	SEE (log t_r) or (log $\dot{e}_m$)
Without S_u	(1)	132	t_r	88.2	0.29
With S_u	(2)	132	t_r	91.4	0.25
Without S_u	(3)	102	$\dot{e}_m$	91.4	0.47
With S_u	(4)	102	$\dot{e}_m$	94.6	0.37

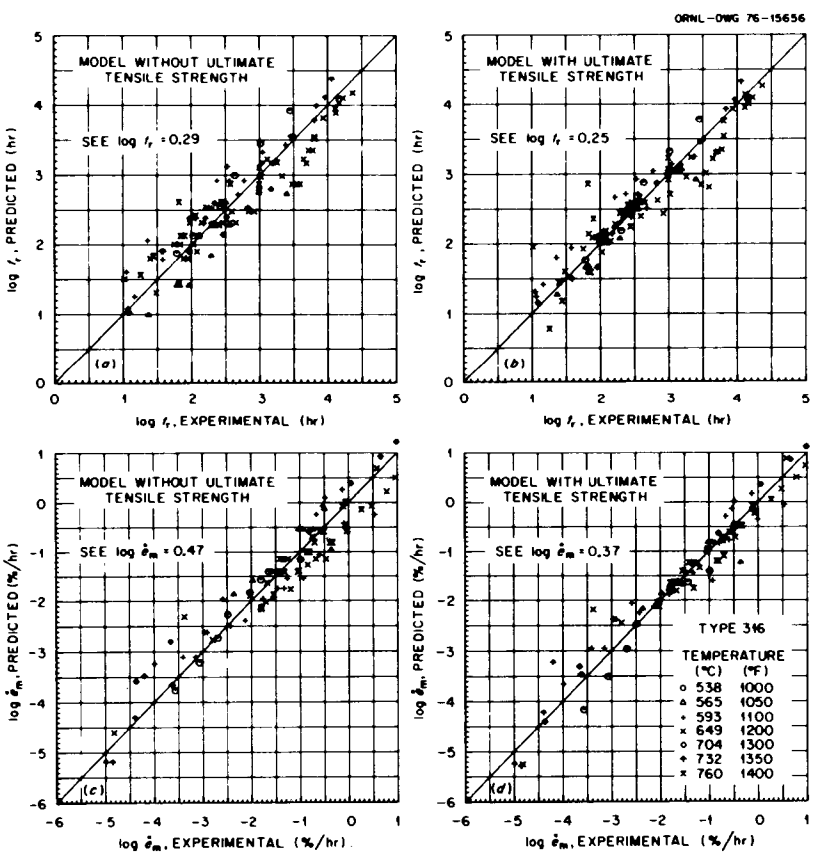

Fig. 3.33. Comparison of Experimental Time to Rupture and Minimum Creep Rate with Predicted Results from Models with and without Ultimate Tensile Strength for Data from Literature on Several Heats of Type 316 Stainless Steel.

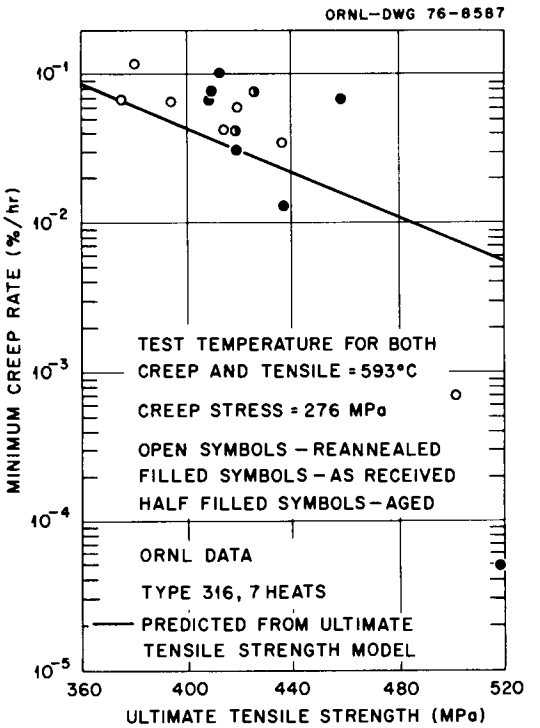

Fig. 3.34. Comparison of ORNL Experimental Minimum Creep Rate Data on Seven Heats of Type 316 Stainless Steel with Values Predicted from the Model Containing S_u.

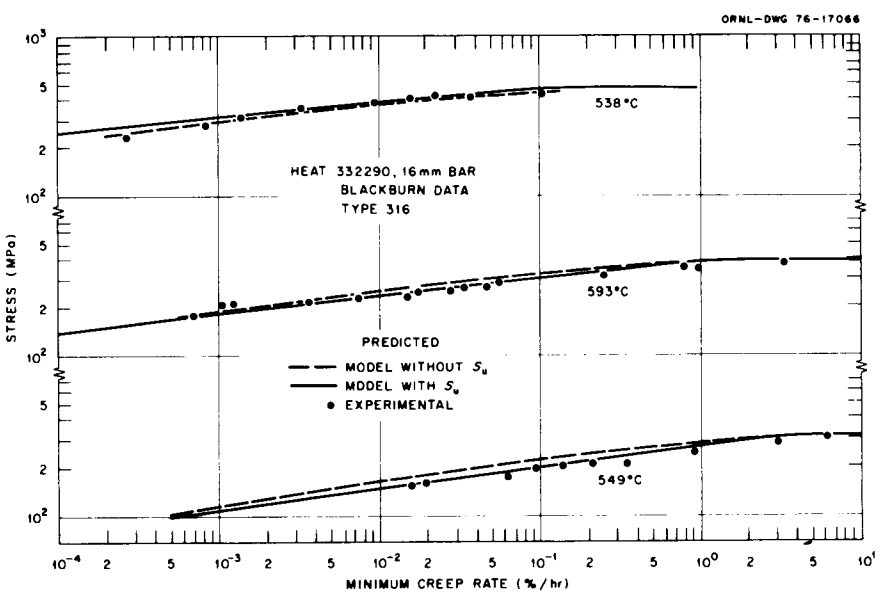

Fig. 3.35. Comparison of Experimental Minimum Creep Rate Data with Values Computed from Models with and without Elevated-Temperature Ultimate Tensile Strength (S_u) for Blackburn Data on Heat 332290 of Type 316 Stainless Steel.

Figure 3.36 shows the plots of minimum creep rate for long-term creep tests on a single heat each of types 304 and 316 stianless steel. Note that these are the first data where the creep rates go to values in the 10^{-7}%/hr range. These data were obtained[21] from NRIM. Included in Fig. 3.36(a) are the predicted values from $\dot{e}_m$ models[20] with and

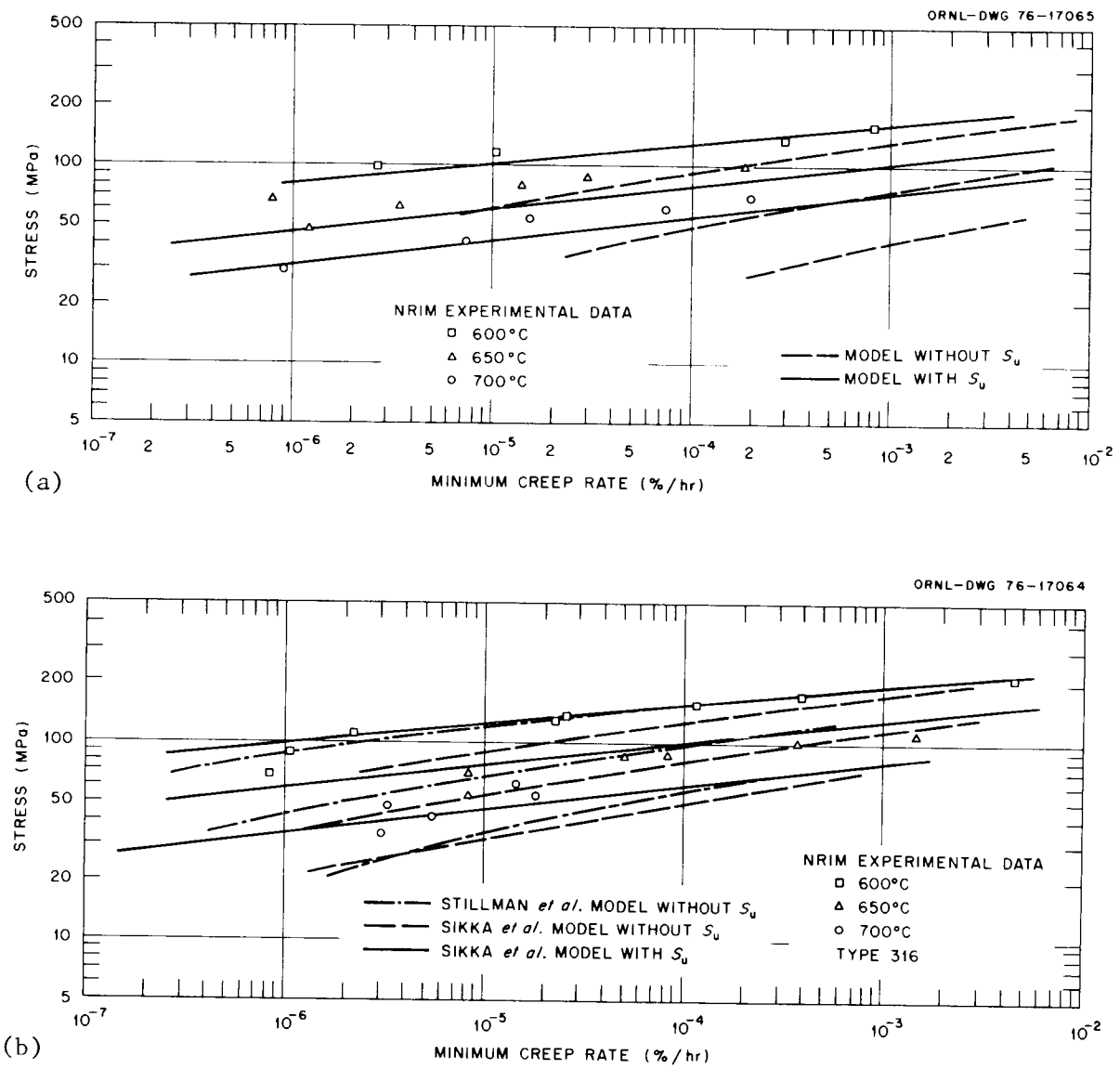

Fig. 3.36. Comparison of Experimental Minimum Creep Rate Data with Values Computed from Models with and without Elevated-Temperature Ultimate Tensile Strength (S_u) for Long-Term Data Obtained from NRIM on (a) Type 304 and (b) Type 316 Stainless Steel.

without S_u. The predicted values from the model without S_u can be off from the experimental value by factors of 100 and greater. However, when the ultimate tensile strength of that particular heat at the creep test temperatures was used in the model with S_u the experimental and predicted values agreed within factors of 10 or less. Thus, with just the knowledge of an elevated-temperature ultimate tensile strength, we can predict with fair accuracy the creep behavior of a new heat.

Figure 3.36(b) compares experimental data on type 316 stainless steel with predicted values from models with and without S_u. The model listed Stillman et al.[23] was derived from heats other than those used in the Sikka et al.[24] model. As mentioned earlier, the Sikka et al.[24] model used only those data points for which elevated-temperature ultimate tensile strength was available. However, that was not the consideration in the selection of data for Stillman et al.[23] model. Figure 3.36(b) indicates that the model with S_u improves significantly the agreement between the experimental and predicted values. Although agreement between the experimental and values predicted from the Stillman et al.[23] model is also fair, it may just be coincidental. However, the model with S_u is always bound to yield a better agreement.

In conclusion the models of t_r and $\dot{e}_m$ containing S_u perform fairly well, even for long-term data. Furthermore, such an excellent agreement between the experimental and predicted values for heats melted in Japan gives additional confidence in the models proposed in the present investigation.

3.2.4 Elastic Properties of Engineering Construction Materials — J. P. Hammond

Precise measurements show that for metals the "elastic" stress-strain relationships are not perfectly linear, even at low stresses and strain levels, and they become progressively more nonlinear as stress increases. Discrepancies thus often occur between elastic constants determined at different strain levels and rates of strain (for example, constants determined by dynamic and static techniques).

The purpose of this program is to correlate the two separate categories of elastic constants (dynamic and static) for reactor materials

of interest. Young's modulus, shear modulus, and Poisson's ratio (E, G, and ν) are being established, with specific attention given to temperature, preference of crystallographic orientation of grains, and other significant test variables. This information is needed to enable more exact and enlightened use of this class of information in engineering design and structural verification work.

3.2.4.1 Program Progress

During the last quarter the dynamic elastic constants were determined for Inconel 617 plate from 24 to 982°C (75—1800°F) by use of our usual accoustical methods. The results presented here supplement comparable information on dynamic elastic constants of 2 1/4 Cr-1 Mo steel,[25] Incoloy 800H,[26] type 304 stainless steel,[27] type 316 stainless steel,[26] and Hastelloy X[28] presented in previous reports. Details of the procedures used with attainable precisions and methods for correcting for systematic errors were recently published.[29]

For establishing the static elastic constants of structural materials, a new method was developed that employs a single test specimen repeatedly for gathering the main body of temperature-dependent data. By using a single specimen repeatedly without disturbing the load train between measurements high resolution of data is assured. Additionally, costs of taking data are reduced. As in the case of determining dynamic moduli, high-accuracy room-temperature values of the constants are established by a separate, more precise method, to which the main body of data is normalized. A cubic polynomial is then fitted to the combined data in a computer by the least squares method to determine best estimates of the constant as a function of temperature. Modifications to the modulus-temperature model to correct for having used the test specimen repetitively may be applied by a bias correction procedure conducted with two or three "fresh" specimens. This static method[30] was recently described in the open literature.[31] Static constants for isothermally annealed 2 1/4 Cr-1 Mo steel (heat 20017) and mill-annealed type 304 stainless steel (heat 9T2796) were presented and compared with results for these materials determined by the dynamic

method. For both materials, values of the Young's moduli decreased characteristically with temperature, with the static curves always falling below the dynamic. The curves for the type 304 stainless steel were virtually straight, and differences between them at any temperature never exceeded 3%. For 2 1/4 Cr-1 Mo steel, the rate of modulus decrease increased somewhat with temperature. The static curve[31] was even farther below the dynamic for 2 1/4 Cr-1 Mo steel than for type 304 stainless steel, falling about 4.3% below at room temperature and 9.3% below at 650°C (1200°F).

The foregoing results on static constants were determined with mechanical extensometers fitted with linear variable differential transformer (LVDT) strain sensors*, and, unfortunately, only Young's modulus was obtainable by this arrangement. In the past year, efforts were made to determine Young's modulus and Poisson's ratio on 2 1/4 Cr-1 Mo steel and type 304 stainless steel with weldable resistance strain gages (AILTECH type MG-425) mounted both longitudinally and laterally to measure axial extension and diametral contraction simultaneously. The gages are of the temperature-compensating type and are designed to correct for differential thermal expansion between gage and test specimen and gage resistivity change to a temperature of 650°C. However, these gages failed to perform as satisfactorily as hoped, and we have since acquired capicator strain gages (HITECH, model HT-DC-100-06) for evaluation and comparison with the weldable resistance gages for this use. Values of Young's modulus determined with the resistance strain gages generally ran 5 to 10% higher than ones established with our extensometer fitted with LVDTs and are suspect. Also the compensation for temperature effects did not appear satisfactory for 2 1/4 Cr-1 Mo steel throughout the test range, nor for type 304 stainless steel above 425°C (800°F).

The problem of temperature compensation is overcome in the present capacitor gage simply by constructing a vital link in the gage of the same material (or equivalent) as the test specimen. The most important source of error in the use of the capacitor gage will be the accuracy

---

*A high-sensitivity model (type 6233) made by Atomic Timing and Control Inc.

to which gage length is known. This length will correspond to the distance between the two effective locations of weld attachment used for mounting the gage. Work is under way to develop suitable means for attaching such gages and accurately assessing gage length. To help alleviate this problem, a large rectangular test specimen was designed to accommodate a 25-mm (1-in.) gage length, both for laterally and longitudinally mounted gages. The other features and procedures to be employed in the use of the capacitor gages are similar in all respects to those developed for the weldable resistance strain gages.

Much of the last quarter was spent securing materials and fabricating specimens for future tests. Table 3.7 lists the various specimens for both dynamic and static testing and gives pertinent information on the materials from which they are being prepared and their orientation in the product forms. All the alloys listed have been received, and the specimens for which their associated heat treating conditions are underlined have been completed.

The future tests embrace the additional materials of interest to the LMFBR, the GCR, and the transition joint programs. Additional tests are included to further evaluate the effects of directionality of testing (anisotropy of constants) and heat-to-heat variations in types 316 and/or 304 stainless steel product forms.

The experiments listed for the nickel-based alloys (Table 3.7, Codes 41—44) are designed to determine the influence of solute additions of increasing ion size on the dynamic constants of a solvent lattice, in this case electron-beam-melted nickel. This information is sought to help explain heat-to-heat variation effects. As discussed in the last quarterly report,[32] dynamic elastic constants appear to decrease with strain to the lattice, whether imparted by alloying or cold working.

Because the anisotropy of elastic constants was found in past experiments to be greatly diminished by taking test specimens from product forms of large dimensions, the rectangular test bars for future static tests are being taken from stock of diameters or thicknesses of 0.1 m (4 in.) or greater (Table 3.7). We have made an exception for the specimen of 2 1/4 Cr-1 Mo steel (Code 24) since material of larger

dimensions was unavailable and prior tests have proven this alloy to be highly isotropic in the 25-mm (1-in.) thickness anyway.[25] The effect of product form dimensions on the anisotropy of dynamic constants in stainless steels will be treated in a future report.

Table 3.7. Specimens for Elastic Properties Study

Code	Material					Orientation of Specimen Axis[a]	Condition[b]			
	Alloy	Dimension (mm)	Dimension (in.)	Form	Heat		Dynamic		Static	
							Blocks	Wire	Round	Rectangular
23	Carbon Steel SA-416-70	102	4	Plate	Lukens A8448	∥ RP	WQ+T	WQ+T	WQ+T	WQ+T
24	2 1/4 Cr-1 Mo	25	1	Plate	20017	∥ RD	IA[c]	IA[c]	IA	IA
25	Inconel 718	107	5	Forging	5-9422	∥ FP	AH	AH	AH	AH
26	Inconel 600	115	4 1/2	Rod		∥ RD	SA	SA	SA	SA
27	Incoloy 800H	152	6	Rod		∥ RD	SA	SA	SA	SA
28	Inconel 606[d]	6	1/4	Rod		∥ SD		SA[c]		
29	Type 16-8-2 SS	6	1/4	Rod		∥ SD		SA		
30	Inconel 82	19	3/4	Weldment		∥ WD			SR	
31	Type 16-8-2SS	19	3/4	Weldment		∥ WD			SR	
32	Type 316SS	13	1/2	Plate	327686	∥ RD	SA			
33	Type 316SS	13	1/2	Plate	327686	in RP, 45°RD	SA			
34	Type 316SS	13	1/2	Plate	327686	in RP, 90°RD	SA			
35	Type 316SS	13	1/2	Plate	327686	⊥RP	SA			
36	Type 316SS	13	1/2	Plate	2P3212	∥ RD	SA			
37	Type 316SS	13	1/2	Plate	500613	∥ RD	SA			
38	Type 304SS	25	1	Plate	8043813	∥ RD	SA,MA			
39	Type 304SS	25	1	Plate	9T2796	∥ RD	SA[e]			
40	Type 304SS	34	1 3/8	Plate	187	∥ RD	SA			
41	Nickel[f]	3	0.1	Wire		∥ SD		SA[g]		
42	Ni-0.1 at.% V	3	0.1	Wire		∥ SD		SA[g]		
43	Ni-0.1 at.% Mo	3	0.1	Wire		∥ SD		SA[g]		
44	Ni-0.1 at.% Nb	3	0.1	Wire		∥ SD		SA[g]		

[a] ∥ = parallel; RP = rolling plane; RD = rolling direction; FD = forging direction; SD = swaging direction; WD = welding direction.

[b] WQ+T = water quenched and tempered; IA = isothermally annealed; AH = age hardened; SA = solution annealed; SR = stress relieved. Underscore indicates specimen already prepared.

[c] Testing on specimen completed earlier.

[d] Wrought form of Inconel 82.

[e] Repeat of an earlier test to compare testing results.

[f] Electron-beam melted Nickel.

[g] Because of limitation on the amount of material, specimen was prepared as wire but to be tested at room temperature to improve accuracy of results.

3.2.4.2 Dynamic Elastic Constants of Inconel 617 — J. P. Hammond and M. W. Moyer*

The dynamic elastic constants were determined parallel to the rolling direction in a plate of Inconel 617 (heat XX00A3US) of 25-mm thickness.

*Laboratory Development, Oak Ridge Y-12 Plant.

The alloy was in the solution-annealed condition. The polynomials established for E, G, and ν are of the usual form:

$$X = X_0[1 + A_x(T - T_0) + B_x(T - T_0)^2 + C_x(T - T_0)^3] ,$$

where

X = the property (E, G, or ν),
X_0 = same at 24°C (75°F),
T = temperature in °C or °F,
T_0 = 24°C (75°F) and
A_x, B_x, and C_x = constants.

The coefficients for the polynomials and standard deviations of fit of data are given in Table 3.8, while graphical displays of the equations with the data points superimposed are presented in Fig. 3.37. The room-temperature elastic constants of Inconel 617, to which the elevated-temperature properties were normalized are:

$$E = 216.4 \pm 0.5 \text{ GPa}$$
$$= 31.38 \times 10^6 \pm 0.07 \times 10^6 \text{ psi}$$
$$G = 82.80 \pm 0.08 \text{ GPa}$$
$$= 12.01 \times 10^6 \pm 0.01 \times 10^6 \text{ psi}$$
$$\nu = 0.3065 \pm 0.0005$$

Table 3.8. Coefficients for Polynomial Fit to Elastic Constants of Inconel 617[a]

Constant	Values of Coefficients				
	X_0	A_x, °C^{-1}	B_x, °C^{-2}	C_x, °C^{-3}	Std Dev of Fit
E	216.4 GPa 31.38×10^6 psi	-2.27189×10^{-4}	-8.67747×10^{-8}	-1.83272×10^{-11}	12.3 GPa 1.78×10^5 psi
G	82.80 GPa 12.01×10^6 psi	-4.33823×10^{-4}	6.18203×10^{-7}	-6.21425×10^{-10}	6.10 GPa 8.85×10^4 psi
ν	0.3065	1.03756×10^{-3}	-3.67059×10^{-6}	3.24225×10^{-9}	1.88×10^{-3}

[a] T_0 = 24°C.

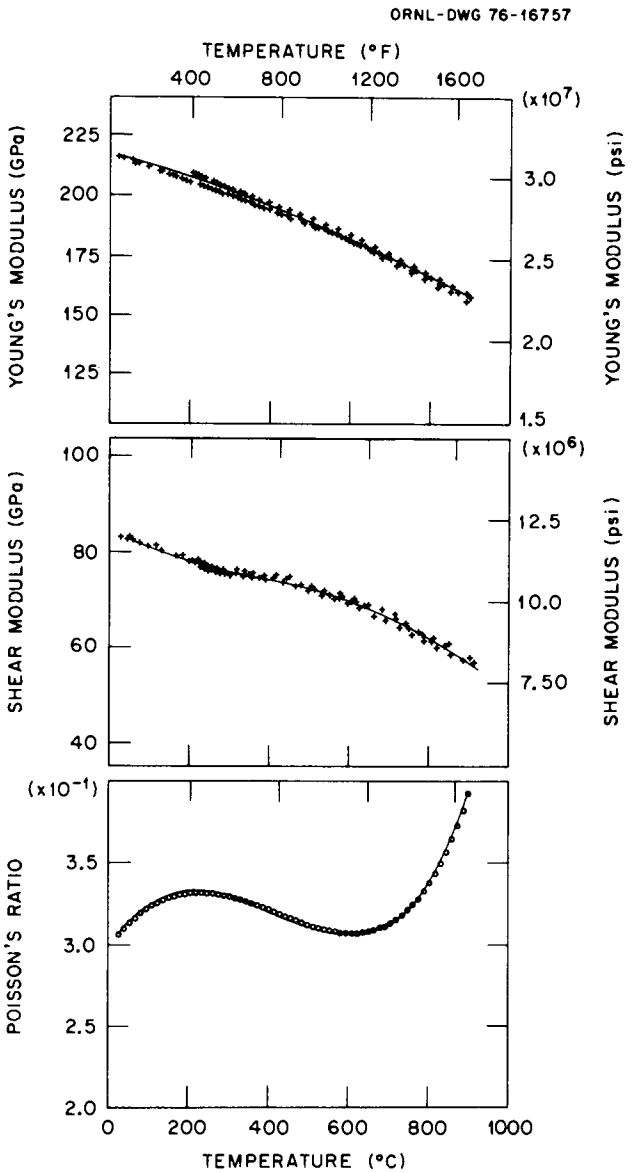

Fig. 3.37. Dynamic Elastic Constants of Inconel 617, Heat XX00A3US.

The elastic properties estimated with the polynomials at 24°C (75°F) and at 28°C (50°F) intervals from 38°C (100°F) to 899°C (1650°F) are given in Table 3.9.

The dynamic Young's and shear moduli of Inconel 617 (Fig. 3.37) decrease characteristically with temperature. The Poisson's ratio curve shows a pronounced sinusoidal effect, tending toward a value of 0.5 at melting.

Table 3.9. Dynamic Elastic Constants of Inconel 617, Heat XX00A3US

Temperature		Young's Modulus		Shear Modulus		Poisson's Ratio
(°C)	(°F)	(GPa)	(psi)	(GPa)	(psi)	
24	75	216.4	31.39×10^6	82.81	12.0×10^6	0.306
38	100	215.7	31.29	82.32	11.94	0.310
66	150	214.4	31.09	81.43	11.81	0.316
93	200	212.9	30.88	80.60	11.69	0.321
121	250	211.5	30.67	79.77	11.57	0.325
149	300	210.0	30.45	79.01	11.46	0.328
177	350	208.4	30.23	78.32	11.36	0.330
204	400	206.9	30.01	77.70	11.27	0.331
232	450	205.3	29.78	77.08	11.18	0.332
260	500	203.7	29.55	76.53	11.10	0.331
288	550	202.1	29.31	75.98	11.02	0.330
316	600	200.4	29.06	75.43	10.94	0.328
343	650	198.7	28.82	74.88	10.86	0.326
371	700	196.9	28.56	74.39	10.79	0.324
399	750	195.1	28.30	73.84	10.71	0.322
427	800	193.3	28.04	73.29	10.63	0.319
454	850	191.5	27.77	72.74	10.55	0.316
482	900	189.6	27.50	72.19	10.47	0.314
510	950	187.7	27.22	71.57	10.38	0.311
538	1000	185.7	26.93	70.88	10.28	0.309
566	1050	183.7	26.64	70.19	10.18	0.308
593	1100	181.6	26.34	69.50	10.08	0.307
621	1150	179.5	26.04	68.67	9.96	0.307
649	1200	177.4	25.73	67.84	9.84	0.308
677	1250	175.3	25.42	66.88	9.70	0.310
704	1300	173.1	25.10	65.91	9.56	0.313
732	1350	170.8	24.77	64.81	9.40	0.318
760	1400	168.6	24.44	63.64	9.23	0.324
788	1450	166.2	24.10	62.33	9.04	0.333
816	1500	164.0	23.76	60.95	8.84	0.343
843	1550	161.4	23.41	59.50	8.63	0.357
871	1600	158.9	23.05	57.92	8.40	0.373
899	1650	156.4	22.69	56.19	8.15	0.393

3.2.5 Inconel Alloy 718 Mechanical Property Program — T. K. Roche

Inconel alloy 718 has been specified for certain structural components of the Clinch River Breeder Reactor at temperatures up to about 649°C (1200°F). For purposes of reactor design and to provide adequate data to support an ASME Code Case application, the mechanical property data base needs to be expanded for the alloy in the commercially heat-treated condition. In support of the program already under way at E. G. and G. Idaho, Inc., mechanical property studies on the alloy were recently initiated at ORNL. Data to be obtained from the overall E. G. and G. and ORNL effort include: tensile, creep-rupture, step-load creep, cyclic creep, stress relaxation, low- and high-cycle fatigue, plasticity, elastic properties, and long-term aging effects. In addition physical properties to be determined include density, thermal expansion, heat capacity, and thermal conductivity.

At the request of E. G. and G., creep-rupture tests are in progress on specimens of Heat 2180-4-9478 [13-mm-thick (1/2-in.) plate], which were supplied in the commercially heat-treated condition, [i.e., 954°C (1750°F) solution anneal plus duplex age]. The chemical analysis of this heat is shown in Table 3.10. The data obtained will be used for developing a creep equation for the alloy at 593, 649, 704, and 760°C (1100, 1200, 1300, and 1400°F). A few tests at 538 and 732°C (1000 and 1350°F) have also been scheduled. Stress levels at each temperature have been selected to obtain rupture lives differing by orders of magnitude within limits from below 100 hr to 10,000 hr guided by the data of Barker et al.[33] Stress-rupture results obtained to date are tabulated in Table 3.11 and compared in Fig. 3.38 with data on the same heat by E. G. and G. and the data from a different heat and product form by Barker et al. For Heat 2180-4-9478 the ORNL results show a slight shift in the direction of longer rupture times relative to the E. G. and G. data, and both sets of these data generally indicate the same shift when compared with the data by Barker et al.

We have on hand hot-forged bar and hot-rolled plate of three additional heats of alloy 718 produced by the same vendor as Heat 2180-4-9478. Chemical analyses can be found in Table 3.10. This material

Table 3.10. Chemical Analysis of Various Heats of Inconel Alloy 718

Element	Content, wt %, for Each Heat			
	2180-4-9478	2180-5-9419	2180-4-9497	2180-5-9422
Al	0.54	0.54	0.57	0.52
B	0.002	0.003	0.006	0.003
C	0.05	0.05	0.05	0.05
Nb + Ta	5.08	5.13	5.08	5.11
Co	0.30	0.27	0.42	0.33
Cr	18.21	18.02	18.15	17.71
Cu	0.02	0.05	0.02	0.03
Fe	Bal	Bal	Bal	19.02
Mn	0.21	0.23	0.17	0.23
Mo	3.05	3.02	3.10	3.07
Ni	52.63	52.63	52.37	Bal
P	0.005	<0.005	<0.005	0.005
S	0.005	<0.002	<0.005	0.002
Si	0.10	0.10	0.03	0.07
Ti	0.97	1.06	0.98	1.02

Table 3.11. Stress-Rupture Properties of Inconel Alloy 718[a]

Test	Test Conditions				Rupture Time (hr)	Strain, %	
	Temperature		Stress			Loading	Time Dependent
	(°C)	(°F)	(MPa)	(ksi)			
17310	538	1000	1034	150.0	2047.4	0.85	2.62
17475	649	1200	758	110.0	86.7	0.55	15.75
17474	649	1200	620	90.0	1023.2	0.44	15.92
17175	649	1200	579	84.0	1990.6	0.55	10.05
17437	704	1300	586	85.0	49.0	0.44	20.21
17576	704	1300	414	60.0	744.3	0.29	18.11
17176	704	1300	365	53.0	1205.0	0.25	19.62
17313	732	1350	310	45.0	487.8	0.23	24.03
17423	760	1400	379	55.0	42.2	0.29	22.34
17179	760	1400	241	35.0	288.3	0.14	25.05
17422	760	1400	172	25.0	797.0	0.12	34.88

[a]Heat 2180-4-9478, 13-mm (1/2-in.) plate. Heat treatment: 954°C (1750°F) solution anneal 1 hr., air cool, age 718°C (1325°F) 8 hr, furnace cool to 621°C (1150°F) and age an additional 8 hr.

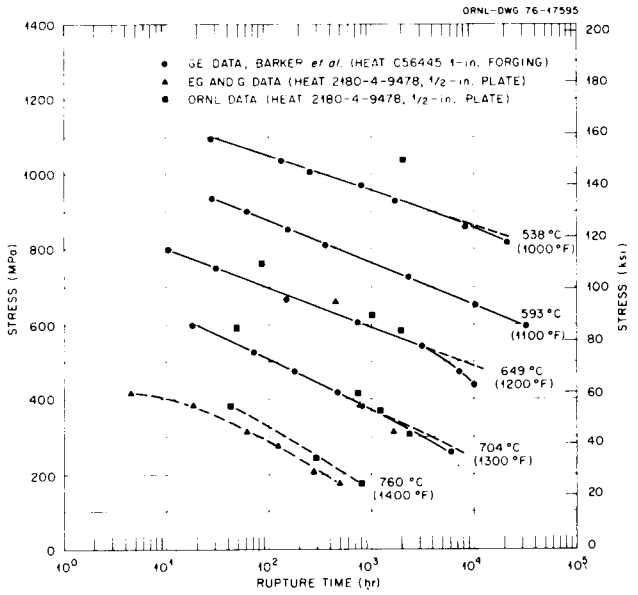

Fig. 3.38. Stress-Rupture Behavior of Inconel Alloy 718 in the Commercially Heat-Treated Condition.

has been sectioned and the types and quantities of specimens machined and heat-treated are listed in Table 3.12. Creep-rupture testing will proceed according to the matrix being followed for Heat 2180-4-9478 and should provide an indication of property variability between heats and product forms. Minimal tensile testing at room and elevated temperature is presently planned, and exploratory stress relaxation tests will be initiated. Furnaces have been scheduled for starting aging heat treatments for times up to three years at 593, 649, 704, and 760°C (1100, 1200, 1300, and 1400°F). The aging blanks are nominally 13 mm diam by 127 mm long (1/2 by 5 in.) and will subsequently be machined into specimens for creep-rupture and other tests.

Table 3.12. Specimens for the Heat-to-Heat Variation Study of Alloy 718

Heat	Product Form	Thickness		Number of Specimens		
		(mm)	(in.)	Creep	Tensile, Relaxation	Aging Blanks
2180-5-9422	Forging	203	8	22	9	34
2180-5-9419	Plate	13	1/2	25	12	53
2180-4-9497	Plate	19	3/4	25	12	34
Total				72	33	121

A relatively large portion of Heat 2180-5-9422 has been designated for step-load and cyclic creep tests, plasticity tests, and determination of elastic properties, including Young's modulus, Poisson's ratio, and shear modulus. Blanks have been cut, and we are preparing specimens for these tests.

Several pieces of Heat 2180-4-9478 were recently obtained from E. G. and G. for physical property studies. Specimens have been prepared, and determination of the coefficient of expansion and thermal conductivity between room temperature and 704°C (1300°F) is in progress.

3.3 MECHANICAL AND METALLURGICAL BEHAVIOR OF WELDMENTS FOR LMFBR*

P. Patriarca, G. M. Slaughter, W. R. Martin, and C. R. Brinkman

3.3.1 Status of Testing on 16-8-2 Submerged-Arc Welds — R. T. King, D. P. Edmonds, and E. Bolling

The creep, tensile, and impact behavior of a type 16-8-2 stainless steel weld made in 25-mm-thick (1-in.) type 316 stainless steel plate is being characterized. The macrostructure of the weld is shown in Fig. 3.39.

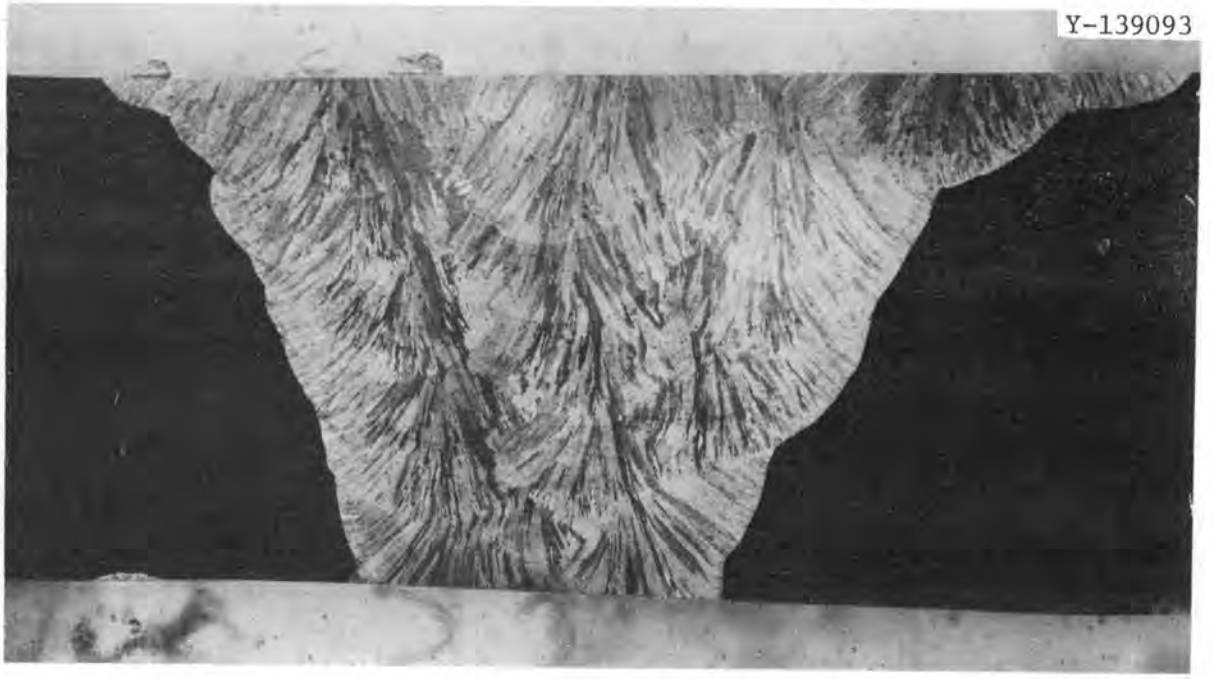

Fig. 3.39. Macrostructure of a Type 16-8-2 Submerged-Arc Weld in 25-mm-Thick Type 316 Stainless Steel Plate. 2.8 ×.

*Progress on work performed under 189a OH024.

The history of the weld and preliminary tensile data have been published previously.[34] Hardness traverses have shown the root pass section to be significantly harder than the surface pass or crown region.[34] Room-temperature tensile tests performed on longitudinal all-weld-metal specimens at 0.004/min nominal strain rate showed that the yield strengths in the root pass region tend to be higher than those measured for surface pass specimens, and that both the weld metal and heat-affected zone have higher yield strengths than as-received base metal[34] (Fig. 3.40). This pattern is common to many as-received austenitic stainless steel welds that have been investigated.[35] Elevated-temperature tensile data showed[34] that while the yield strength of the weld metal exceeds minimum properties for type 316 stainless steel base metal, the ultimate tensile strengths can be below the minimum trend curve for type 316 stainless steel base metal from 204 to 649°C (400–1200°F).

Several creep tests have been run at 649 and 566°C on both longitudinal and transverse all-weld-metal specimens. The available data are summarized in Table 3.13, and creep-rupture data are plotted

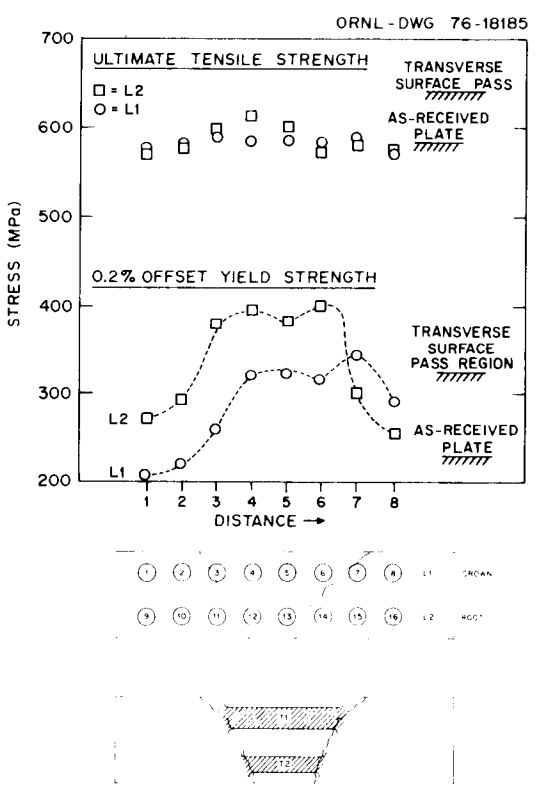

Fig. 3.40. Tensile Strength Properties of Variously Located Specimens in 16-8-2 Submerged-Arc Weld and Weldments.

Table 3.13. Creep-Rupture Test Data for Babcock and Wilcox Type 16-8-2 Stainless Steel Submerged-Arc Welds

Stress (MPa)	Stress (ksi)	Specimen Type and Number	Test	Rupture Time (hr)	Time to Tertiary Creep: Linearity	Time to Tertiary Creep: 0.2% Offset	Total Strain, %: Onset of Tertiary Creep: Linearity	Total Strain, %: Onset of Tertiary Creep: 0.2% Offset	Total Strain, %: Rupture	Reduction of Area (%)
				Tests at 649°C (1200°F)						
172	25	L1 776-L35	FWB-239	31.5	1.2	1.75	1.37	1.7	44.2	58.4
138	20	L1 775-L1	FWB-249	478.5	25	58	1.46	3.0	42.5	54.0
110	16	L1 775-L6	FWB-250	3656.0					∿60	
172	25	L2 776-L37	FWB-237	73.9	∿4	∿5.7	∿0.8	∿1.1	48.5	50.1
138	20	L2 775-L14	FWB-254	609.4	34	73	0.6	1.1	44.2	56.1
110	16	L2 775-L10	FWB-257	3401.6					∿48	
172	25	T1 776-T3	FWB-240	121.3	6	11.5	∿0.96	∿1.6	30.7	37.7
138	20	T1 776-T1	FWB-252	1334.6	710	180	∿1.2	∿2.3	30.3	32.5
110	16	T1 775-T5	FWB-253	>3684					>14	
172	25	T2 776-T6	FWB-246	111.8	11.4	20	0.9	1.75	34.7	49.0
138	20	T2 775-T6	FWB-256	1009.0	250	300	1.1	1.39	15.7	36.9
				Tests at 566°C (1050°F)						
310	45	L1 776-L34	FWB-241	45.8	29	31	9.8	11.0	44.1	45.6
276	40	L1 775-L2	FWB-255	209.3	105	124	7.9	9.2	23.3	29.3
276	40	L1 775-L3	FWB-259	174.0	85	95	17.0	18.4	40.3	38.0
310	45	L2 775-L5	FWB-248	78.8	27.5	29	8	8.4	34.7	36.2
241	35	L2 775-L3	FWB-259	699.8	323	395	4.4	5.4	26.2	62.0
310	45	T1 776-T1	FWB-238	75.3	37.5	41.8	19.9	21.2	42.8	25.6
276	40	T1 775-T3	FWB-263	201.5	137.5	198	7.6	9.5	14.0	15.6
241	35	T1 775-T7	FWB-260	1279.5	880	1240	3.0	3.8	7.7	12.5
310	45	T2 776-T2	FWB-245	109.6	2.8	38.4	1.6	3.0	11.5	13.9
310	45	T2 775-T4	FWB-264	142.5	38	55	2.6	3.5	14.0	18.4

in Fig. 3.41. The rupture times for the weld metal are all below the average rupture times for type 316 stainless steel base metal,[36] and the data frequently fall below the average − 1.65σ "minimum" curves for type 316 base metal. At least one of the transverse weld specimens failed in the heat-affected zone (HAZ), because the fusion line was contained at one end of the gage length as a result of either machining error or a slightly narrower weld region than was anticipated. This test (FWB-263) is to be repeated. However, another transverse weld specimen (Test FWB-245) failed in the weld metal with clear indications of a substructural fracture morphology.[34] Close attention will be paid to the failure mode of transverse specimens in the final report on those tests. The creep testing program is now aimed at completing the tests at 566°C (1050°F) at 241 and 207 MPa (35 and 30 ksi) stress levels.

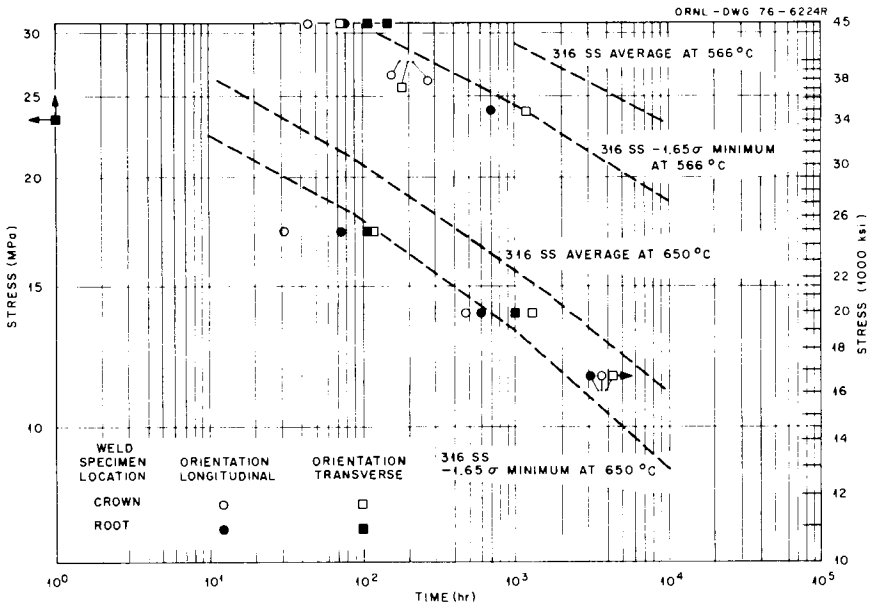

Fig. 3.41. Comparison of Creep-Rupture Properties of Type 16-8-2 Stainless Steel Submerged-Arc Weld Specimens with Type 316 Stainless Steel Base Metal (after Blackburn).

A series of whole-weld sections was aged in an air furnace for times to 500 hr at 566 and 649°C. Transverse-to-the-weld Charpy impact specimens were then machined from the aged welds and from as-welded sections. Specimens were cut from both the surface and root pass regions. Ferrite numbers were then determined at three locations corresponding to both the crown and root surfaces of the weld, as shown in Fig. 3.42. The data, shown in Table 3.14, have not been statistically analyzed. However, they show a trend toward lower ferrite numbers in the root pass region than at the crown. The ferrite numbers vary with location on the surface. Comparisons of the readings (Table 3.14, Fig. 3.42) at location 1 with locations 3 and 4 and of the readings at location 2 with locations 5 and 6 indicate the magnitude of these variations. If there is a trend, it is probably toward lower ferrite numbers near the fusion line.

The as-received Charpy weld specimens were notched and broken in sets of three, so that the notches propagated in the weld direction. One set of tests (Fig. 3.43) showed that the two test welds used for as-welded properties had comparable impact behavior at −184°C (−300°F), room

ORNL-DWG 76-18186

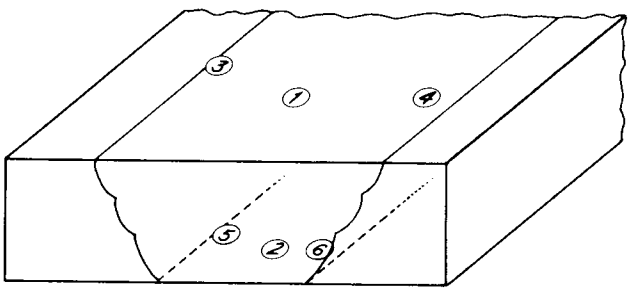

Fig. 3.42. Locations at Which Ferrite Numbers Were Measured in Submerged-Arc Type 16-8-2 Stainless Steel Welds.

Table 3.14. Ferrite Numbers of Submerged-Arc Type 16-8-2 Stainless Steel Welds Measured on Untested Charpy V-Notch Specimens Taken from Various Locations in the Weld

Aging Treatment			Ferrite Number at Various Locations[a]					
(hr)	(°C)	(°F)	Crown 1	Root 2	Crown 3	Crown 4	Root 5	Root 6
0			2.3, 2.1, 2.3 2.0, 2.0, 2.1	1.3, 1.6, 1.5 1.4, 1.8, 1.4	1.6	1.3	1.0	0.9
10	649	1200	1.3, 1.5, 1.3	0.9, 0.9, 0.8	1.0	1.0	0.9	0.7
100	649	1200	2.0, 1.8, 2.2	0.8, 0.8, 0.8	1.4	1.6	1.7	0.5
500	649	1200	1.4, 1.6, 1.7	1.1, 0.7, 0.8	1.2	3.0	0.6	0.7
100	566	1050	1.0, 1.2, 1.0	0.6, 0.5, 0.5	0.8	1.4	0.5	0.5
500	566	1050	1.3, 1.4, 1.3	0.8, 0.8, 0.8	1.0	0.9	0.8	0.7

[a]The locations are identified in Fig. 3.42. Each value given represents one FN reading by a Ferritescope. Six as-welded specimens and three aged at each set of conditions were measured at locations 1 and 2; only one for each condition was measured at the other locations. Specimens were machined and macroetched.

temperature, and 288°C (550°F). The highest energy absorptions were for room-temperature tests. A series of tests on crown and root pass specimens from aged welds is shown in Fig. 3.44. Aging at 566°C reduced impact energy absorption to below 68 J (50 ft-lb) for both surface and root pass specimens. The notches in the specimens were machined from near the fusion line of welds aged for 500 hr at 649°C. The data are thus not comparable with the balance of the data, all of which involved notches in the center of the weld. Fresh specimens have been aged but not tested.

ORNL-DWG 76-18187

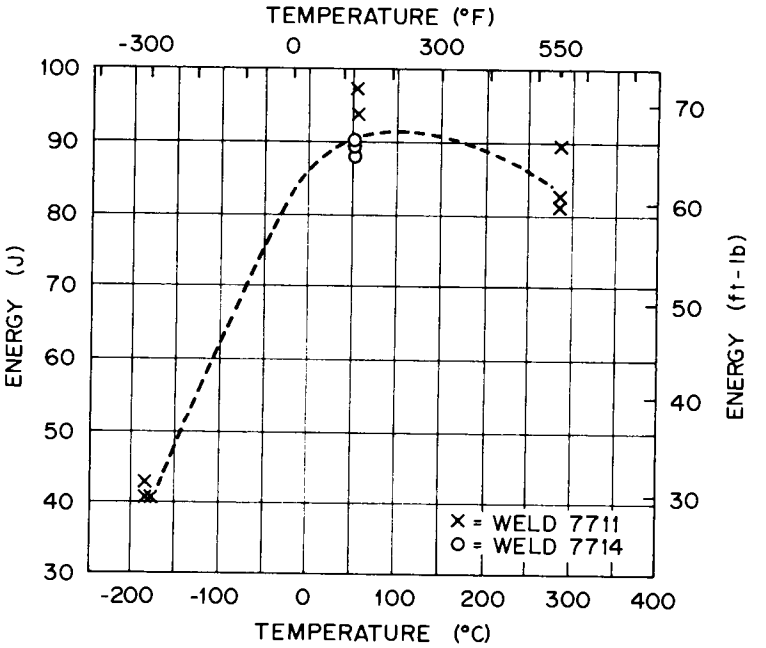

Fig. 3.43. Effect of Temperature on C_V Impact Energy for Notches Propagating in Weld Direction, 16-8-2 SA Welds.

ORNL-DWG 76-18188

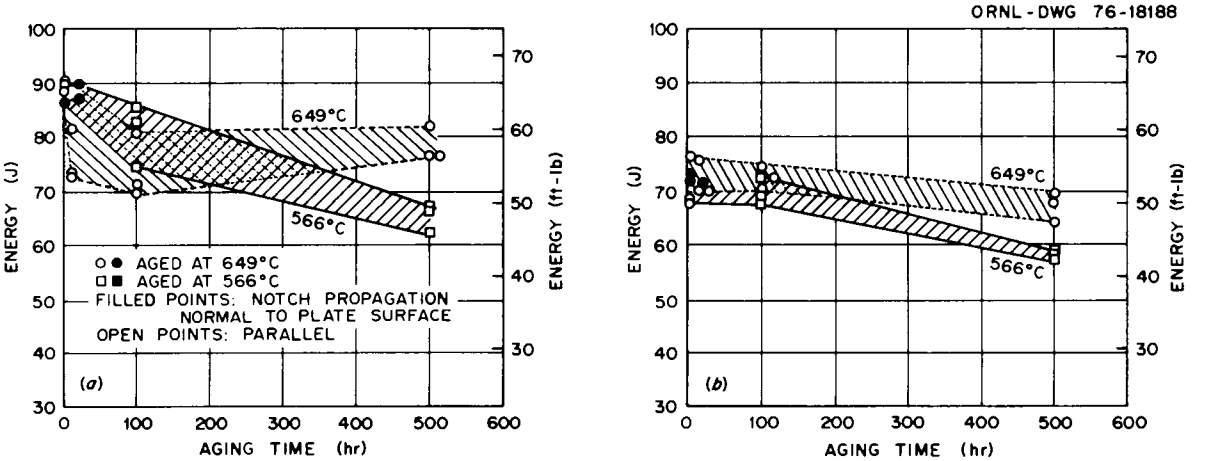

Fig. 3.44. Effect of Aging at 649 and 566°C on C_V Impact Energy for Notches Propagating in Weld Direction, 16-8-2 SA Welds. (a) Surface (crown) specimens. (b) Root specimens.

3.3.2 Mechanical Properties of Welds in LMFBR Primary Piping Materials — R. T. King

A report entitled *Mechanical Properties of LMFBR Primary Piping Materials* by C. R. Brinkman, V. K. Sikka, and R. T. King was issued giving the current status of our work in this area.[37] Tensile data for type 308 stainless steel welds and weldments were compiled and compared with the properties of type 304 stainless steel base metal. Creep data for type 308 welds were not presented because type 304 stainless steel use is presently likely to be limited to cold legs of LMFBR piping systems. On the other hand, type 316 stainless steel welds are likely to occur in the hot legs of piping systems where Code Case 1592 requires consideration of time-dependent deformation of austenitic materials in Class 1 systems at temperatures above 427°C (800°F). Creep-rupture data for 16-8-2 and type 316 stainless steel welds were compiled and compared with the range of creep-rupture properties for type 316 stainless steel base metal for temperatures to 649°C (1200°F) (Fig. 3.45). Since ductility of austenitic weldments is an important concern, the

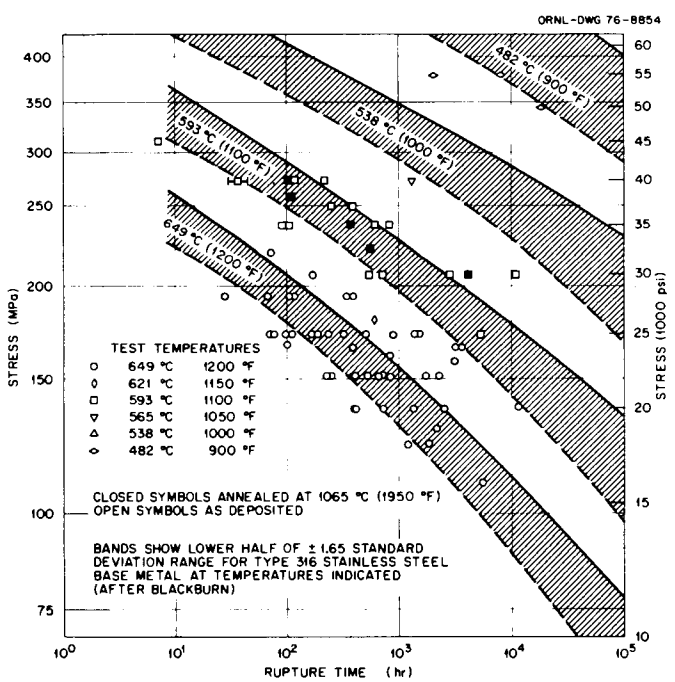

Fig. 3.45. Creep-Rupture Behavior of Type 16-8-2 Weld Metal Deposited by Gas Tungsten-Arc and Shielded Metal-Arc Processes.

total elongation measured in creep tests for types 16-8-2 and 316 stainless steel weld metals were compiled and plotted as functions of rupture time (Fig. 3.46).

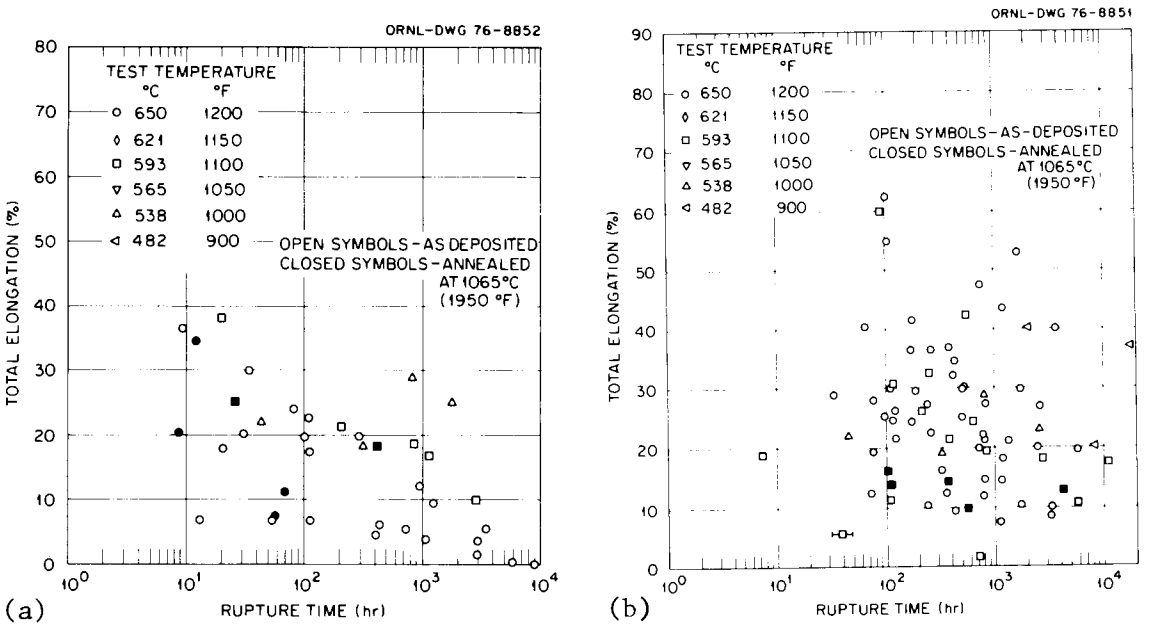

Fig. 3.46. Strain at Rupture of (a) Type 316 Stainless Steel and (b) 16-8-2 Weld Metal from Gas Tungsten-Arc and Shielded Metal-Arc Deposits.

3.3.3 Novel Measurement of Ultrasound Velocity in Type 308 Stainless Steel Weld Metal — L. Adler* and K. V. Cook

Studies of mechanical properties of austenitic stainless steel weld metal have shown that the elastic properties of weldments are anisotropic. Recent measurements[38] with both longitudinal and shear wave ultrasonic techniques detected velocity changes along special planes of the weldment. The macrostructure of specimens of a single-pass stainless steel (type 308) electroslag weld leads us to expect either orthotropic or special orthotropic (transversely isotropic) symmetry for the elastic constants. All together nine elastic constants are required to relate stress and elastic strain for orthotropic symmetry. The relationship between the

*Consultant from the University of Tennessee.

elastic stiffness constants and the ultrasonic velocity may be obtained in matrix form by use of the Christoffel relations. By measuring ultrasonic velocities the components of the elastic stiffness matrix may be obtained. For our initial work, sections were taken from the weldment, and contact methods were used to measure velocity changes in directions governed by the planes of the sections. This approach is slow and costly and limits the information that can be obtained. Therefore, we devised a special mechanical goniometry system that uses immersion techniques for coupling the transducer to the test weld.

Ultrasonic velocity was measured in various orientations of the weld structure with this immersed ultrasonic through-transmission system on cylindrical specimens taken from the three orthogonal directions in the weld. In each cylindrical sample velocity changes were measured as a function of rotation (or angle). Both longitudinal and shear wave velocities vary with sample rotation. The longitudinal velocity varies by as much as 15% and the shear 30% in the 1-3 plane for the type 308 stainless steel weld metal, as shown in Fig. 3.47. The solid curves in Fig. 3.47 are calculated from Christoffel's equation for the assumed orthotropic symmetry, and the points are experimental. Data such as those presented in Fig. 3.47 can be applied to deformation analyses for real weldments, as we previously indicated.[38] These results have

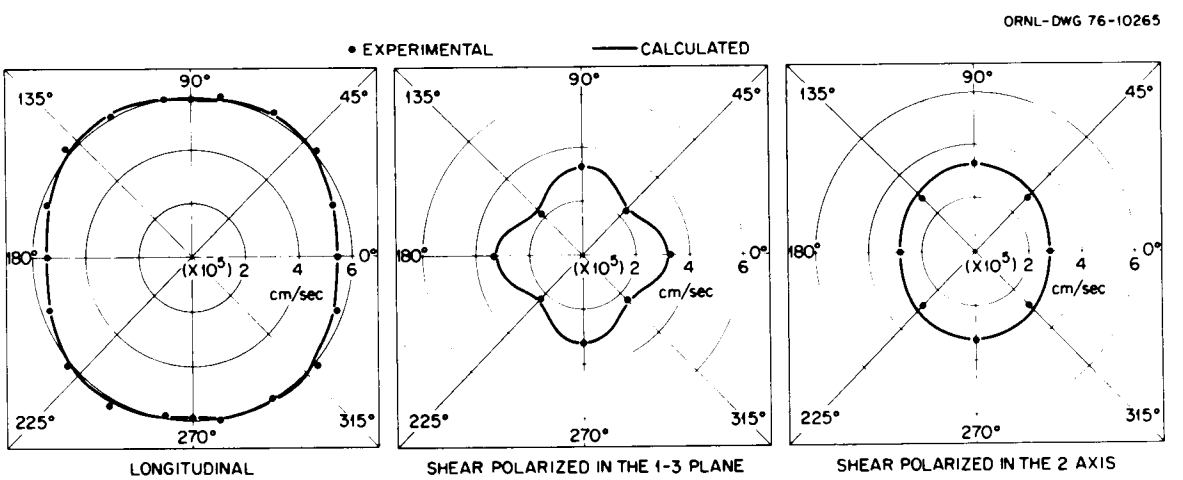

Fig. 3.47. Variation of Ultrasonic Velocities with Orientation in a "Single Pass" Stainless Steel Weldment in the 1-3 Plane.

significance in the field of ultrasonic inspection of weld material, where variation of the ultrasonic velocities with structure, material, and orientation can be important.

The interface between base metal and weld metal may introduce two very important variables not presently considered in routine angle beam testing. These variables are sound transmission changes and angle changes. Thus, both amplitude reflection (apparent attenuation) and location of signals from reflections (time changes) such as flaws are affected. These variations must be determined for each weldment material to assume meaningful testing.

3.3.4 Measurement of Ultrasound Velocity in Type 308 Stainless Steel Weld Metal — L. Adler* and K. V. Cook

As reported in Sect. 3.3.3, studies of mechanical properties and ultrasonic measurements have been correlated for type 308 stainless steel single-pass weld metal by use of a novel ultrasonic immersion method. The reference coordinate axes and an electroslag weld with the idealization of all solidification directions parallel is shown in Fig. 3.48.

*Consultant from the University of Tennessee.

ORNL-DWG 75-13166R

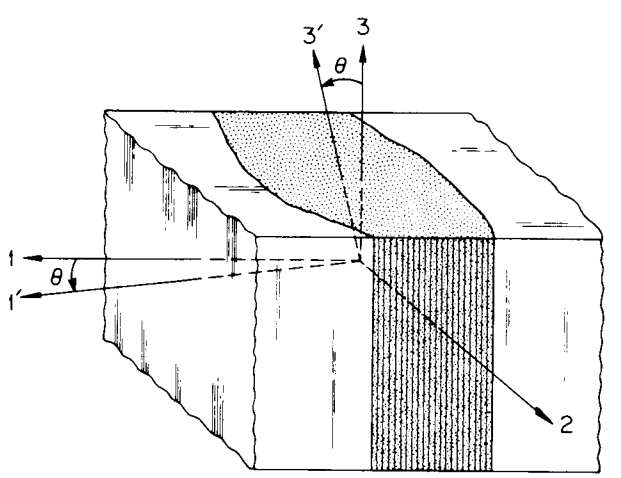

Fig. 3.48. The Reference Coordinate Axes and an Illustration of an Electroslag Weld with the Idealization of all Solidification Directions Parallel.

Both longitudinal and shear wave velocities varied (Sect. 3.3.3) in the 1—3 plane by significant percentages. Further measurement in the 2—3 plane has shown similar velocity variation, which is also due to anisotropy in the weld structure. In the 1—2 plane (Fig. 3.49) velocity varied very little with orientation, indicating that this is nearly a plane of isotropy.

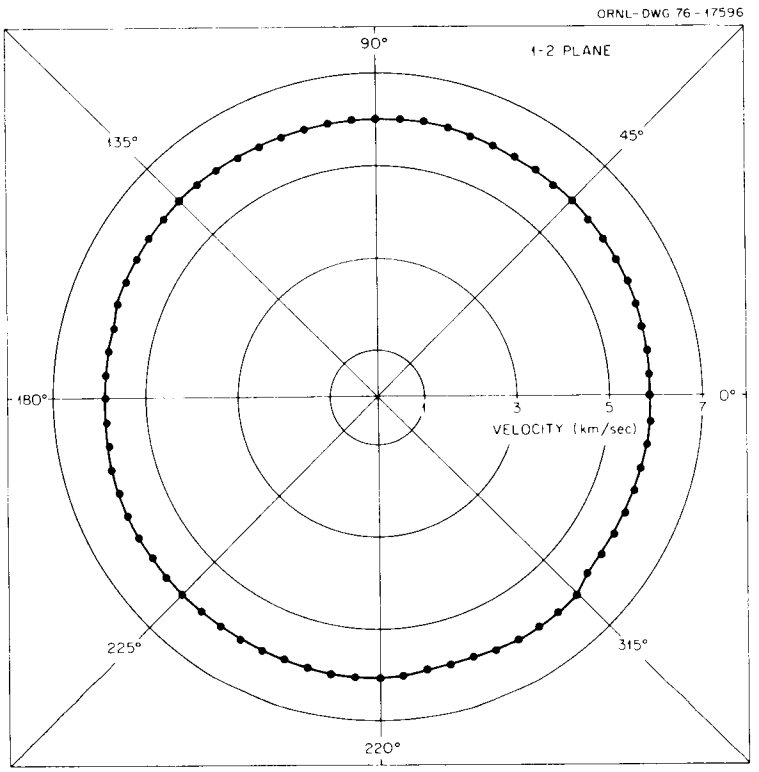

Fig. 3.49. Longitudinal Velocity Versus Various Rotational Angles in the 1—2 Plane of a Type 308 Stainless Steel Single-Pass Weld.

3.3.5 Model for Residual Stress in Welded Steel Pipe and its Correlation with Ultrasonic Rayleigh Waves — K. V. Cook, L. Adler,* and B. R. Dewey*

Residual internal stress in metal objects can exist after removal of all external force. The residual stress may be the result of many

*Consultant from the University of Tennessee.

fabrication processes where large thermal gradients and/or differential thermal expansions occur. For example, obvious visible deformation should indicate the presence of residual stress in two large-diameter pipes butt welded together with a circumferential weldment. The Mechanical Properties Group will attempt residual stress measurements on these samples using strain gage monitoring before, during, and after cutting. Since the ultrasonic surface wave (Rayleigh wave) velocity is known to be influenced by strain in the medium and, hence, by the residual stress, we decided to measure surface wave velocity variations and relate them to both theoretical and destructive test data. The approach was limited to a feasibility effort but has produced some interesting results. We introduced a mathmatical model treating the welded pipe as an infinitely thin-walled cylindrical shell with a circumferential line loading. The stress distribution[39] along the axis of an infinite shell is governed by the equation

$$\frac{dw^4}{dx^4} + 4\beta^4 w = 0 \ , \tag{1}$$

where w is the displacement along the radius,

x is a distance along the cylinder axis,

and $\beta^4 = 3(1 - \nu^2)/a^2h^2$,

where ν = Poisson's ratio

a = radius of the shell,

h = wall thickness of the shell.

Figure 3.50 shows an experimental system to measure surface wave velocity on two welded pipes. The apparatus on top of the pipe is used for outer surface measurements; a similar device was used to measure inner surface wave velocity variations.

When a solution of Eq. (1) in the form $w = w(x)$ is found, it follows that the surface stress is directly proportional to d^2w/dx^2. In Fig. 3.51,

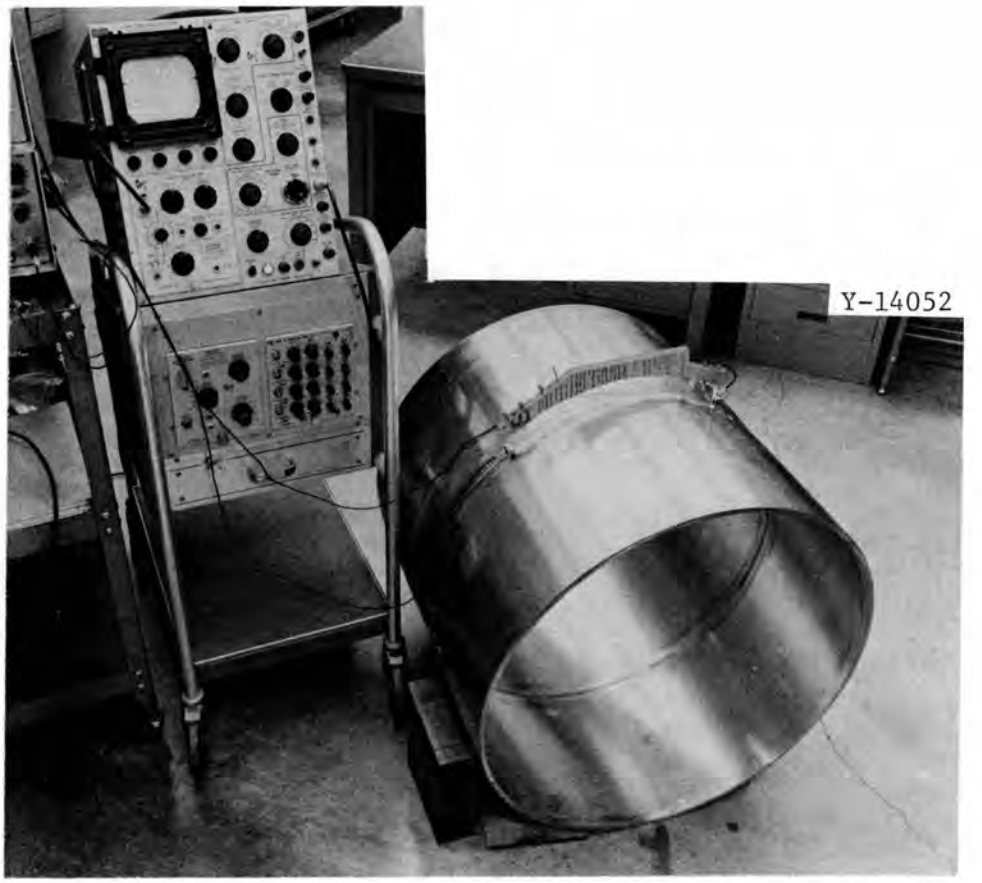

Fig. 3.50. Ultrasonic Rayleigh Wave Velocity Measuring System. The electronic part of the system is on the left of the photograph. The apparatus on top of the pipe is used to measure surface wave velocity on the outer surface as a function of both its longitudinal and circumferential positions as related to the weldment.

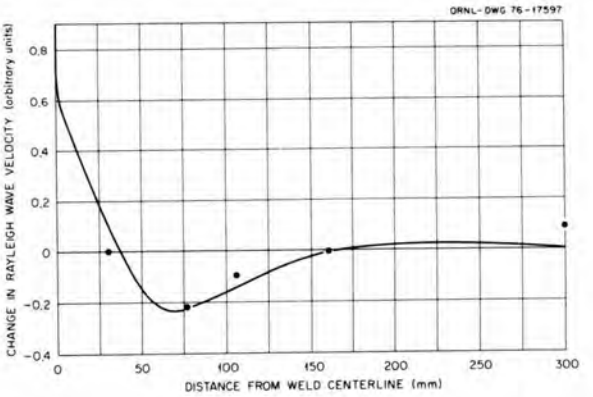

Fig. 3.51. Comparison of the Variation of Circumferential Rayleigh Velocity (ΔV_R) and Surface Stress Distribution from Shell Theory (the Scale is Arbitrary).

the predicted variation of a nondimensional surface stress is plotted along with the experimental points from surface wave velocity variation. The scale has been adjusted so that the maxima coincide. The ultrasonic results clearly correlate with those of shell theory.

3.4 MECHANICAL PROPERTIES OF STEAM GENERATOR MATERIALS* — C. R. Brinkman

3.4.1 Creep and Rupture Behavior of 2 1/4 Cr-1 Mo Steel — R. L. Klueh

Because 2 1/4 Cr-1 Mo steel is to be used as the structural material for the steam generators of the CRBR, we have been studying the creep and rupture behavior of 2 1/4 Cr-1 Mo steel. We have previously reported on the effect of heat treatment on the creep-rupture behavior of annealed 2 1/4 Cr-1 Mo steel,[40,41] and last quarter[42] we reported on the tertiary creep behavior in those tests.

In those studies, creep tests were made at 454, 510, and 566°C (850, 950, and 1050°F) on specimens taken from pieces of 25.4-mm-thick (1-in.) plate (from a single heat of steel) given the following heat treatments: annealed (full anneal) labeled AN-1, which was slowly cooled from the austenitizing temperature; annealed labeled AN-2, which was cooled at a faster rate; and isothermally annealed labeled IA. For all three heat treatments, the microstructure was primarily proeutectoid ferrite.[40]

For many of the test conditions, nonclassical creep curves were observed. Instead of single primary (transient), secondary (steady-state), and tertiary creep stages, a curve with two steady-state stages was observed. The creep curve shape was found to be a function of stress. With increasing stress, curves went from classical to nonclassical then back to classical. The "classical" curves in the high-stress regime were decidedly different from those developed at low stresses:[42] the strains to tertiary creep for the high-stress classical curves were considerably less than those developed at the low stresses.

In the following, we will attempt to give a metallurgical explanation for those observations. Hopefully, if the metallurgy of the system is

---

*Progress on work performed under 189a OH028.

understood, we will be able to make appropriate extrapolations for creep parameters to stresses of interest to the designer with more confidence.

The explanations for the kinds of behavior noted in these tests are all involved with the evolution of the microstructure during elevated-temperature exposure and deformation. That is, the microstructure developed during the heat treatment is not metallurgically stable, and a continuous change occurs during a creep test or elevated-temperature exposure. These changes can strongly influence the creep properties.

Glen[43] has suggested that the creep resistance of most alloys is "compounded of two parts: the initial creep resistance," which he states "depends on the microstructure before testing," and a "latent creep resistance that arises from the effect of various strain-aging phenomena and has no effect initially." Further, Glen notes that "a third effect must also be considered, namely, the overaging or spheroidization of precipitates, since this tends to reduce creep resistance." All three of these effects are involved in the interpretation of the present results.

Although different amounts of bainite are present in the microstructures of the three differently heat-treated plates, in each case it makes up only a small fraction of the total microstructure. Therefore, as was previously shown for the elevated-temperature tensile properties,[44] the creep properties will be determined primarily by the properties of the proeutectoid ferrite. During the heat treatment, Mo_2C will begin to precipitate in the proeutectoid ferrite, and the matrix will be supersaturated with respect to this carbide. When heated at an elevated temperature (in service or during a creep test), the Mo_2C precipitation reaction will proceed, giving rise to one of Glen's "latent creep resistance" effects.

However, Mo_2C is not the stable carbide in proeutectoid ferrite, and eventually it gives way to eta-carbide.[45] (Although eta-carbide is generally referred to as M_6C, in 2 1/4 Cr-1 Mo steel it is[46] more nearly M_4C.) In the bainite, M_3C and Mo_2C form. These precipitates are eventually replaced by M_7C_3, $M_{23}C_6$, and eta-carbide; the M_7C_3 eventually is replaced by eta-carbide. The carbide of the pearlite plates is $M_{23}C_6$, and it partially gives way to eta-carbide.[47,48] Therefore,

regardless of the microstructure after the original heat treatment, with time it will evolve to a ferrite matrix containing globular $M_{23}C_6$ and eta-carbide.[45,47,48]

We feel that most of the precipitate strengthening takes place while the high density of small Mo_2C particles is present, and the large globular particles of $M_{23}C_6$ and eta-carbide have much less strengthening effect.[44,49]

If we focus on the proeutectoid ferrite, which primarily determines the properties, we see that the matrix starts out supersaturated with respect to Mo_2C and contains a high density of fine Mo_2C precipitate particles.[44,47] As seen below, the amount of supersaturation (and precipitate) will depend on the anneal heat treatment (i.e., the cooling rate). With time at an elevated temperature, the supersaturation is relieved by the continued formation of Mo_2C. Eventually, the Mo_2C particle density reaches a maximum, which corresponds to an optimum hardening. Then the Mo_2C begins to agglomerate and is simultaneously replaced by eta-carbide, a change that goes hand in hand with a decrease in strength.

In addition to the precipitate changes that occur during elevated-temperature exposure, solid solution effects occur in the supersaturated proeutectoid ferrite matrix. These effects give rise to "latent creep resistance" effects and can explain some of the interesting observations made in the present study. These same solution effects lead to dynamic strain aging effects, which give rise to peaks in the ultimate tensile strength-temperature relationships.[44] (Similar processes occur in the bainite, but the magnitude of the effect is considerably reduced.[44,50])

Dynamic strain aging can result from two types of interaction between solute atoms and dislocations.[51] In the first type, the interaction involves the interstitial solutes carbon and nitrogen. The second type of interaction is more complex and arises from the simultaneous presence in solid solution of substitutional and interstitial atoms that have an affinity for one another. Baird and Jamieson[52] have shown that the second dynamic strain aging mechanism occurs in alloys that contain substitutional elements that have a strong affinity for the interstitial

elements carbon and/or nitrogen. This strengthening mechanism, which Baird and Jamieson termed "interaction solid solution hardening," extends the dynamic strain aging effect to higher temperatures. This effect is also important in creep.[53,54]

We previously showed[44] that "interaction solid solution hardening" caused by carbon and molybdenum could account for the differences in the tensile properties of AN-1, AN-2, and IA. We now feel that the differences observed in the creep and rupture properties for these different heat treatments are also largely the result of similar interaction solid solution hardening.

Baird and Jamieson[53,54] have studied the effect of interaction solid solution hardening on the creep behavior of Fe-Mo-C and Fe-Cr-C alloys. By following changes in the amounts of solute in solution during a creep test, they showed that changes in creep behavior could be attributed to changes in the amounts of carbon and molybdenum in solution. In certain Fe-Mo-C alloys they noted two steady-state creep stages similar to those noted in the present study. They concluded that the first steady-state stage was due to interaction solid solution hardening.

More than one period of "steady-state creep" has been observed for numerous alloys,[43,53-58] including 2 1/4 Cr-1 Mo steel.[59] In all cases the observations are attributed to metallurgical instabilities. Baird and Jamieson were the first to attribute the effects to interaction solid solution hardening. However, their studies were made at only a limited number of stresses and temperatures. Our studies appear to be the first to cover a wide range of temperatures and stresses and are also the first extensive observations on interaction solid solution hardening effects on creep in a commercial alloy.

As described by Baird and Jamieson,[52,53] atoms of molybdenum (which is a strong carbide former) interact with carbon atoms in solution to form Mo-C atom pairs or atom clusters (where more than one molybdenum atom is associated with each carbon atom). Now, according to Baird,[60] "two possible strengthening mechanisms can be envisaged in the range where these groupings (of atoms) cannot diffuse with dislocations; (i) if interstitial atoms are more tightly bound to substitutional

atoms than to dislocations, then the marked solid-solution strengthening effect of interstitial atoms will be extended to much higher temperatures than is the case in pure iron, and (ii) if interstitial atoms are bound more tightly to dislocations than to substitutional atoms, then dislocations carrying interstitial solute atmospheres will interact with relatively immobile substitutional solute atoms (single or paired), thus extending dynamic strain-aging effects to higher temperatures than in pure iron." These dislocation atmospheres of molybdenum and carbon atoms or atom clusters, which cannot move with the dislocations even at quite high temperatures, are the basis for interaction solid solution hardening.

Baird and Jamieson studied mainly ternary alloys of the type Fe-A-X, where A was Mo, Cr, or Mn and X was C or N. Of the Cr and Mo alloys, only the Fe-Mo-C alloys appeared to show extensive interstitial solid solution strengthening. In fact, when Cr was added to Fe-Mo-C alloys, the strengthening effect was reduced.[60] For this reason, as well as the previous work on tensile properties,[44] we would conclude that an Mo-C interaction is occuring in the 2 1/4 Cr-1 Mo steel. This is reasonable, since Mo_2C is the first precipitate to form in the proeutectoid ferrite, and precipitate formation requires the same pre-precipitate agglomeration in solution that is required for interaction solid solution hardening.

Dislocation behavior during creep can be described by two theories: recovery-controlled creep and glide or climb-controlled creep.[61] Stress decrement tests by Baird et al.[55] indicate that either of these processes can occur, depending upon the heat treatment that the ferritic steel receives. More such tests are needed to determine the exact creep mechanism in these steels. However, both mechanisms are based on dislocation movement within the subgrains, and therefore a qualitative explanation of our observations is possible, regardless of the mechanism.

For a material that shows a typical creep curve with single primary (transient), secondary (steady-state), and tertiary stages, the dislocation density within the subgrains increases gradually in the primary stage and beomes approximately constant in the secondary stage.[61] On the

recovery-controlled creep model, the steady-state creep stage is then one where the rates of recovery and work hardening are equal. On the climb-controlled model, dislocations from a source are essentially piled up against some barrier — a precipitate particle or dislocation stress field. Because of the back stress by the piled up dislocations, the dislocation source would cease to operate (creep would cease) if the dislocation could not bypass the barrier. The lead dislocation can bypass the barrier by climb. Creep therefore continues with the creep rate determined by the climb rate.

For either model, the rate-controlling processes for the two steady-state stages have the same explanation. When a test is loaded and creep begins, the dislocations that form attract an atmosphere of molybdenum and carbon atoms or atom clusters, which restrict their movement. The dislocation sources may also be affected. Since strain requires dislocation movement, the amount of strain that occurs during the first steady-state stage is severely limited, as observed.[41] In Fig. 3.52 the creep curve for AN-1 at 566°C (1050°F) and 138 MPa (20 ksi) is enlarged. Note that the initial steady-state region extends only to about 15 hr before a quasi-tertiary state begins. Because dislocation motion is severely limited by the atmospheres during these initial "primary and steady-state stages," only 0.025% strain occurs.

With time at temperature and stress, the amount of carbon in solution decreases: it is incorporated into the Mo_2C precipitate and dislocation atmospheres. Precipitate probably forms on the immobilized dislocations.[51,53] As further dislocation generation proceeds, less and less carbon is available to participate in interaction solid solution strengthening. The dislocation density must thus increase toward the level that is present for the normal steady-state stage, and the dislocations that now determine the creep rate are those that have not attracted an atmosphere. Creep in the second steady-state stage is probably determined by the movement of the dislocations through the proeutectoid ferrite, which contains a high density of Mo_2C precipitate particles.

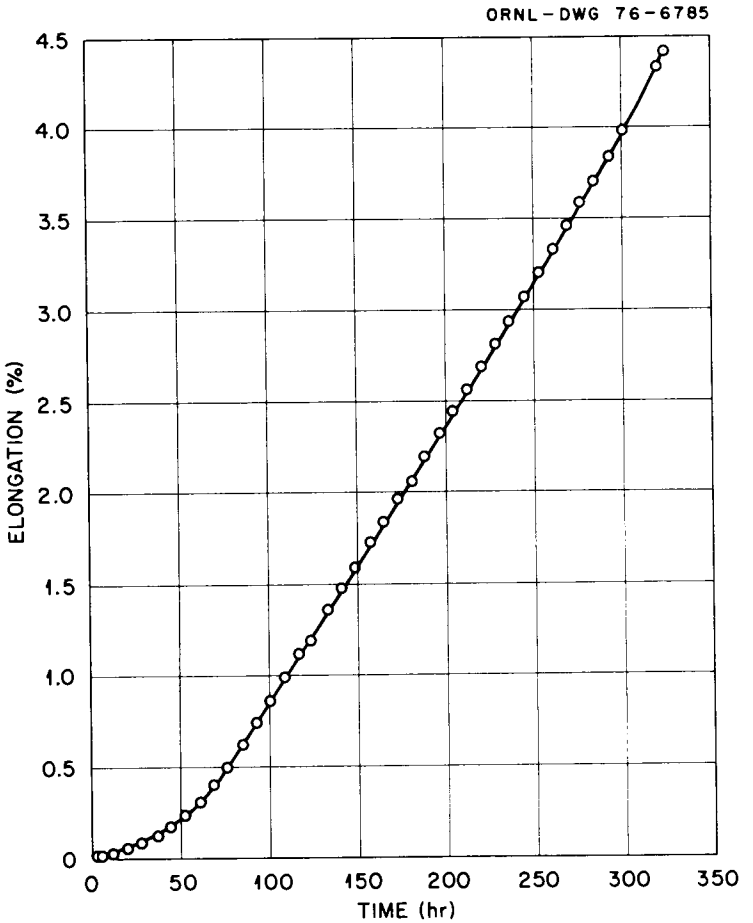

Fig. 3.52. Early Part of Creep Curve for AN-1 at 138 MPa (20 ksi) and 566°C (1050°F). In about 15 hr, the first steady-state stage is complete. After about 80 hr, the second steady-state stage has begun.

We found[41,42] that at 566°C, the creep curves with two steady-state regions were observed at 138 MPa (20 ksi), but not at 124 MPa (18 ksi). That conclusion was based on examinations of the complete curve shown in Fig. 3.53(a). When the early part of the curve is enlarged as shown in Fig. 3.53(b), a slight discontinuity in the creep rate at very short times is readily apparent (there is still really only a single steady-state stage). Because of its limited duration relative to the second steady-state region, this discontinuity was not detected when the overall curve was examined. However, at 103 MPa (15 ksi), even when the curve was enlarged as shown in Fig. 3.54, only one steady-state stage was observed. The observation,[41,43] therefore,

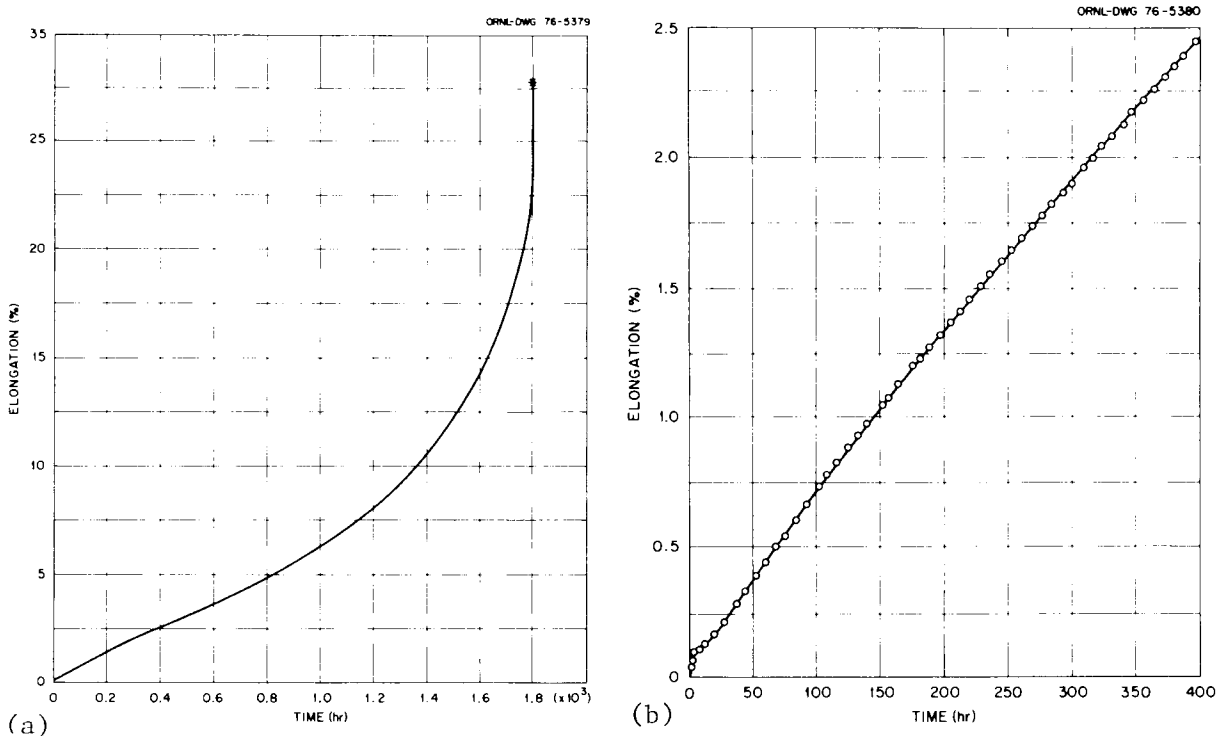

Fig. 3.53. Creep Curve for AN-1 at 124 MPa (18 ksi) at 566°C (1050°F). (a) Complete curve. (b) Early part of curve. In (b) note the slight discontinuity in the early part of the curve.

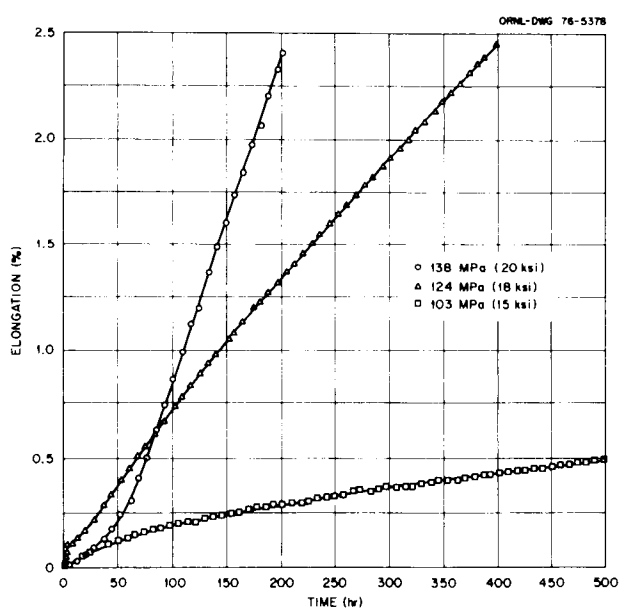

Fig. 3.54. Creep Curves for AN-1 at 103, 124, and 138 MPa (15, 18, 20 ksi) at 566°C. Note how the strain of the 138-MPa test for early times falls below that for the lower stress tests.

that below some stress the creep curve has a classical shape appears to be real. Noting the limited effect at 124 MPa, we concluded that this stress is close to that at which the creep curves become classical.

Not only does Fig. 3.54 illustrate the fact that interaction solid solution hardening ceases at a stress of about 124 MPa, it also illustrates the strengthening effect of interaction solid solution hardening (i.e., the limiting strain) discussed above. In addition to the 103-MPa (15-ksi) test, Fig. 3.54 also shows the creep curves observed for AN-1 at 124 and 138 MPa (18 and 20 ksi). Note that for the first 25 hr of the tests, the creep strain for the 138-MPa test falls below that for both the 124- and 103-MPa tests, certainly an unexpected result if similar mechanism were occurring for each stress. This result can be explained, however, by the fact that at 138 MPa interaction solid solution hardening limits the strain in the first steady-state stage, but at stresses of 124 MPa and below, interaction solid solution hardening has no effect.

If the solute drag mechanism applies, as stress decreases we would expect a change from a nonclassical creep curve (one with two steady-state stages) to a classical creep curve. As the stress decreases the dislocation velocity decreases, and at some stress the dislocation velocity will be equal to that of the diffusing Mo-C atom clusters. Below the critical velocity, the Mo-C atom clusters can diffuse at a rate greater than or equal to the dislocation velocity. Hence, interaction solid-solution hardening no longer occurs, and a classical creep curve results.

When the temperature is decreased, this critical velocity will decrease, since the diffusion rate for the Mo-C atom clusters will decrease. It follows from this that for a given stress, the lower the temperature, the longer the period of the first steady-state stage. In keeping with these observations, most of the AN-1 and IA tests at 510°C displayed two steady-state stages. The AN-2 specimens, which apparently displayed "classical" creep curves at 510°C (950°F) (except possibly at 207 MPa — 30 ksi) appear to be a special case.[41,42]

Figure 3.55 shows the creep curves for AN-1, AN-2, and IA at 138 MPa (20 ksi) at 566°C. All three curves have two steady-state stages, with AN-2 displaying the longest first steady-state stage. This is expected, since the faster cooling rate for this steel allowed more molybdenum and carbon to remain in solution, thus making more of these species available for interaction solid solution hardening. A similar observation was made for the tensile properties to account for the greater amount of dynamic strain aging for this heat treatment.[44]

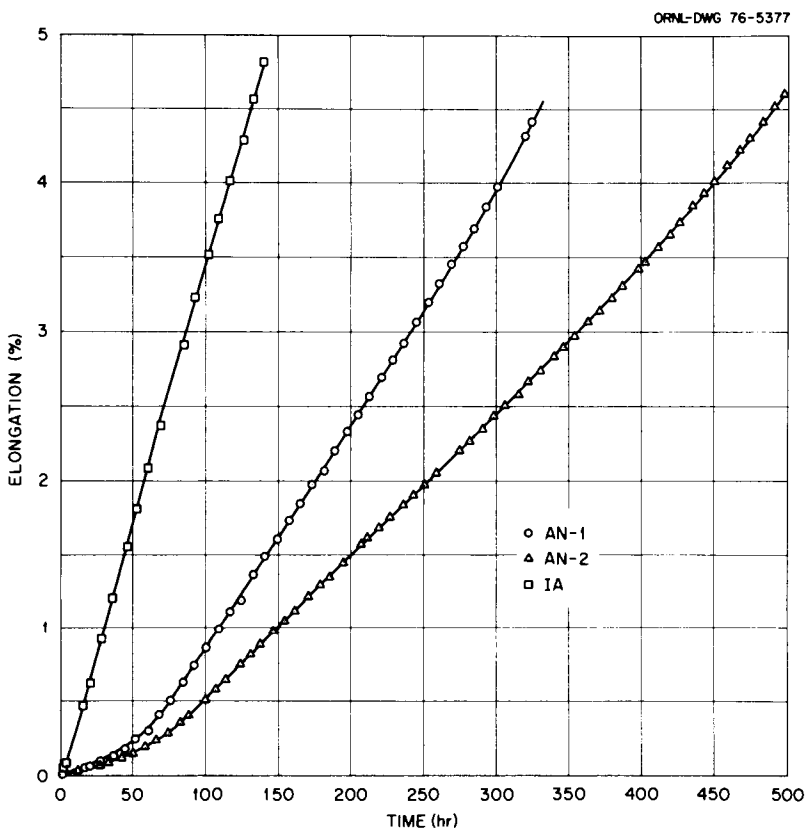

Fig. 3.55. Creep Curves for AN-1, AN-2, and IA at 138 MPa (20 ksi) at 566°C (1050°F). Note that only the early part of these curves is shown. At this high temperature, the length of the second steady-state stage is much greater than the first. On this enlarged scale, IA displays little first steady-state stage.

Since AN-2 shows the greatest amount of interaction solid solution hardening at 566°C, a similar conclusion should apply at 510°C, where all but two of the AN-1 and IA tests displayed two steady-state stages.

In fact, from the above discussion, we would expect most of the tests on AN-2 at 510°C to have two steady-state stages. To explain this apparent dichotomy and the results at 454°C, it is of interest to reexamine the strains developed during the steady-state stages. As pointed out previously[42] the strains to the end of the steady-state stages fall into three distinct categories: (1) less than 1.5% (most less than 0.7%) for the end of the first steady-state stage of nonclassical curves, (2) 4–7% to the end of the second steady-state stage and to the end of the steady-state stage of classical curves at 566°C, and (3) 1.5–2.5% for the classical curves at 454°C and high-stress tests for AN-2 at 510°C and the high-stress tests for AN-1 at 510 and 566°C.

For the AN-2 tests at 510°C we found[42] that the strains for the low-stress tests (<310 MPa, 45 ksi) fall into the first category (<1.5%). Therefore, the steady-state stage that was observed was really the first steady-state stage (i.e., the one controlled by interaction solid solution hardening). Because of the length of that stage for AN-2, the second steady-state stage was never observed. In other words, by the time the first steady-state stage is finished, the second steady-state stage is so short that it occurs by itself only over a very short period of time.

If the above conclusion is correct, both steady-state stages should be observed on an AN-2 specimen tested at 510°C at a lower stress, where the length of the first steady-state stage does not interfere with the second steady-state stage. We did this at 152 MPa (22 ksi). As seen in Fig. 3.56, two steady-state stages are observed; the specimen is still in the second steady-state stage after 1% strain. The length of the first steady-state stage was approximately 1100 hr, as compared with about 800 hr for AN-1 at the same stress. Although the length of the first steady-state stage is expected to decrease somewhat with increasing stress, the reason for the overlap for both heat treatments at rupture times less than several hundred hours is easily seen. Hence, at an intermediate stress level, a "classical" creep curve is observed because the two steady-state stages overlap.

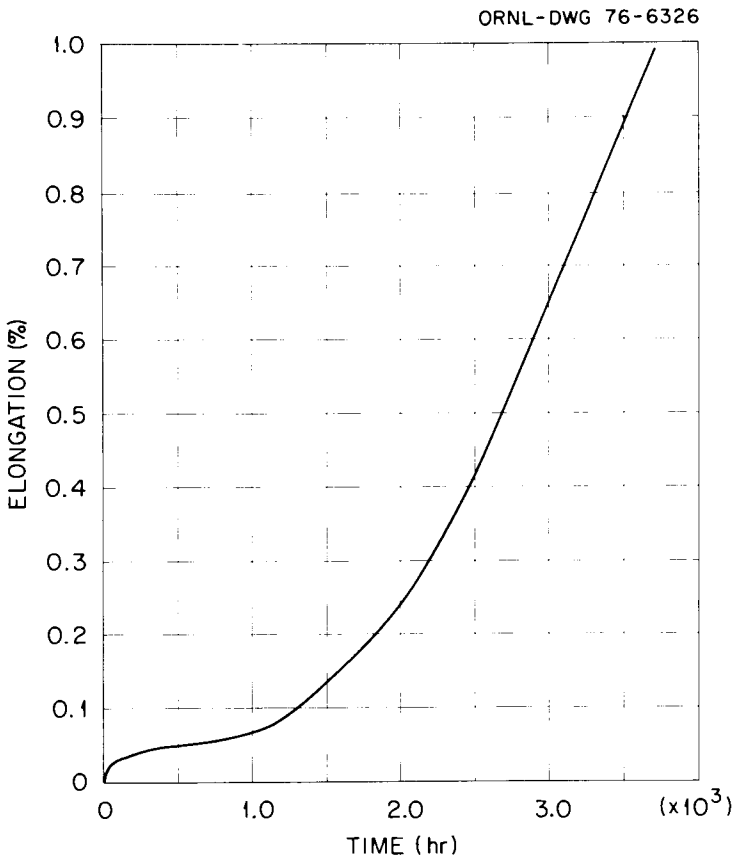

Fig. 3.56. Creep Curve for AN-2 at 152 MPa (22 ksi) at 510°C. The test, as shown, is still in the second steady-state stage.

Although the "classical" curves with 1.5 to 2.5% strain at 454°C and for tests on AN-2 at high stresses could also be the result of an inability to delineate the second steady-state stage as explained above, the fact is that the strains are substantially greater than they are for the first stage of the obviously nonclassical curves (<1.5%) and for the intermediate-stress tests on AN-2, where the above explanation was applied. Furthermore, as pointed out in the last quarter,[42] as a result of a reduced rupture elongation, the $\varepsilon_2/\varepsilon_R$ values at 454°C are quite similar to those at 510 and 566°C, and substantially above those for AN-2 at intermediate stresses (they are also substantially above $\varepsilon_2/\varepsilon_R$ when ε_2 is taken as the end of the first steady-state stage). These observations all indicate that the 454°C "classical" curves and the high-stress tests on AN-1 and AN-2 may require a separate explanation. All the tests in question have $\varepsilon_2/\varepsilon_R \geqslant 7$.

The creep rate depends on the dislocation density, which in turn depends on stress: the greater the stress, the larger the dislocation density. It may therefore be that above some stress, dislocations are generated faster than they can be tied up by Mo-C clusters. Hence, the creep rate is determined by some combination of the processes that operate in the two stages for materials that display nonclassical creep.

Regardless of what the mechanism is, it must go hand in hand with the lower ductility (primarily total elongation) noted above for the 454°C tests. A similar reduced elongation was noted[40] for the high-stress tests (above about 276 MPa) at 510°C for all three heat treatments. That is, at 510°C at the highest stresses tested, an increase in stress was accompanied by a decrease in elongation. For most metals and alloys, just the opposite is observed: high creep stresses correspond to increased ductility.

From the above observations we would expect that as the stress is lowered, a stress regime would be reached at 454°C where nonclassical creep curves should be observed. Note that tests at 454°C at the lowest stresses show about 1.5% strain to the onset of tertiary creep,[40] somewhat below strains in most of the other tests at this temperature. This may indicate that the stress is near the upper end of the regime for nonclassical curves. The total elongation for the 338-MPa (49-ksi) test (the lowest stress test) for the IA also appears higher than for the higher stresses (24% vs 17%). Similar changes in total elongation were observed at 510 and 566°C as the stress regime for nonclassical creep curves was approached.[40]

With the aid of Table 3.15, the above discussion on interaction solid solution hardening can now be summarized. Nonclassical creep curves are the result of interaction solid solution hardening. By the interaction of molybdenum and carbon atoms or atom clusters with dislocations to form an atmosphere, a pseudo-steady-state creep stage is observed shortly after the start of a creep test. This steady-state stage exists until the number of molybdenum and carbon atoms in solution decreases until there are insufficient atoms to form atmospheres on freshly generated dislocations (i.e., because of precipitate formation or prior formation of dislocation atmospheres). As the carbon becomes

Table 3.15. Summary of Observations on Creep Curve Shapes

Stress	Behavior	Event	Strain Limits, %	
			All Cases	Most Cases
Lowest	Classical	onset of tertiary	4–7	
Intermediate	Nonclassical	end of first steady state	<1.5	<0.7
		end of second steady state	4–7	
	Classical-I	onset of tertiary	<1.5	<0.7
Highest	Classical-II	onset of tertiary	1.5–3	2–3

exhausted, the creep rate begins to increase and eventually approaches a second steady-state stage. This later steady state is one in which dislocation movement through the proeutectoid ferrite matrix controls creep rate; the proeutectoid ferrite contains a high density of Mo_2C precipitate particles. When this second steady state ends, tertiary creep ensues, leading to failure.

The effect of the heat treatment can be explained in terms of the amount of Mo_2C formed during the initial heat treatment. The more slowly the steel is cooled from the austenitizing temperature, the greater is the amount of Mo_2C precipitate formed, and less molybdenum and carbon are left in solution for interaction solid solution hardening. Hence, the slower the cooling rate, the less molybdenum and carbon are in solution, and the shorter is the length of the first steady-state stage.

As the creep stress is decreased, the dislocation velocity decreases and the Mo-C atmosphere will be able to diffuse with the dislocation. At this point the first steady-state stage will no longer appear. A classical creep curve with primary, secondary, and tertiary stages will then be observed. At 566°C, this occurs at about 124 MPa (18 ksi). Since the rate of diffusion decreases with decreasing temperature, the stress for the critical velocity will decrease; it was not observed at 510°C.

In addition to the low-stress classical creep curves, two types of classical curves are observed when the stress is raised. When the first steady-state stage is prolonged, it can obliterate the second steady-state stage, giving rise to what appears to be a classical creep curve — classical-I. This was observed at intermediate stresses for AN-2 at 510°C. At still higher stresses a second type of "classical" creep curve appears — classical-II.

The classical-II curves may possibly be the result of the simultaneous operation of the processes that give rise to the two steady-state stages. Whatever the mechanism, it results in reduced ductility. In Table 3.15 the observations are summarized, along with the ductilities that are found in each stress regime.

As pointed out previously,[42] tertiary creep has at times been stated to occur prematurely in 2 1/4 Cr-1 Mo steel. Indeed, if the end of the first steady-state stage is taken as the onset of tertiary creep, it would be quite premature. For instance, in Fig. 3.56 tertiary creep would occur after about 1000 hr and less than 0.1% creep strain; this would be after less than 10% of its life (rupture is estimated at greater than 10,000 hr). However, as we have shown above, the increase in creep rate at this point of the curve is the result of a metallurgical instability, not the gross structural instability that the designer wishes to avoid. The "tertiary creep" that the designer is interested in occurs at the end of the second steady-state stage. As we showed last quarter,[42] the end of this stage occurred at approximately 50% of the lifetime of all the tests, just as it does for the tests that display classical creep curves.

These results also point up the obvious need for caution when one extrapolates results of tests at high stresses to the low stresses of interest for design. For example, at 454°C the tests were conducted at stresses where only the high-stress classical creep curve shape was observed. If the above discussion is correct, with decreasing stress the curves will become nonclassical. Eventually, curves may again become classical, but different from the classical curves at the high stresses. Thus, direct extrapolation of creep parameters from the

high-stress regime to the low-stress regime without taking the above results into consideration could lead to erroneous conclusions.

3.4.2 Heat-to-Heat Variation of 2 1/4 Cr-1 Mo Steel — R. L. Klueh

As a result of the decision to use 2 1/4 Cr-1 Mo steel as the structural material for the CRBR steam generators, we have been involved in the determination of the elevated-temperature mechanical properties of 2 1/4 Cr-1 Mo steel over the temperature and stress ranges of interest for design.[40,62] The peak sodium temperature in the steam generators will be approximately 510°C (950°F). Tensile, creep, and cyclic studies[40,62,63] have been made over the range 454 to 566°C (850–1050°F) to determine accurate properties for use in the constitutive equations[64] for this steel. Those studies[40,62,63] were done on a single heat of the steel, an air-melted 25.4-mm-thick (1-in.) plate (heat 20017). In that work the mechanical property characteristics were of most importance, and property variations due to differences arising in different heats, product forms, or melting practices were ignored. Code allowable stresses for high-temperature design of nuclear components are given by Code Case 1592. To set the allowable design stresses, average values are determined from all available data taken from steel that meets the appropriate ASME specifications; the ASME specifications usually correspond to applicable ASTM specifications. Minimum values are determined from such a data compilation, and the allowable stresses are conservatively estimated from these minimum values.

Smith[65] has gathered all the available elevated-temperature tensile and creep-rupture data for 2 1/4 Cr-1 Mo steel, and mainly these data were used to determine the allowable stresses for Code Case 1592. These same and later data were used by analysts at ORNL to determine data correlations for the *Nuclear Systems Materials Handbook*.[8] When the compiled data for the tensile and creep properties are examined, large variations in properties are observed. For example,[8] ultimate tensile strength values for annealed 2 1/4 Cr-1 Mo steel varied by about 125 MPa (18 ksi) at 25°C (77°F) and by almost 250 MPa (36 ksi) at 371 and 538°C (700 and 1000°F). Since conservative design values are required, they are based on minimum values.

When correlations or allowable stresses were determined from such data, all annealed data that meet the appropriate specifications are used, regardless of melting practice or product form. In most cases the material from which the allowable stresses for ASME Code Case 1592 were determined or from which the *Nuclear Systems Materials Handbook* correlations were arrived at came from air-melted 2 1/4 Cr-1 Mo steel. Likewise, the data used for constitutive equation development was from an air-melted heat.[40,62,63] To ensure that the tube-to-tubesheet welds will be made on steel free from inclusions and porosity, vacuum-arc remelted (VAR) steel will be used for the tubesheet forgings and electroslag remelted (ESR) steel for the tubing. Few data appear to be available for 2 1/4 Cr-1 Mo steel remelted by these practices, and none appear to have been used in the correlations or for Code Case 1592.

The effect of heat-to-heat variations on the elevated-temperature mechanical properties of types 304 and 316 stainless steel has been studied.[10,66] For these austenitic steels, much of the effect could be traced to differences in chemical composition and grain size. The amounts of carbon, nitrogen, and niobium significantly affected the properties. For a ferritic steel such as 2 1/4 Cr-1 Mo steel, the heat treatment will have a very definite influence on the properties. Obviously, a pronounced difference will be observed between steels that are annealed, normalized and tempered, and quenched and tempered. However, we have shown that differences can also occur in annealed steels that are cooled at slightly different rates.[40,44]

The present work has the following objectives:

1. the determination of heat-to-heat variations in annealed 2 1/4 Cr-1 Mo steel for selected heats;
2. the examination of differences in various product forms — namely, tubing, forgings, and plates;
3. the examination of differences in steel produced by various processes — namely, air melted, vacuum-arc remelted (VAR), and electroslag remelted (ESR);
4. the identification of the causes of heat-to-heat variation in mechanical properties.

We are testing specimens taken from 12 different heats: five air-melted tubing heats, two pieces from VAR forgings, two pieces from ESR plates, one air-melted forging, and two air-melted plates. The chemical composition for all but one of the heats satisfied the ASME specifications (Table 3.16). The exception was one VAR forging heat (C60570), which contained 0.034 wt % S (the specifications allow 0.030 max). Since many of these heats were obtained before the RDT Standards had been issued, several do not meet them for carbon (0.11 max) and/or sulfur (0.015 max). These include the tubing heats 36202 and 72871, the VAR heats 13812 and C60570, the ESR plate XXR, and the air-melted plate 3P5601. However, the ASME code allowable stresses and the *Nuclear Systems Materials Handbook* correlations were determined on a similar cross section of steels (annealed 2 1/4 Cr-1 Mo steel that met ASME specifications), and the Clinch River Breeder Reactor steam generators will be designed according to those allowable stresses and correlations.

Table 3.16. Chemical Composition and Grain Size of 2 1/4 Cr-1 Mo Steel as Reported by Vendors

Heat	Chemical Composition, wt %							Grain Size (ASTM)
	C	Mn	S	P	Si	Cr	Mo	
				Tubing Heats				
36018	0.11	0.47	0.015	0.019	0.23	2.29	0.96	
36202	0.12	0.47	0.021	0.014	0.36	2.32	0.98	6–7
72768	0.09	0.44	0.011	0.011	0.38	2.22	0.95	6–7
72871	0.13	0.50	0.022	0.016	0.33	2.27	0.99	6
X6216	0.11	0.46	0.015	0.011	0.27	2.20	1.03	7
				VAR Forging Heats				
13812	0.10	0.50	0.024	0.006	0.31	2.33	0.9	
C60570	0.10	0.37	0.034	0.009	0.37	2.24	1.02	
				ESR (Lectrefine) Plates [0.15 m (6 in.) thick]				
R0110	0.10	0.44	0.004	0.014	0.17	2.44	0.97	8
XXR	0.13	0.45	0.006	0.010	0.18	2.32	0.97	
				Air Melted Forging				
NF60-8746	0.09	0.39	0.009	0.009	0.35	2.40	1.01	4–6
				Air Melted Plate [25 mm (1 in.) thick]				
20017	0.11	0.55	0.011	0.014	0.29	2.13	0.90	
3P5601	0.12	0.35	0.022	0.009	0.27	2.30	0.96	

The five tubing heats and the two air-melted plates were obtained from Babcock and Wilcox Corporation. The 38-mm-diam (1.5-in.) tubing had wall thicknesses of 4.8 (heats 36018 and 72871), 7.3 (heats 36202 and X6216), and 9.0 mm (heat 72768) (0.19, 0.29, and 0.35 in.). The VAR forgings were small pieces of material obtained through courtesy of the Foster Wheeler Corporation: one (13812) had been obtained from Jorgensen Company and the other (C60570) from Coulter Company. Both the ESR materials were pieces of 152-mm-thick (6-in.) plate produced by Lukens Steel Company and are sold commercially under the trade name Lectrefine: heat R0110 was obtained from Lukens via General Electric Company; heat XXR was obtained via Foster Wheeler Corporation (XXR was arbitrarily assigned by our laboratory, since no vendor heat number was available). The air-melted forging (NF 60-8746) was one of three tubesheet forgings that were purchased from National Forge Company. These forgings, which were manufactured by the electric furnace, air-melted, vacuum-degassed process, were obtained before the decision was made to use VAR material. The tubesheet forging from which these specimens were taken was a cylinder 0.84 m diam by 0.483 m thick (33 × 19 in.).

The tubing, forgings, and ESR plates were tested in the as-received condition. The tubing and air-melted forging had been "annealed" and the two VAR forgings and the two ESR plates were normalized and tempered. The two air-melted 25.4-mm-thick (1-in.) plates were received in a normalized-and-tempered condition. Because the microstructures contained large amounts of bainite and the room-temperature strengths were considerably above those allowed by the appropriate ASME specifications and RDT Standards, the as-received material was not studied for these two heats.

In order that all the heats could be compared from a common basis, material from each of the heats was similarly isothermally annealed in our laboratory. They were austenitized by heating 1 hr at 927°C (1700°F), furnace cooled to 704°C (1300°F), held at 704°C for 2 hr, then furnace cooled to room temperature.

We previously reported on the metallography and tensile properties of the two VAR heats (13812 and C60570) and the one ESR heat (XXR) in the as-received[67] and the isothermally-annealed[68] conditions. Likewise, such data have also been made available on the air-melted forging[69]

and the two air-melted plate heats (20017[44] and 3P5601[70]) in the isothermal annealed condition. Microhardness and grain size determinations were made (Table 3.17); grain size was determined by the line intercept method.

Table 3.17. Grain Size as Determined by Intercept Method and DPH Microhardness for 2 1/4 Cr-1 Mo Steel Heats

Heat	Grain Size, ASTM		Microhardness, DPH	
	AR[a]	LIA[b]	AR[a]	LIA[b]
		Tubing Heats		
36018	8.2	7.3	146	143
36202	7.7	7.8	143	146
72768	8.8	7.3	157	145
72871	8.8	8.2	149	141
X6216	7.9	6.5	163	146
		VAR Forging Heats		
13812	4.8	6.5	163	133
C60570	7.6	8.4	148	148
		ESR(Lectrefine) Plates (0.15 m thick)		
R0110	6.2	7.8		
XXR	6.8	7.5	168	136
		Air-Melted Forging		
NF-60-8746	4.5	5.3	153	150
		Air-Melted Plates (25 mm thick)		
20017		5.2		156
3P5601		4.8		133

[a]As received.

[b]Laboratory isothermally annealed.

For the tubing heats in both the as received and isothermally annealed conditions, the microstructures were primarily proeutectoid ferrite with varying amounts of precipitate, presumably carbides (Figs. 3.57—3.61). At high magnification (750× or greater), some of the precipitate could be resolved as a fine pearlite (the dark patches);

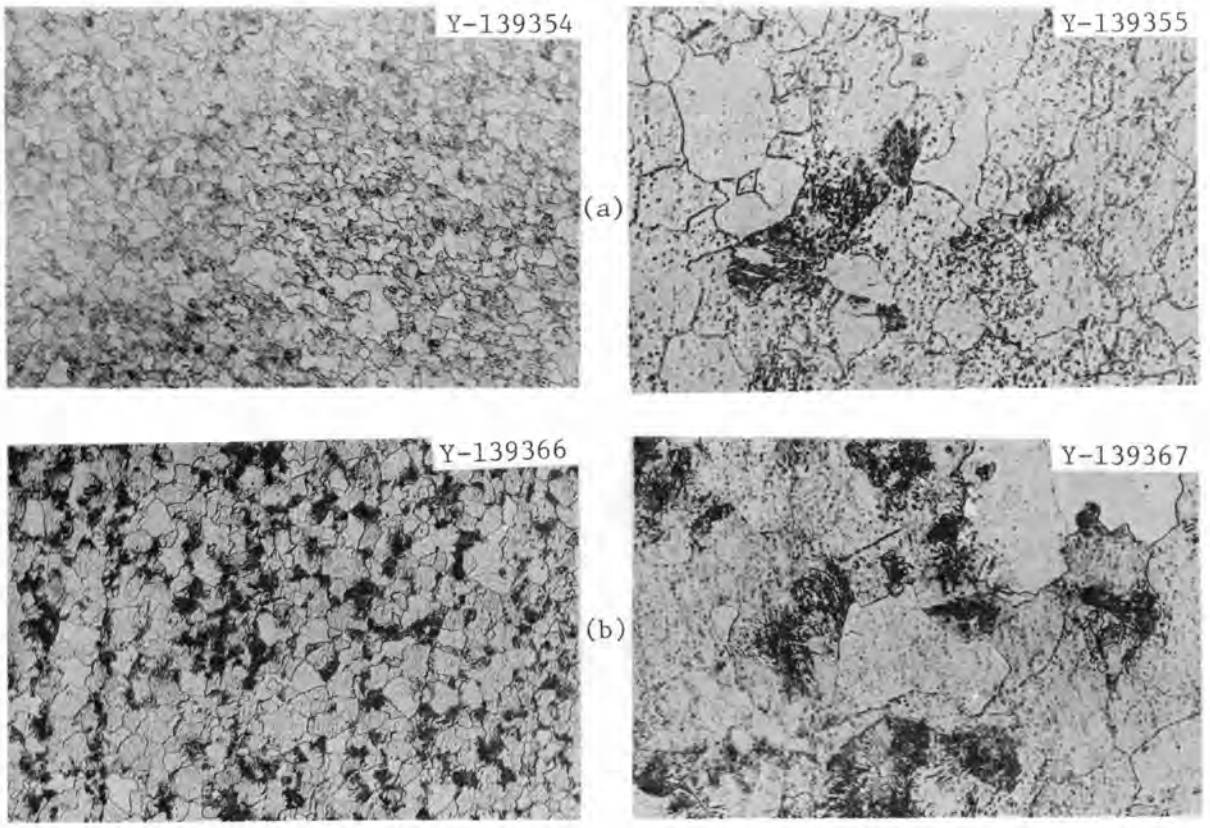

Fig. 3.57. Microstructure of 2 1/4 Cr-1 Mo Steel Tubing Heat 36018. (a) As received. (b) After laboratory isothermal anneal. Left 100×; right 500×.

also, varying amounts of spherical carbide particles were spread through the proeutectoid ferrite matrix. Even at the high magnification bainite could not be detected in the microstructure. The main difference that can be seen from heat to heat is the amount of pearlite and spherical carbide in the microstructures. However, it is difficult to say whether there are large differences in the carbides, because of differences in etching characteristics of the different heats. In most cases the as-received material appears to contain less carbide precipitate than the material that received the laboratory isothermal anneal (Figs. 3.57—3.61), although at higher magnification the differences do not appear as great. The precipitates appear to be more dispersed in the as-received steel. In most cases the grain size of the as-received tubing is slightly smaller (larger grain size number) than it is after the laboratory isothermal anneal (Table 3.17).

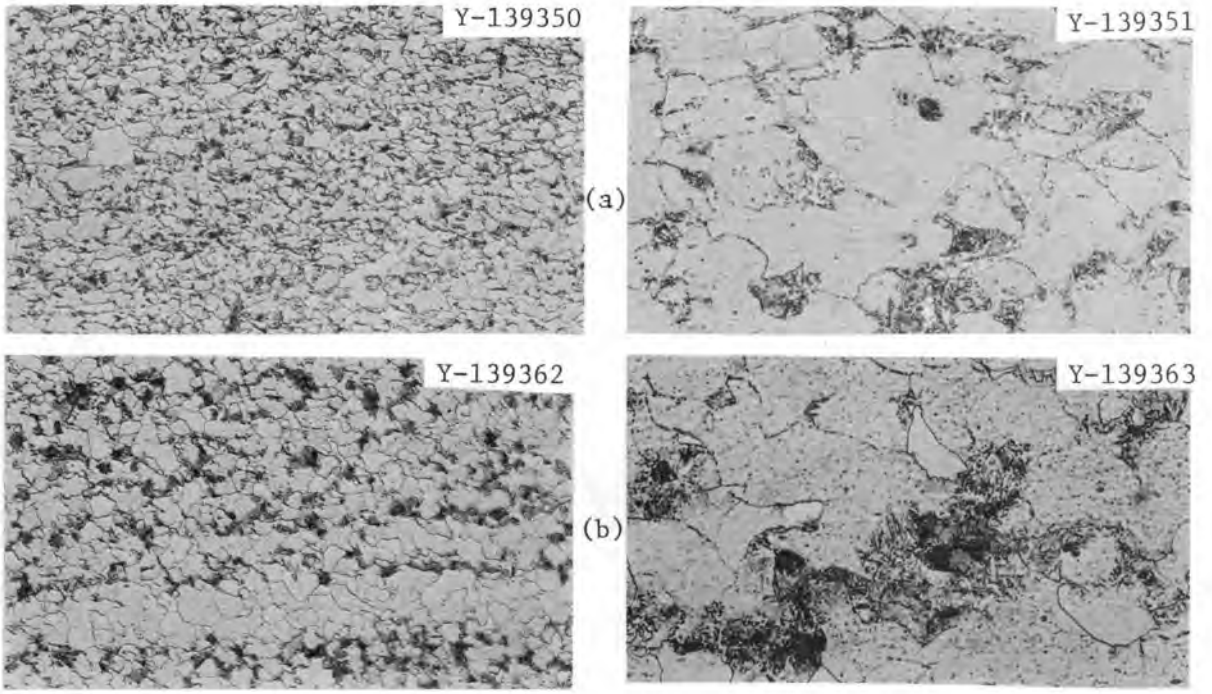

Fig. 3.58. Microstructure of 2 1/4 Cr-1 Mo Steel Tubing Heat 36202. (a) As received. (b) After laboratory isothermal anneal. Left 100×; right 500×.

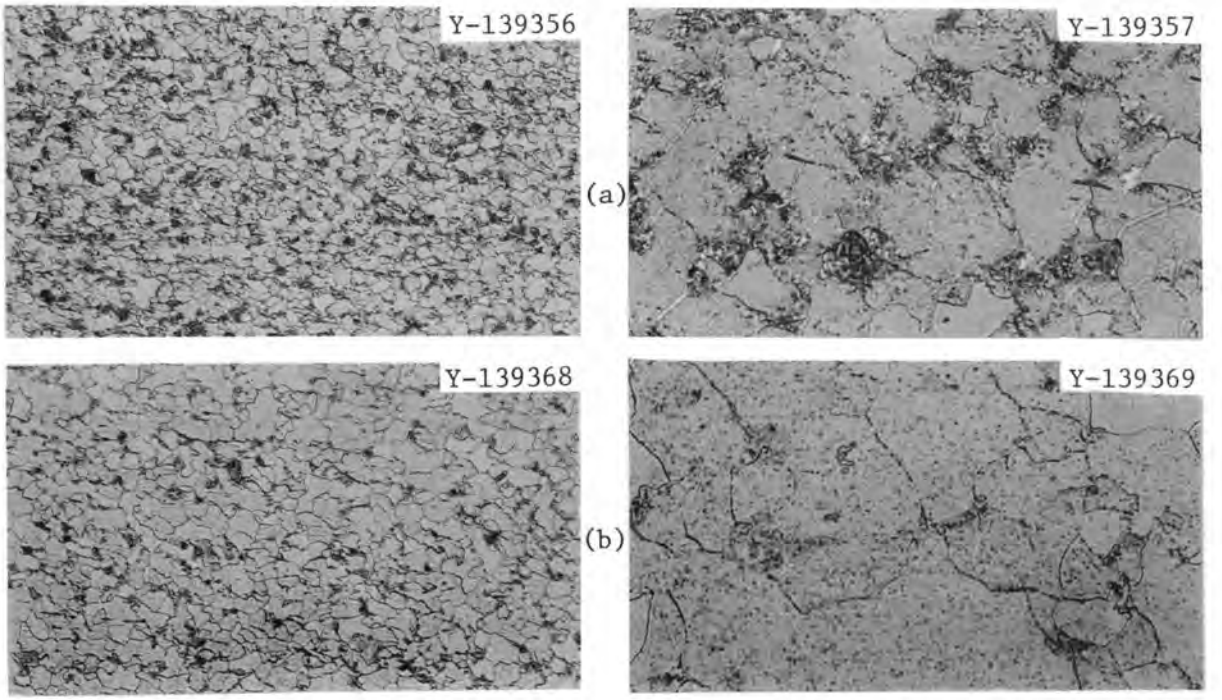

Fig. 3.59. Microstructure of 2 1/4 Cr-1 Mo Steel Tubing Heat 72768. (a) As received. (b) After laboratory isothermal anneal. Left 100×; right 500×.

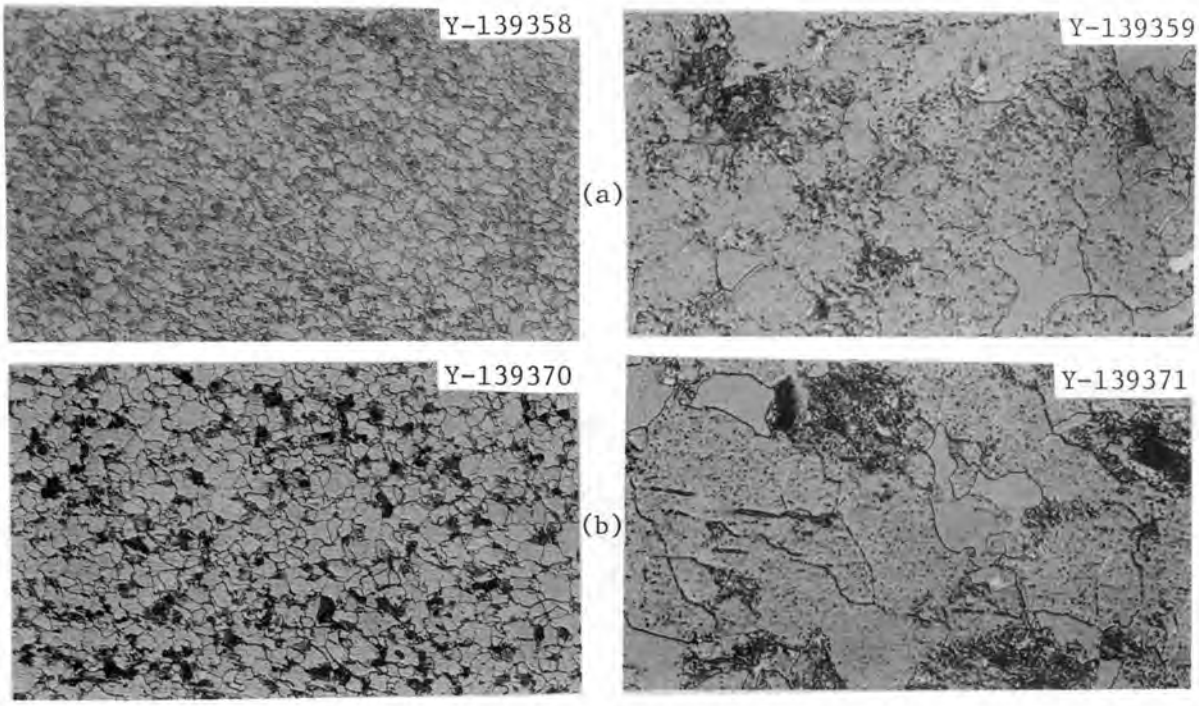

Fig. 3.60. Microstructure of 2 1/4 Cr-1 Mo Steel Tubing Heat 72871. (a) As received. (b) After laboratory isothermal anneal. Left 100×; right 500×.

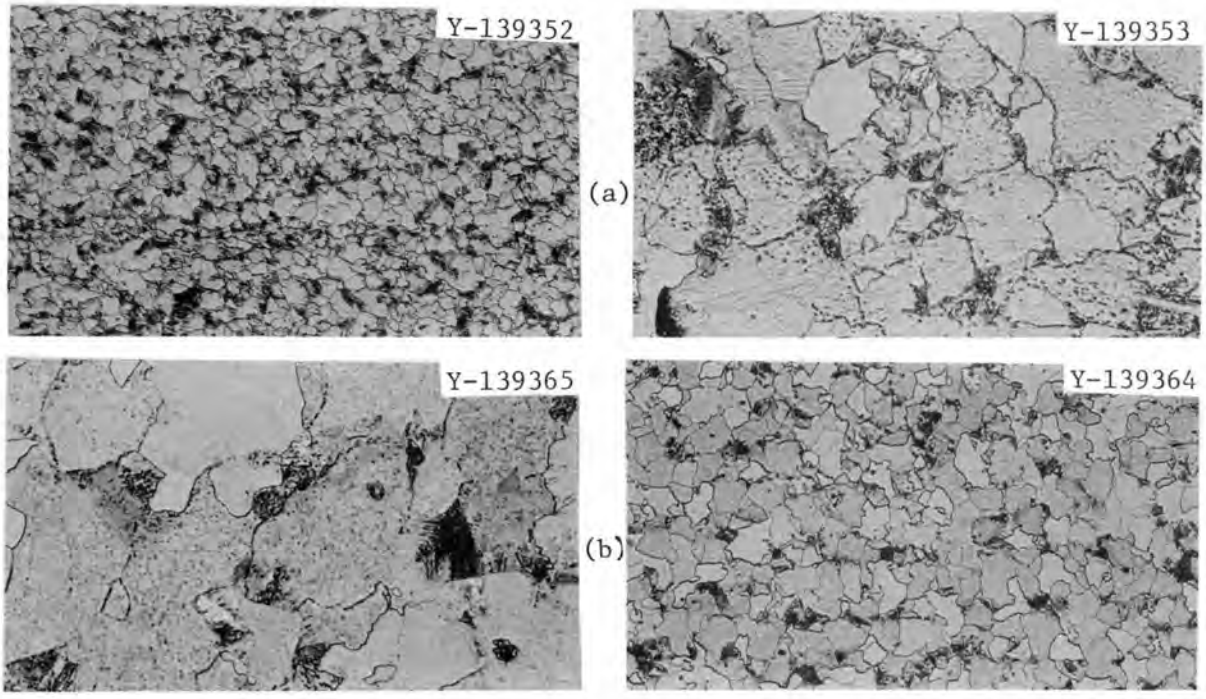

Fig. 3.61. Microstructure of 2 1/4 Cr-1 Mo Steel Tubing Heat X6216. (a) As received. (b) After laboratory isothermal anneal. Left 100×; right 500×.

The VAR and ESR steels were received in the normalized and tempered condition. Thus, the as-received microstructures contained considerable bainite (about 25–40%).[67] After the laboratory isothermal anneal, the microstructures were primarily proeutectoid ferrite and pearlite.[68] In this case, the grain size was smaller after the isothermal anneal (Table 3.17).

The specimens from the air-melted forging were taken from about 0.25 to 0.28 m (10–11 in.) from the center of the cylindrical forging, At this distance into the forging, considerable bainite (15–25%) was observed.[69] After the laboratory isothermal anneal, the microstructure was primarily proeutectoid ferrite with small amounts of pearlite and bainite.[69] After a laboratory isothermal anneal, the microstructure of the air-melted plate heat 20017 was primarily proeutectoid ferrite with small amounts of pearlite and bainite.[44] Heat 3P5601 was primarily proeutectoid ferrite and pearlite. The grain sizes of the air-melted plates and the air-melted forging are considerably larger than for both the as-received and laboratory isothermally annealed tubing heats (Table 3.17); they are also considerably larger than for the ESR plates and the one VAR forging after the laboratory isothermal anneal.

The tensile properties for all heats were determined at 25, 204, 371, 454, 510, and 566°C at a nominal strain rate of about 7×10^{-4}/sec. As stated above, the tensile data for all but the tubing heats and one of the ESR heats (R0110) were previously presented.[44,67–70] The tubing data and those for the ESR heat are given in Tables 3.18 through 3.20. A graphical presentation of the entire data compilation is difficult, since much of the data overlap. Therefore, the strengths for the various product forms in the as-received and laboratory isothermally annealed conditions are presented separately, along with comparisons of as-received and laboratory isothermally annealed steels for given product forms or melting practices (Figs. 3.62–3.64).

The as-received tubing heats show considerable scatter [Fig. 3.62(a)], with heat X6216 considerably stronger than the others in both the 0.2% yield strength and the ultimate tensile strength. After the laboratory isothermal anneal, the properties of the five heats differ much less

Table 3.18. Tensile Properties[a] of Annealed 2 1/4 Cr-1 Mo Steel Tubing — As Received

Temperature		Stress, MPa (ksi)			Strain, %		Reduction of Area (%)
(°C)	(°F)	Yield	Ultimate	Fracture	Uniform	Total	
			Heat 36018				
25	77	324(47.0)	495(71.9)	288(41.8)	15.0	25.3	73.6
204	400	270(39.2)	452(65.6)	282(40.9)	9.4	16.3	65.8
371	700	220(31.9)	513(74.4)	327(47.4)	9.6	15.8	62.9
454	850	217(31.5)	478(69.4)	277(40.2)	8.6	16.4	68.4
510	950	201(29.1)	435(63.2)	213(30.9)	9.5	19.5	70.5
566	1050	196(28.5)	374(54.3)	152(22.0)	11.5	26.1	80.6
			Heat 36202				
25	77	299(43.4)	504(73.1)	276(40.0)	14.4	23.7	76.4
204	400	263(38.2)	450(65.3)	263(38.1)	9.5	16.6	70.8
371	700	229(33.3)	508(73.8)	300(43.6)	9.1	16.3	65.3
454	850	207(30.0)	449(65.2)	207(30.0)	9.2	18.0	72.3
510	950	209(30.3)	422(61.2)	174(25.2)	9.1	19.7	80.0
566	1050	199(28.9)	347(50.3)	123(17.8)	11.1	26.4	84.7
			Heat 72768				
25	77	339(49.2)	548(79.6)	314(45.5)	13.0	22.7	69.3
204	400	281(40.8)	477(69.3)	287(41.7)	11.1	18.4	68.8
371	700	240(34.8)	533(77.3)	327(47.4)	9.3	15.8	65.2
454	850	229(33.2)	480(69.6)	254(36.8)	10.0	18.2	68.8
510	950	221(32.1)	431(62.6)	192(27.8)	8.4	20.1	73.7
566	1050	203(29.4)	348(50.5)	123(17.8)	10.1	29.2	82.8
			Heat 72871				
25	77	319(46.3)	500(72.5)	280(40.6)	14.6	25.3	73.0
204	400	260(37.8)	446(64.8)	263(38.2)	9.8	17.6	72.2
371	700	225(32.7)	511(74.1)	305(44.2)	9.5	16.0	66.7
454	850	208(30.2)	464(67.4)	241(35.0)	9.7	18.0	69.5
510	950	204(29.6)	409(59.3)	174(25.3)	9.0	21.0	79.2
566	1050	181(26.2)	325(47.2)	106(15.4)	9.4	28.3	82.8
			Heat X6216				
25	77	353(51.3)	562(81.5)	324(47.0)	12.4	20.0	71.1
204	400	314(45.5)	510(74.0)	312(45.3)	8.8	15.3	66.8
371	700	288(41.8)	565(82.0)	349(50.6)	9.0	15.9	61.0
454	850	291(42.2)	516(74.9)	265(38.4)	8.7	16.6	71.2
510	950	260(37.8)	467(67.8)	202(29.3)	8.6	17.8	75.4
566	1050	254(36.9)	391(56.7)	147(21.3)	8.7	23.5	79.9

[a]Crosshead speed: 0.02 mm/sec (0.05 in./min); nominal strain rate: 7.3×10^{-4}/sec.

Table 3.19. Tensile Properties[a] of Annealed 2 1/4 Cr-1 Mo Steel Tubing — Laboratory Isothermally Annealed

Temperature		Stress, MPa (ksi)			Strain, %		Reduction of Area (%)
(°C)	(°F)	Yield	Ultimate	Fracture	Uniform	Total	
			Heat 36018				
25	77	313(45.4)	505(73.3)	306(44.4)	13.1	23.8	71.9
204	400	279(40.5)	479(69.5)	323(46.9)	7.5	14.0	67.4
371	700	233(33.8)	525(76.2)	344(49.9)	8.9	14.7	60.9
454	850	206(29.9)	483(70.1)	255(37.0)	9.3	17.1	71.0
510	950	193(28.0)	440(63.8)	198(28.8)	9.0	17.7	70.1
566	1050	185(26.9)	340(49.4)	107(15.5)	9.4	27.5	85.3
			Heat 36202				
25	77	305(44.2)	514(74.6)	309(44.8)	13.5	24.5	72.4
204	400	263(38.2)	473(68.6)	311(45.2)	8.7	18.3	67.8
371	700	238(34.6)	521(75.6)	344(49.9)	9.3	15.8	58.9
454	850	187(27.2)	480(69.6)	263(38.2)	10.5	17.7	68.7
510	950	185(26.9)	427(62.0)	201(29.2)	9.5	20.3	74.7
566	1050	172(24.9)	340(49.4)	123(17.9)	9.0	31.1	84.6
			Heat 72768				
25	77	303(44.0)	485(70.4)	268(38.9)	14.2	24.7	80.1
204	400	251(36.4)	456(66.2)	274(39.7)	8.7	16.7	73.9
371	700	232(33.6)	505(73.3)	304(44.1)	9.1	16.7	67.9
454	850	187(27.1)	460(66.8)	235(34.1)	8.5	16.8	78.6
510	950	172(24.9)	416(60.4)	178(25.9)	9.2	19.0	72.4
566	1050	165(23.9)	328(47.6)	101(14.6)	11.3	28.4	84.7
			Heat 72871				
25	77	315(45.7)	511(74.2)	297(43.1)	13.7	23.2	77.0
204	400	260(37.8)	456(66.2)	280(40.7)	8.7	16.5	72.2
371	700	238(34.5)	516(74.9)	319(46.3)	9.5	16.2	63.4
454	850	194(28.2)	475(68.9)	251(36.5)	9.1	18.1	65.1
510	950	179(25.9)	424(61.5)	184(26.7)	9.0	19.4	73.6
566	1050	163(23.7)	306(44.4)	100(14.5)	8.2	33.1	86.0
			Heat X6216				
25	77	323(46.9)	523(75.9)	299(43.4)	12.7	21.0	73.4
204	400	271(39.4)	484(70.3)	299(43.4)	7.4	14.1	70.8
371	700	251(36.4)	546(79.2)	345(50.0)	8.9	15.6	64.8
454	850	224(32.5)	496(72.0)	253(36.7)	8.2	16.3	72.1
510	950	216(31.3)	441(64.0)	181(26.3)	8.9	20.3	79.0
566	1050	205(29.7)	332(48.0)	89(12.9)	6.8	27.0	85.4

[a]Crosshead speed: 0.02 mm/sec (0.05 in./min); nominal strain rate: 7.3×10^{-4}/sec.

Table 3.20. Tensile Properties[a] of an ESR Plate (Heat R0110) in the As Received and Isothermally Annealed Conditions

Temperature		Stress, MPa (ksi)			Strain, %		Reduction of Area
(°C)	(°F)	Yield	Ultimate	Fracture	Uniform	Total	(%)
				As Received			
25	77	313(45.5)	521(75.6)	271(39.4)	11.5	22.9	76.5
204	400	269(39.1)	446(64.8)	229(33.2)	9.9	18.7	72.5
371	700	282(40.9)	455(66.1)	276(40.1)	7.9	15.6	68.2
454	850	269(39.1)	427(62.0)	229(33.2)	8.5	17.8	72.3
510	950	257(37.3)	376(54.5)	172(24.9)	6.8	18.3	74.9
566	1050	240(34.9)	318(46.2)	114(16.5)	6.8	30.8	81.8
				Laboratory Isothermally Annealed			
25	77	267(38.7)	476(69.1)	282(40.9)	14.2	23.3	73.7
204	400	237(34.4)	433(62.9)	263(38.2)	10.9	19.2	73.0
371	700	206(29.9)	464(67.4)	311(45.1)	8.2	14.9	63.5
454	850	190(27.6)	442(64.1)	255(37.0)	8.7	17.2	66.4
510	950	194(28.2)	416(60.4)	217(31.5)	9.6	20.0	67.1
566	1050	186(27.0)	342(49.7)	136(19.7)	10.0	27.2	82.3

[a]Crosshead speed: 0.02 mm/sec (0.05 in./min); nominal strain rate: 7.3×10^{-4}/sec.

although X6216 is still the strongest [Fig. 3.62(b)]. With the exception of the as-received strength of X6216, difference between the strength properties before and after the laboratory isothermal anneal [Fig. 3.62(c)] is not large. The ultimate tensile strengths are comparable, but the yield strengths of the laboratory isothermally annealed steels fall slightly below those of the as-received tubing at the higher temperatures.

The strength properties of the VAR forgings and the ESR plates determined previously[44,67] along with the data of Table 3.20 are plotted together (Fig. 3.63). Again, after the laboratory isothermal anneal, the differences in strengths are considerably reduced. As might be expected, since the as-received material is normalized and tempered, it is stronger than the laboratory annealed material [Fig. 3.63(c)]. The yield strengths are considerably greater at all temperatures; however, the ultimate tensile strengths of the as-received and laboratory isothermally annealed steels approach each other above 454°C [Fig. 3.639c)].

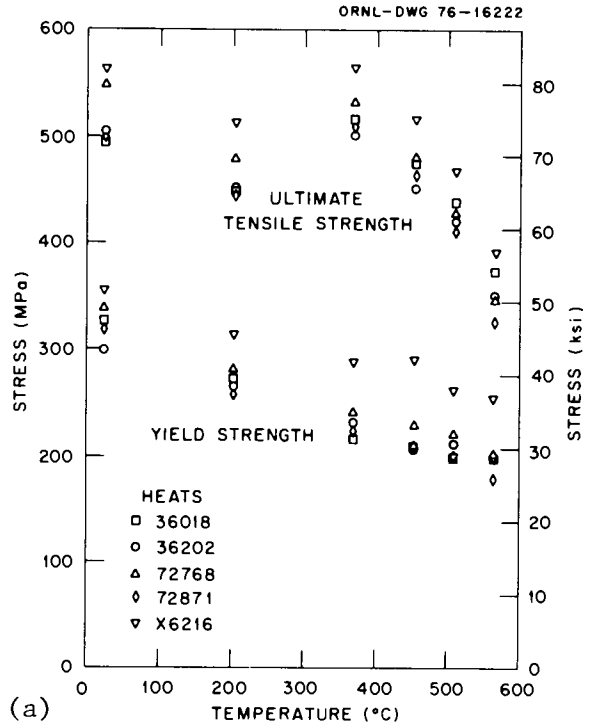

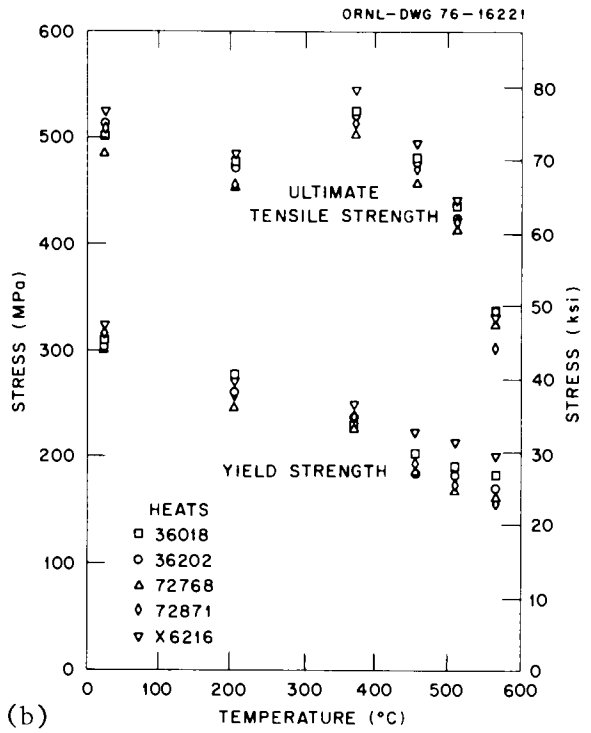

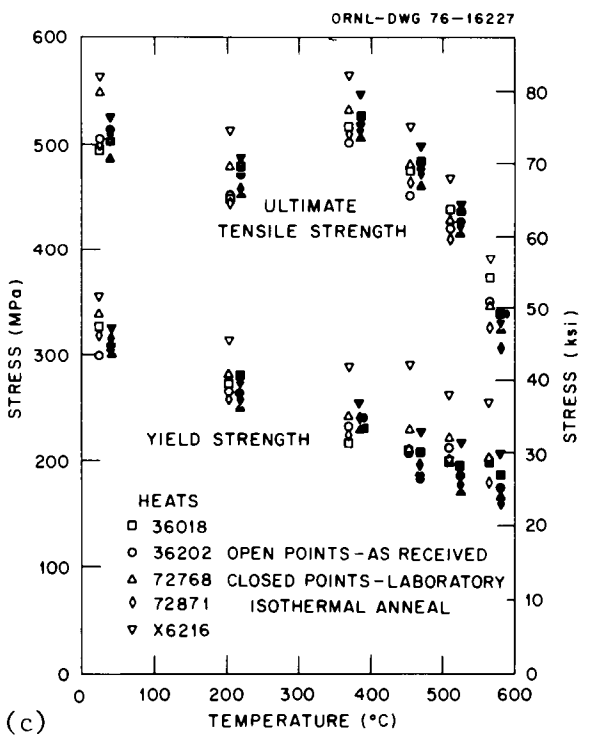

Fig. 3.62. The 0.2% Yield and Ultimate Tensile Strengths as Functions of Temperature for Five Tubing Heats. (a) As received. (b) After laboratory isothermal anneal. (c) Both combined (points for annealed material are shifted to the right to avoid overlap).

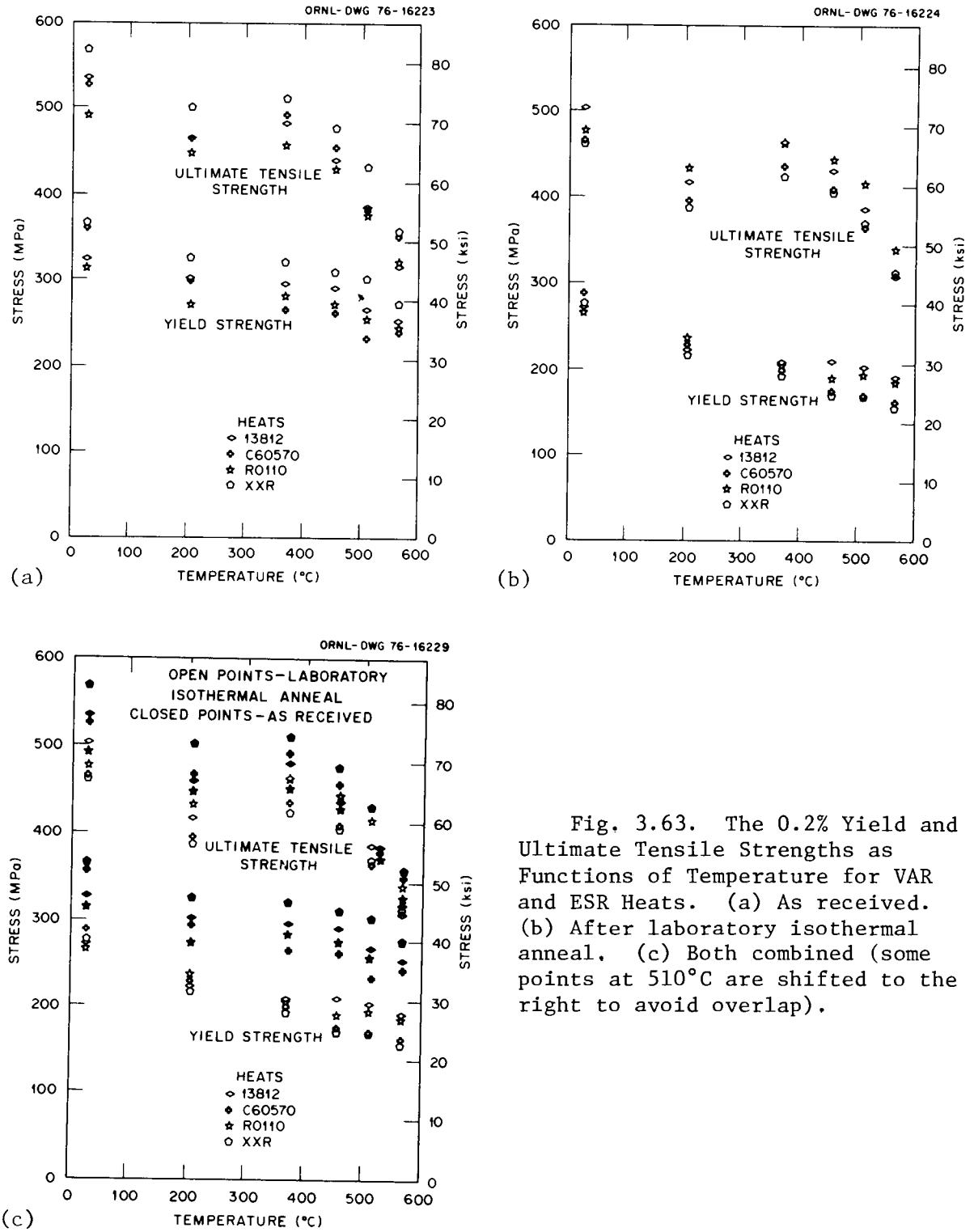

Fig. 3.63. The 0.2% Yield and Ultimate Tensile Strengths as Functions of Temperature for VAR and ESR Heats. (a) As received. (b) After laboratory isothermal anneal. (c) Both combined (some points at 510°C are shifted to the right to avoid overlap).

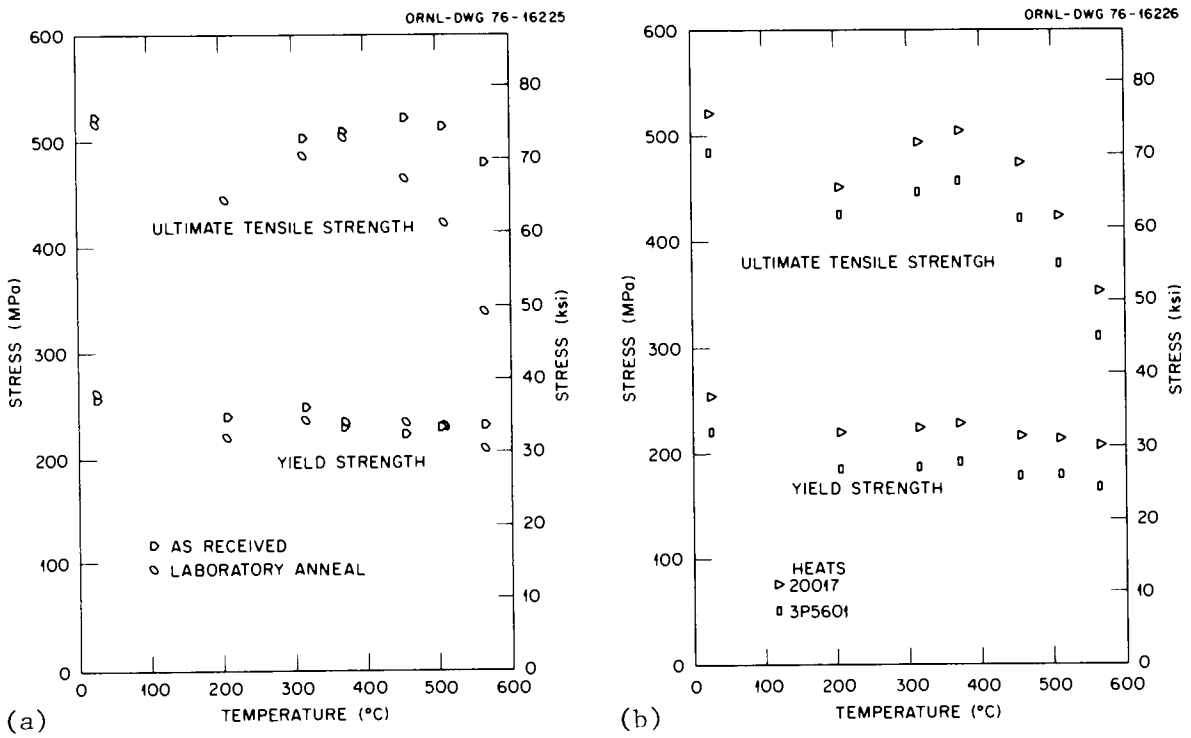

Fig. 3.64. The 0.2% Yield Strength and Ultimate Tensile Strength for Air-Melted 2 1/4 Cr-1 Mo Steel. (a) As-received and laboratory isothermally annealed forging. (b) Laboratory isothermally annealed plates. plates.

The narrow range of the properties of the four steels shows that the VAR and ESR strengths differ little after they have been similarly heat-treated [Fig. 3.63(b)].

When the VAR and ESR steels are compared with the air-melted tubing heats after both have received a laboratory isothermal anneal, the tubing heats are considerably stronger. Except at 566°C, where the properties are similar, the ultimate tensile strengths of all the tubing heats are considerably greater than those of the VAR and ESR heats. Similarly, the yield strengths are considerably greater above 454°C, where the scatter bands for the different types of steels begin to intersect. The most noticeable difference appears to be that the dynamic strain aging peak in the ultimate tensile strength-temperature representation for the tubings (Fig. 3.62) is higher (relative to the properties at room temperature) than it is for the ESR and VAR materials (Fig. 3.63).

Although the yield strengths for the air-melted forging in the as-received condition (isothermally annealed) and the laboratory isothermally

annealed forging are similar, the ultimate tensile strengths for the two heat treatments differ considerably above 371°C. This difference is primarily due to the difference in the temperature of the dynamic strain aging peak for the two different heat treatments. The peak occurs near 454°C for the as-received forging but near 371°C for the laboratory isothermally annealed material. Above the peak temperatures, the strength drops off considerably faster for the laboratory isothermally annealed steel [Fig. 3.64(a)]. A comparison of the tubing results with the forging results indicates that with the exception of the ultimate tensile strength of the as-received forging above 454°C, the properties of the different product forms compare quite favorably. Since the tubings had higher ultimate tensile strengths than the laboratory annealed VAR and ESR products, the air-melted forging is also stronger than the VAR and ESR products.

In the isothermally annealed condition, heat 20017 was the stronger of the two air-melted plates [Fig. 3.64(b)]. It also exhibited a higher dynamic strain aging peak relative to the room-temperature ultimate tensile strength. Below 371°C, the yield strengths of the air-melted plates were less than those for the tubing heats; above 371°C, the yield strengths were comparable. The ultimate tensile strengths for heat 20017 were comparable to those of the tubing heats, while those for 3P5601 were consistently below those of the tubing heats.

The ductilities for these different product forms were all quite similar[44,67-69] (Tables 3.18–3.20). With a few exceptions, at 25°C the total elongation was between 20 and 30%, the reduction of area between 70 and 80%; the uniform elongation for all heats was between 10 and 15%. The exceptions for the total elongation or the reduction of area include the as-received VAR and ESR steels,[67] the as-received air-melted forging[69] and the air-melted plate[70] heat 3P5601. The as-received VAR and ESR steels are normalized and tempered and are expected to have a reduced ductility. Actually, their ductilities fall only slightly below the range of values cited above.[67] Similarly most of the other exceptions fall only slightly below the range of values noted. Although the air-melted forging in the

as-received condition had only a 52% reduction of area,[69] it had a total elongation of almost 28%. It also exhibited a greater than average uniform elongation.

The ductility behavior with temperature is also similar for all heats: the total elongation and reduction of area go through a minimum with increasing temperature; the highest values for these indices occur at 566°C, the highest test temperature, where the reduction of area generally exceeds 70% and the total elongation exceeds about 24%. Two of the normalized-and-tempered heats (13812 and XXR) had slightly smaller total elongations. Both the total elongation and reduction of area of the as-received air-melted forging fall[69] below these values. The reduction of area is only 52%, considerably below the 70% or more observed for all other heats. Furthermore, this forging had been isothermally annealed by the National Forging Company.

The uniform elongation shows a general decrease with increasing temperature. It is of interest to note that the uniform elongation values for the as-received air-melted forging were quite a bit larger than for the laboratory isothermally annealed condition,[69] just the opposite of the observations on total elongation and reduction of area discussed above. Similarly, a comparison of Tables 3.18 and 3.19 for the tubing heats indicates that the uniform elongations of the as-received steels are generally greater than those that received the laboratory isothermal anneal. The laboratory isothermal anneal generally led to slightly greater total elongations and reductions of area and lower strengths than those of the as-received tubing.

3.4.3 Thermal Aging Effects on 2 1/4 Cr-1 Mo Steel — R. L. Klueh

The Clinch River Breeder Reactor steam generators will operate at temperatures to 510°C. Since the reactor is designed to operate for 30 years, a knowledge of the effect of time at temperature on the mechanical properties of the steam generator structural material is of interest.

We have started an aging program on annealed 2 1/4 Cr-1 Mo steel. In the first series of tests, specimens from four commercial heats of tubing were aged. These heats are: 36202, 72768, 72871, and X6216

from the heat-to-heat variation study discussed in Sect. 3.4.2. Plans call for the specimens to be aged at 454, 510, and 566°C (850, 950, and 1050°F) for 1000, 2500, 5000, 10,000, and 20,000 hr. Specimens were taken from the commercially annealed tubes and were aged in the as-received condition (the specimens were stress relieved for 0.25 hr at 649°C before aging). Tensile and creep tests are to be made on these aged specimens. We are also aging annealed material from heat 20017. Considerable tensile and creep testing was previously done on this heat in the unaged condition, and we plan to conduct somewhat more extensive testing on that heat of steel after aging than on the four tubing heats.

During this quarter we concluded tensile tests on specimens of the four tubing heats that had been aged for 1000 and 2500 hr at 454, 510, and 566°C (850, 950, and 1050°F). All four heats were tested at room temperature and at the aging temperature. The results for heats 36202, 72768, 72871, and X6216 are given in Tables 3.21 and 3.22.

Table 3.21. Room-Temperature Tensile Properties of Aged Commercial Tubing Heats of 2 1/4 Cr-1 Mo Steel

Aging Temperature (°C)	Aging Time (hr)	Strength, MPa (ksi)			Elongation, %		Reduction of Area (%)
		Yield	Ultimate	Fracture	Uniform	Total	
			Heat 36202				
454	0	299 (43.4)	504 (73.1)	276 (40.0)	14.4	23.7	76.4
	1000	319 (46.3)	570 (82.7)	399 (49.2)	12.4	22.0	71.0
	2500	323 (46.9)	577 (83.7)	337 (48.9)	11.7	21.9	72.1
510	1000	322 (46.8)	576 (83.6)	340 (49.3)	11.2	21.4	71.9
	2500	312 (45.3)	573 (83.1)	326 (47.3)	11.0	21.3	73.8
566	1000	325 (47.1)	572 (83.0)	322 (46.8)	10.9	21.6	72.8
	2500	282 (40.9)	566 (82.1)	314 (45.6)	10.1	21.5	72.9
			Heat 72768				
454	0	339 (49.2)	548 (79.6)	314 (45.5)	13.0	22.7	69.3
	1000	244 (35.4)	487 (70.7)	285 (41.4)	14.3	24.9	74.6
	2500	237 (34.4)	488 (70.8)	285 (41.4)	15.1	25.0	74.7
510	1000	287 (41.6)	544 (79.0)	313 (45.5)	13.0	23.0	70.5
	2500	234 (34.0)	491 (71.3)	285 (41.4)	16.3	24.5	70.5
566	1000	241 (35.0)	492 (71.4)	282 (41.0)	14.5	24.6	73.0
	2500	222 (32.2)	493 (71.6)	285 (41.4)	14.1	24.5	71.4
			Heat 72871				
454	0	319 (46.3)	500 (72.5)	280 (40.6)	14.6	25.3	73.0
	1000	305 (44.2)	514 (74.6)	288 (41.8)	13.1	24.0	74.5
	2500	249 (36.1)	508 (73.8)	291 (42.3)	13.7	22.8	72.2
510	0	319 (46.3)	500 (72.5)	280 (40.6)	14.6	25.3	73.0
	1000	258 (37.5)	511 (74.1)	293 (42.5)	13.9	23.9	73.7
	2500	234 (34.0)	509 (73.9)	287 (41.6)	13.8	23.9	73.8
566	0	319 (46.3)	500 (72.5)	280 (40.6)	14.6	25.3	73.0
	1000	245 (35.5)	515 (74.8)	289 (42.0)	13.8	24.1	73.8
	2500	238 (34.6)	508 (73.8)	284 (41.2)	12.9	22.5	75.4
			Heat X6216				
454	0	353 (51.3)	562 (81.5)	324 (47.0)	12.4	20.0	71.1
	1000	278 (40.3)	533 (77.3)	304 (44.1)	11.9	21.9	70.4
	2500	276 (40.1)	531 (77.0)	302 (43.9)	12.6	22.3	71.3
510	0	353 (51.3)	562 (81.5)	324 (47.0)	12.4	20.0	71.1
	1000	281 (40.9)	535 (77.7)	309 (44.8)	12.4	22.1	68.6
	2500	274 (39.8)	537 (77.9)	300 (43.5)	11.7	20.4	69.3
566	0	353 (51.3)	562 (81.5)	324 (47.0)	12.4	20.0	71.1
	1000	305 (44.2)	557 (80.8)	310 (45.0)	11.0	20.5	72.9
	2500	255 (37.0)	520 (75.4)	287 (41.7)	11.5	21.2	75.3

Table 3.22. Aging-Temperature Tensile Properties of Aged Commercial Tubing Heats of 2 1/4 Cr-1 Mo Steel

Aging and Test Temperature (°C)	Aging Time (hr)	Strength, MPa (ksi)						Elongation, %		Reduction of Area (%)
		Yield		Ultimate		Fracture		Uniform	Total	
				Heat 36202						
454	0	207	(30.0)	449	(65.2)	207	(30.0)	9.2	18.0	72.3
	1000	263	(38.1)	495	(71.9)	275	(39.9)	11.0	18.9	68.6
	2500	265	(38.5)	471	(68.3)	262	(38.0)	9.8	19.8	70.4
510	0	209	(30.3)	422	(61.2)	174	(25.2)	9.1	19.7	80.0
	1000	251	(36.5)	420	(60.9)	194	(28.1)	9.5	23.2	76.9
	2500	244	(35.4)	391	(56.8)	179	(26.0)	9.0	22.7	77.8
566	0	199	(28.9)	347	(50.3)	123	(17.8)	11.1	26.4	84.7
	1000	224	(32.5)	326	(47.3)	118	(17.1)	8.2	31.7	82.8
	2500	205	(29.8)	306	(44.4)	113	(16.4)	7.4	29.7	81.2
				Heat 72768						
454	0	229	(33.2)	480	(69.6)	254	(36.8)	10.0	18.2	68.8
	1000	223	(32.4)	447	(64.9)	244	(35.4)	10.6	19.6	75.4
	2500	216	(31.4)	420	(60.9)	230	(33.4)	10.5	20.2	73.8
510	0	221	(32.1)	431	(62.6)	192	(27.8)	8.4	20.1	73.7
	1000	182	(26.4)	379	(55.0)	174	(25.2)	12.1	24.3	73.9
	2500	214	(31.0)	358	(52.1)	162	(23.5)	10.6	26.5	78.6
566	0	203	(29.4)	348	(50.5)	123	(17.8)	10.1	29.2	82.8
	1000	189	(27.5)	298	(43.3)	106	(15.4)	7.6	33.7	81.4
	2500	184	(26.7)	287	(41.6)	112	(16.3)	7.3	32.7	82.7
				Heat 72871						
454	0	208	(30.2)	464	(67.4)	241	(35.0)	9.7	18.0	69.5
	1000	198	(28.7)	424	(61.6)	227	(33.0)	11.1	20.8	72.9
	2500	192	(27.8)	395	(57.3)	213	(30.9)	10.9	21.5	73.0
510	0	204	(29.6)	409	(59.3)	174	(25.3)	9.0	21.0	79.2
	1000	182	(26.4)	356	(51.7)	152	(22.0)	11.5	26.9	79.9
	2500	176	(25.6)	336	(48.8)	140	(20.3)	8.8	31.3	80.6
566	0	181	(26.2)	365	(47.2)	106	(15.4)	9.4	28.3	82.8
	1000	165	(24.0)	282	(41.0)	88	(12.7)	10.4	33.1	89.2
	2500	172	(24.9)	273	(39.6)	84	(12.2)	8.6	34.9	89.2
				Heat X6216						
454	0	291	(42.2)	516	(74.9)	265	(38.4)	8.7	16.6	71.2
	1000	282	(41.0)	492	(71.4)	257	(37.3)	9.5	18.5	70.3
	2500	281	(40.9)	472	(68.5)	248	(36.0)	9.6	19.0	67.6
510	0	260	(37.8)	467	(67.8)	202	(29.3)	8.6	17.8	75.4
	1000	258	(37.4)	409	(59.3)	174	(25.3)	9.9	20.4	73.0
	2500	240	(34.9)	373	(54.2)	147	(21.3)	9.2	23.4	80.5
566	0	254	(36.9)	391	(56.7)	147	(21.3)	8.7	23.5	79.9
	1000	222	(32.2)	313	(45.4)	96	(13.9)	8.1	29.7	78.7
	2500	184	(26.7)	274	(39.8)	76	(11.0)	7.9	37.4	84.6

For the limited amounts of short-time aging data available, no detailed conclusions are possible. In general, the longer the aging time, the greater the effect on the strength. Since aging is expected to be thermally activated, the higher the aging temperature, the greater the effect on strength. In most instances, the 0.2% yield strength and ultimate tensile strength decreased with increased aging time, the decrease being the greater the higher the temperature, although there are some exceptions to these general trends. However, only when further data become available will the overall behavior be clear. Hence, we will defer detailed comment until such data are available.

3.4.4 Effect of Sodium on the Mechanical Properties of 2 1/4 Cr-1 Mo Steel — R. L. Klueh

The effect of sodium on the mechanical properties of 2 1/4 Cr-1 Mo steel is of interest for the steam generators of the CRBR because decarburization by sodium is possible[48] under the conditions of the 2 1/4 Cr-1 Mo steel in the steam generators. Last quarter[71] we reported on the tensile properties of 2 1/4 Cr-1 Mo steel specimens exposed to sodium for 26,500 hr at 566°C (1050°F). Results were also presented for specimens that had been thermally aged for 26,500 hr at 566°C in a helium (nondecarburizing) atmosphere.

Specimens that were decarburized and aged for 26,500 hr at 566°C are now being creep-rupture tested. The specimens were decarburized and aged by MSA Corp., Evans City, Pennsylvania.[71] We obtained 23 decarburized specimens, but only five aged specimens were available. Since no starting material was available, the effect of decarburization and aging will have to be inferred by comparison with literature data.

Creep-rupture tests are being made at 510 and 566°C (950 and 1050°F) on lever arm creep frames with a 12:1 ratio; the specimens are heated in a Marshall resistance furnace. During test the temperature is monitored and controlled by three Chromel vs Alumel thermocouples attached along the specimen gage section. Temperatures are controlled to ±1°C, and the temperature varies less than ±3°C along the gage length.

Creep strains are measured with a mechanical extensometer attached to the gage section, and the strain is read periodically on a dial gage with a sensitivity of 3 mm (10^{-5} in.).

The creep-rupture results at 510 and 566°C obtained to date on the sodium-decarburized steel are given in Table 3.23. Also shown are the results obtained on the helium-aged specimens. We previously compared the results for the helium-aged specimens with the values given by ASME Code Case 1592; they fell substantially below the expected minimum[72] given in Code Case 1592. The results for the sodium-exposed specimens fall slightly below those previously given for the helium-aged specimens. However, these are rather high-stress (short-rupture-life) tests. Extrapolation of these short-rupture-time tests to longer times and lower stresses indicates that the properties of the helium-aged steel will approach the ASME values at longer rupture times.[72] We presently have tests in progress at 55 MPa (8 ksi) on both helium-aged and sodium-decarburized specimens. Once these long-time tests are completed, we should be better able to evaluate the trends for the effect of sodium after 26,500 hr at 566°C.

Table 3.23. Creep-Rupture Properties of 2 1/4 Cr-1 Mo Steel Decarburized in Sodium or Aged in Helium for 26,500 hr at 566°C (1050°F)

Test Temperature		Stress		Rupture Life	Elongation	Reduction of Area	Minimum Creep Rate
(°C)	(°F)	(MPa)	(ksi)	(hr)	(%)	(%)	(%/hr)
				Decarburized			
566	1050	138	20.0	10.0	56.7	54.4	2.44
		103	15.0	114.0	76.8	62.4	0.24
		83	12.0	395.5	79.8	66.7	0.0817
		69	10.0	1517.5	64.0	53.2	0.0184
510	950	172	25.0	26.5	66.3	53.3	1.07
		138	20.0	190.5	77.5	61.0	0.159
		121	17.5	463.2	76.0	74.7	0.0646
				Aged			
566	1050	102	15.0	158.0	90.5	64.5	0.202
		83	12.0	692.0	108.5	62.3	0.0475
		69	10.0	2940.1	67.0	46.3	0.0109

3.4.5 Fatigue Behavior of 2 1/4 Cr-1 Mo Steel — C. R. Brinkman

3.4.5.1 Specimen Geometry Effects — J. P. Strizak

We have compared data from strain-controlled fatigue tests involving hourglass and uniform-gage specimens employed by ORNL and its subcontractors, including Mar-Test Inc. and the Battelle-Columbus Laboratory. The intent was to gain insight as to possible specimen geometry effects on experimental fatigue data.

The hourglass and uniform-gage specimen configurations employed to date in characterizing the fatigue behavior of 2 1/4 Cr-1 Mo steel are shown in Figs. 3.65 and 3.66 respectively. It should be noted that,

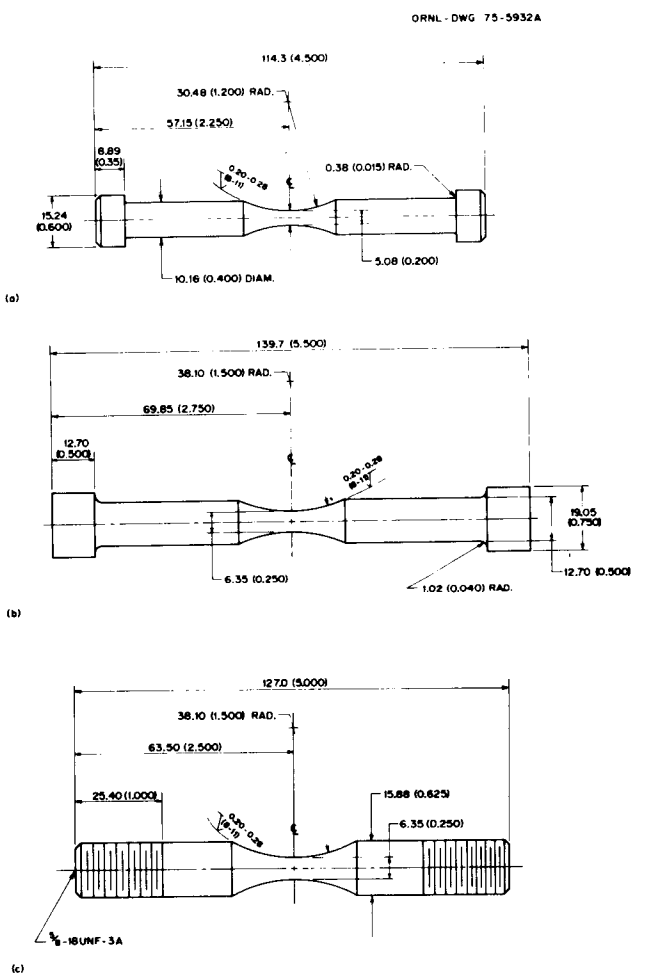

Fig. 3.65. Sketches of Hourglass Specimens. All dimensions are in millimeters (inches) except surface finishes, which are in micrometers (microinches). (a) ORNL specimen. (b) Mar-Test specimen. (c) Battelle-Columbus specimen.

ORNL-DWG 76-18191

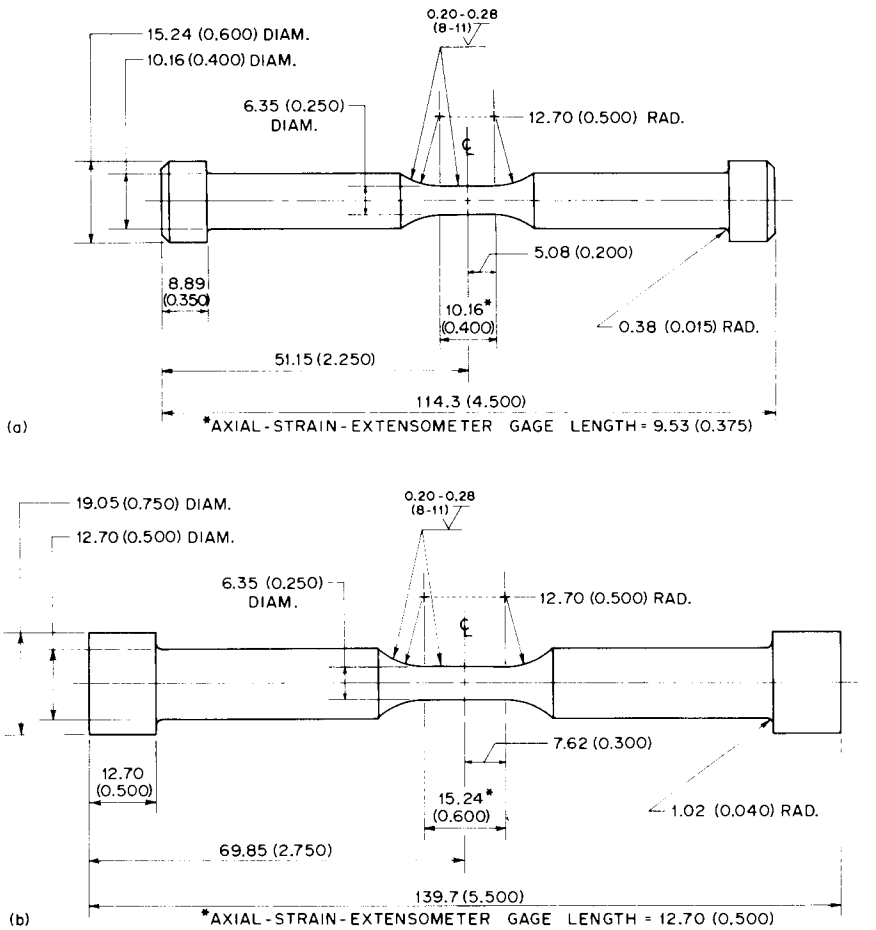

Fig. 3.66. Sketches of Uniform-Gage Specimens. All dimensions are in millimeters (inches) except surface finishes, which are in micrometers (microinches). (a) ORNL specimen. (b) Mar-Test specimen.

while the minimum diameters of the two buttonhead specimens shown in Fig. 3.65 are different, the specimens have the same radius-to-minimum diameter (R/D) ratio of 6, where R is the radius of curvature of the hourglass section. Also, the uniform-gage specimens shown in Fig. 3.66 differ in specimen gage length and axial-strain-extensometer gage length. Particularly attractive features of the hourglass specimens include resistance to buckling when loaded in compression and ease of heating since only a small part of the specimen needs to be at a uniform test temperature.

Final machining of the test areas of both the hourglass and uniform-gage specimens was accomplished in the same manner: (1) Rough machine

to leave 0.25 mm (0.010 in.) stock material on the radius over the final dimension. (2) Set up a grinding wheel of specified radius with its shaft at 90° to the specimen longitudianl axis. Grind wet. (3) Remove 5 μm (0.0002 in.) of stock material each pass while rotating the specimen at 325 rpm about its longitudinal axis. (4) Buff to a 0.20 to 0.28 μm (8–11 μin.) surface finish by polishing parallel to the specimen longitudinal axis. (5) Polish the reduced area longitudinally to remove all circumferential work marks visible at approximately 20× magnification under an optical microscope.

Fully reversed axial-strain-controlled push-pull testing was accomplished in closed-loop electrohydraulic fatigue machines. Axial strain control was maintained directly by employing an axial strain extensometer attached to the gage length of the uniform-gage specimen. On the other hand, a diametral extensometer was employed on the hourglass (zero gage length) specimens, and conversion to axial strain was accomplished by a simple diametral-to-axial strain computer. Total strain range, $\Delta\varepsilon_t$, was thus determined by the relation

$$\Delta\varepsilon_t = \left(\frac{\Delta\sigma}{E}\right)\left(1 - 2\nu\right) + 2\Delta\varepsilon_d ,$$

where E is Young's Modulus at the test temperature, ν is Poisson's ratio, $\Delta\varepsilon_d$ is the diametral strain range, and $\Delta\sigma$ is the peak-to-peak stress range from the hysteresis loops. Constant-strain-rate tests were conducted by employing a triangular wave form. The specimens were heated by induction in air, with thermocouples attached to the specimens some distance removed from the extensometer gage areas.

Data from tests on a single heat of isothermally annealed 2 1/4 Cr-1 Mo steel are compared in Table 3.24. Elastic, plastic, and total strain ranges are plotted against cycles to failure in Figs. 3.67 and 3.68 for room temperature and 538°C (1000°F) respectively. Results at room temperature in Fig. 3.67 are essentially the same for both hourglass and uniform-gage specimen configurations at the higher strain ranges. On the other hand, cyclic life at 538°C (1000°F) is reduced by a factor less than 2 for the uniform-gage data in comparison with hourglass

Table 3.24. Comparison of Data from Strain-Controlled Fatigue Tests Involving Hourglass and Uniform-Gage Specimen Configurations[a]

Temperature		Specimen[b]	Total Strain Range $\Delta\varepsilon_t$, %	Specimen Geometry	Stress Range, $\Delta\sigma$		Tensile Stress Amplitude σ_t		Compressive Stress Amplitude σ_c		Strain Range, %		Cycles to Failure, N_f
(°C)	(°F)				(MPa)	(ksi)	(MPa)	(ksi)	(MPa)	(ksi)	Elastic $\Delta\varepsilon_e$	Plastic $\Delta\varepsilon_p$	
20	70	ITT-5	2.00	Hourglass	759	110.1	369	53.5	390	56.5	0.27	1.73	958
20	70	IUL-14	1.98	Uniform	736	106.8	366	53.2	370	53.7	0.36	1.62	1,042
20	70	ITL-76	1.02	Hourglass	656	95.2	324	47.1	332	48.2	0.32	0.70	4,042
20	70	IUL-18	1.00	Uniform	619	89.8	309.5	44.9	309.5	44.9	0.30	0.70	4,079
20	70	IUL-16	0.51	Uniform	528	76.6	254	36.8	274	39.8	0.26	0.25	32,403
20	70	ITT-6	0.35	Hourglass	486	70.5	234	33.9	252	36.6	0.23	0.12	140,235
20	70	IUL-19	0.35	Uniform	489	70.9	246	35.6	244	35.3	0.24	0.11	115,121
538	1000	BIL-16	2.09	Hourglass	549	79.6					0.36	1.73	846
538	1000	IUL-10	1.99	Uniform	558	80.9	274	39.7	284	41.2	0.32	1.67	679
538	1000	BIL-15	1.03	Hourglass	467	67.8					0.27	0.76	2,477
538	1000	IUL-8	0.97	Uniform	477	69.2	239	34.5	239	34.7	0.27	0.70	2,000
538	1000	BIL-11	0.50	Hourglass	248	62.0					0.27	0.23	16,185
538	1000	MIL-10	0.50	Hourglass	391	56.7	192	27.8	199	28.9	0.22	0.28	16,036
538	1000	ITL-17	0.50	Hourglass	386	56.0	189	27.4	197	28.6	0.22	0.28	15,164
538	1000	MIL-31	0.50	Uniform	410	59.5	204	29.6	206	29.8	0.23	0.27	9,353
538	1000	IUL-6	0.50	Uniform	412	59.8	204	29.6	208	30.1	0.24	0.26	10,764
538	1000	ITT-7	0.38	Hourglass	414	60.1	209	30.3	206	29.8	0.24	0.14	63,906
538	1000	IUL-7	0.35	Uniform	393	57.0	197	28.6	196	28.5	0.22	0.13	73,256

[a]All test conducted at a strain rate, $\dot{\varepsilon}$, of 4×10^{-3}/sec.

[b]All specimens from heat 3P5601 in an isothermally annealed condition.

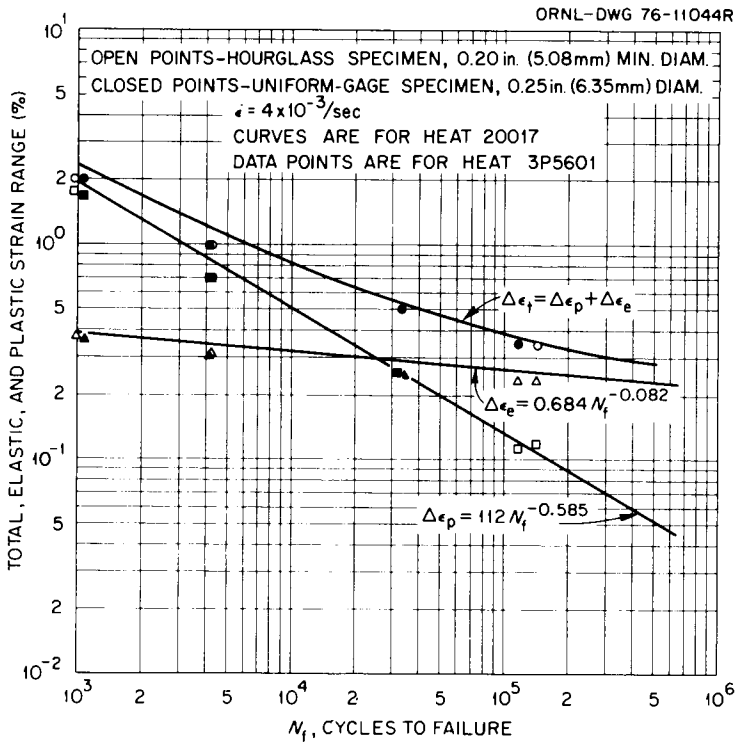

Fig. 3.67. Comparison of Specimen Geometry Effects on the Fatigue Behavior of 2 1/4 Cr-1 Mo Steel at Room Temperature.

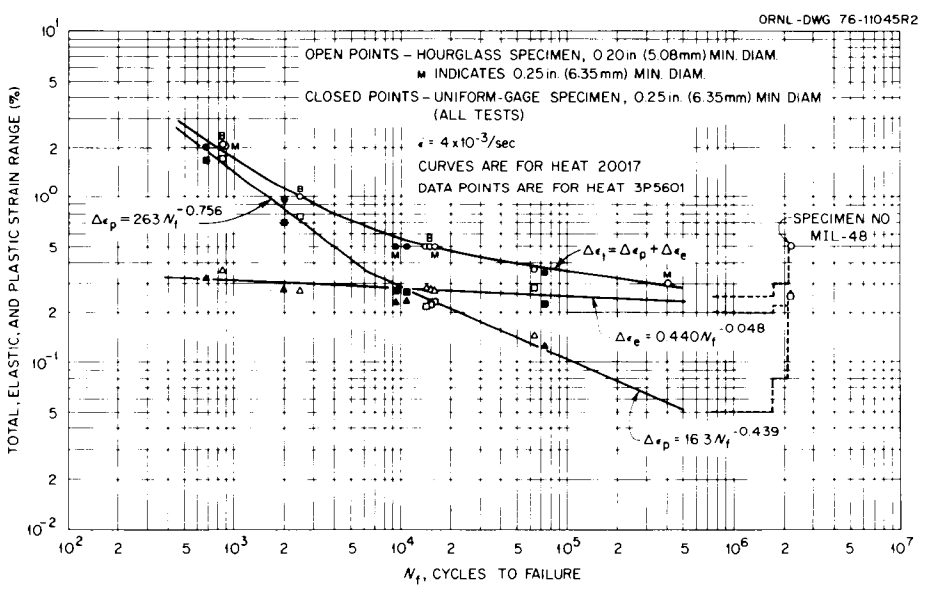

Fig. 3.68. Comparison of Specimen Geometry Effects on the Fatigue Behavior of 2 1/4 Cr-1 Mo Steel at 538°C (1000°F).

specimen data. Some evidence of increased stresses is indicated for the uniform-gage data at 538°C (1000°F) in Table 3.24. Finite element analysis of the stress concentration[73] occurring near the transition radii in a uniform-gage specimen showed that the portion of the specimen gage area removed from the transition radii by a distance approximately equal to one diameter has a fairly uniform stress over the entire cross section. Reference to Fig. 3.66 would indicate that some area of stress concentration may be encountered near the extremes of the gage length of both axial extensometers that were used. In addition, the relatively large surface area of the uniform-gage configuration would enhance the probability of crack initiation sites, thus leading to earlier failure, particularly at low strain ranges — say below 0.5% — and at elevated temperatures. Temperature gradients over the gage length and accuracy of strain measurements in both hourglass and uniform-gage specimen configurations would also add to the observed differences in fatigue life at like values of nominal (engineering) strain ranges.

The letter designations B and M appearing by individual data in Fig. 3.68 indicate the laboratory performing the particular test, (i.e., Battelle-Columbus Laboratory and Mar-Test, Inc., respectively); the remaining tests were performed at ORNL. Where comparisons can be made (see Fig. 3.68), slight lab-to-lab variability in testing equipment or techniques shows no apparent effect. Further, at a total strain range of 0.5%, no noticeable difference is observed in results for either 5.08 or 6.35-mm-diam (0.200 or 0.250-in.) hourglass specimens.

3.4.5.2 Subcritical Crack Growth Studies — W. R. Corwin

This study uses isothermally annealed 2 1/4 Cr-1 Mo steel from two Babcock and Wilcox heats, 20017 and 3P5601, and one, 50057, supplied by Sumitomo Metal Industries of Japan. Their mechanical properties have been reported in previous quarterlies.

Efforts this quarter were concentrated on testing in air to expand on effects of temperature and frequency on fatigue crack propagation (FCP) of 2 1/4 Cr-1 Mo steel. Also limited work was performed to investigate effects of carbon content and aging.

To allow a wider range for the evaluation of thermal effects on the FCP behavior of 2 1/4 Cr-1 Mo steel, limited testing was performed at −46°C (−50°F). The results, shown in Fig. 3.69, along with others reported previously* show the continued dependence of the FCP rate on temperature into this range. Inasmuch as thermally induced deformation mechanisms are inactive at these temperatures, the increased fatigue resistance from that observed at room temperature is attributed to either increases in the mechanical strength and/or decreased oxidation at the crack tip at the lower temperature. The strong effect of the presence of oxygen, which has been demonstrated[74] on the FCP rate of 2 1/4 Cr-1 Mo steel at higher temperatures, may still be important at room temperature and below.

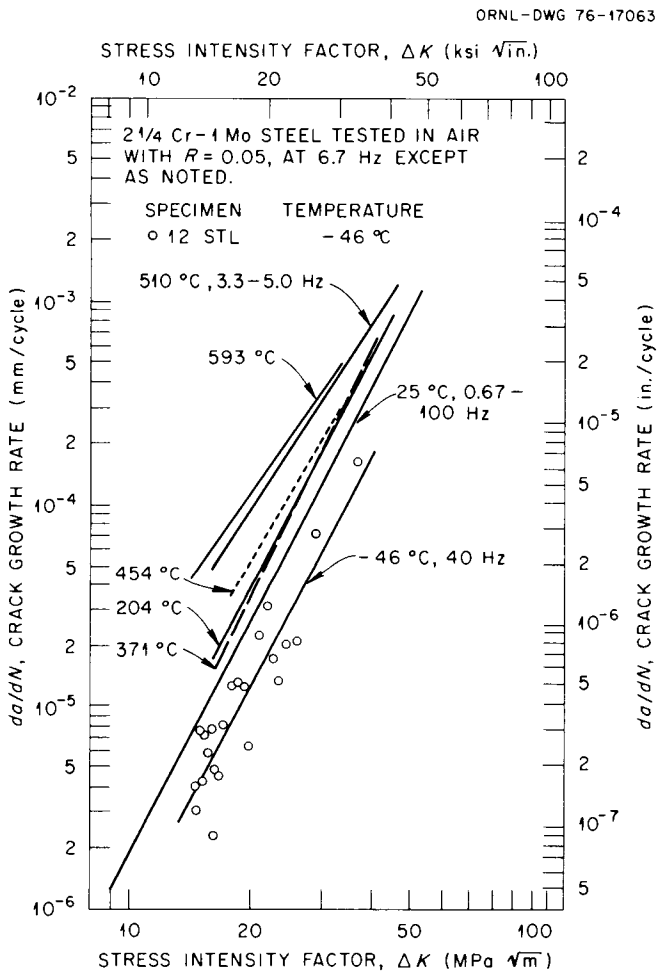

Fig. 3.69. Effect of Test Temperature on Fatigue Crack Growth Rate.

*Trend line at 371°C (700°F) is averaged results from both heats 20017 and 3P5601.

Effects of frequency were further examined at 593°C (1100°F) with testing at ν = 50 Hz, at 510°C (950°F) with testing at 0.0067 and 0.00067 Hz and at 371°C (700°F) with testing at 0.067 Hz. It is apparent from comparison of the results obtained at 593°C (1100°F), shown in Fig. 3.70, with previous results, that a strong time dependence of the FCP rate still exists even at the high frequency of 50 Hz. The FCP rate monotonically decreases at constant ΔK with increasing frequency; this is attributed primarily to the environmental aspects of oxidation at the crack tip.

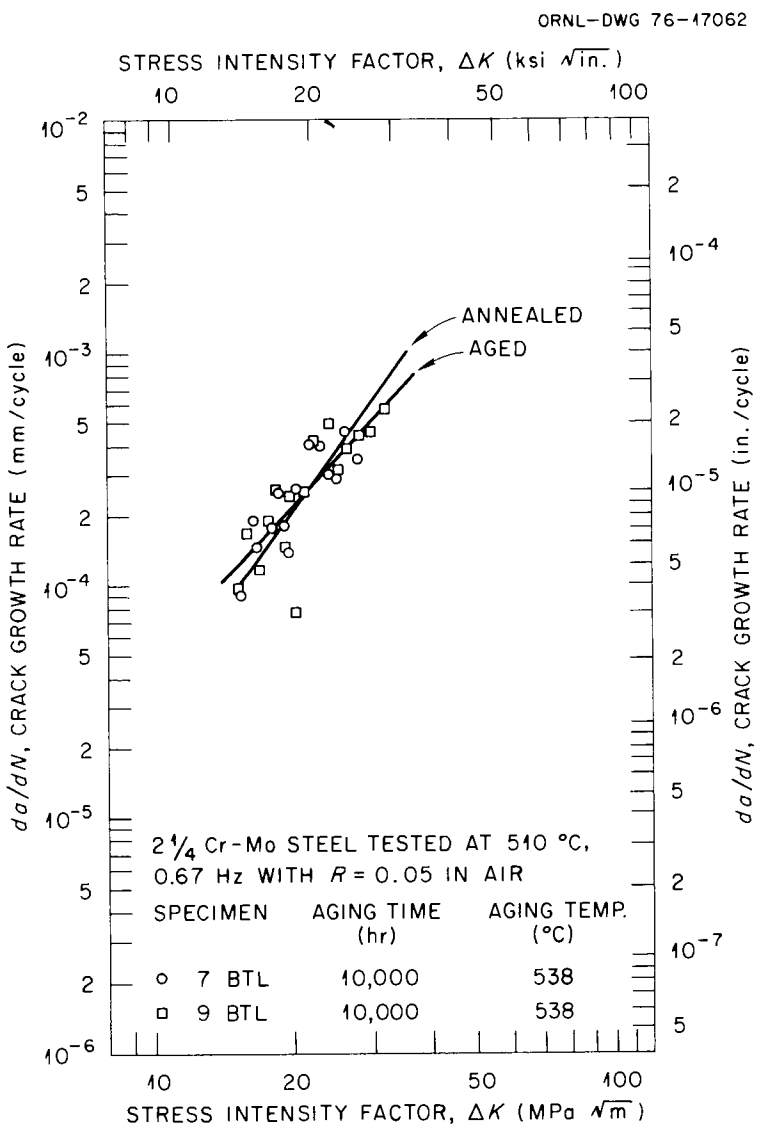

Fig. 3.70. Effect of Test Frequency on Crack Growth Rate.

Results of low-frequency testing at 510°C (950°F) show a similar trend over the range of frequency from 5.0 to 0.0067 Hz, the lowest frequency investigated at 593°C (1100°F). However the results at the lowest frequency determined at 510°C (950°F) do not show expected further increases in crack growth, as would be expected. Rather the opposite is true as shown in Fig. 3.71. This crack growth rate per cycle is faster at 0.0067 Hz than at 0.00067 Hz. This appears due primarily to two causes. At the longest cycle time (25 min/cycle) apparently both crack tip blunting due to creep as well as relaxation of the high crack tip stress occur, so the calculated stress intensity factor overestimates the actual crack extension during force.

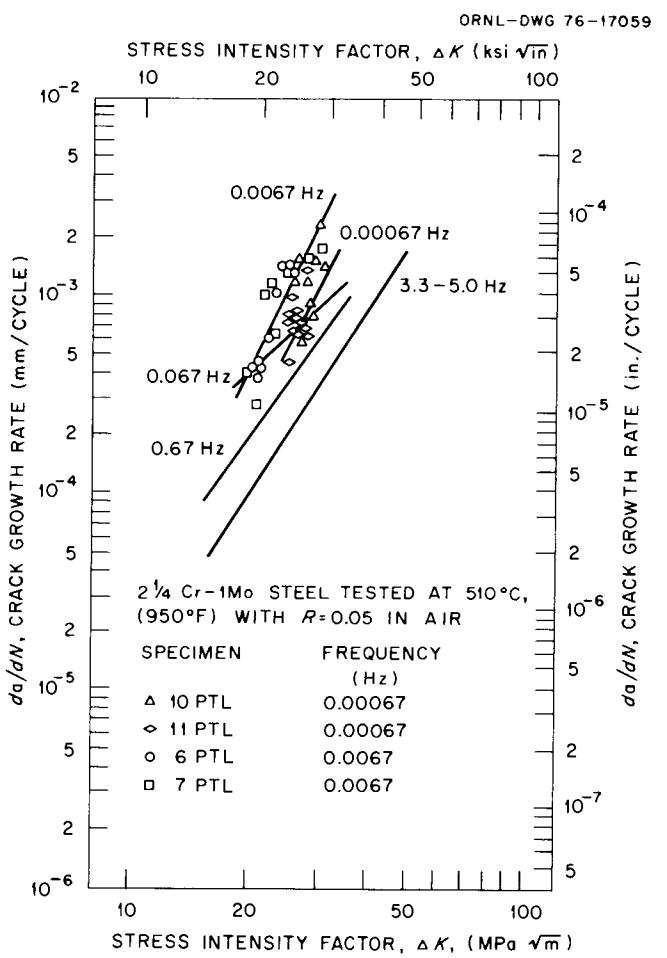

Fig. 3.71. Effect of Test Frequency on Fatigue Crack Growth Rate at 510°C.

The evaluation of frequency effects at 371°C (700°F) is complicated by heat-to-heat variations of the crack growth rate. As reported earlier,[75] the only conditions we have observed under which heat-to-heat effects on the FCP rate are significant in 2 1/4 Cr-1 Mo steel are in the temperature range in which dynamic strain aging occurs, 316 to 426°C (600–800°F). Comparing the results of testing material from heat 3P5601 at 6.7 Hz and 0.067 Hz in Fig. 3.72 shows a minimal effect of test frequency on the crack growth rate. However, the trend line representing data at 6.7 Hz for heat 20017 shows significantly lower crack growth rates than for heat 3P5601 at either frequency. This agrees with other observations[76] that heat 20017 experiences a greater degree of dynamic strain aging at 371°C (700°F).

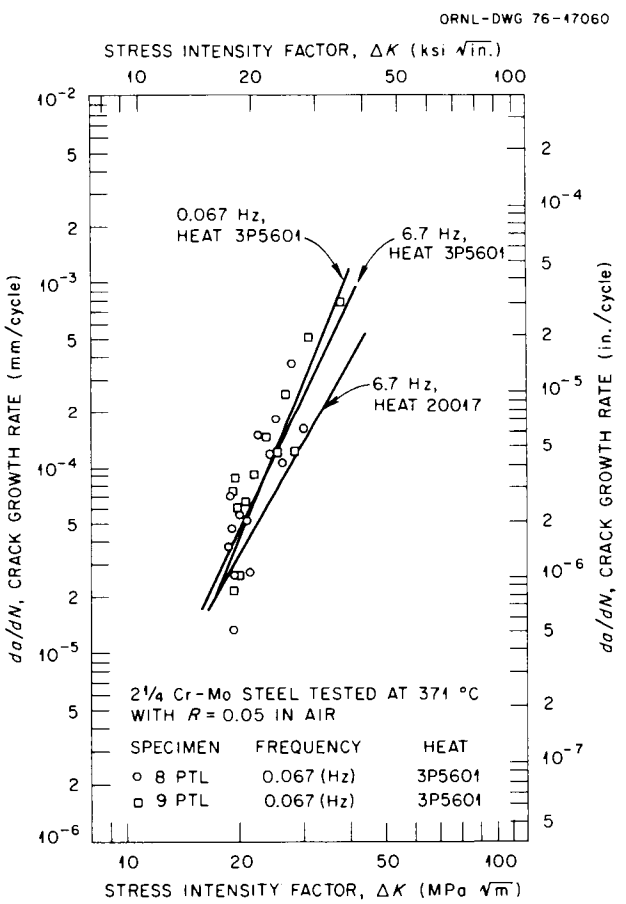

Fig. 3.72. Effect of Frequency on Fatigue Crack Growth Rate at 371°C (700°F).

Since some decarburization may occur during system service comparative testing on a low-carbon heat of 2 1/4 Cr-1 Mo (heat 50057, 0.026% C) was performed. The results obtained at 510°C (950°F), ν = 0.67 Hz in air are compared in Fig. 3.73 with those obtained under identical testing conditions on heats 3P5601 and 20017 with 0.119 and 0.135% C, respectively. Very little difference was observed. What small effect there is was evident at the higher levels of ΔK. The tests on heat 50057 had to be terminated at shorter crack length and lower stress intensity factors than tests on the other heats because of excessive plasticity. This presumably was due to the lower tensile strength of this low-carbon material. The difference in slope of the da/dN was ΔK plot is not particularly significant inasmuch as the range of ΔK is so short that the scatter in the data can very easily affect the slope of a least squares fit.

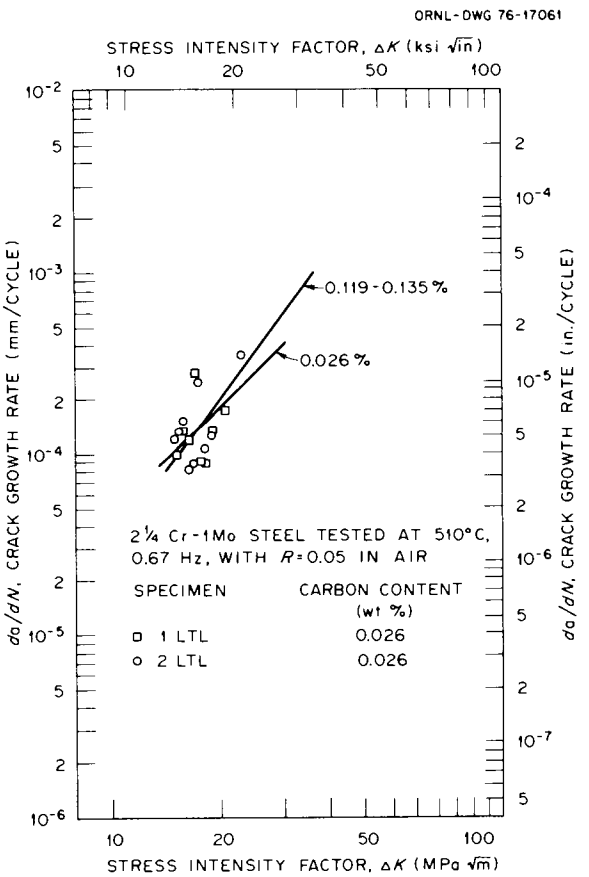

Fig. 3.73. Effect of Carbon Content on Fatigue Crack Growth Rate.

Also examined last quarter was the effect of aging on the FCP behavior of 2 1/4 Cr-1 Mo steel. Specimen blocks from heat 20017 were aged for 10,000 hr at both 482 and 538°C (900 and 1000°F) in argon. Specimens were then fabricated and tested at 510°C (950°F), ν = 0.67 Hz in air and the results compared with identical tests on isothermally annealed unaged material. As seen in Fig. 3.74 there is no appreciable effect of 10,000 hr at 538°C (1000°F) on the subsequent crack growth behavior at 510°C under the conditions examined. The specimens aged at 482°C will be tested next quarter.

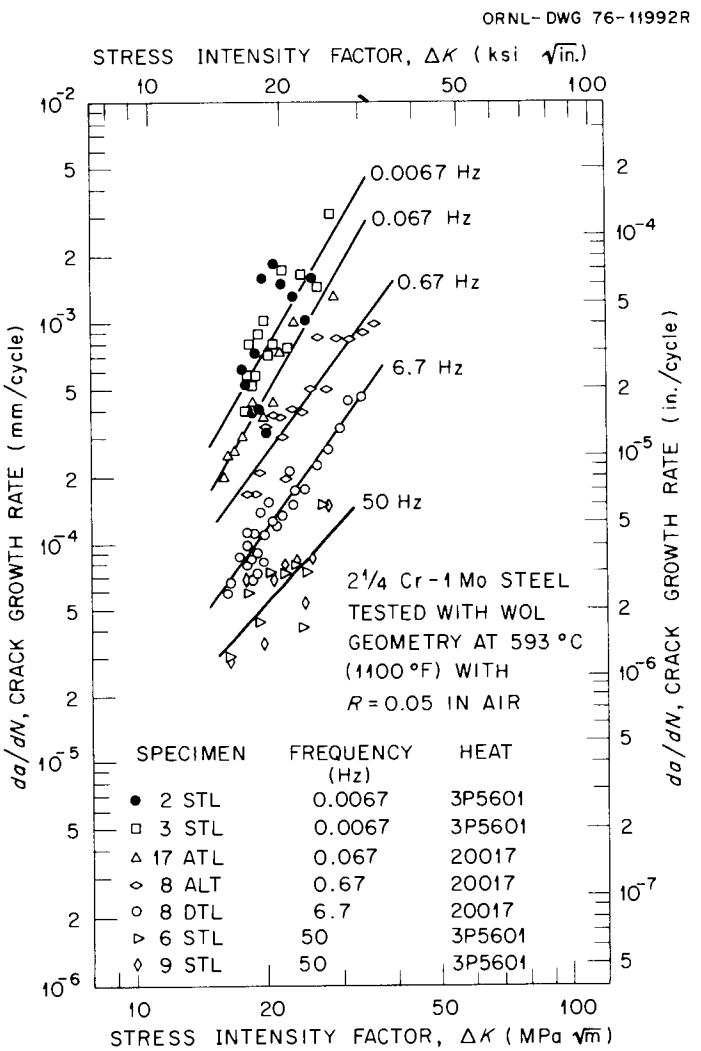

Fig. 3.74. Effect of Aging on Fatigue Crack Growth Rate.

3.4.6 Creep and Tensile Properties of Transition Weld Joint Materials — R. L. Klueh and J. F. King

Since the intermediate heat exchanger of the CRBRP is to be constructed of an austenitic stainless steel and the steam generator from ferritic 2 1/4 Cr-1 Mo steel, a welded transition joint is required. To minimize the difference in the coefficients of thermal expansion between type 316 stainless steel and 2 1/4 Cr-1 Mo steel, an intermediate spool piece of Incoloy 800 is to be used. The joint therefore would include these three base metals plus two weld metals, probably type 16-8-2 filler metal to join the Incoloy 800 and type 316 stainless steel, and Inconel 82 filler metal for the Incoloy 800 and 2 1/4 Cr-1 Mo steel. Because little is known about such weldments, we are presently determining the mechanical properties of the filler metals and transverse weldments that are appropriate for these joints.

3.4.6.1 Tensile Properties of Transverse Weldments

During this quarter we received two different kinds of welded plates from General Electric. In one weld 19-mm-thick (3/4-in.) plates of Incoloy 800 and 2 1/4 Cr-1 Mo steel were welded with Inconel 82 filler metal; in the other, 19-mm-thick plates of Incoloy 800 and type 316 stainless steel were welded with type 16-8-2 filler metal. Composite specimens were obtained from these plates. These specimens contain both weld metal and the two base metals in the gage section.

Tensile tests were started on the 2 1/4 Cr-1 Mo steel/Inconel 82/Incoloy 800 specimens. These tests are being made over the temperature range 25 to 732°C (77–1350°F). Although the data evaluation is not yet complete, the specimens were observed to fail in the 2 1/4 Cr-1 Mo steel. This is in agreement with what is known about the relative strengths of the individual base metals and weld metal.

During the next quarter we will evaluate the strength data from these tests, and tensile tests will also be made on the Incoloy 800/16-8-2/type 316 stainless steel specimens.

3.4.6.2 Creep and Rupture Behavior of Inconel 82 Weld Metal

Last quarter[77] we reported on the creep and rupture behavior of Inconel 82 weld metal at 454, 510, and 566°C. We have now completed several more tests at these temperatures, and the results are given in Table 3.25. Since the completed tests did not substantially change the creep-rupture curves and the curves for stress as a function of minimum creep rate that were presented last quarter, updated curves will not be presented at this time.

We have now begun tests at 621, 677, and 732°C. The results for tests completed to date along with the tests in progress are given in Table 3.26.

Table 3.25. Creep-Rupture Properties of Inconel 82 Weld Metal

Stress (MPa)	Stress (ksi)	Rupture Life (hr)	Total Elongation (%)	Reduction of Area (%)	Minimum Creep Rate (%/hr)
Tests at 454°C (850°F) on Welds in 19-mm (3/4-in.) Plate					
414	60.0	a			0.0000250
434	63.0	a			0.0000318
455	66.0	a			0.000160
483	70.0	b			0.000273
483	70.0	68.1	37.0	54.2	0.00769
483	70.0	75.1	33.4	50.5	0.0187
489	71.0	1075.4	33.2	55.2	0.00063
496	72.0	1012.6	36.0	38.5	0.000938
510	74.0	142.3	40.2	52.5	0.013
517	75.0	3.2	33.7	53.0	0.125
Tests at 510°C (950°F) on Welds in 13-mm (1/2-in.) Plate					
379	55.0	6770.4	15.7	15.2	0.0000187
396	57.5	3255.0	11.5	15.6	0.0000440
414	60.0	1645.4	23.6	19.7	0.000463
434	63.0	1205.1	33.7	29.3	0.000536
448	65.0	357.1	39.1	35.9	0.00459
455	66.0	4.0	40.4	39.0	0.150
455	66.0	39.4	38.7	42.9	0.138
465	67.5	37.1	48.4	51.8	0.209
483	70.0	10.9	48.4	53.7	0.395
Tests at 566°C (1050°F) on Welds in 13-mm (1/2-in.) Plate					
328	47.5	a			0.0000149
345	50.0	778.8	14.5	15.6	0.000324
345	50.0	6003.3	8.3	6.4	0.0000330
365	53.0	1087.5	17.2	18.2	0.000611
379	55.0	841.1	18.9	18.9	0.00105
396	57.5	448.2	21.4	19.6	0.00280
396	57.5[c]	124.6	21.9	25.6	0.0652
396	57.5[c]	63.8	22.2	30.9	0.133
414	60.0	112.8	29.7	27.4	0.0331
434	63.0	29.5	37.6	36.8	0.231

[a]Test discontinued before rupture.

[b]Temperature overshot and test failed after 2430 hr.

[c]Tests made on 19-mm (3/4-in.) plate.

Table 3.26. High-Temperature Creep-Rupture Properties of Inconel 82 Weld Metal Taken from Welds in 19-mm (3/4-in.) Plate

Stress (MPa)	Stress (ksi)	Rupture Life (hr)	Total Elongation (%)	Reduction of Area (%)	Minimum Creep Rate (%/hr)
		Tests at 621°C (1150°F)			
241	35.0	a			
276	40.0	a			
293	42.5	a			
310	45.0	295.1	14.1	39.7	0.0251
379	55.0	21.2	25.4	33.7	0.660
		Tests at 677°C (1250°F)			
138	20.0	a			
172	25.0	a			
207	30.0	215.0	17.7	30.8	0.022
241	35.0	89.0	25.2	39.7	0.080
276	40.0	26.0	33.4	49.1	0.326
		Tests at 732°C (1350°F)			
83	12.0	a			
103	15.0	a			
138	20.0	103.6	26.8	50.0	0.0603
172	25.0	30.7	41.8	40.6	0.342

[a]Tests in progress.

3.5 HIGH-TEMPERATURE DESIGN — J. M. Corum* and C. E. Pugh*

These programs now report semiannually, so there is no report this quarter.

3.6 MECHANICAL PROPERTIES OF HTGR STEAM GENERATOR AND PRIMARY CIRCUIT MATERIALS† — J. R. DiStefano

The major overall objectives of this program are to (1) determine the compatibility of alloys planned for use in the HTGR steam-cycle

*Reactor Division

†This work is supported by the Division of Nuclear Research and Application.

system with their environment and (2) determine, compile, and analyze materials design data for the commercial HTGR. To achieve these objectives it is necessary to study the mechanical behavior (tensile, creep, low-cycle fatigue, and crack growth) of HTGR alloys at temperatures and in environments (helium and steam) appropriate to their service in the reactor.

3.6.1 Tensile Testing — A. Lystrup*

The FY 1976 work plan for tensile tests has been completed.

3.6.2 Environmental Creep Testing — A Lystrup*

Environmental creep tests of HTGR structural alloys in simulated primary coolant helium and comparison tests in air have continued during the quarter. Eight tests (16126, 16263, 16268, 17330, 17334, 17375, 17377, and 17495) were completed during this period, and the results from those tests are shown in Table 3.27 together with results from all the previous tests. Not all the data from tests 16126, 16263, and 17375 have been determined yet. The tests in progress are listed in Table 3.28. Maximum time in test is approaching 14,000 hr on test 15046.

Stress-rupture data from helium environmental tests conducted at ORNL and at General Atomic (GA) are compared with data from air tests of Hastelloy X and 2 1/4 Cr-1 Mo steel in Fig. 3.75. In both plots the solid lines represent the average of many air tests and the points are data from helium tests available at present. No significant differences appear between the stress-rupture data from the helium environmental tests and from the air tests at the temperature-stress-time (max 10,000 hr) combinations.

At 704°C (1300°F) the corrosion behavior of Hastelloy X in HTGR helium was similar to that in air, whereas at 760°C (1400°F) air appeared to be the more corrosive environment. In 4500 hr at 704°C (1300°F) the oxide layer at the shoulder of the specimen (where the stress was one-fourth that at the gage section) grew to a thickness of 2 μm in the helium environment and to a thickness of 3 μm in air

*On assignment from Risö, Denmark.

Table 3.27. Creep Tests Completed on HTGR Structural Materials

Test	Material	Heat	Temperature (°C)	Temperature (°F)	Stress (MPa)	Stress (ksi)	Environment	Time, hr, for Indicated Creep Strain (2%)	Time, hr, for Indicated Creep Strain (5%)	Steady State Creep Rate (hr^{-1})	Time to Tertiary Creep (hr)	Rupture Life (hr)	Elongation (%)
15377	9 Cr-1 Mo	316381-1A	482	900	172	25.0	He					1317[a]	1.9
17495	2 1/4 Cr-1 Mo	72768	649	1200	69	10.0	He	59	137	3.1×10^{-4}	100	288	47.2
17333	2 1/4 Cr-1 Mo	X-6216	593	1100	138	20.0	He	11	34	13	42	89.5	42.1
16882	2 1/4 Cr-1 Mo	72768	593	1100	103	15.0	He	3	81	0.44	600	1337	51.3
17377	2 1/4 Cr-1 Mo	72768	593	1100	103	15.0	He	30	92	4.9	130	328	50.8
16266	2 1/4 Cr-1 Mo	72768	593	1100	103	15.0	Air	26	90	4.8	175	388	52.5
16883	2 1/4 Cr-1 Mo	36202	593	1100	103	15.0	He	48	144	3.1	188	436	46.8
17334	2 1/4 Cr-1 Mo	X-6216	593	1100	103	15.0	He	105	306	1.4	365	793	44.5
15023	2 1/4 Cr-1 Mo	X-6216	593	1100	69	10.0	He	4930	7380	0.024	3750	9660	38.9
15047	2 1/r Cr-1 Mo	X-6216	593	1100	69	10.0	He	4660	6540	0.025	3150	7784	26.6
15045	2 1/4 Cr-1 Mo	X-6216	593	1100	69	10.0	He			0.022		3186[a]	2.8
15373	2 1/4 Cr-1 Mo	36202	482	900	207	30.0	He	787	1660	0.11	500	3494	35.7
16263	2 1/4 Cr-1 Mo	36202	482	900	207	30.0	Air					6611	
16126	Hastelloy X	2600-3-4936	871	1600	34	5.0	He					6527	
16054	Hastelloy X	2600-3-2792	871	1600	62	9.0	He	197	327	0.93	205	554	34.8
16269	Hastelloy X	2600-3-4936	816	1500	69	10.0	Air	940[b]	1720[b]	0.1[b]	650[b]	3453	18.8
17375	Hastelloy X	2600-3-4936	816	1500	69	10.0	Air					1905	
16031	Hastelloy X	2600-3-2792	760	1400	152	22.0	He	15	38	12	44	159	57.5
16125	Hastelloy X	2600-3-4936	760	1400	138	20.0	He	30	103	4.0	142	305	38.9
17330	Hastelloy X	2600-3-4936	760	1400	138	20.0	Air	35	95	4.6	113	297	52.4
16490	Hastelloy X	2600-3-4936	760	1400	103	15.0	He	1110	2180	0.12	1480	2690	18.7
15771	Hastelloy X	2600-3-4936	704	1300	172	25.0	He	104	321	1.4	510	1007	35.4
15058	Hastelloy X	2600-3-4936	704	1300	138	20.0	He	344	1920	0.17	1950	4045	21.4
15792	Hastelloy X	2600-3-4936	704	1300	138	20.0	He	500	2590	0.11	2000	4588	23.0
16268	Hastelloy X	2600-3-4936	704	1300	138	20.0	Air	297	2139	0.12	1950	4504	18.3
15772	Hastelloy X	2600-3-4936	649	1200	172	25.0	He	850	2170	0.17	3950	6466	34.9

[a]Terminated short of rupture.

[b]Estimated value. Bad extensometer readings through the whole test.

Table 3.28. Current Environment and Air Creep Tests

Test	Test Frame	Material	Heat	Temperature (°C)	Temperature (°F)	Stress (MPa)	Stress (ksi)
			He Environment Tests				
17332	I-160	Hastelloy X	2600-3-4936	816	1500	69	10.0
15046	I-161	2 1/4 Cr-1 Mo	X-6216	538	1000	103	15.0
17328	I-162	Hastelloy X	2600-3-4936	704	1300	103	15.0
15363	I-163	9 Cr-1 Mo	316381-1A	538	1000	103	15.0
15369	I-164	2 1/4 Cr-1 Mo	36202	538	1000	103	15.0
15374	I-165	2 1/4 Cr-1 Mo	36202	482	900	172	25.0
Being Loaded	I-166	Hastelloy X	2600-3-4936	649	1200	207	30.0
17329	I-167	Hastelloy X	2600-3-4936	649	1200	138	20.0
Being Loaded	I-168	2 1/4 Cr-1 Mo	X-6216	649	1200	69	10.0
17494	I-169	2 1/4 Cr-1 Mo	X-6216	482	900	207	30.0
			Air Tests				
Being Loaded	I-170	2 1/4 Cr-1 Mo	36202	482	900	172	25.0
16264	I-171	2 1/4 Cr-1 Mo	36202	538	1000	103	15.0
16360	I-172	2 1/4 Cr-1 Mo	72768	593	1100	69	10.0
16267	I-173	Hastelloy X	2600-3-4936	649	1200	172	25.0
17376	I-174	Hastelloy X	2600-3-4936	704	1300	103	15.0
Being Loaded	I-175	Hastelloy X	2600-3-4936	871	1600	34	5.0

(Fig. 3.76). In 300 hr at 760°C (1400°F) the oxide layer was 1 μm thick on the specimen exposed to helium and 3 μm thick on the specimen exposed to air, as shown in Fig. 3.77.

The corrosion rate of 2 1/4 Cr-1 Mo steel at 593°C (1100°F) in HTGR helium decreases with increasing time. This is shown on the curve in Fig. 3.78 together with micrographs of the edge of a cross section of the shoulder of 2 1/4 Cr-1 Mo steel creep specimens from five different tests. One of the tests was conducted in air, and the corrosion resistance of 2 1/4 Cr-1 Mo steel at 593°C (1100°F) appears much better in HTGR helium than in air. The depth of attack reached 24 μm in 388 hr in air, whereas it reached only 20 μm in 9660 hr in the helium.

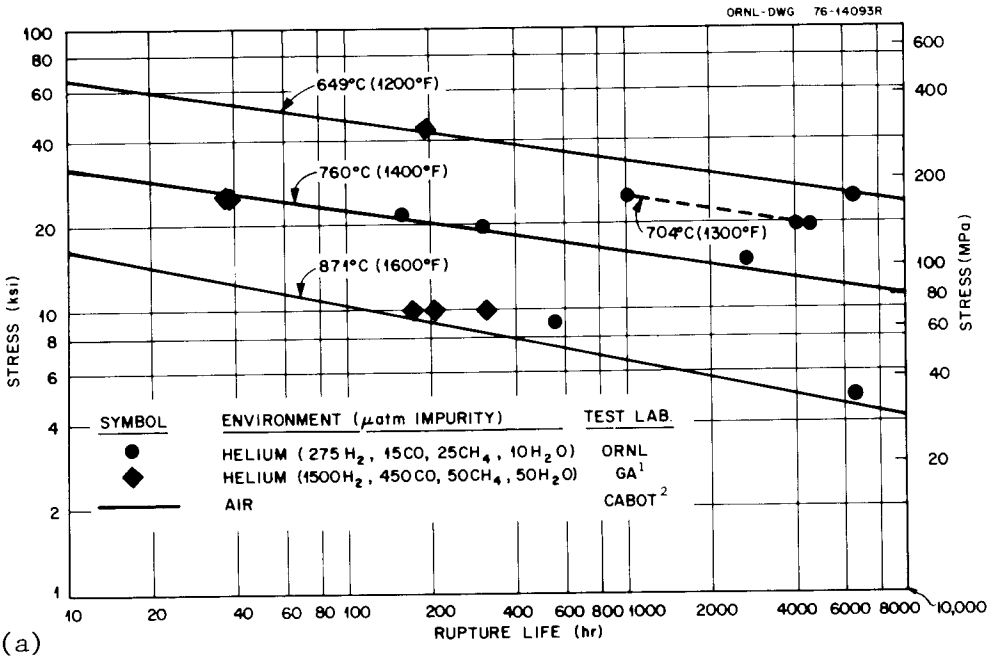

(a)

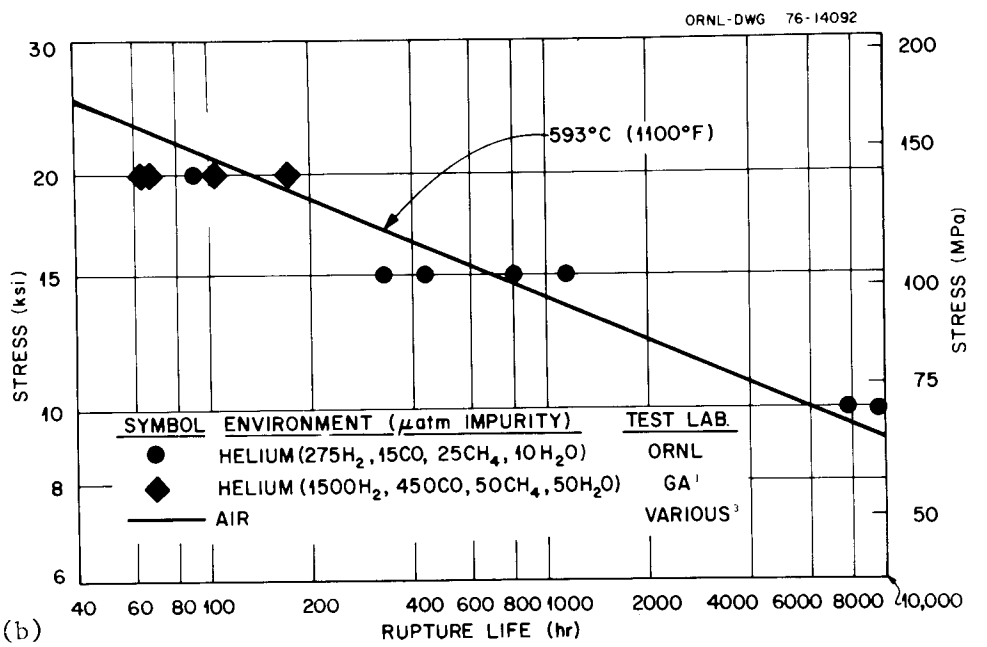

(b)

Fig. 3.75. Rupture Life vs Stress in HTGR Environment and Air. (a) Hastelloy X at various temperatures. (b) 2 1/4 Cr-1 Mo steel at 593°C (1100°F). References: [1]R. J. Wolwowicz, *Creep-Rupture Properties of Incoloy 800H, 2 1/4 Cr-1 Mo, and Hastelloy X Alloys in Simulated HTGR Environment*, GA-A13876 (June 1976). [2]J. W. Tackett, *The Creep Rupture Properties of Hastelloy Alloy S Sheet*, Tech. Dept. Report 8745, Stellite Division, Cabot Corp., Kokomo, Ind. (1975). [3]M. K. Booker, T. L. Hebble, D. O. Hobson, and C. R. Brinkman, *Mechanical Properties Correlations for 2 1/4 Cr-1 Mo Steel in Support of Nuclear Reactor Systems Design*, ORNL/ ORNL/TM-5329 (June 1976).

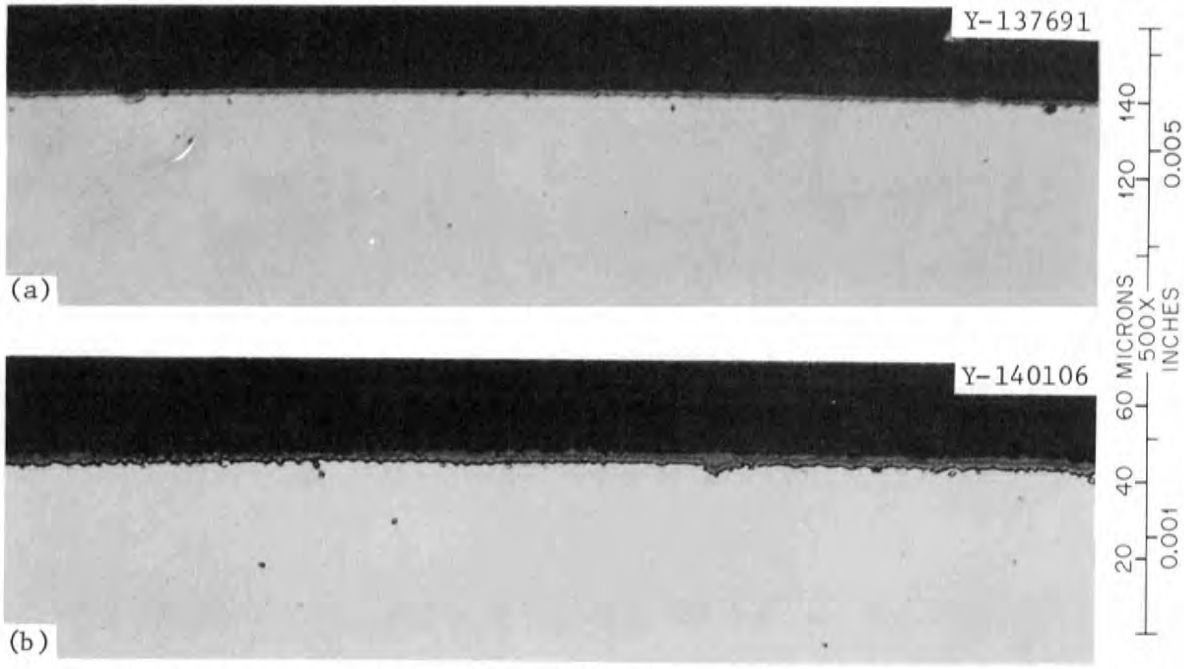

Fig. 3.76. Edge of Cross Section of the Shoulder of Hastelloy X Creep Specimens. (a) Test 15792, HTGR-helium exposed for 4588 hr at 704°C (1300°F). (b) Test 16268, air exposed for 4504 hr at 704°C (1300°F).

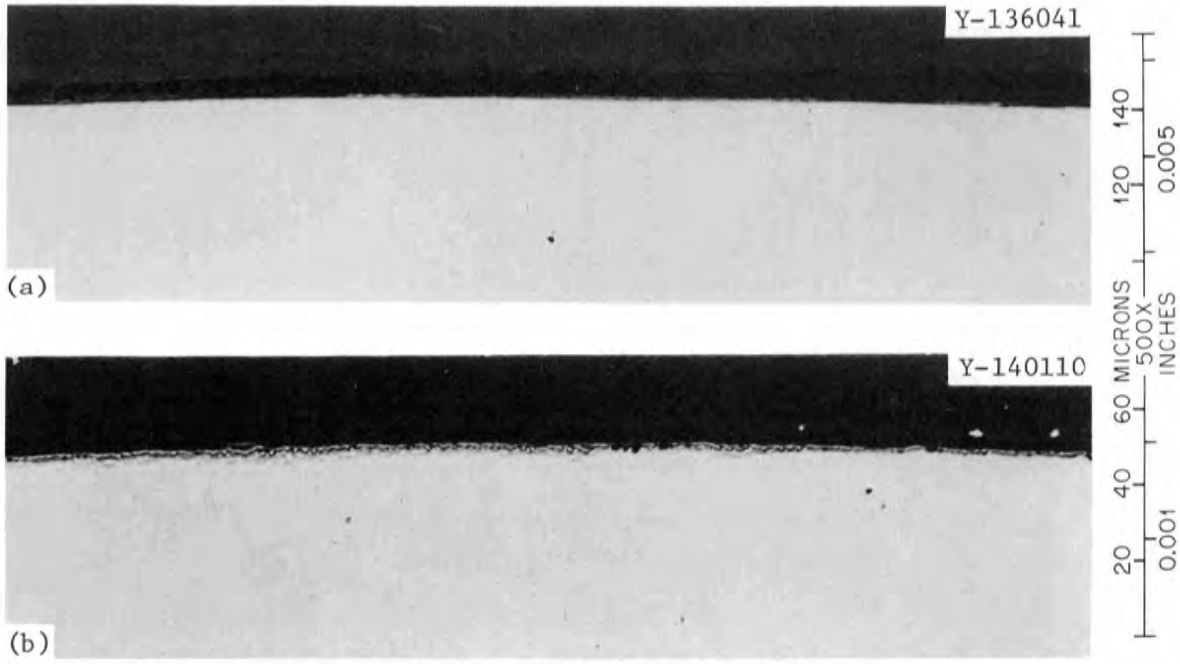

Fig. 3.77. Edge of Cross Section of the Shoulder of Hastelloy X Creep Specimens. (a) Test 16125, HTGR-helium exposed for 305 hr at 760°C (1400°F). (b) Test 17330, air exposed for 297 hr at 760°C (1400°F).

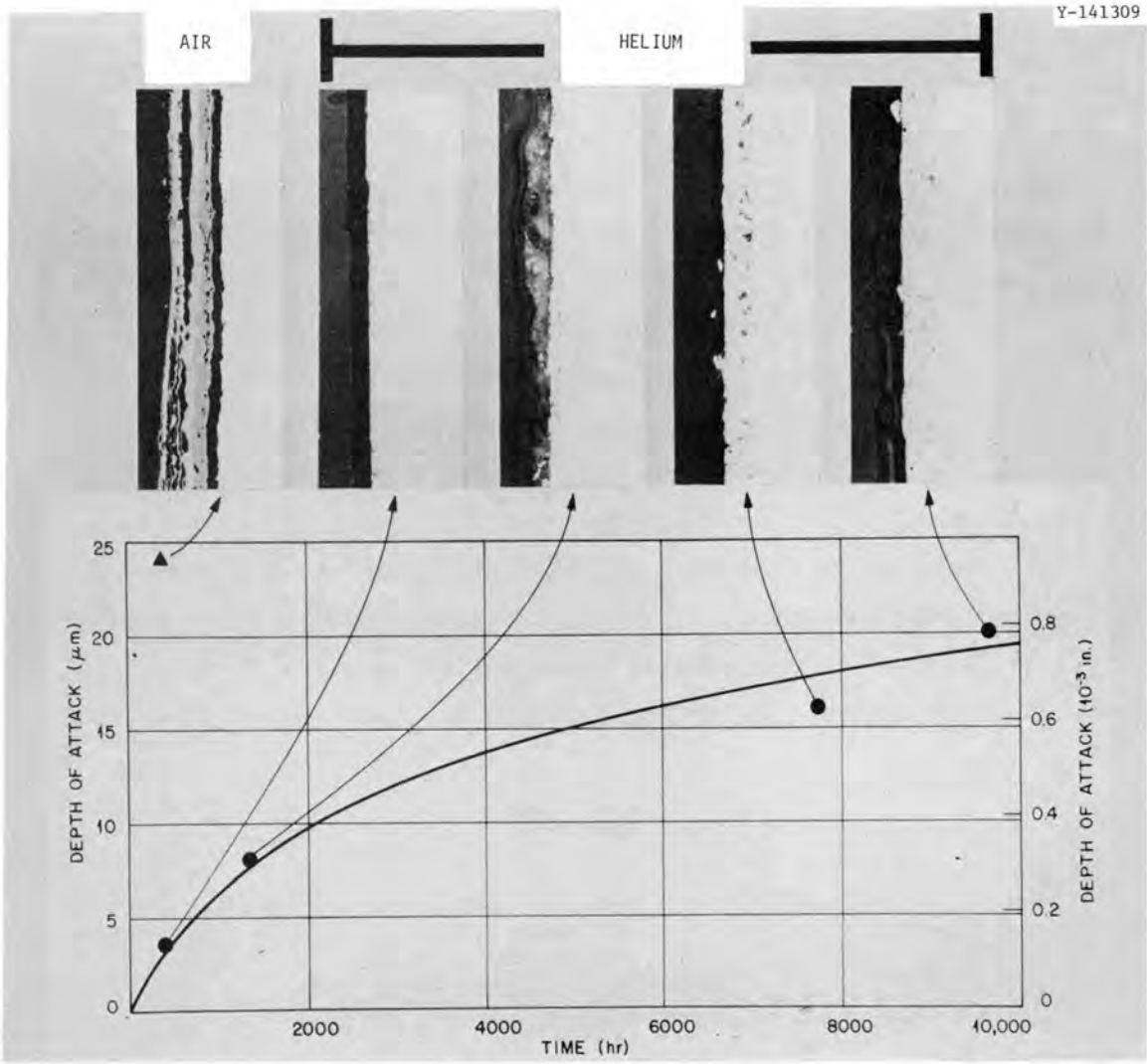

Fig. 3.78. Corrosion Behavior of 2 1/4 Cr-1 Mo Steel at 593°C (1100°F) in HTGR-Helium Environment and Air. The micrographs are from the following tests (from left to right): 16266, 16883, 16882, 15047, and 15023.

3.6.3 Environmental Fatigue and Creep-Fatigue Interaction — J. P. Strizak

The objective of this effort is to collect the necessary elevated-temperature fatigue and creep-fatigue design data on a number of structural alloys so as to permit their utilization in HTGR systems. Materials of interest include Hastelloy X, 2 1/4 Cr-1 Mo steel, and Inconel 617, while testing environments include air, vacuum, and helium with controlled impurity levels adjusted to expected HTGR conditions.

Material heat-to-heat variability is also under consideration in that two heats of 2 1/4 Cr-1 Mo steel are currently under test and material from several heats of Hastelloy X is available.

Since the last reporting period,[78] tests involving a compressive load hold period as a part of a fully reversed cycle sequence have been emphasized. These tests are being conducted in air at 538°C (1000°F) and use a bumpless transfer computer system, which keeps the test in strain control for a given cycle except during the hold period, when the test is in load control. Switching from strain control to load control occurs at the onset of the hold period, when a predetermined load is achieved, while switching from load control to strain control occurs at the end of the cycle hold period when a predetermined strain level is achieved. Creep deformation thus occurs each cycle as shown in Fig. 3.79. Figure 3.79 also shows a general acceleration in creep rates as the cycles are continued toward specimen failure. Conducting cyclic creep tests in

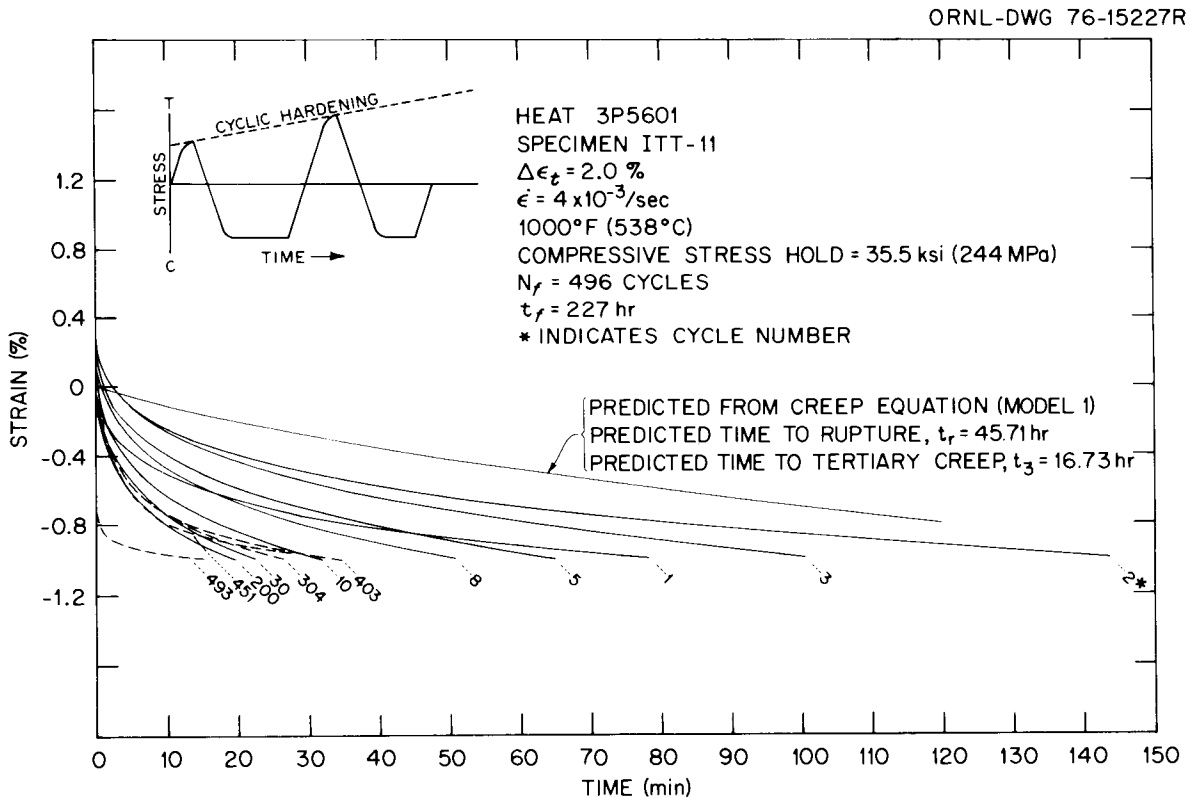

Fig. 3.79. Creep Strain vs Time During a Creep-Fatigue Test with a Compressive Stress Hold Period for 2 1/4 Cr-1 Mo Steel, Heat 3P5601, Tested at 538°C (1000°F).

this fashion permits one to accumulate considerable amounts of compressive time-dependent inelastic deformation, $\Delta\varepsilon_{pc}$, in a relatively short test period. These tests are being conducted and the data analyzed according to the technique of strain range partitioning to determine the influence of temperature, heat-to-heat variations, melting practice, and heat treatment on the overall predictability of the method. Figure 3.80 compares recent results (half darkened data points) generated with the use of compressive hold periods, the most damaging mode for 2 1/4 Cr-1 Mo steel, for several heats of this material with the results of Manson et al[79] (dark data points). While heat-to-heat variation scatter in the data is apparent, no trends have yet been identified. We are now testing this material in a tensile hold mode only.

An environmental chamber capable of containing helium with controlled amounts of impurities or high vacuum has been procured. It is a stainless steel vessel with several viewing and instrumentation ports. Vacuum is achieved via an oil diffusion or an ion pump working in conjunction with a mechanical pump. The chamber has been installed on one of the closed-loop electrohydraulic machines. Currently, auxiliary instrumentation is being installed in preparation for system check-out.

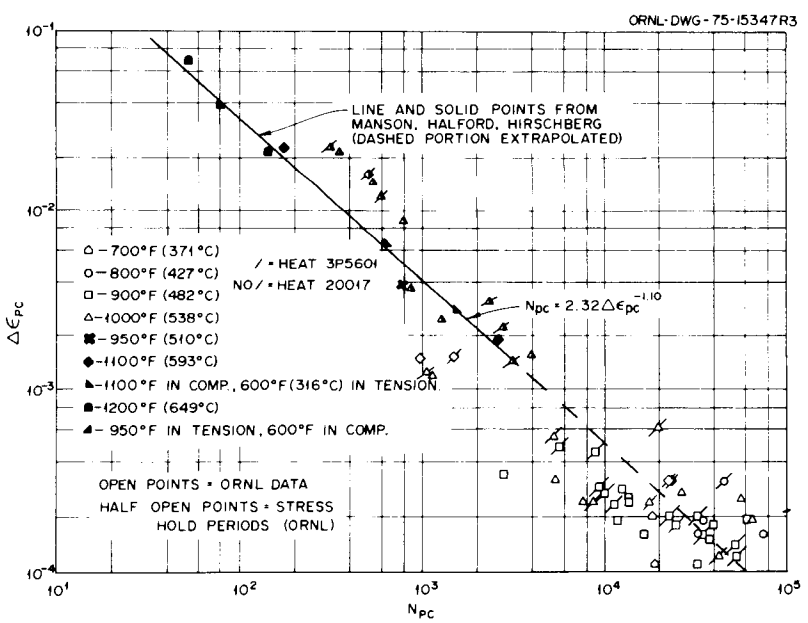

Fig. 3.80. Compressive Creep-Fatigue Data for 2 1/4 Cr-1 Mo Steel.

3.7 FATIGUE STUDIES IN SUPPORT OF THE ISX* — W. R. Corwin

The ISX, an experimental Tokamac-type fusion experiment is currently being designed and built for the Fusion Energy Division at ORNL. It will employ a pulsed magnetic field to contain ionized plasma within its toroidal containment vessel. Hence the material of which the magnetic coils are made will be repetitively loaded. The electromagnetic loading of the material will go from zero to maximum tension and back in a load-controlled nature, and current design calls for loading to approximately 10^5 cycles. This present study is to determine the fatigue resistance of the material chosen for the coils. The material, CDA 182, Cu—1.08% Cr, was selected on the basis of good mechanical strength and high electrical conductivity, 89%, IACS. Its product form is 25-mm (1-in.) plate and it was delivered and tested in the half-hard temper. Its mechanical properties are given in Table 3.29.

Table 3.29. Mechanical Properties of CDA 182 (Cu—1.08% Cr)

Property	Longitudinal	Transverse
Yield strength, 0.5% offset, MPa (ksi)	352(51)	358(52)
Ultimate tensile strength, MPa (ksi)	400 (58)	410(59.4)
Elongation in 50.8 mm (2.00 in.), %	23	23
Rockwell Hardness B	71	71

Two types of fatigue tests have been performed, uniaxial tests employing a standard buttonhead hourglass fatigue specimen shown in Fig. 3.65(a) and full-scale prototypic part tests. The uniaxial tests have been used to establish the basic engineering stress amplitude, σ_A, vs number of cycles to failure, N_F, for the material. Testing was performed in load control to simulate service conditions. Test conditions and results are summarized in Fig. 3.81. Numerous fully reversed tests

*Work done for the Fusion Energy Division.

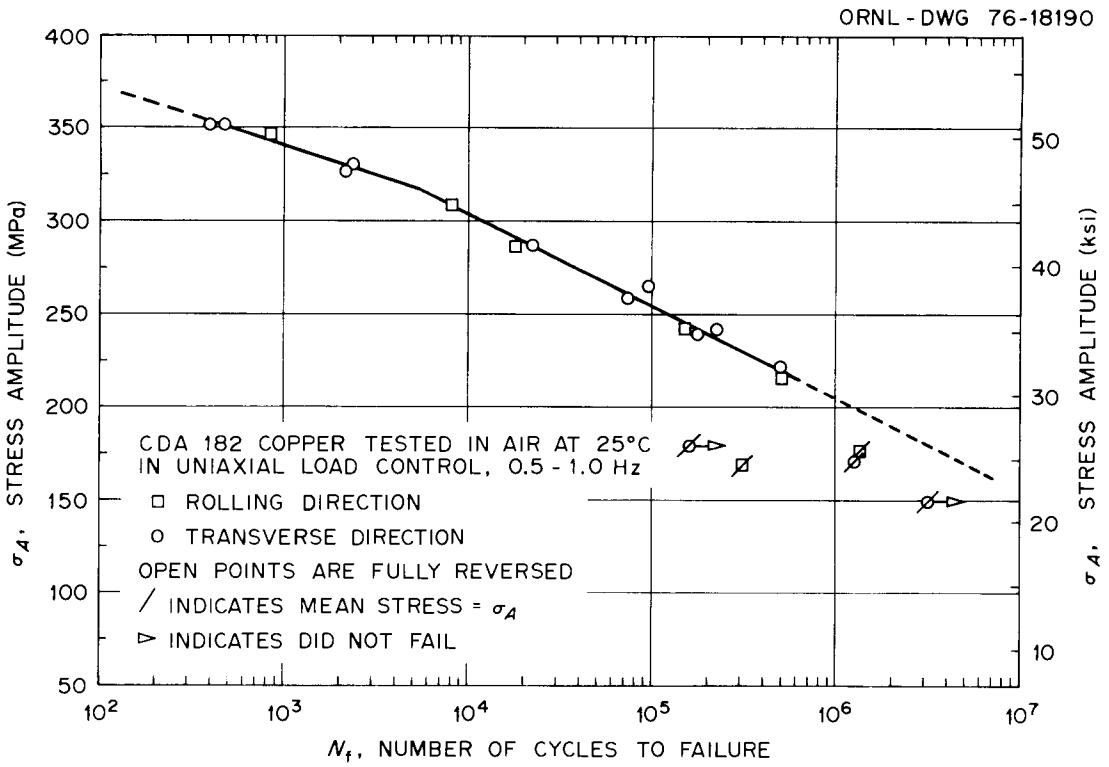

Fig. 3.81. Fatigue Life vs Number of Cycles to Failure of a Cu–1% Cr Alloy in the Half Hard Temper.

and limited tests in which the mean stress, σ_m, is equal to σ_A have been completed. More tests with $\sigma_m = \sigma_A$ are scheduled. When completed, this series of tests will be used with the results of prototype tests to estimate the effective fatigue stress concentration factor, K_f, in the prototypic part.

In the construction of the magnetic coils it will be necessary to mechanically join pieces of the copper approximately 25 mm thick by 150 mm wide (1 × 6 in.) so as to maintain good electrical continuity as well as good tensile strength in the joint. The design chosen is of the interlocking finger type and shown schematically in Fig. 3.82. Stress analyses have shown this joint to be the most highly stressed portion of the structure during operation; hence two full-scale mockup joints have been fatigue tested under prototypic loading conditions. Actual loading in service has been estimated to go from zero to 89 kN (20,000 lb) and back once every 10 sec, with the pulse lasting about 0.1 sec. The

ORNL-DWG 76-18189

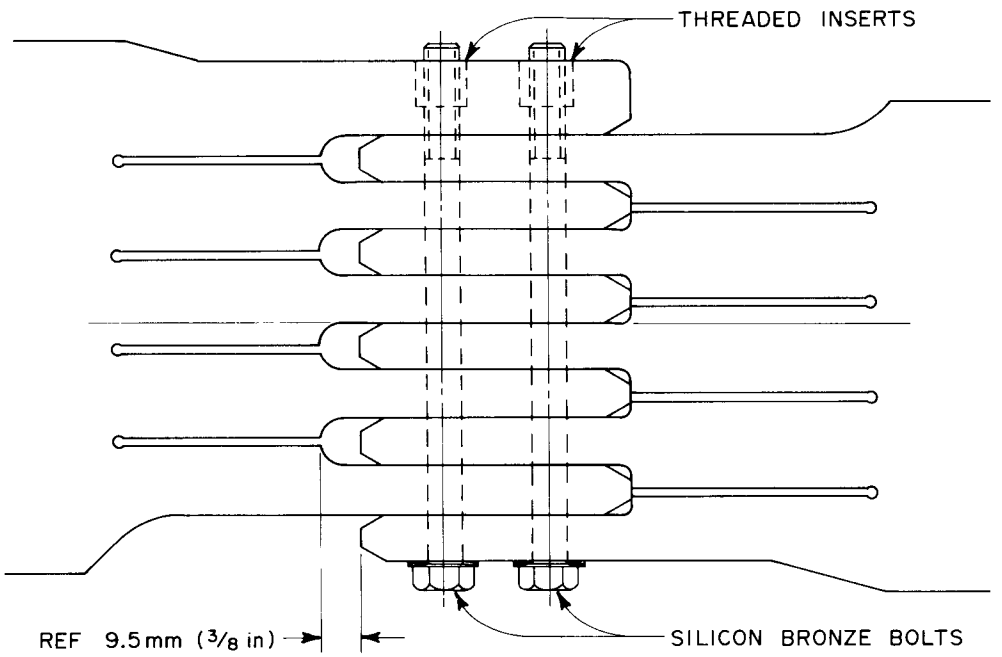

Fig. 3.82. Schematic Drawing of ISX Finger Joint.

first finger-joint specimen was loaded from zero to 89 kN (20,000 lb) in tension and unloaded back to zero at room temperature at 1 Hz. After 1,023,015 cycles with no visible evidence of plasticity or fatigue cracking apparent, the maximum load was raised to 133.4 kN (30,000 lb) for 82,869 cycles. Still no damage was visible and the maximum load was raised to 222.3 kN (50,000 lb). Failure then occurred after 20,954 cycles, by fracture of the bolts first, and then three fingers. There was evidence on the finger fracture surfaces of fatigue cracking and then ductile rupture. Pictures both before and after test are shown in Fig. 3.83.

The second specimen was tested in the same manner as the first but with a maximum load of 133.4 kN (30,000 lb) throughout the test. After 582,000 cycles with no damage visible testing was discontinued, and the specimen was set aside for examination or possibly more testing. Analysis for maximum values of K_f for the finger joint is planned once the uniaxial testing is complete.

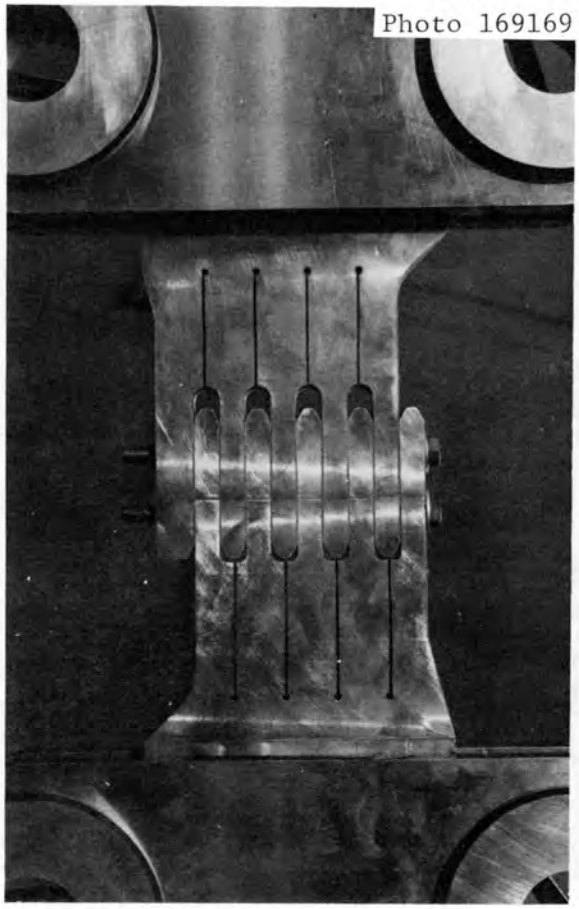

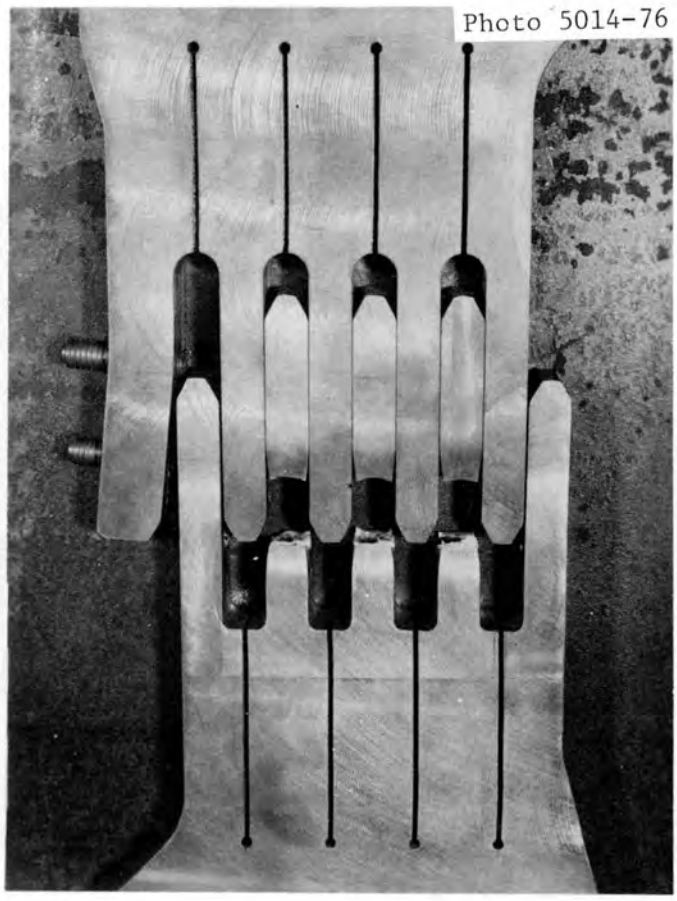

Fig. 3.83. ISX Finger Joint Fatigue Test Specimen. (a) Before testing, in testing fixture. (b) After failure.

3.8 REFERENCES

1. J. M. Steichen, *Effect of Thermal Aging on the High Strain Rate Tensile Properties of Type 304 Steel,* HEDL-TME-74-38 (July 1974).
2. J. M. Steichen, Hanford Engineering Development Laboratory, private communication, May 1976.
3. L. D. Blackburn, Hanford Engineering Development Laboratory, private communication, November 1973.
4. V. K. Sikka, T. L. Hebble, M. K. Booker, and C. R. Brinkman, *Influence of Laboratory Annealing on Tensile Properties and Time-Independent Design Stress Intensity Limits for Type 304 Stainless Steel,* ORNL-5175 (in preparation).
5. G. E. Dieter, "Introduction to Ductility," pp. 1—27 in *Ductility,* American Society for Metals, Metals Park, Ohio, 1968.
6. D. J. Wilson, "The Influence of Simulated Service Exposure on the Rupture Strengths of Grade 11, Grade 22, and Type 304 Steels," *J. Eng. Mater. Technol.* 96: 10—21 (1974).
7. R. J. Beaver and W. R. Martin, *Procurement of Type 316 Stainless Steel Reference Heat for LMFBR Research and Development Program,* ORNL/TM-5196 (January 1976).
8. Hanford Engineering Development Laboratory, *Nuclear Systems Materials Handbook,* TID-26666 (continually updated).
9. J. E. Hillard, "Estimating Grain Size by the Intercept Method," *Met. Progr.* 85: 99—102 (1964).
10. H. E. McCoy, Jr., and R. D. Waddell, Jr., "Mechanical Properties of Several Product Forms of a Single Heat of Type 304 Stainless Steel," *J. Eng. Mater. Technol.* 97: 343—49 (1975).
11. R. W. Swindeman, W. J. McAfee, and V. K. Sikka, "Product Form Variability in the Mechanical Behavior of Type 304 Stainless Steel at Room Temperature and 593°C (1100°F)," paper submitted for publication in the ASTM Symposium on Reproducibility and Accuracy of Mechanical Tests, St. Louis, Missouri, May 1976.
12. V. K. Sikka, C. R. Brinkman, R. W. Swindeman, and M. K. Booker, *Residual Cold Work and Its Influence on Tensile and Creep Properties of Types 304 and 316 Stainless Steels,* ORNL/TM-5192 (January 1976).

13. W. E. Leyda and C. C. Schultz, "Variability in Creep and Rupture Test Results in a Single Heat of Type 304 Stainless Steel," Babcock and Wilcox Report ORNL-Sub-3654-3 (September 1975).

14. V. K. Sikka and M. K. Booker, "Assessment of Tensile and Creep Data for Types 304 and 316 Stainless Steel," ASME Paper No. 76-PVP-31, 1976, accepted for publication in *Journal of Pressure Vessel Technology*.

15. V. K. Sikka, R. W. Swindeman, and C. R. Brinkman, "Elevated Temperature Tensile Ductility Minima in Types 304 and 316 Stainless Steel," accepted for publication in the Fourth International Conference on Fracture, to be held at Waterloo, Canada, June 19–24, 1977.

16. W. F. Simmons and J. A. Van Echo, *Report on the Elevated-Temperature Properties of Stainless Steels, ASTM Data Ser.* DS 5 S1, American Society for Testing and Materials, Philadelphia, 1965.

17. G. V. Smith, "An Evaluation of the Yield, Tensile, Creep, and Rupture Strength of Wrought 304, 316, 321, and 347 Stainless Steels at Elevated Temperatures, *ASTM Data Ser.* DS 5 S2, American Society for Testing and Materials, Philadelphia, February 1969.

18. J. Odar, Republic Steel Co., Canton, Ohio, private communication.

19. V. K. Sikka and C. R. Brinkman, "Relation Between Short- and Long-Term Elevated-Temperature Properties of Several Austenitic Stainless Steels," *Scr. Metall.* 10: 25–28 (1976).

20. V. K. Sikka, "Time to Rupture and Minimum Creep Rate Modeling for Type 304 Stainless Steel," *Mechanical Properties Test Data for Structural Materials Quart. Prog. Rep. July 31, 1976,* ORNL-5200, pp. 89–109.

21. Yoshio Monma, National Research Institute for Metals, Tokyo, 153, Japan, private communication, March 1976.

22. M. K. Booker, *Mathematical Description of the Elevated-Temperature Creep Behavior of Type 304 Austenitic Stainless Steel,* report in preparation.

23. W. E. Stillman, M. K. Booker, and V. K. Sikka, "Mathematical Description of the Creep Strain-Time Behavior of Type 316 Stainless Steel," pp. 424–48 in *Proc. 2nd Int. Conf. Mechanical Behavior of Materials,* American Society for Metals, Metals Park, Ohio, 1976.

24. V. K. Sikka, M. K. Booker, and C. R. Brinkman, *Use of Tensile Strength in Correlating and Predicting Creep and Creep Rupture Behavior of Types 304 and 316 Stainless Steel,* ORNL-5175 (in press).

25. J. P. Hammond and M. W. Moyer, "Elastic Properties Determined by Dynamic Tests," *Mechanical Properties Test Data for Structural Materials Quart. Prog. Rep. July 31, 1975,* ORNL-5106, pp. 104–11.

26. Ibid., *April 30, 1976,* ORNL-5150, pp. 130–35.

27. J. P. Hammond and M. W. Moyer, "Elastic Properties Determined by Dynamic Tests," *Fuels and Materials Development Program Quart. Prog. Rep. Sept. 30, 1974,* ORNL-TM-4726, pp. 139–42.

28. J. P. Hammond and M. W. Moyer, "Elastic Constants of Hastelloy X," *Mechanical Properties Test Data for Structural Materials Quart. Prog. Rep. July 31, 1976,* ORNL-5200, pp. 130–35.

29. M. W. Moyer and J. P. Hammond, *Ultrasonic Measurement of Elastic Constants at Temperatures from 20 to 1100°C,* Y-2047 (September 1976).

30. J. P. Hammond, "Elastic Properties Determined by Static Tests," *Mechanical Properties Test Data for Structural Materials Quart. Prog. Rep. Jan. 31, 1976,* ORNL-5112, pp. 77–80.

31. J. P. Hammond, M. W. Moyer, and C. R. Brinkman, "Effects of Materials and Test Variables on Elastic Constants of 2 1/4 Cr-1 Mo Steel and Type 304 Stainless Steel," pp. 1037–41 in *Proc. 2nd National Conf. Mechanical Behavior of Materials* (held 16–20 August 1976, Boston) American Society for Metals, Metals Park, Ohio, 1976.

32. J. P. Hammond and M. W. Moyer, "Effects of Heat-to-Heat Variations on the Elastic Constants of Type 304 Stainless Steel," *Mechanical Properties Test Data for Structural Materials Quart. Prog. Rep. July 31, 1976,* ORNL-5200, pp. 132–39.

33. J. F. Barker et al., "Long Time Stability of Inconel 718," *J. Met.* 22: 31–41 (January 1970).

34. R. T. King, E. Bolling, and D. P. Edmonds, "Structure and Properties of a 16-8-2 Submerged-Arc Weld," *LMFBR Materials Development Program Quart. Prog. Rep. March 31, 1976*, ORNL-5157, pp. 106–17.

35. R. T. King, D. A. Canonico, and C. R. Brinkman, "Elevated Temperature Weldment Behavior as Related to Nuclear Design Criteria," *Weld. J. (Miami)* 54(8): 265-s–275-s (August 1975).

36. L. D. Blackburn, "Isochronous Stress-Strain Curves for Austenitic Stainless Steels," pp. 15–48 in *The Generation of Isochronous Stress-Strain Curves*, ed. by A. O. Schaefer, American Society of Mechanical Engineers, New York, 1972.

37. C. R. Brinkman, V. K. Sikka, and R. T. King, *Mechanical Properties of LMFBR Primary Piping Materials*, ORNL/TM-5594 (October 1976).

38. B. R. Dewey, L. Adler, R. T. King, and K. V. Cook, "Measurements of Anisotropic Elastic Constants for Weld Metal," Society for Experimental Stress Analysis Paper WR-11-1975, May 1976, presented at the 1976 SESA Spring Meeting, Silver Spring, Md., May 9–14, 1976; submitted for publication to the *Journal of Experimental Mechanics*.

39. S. Timoshenko and S. Woinowsky-Krieger, *Theory of Plates and Shells*, McGraw-Hill, 1959.

40. R. L. Klueh, "Creep-Rupture Properties of 2 1/4 Cr-1 Mo Steel," *Mechanical Properties Test Data for Structural Materials Quart. Prog. Rep. Oct. 31, 1975*, ORNL-5107, pp. 141–54.

41. Ibid., *Apr. 30, 1976*, ORNL-5150, pp. 148–51.

42. R. L. Klueh, "Creep and Rupture Behavior of 2 1/4 Cr-1 Mo Steel," *Mechanical Properties Test Data for Structural Materials Quart. Prog. Rep. July 31, 1976*, ORNL-5200, pp. 154–67.

43. J. Glen, "A New Approach to the Problem of Creep," *J. Iron Steel Inst.* 189: 333–43 (1958).

44. R. L. Klueh, *Heat Treatment Effects on the Tensile Properties of Annealed 2 1/4 Cr-1 Mo Steel*, ORNL-5144 (May 1976).

45. R. G. Baker and J. Nutting, "The Tempering of 2 1/4 Cr-1 Mo Steel After Quenching and Normalizing," *J. Iron Steel Inst.* 192: 257–68 (1959).

46. J. M. Leitnaker, R. L. Klueh, and W. R. Laing, "The Composition of Eta-Carbide Phase in 2 1/4 Cr-1 Mo Steel," *Metall. Trans.* 6A: 1949–55 (1975).

47. K. F. Hale, "Study of Creep in a Chromium-Molybdenum Steel," pp. 650–58 in *Proc. 4th Intern. Conf. Electron Microscopy,* Vol. 1, Springer-Verlag, Berlin, 1960.

48. R. L. Klueh and J. M. Leitnaker, "An Analysis of the Decarburization and Aging Processes in 2 1/4 Cr-1 Mo Steel," *Metall. Trans.* 6A: 2089–93 (1975).

49. K. J. Irvine, J. D. Murray, and F. B. Pickering, "Structural Aspects of Creep-Resisting Steel," pp. 246–75 in *Structural Processes in Creep,* Iron and Steel Institute, London, 1961.

50. R. L. Klueh and R. E. Oakes, Jr., *Strain Rate Effects on the Tensile Properties of a Bainitic (Normalized-and-Tempered) 2 1/4 Cr-1 Mo Steel,* ORNL-5134 (April 1976).

51. J. D. Baird, "The Effects of Strain-Aging Due to Interstitial Solutes on the Mechanical Properties of Metals," *Metallurgical Review No. 149, Metals and Mater.* 5: 1–18 (1971).

52. J. D. Baird and A. Jamieson, "High-Temperature Tensile Properties of Some Synthesized Iron Alloys Containing Molybdenum and Chromium," *J. Iron Steel Inst.* 210: 841–46 (1972).

53. J. D. Baird and A. Jamieson, "Creep Strength of Some Synthesized Iron Alloys Containing Manganese, Molybdenum, and Chromium," *J. Iron Steel Inst.* 210: 847–56 (1972).

54. A. Jamieson et al., "Effects of Composition and Structure on the Creep Strength of Molybdenum Bearing Ferritic Steels," pp. 196–206 in *Creep Strength in Steels and High-Temperature Alloys,* The Metals Society, London, 1972.

55. J. D. Baird et al., "strengthening Mechanisms in Ferritic Creep Resistant Steels, pp. 207–16 in *Creep Strength in Steels and High-Temperature Alloys,* The Metals Society, London, 1972.

56. J. Glen, "The Effect of Alloying Elements on Creep Behavior," *J. Iron Steel Inst.* 190: 114–35 (1958).

57. J. Glen, "The Shape of Creep Curves," *J. Basic Eng.* 85: 595–600 (1963).

58. B. B. Argent, M. N. van Niekerk, and G. A. Redfern, "Creep of Ferritic Steels," *J. Iron Steel Inst.* 208: 830–43 (1970).

59. R. L. Klueh, "The Relationship Between Rupture Life and Creep Properties of 2 1/4 Cr-1 Mo Steel," *Nucl. Tech.* 26: 287–96 (1975).

60. J. D. Baird, "The Relationship Between Microstructure and Creep Strength in Ferritic Steels," *Jernkont. Ann.* 155: 311–21 (1971).

61. R. Lagneborg, "Dislocation Mechanisms in Creep," *Intern. Metall. Rev.* 17: 130–46 (1972).

62. R. L. Klueh and R. E. Oakes, Jr., *High-Strain-Rate Tensile Properties of Annealed 2 1/4 Cr-1 Mo Steel,* ORNL-TM-5028 (October 1975).

63. C. E. Jaske et al., "Monotonic and Cyclic Stress-Strain Response of Annealed 2 1/4 Cr-1 Mo Steel," pp. 191–212 in *Structural Materials for Service at Elevated Temperatures in Nuclear Power Generation,* American Society of Mechanical Engineers, New York, 1975.

64. C. E. Pugh et al., *Background Information for Interim Methods of Inelastic Analysis for High-Temperature Reactor Components of 2 1/4 Cr-1 Mo Steel,* ORNL/TM-5226 (May 1976).

65. G. V. Smith, *Supplemental Report on the Elevated-Temperature Properties of Chromium-Molybdenum Steels (An Evaluation of 2 1/4 Cr-1 Mo Steel), ASTM Data Ser.* DS 6 S2, American Society for Testing and Materials, Philadelphia, March 1971.

66. V. K. Sikka, H. E. McCoy, M. K. Booker, and C. R. Brinkman, "Heat-to-Heat Variations in Creep Properties of Types 304 and 316 Stainless Steels," *J. Pressure Vessel Technol.* 97: 243–51 (1975).

67. R. L. Klueh, "Heat-to-Heat Variation of 2 1/4 Cr-1 Mo Steel," *Mechanical Properties Test Data for Structural Materials Quart. Prog. Rep. April 30, 1975,* ORNL-5105, pp. 197–200.

68. Ibid., *Jan. 31, 1975,* ORNL-5104, pp. 206–13.

69. R. L. Klueh and J. L. Griffith, "Mechanical Properties of a 2 1/4 Cr-1 Mo Steel Forging for LMFBR Tubesheets," *Mechanical Properties Test Data for Structural Materials Quart. Prog. Rep. July 31, 1976,* ORNL-5200, pp. 169–81.

70. C. R. Brinkman et al., "Fatigue Behavior of 2 1/4 Cr-1 Mo Steel," *Mechanical Properties Test Data for Structural Materials Quart. Prog. Rep. April 30, 1975,* ORNL-5105, pp. 200–202.

71. R. L. Klueh, "Effect of Sodium on the Mechanical Properties of 2 1/4 Cr-1 Mo Steel," *Mechanical Properties Test Data for Structural Materials Quart. Prog. Rep. July 31, 1976,* ORNL-5200, pp. 181–84.

72. C. R. Brinkman et al., *Time Dependent Mechanical Properties of 2 1/4 Cr-1 Mo Steel for Use in Steam Generator Design,* ORNL-5125 (March 1976).

73. B. R. Dewey, "Finite Element Analysis of Creep and Plasticity Tensile Test Specimens," *Exp. Mech.* 16: 16–20 (January 1976).

74. W. R. Corwin and C. R. Brinkman, "Effects of Steam and Helium Environments on the Elevated-Temperature Subcritical Crack Growth Properties of 2 1/4 Cr-1 Mo Steel," pp. 1498–1502 in *Proc. 2nd Int. Conf. Mechanical Behavior of Materials,* American Society for Metals, Metals Park, Ohio, 1976.

75. W. R. Corwin, "Subcritical Crack Growth Studies," *Mechanical Properties Test Data for Structural Materials Quart. Prog. Rep. Jan. 31, 1976,* ORNL-5112, pp. 168–72.

76. C. R. Brinkman, M. K. Booker, J. P. Strizak, W. R. Corwin, J. M. Leitnaker, and J. L. Frazier, "Fatigue Behavior of 2 1/4 Cr-1 Mo Steel," *Mechanical Properties Test Data for Structural Materials Quart. Prog. Rep. April 30, 1975,* ORNL-5105, pp. 200–30.

77. R. L. Klueh and J. F. King, "Creep Properties of Inconel 82 Weld Metal," *Mechanical Properties Test Data for Structural Materials Quart. Prog. Rep. July 31, 1976,* ORNL-5200, pp. 227–30.

78. J. P. Strizak, "Fatigue-Life Testing," *Mechanical Properties Test Data for Structural Materials Quart. Prog. Rep. July 31, 1976,* ORNL-5200, pp. 267–72.

79. S. S. Manson, G. R. Halford, and M. H. Hirschberb, *Creep-Fatigue Analysis by Strain-Range Partitioning,* NASA-TM-67838 (1971).

4. NAVAL RESEARCH LABORATORY

L. E. Steele

4.1 INTRODUCTION - L. E. Steele

The research program of the NRL Engineering Materials Division, Thermostructural Materials Branch, includes the study of the behavior of structural materials useful in reactor construction. Within the scope of the title above much unirradiated data are developed. This report is developed using such data to support the USERDA and USNRC objective of compiling structural materials properties data for use in national reactor development programs. The NRL program is sponsored by the Office of Naval Research, the U. S. Energy Research and Development Administration, the U. S. Nuclear Regulatory Commission, and the U. S. Army Engineer Power Group. The unirradiated materials properties data contributed here include that developed in the course of research in the areas of high temperature materials, radiation damage, and fracture mechanics.

4.2 SIGNIFICANCE OF WELDING VARIABLES, LONG TERM AGING, AND TENSION HOLD TIMES ON FATIGUE CRACK GROWTH IN TYPE 316 STAINLESS STEEL WELDS - J. R. Hawthorne and H. E. Watson

4.2.1 Background

Material evaluations being conducted by the Naval Research Laboratory (NRL) in support of the Army MH-1A reactor operation include studies of fatigue crack growth resistance with and without radiation exposure. The MH-1A vessel operates at a nominal 500°F (260°C) and is composed of a central AISI Type 316 stainless steel forging, an upper nozzle and flange assembly, and a lower vessel head joined by submerged arc welds (AISI Type 316 filler). The NRL studies are evaluating both vessel forging and weld metal to identify that material having the greater propensity for fatigue crack growth in service and the fatigue crack growth rate corresponding to the worst

possible condition of service environment and stress loading condition. Load-hold time effects and long term thermal conditioning effects were felt to be key questions in planning the investigation.

Only archive forging material (vessel nozzle dropouts) and not weld metal was secured at the time of vessel manufacture for reactor surveillance testing and other investigations. A detailed study of the effects of welding parameters, materials, and conditions on weld metal properties was therefore requested by Army sponsors as part of the overall investigations. Three submerged arc test welds were made using direct current, reverse polarity (dcrp) welding conditions following the MH-1A practice. Variations included the use of more than one weld filler and flux lot combination to explore the influence of welding materials on fatigue resistance.

The first set of exploratory studies on welds with fatigue tests in air at 500°F (260°C) have been completed and are reported here.

4.2.2 Materials

The chemical compositions and tensile strengths of the weld deposits are given in Table 4.1. Welding parameters, conditions, and the specific materials used for the individual weldments are given in Table 4.2. It should be noted that one lot of filler wire was used for welds V23 and V25 and a different lot was used for weld S83.

4.2.3. Specimen Design and Evaluation

A single-edge-notched (SEN) cantilever fatigue specimen (Fig. 4.1) was employed for the weld deposit evaluations wherein the plane of the crack was oriented parallel to the welding direction and perpendicular to the weldment surface. All tests were conducted at 500°F (260°C) using a zero-tension-zero loading cycle. Specimen temperatures were provided by induction heating and were monitored continuously during testing by thermocouples. Tests normally were interrupted during non-

Table 4.1 - Chemical Composition of Submerged Arc Test Welds

Material	Chemical Composition (wt-%)									
	C	Mn	P	S	Si	Ni	Cr	Mo	Cu	N
Weld 1 (Code V23)	0.047	1.44	0.024	0.012	0.68	11.19	19.06	2.45	0.15	0.0447
Weld 2 (Code V25)	0.045	1.52	0.023	0.011	0.67	10.91	19.01	2.37	0.15	0.0459
Weld 3[a] (Code S83)	0.042	1.95	0.019	0.008	0.62	11.84	18.97	2.53	0.05	0.0397

[a]- preliminary determination

Table 4.2 - Welding Parameters, Materials and Conditions for Submerged Arc Welds (AISI Type 316 Stainless Steel)

Parameter/ Condition	Weld Identification Code		
	V23	V25	S83
Base Plate	a	a	a
Weld Procedure	b	b	b
Filler Type	Type 316[c] (5/32-in. dia)	Type 316[c] (5/32-in. dia)	Type 316[d] (1/8-in. dia)
Flux	Arcos S-16 (Lot 3K1F)	Arcos S-16 (Lot 2F4F)	Arcos S-16 (Lot 2F4F)
Backing	Type 316 (5/16 x 1-in.)	Type 304 (1/4 x 1-in.)	Type 316 (1/4 x 1-in.)
Joint	c	e	f
Restraint	Full,Mech.	Full,Mech.	Full,Mech.
Current	500A, dcrp	420A, dcrp	420A, dcrp
Voltage	32V	30V	30-32V
Travel	17 ipm	12 ipm[g]	12 ipm[g]
Energy Input	56 kJ/in.	63 kJ/in.	63-67 kJ/in.
Stickout	1-1/4 in.	1-1/4 in.	1-1/4 in.
Torch Angle	90 degree	90 degree	90 degree
Interpass (^{o}F max.)	300	300	300
Interpass Cleaning	h	h	h
Postweld HT	None	None	None
Inspection	-	-	X-ray
Delta Ferrite (Ferrite #1)[i]	11.6	11.5	11.1

a- AISI Type 315 plate (1-in.), Al heat 65803
b- Submerged arc (S/A), single electrode
c- Arcos lot E2061R316
d- Unibraze heat 13811120
e- Single Vee (1/r-in. root opening; 90 deg incl. angle)
f- Single Vee (1/8-in. root opening; 90 deg incl. angle)
g- Root pass was at 16 ipm
h- Acetone, wire brush
i- Magne Gage determination (avg)

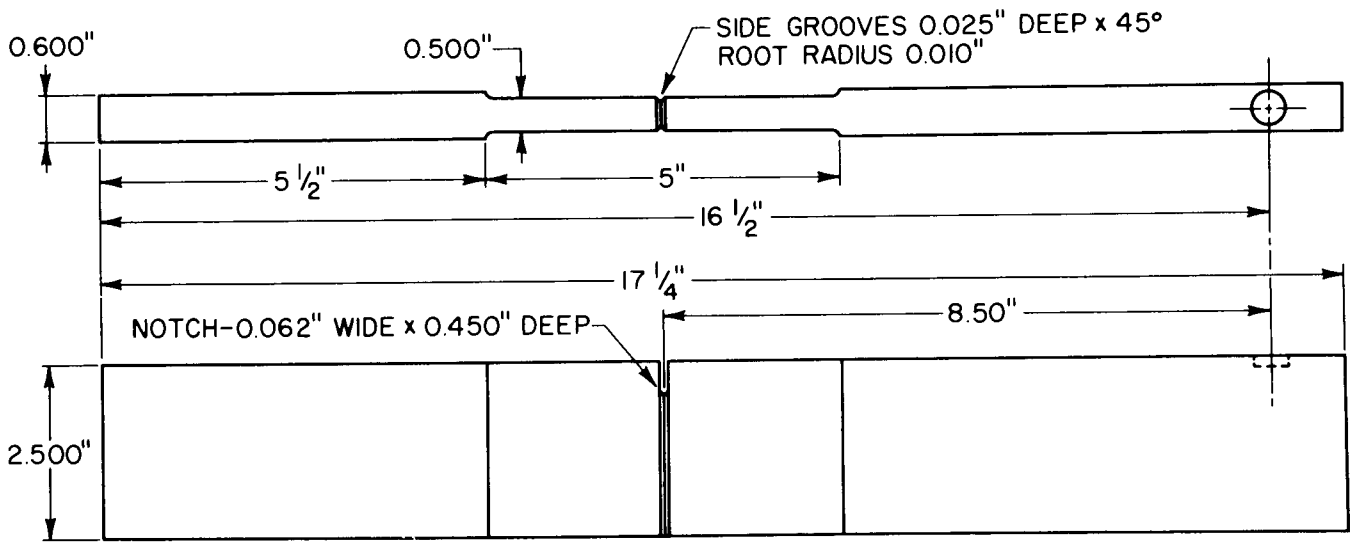

Fig. 4.1 - Design of single-edge-notched (SEN) cantilever fatigue test specimen

working hours and were resumed only after the specimens had again reached temperature. No noticeable effect of this procedure was seen in the data. Crack length measurements were accomplished in the hot cell by means of a high resolution, closed circuit television system and out-of-cell by means of a traveling microscope at a magnification of 35X. Rates of crack growth were established from plots of crack length vs number of cycles using the ASTM-recommended incremental polynominal method. Crack growth rates (da/dN) were related to stress intensity factor range (ΔK) using the expression for K for pure bending developed by Gross and Srawley:[1]

$$K = [6PL/(BB_n)^{1/2} W^{3/2}] Y.$$

In general, the data for all materials appeared to be well described by a power law relationship of the form:

$$da/dN = C(\Delta K)^m.$$

4.2.4 Experimental Test Matrix

The test matrix developed for the study is outlined in Table 4.3. For the weld deposits, the matrix enables a determination of the separate effects of 500°F (260°C) - 2500 hour thermal conditioning, fatigue cycling rate (10 cpm vs 1 cpm) with and without a load-hold and weld variability as a function of filler lot and flux lot.

4.2.5 Results and Discussion

4.2.5.1 Effect of Thermal Aging

Experimental results for thermally-aged vs as-welded conditions are illustrated in Fig. 4.2 for welds V23 and V25. From Table 4.3, it is recalled that the two welds represent different flux lots and somewhat different welding conditions. (For the purposes of this study, the difference in welding heat inputs between welds V23 vs V25 and S83 is considered secondary to flux lot and filler lot differences). In each case, no influence of thermal aging on fatigue crack growth behavior is evident in the data. That is, the data overlap

Table 4.3 - Experimental Test Matrix

Material No.	Filler Lot	Flux Lot	Welding Conditions	As-Welded Condition 10 cpm (0)[1]	As-Welded Condition 1 cpm (Δ)	Thermally Aged 500°F(260°C)-2500 hr 10 cpm (□)
Weld V23	1	1	1 (56 kJ/in.)	#4	#3	#6
Weld V25	1	2	2 (63 kJ/in.)	#3	-	#2
Weld S83	2	2	2	-	#3	-

[1]Symbol used for data plots

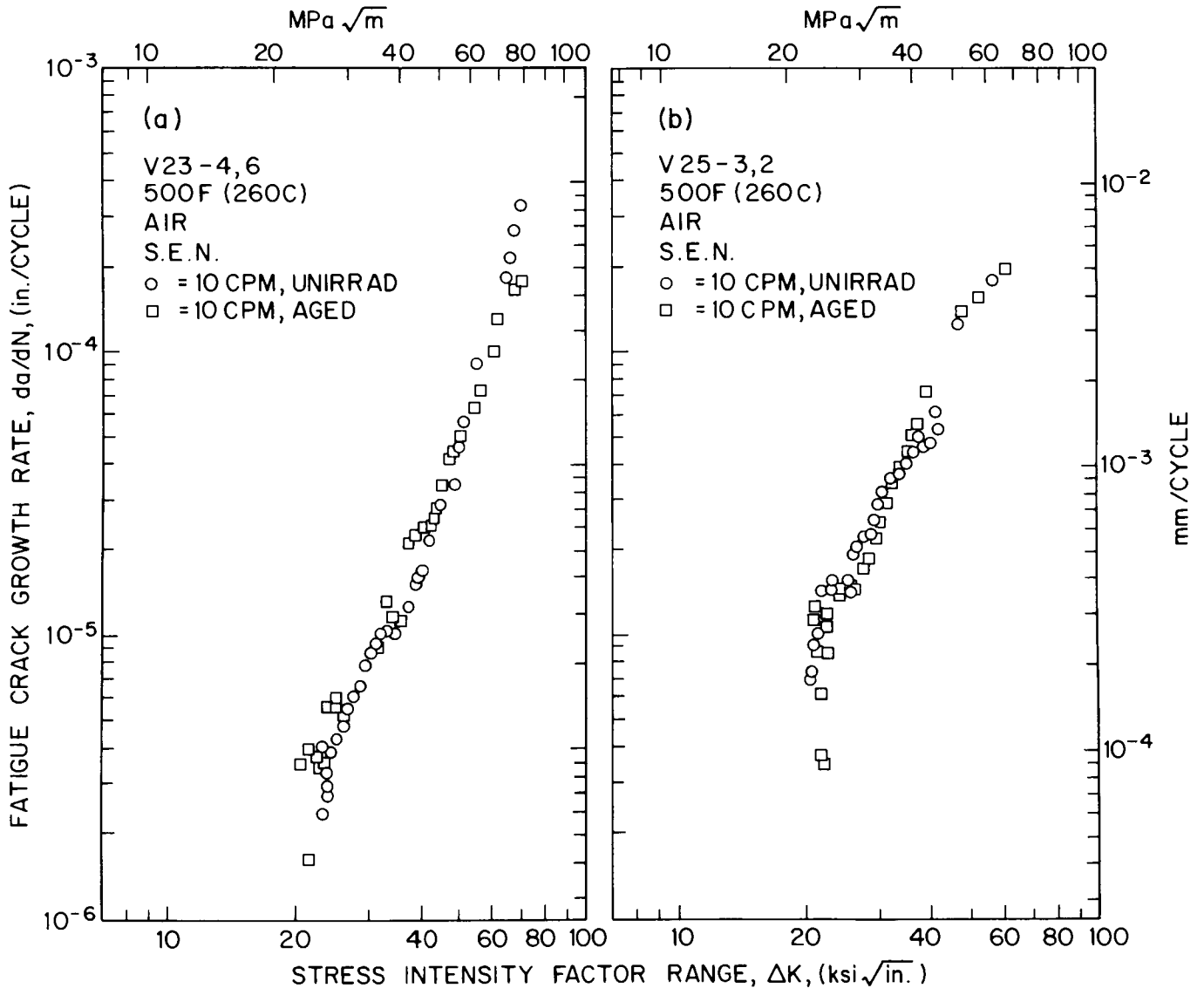

Fig. 4.2 - Comparisons of thermally-aged vs as-welded conditions for welds V23 (left graph) and V25 (right graph).

sufficiently to be considered a single data set.

4.2.5.2 Effect of Fatigue Cycling Rate With Load-Hold Time

Figure 4.3 illustrates the effect of fatigue cycling rates of 10 cpm vs 1 cpm. In the case of 10 cpm cycling, the loading pattern was a sawtooth configuration having 6 second loading and 0.6 second unloading times. In contrast, the loading pattern for 1 cpm was a modified trapezoid pattern with the peak load maintained for 54 seconds between 6 second loading and 0.6 second unloading periods. For the weld illustrated, cycling rate as described appears to have a significant effect on crack growth behavior only above a ΔK value of about 43 ksi$\sqrt{in}$. Above this value, a load-hold time appears to be somewhat beneficial to performance. Overall, the results suggest that, for tests in air, fatigue cycling rates below 10 cpm are not required to reveal worst case performance.

4.2.5.3 Effect of Welding Materials - Flux Lot

The comparison presented in Fig. 4.4 for welds V23 vs V25 shows a very clear influence of flux lot on weld performance. Here, a factor of three difference in performance is noted. The flux lots in this case were manufactured about 1-1/2 years apart and were to the same production formulation.

4.2.5.4 Effect of Welding Materials - Filler Lot

In Fig. 4.5, the results denote an effect of filler lot on weld performance which approaches the effect of flux lot in magnitude. The comparison assumes that fatigue cycling rate is not a primary variable. At a minimum, the 10 cpm fatigue performance of weld S83 would be projected somewhat above the data shown for 1 cpm testing with hold time and thus, would enhance the observed difference between the two welds.

4.2.5.5 Effect of Welding Materials - Filler and Flux Lots

The most dramatic variation in behavior noted by the

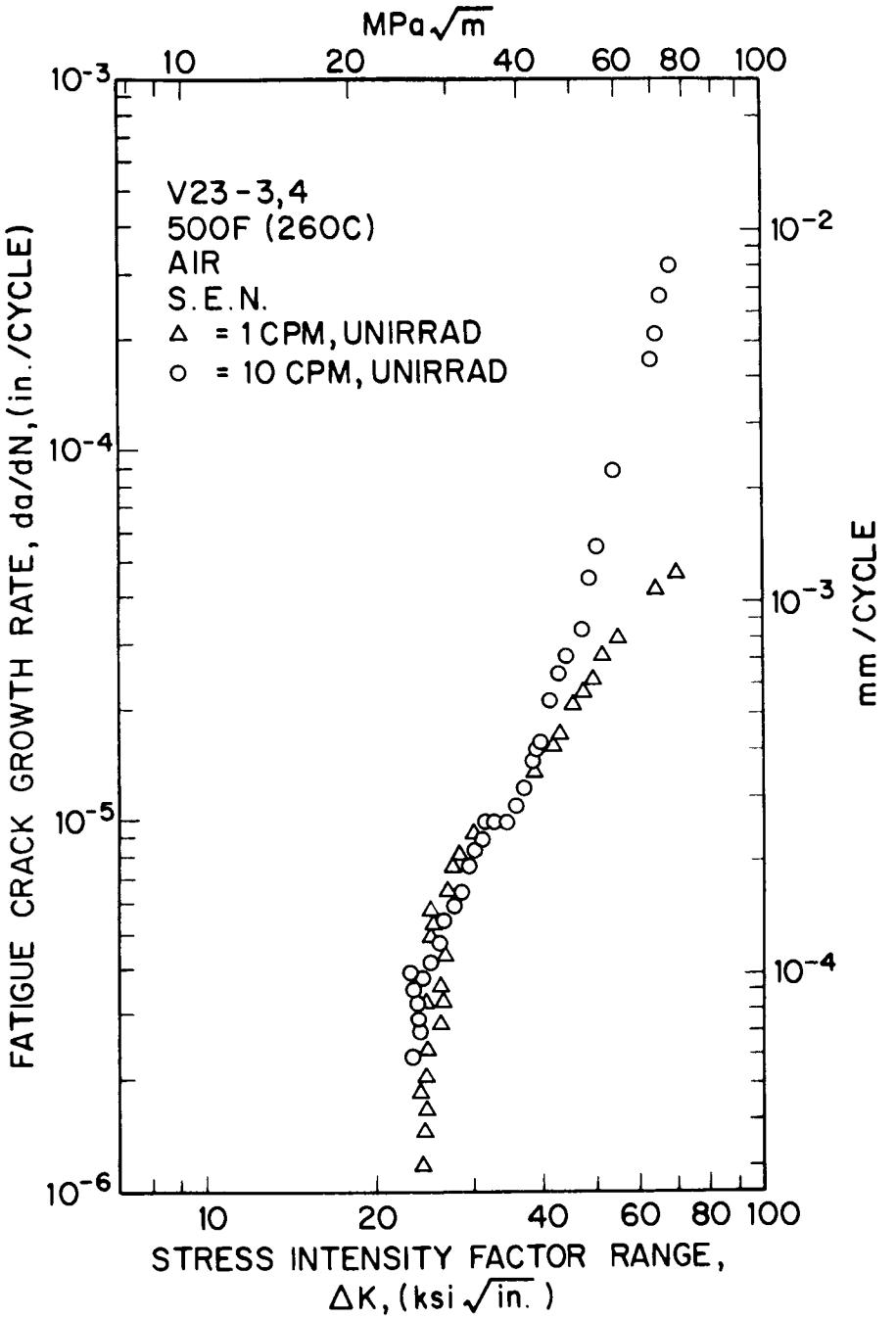

Fig. 4.3 - Comparison of fatigue crack growth rates in weld V23 with and without load hold time from 1 cpm vs 10 cpm cycling rates

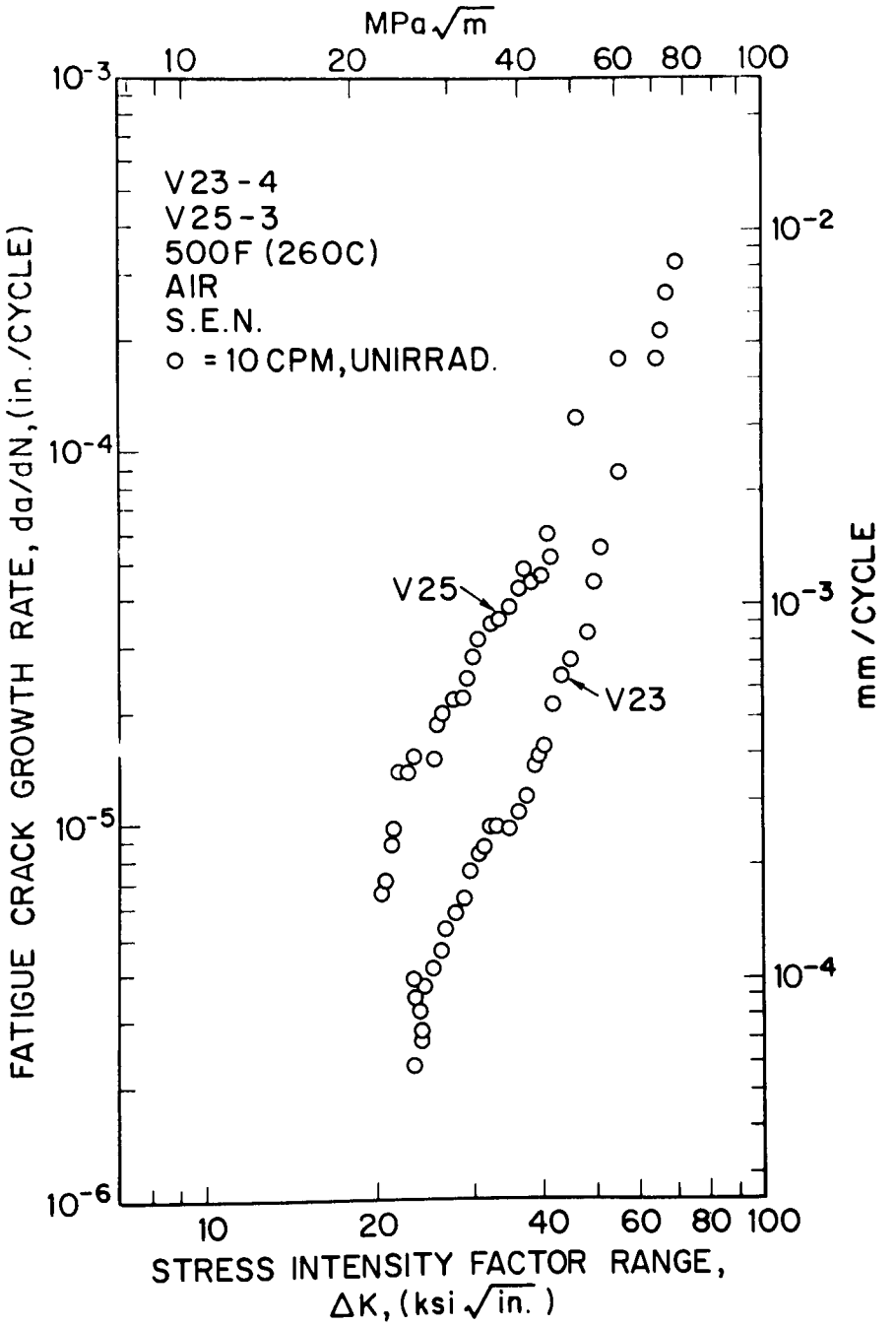

Fig. 4.4 - Crack growth rates for welds V23 and V25 demonstrating an influence of flux lot on fatigue performance. A factor of three difference in fatigue crack growth rate is shown.

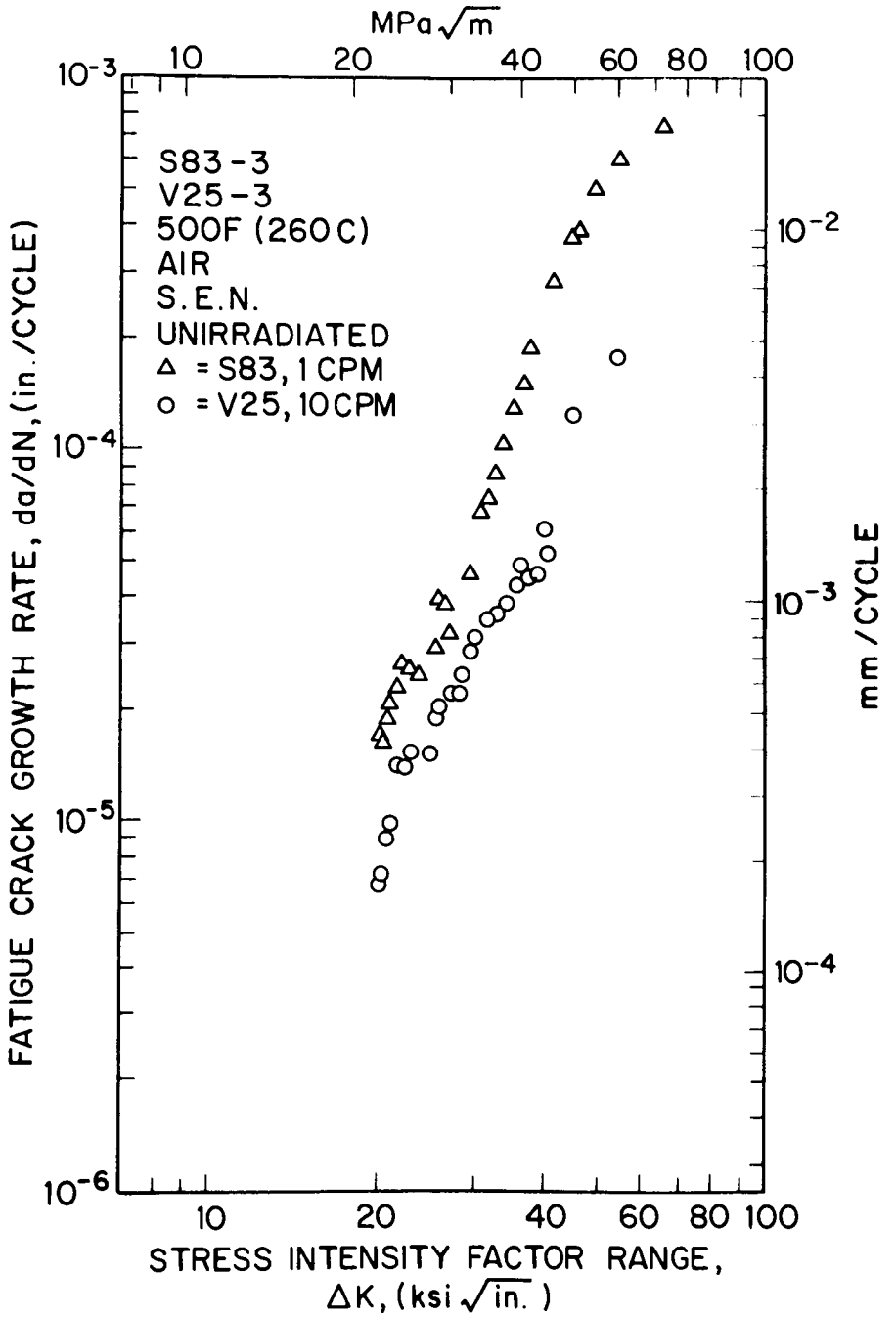

Fig. 4.5 - Crack growth rates for welds S83 vs V25 showing an influence of filler lot on fatigue performance.

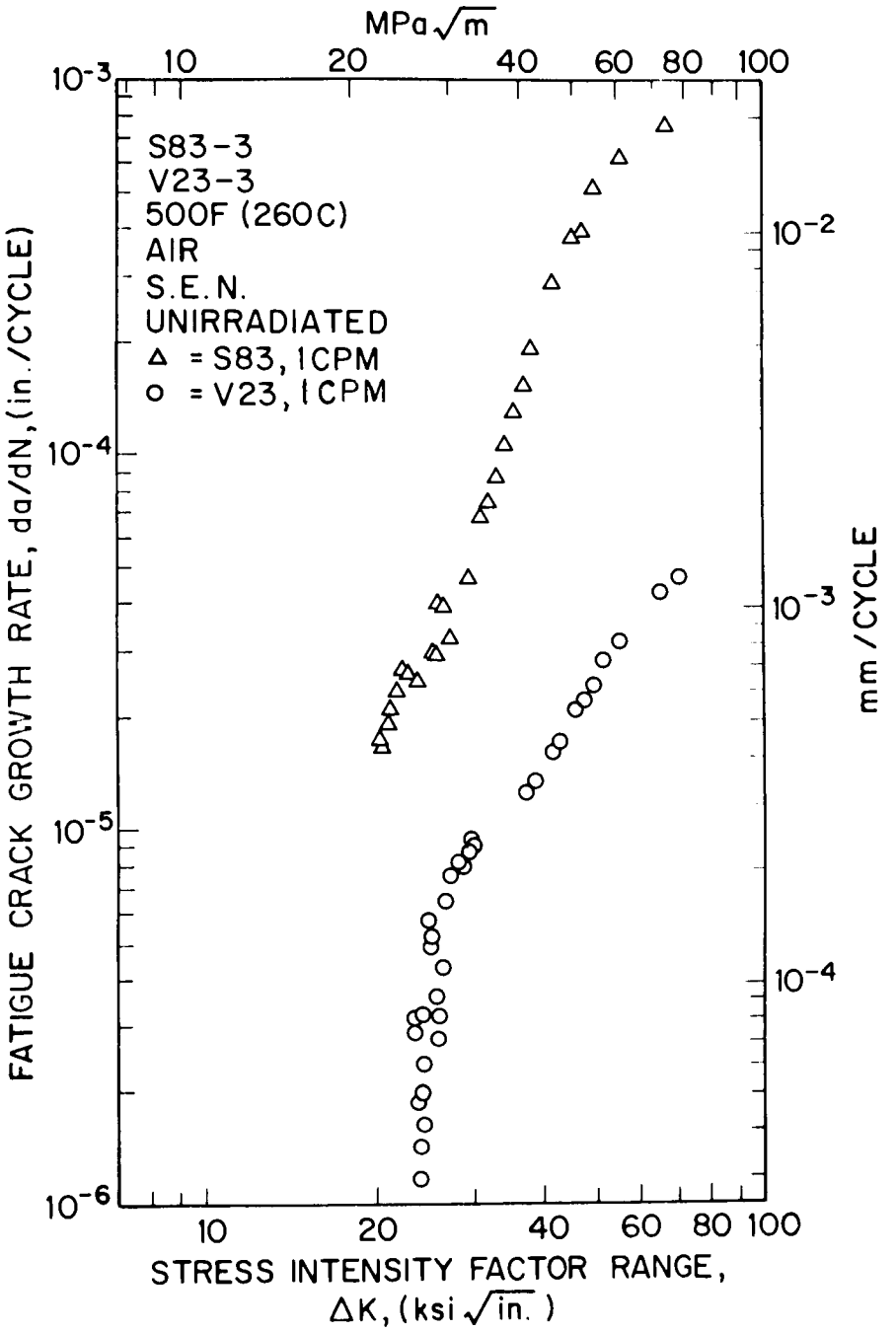

Fig. 4.6 - Crack growth rates for welds S83 vs V23 representing different filler and flux lots. A factor of ten difference in fatigue crack growth rate is illustrated.

investigation is that illustrated in Fig. 4.6. The results demonstrate the possibility for a factor of 10 difference in fatigue crack growth resistance among welds with random filler lot-flux lot combinations. The metallurgical factors responsible for the observed difference have not been isolated nor can probable explanations be tendered at this time. Regardless, the results are viewed as having great impact on reactor surveillance or other situations where component performance is often judged from that of "representative" rather than "duplicate" welds. Without question, the isolation of the metallurgical causes of the observed weld-to-weld differences should be a near term objective.

4.2.6 Weld Deposit vs ASME Code Section XI Design Curve

In Fig. 4.7, the ASME Code, Section XI, design curve for fatigue crack growth in low alloy steel is shown.[2] The curve, developed as a worst case projection of fatigue behavior with an added allowance for conservatism, should lie to the left of any experimentally developed data. However, the results of the present study demonstrate that the design curve is inappropriate for stainless steel weld deposits. That is, the experimental fatigue crack growth data developed for weld S83 (and weld V25, not shown) fall to the left of this curve.

4.2.7 Conclusions

Based on the determinations of this study, the following assessments and conclusions are possible concerning 500°F (260°C) fatigue test performance in air.

a. Significant variability in fatigue crack growth resistance can be exhibited by submerged arc weld deposits. A factor of three difference was shown possible from different flux lots; a factor of ten difference was observed between welds made with different filler and flux lots.

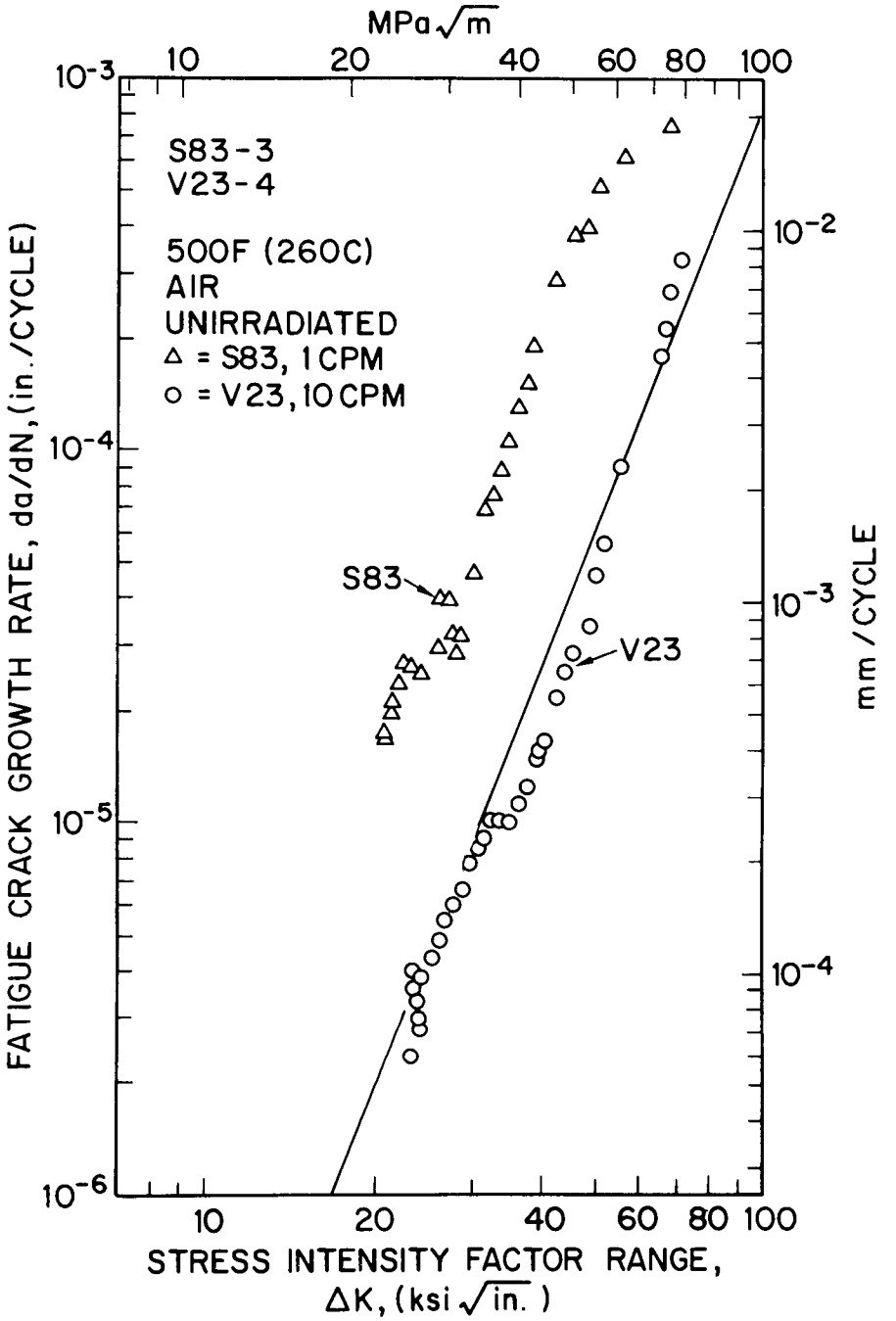

Fig. 4.7 - The fatigue crack growth resistance of welds S83 and V23 relative to the ASME Code, Section XI, design curve for low alloy steel. The design curve is shown to be unconservative for these particular stainless steel materials.

b. Fatigue cycling at 10 cpm in a sawtooth mode is as severe as 1 cpm fatigue cycling with a 54 second hold time for weld deposits. At ΔK values greater than about 43 ksi $\sqrt{in.}$, fatigue cycling at 10 cpm produced faster growth rates than the 1 cpm fatigue cycling mode.

c. Long term (2500 hour) thermal conditioning at 500°F (260°C) does not have a pronounced effect (beneficial or detrimental) on fatigue crack growth resistance of welds (unirradiated, as-welded condition).

d. Crack growth rates observed for two of the three welds evaluated exceeded design curve projections of the ASME Code, Section XI, for low alloy steels. Accordingly, the design curve is inappropriate, i.e., unconservative, for estimating AISI Type 316 stainless steel weld performance.

4.3 CHARPY-V NOTCH DUCTILITY OF SELECTED ALLOY 718 PLATE, WELD DEPOSIT, AND FORGING MATERIALS - J. R. Hawthorne

4.3.1 Background

Investigations of postirradiation mechanical properties retention by Alloy 718 in various product forms are currently underway at NRL. The focus of present research is on notch ductility and fatigue resistance changes after irradiation at temperatures ranging from 800 to 1200°F (427 to 649°C). To accomplish preirradiation versus postirradiation comparisons,preirradiation properties are being developed for the same temperature range and for ambient temperature. Reference notch ductility properties were recently secured for four materials including vacuum arc remelted (VAR) and electroslag remelted (ESR) plates, a GTA weld deposit, and a VAR forging. The plates and weld deposits received the Idaho Nuclear Engineering Laboratory (INEL)-developed heat treatment; the forging material received a standard commercial heat treatment which involved a lower solution annealed temperature. Charpy-V results for the respective materials are presented here.

4.3.2 Materials

Material compositions are given in Table 4.4 together with documentation on melt identification. The weld deposit was specially fabricated

Table 4.4 - Chemical Compositions of Alloy 718
Plates, Weld Deposit and Forging

Material	Thickness (in.)	Melt No.	Chemical Composition (wt-%)														
			C	P	S	B	Ti	Al	Mn	Fe	Co	Mo	Cr	Cu	Si	Ni	Cb
VAR Plate (NRL V-17)	3/4	9247	.05	<.005	<.005	.004	.99	.57	.10	Bal	.40	3.13	18.15	-	.08	51.52	5.14
ESR Plate (NRL V-47)	1	9407	.04	.005	.005	.003	1.00	.52	.19	Bal	.43	3.12	17.96	.02	.05	51.14	5.19
GTA Weld* (NRL V-48)	1	60C7E (Filler)	.04	.010	.007	.0042	1.01	.55	.09	17.97	.03	3.00	18.04	.10	.18	53.84	5.11
VAR Forging (NRL V-37)	2	93074 (Pancake) (55537)	.045	<.005	.004	.0047	.86	.46	.06	17.93	.06	3.09	18.37	.05	.10	53.88	5.37

*Based on filler chemistry.

for NRL by INEL. The forging represents excess material from the fabrication of the FBR thermal baffle assembly and was received courtesy of Westinghouse Atomic Research Division (WARD) and ERDA. Material heat treatments are given in Table 4.5. As discussed below, three adaptations of the basic INEL heat treatment specification were evaluated for the plates and the weld deposits. Observed differences point up a special problem in heat treating weldments. The forging was received fully heat treated by the vendor.

Charpy-V specimens were removed from the plates primarily in the transverse (TL-weak) test direction; the tangential direction (TL) was the primary test direction for the forging pancake. Weld deposit specimens were taken with the long specimen dimension perpendicular to the welding direction only. For all three materials, the specimen notch was perpendicular to the weldment surface.

4.3.3 Results

Table 4.4 summarizes Charpy-V energy determinations for the materials. As expected, the forging exhibited better energy absorption levels than the VAR plate but somewhat lower energy levels than the ESR plate More importantly, the weld deposit exhibited unusually low test values both at ambient temperature and at elevated temperatures, following the first heat treatment scheme (Scheme No. 1) used. In terms of prior INEL experience, the weld results were anomalous.[3]

A review of the weld deposit heat treatment history suggested three potential contributions to the low weld notch toughness: (a) the use of step cooling versus continuous cooling to yield the required cooling rate of 100°F (56°C) ±25°F (14°C) per hour; (b) furnace operation at the low end of the specification range for the solution anneal, i.e., 1950°F (1066°C) rather than at 2000°F (1093°C); and (c) a solution anneal time at temperature less than 1 hour resulting from the heatup lag of the particular furnace load involved. Variations of the original basic heat treatment procedure were subsequently devised to assess these possible contributions. Scheme No. 2 (see Table 4.5) reproduced heat treatment specification ideally [2000°F (1093°C)-1 hr solution anneal via specimen thermocouple plus continuous cooling at prescribed rate]. Scheme No. 3

Table 4.5 - Charpy-V Notch Ductility of Alloy 718

Plates, Weld Deposit and Forging

Material	Thickness	Melt No.	Heat Treatment[a]	Test Orientation[b]	Charpy-V Energy (ft-lb) 75°F (24°C)	800°F (427°C)	1160°F (627°C)
VAR Plate (NRL V-17)	3/4-in.	9247	INEL (No.1)	TL	16,16	22,22	22,25
				LT	13,14	20,21	--
			INEL (No.2)	TL	20,20	28,29	--
			INEL (No.3)	TL	19	26,28	--
ESR Plate (NRL V-47)	1-in.	9407	INEL (No.1)	TL	--	--	--
				LT	30,31	40,41	--
			INEL (No.2)	TL	29,30	37,38	--
			INEL (No.3)	TL	29	37,37	--
GTA Weld (NRL V-48)	1-in.	60C7E (Filler)[c]	INEL (No.1)	TL	12,16	21,22	15,18
(V-47 Plate)		9407 (Parent)	INEL (No.2)	TL	24,27	31,33	--
			INEL (No.3)	TL	--	32,34	--
VAR Forging (NRL V-37)	2-in.	93074 (Pancake 55537)	COMMERCIAL	TL	22,23,22,21	33,30,26	32,36
				LT	17,20.5	27,21	--

[a]INEL Heat Treatment, Scheme No.1 - 1950°F (1066°C)-1 h total (heat up and time at temperature); furnace cool at 100°F (56°C) ±25°F (14°C)/h to 1325°F (719°C) by step cooling 100°F (56°C) each hour; age 1325°F (719°C)-4 h; furnace cool at 100°F (56°C)/h by step cooling to 1150°F (621°C); hold at 1150°F (621°C); furnace cool.

INEL Heat Treatment, Scheme No.2 - 2000°F (1093°C)-1 h - (time at temperature); furnace cool continuously at 100°F (56°C) ±25°F (14°C)/h to 1325°F(719°C); age 1325°F (719°C)-4 h; furnace cool continuously at 100°F (56°C) ±25°F (14°C)/h to 1150°F (621°C); hold at 1150°F (621°C)- 16 h; furnace cool.

INEL Heat Treatment, Scheme No.3 - 1950°F (1066°C)-1 h total (heat up and time at temperature); furnace cool continuously at 100°F (56°C) ±25°F (14°C)/h to 1325°F (719°C); age 1325°F (719°C)-4 h; furnace cool continuously at 100°F (56°C) ±25°F (14°C)/h to 1150°F (621°C); hold at 1150°F (621°C)-16 h; furnace cool.

Commercial Heat Treatment - 1775°F (969°C)-1 h; water quenched; aged 1325°F(719°C)-8 h; furnace cool at 100°F (56°C) h to 1150°F (621°C); hold at 1150°F (621°C)-8 h; air cool

[b]TL - transverse test orientation
LT - longitudinal test orientation

[c].062-in. diameter wire

reproduced heat treatment Scheme No. 1 except for cooling rate which was the same as for Scheme No. 2. The results of both alternate schemes reveal that the low notch toughness observed initially due to the step cooling procedure only and not to solution annealing temperature or time variations. From examination of the transformation diagram for Alloy 718,* these last two variables would not be expected to contribute significantly in this case.

To summarize,the study has revealed that, unlike the good latitude given by Alloy 718 in heat treating time or temperature, the procedure used to accomplish the specified cooling rate in heat treatment Alloy 718 weldments appears extremely critical to weld deposit notch ductility. Accordingly, proposed commercial heat treating practices for Alloy 718 must be weighed carefully to assure the development of desired weld properties.

4.4 REFERENCES

1. Gross, B. and Srawley, J. E., "Stress-Intensity Factors for Single-Edge-Notch Specimens in Bending or Combined Bending and Tension by Boundary Collocation of a Stress Function," NASA-TN-D-2603, National Aeronautics and Space Administration, January 1965.

2. "Rules for Inservice Inspection of Nuclear Power Plant Components," Section XI,1974 Edition, ASME Boiler Code, July 1974, p. 127.

3. Telecon,W.Reuter (INEL) and J. R. Hawthorne (NRL) on 22 Sep 1976.

4. Keiser, D. D. and Brown, H. L., "A Review of the Physical Metallurgy of Alloy 718," ANCR-1292, Aerojet Nuclear Company Report, February 1976.

5. HANFORD ENGINEERING DEVELOPMENT LABORATORY

H. H. Yoshikawa

5.1 INTRODUCTION

The objectives of the structural materials investigation conducted at the Hanford Engineering Development Laboratory are mainly to provide control data for in-reactor and postirradiation tests and to provide direct and timely assistance to FFTF and Demonstration plant structural design and analysis programs. The HEDL efforts involve evaluation of mechanical properties of structural materials in the areas of normal and high strain rate tensile testing, creep, low cycle fatigue, fatigue crack growth and fracture toughness. Materials generally represented are austenitic stainless steels, nickel base alloys, ferritics and welds. They are used in such structures as reactor vessels, guard vessels, reflectors, shielding, core support structures, core formers, upper internals and piping. Those test results and analyses appropriate to the "Structural Materials Quarterly Report" will be reported here; however, those investigations associated with irradiation effects per se will be reported in HEDL publications.

5.2 LMFBR STRUCTURAL MATERIALS - J. J. Holmes and R. L. Knecht

5.2.1 Effect of a Liquid Sodium Environment Upon Fatigue-Crack Growth in a Pressure Vessel Steel - L. A. James and R. L. Knecht

5.2.1.1 Objective

The objective of this report is to characterize the effects of various parameters upon the fatigue-crack propagation behavior of reactor structural materials for use in design, safety analysis and operations support.

5.2.1.2 Accomplishments and Status

The specimens employed in this study were of the ASTM "Compact Type" design (W=2.00 in., B=0.50 in.). Feedback-controlled electro-hydraulic systems were utilized for applying the cyclic loads. The loading waveforms were sinusoidal and, depending upon the test, stress ratios

($R=K_{min}/K_{max}$) were either 0.05 or 0.50, and cyclic frequencies were either 40 cpm (0.667 H_{20}) or 400 cpm (6.67 Hz). An air-circulating furnace was employed for those specimens tested in an air environment. An environmental chamber, which has been previously described[1] was utilized for the test conducted in a flowing sodium environment.

The SA-387 Grade D material used in this study was procured in the form of 88.9 mm (3.5 in.) plate (Lukens heat B8238). Prior to machining test specimens, the plate was heated to 1700°F (926°C) and held at that temperature for 3.5 hours. It was then cooled at a rate no faster than 100°F per hour (56°C/hr.) to 600°F (316°C), at which time it was cooled in still air to room temperature. The chemical compositions and mechanical properties of this material are given in Tables 5.1 and 5.2, respectively.

TABLE 5.1

Chemical Composition (percent by weight)

C	Mn	P	S	Si	Cr	Mo	Ni
0.12	0.50	0.010	0.020	0.22	2.30	0.98	0.10

* SA-387 Grade D is equivalent to SA-387 Grade 22 Class 1.

TABLE 5.2

Mechanical Properties

(Strain rate = 3×10^{-5} sec^{-1})

Test Temp.	0.2% Offset Yield	Ultimate Strength	Uniform Elong.	Total Elong.	Red. in Area	Site Sequence No.*
24°C	247.1 MPa	492.7 MPa	13.31%	20.13%	59.35%	H03001
75°F	36,850 psi	71,460 psi				
427°C	226.0 MPa	474.2 MPa	9.60%	15.45%	56.91%	H03006
800°F	32,930 psi	68,780 psi				

* HEDL LMFBR Fuel Cladding Information Center

Fatigue-crack growth tests were conducted in air and sodium environments at 800°F (427°C), and the results are shown in Figure 5.1. Limited testing was also done in an air environment to survey the effect of cyclic frequency at 800°F (427°C), and these results are shown in Figure 5.2.

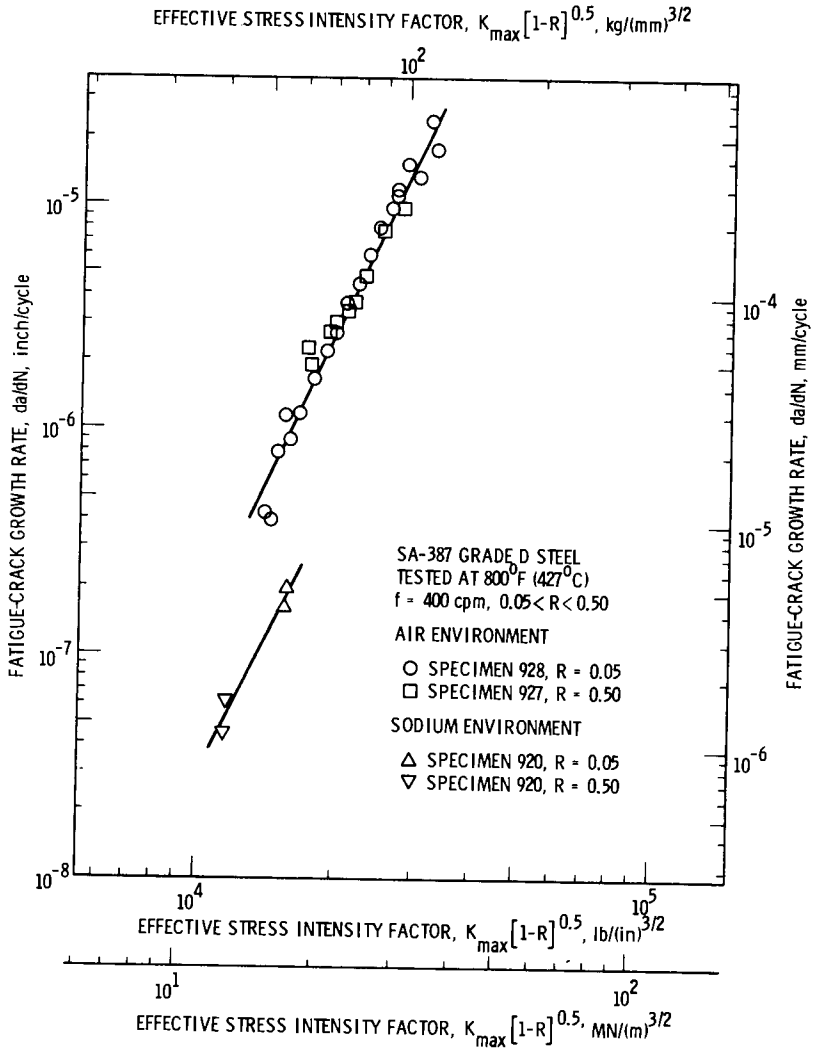

Figure 5.1. Comparison of fatigue-crack growth behavior of 2-1/4 Cr-1Mo Steel in air sodium environments at 800°F.

It will be noted in Figure 5.1 that two different stress ratios (R=0.05 and R=0.50) are employed, and that the results are expressed in terms of the "effective stress intensity factor" (K_{eff}) rather than the more familiar "stress intensity factor range" (ΔK). Stress ratio can have a significant effect upon crack growth rates when expressed as a function of ΔK, and it has been shown that use of K_{eff} generally produces an excellent correlation of crack growth rates over a wide range of stress ratios[2].

The effect of sodium upon the crack growth behavior may be seen in Figure 5.1. Fatigue-crack growth rates are approximately a factor of five lower in a sodium environment (oxygen content 1-3 ppm) than in an air environment at the same temperature. This is in qualitative agreement with similar tests on austenitic stainless steels[1,3,4,5] and nickel-base alloys[6,7]. Similar trends were also noted for a 2-1/4 Cr-1Mo steel tested in air and helium environments at temperatures of 950°F (510°C) and 1100°F (593°C)[8]. It is believed that the very low oxygen levels present in liquid sodium environments prototypic of LMFBR systems are responsible for the low crack growth rates experienced in such environments[1].

The effect of cyclic frequency in an air environment at 800°F (427°C) was surveyed at 40 cpm (0.667 Hz) and 400 cpm 6.67 Hz). The results, shown in Figure 5.2, indicate little or no effect of frequency over this narrow range at this temperature. This is in agreement with tests on another ferritic pressure vessel steel in an air environment at 550°F (288°C) over the frequency range 1-600 cpm (0.017-10.0 Hz)[9]. However, the effect of frequency in an air environment is definitely temperature dependent, since there is an effect for 2-1/4 Cr-1Mo steel tested in air at temperatures of 950°F (510°C) and 1100°F (593°C)[10].

5.2.1.3 Expected Achievements During Next Reporting Period

Testing to characterize the crack growth behavior of bi-metallic weldments (IN-718/IN-600, IN-718/Type 316, IN-600/Type 316, all utilizing IN-82 filler metal) will continue.

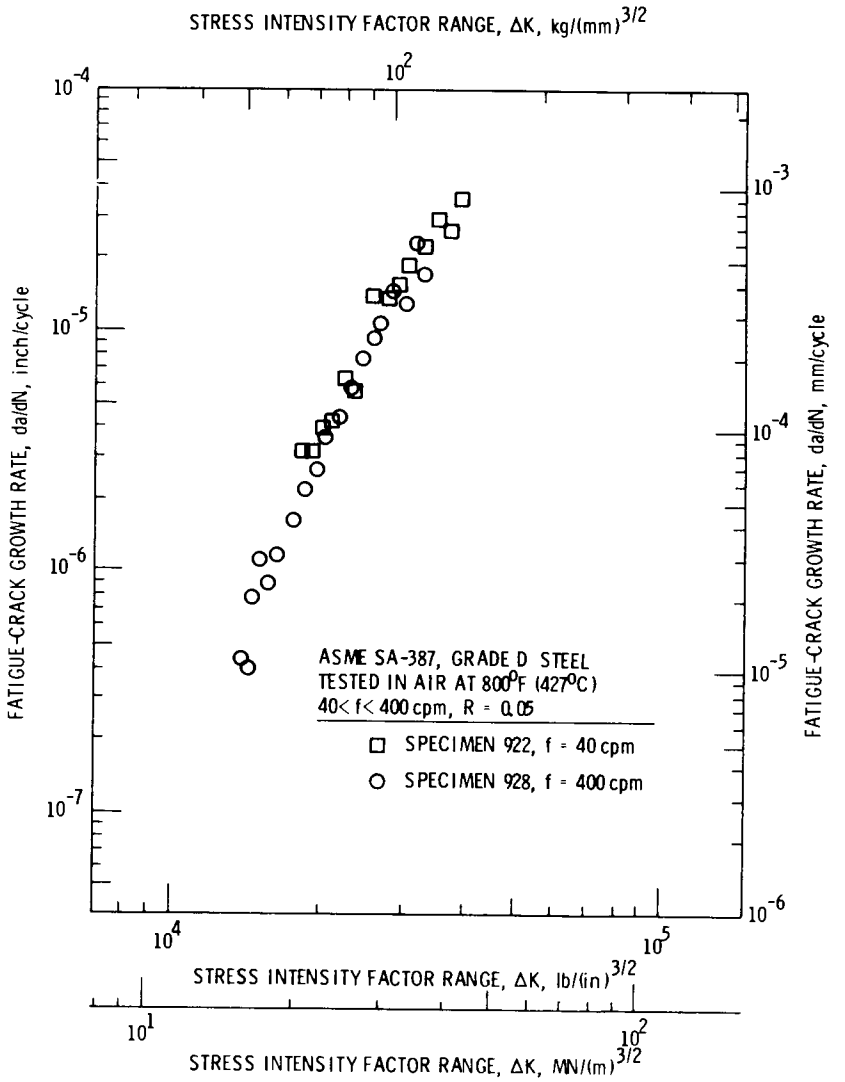

Figure 5.2. Comparisons of fatigue-crack growth behavior of 2-1/4 Cr-1Mo Steel at two frequencies in an air environment at 800°F.

5.2.2 THE EFFECT OF HEAT TREATMENT ON THE FRACTURE TOUGHNESS RESPONSE OF INCONEL 718 AT 75°F AND 800°F - W. J. Mills, R. L. Knecht

5.2.2.1 Objective

The objective of this work is to characterize the fracture toughness response of LMFBR structural alloys. This information supports the design, operation, and safety analyses of LMFBR structural components.

5.2.2.2 Accomplishments and Status

The effect of heat treatment on the room temperature and elevated temperature fracture toughness response of Inconel 718 has been characterized. The Inconel 718 "Conventional" and INEL heat treatments are reported in Table 5.3. Chemical analysis and mechanical properties are given in Tables 5.4 and 5.5, respectively.

Fracture tests were performed on deeply cracked (fatigue precracked to a/W>0.6) .577T (thickness - 0.495 inch) compact tension specimens oriented in the T-L direction. Values of J_{Ic} were determined by the R-curve technique outlined in Reference 11.

The R-curves for Inconel 718 at 75°F and 800°F (Figures 5.3 and 5.4, respectively) illustrate that the ductile fracture toughness response of the INEL heat treated Inconel 718 was superior to that of the Conventionally heat treated alloy at both test temperatures. It should be noted that the yield strength and ultimate tensile strength resulting from the Conventional heat treatment were only slightly greater than those associated with the INEL heat treatment (Table 5.5). Hence, the Conventionally heat treated Inconel 718 pays a large penalty in fracture toughness for its marginal increase in strength.

Figures 5.3 and 5.4 also show that the elevated temperature (800°F) value of J_{Ic} for the Conventionally heat treated Inconel 718 (435 in-lb/in^2) was essentially the same as the room temperature fracture toughness (414 in-lb/in^2). On the other hand, J_{Ic} for the INEL heat treatment decreased from 839 in-lb/in^2 at 75°F to 720 in-lb/in^2 at 800°F. This phenomenon is consistent with the fracture toughness response of another heat of Inconel 718 (Haynes/2180-1-0345, INEL heat treatment)

TABLE 5.3

HEAT TREATMENTS FOR INCONEL 718

Conventional Heat Treatment

Annealed at 1750°F, air cooled to room temperature. Aged 8 hours at 1325°F, furnace cooled to 1150°F and held at 1150°F for a total aging time of 18 hours, air cooled to room temperature.

INEL Heat Treatment

Solution annealed 1 hour at 2000°F, cooled to 1325°F at 100°F/hour, aged 4 hours at 1325°F, cooled to 1150°F at 100°F/hour, aged 16 hours at 1150°F, air cooled to room temperature.

TABLE 5.4

CHEMICAL COMPOSITION (percent by weight)

Material	Produced/Heat No.	C	Mn	Fe	S	Si	Cu	Ni	Cr	Al	Ti	Co	P	Mo	B	Cb&Ta
Inconel 718	Haynes/2180-1-9327	0.04	0.08	Bal.	0.005*	0.07	0.02	51.60	18.30	0.52	1.01	0.12	0.005*	3.10	0.004	5.26

* Less than

TABLE 5.5

MECHANICAL PROPERTIES

Inconel 718 (2180-1-9327

Heat Treatment	Temperature (°F)	Specimen No.	0.2% Yield Strength (psi)	Ultimate Strength (psi)	Flow Strength (psi)	Total Elongation (%)	Reduction In Area (%)
Conventional	75	T490	167,200	205,500	186,350	12.5	37.0
Conventional	800	T489	136,600	178,000	157,300	11.7	38.2
INEL	75	T493	148,900	193,300	171,100	12.4	37.8
INEL	800	T491	133,800	165,800	149,800	12.5	40.8

Strain Rate = 1.78×10^{-3} min^{-1}

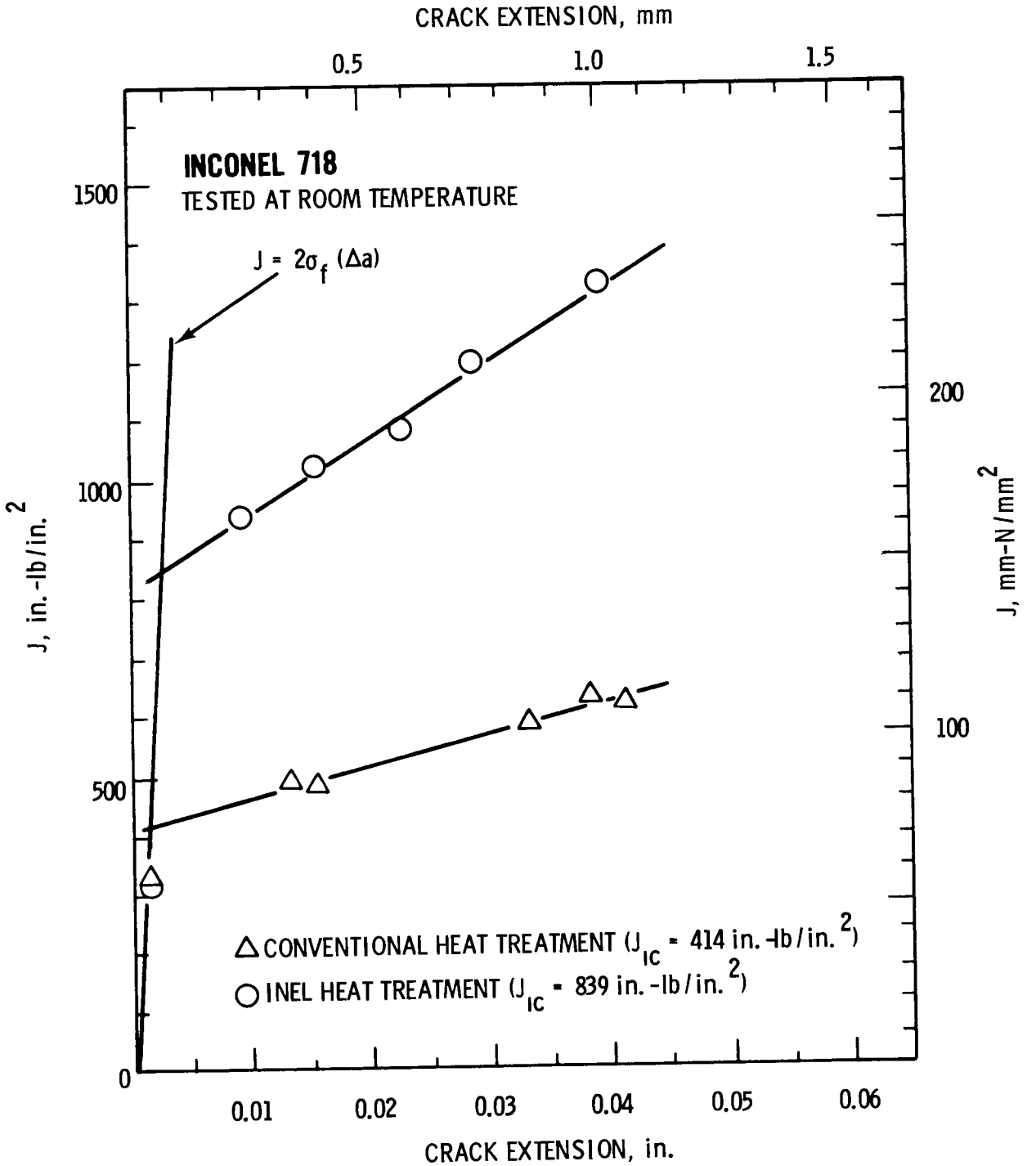

FIGURE 5.3 R-curves for Inconel 718 (INEL and Conventional Heat Treatments) Tested at Room Temperature.

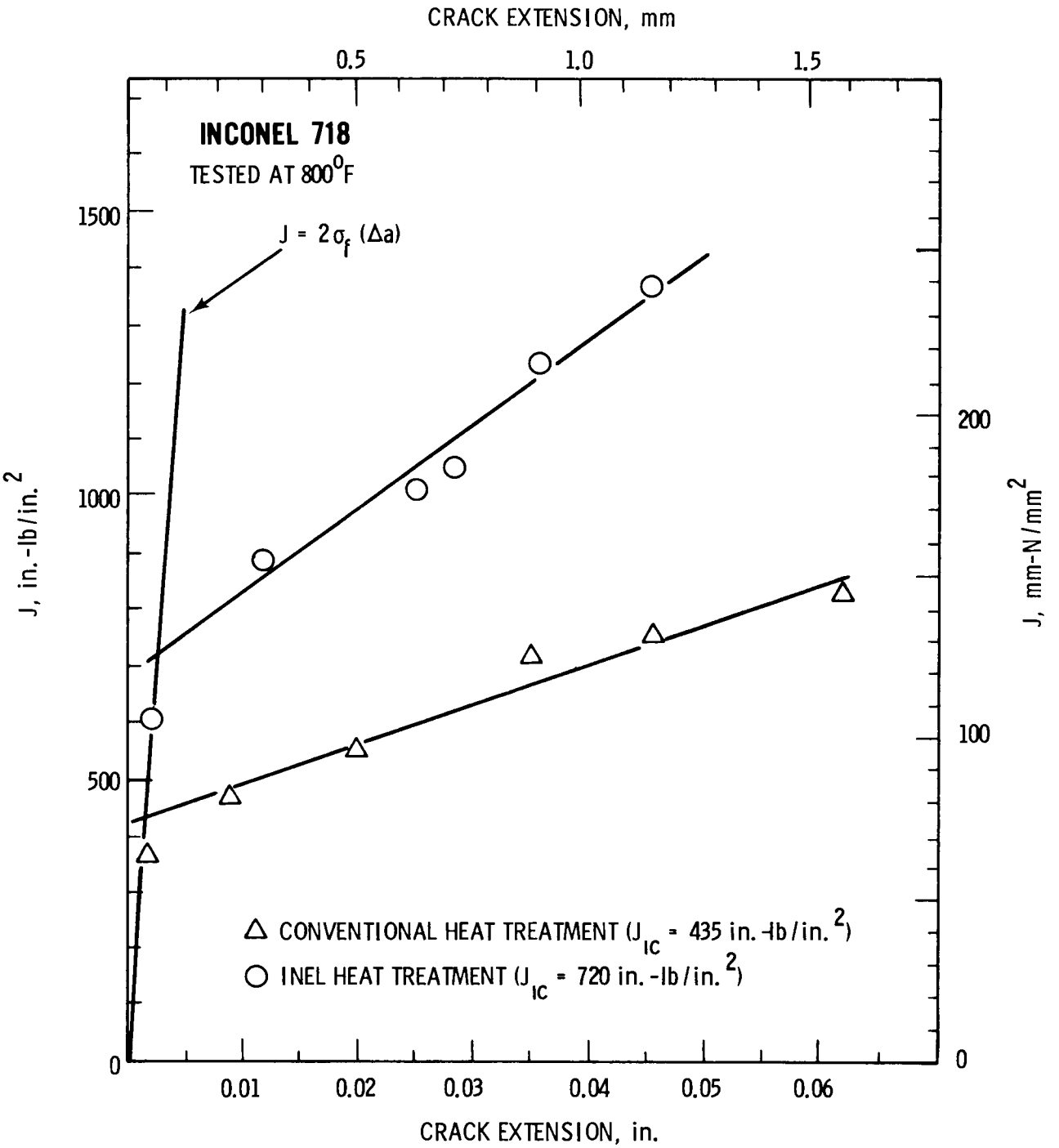

FIGURE 5.4 R-curves for Inconel 718 (INEL and Conventional Heat Treatments (Tested at 800°F).

where J_{Ic} decreased from 727 in-lb/in^2 at 75°F to 555 in-lb/in^2 at 800°F.[12] Comparison of the fracture toughness behavior of the two Inconel 718 heats reveals that J_{Ic} values for Haynes Heat 2180-1-9345 were slightly lower than those obtained during the current investigation from Haynes Heat 2180-1-9327. This apparent anomoly is believed to be associated with heat-to-heat variations; additional testing is currently underway at HEDL in order to resolve this issue.

5.2.2.3 Expected Achievements in the Next Reporting Period

Room temperature and elevated temperature elastic-plastic fracture toughness testing of nickel-base alloys, A-286 stainless steel, and ferritic steels will continue. In addition, fractographic examination of fracture specimens will be performed in order to fully characterize the fracture response of these alloys.

5.2.3 CREEP-RUPTURE BEHAVIOR OF INCONEL 600 AFTER THERMAL EXPOSURE - L. D. Blackburn, J. M. Steichen and R. L. Knecht

5.2.3.1 Objective

The objective of this work is to characterize the creep-rupture behavior of unirradiated Inconel 600 for subsequent comparison with post-irradiation test results.

5.2.3.2 Accomplishments and Status

5.2.3.2.1 Scope. Creep-rupture behavior of annealed Inconel 600 was reported in the previous quarterly report. This report presents similar correlations for the same material subjected to thermal exposures prior to testing. Durations of thermal exposures were 1000, 4000 and 10,000 hours at temperatures of 811 K (1000°F), 922 K (1200°F) and 1033 K (1400°F); creep-rupture tests were conducted at the prior thermal exposure temperature.

5.2.3.2.2 Results. Inspection of the creep-rupture data suggested that the 4000-hour and 10,000-hour exposures could be treated together,

and the experimental results were described analytically by lease squares fitting to equations of the form

$$\log P = A_p + n_p \log \sigma \qquad [13]$$

where P is a particular property, σ is the stress, and A_p and n_p are constants. Values of n_p were compared with results for annealed material using the multiple comparison approach described by Acton,[1] and where differences were not statistically significant, n_p values for annealed material were adopted. For the 1000-hour exposures, data were obtained at only two stress levels so analytical descriptions were not formulated.

Experimental results for time to rupture (t_r) are presented in Figure 5.5. Data at 811 K (1000°F) and 1033 K (1400°F) show that thermal exposure decreases t_r relative to annealed material but leaves the stress dependence unchanged. The 922 K (1200°F) t_r values are very similar to those of annealed material, but the analysis indicates a stronger stress dependence after thermal exposure. At all temperatures, t_r is slightly larger for the 1000-hour exposure than for the two longer exposures.

Results for time to the onset of tertiary creep (t_2) are presented in Figure 5.6. At 811 K (1000°F), t_2 is reduced relative to annealed material but retains the same stress dependence. The stress dependence of t_2 is increased markedly after the 4000-hour and 10,000-hour exposures at 922 K (1200°F), leading to much larger t_2 values at low stresses. The stronger stress dependence after thermal exposure is clearly evident in the t_2 data, and this behavior supports the stronger stress dependence of t_r in exposed material at 922 K (1200°F) discussed above. However, the limited data suggest that the stress dependence of t_2 after the 1000-hour exposure is the same as that of annealed material. At 1033 K (1400°F), thermal exposure leads to larger t_2 values but does not change the stress dependence.

Thermal exposure at all temperatures produces an increase in minimum creep rate ($\dot{\varepsilon}_m$) without a change in stress dependence, as shown in Figure 5.7. The magnitude of the increase in $\dot{\varepsilon}_m$ varies with temperature, and the increase for the 1000-hour exposure tends to be somewhat smaller than that for the two longer exposures. Similar behavior is observed for the

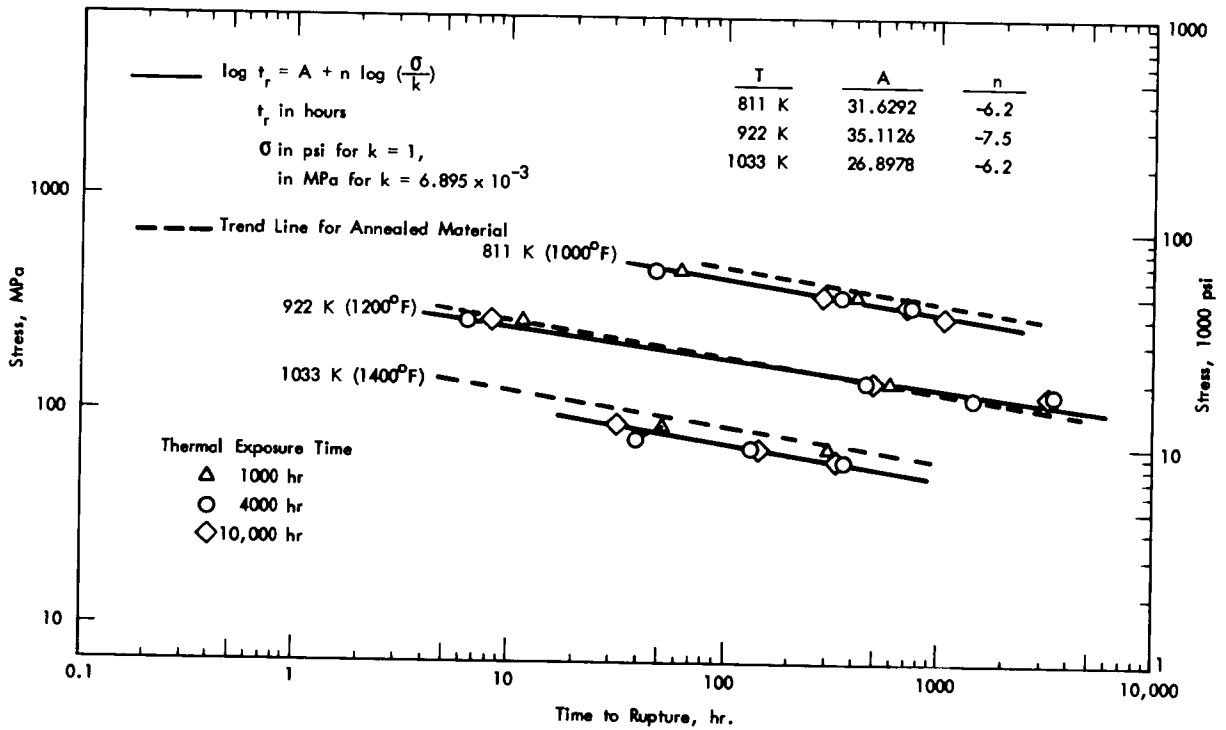

FIGURE 5.5 Variation of Time to Rupture With Stress for Inconel 600 After Prior Thermal Exposure

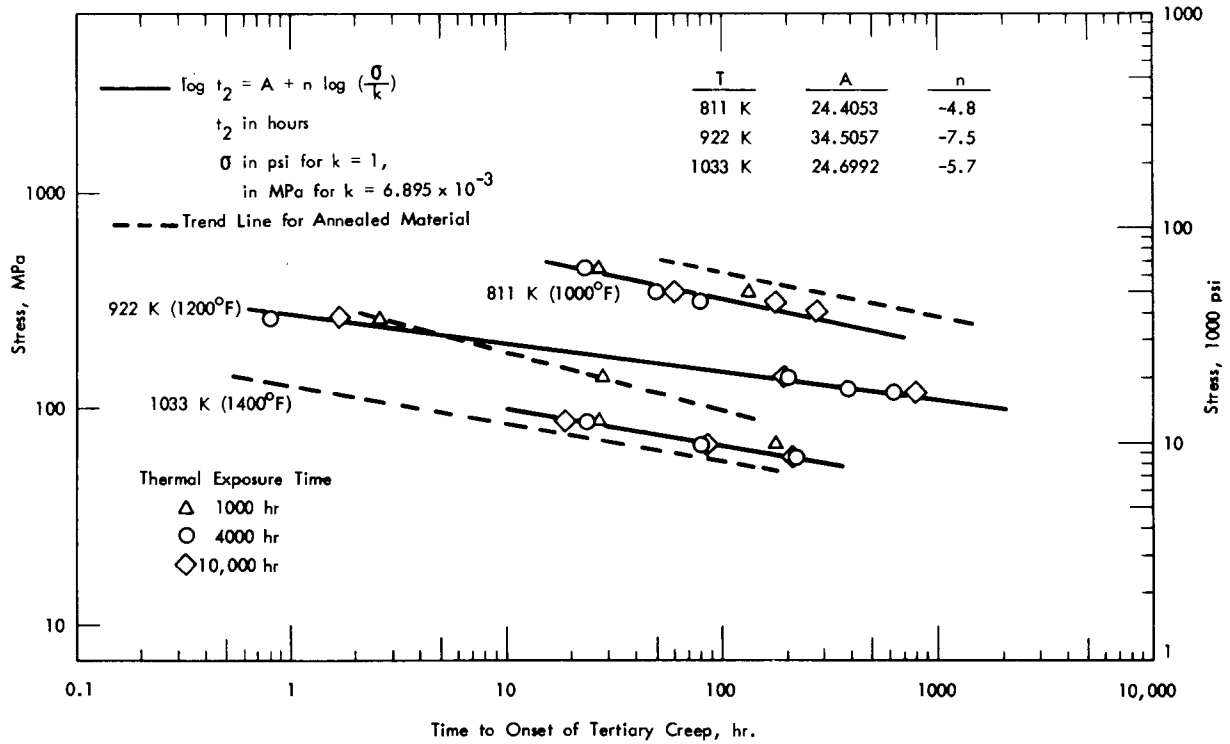

FIGURE 5.6 Variation of Time to Onset of Tertiary Creep With Stress for Inconel 600 After Prior Thermal Exposure

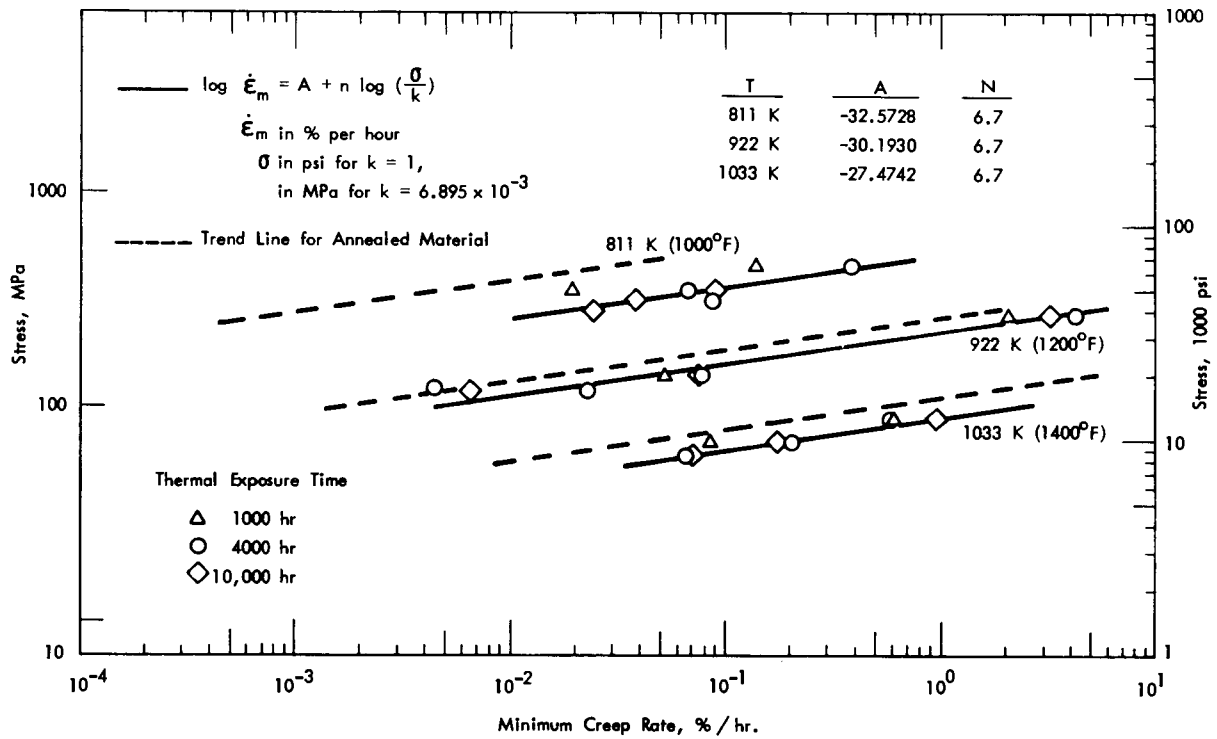

FIGURE 5.7 Variation of Minimum Creep Rate With Stress for Inconel 600 After Prior Thermal Exposure

average creep rate to rupture and the average creep rate to the onset of tertiary creep, as shown in Figures 5.8 and 5.9.

Creep strain at rupture (ε_r) data are presented in Figure 5.10 along with the trend curve predicted from the analytical descriptions from Figures 5.6 and 5.8. Thermal exposure produces a significant increase in ε_r at 811 K (1000°F), but leads to relatively minor differences at the other temperatures. However, the increased stress dependence of t_r at 922 K (1200°F) leads to a predicted trend curve of increasing ε_r with increasing t_r for exposed material in contrast to the decreasing ε_r trend curve for annealed material at this temperature. Thermal exposure produces significant increases in the creep strain at the onset of tertiary creep at all temperatures, as shown in Figure 5.11.

The correlations presented should be an adequate description of the effect of thermal exposure on the creep-rupture properties of Inconel 600 for subsequent use in interpreting postirradiation test results.

5.2.3.3 Expected Accomplishments

The characterization of creep-rupture properties of unirradiated Inconel 600 is complete.

5.2.4 ELEVATED TEMPERATURE HIGH STRAIN RATE TENSILE PROPERTIES OF ALLOY 600 - J. M. Steichen, A. L. Ward, and R. L. Knecht

5.2.4.1 Objective

The objective of this work is to characterize the effects of test temperature and strain rate on the tensile properties of Alloy for subsequent comparison to postirradiation test results.

5.2.4.2 Accomplishments and Status

5.2.4.2.1 Scope. This report presents the results of a study to determine the effects of test temperature and strain rate on the tensile properties of annealed Alloy 600. Test parameters included temperatures from 22 to 760°C (72 to 1400°F) and nominal strain rates from 3×10^{-5} to 1.0 sec^{-1}. The results described herein provide a detailed characterization of unirradiated tensile properties and the basis for ascertaining

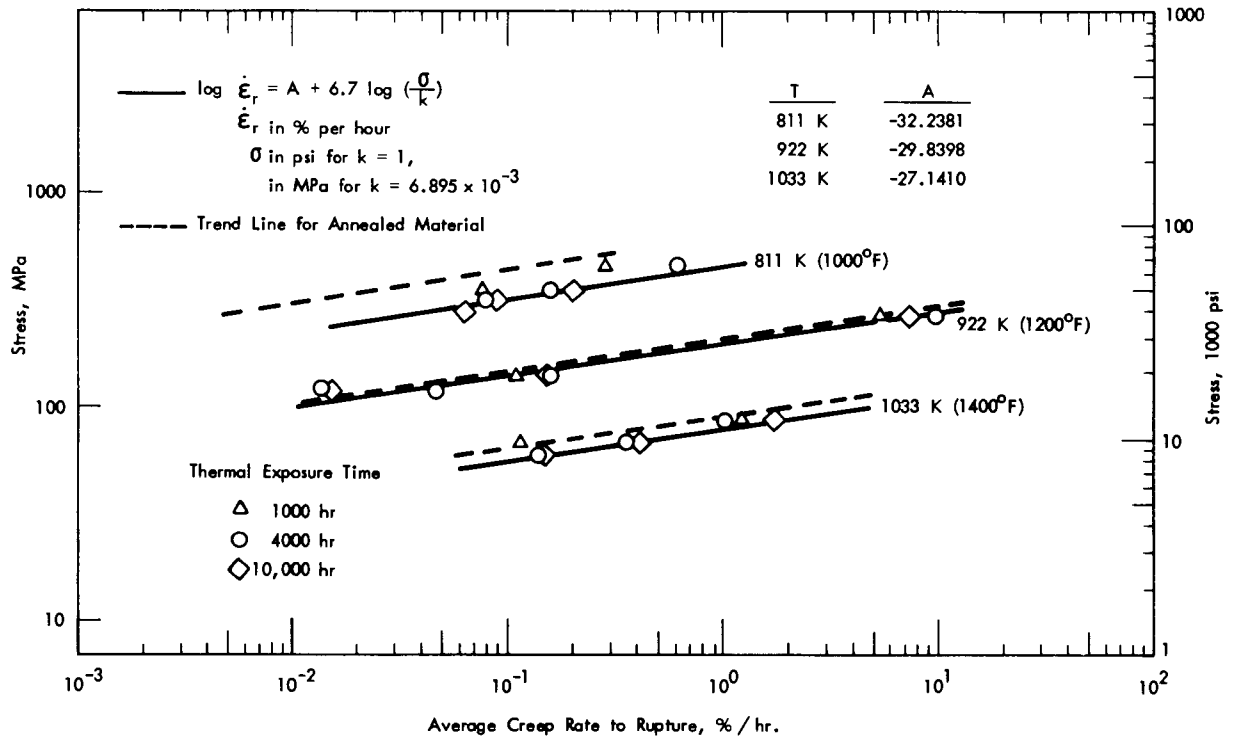

FIGURE 5.8 Variation of Average Creep Rate to Rupture With Stress for Inconel 600 After Prior Thermal Exposure

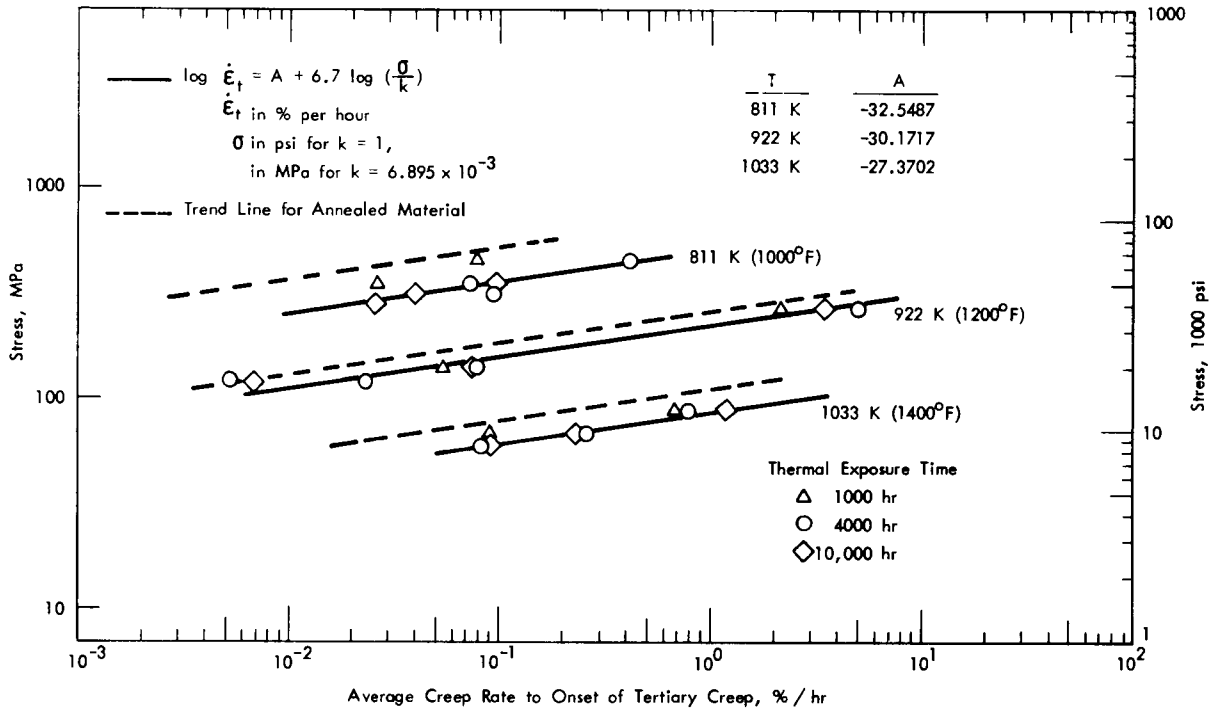

FIGURE 5.9 Variation of Average Creep Rate to Onset of Tertiary Creep With Stress for Inconel 600 After Prior Thermal Exposure

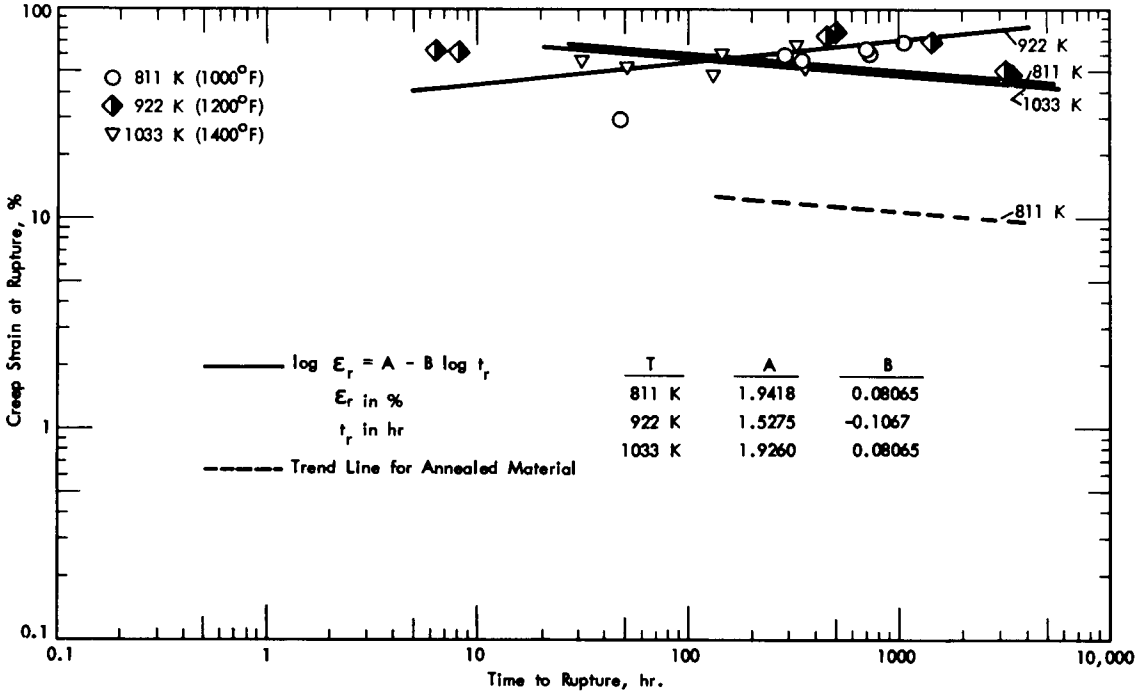

FIGURE 5.10 Variation of Creep Strain at Rupture with Time to Rupture for Inconel 600 After Prior Thermal Exposure

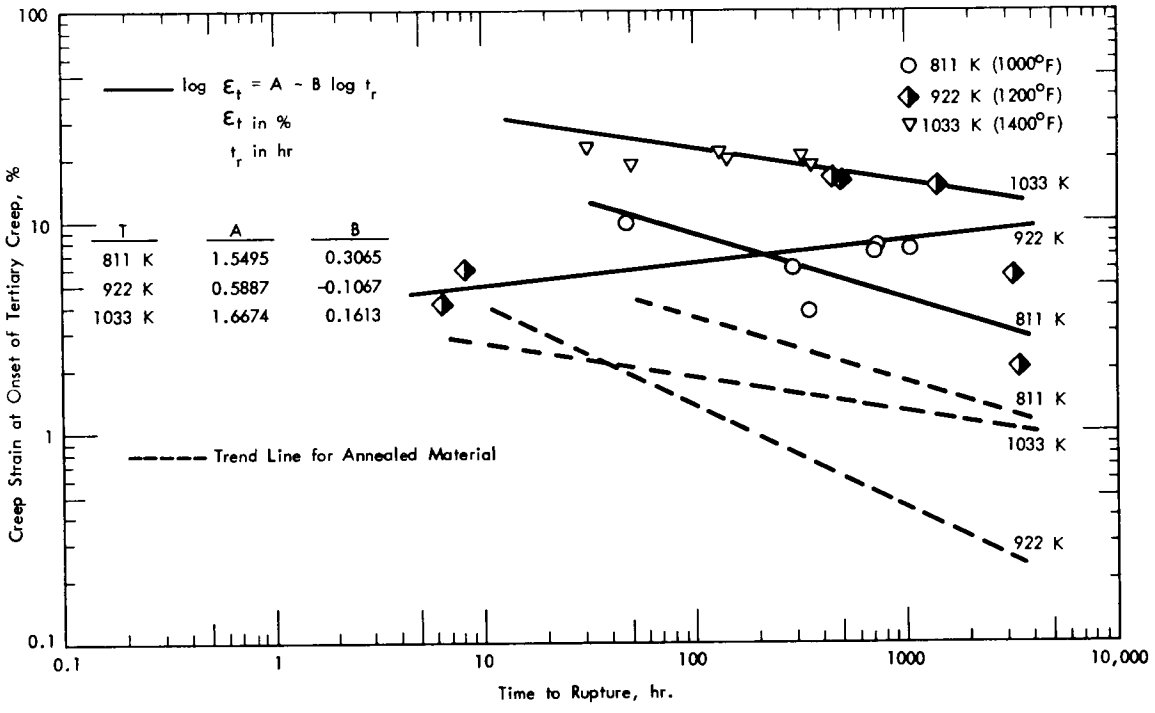

FIGURE 5.11 Variation of Creep Strain at Onset of Tertiary Creep With Stress for Inconel 600 After Prior Thermal Exposure

the effects of neutron irradiation on those properties. Irradiation effects results will be reported as the data become available.

5.2.4.2.2 Results

5.2.4.2.2.1 Temperature Effects. The tensile properties of Alloy 600 measured at a nominal strain rate of 3×10^{-5} sec^{-1}, are given as a function of deformation temperature in Figure 5.12. Data presented in this figure represent average results from multiple tests (see Table 5.6). The strength properties (ultimate and 0.2% yield) decrease initially to plateau regions and then fall rapidly at the higher temperatures. Such plateaus, observed in austenitic stainless steels, have been attributed, at least in part, to dynamic strain aging,[14-16] and in fact, the beginning of the plateaus and the slight increase in ultimate strength correspond to the appearance of serrations in the flow curves (Figure 5.13). Dynamic strain aging has been shown to increase the rate of strain hardening ($d\sigma/d\varepsilon$) in austenitic materials[14-16] thereby increasing strength and associated ductility parameters. Data for Alloy 600 in this study are consistent with this observation since total and uniform elongation are enhanced in the temperature regime where dynamic strain aging is observed (∿300 to 600°C) (Figure 5.12).

Fahr[16] has related various deformation mechanisms in Type 316 stainless steel to a number of distinct types of serrated or jerky flow. All serration types are believed associated with interactions of dislocations and interstitial (primarily carbon and nitrogen) solute atoms. Since the interactions involve relative rates of solute diffusion and dislocation motion, deformation is necessarily dependent on time and temperature. At the relatively low strain rate of 3×10^{-5} sec^{-1} represented by the data in Figure 5.12, sufficient time is available at certain temperatures to significantly influence ultimate strength and total and uniform elongation. The 0.2% yield strength is affected a much lesser extent since it is obtained very early in a test. Little or no effect of strain aging on the reduction of area would be expected since this property is dominated by unstable flow and fracture.

For temperatures above ∿600°C, serrations are no longer observed in the flow curves and properties depart from the lower temperature behavior.

TABLE 5.6

ELEVATED TEMPERATURE TENSILE PROPERTIES OF
ALLOY 600 AT VARIOUS STRAIN RATES

Strain Rate Sec^{-1}	Test Temp. °C	Strength-MPa (Ksi) PEL	0.2% Yield	Ultimate	Elongation-% Total	Uniform	Reduction of Area-%	Test Ident.
3×10^{-5}	22	168 (24.4)	283 (41.1)	655 (95.0)	39.8	36.6	65.3	600-1
	22	197 (28.5)	290 (42.1)	678 (98.3)	36.8	34.0	60.2	2
	232	182 (26.4)	244 (35.4)	621 (90.1)	37.7	33.9	69.1	24
	232	208 (30.2)	270 (39.2)	642 (93.1)	33.9	30.3	65.9	25
	316	197 (24.6)	248 (36.0)	647 (93.8)	41.4	40.1	59.0	3
	427	197 (38.5)	261 (39.3)	654 (94.9)	38.0	34.3	52.8	4
	427	154 (22.4)	232 (33.7)	611 (88.6)	40.5	36.2	61.8	5
	538	168 (24.4)	268 (38.9)	597 (86.6)	34.2	31.3	46.3	6
	538	140 (20.3)	221 (32.1)	571 (82.8)	40.4	37.3	50.4	7
	538	178 (25.8)	235 (34.1)	575 (83.4)	36.1	32.9	51.6	16
	593	140 (20.3)	248 (35.9)	551 (72.6)	30.0	20.4	40.7	8
	593	168 (24.4)	216 (31.3)	508 (73.7)	30.0	26.6	32.5	9
	649	162 (23.5)	220 (31.9)	375 (54.4)	44.4	10.0	62.3	10
	649	197 (24.6)	239 (34.7)	396 (57.5)	32.1	9.5	54.9	11
	649	158 (22.9)	202 (29.3)	392 (56.9)	24.8	14.0	41.0	17
	760	121 (17.6)	151 (21.9)	163 (23.6)	66.0	2.3	86.1	12
	760	127 (18.4)	158 (22.9)	168 (24.3)	71.7	2.1	80.3	13
3×10^{-3}	22	254 (36.9)	326 (47.3)	675 (97.9)	34.2	29.9	65.6	32
	22	263 (38.2)	340 (49.3)	695 (100.8)	33.1	26.6	73.2	33
	232	223 (32.3)	288 (41.8)	622 (90.2)	34.6	30.1	67.7	34
	232	234 (33.9)	275 (39.9)	275 (91.9)	33.3	29.9	73.4	35
	427	226 (32.8)	276 (40.0)	656 (95.2)	38.0	34.4	59.0	36
	427	190 (27.6)	235 (34.1)	616 (80.3)	39.2	36.8	57.7	37
	538	179 (26.0)	220 (31.9)	603 (87.4)	40.2	34.8	59.3	38
	538	198 (28.7)	250 (36.2)	613 (88.9)	34.7	31.8	63.1	39
	593	185 (26.8)	215 (31.2)	558 (80.9)	34.3	30.8	57.7	40
	593	197 (28.5)	252 (36.6)	572 (82.9)	34.0	31.0	52.0	41
	649	198 (28.7)	226 (32.8)	521 (75.6)	32.2	27.1	63.1	42
	649	168 (24.4)	201 (29.2)	497 (72.1)	36.7	27.3	42.3	43
	760	168 (24.4)	197 (28.5)	298 (43.2)	67.5	9.8	80.5	44
	760	181 (26.2)	211 (30.6)	314 (45.6)	67.5	8.8	80.3	45

TABLE 5.6 (cont'd)

Strain Rate Sec^{-1}	Test Temp. °C	Strength-MPa (Ksi) PEL	0.2% Yield	Ultimate	Elongation-% Total	Uniform	Reduction of Area-%	Test Ident.
6×10^{-2}	22	250 (36.2)	316 (45.9)	706 (102.4)	36.7	30.9	59.6	600-55
	232	258 (37.4)	299 (43.4)	645 (93.5)	31.4	24.2	64.5	56
	427	204 (29.6)	254 (36.9)	616 (89.3)	34.1	29.3	60.2	57
	538	230 (33.3)	252 (36.6)	609 (88.3)	38.4	33.5	57.7	58
	593	182 (26.4)	228 (33.1)	573 (83.1)	35.6	31.3	57.3	59
	649	177 (25.7)	226 (32.8)	558 (81.0)	31.9	27.9	53.7	60
	760	207 (30.0)	221 (32.0)	414 (60.1)	38.1	17.3	70.7	61
1.0	22	270 (39.2)	322 (46.7)	747 (108.4)	35.4	31.0	63.9	62
	232	200 (29.0)	292 (42.4)	623 (90.3)	34.4	29.9	69.4	63
	457	212 (30.7)	265 (38.5)	592 (85.9)	34.7	30.4	63.9	64
	538	219 (31.7)	267 (38.7)	600 (87.0)	38.0	33.9	61.8	65
	593	182 (26.4)	231 (33.5)	541 (78.4)	34.4	29.8	62.1	66
	649	196 (28.6)	233 (33.8)	538 (78.0	31.8	27.3	57.7	67
	760	174 (25.3)	208 (30.2)	450 (65.3)	28.1	21.1	66.1	68

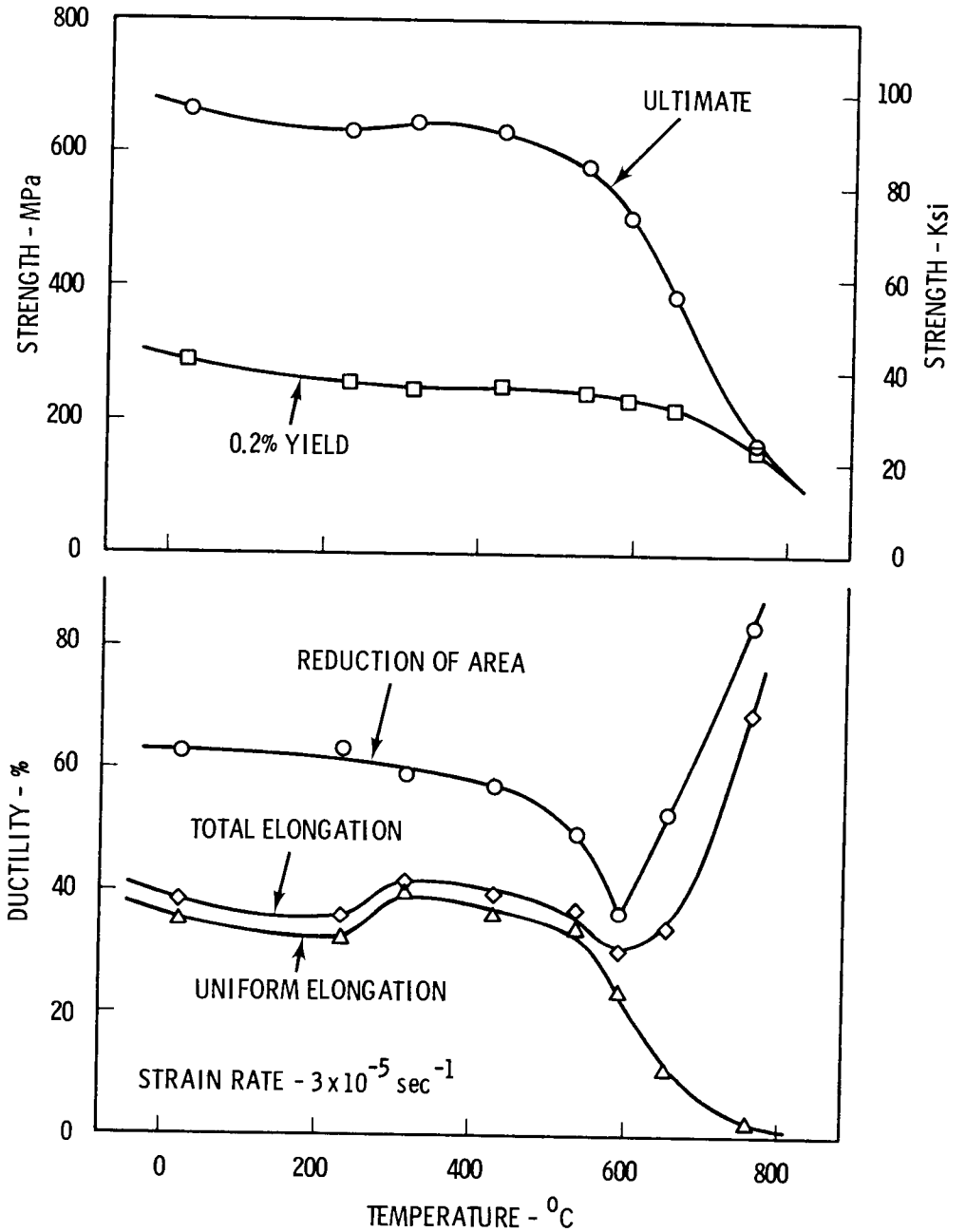

FIGURE 5.12 Temperature Dependence of Alloy 600 Tensile Properties

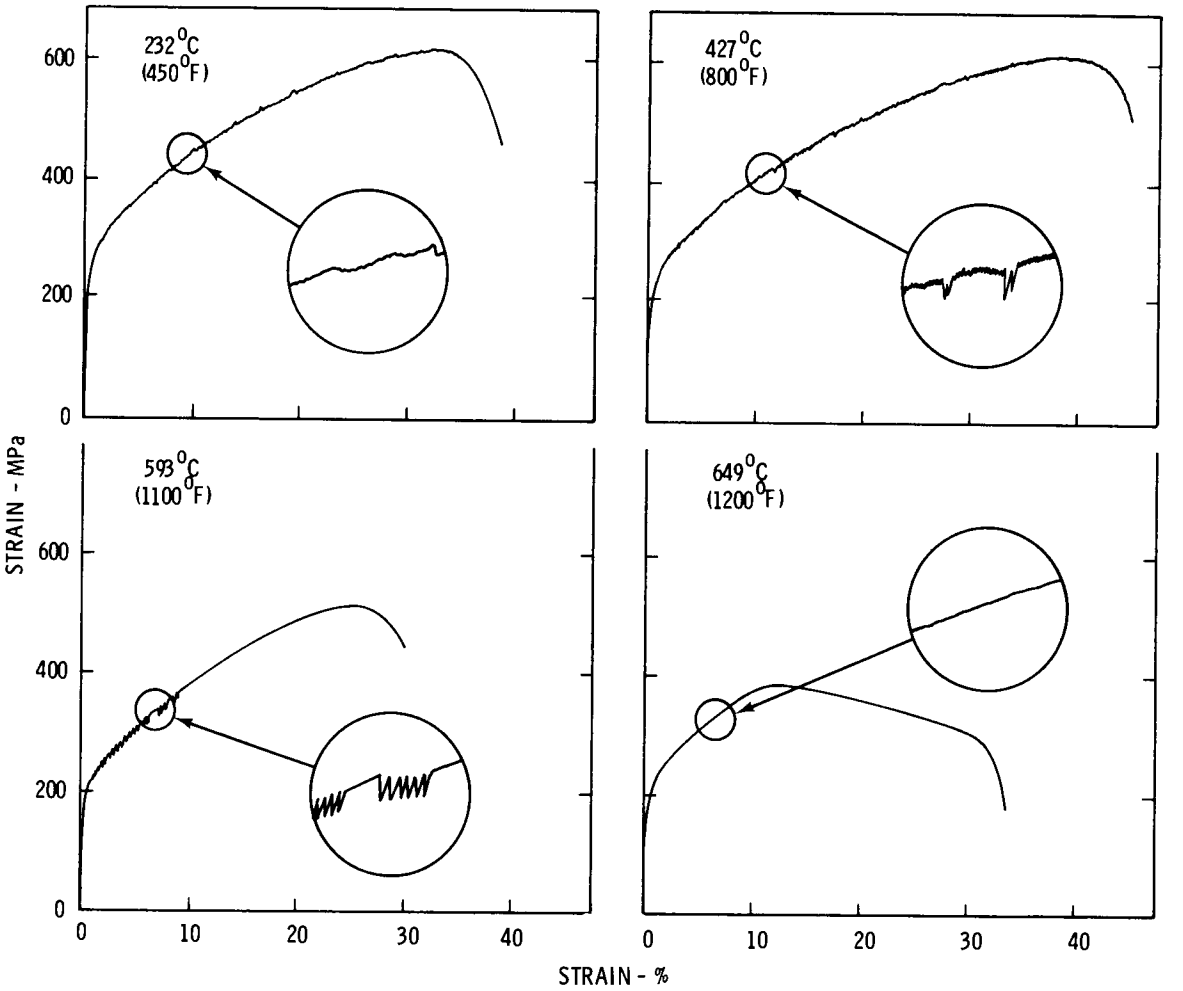

FIGURE 5.13 Serrated Flow in Alloy 600 at 3×10^{-5} sec^{-1} and Various Temperatures.

Both strength parameters fall rapidly as does uniform elongation, and total elongation and reduction of area increase sharply. At these high temperatures, diffusion rates of all constituents increase to a point such that thermal creep processes (diffusion controlled) control deformation and result in decreased strength. The strong increases in total elongation and reduction of area are attributed to recrystallization which occurs during deformation at the higher temperatures (>600°C) and effectively restricts the growth of intergranular cracks[17]. At 593°C (1100°F) intergranular fracture limits ductility resulting in minima in total elongation and reduction of area. The recrystallization process at this temperature is not sufficiently active to restrict growth of intergranular cracks (Figure 5.14).

5.2.4.2.2.1 Strain Rate Effects. The strain rate dependence of the ultimate strength of Alloy 600 at the various test temperatures is illustrated in Figure 5.15 (also see Table 5.6). At room temperature (22°C) a positive strain rate sensitivity is observed, i.e., ultimate strength increases with increasing strain rate. In the temperature range from 232 to 538°C (450 to 1000°F) the ultimate strength is essentially insensitive to strain rate. For temperatures of 649 and 760°C (1200 and 1400°F), the strain rate dependence is distinctly different from that ovserved at the lower temperatures. For rates below about 7×10^{-3} sec^{-1} at 649°C (1200°F) and 2×10^{-1} sec^{-1} at 760°C (1400°F), the ultimate strength exhibits a strong positive strain rate dependence. Such dependence, reported previously for other austenitic materials[18-20], has been attributed to the dominance of creep deformation at these temperatures and low strain rates. As strain rate is increased, creep (time and temperature dependent) is progressively restricted until it no longer exerts a pronounced influence at the higher strain rates.

The strain rate dependence of the ultimate strength of Alloy 600 is very similar to that previously reported for austenitic stainless steels and nickel alloys[18-20]. For intermediate test temperatures (232 to 538°C) the ultimate strength remains constant or decreases slightly with strain rate. The ultimate strength at low strain rates has been previously related to dynamic strain aging and progressive elimination of this dynamic process

(a) 250x

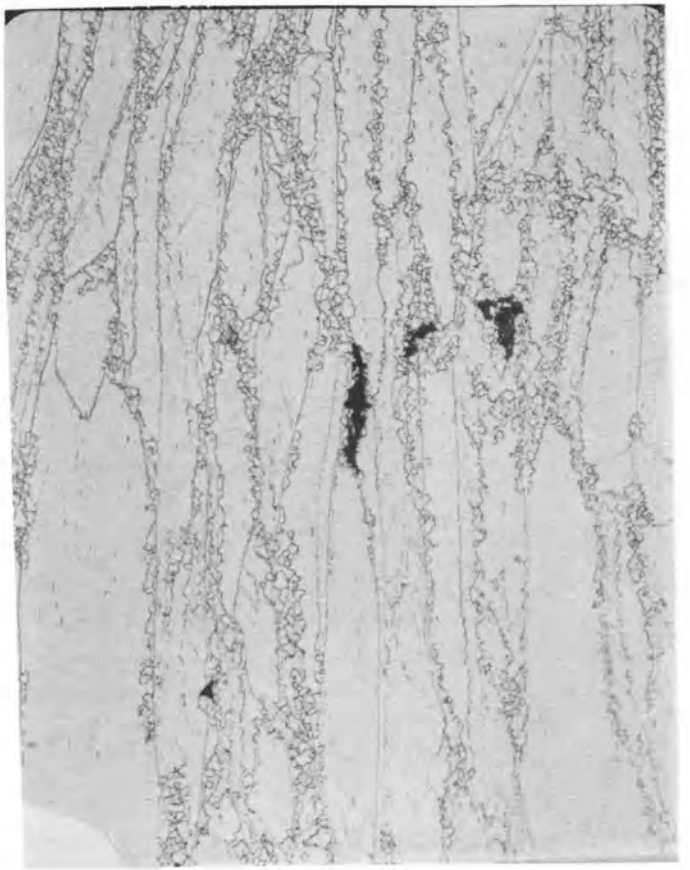

(b) 250x

FIGURE 5.14 Fracture Behavior of Annealed Alloy 600 at 3×10^{-5} sec^{-1}
(a) 593°C (1100°F) (b) 649°C (1200°F)

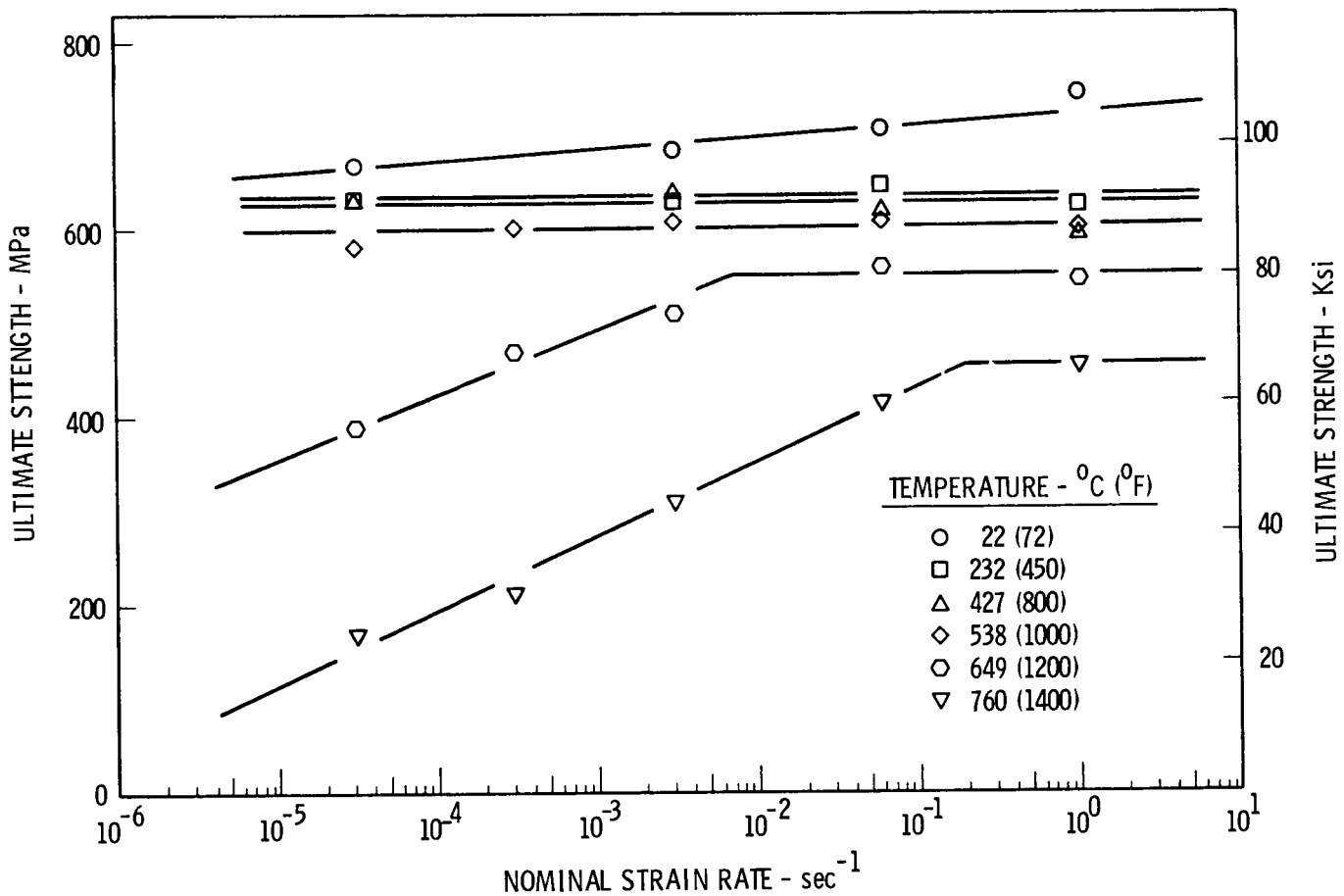

FIGURE 5.15 Strain Rate and Temperature Dependence of the Ultimate Strength of Alloy 600.

with increasing strain rate accounts for the slight reduction in ultimate strength[16,18]. At the higher temperatures (649 and 760°C), creep dominates deformation at low strain rates; however, as strain rate increases, interstitial atoms begin to retard dislocation movement and serrations in the flow curves are observed (Figure 5.16). Although creep and dynamic strain rate, it is apparent that creep processes are dominant for those test conditions where the ultimate strength is strongly dependent on both strain rate and temperature.

The dependence of the 0.2% yield strength on temperature and strain rate is similar to that observed for the ultimate strength (Figure 5.17). For temperatures to 649°C (1200°F) positive strain rate sensitivity is observed with the largest increases apparent at the lower temperatures. At 760°C (1400°F) the 0.2% yield stress increases rapidly with strain rate to a rate of 3×10^{-3} sec^{-1} and above this rate remains constant. At this high temperature, creep apparently exerts a slight influence on behavior at the lower test rates.

Total elongation, uniform elongation, and reduction of area are illustrated in Figures 5.18, 5.19, 5.20, respectively. For temperatures to 538°C (1000°F) these ductility parameters are essentially unaffected by increasing strain rate and all specimens exhibited transgranular fractures. At the higher temperatures the effect of strain rate can be related to changes in fracture mode. At 649°C (1200°F) and the lowest test rate, intergranular fractures were observed as were low reduction of area and uniform elongation values. Increasing strain rate significantly enhances these ductility parameters and completely transgranular fractures were observed at the higher strain rates. This behavior is consistent with that reported previously for Type 304 stainless steel[18]. At 760°C (1400°F) and the lowest rate, recrystallization occurs during testing resulting in transgranular fractures (Figure 5.14) and high reduction of area and total elongation values. Increasing strain rate reduces the time for recrystallization, hence, reduction of area and total elongation values decrease. Results of Shapiro and Dieter[17], which are in agreement with this observation, revealed that recrystallization is eliminated when Alloy 600 is tested at 2.5 sec^{-1} and a temperature of 816°C (1500°F). All three

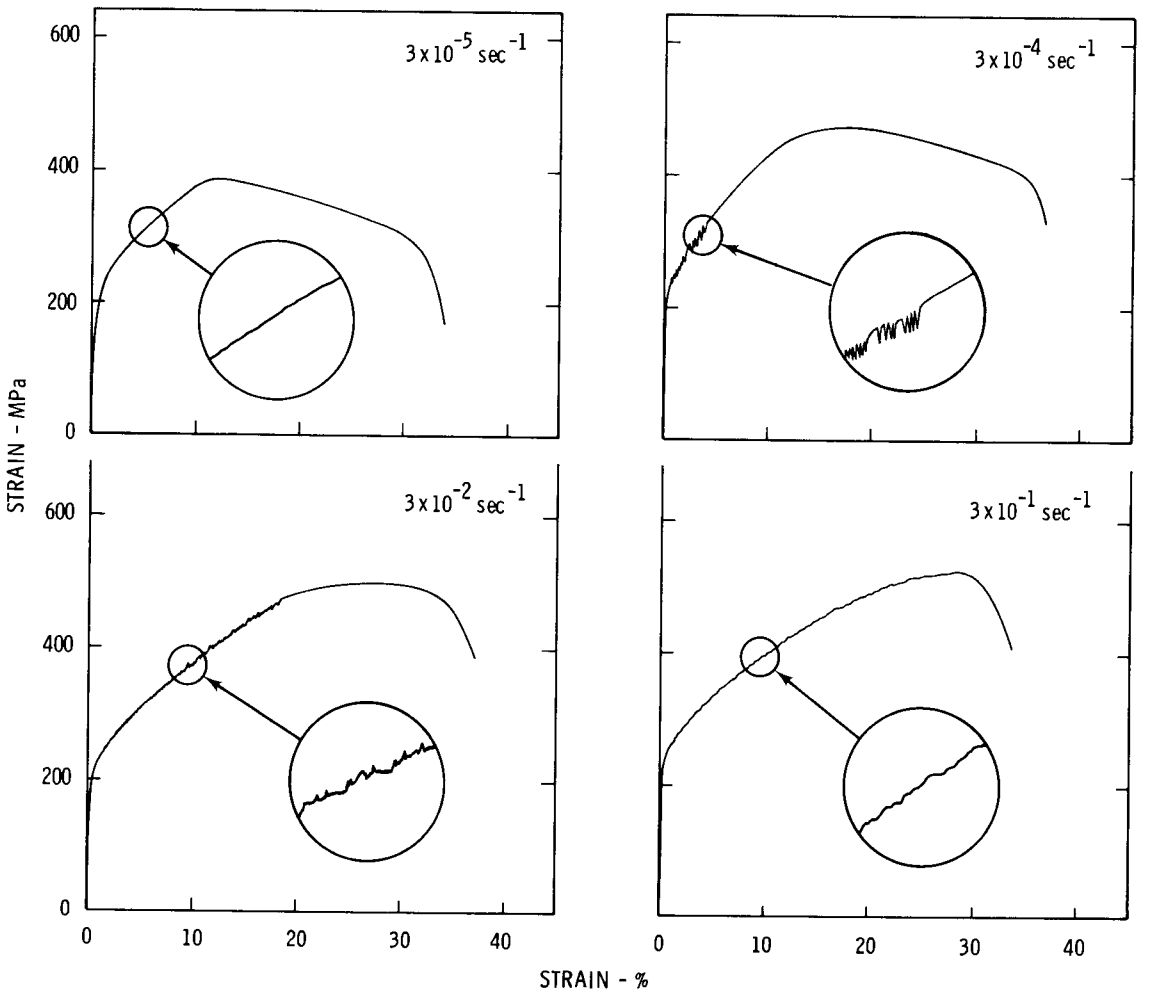

FIGURE 5.16 Strain Rate Effects on Serrated Flow in Alloy 600 at 649°C (1200°F)

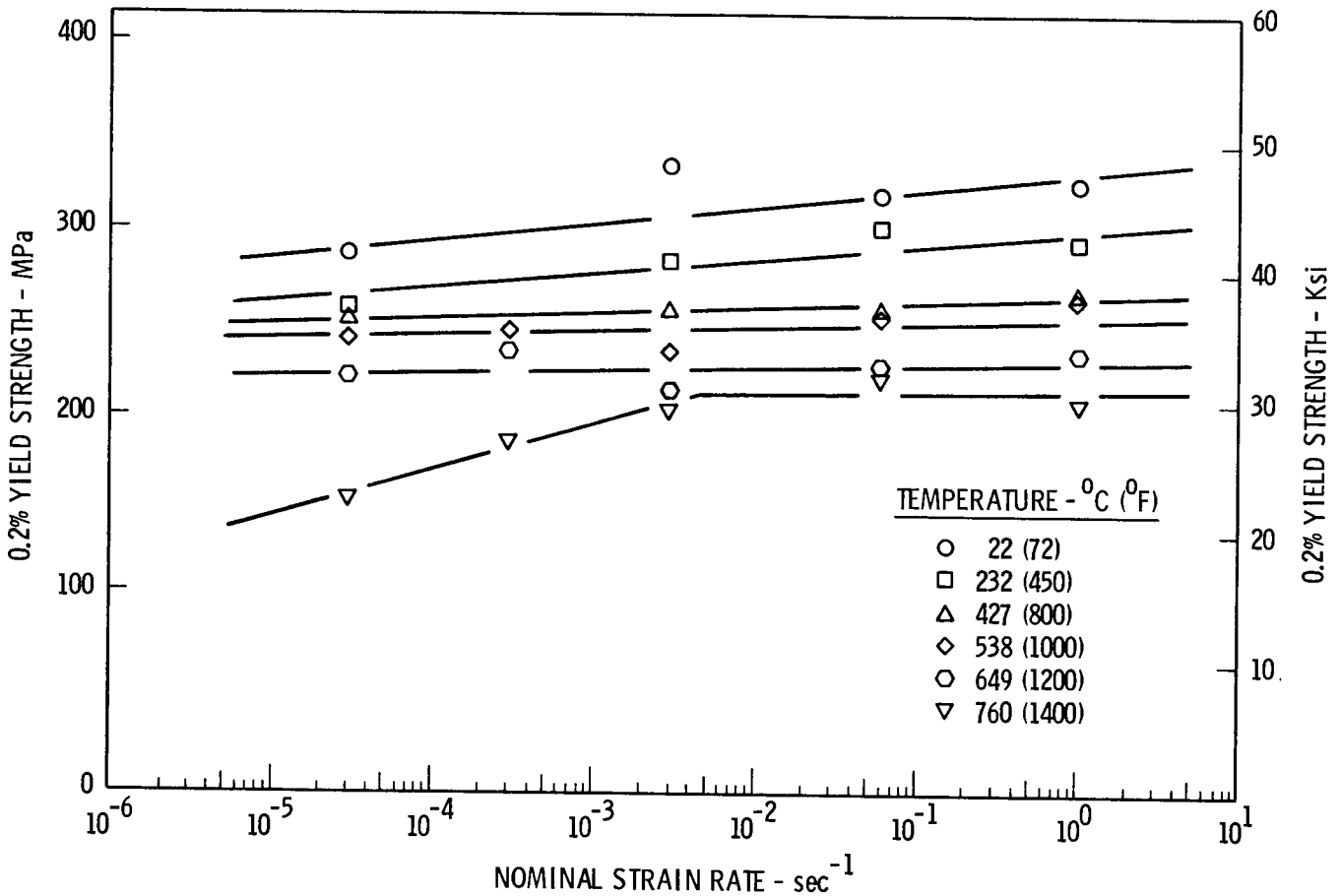

FIGURE 5.17 Strain Rate and Temperature Dependence of the 0.2% Yield Strength of Alloy 600.

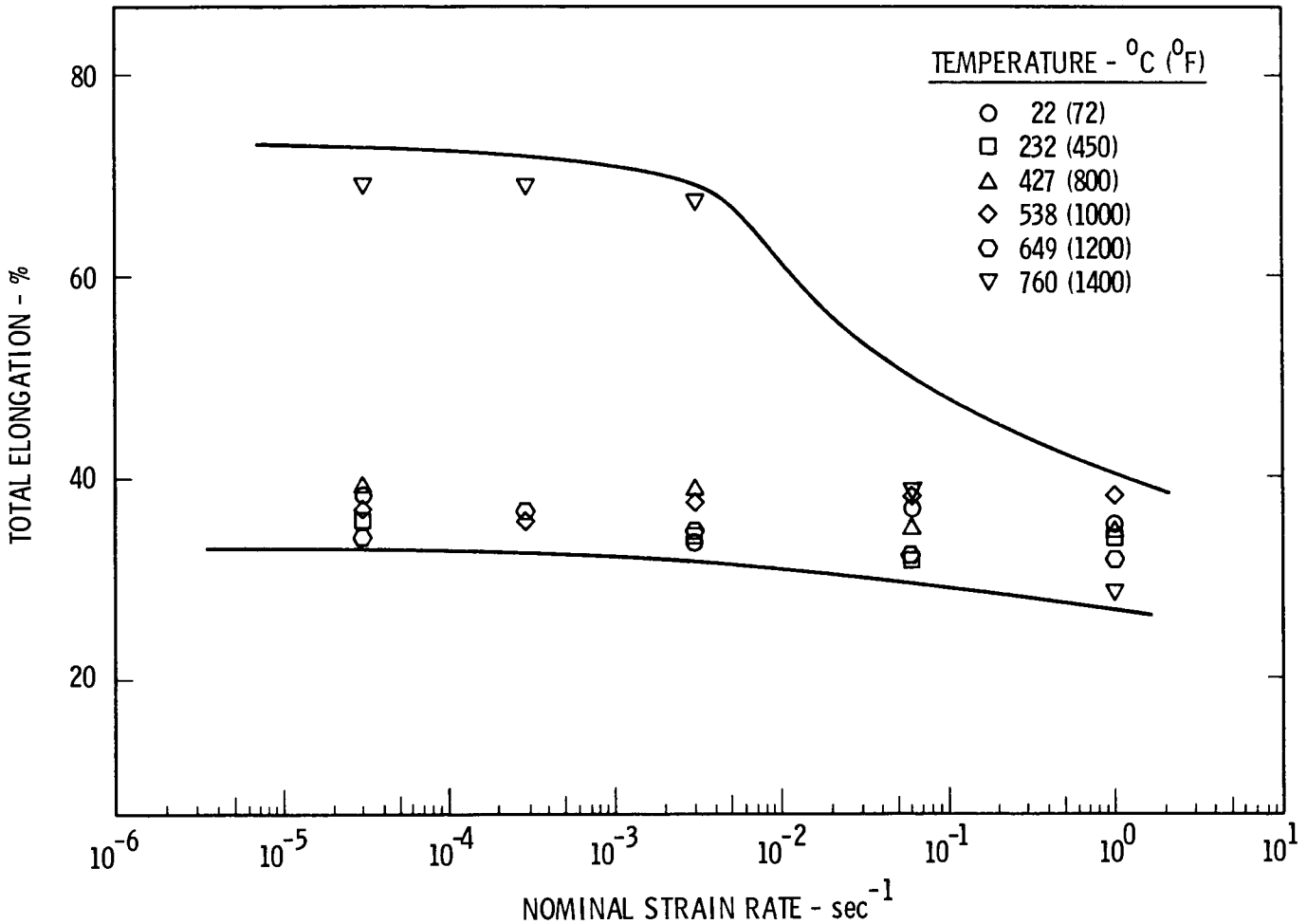

FIGURE 5.18 Strain Rate and Temperature Dependence of the Total Elongation of Alloy 600.

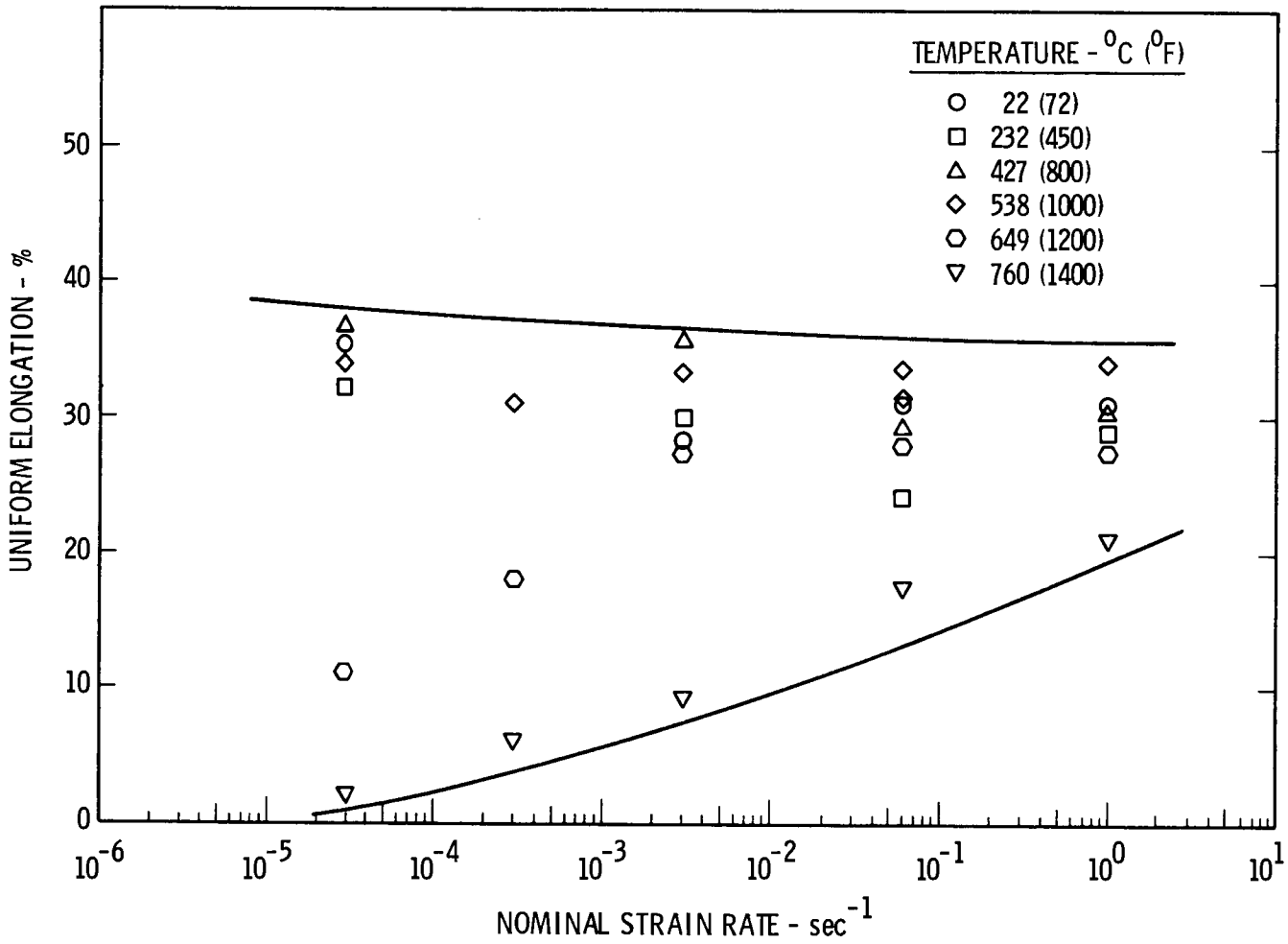

FIGURE 5.19 Strain Rate and Temperature Dependence of the Uniform Elongation of Alloy 600.

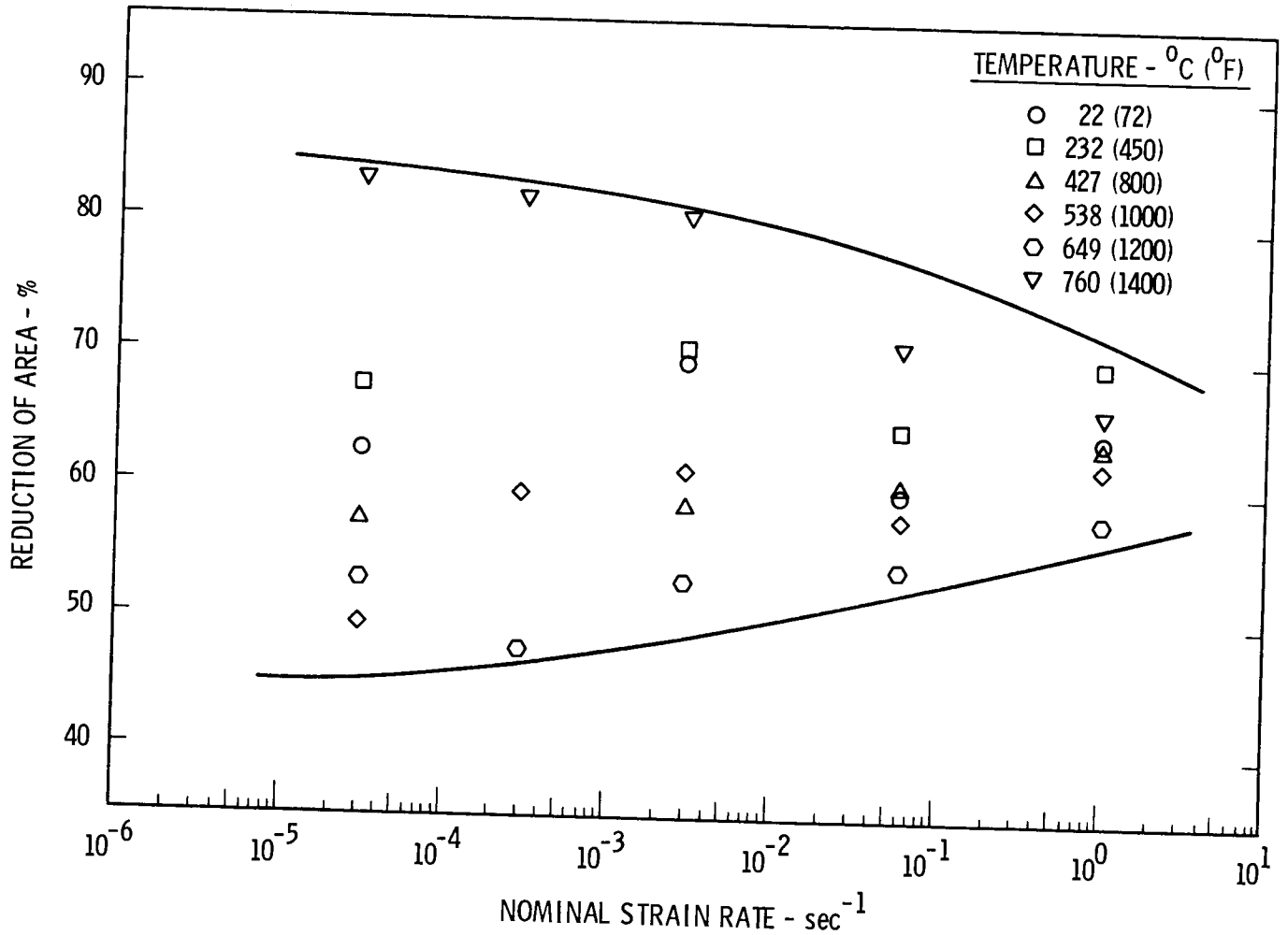

FIGURE 5.20 Strain Rate and Temperature Dependence of the Reduction of Area and of Alloy 600.

ductility parameters are more dependent on temperatures at the lower test rates than at the higher rates.

5.2.4.3 Expected Accomplishments

Characterization of the tensile properties of Alloy 600 thermally exposed for 10,000 hours will be completed during the next reporting period.

5.3 MATERIALS INFORMATION DOCUMENTATION - J. C. Spanner, R. A. Moen, and M. F. Marchbanks

5.3.1 Objective

The objective of this program is to manage, coordinate, and publish the reference for advanced nuclear energy systems programs.

5.3.2 Accomplishments and Status

Nuclear Systems Materials Handbook

Update Package No. 4 was completed in terms of Advisory Group review/approval, final page preparation, and printing. The 103-page package contained new pages describing:

- Effect of neutron irradiation on the stress-strain behavior of annealed and 20 percent cold worked Type 316 stainless steel.
- Effect of strain rate on the flow stress behavior of annealed and 20 percent cold worked Type 316 stainless steel for both unirradiated and irradiated material.

Update Package No. 5 progressed to the point of approval by the Advisory Group, and final page preparations are 90 percent complete. That package contains over 70 pages describing:

- Tensile and yield strength of 2-1/4 Cr-1Mo steel.
- Introductory pages for Inconel X-750.
- Introductory pages and tensile properties (strength and ductility) for 6061-T6 aluminum.

Draft 2 of the initial contents of Volume 3, "Materials and Processes: Selection and Control" has been completed and is currently in the Advisory Group review cycle. Sections have been prepared in the following areas:

- Cost and Factors Affecting Costs
- Special Process Precautions
- Metal Removal
- Thermal Treatments
- Surface Treatments
- Marking Materials
- Handling and Preparation for Shipping and Storage

Computer capabilities in terms of equipment and software were enhanced during the reporting period. A 2000 baud interface was installed for the telephone connection between the Tektronix large screen cathode ray tube (CRT) terminal and the CYBER computer. This coupled with the digitizer and hard-copy unit helps to expedite page preparation activities. A computer program used to produce camera-ready graph pages has been revised to utilize various enhanced character or type styles to give the finished masters a more pleasing and professional appearance. Additional computer software has been developed to aid in preparation of data pages. The new software enables interactive development of non-linear and linear curve fits, and display of the results on the CRT terminal screen.

Guidelines used in operation of the Handbook program were revised and reissued to all Working Group chairmen and Advisory Group members. These guidelines were provided in Rev. 1 of General Operating Guide, HEDL-MG-45, Part A. A companion document, Personnel Directory, HEDL-MG-45, Part B, was also revised and provided to key program participants as a continued means of enhancing communications.

5.3.3 Expected Achievements in the Next Reporting Period

Update Package No. 4 will be distributed in early October to over 650 current Handbook users. Update Package No. 5 will be printed and distributed near the end of the quarter.

The sixth semiannual meeting of the Advisory Group will take place at Atomics International on November 4 and 5, 1976.

5.4 REFERENCES

1. L. A. James and R. L. Knecht, "Fatigue-Crack Propagation Behavior of Type 304 Stainless Steel in a Liquid Sodium Environment", Metallurgical Transactions, Vol. 6A, No. 1, pp. 109-116, 1975.
2. L. A. James, "The Effect of Stress Ratio Upon the Elevated Temperature Fatigue-Crack Growth Behavior of Several Reactor Structural Materials", Report HEDL-TME 75-20, Westinghouse Hanford Co., 1975.
3. P. Marshall, "The Fatigue Behavior of Annealed AISI 316 Stainless Steel in Air and High Temperature Sodium: Review and Preliminary Results", Report RD/B/N3236, Central Electricity Generating Board, 1974.
4. E. K. Priddle and C. Wittshire, "The Measurement of Fatigue-Crack Propagation in Specimens Immersed in Liquid Sodium at Elevated Temperatures", International Journal of Fracture, Vol. 11, No. 4, pp. 697-700, 1975.
5. J. F. Copeland and G. R. Dodson, in "Sixth Quarterly Report, STeam Generator Materials Engineering", Report GEAP-14029-6, p. 5-1, General Electric Co., 1976.
6. L. A. James, "Fatigue-Crack Propagation Behavior of Inconel 718", Report HEDL-TME 75-80, Westinghouse Hanford Co., 1976.
7. L. A. James, "Fatigue-Crack Propagation Behavior of Inconel 600", Report HEDL-TME 76-43, Westinghouse Hanford Co., 1976.
8. W. R. Corwin and C. R. Brinkman, "Effects of Steam and Helium Environments on the Elevated Temperature Subcritical Crack Growth of 2-1/4 Cr-1Mo Steel", Proc. 2nd Int. Conf. Mech. Behavior of Materials, pp. 1498-1502, American Society for Metals, 1976.
9. L. A. James and J. A. Williams, "Fatigue-Crack Propagation in Unirradiated and Irradiated ASTM A533-B Steel at Low Cyclic Frequency", Journal of Nuclear Materials, Vol. 49, No. 3, pp. 241-243, 1973.
10. C. R. Brinkman, W. R. Corwin, M. K. Booker, T. L. Hebble and R. L. Kleuh, "Time Dependent Mechanical Properties of 2-1/4 Cr-1Mo Steel for Use in Steam Generator Design", Report ORNL-5125, Oak Ridge National Laboratory, 1976.

11. J. D. Landes and J. A. Begley, "Test Results from J-Integral Studies: An Attempt to Establish a J_{Ic} Testing Procedure," ASTM STP 560, 1974, p. 170.

12. W. J. Mills, "The Ductile Fracture Toughness Response of Inconel 718 and Inconel X-750 at 75°F and 800°F," Reference Core and Structural Materials Quarterly Report, HEDL Report TC-675, April-June 1976.

13. F. S. Acton, Analysis of Straight Line Data, John Wiley & Sons, Inc.; New York, 1959, pp. 184-187.

14. C. F. Jenkins and G. V. Smith, "Serrated Plastic Flow in Austenitic Stainless Steel", Transactions AIME, Vol. 245, October 1969, pp. 2149-2156.

15. D. E. Scnon and G. V. Smith, "Effect of Grain Size and Temperature on the Strengthening of Nickel and a Nickel-Cobalt Alloy by Carbon", Transactions AIME, Vol. 242, August 1968, pp. 1527-1533.

16. D. Fahr, "Analysis of Stress-Strain Behavior of Type 316 Stainless Steel", Oak Ridge National Laboratory, ORNL-TM-4292, November 1973.

17. E. Shapiro and G. E. Dieter, "High Temperature-High Strain RAte Fracture of Inconel 600", Metallurgical Transactions, Vol. 1, June 1960, pp. 1711-1719.

18. J. M. Steichen, "High Strain Rate Tensile Properties of AISI Type 304 Stainless Steel", Journal of Engineering Materials and Technology, Vol. 95, July 1973, pp. 182-185.

19. G. L. Dotson, "The Effect of Slow-Constant Strain Rates on the Tensile Properties of Selected Alloys at Room and Elevated Temperatures", Journal of Engineering Materials and Technology, Vol. 95, Oct. 1973, pp. 42-49.

20. R. W. Swindeman, "Representation of the High-Temperature Tensile Behavior Reannealed Type 304 Stainless Steel by the Voce Equation", Journal of Engineering Materials and Technology, Vol. 97, No. 2, April 1975, pp. 98-106.

6.0 WESTINGHOUSE ADVANCED REACTORS DIVISION

E. C. Bishop, W. E. Ray

6.1 INTRODUCTION

Two programs are being performed at Westinghouse Advanced Reactors Division (ARD). The first program is "Validation of High Temperature Design Methods and Criteria" (189a CW063). Two of the tasks in this program are "Basic Specimen Testing" and "Tubular Specimen Testing". The specimen material for both tasks was supplied from ORNL reference heats of Type 304 and 316 stainless steel. The second program is "Component Materials Compatibility" (189a CW065). One of the tasks in this program is "Mechanical Properties".

The basic specimen tests are performed on plates and bars loaded at 1100°F (593°C). Specimen designs have been selected to provide nonuniform stress distributions (uniaxial, plane stress, and plane strain) and to determine the effects of holes, notches, and welds in various orientations. Uniform and stepped loading is applied at levels sufficient to cause significant creep strain in hundreds of hours and rupture in several thousand hours. Test data are used for: verification of constitutive equations for time-dependent material response, validation of analytical techniques for nonuniform stress states, and investigation of strain limits in base metal, welds, and at geometrical discontinuities.

The tubular specimen tests are being run at 1100°F (593°C) with various combinations of internal pressure and axial load to produce a uniform stress state with a range of biaxiality. Load levels have been selected to determine secondary creep rates in 2000 hours with both steady state and step loading. A limited number of tests will be continued to rupture with geometrical discontinuities. The test data are primarily used for verification of constitutive equations and validation of analytical techniques for shells under multiaxial states of stress.

Westinghouse ARD is performing experiments to identify the effects of a flowing sodium environment on the mechanical properties of LMFBR

structural components. The present scope of the program involves three materials: Type 316 Stainless Steel, Type 304 Stainless Steel, and Inconel 718. Work on these materials is in support of the CRBRP upper plenum and hot leg piping components design. Inconel 718 is also being evaluated on a limited basis, relative to the thermal transients to be experienced by the thermal baffles in the upper plenum of the FFTF reactor. More extensive evaluations in the material for the CRBRP will follow. Low-cycle fatigue, creep-fatigue, and creep-rupture experiments are being performed in flowing sodium at elevated temperatures on as-fabricated, aged, and sodium pre-exposed samples in order to identify the environmental effects. In addition, in-air experiments are being performed on the same materials to obtain baseline data.

This report covers the periods: Sections 6.2 and 6.3 - June 1, 1976 through August 31, 1976 and Section 6.4 - May 1, 1976 through July 31, 1976.

6.2 BASIC SPECIMEN TESTING - M. J. Manjoine (Westinghouse Research Laboratories)

6.2.1 Type 304 Stainless Steel Testing

6.2.1.1 BTW-2 Transverse Weld in B-Type Model at 19 ksi (131 MPa) and 1100°F (593°C)

After 9689 hours the overall creep had reduced to 6×10^{-5}% per hour. The accumulated strain at that time was 1.45%. The specimen was cooled and unloaded for photographic measurement and inspection at 10,672 hours. No visible evidence of crack initiation could be detected. This life equals that of the base metal specimen of this geometry. The test will be continued to observe crack initiation and growth.

6.2.1.2 BAW-2 Axial Weld in B-Type Model at 22 ksi (151.7 MPa) and 1100°F (593°C)

This test was interrupted at 4500 hours for photographic inspection. Cracks had developed over the middle inch of the three-inch gauge length.

The major cracks had grown to 0.1 inch (2.5 mm) in length with an average spacing of 0.15 inch (3.81 mm).

The test was restarted and failure occurred at 5,040 hours with an overall creep strain of about 13.6%. The cracks had propagated about 25% of the width on each side of the weld. This test confirms the result obtained from BAW-1 indicating that the life of an axial weld specimen is longer than that for a comparable base metal specimen.

6.2.1.3 C-4 B-Type Model with Central Hole 18 ksi (124.1 MPa) and 1100°F (593°C)

The test was interrupted at 3043 hours for photographic inspection. The specimen had cracked through the thickness at the central hole at the mid-length diameter. The crack had propagated about .06 inch (1.5 mm) across the width at each side of the mid-length diameter.

The test was again interrupted at 4005 hours for photographic inspection. The cracks which had initiated at the minimum section at the edges of the hole had forked at the .06 inch (1.5 mm) length with an included angle of about 60°.

After 4520 hours the cracks were again photographed. The maximum extent of the crack was about 0.23 inch (5.9 mm) from the edge of the hole. The general path of the forked cracking is still perpendicular to the direction of the axial load or principal stress. The test is being continued.

6.2.2 Type 316 Stainless Steel Tests

6.2.2.1 6A1 Type A Model at 32.5 ksi (224.1 MPa) and 1100°F (593°C)

The proportional limit of this specimen was 13.7 ksi (94.4 MPa) and the overall plastic deflection at 32.5 ksi (224.1 MPa) was 0.156 inches (3.96 mm). The nominal loading strain was 5.2% for the three inch gage length. At 264 hours the specimen was in to third stage creep and the minimum creep rate had been about 1×10^{-2}% per hour. Rupture occurred after 604 hours.

6.2.2.2 6D2 Notched Bar at 28 ksi (193 MPa) and 1100°F (593°C)

After 2562 hours, the overall deflection of this specimen was 0.015 inch (.38 mm) which is equal to the failure strain of the specimen 6D1 tested at 35 ksi (224.1 MPa). After 3353 hours the deflection rate had decreased at 2.7×10^{-6} in/hr (6.8×10^{-7} mm/hr) and the life was six times that estimated for similar specimens made from 304 SS. This specimen is now at 4075 hours and is deforming at a steady overall deflection of 2×10^{-6} in/hr. (5×10^{-7} mm/hr).

6.2.2.3 6D3 Notched Bar at 25 ksi (172.4 MPa) and 1100°F (593°C)

After 4120 hours the overall deflection is .011 inch (.28 mm) and the deflection rate is steady at 1.6×10^{-6} in/hr. (4.1×10^{-7} mm/hr).

6.3 TUBULAR SPECIMEN TESTING - C. Daniels, K. C. Thomas, P. C. S. Wu

6.3.1 Type 304 SS Testing and Analysis

Constant condition creep and rupture testing of Type 304 SS has previously been completed. A paper presenting these results was given at the 2nd International Conference of Mechanical Behavior of Materials in Boston, Mass. on August 18, 1976. It was entitled "Multiaxial Creep Behavior of Type 304 Stainless Steel Tubular Specimens" and authored by P. C. S. Wu, C. Daniels and K. C. Thomas. This paper presented in concise form all of the corrected results for these tests and most of the final analysis. All of this information was previously published in the quarterly reports.

Creep testing of tubular specimens under variable stress conditions has been completed. The testing of these specimens to rupture is currently proceeding. Preliminary analysis of these tests are underway. The basic data has been reduced. Each segment which is under constant stress will be evaluated separately. The segments will be related to the master equation developed for the constant condition creep tests. An additional function will be developed to account for the creep history of each segment.

6.3.2 Type 316 SS Heat Treatment

Heat treatment tests were carried out to determine the heat treatment procedure to be used for reference heat Type 316 SS. The object is to have annealed material which conforms to ORNL guidelines which are:

0.2% yield strength	28-32 ksi (193-220 MPa)
ASTM grain size	3-5
Hardness R_B	64-74
Annealing temperature	1950°F ± 50 (1068° C ± 25)

Flat tensile specimens 0.050" (1.3 mm) thick were machined from the reference heat Type 316 SS, heat treated and tested in a tensile machine at room temperature. The annealing temperature was held constant and the hold time at temperature was varied. A listing of these results is shown in Table 6.1.

A hold time of 30 min. produced the optimum combinations of the properties within the tolerance bands. More tests are planned to confirm these results.

In anticipation of acceptable heat treatment results, eight full sized tubular specimens were machined. They are presently undergoing inspection. Upon release from quality assurance, the gage lengths will be heat treated. Then the end caps will be welded and the specimens final machined.

6.4 SODIUM EFFECTS ON MECHANICAL PROPERTIES OF STRUCTURAL MATERIALS

P. N. Flagella, J. Kahrs, J. Denne, P. Wu, S. L. Schrock

Westinghouse ARD is performing experiments to identify the effects of a flowing sodium environment on the mechanical properties of LMFBR materials used for structural components. The present scope of the program involves Type 316 stainless steel and Inconel 718. Work on these materials is in support of the CRBRP design efforts on the upper plenum and hot leg piping components. Low cycle fatigue, creep fatigue, and creep rupture experiments are being performed in flowing sodium at elevated temperatures on as-fabricated, aged, and sodium pre-exposed samples

Table 6.1 Heat Treatment Results of Type 316 Stainless Steel at 1950°F

Specimen Number	Hold Time (min.)	Hardness Before Heat Treating (R_B)	Hardness After Heat Treating (R_B)	Grain Size ASTM	Yield Stress at .2% (ksi)
167A	0	-	76	6 1/2	32
167H	0	76	73	6 1/2	34
167B	10	75	70	5	32
167C	10	75	69	5	31.6
167D	15	75	69	5 and 4	30.8
167E	20	77	69	5	28
167F	20	75	67	5 and 4	32
167G	30	75	67	5 and 4	28.4

in order to identify the environmental effects. In addition, in-air experiments are being performed on the same materials to obtain baseline data.

The present report describes the results obtained to date on creep rupture and low cycle fatigue tests in flowing sodium of solution annealed Type 316 stainless steel with various pre-treatments.

6.4.1 Type 316 Stainless Steel

During this reporting period, additional creep-rupture and low cycle fatigue tests were performed on material from Heat 65805 in flowing sodium. The material was received in plate form as 2.5 cm (1 inch) thick and solution annealed. After cutting the plate into 2.5 cm square bars, in the major rolling direction of the plate, test samples were machined with the gage section 0.63 cm dia. x 1.27 cm long. Some samples were tested in the as-fabricated condition (solution annealed) and others were exposed to sodium prior to testing. Results of the low-cycle strain-controlled fatigue tests ($\dot{\varepsilon} = 4 \times 10^{-3}$ sec^{-1}) obtained to date are given in Table 6.2, with the fatigue curves shown in Figure 6.1. The data show a significant decrease in fatigue life after sodium exposure at 593°C for 2000 hours, especially for total strain ranges less than approximately 0.7%, when compared to the results obtained for as-fabricated material. The additional decrease in fatigue life is much less for the material sodium pre-exposed at 593°C for 5000 hours. The data in Figure 6.1 also shows a slope change for the plastic strain range curve beyond approximately 20,000 cycles to failure (commonly referred to as the transition fatigue life). Figures 6.2, 6.3, and 6.4 present the cyclic stress response for the test identified in Table 6.2. The curves for as-fabricated material in Figure 6.2 show a significantly higher saturation stress for the same total strain range, than that required for the pre-exposed material (Figures 6.3 and 6.4). In addition, at total strain ranges less than 1%, significant secondary hardening is identified, with the magnitude increasing as the strain range is decreased (and fatigue life increases). A similar trend in secondary hardening is shown for the sodium pre-exposed samples (Figures

Table 6.2 Low Cycle Fatigue[a] Results for Solution Annealed Type 316 Stainless Steel[b] Tested in Flowing Sodium[c] at 593°C

Sample Number	Sodium Pre-Exposure Hours at 593°C	Stress Range[d]		Strain Range, %		N_f
		ksi	MPa	$\Delta\varepsilon_t$	$\Delta\varepsilon_t$	
32	5000	85.0	586.1	1.05	0.65	2,355
33	5000	56.8	391.6	0.45	0.18	59,592
36	5000	53.7	370.3	0.36	0.11	491,617
50	2000	113.2	780.5	2.00	1.48	331
45	2000	86.0	593.0	1.09	0.69	1,927
47	2000	74.6	514.4	0.72	0.37	7,864
105	2000	58.2	401.3	0.39	0.12	382,119
144	0	121.4	837.0	2.01	1.45	394
141	0	97.2	670.2	1.10	0.65	2,265
170	0	72.0	496.5	0.58	0.25	16,467
160	0	73.8	508.8	0.49	0.15	124,900

(a) Strain Rate: 4×10^{-3} sec^{-1}
Control Mode: Axial Strain
Wave Form: Triangular, zero mean strain

(b) Heat 65805, 2.5 cm thick plate

(c) Oxygen content of sodium, 1.5 to 2.0 ppm (cold trap at 145° to 150°C)

(d) at $N_f/2$

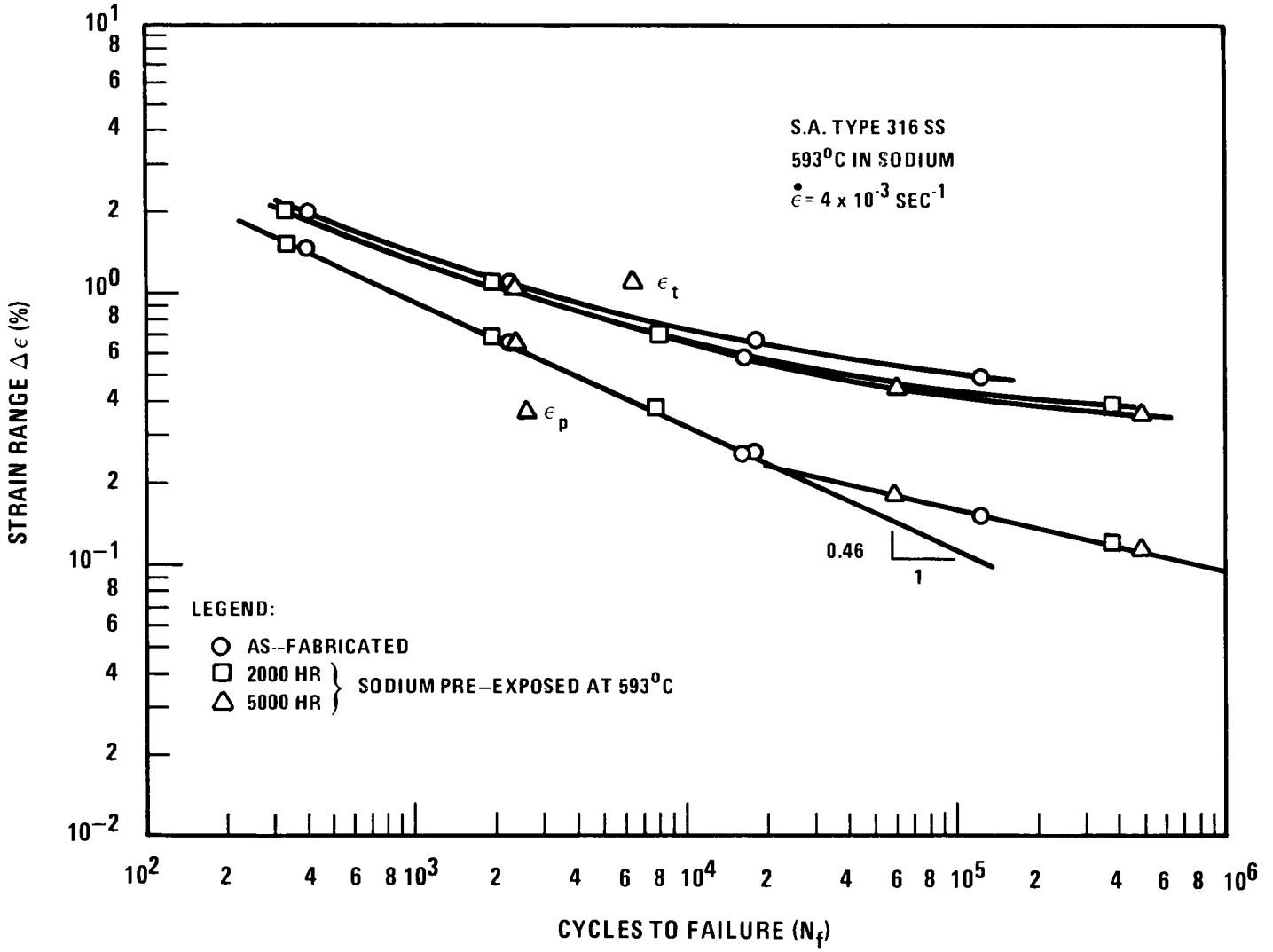

Figure 6.1 Low Cycle Fatigue Curves for Solution Annealed Type 316 Stainless Steel Tested in Flowing Sodium at 593°C

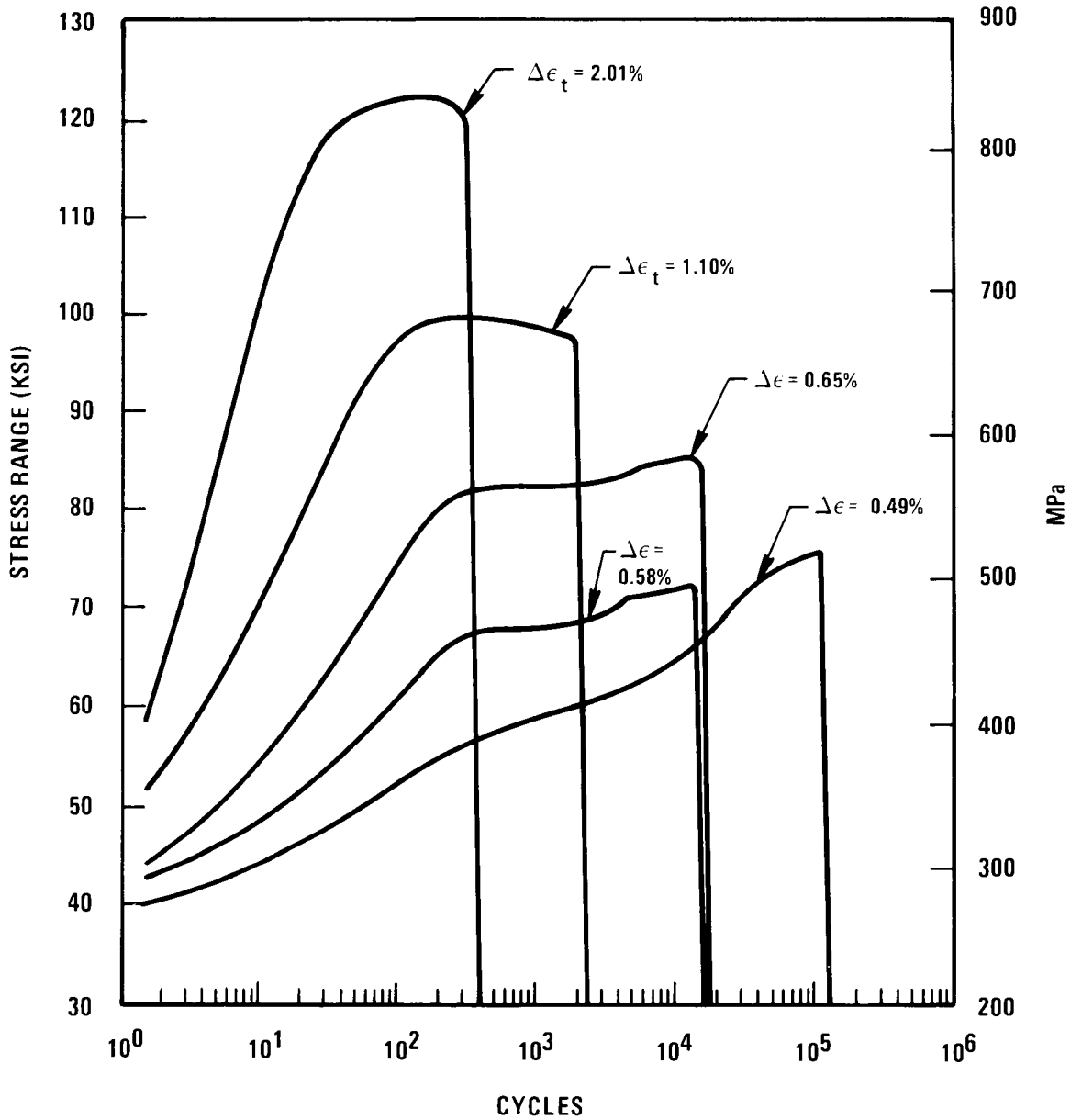

Figure 6.2 Stress Range Curves for As-Fabricated Solution Annealed Type 316 Stainless Steel Tested in Sodium at 593°C

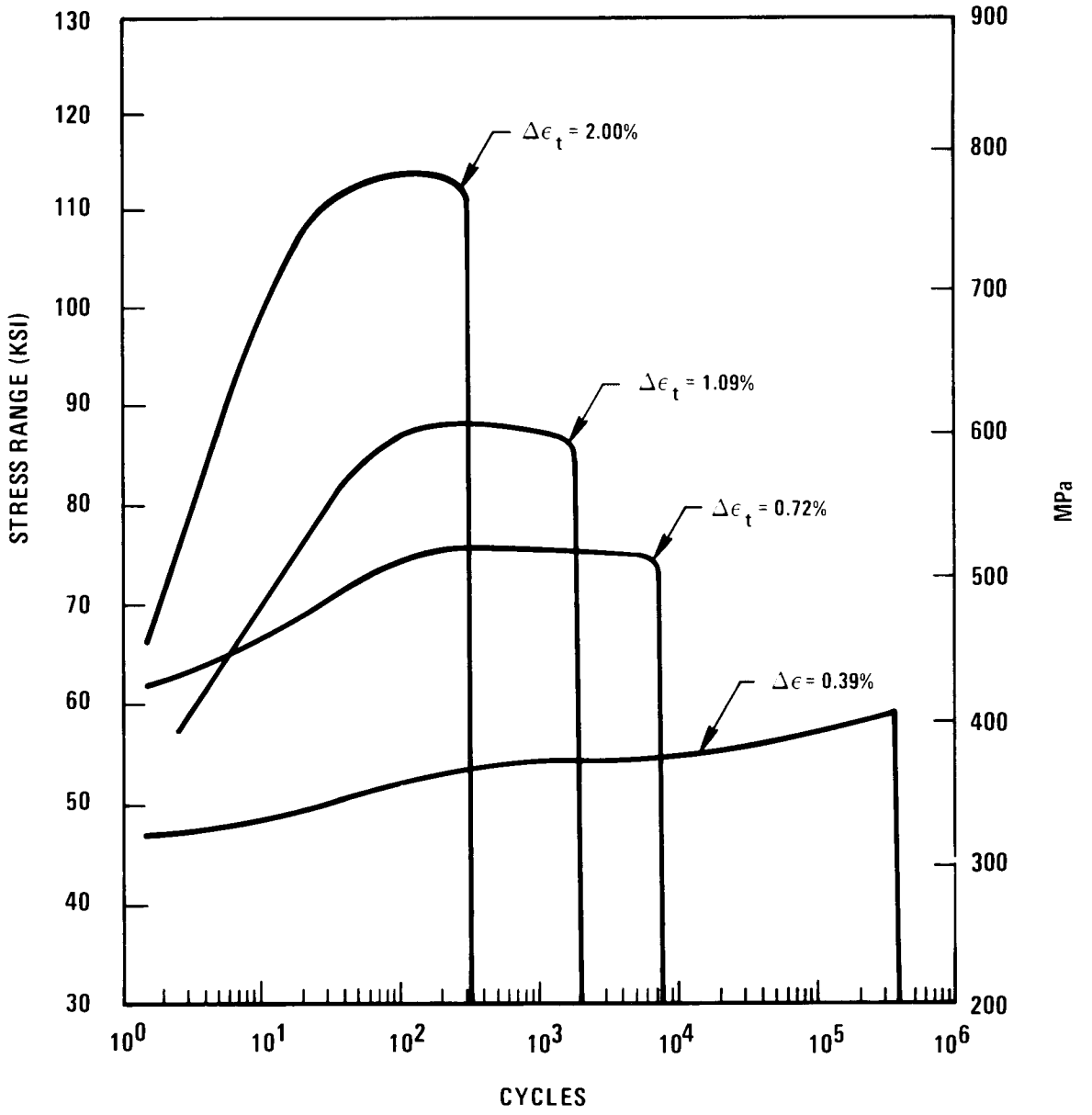

Figure 6.3 Stress Range Curves for Solution Annealed Type 316 Stainless Steel After Sodium Exposed at 593°C for 2000 Hours. Tested in Sodium at 593°C

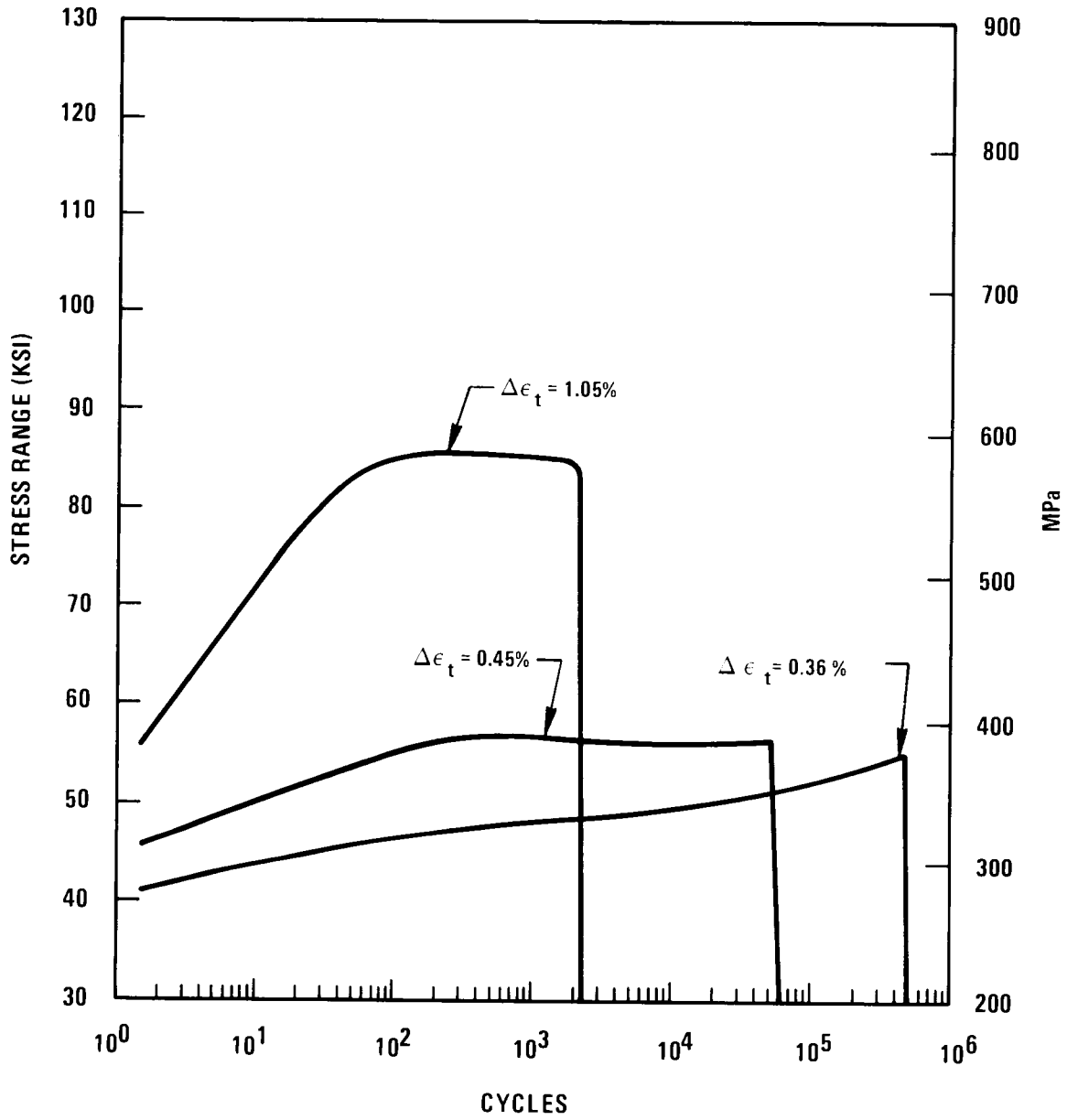

Figure 6.4 Stress Range Curves for Solution Annealed Type 316 Stainless Steel After Sodium Exposure at 593°C for 5000 Hours. Tested in Sodium at 593°C

6.3 and 6.4) but of a lower magnitude and begins to appear at lower strain ranges. These differences are probably mainly related to the aging of the material during the sodium pre-exposure, resulting in microstructural changes. Metallographic evaluations will be performed to identify the differences in microstructure.

Additional creep-rupture tests of the solution annealed Type 316 stainless steel material from Heat 65805 were performed in flowing sodium at 593°C. A tabulation of the results obtained to date for tests performed at 32.5 and 40 ksi are given in Table 6.3. Figures 6.5 and 6.6 present the creep curves for the same tests. The samples sodium pre-exposed show a large increase in rupture life and ductility at both stress levels when compared to results for the as-fabricated samples. The minimum creep rate for the pre-exposed material is also higher than the as-fabricated material. The results also show a decrease in rupture life and an increase in minimum creep rate as the pre-exposure time is increased from 2000 to 5000 hours. At the same time, the strain-on-loading values decrease, rather than increase, as the pre-exposure time is increased. This implies that the material with the longer pre-exposure time has the highest yield strength. Short term tensile tests and metallurgical evaluations will be required to confirm the interpretation. Testing at lower stress levels (and longer times) are in progress to determine if the differences mentioned above persist.

6.5 REFERENCES

(1) "Validation of High Temperature Design Methods and Criteria Quarterly Progress Report for Period Ending November 30, 1973," W-ARD-HT-3045-4, March 1974 (Availability: Technical Information Center).

Table 6.3 Creep-Rupture Results for Solution Annealed Type 316 Stainless Steel[a] Tested in Flowing Sodium[c] at 593°C

Sample Number	Na Pre-Exposure Hours at 593°C	Stress[b] ksi	Stress[b] MPa	Loading Strain %	Hours to Indicated Creep Strain, % 0.5	1.0	2.0	3.0	5.0	7.0	10.0	Min. Creep Rate, %/hr	0.2% Offset Time, hr	0.2% Offset Strain, %	Time to Rupture, hr	Total Elong., % Creep Curve	Total Elong., % Post Test
146	0	32.5	224.1	4.61	12.5	39.0	130	250	412	504	580	8.5×10^{-3}	350	4.1	640	20.3	21.8
080	2000	32.5	224.1	4.48	4.2	14.0	66.2	143	310	440	599	1.1×10^{-2}	320	5.1	1188	64.5	65.6
026	5000	32.5	224.1	3.78	17.7	49.0	118	183	289	382	520	1.5×10^{-2}	250	4.2	1144	72.9	76.5
149	0	40.0	275.8	10.74	4.7	12.6	24.8	37.1	60.6	73.6	--	8.1×10^{-2}	64.4	5.4	75.2	18.5	20.3
084	2000	40.0	275.8	8.60	1.0	2.6	6.5	11.0	22.0	33.2	50.4	1.8×10^{-1}	61.0	12.0	129	67.6	70.3
017	5000	40.0	275.8	6.73	1.0	2.3	5.2	8.6	16.4	24.4	36.3	2.5×10^{-1}	47.0	19.6	110	67.8	68.7

(a) Heat 65805, 2.5 cm thick plate

(b) Gage Section 0.63 cm dia. x 2.54 cm long

(c) Oxygen content of sodium, 1.5 x 2.0 ppm (cold trap at 145° to 150°C)

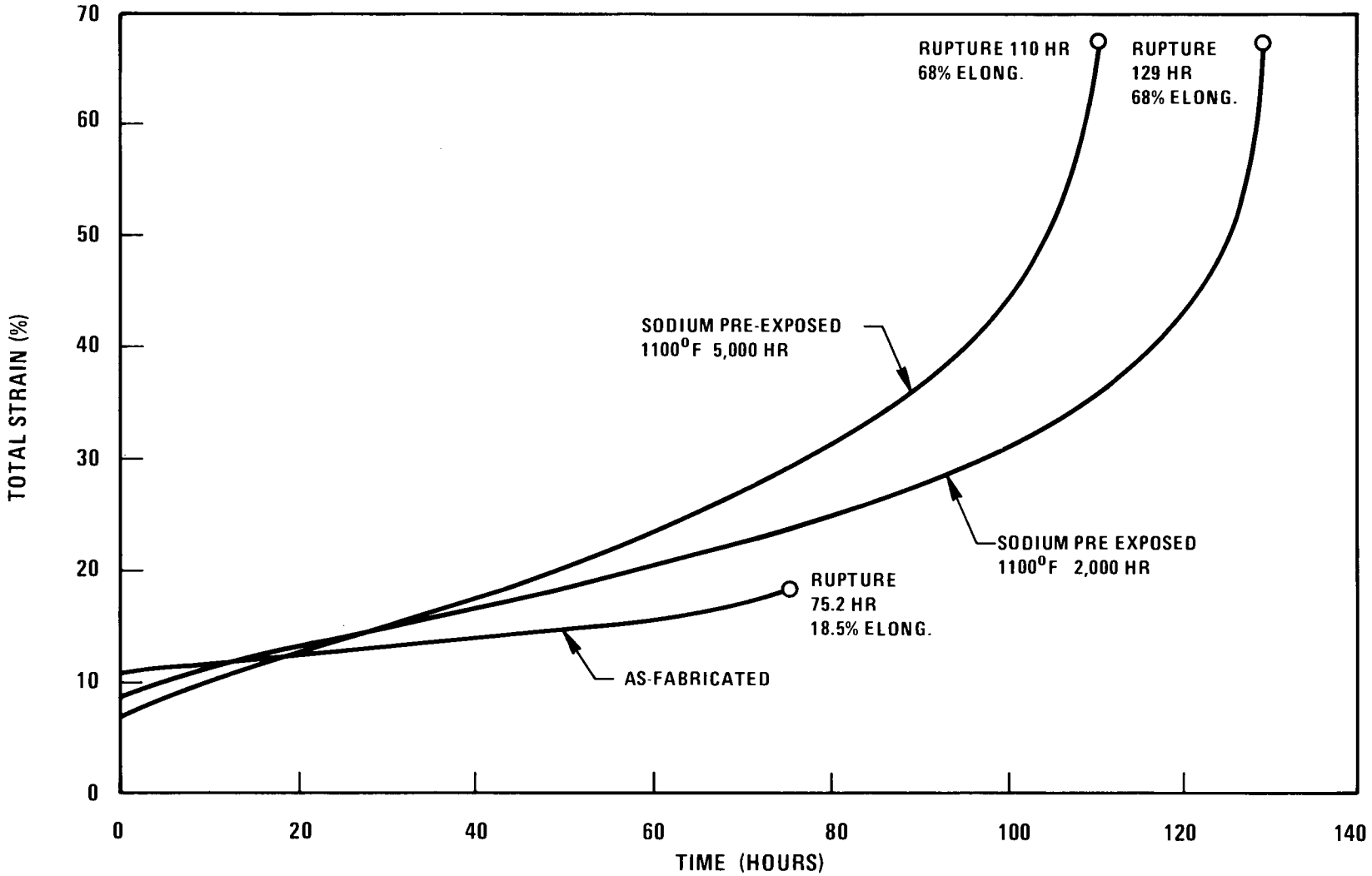

Figure 6.5 Creep-Rupture Curves for Solution Annealed Type 316 Stainless Steel Plate Tested at 593°C and 40.0 ksi in Flowing Sodium

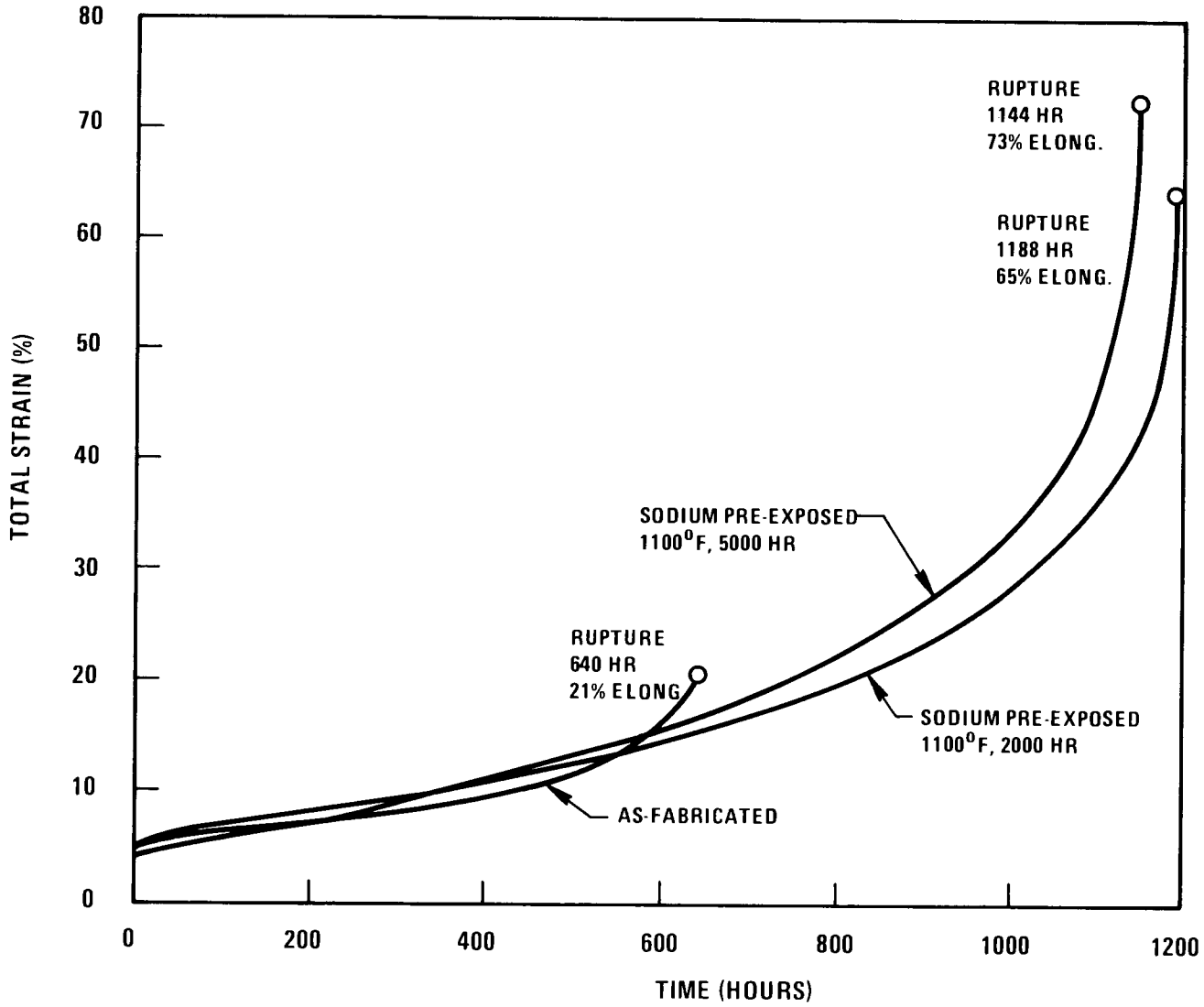

Figure 6.6 Creep-Rupture Curves for Solution Annealed Type 316 Stainless Steel Plate Tested in Flowing Sodium at 593°C and 32.5 ksi

7. UNIVERSITIES

7.1. UNIVERSITY OF CINCINNATI

J. Moteff

7.1.1. INTRODUCTION

The objective of this program is to (a) evaluate the time, temperature, and stress-dependent mechanical properties of reactor structural materials, (b) determine the relationship of these properties to the microstructure, (c) show the contribution of the microstructure to the internal stress fields and the subsequent influence on microcracking and the grain boundary sliding behavior during the normal plastic deformation at elevated temperatures, and (d) demonstrate the relationship of the hot micro-hardness properties with the hot-tensile properties of a class of commercial and advanced alloys presently under investigation at other laboratories. Special consideration is being given to operating conditions typical of nuclear reactor applications, including the knowledge that radiation environment can influence the substructure of these metals, a circumstance which can lead to significant changes in the conventional mechanical property behavior.

7.1.2. EXPERIMENTAL PROGRAM

Transmission electron microscopy has been used as the primary tool to study the deformation substructure of reactor structural materials resulting from creep, fatigue, and tensile testing at elevated temperatures. Complementary work using optical microscopy, scanning electron microscopy, and

hot-hardness testing has been performed to characterize the deformation and failure behavior. New work is underway to perform similar studies on the Commercial, the Developmental, and the Fundamental alloys being evaluated in the National Alloy Developmental Program with particular attention on the application of hot-hardness measurement as a strength microprobe.

7.1.2.1. Activation Energy for Creep of AISI 310 Stainless Steel and Inconel 718 Calculated from Hot-Hardness Data (R. Dorning)

Hot-hardness tests were performed in a high purity argon (99.999%) atmosphere on AISI 310 stainless steel and preliminary tests on Inconel 718. As shown in Fig. 7.1, the hardness curve of AISI 310 stainless steel is similar to that of AISI 330 stainless steel at temperatures above 300°C. The difference at lower temperatures is believed to be due to heat treatment variance. Sample preparation also effects the hardness at low temperatures since a cold work surface layer is introduced by cutting and polishing. Electro polishing was employed to minimize surface stress.

Tests above 0.75 T_m have been completed on Inconel 718 which displays the same general characteristics on the AISI 310 and 330 stainless steels at similar temperatures.

In a continuation of the work done on AISI 330 stainless steel the apparent activation energy for indentation hardness and the activation energy for creep have been calculated on

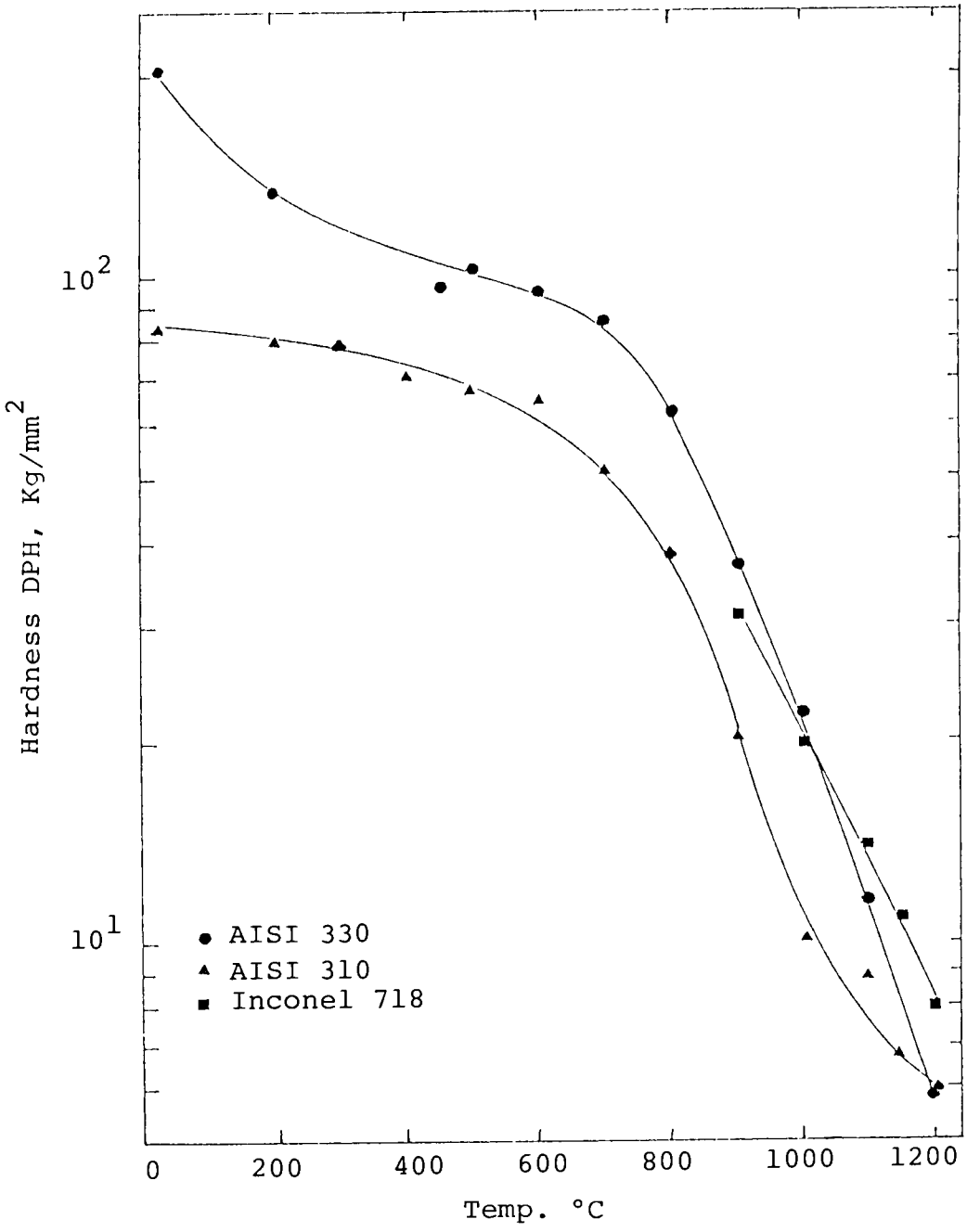

Fig. 7.1. Hardness versus Temperature for AISI 310 and Inconel 718 Compared to AISI 330.

AISI 310 stainless steel and Inconel 718. The apparent activation energy for indentation hardness was determined using the Larsen-Badse relation[1]

$$H = A \exp^{2Q'/RT} \qquad [7.1]$$

where the slopes in Fig. 7.2 are equal to 2Q'/R.

The results for AISI 310 stainless steel are

$$Q' = 6{,}200 \text{ cal/mole} \quad \text{for } T > 0.55 \text{ Tm}$$

$$Q' = 140 \text{ cal/mole} \quad \text{for } T < 0.55 \text{ Tm}$$

and for Inconel 718

$$Q' = 6{,}100 \text{ cal/mole} \quad \text{for } T > 0.55 \text{ Tm.}$$

The low apparent activation energy for indentation hardness has been explained by Sherby and Armstrong[2]. By using the expression

$$H/E = G \exp (Q/nRT) \qquad [7.2]$$

the activation energy for creep can be determined. The modulus compensated hardness data for AISI 310 stainless steel and Inconel 718 above 0.55 Tm versus 1/T are given in Fig. 7.3. The AISI 310 stainless steel displayed the same break at 0.75 Tm as the AISI 330 stainless steel (previous report). For a value of n = 5 in Equation 7.2, the activation energy for creep of 85,100 cal/mole for AISI 310 stainless steel and 63,500 cal/mole for Inconel 718 were obtained for T > 0.75 Tm.

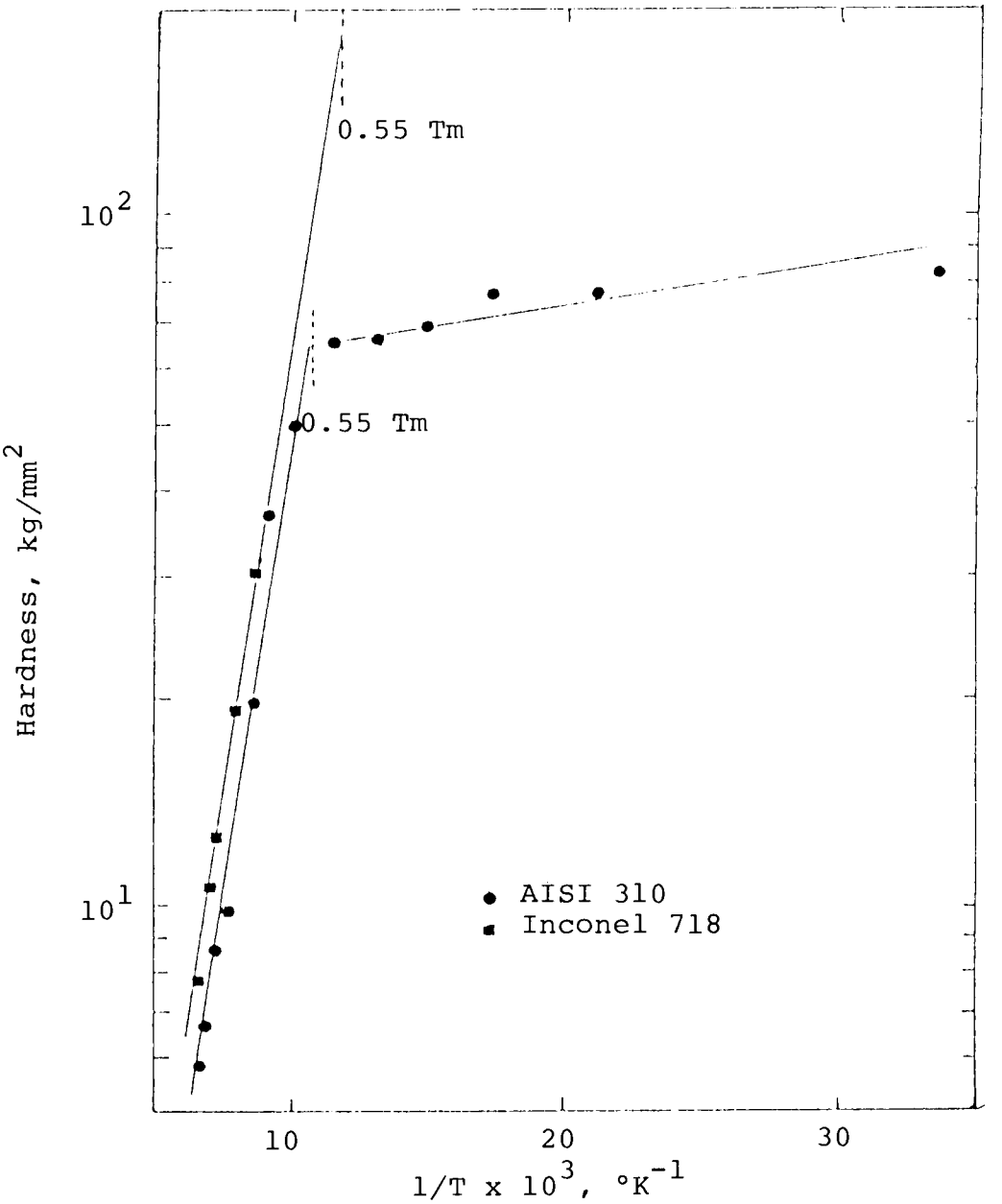

Fig. 7.2. Log Hardness versus 1/T for AISI 310 and Inconel 718.

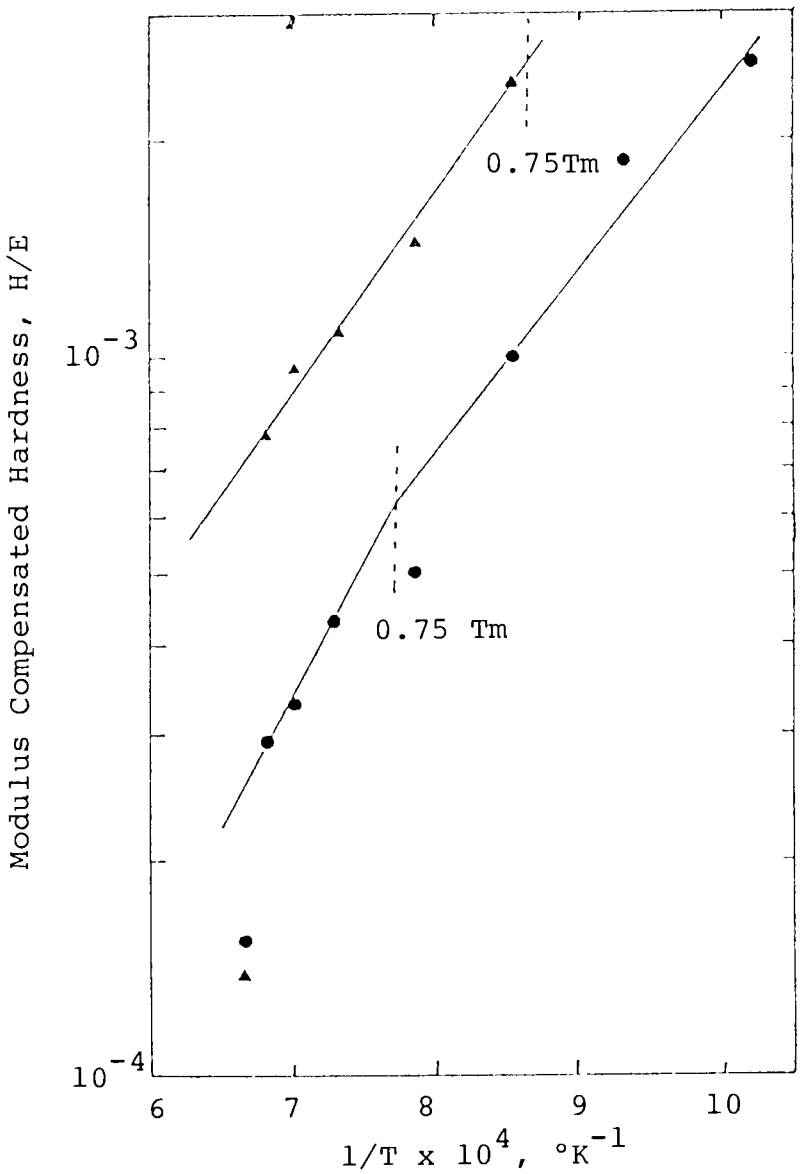

Fig. 7.3. Modulus Compensated Hardness versus 1/T for AISI 310 and Inconel 718.

7.1.2.2. A Study on Subgrain/Cell Development During Creep Deformation (J. Foulds)

Three tests were run to rupture on AISI 330 stainless steel at 652°C (0.57 Tm) and 35 ksi, the curves obtained being sufficiently identical to warrant the running of interrupted tests. Interrupted tests were run as shown in Fig. 7.4 and Table 7.I. Table 7.II contains the rupture data for the test (Specimen #AN330-CF01).

Interrupted tests at 652°C and 25 ksi have been postponed due to the variation obtained in the rupture data for the three tests run. The possible reasons for the variation are under investigation.

Straining during the interrupted tests was carefully monitored noting a less than 1 percent strain deviation from the curve in Fig. 7.4, indicating the validity of the microstructural data to be obtained from the tested specimens.

The fractured surface of the ruptured specimen AN330-CF01 indicated a highly (>95%) transgranular cracking mechanism when observed on the scanning electron microscope. Preliminary TEM observation on the same specimen revealed a "not so well defined" cellular structure with the presence of a second phase (not yet identified) having the same crystal structure as the matrix. All micrographs will be reported at the time of quantitative evaluation of the microstructural data.

With regard to the "as-annealed" material the grains were

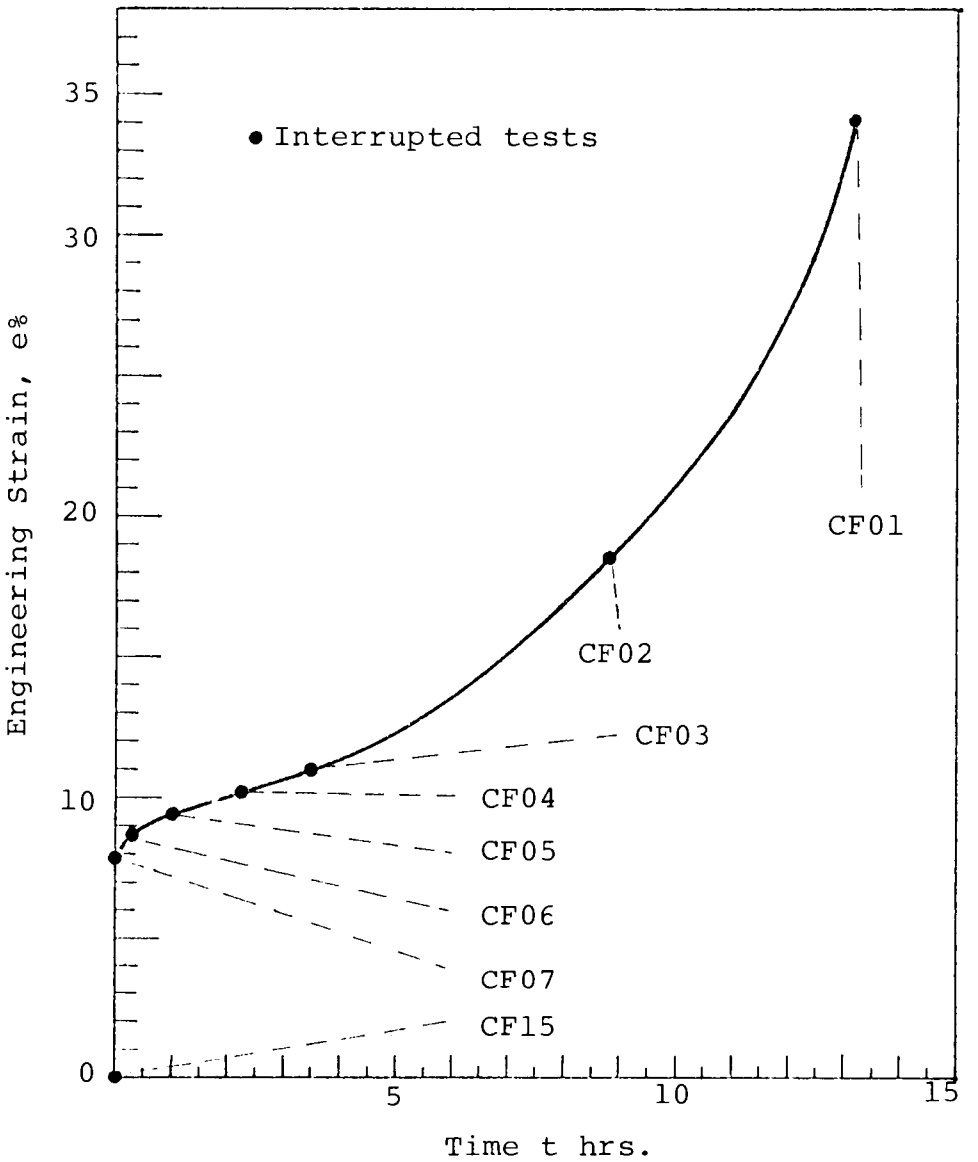

Fig. 7.4. Strain Behavior of AISI 330 Stainless Steel at 652°C and 35 ksi Applied Stress.

TABLE 7.I

AISI 330 INTERRUPTED TEST DATA AT 652°C AND 35 KSI

Sample Number	e%	t hr.	R.A.%	Expected e% from Fig. 7.4
AN330-CF02	21.10	9.0	19.44	18.90
-CF03	10.30	3.5	8.40	10.95
-CF04	9.85	2.25	10.90	10.20
-CF05	8.80	1.0	7.80	9.40
-CF06	7.60	0.3	6.80	8.65
-CF07	7.30	0.0	7.04	7.80

e = Strain at interruption.

t = Time of test.

RA = Reduction in cross-sectional area.

TABLE 7.II

LOW CYCLE FATIGUE DATA FOR
AISI 304 SS (9 T 2796) TESTED IN AIR AT 649°C

Number of Cycles at Interruption[b] N, (Cycles)	Number of Surface Cracks[c]	Number of Surface Cracks per (mm^2)	Largest Crack (μm)
0	0	0	0
1/4	0	0	0
3/4	0	0	0
2 3/4	0	0	0
6 3/4	8	0.25	3
80	66	2.11	20
361	138	4.41	147
722[a]	165	4.46	350

(a) This specimen was tested until failure.

(b) All tests were initiated in the compression mode and interrupted at the peak of tension cycling with the exception of the 1/4 cycle care which was terminated at the end of compressive cycling.

(c) All specimens were examined in the polished condition at 1000X mag.

observed to be equiaxed with the average grain size = 87 microns measured both on longitudinal and diametrial sections while the average microhardness was found to be 128 DPH for the same.

7.1.2.3. Fatigue Crack Characteristics as a Function of the Fatigue Life of AISI 304 Stainless Steel Tested at 649°C (J. Costa)

This study was accomplished in conjunction with the high temperature fatigue substructure development work reported earlier[3]. Since these tested specimens were used in this study, the reference heat number, heat treatment, and chemical analysis are the same.

Seven hour-glass specimens have been tested to different fractions of the fatigue life and to failure (complete separation) under the identical testing conditions of temperature (649°C), total strain range (2%), and cyclic strain rate ($4 \times 10^{-3} sec^{-1}$). The number of cycles at the termination of the respective fatigue tests and their test details are given in Table 7.II. All tests were initiated at the peak of the tension cycle, with the exception of the 1/4 cycle case.

Montages of the fractured surface, as photographed by a scanning electron microscope (Fig. 7.5), were assembled in order to count striation fringes. Recognizing that there is normally a one-to-one relationship between a striation and a fatigue cycle during crack propagation, the number of striations per unit length (dN/da) counted at various positions

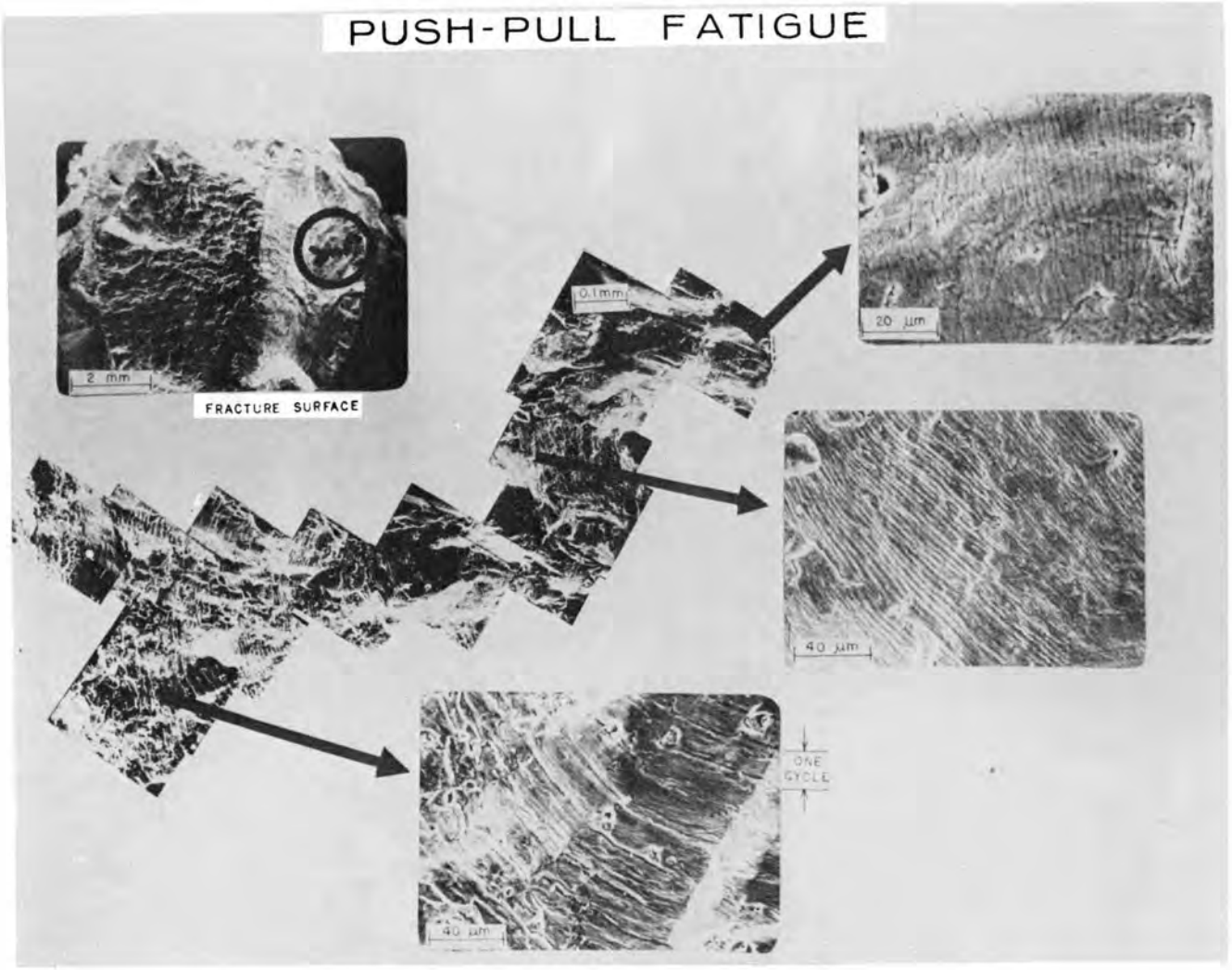

Fig. 7.5. AISI 304 SS Hour-Glass Specimen Montage of the Fractured Surface as Photographed by a Scanning Electron Microscope.

positions along the montage was determined. This value, dN/da, called the striation density, was plotted against crack length, a, which produced a curve (Fig. 7.6 a) from which, by integration, Np(s), the number of cycles for crack propagation was calculated. Similarly, $\ell n(a)$ versus N plots were constructed as shown in Fig. 7 b, to determine N_o, the number of cycles to initiate a crack of length, a_o ($\sim$ 1 grain diameter $\simeq$ .1 mm). These techniques employed in separating N_o and Np were developed by other investigators[4-6].

The remaining six specimens interrupted before failure were sectioned and prepared for metallographic examination and for micro-hardness evaluation. Unetched metallographic specimens showed the development of a crack during crack initiation and propagation periods (Fig. 7.7). Maximum observable crack lengths at various cyclic times agreed with the predicted values calculated using the $\ell n(a)$ versus N plots. Furthermore, Tukon micro-hardness measurements correlated well with stress amplitude readings at interruption (Fig. 7.7) and with the substructure development investigated by Nahm.

7.1.2.4. Stress-Temperature Effects on Substructures

(B. Billings)

Table 7.III presents the raw creep data accumulated to date for AISI 330 stainless steel. The stress levels used in the constant load tests range from 10 ksi (69.9 MPa) to 40 ksi (279.4 MPa). Three test temperatures have been used at

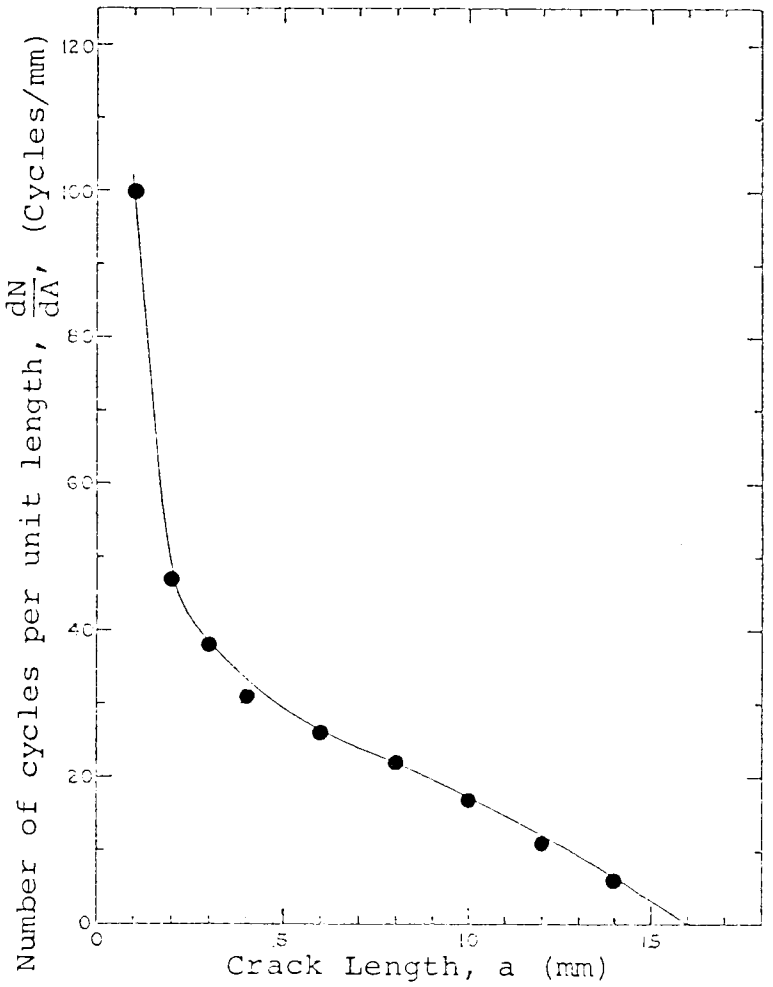

Fig. 7.6 a. Striation Density (dN/da) or the Number of Cycles per Unit Length Plotted Against Crack Length, a.

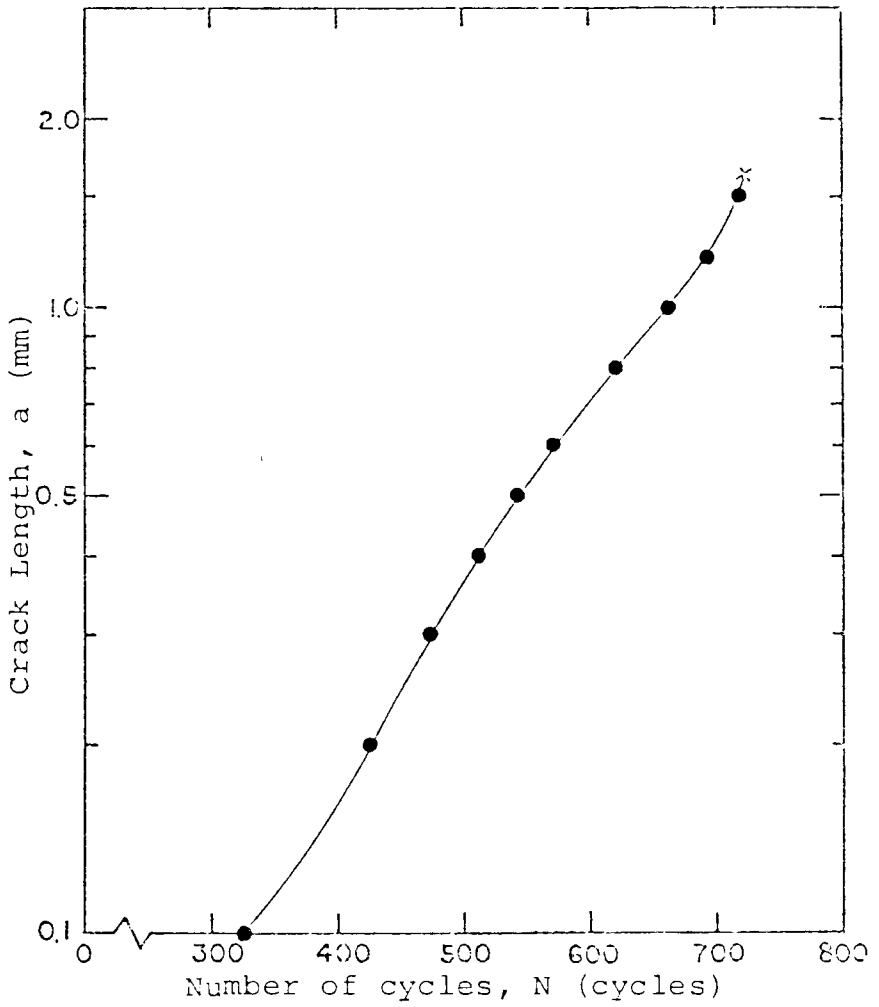

Fig. 7.6 b. ℓn a Versus N Plots of AISI 304 SS at 649°C in Air.

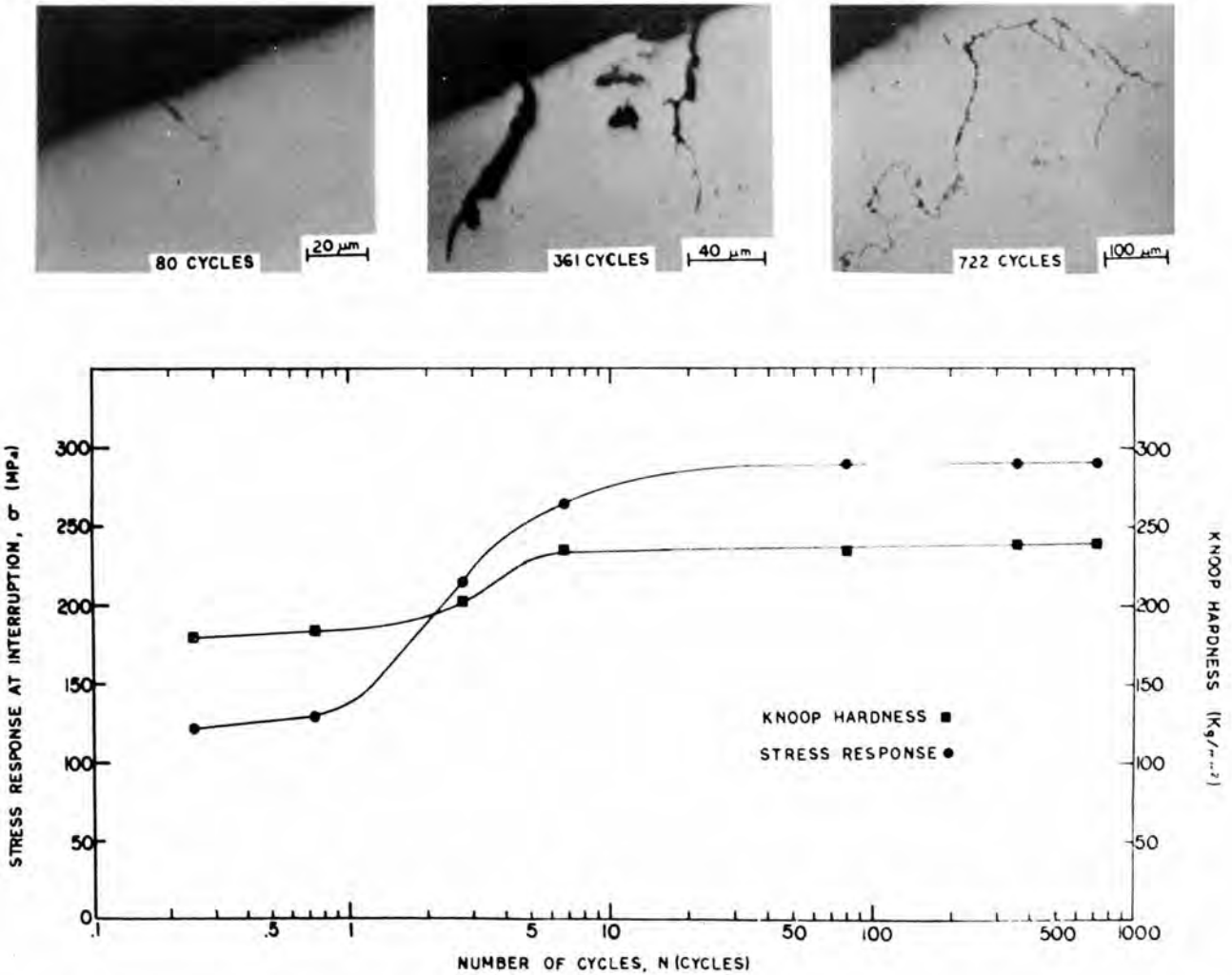

Fig. 7.7. Unetched Metallographic Specimens, Interrupted Before Failure, Showing the Development of a Crack During Crack Initiation and Propagation Periods. Plots Correlating Microhardness and Stress Response as a Function of N (Cycles).

present: 652°C (.58 Tm), 701°C (.6 Tm), and 800°C (.66 Tm). In addition to the data in Table 7.III, one test is presently in progress: sample number AN330-CB08, σ_a = 20 ksi, T = 600°C, e_p = 1.1%. This test has been underway for over 500 hours with an observed total strain of 1.6%. The sample geometry and testing procedures used to generate these data are reported elsewhere[7].

Figure 7.8 shows the constant load creep curves for the previously unreported specimens in Table 7.III, i.e. for specimens numbered AN330-CB05, 06, and 07. For the test conditions of these specimens see Table 7.III.

Figure 7.9 and Fig. 7.10 show the dependencies of the steady state creep rate and the time to rupture, respectively, on the applied stress.

In Fig. 7.9 the relationship between the steady state creep rate and the applied stress may be given by a power law as:

$$\dot{\varepsilon}_s = A\sigma_a^{\,n}$$

where $\dot{\varepsilon}_s$ is the steady state creep rate (hr^{-1}), σ_a is the applied stress (psi), n is a dimensionless constant, and A is a constant ($psi^{-n}hr^{-1}$).

In the present case,

at T = 800°C $\quad \dot{\varepsilon}_s = 8.7 \times 10^{-32}(\sigma_a)^{7.13}$

at T = 701°C $\quad \dot{\varepsilon}_s = 1.23 \times 10^{-34}(\sigma_a)^{7.35}$

It should be noted that these equations are the result of a

TABLE 7.III

AISI 330 RAW CREEP-RUPTURE TEST DATA

Sample Number	Applied Stress, ksi	Temp. °C[°F]	e_p %	e_t %	$\dot{e}_s$ %/hr	t_z hr	t_R hr	e_r %	RA %
AN330-CB01	40	701[1294]	5.0	12.0	83.7	0.15	0.75	60.0	44.1
-CB02	35		1.5	2.7	8.82	0.85	2.9	65.0	56.4
-CB03	30		2.7	6.0	33.3	0.17	0.68	64.0	54.1
-CB04	20		0.19	0.95	0.605	5.0	33.6	62.3	58.5
-CB05	15		1.13	3.5	0.057	41.5	251.1	62.5	52.2
-CB06	20	800[1472]	0.45	3.5	39.8	0.2	0.75	70.5	60.2
-CB07	10		0.09	1.55	0.284	24.8	64.9	30.3	31.0
-CF01	35	652[1206]	7.8	9.4	0.618	4.8	13.2	34.0	36.15

e_p = Plastic loading strain.

e_t = Cumulative strain at end of primary creep.

$\dot{e}_s$ = Minimum secondary creep rate.

t_2 = Time to reach end of secondary creep.

t_R = Time to rupture

e = Rupture strain

e_R = Rupture strain.

%RA = % reduction in cross-sectional area

NOTE: Values obtained through graphical methods.

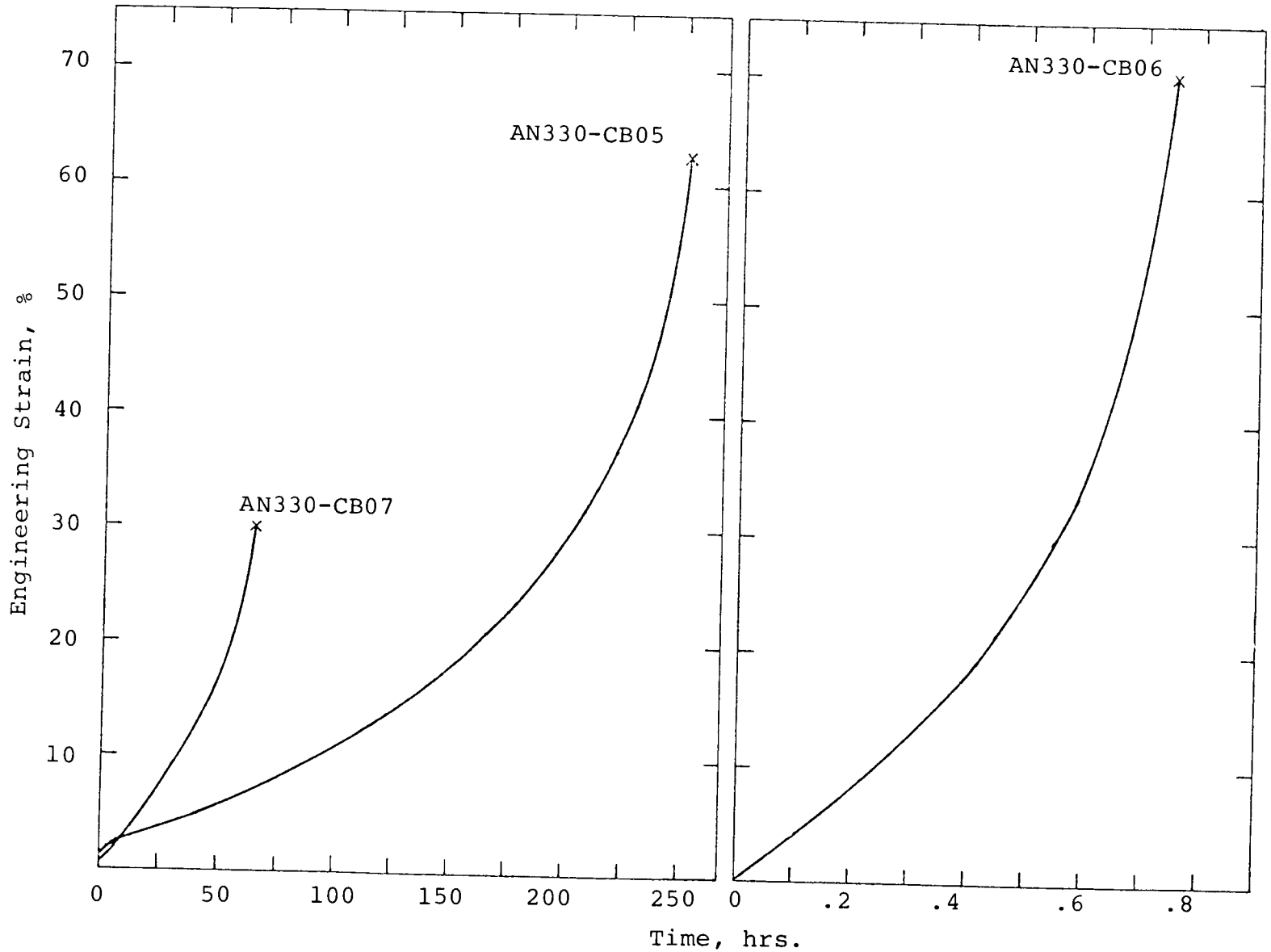

Fig. 7.8. Constant Load Creep-Rupture Curves for AISI 330 Stainless Steel Tested Various Conditions.

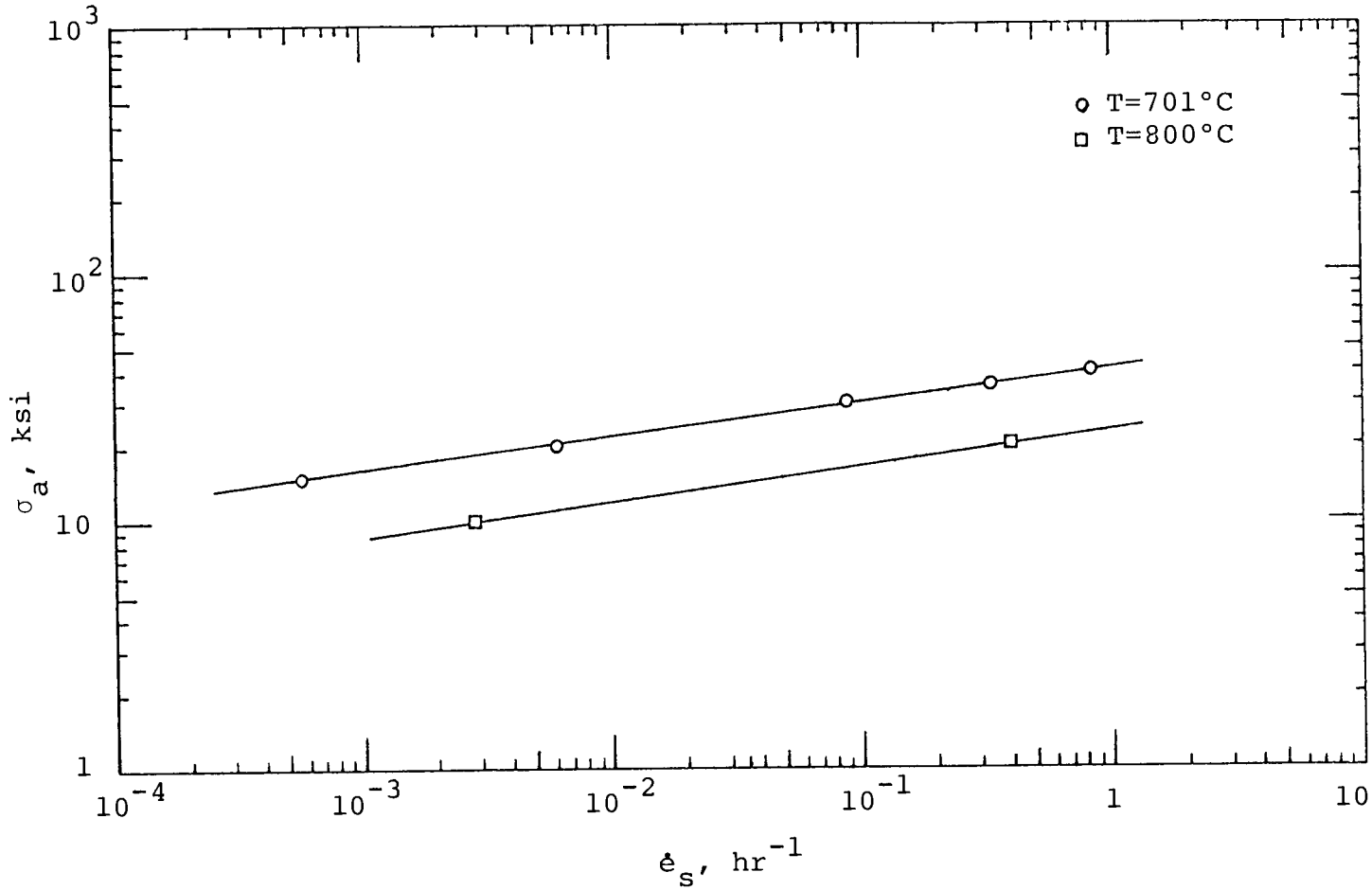

Fig. 7.9. Applied Stress, σ_a, versus Steady State Creep Rate, $\dot{e}_s$, for AISI 330 Stainless Steel Crept at Various Temperatures and Stresses.

least squares fit to a relatively small number of data points. Therefore, the accuracy of the values of A and n and the equations above is limited. As more creep rupture data is generated, these equations will be significantly refined.

In Fig. 7.10 the relationship between the time to rupture can be interpreted in terms of a power law of the form:

$$t_R = A\sigma_a^{-n}$$

where t_R is the time to rupture (hours), σ_a is the applied stress (psi), n is a dimensionless constant, and A is a constant ($(psi)^n hr$). Again, it should be noted that the equations for the curves are the result of an analysis of a small number of data points, hence they are inherently uncertain. Moreover, the power law equation itself is not sufficient to explain the stress dependence of the rupture life[8]. Various parameters have been used to obtain the rupture life from the stress. Examples of such parameters are the Larson-Miller, the Manson-Succop, and the Orr-Sherby-Dorn parameters[9]. However, the power law fit yields a first approximation of the functional dependency of the time to rupture on stress for the 330 alloy for a small data population.

Figure 7.10 actually shows the inverse relationship of that proposed above. The figure is plotted after Garofalo[8] and it can be noted that no change in slope occurs in any one curve. This indicates that the fracture mode remained constant for all samples tested at the same temperature[10].

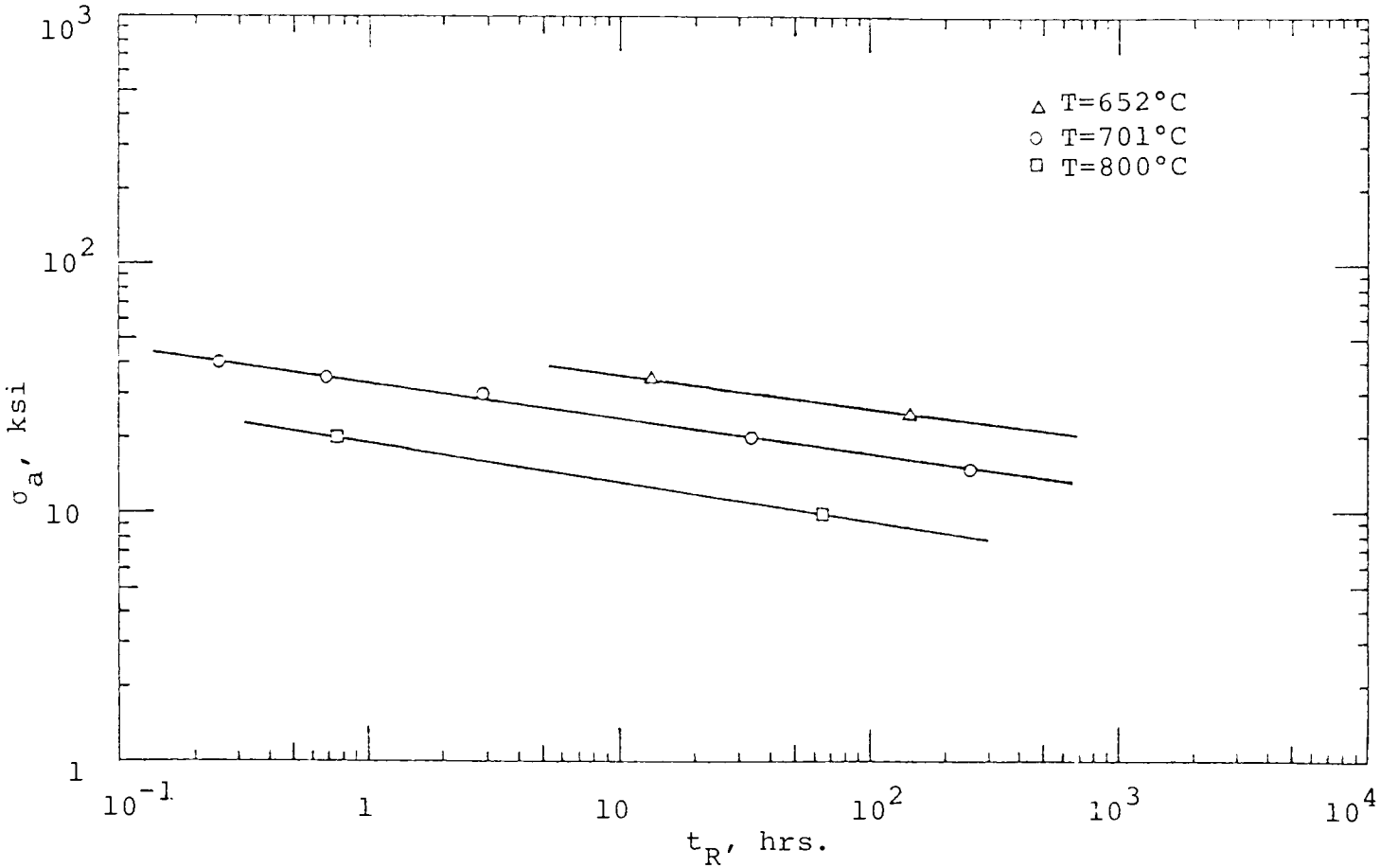

Fig. 7.10. Applied Stress, σ_a, versus Time to Rupture, t_R, for AISI 330 Stainless Steel Crept at Various Temperatures and Stresses.

The fracture surfaces of the ruptured samples from Table 7.III have been observed in the Scanning Electron Microscope (SEM). The major fracture mode observed was the transgranular mode.

Figure 7.11 is a plot of the secondary creep rate versus the reciprocal temperature. After Garofalo[8], the slope of this curve is equal to $-\frac{\Delta H_c}{R}$ where ΔH_c is the apparent activation energy for creep (cal/mole) and R is the gas constant. This is only true if it is assumed that temperature has no effect on the substructure developed during steady state creep. Because of this assumption, Fig. 7.11 is shown at a constant applied stress. The slope calculations from this figure yield an activation energy ΔH_c = 100 kcal/mole. This value for ΔH_c is in good agreement with that obtained from hot hardness measurements on the same alloy (93.4 kcal/mole)[11]. However, it must be noted that only three data points have been used to define the curve in Fig. 7.11. The curve was fit to these points by a least squares method, hence the ΔH_c = 100 kcal/mole value obtained from the curve may be slightly uncertain.

A limited study into the cracking behavior of AISI 330 has been initiated. It is known that the cracking characteristics of an alloy depend on the stress, temperature, and strain-rate conditions to which the alloy is subjected[12]. The rupture of an alloy is directly related to growth and interlinking of cracks which appear during deformation[13,14]. Hence, an investigation into the cracking behavior of AISI

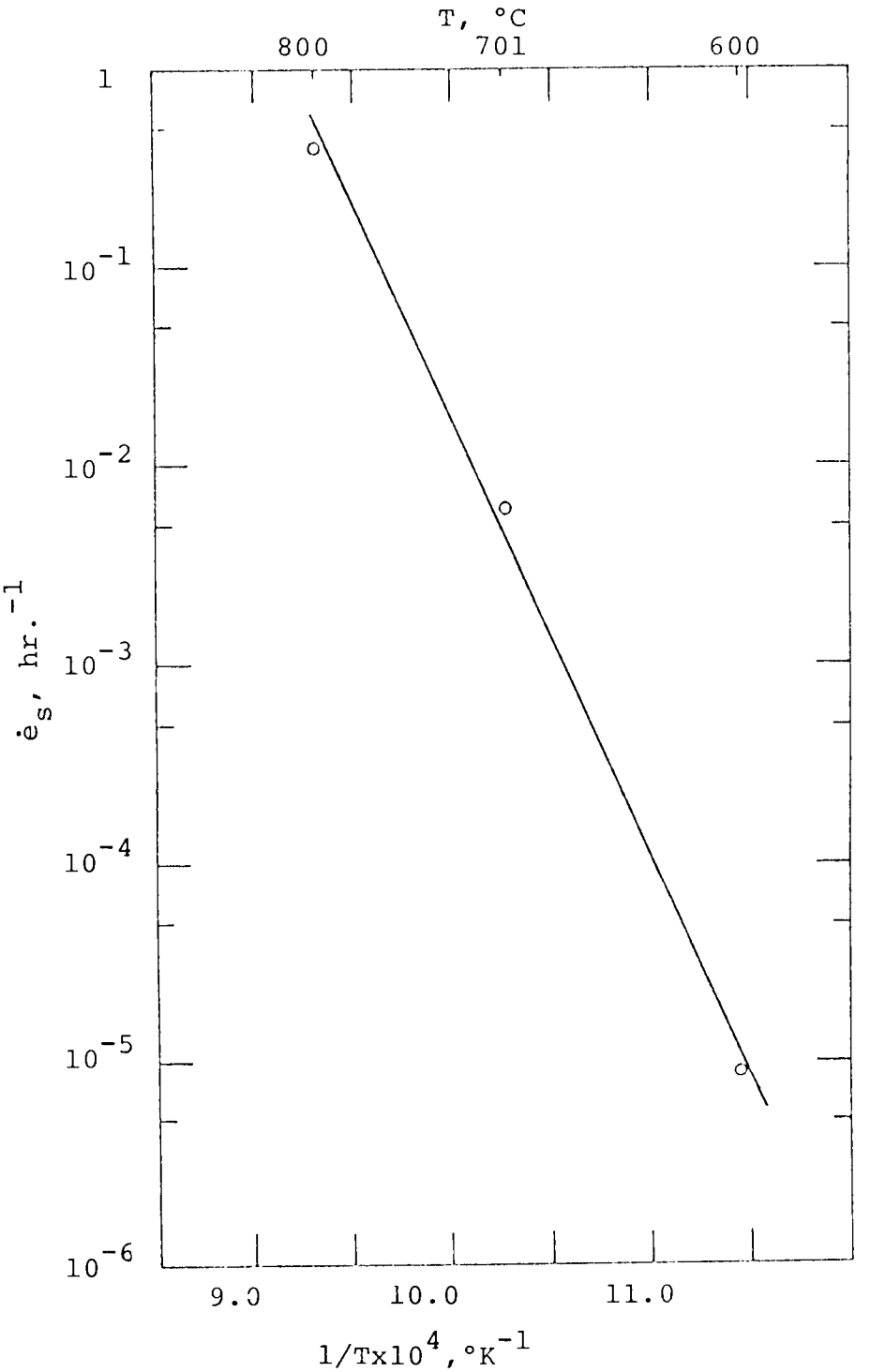

Fig. 7.11. Steady State Creep Rate, e_s, versus 1/T for AISI 330 Stainless Steel Crept at σ_a=20 ksi at Different Temperatures.

330 stainless steel is appropriate.

No quantitative microstructural evaluation is available at this time.

7.1.3. REFERENCES

1. J. Larsen-Badse, Trans. JIM 9 (1968) 312.
2. O. P. Sherby and P. E. Armstrong, Met. Trans. 2 (1971) 3479.
3. H. Nahm, Ph.D. Thesis, University of Cincinnati,Cincinnati, Ohio (1975).
4. P. S. Maiya, Scripta Met. 9 (1975) 1141.
5. P. S. Maiya, Scripta Met. 9 (1975) 1277.
6. J. Moteff, H. Nahm, and A. Ermi, paper in preparation.
7. Oak Ridge National Laboratory, Mechanical Properties Test Data for Structural Materials Quarterly Progress Report for Period Ending April 30, 1976, ORNL-5150, pp. 374-379.
8. F. Garofalo, Fundamentals of Creep and Creep-Rupture in Metals, The Macmillan Company, New York, 1966, pg. 211.
9. M. K. Booker, C. R. Brinkman, and V. K. Sikka, Correlation and Extrapolation of Creep Ductility Data for Four Elevated-Temperature Structural Materials, Symposium on Structural Materials for Service at Elevated Temperatures in Nuclear Power Generation, ASME, 1975, pp. 108-145.
10. R. E. Reed-Hill, Physical Metallurgy Principles, D. Van Nostrand Company, New York, 1964, pg. 879.
11. Oak Ridge National Laboratory, Mechanical Properties Test Data for Structural Materials Quarterly Progress Report for Period Ending July 31, 1976, ORNL-5200, pg. 372.
12. H. Nahm, M.S. Thesis, University of Cincinnati,Cincinnati, Ohio (1973).
13. H. Nahm, D. J. Michel, and J. Moteff, J. of Material Science 8, (1973) 104-108.
14. U. Lindborg, Acta Met. 17 (1969) 157-165.

7.2 UNIVERSITY OF CALIFORNIA, LOS ANGELES - A. J. Ardell, K. Ono and A. S. Tetelman

7.2.1 Mechanical Properties Evaluation of Carburized Type 304 Stainless Steel (P. L. Jones and A. S. Tetelman)

During the last reporting period, work has continued on the characterization of elevated temperature static load crack extension in Type 304 stainless steel. As reported previously[1], we have found that in an inert or carburizing atmosphere at 750°C, crack growth rates can be correlated with either net section stress, $\sigma_{(net)}$, or stress intensity factor, K, using equations of the form

$$\frac{da}{dt} = D\sigma_{(net)} \tag{1}$$

and

$$\frac{da}{dt} = CK^n \ . \tag{2}$$

Additional tests have been performed over a range of temperatures in an inert atmosphere and the results correlated with $\sigma_{(net)}$ and K.

Materials characterization, specimen configuration, and general test procedures have been discussed in previous reports[1,2]. Crack growth experiments were performed in a helium atmosphere at 650, 700, and 800°C using a static load creep frame with a 9.5 to 1 lever ratio. Tests were interrupted periodically and crack depth and length recorded. Crack growth rates were determined graphically and subsequently correlated with stress intensity and net section stress, and the results were compared to those obtained at 750°C.

The results are displayed in Figures 1 and 2. Figure 1 is a log-log plot of crack growth rate as a function of stress intensity factor for tests conducted in a helium atmosphere at 650, 700, 750 and 800°C, while Figure 2 compares crack growth rate to net section stress over the same temperature range. A linear regression analysis was performed on the data using relations of the form of Eq. (1) and (2).

The results are summarized in Table I. It is interesting to note that while the net section stress exponent, m, ranged from 12.9 at 650°C to 6.0 at 800°C, the stress intensity exponent, n, determined over the same temperature range, varied less than 10%, with a mean value of 3.4.

Because the exponent, n, is essentially constant when crack growth rate is compared to stress intensity factor, an attempt was made to determine the physical significance, if any, of the apparent activation energy for creep crack growth obtained from an Arhennius relation of the form

$$\frac{da}{dt} = A \exp(-Q/RT). \qquad (3)$$

Figure 3 is a semi-log plot of crack growth rate versus 1/T for the data obtained between 650°C and 800°C at constant values of K. A linear regression analysis of the data gives an apparent energy of 39.8 kcal/mole, which is close to one half the activation energy for self diffusion in austensite[3]. This would imply that grain boundary diffusion is the rate controlling process[4], which is consistent with the observation that all the specimens tested exhibited an intergranular fracture mode.

Although creep crack extension rates can be correlated with either stress intensity factors or net section stress, it appears that from a

TABLE I

$\frac{da}{dt}(in/min) = D\sigma_{(net)}^{m}$ $[\sigma_{(net)} = ksi]$ $\frac{da}{dt}(in/min) = CK^{n}$ $[K = ksi\sqrt{in}]$

Temperature (°C)	D	m	Variance (r^2)	C	n	Variance (r^2)
650	2.12×10^{-24}	12.9	.966	2.02×10^{-8}	3.3	.986
700	3.35×10^{-15}	7.1	.993	3.37×10^{-8}	3.6	.991
750	6.74×10^{-14}	7.0	.994	1.79×10^{-7}	3.3	.994
800	5.25×10^{-12}	6.0	.984	3.09×10^{-7}	3.5	.996

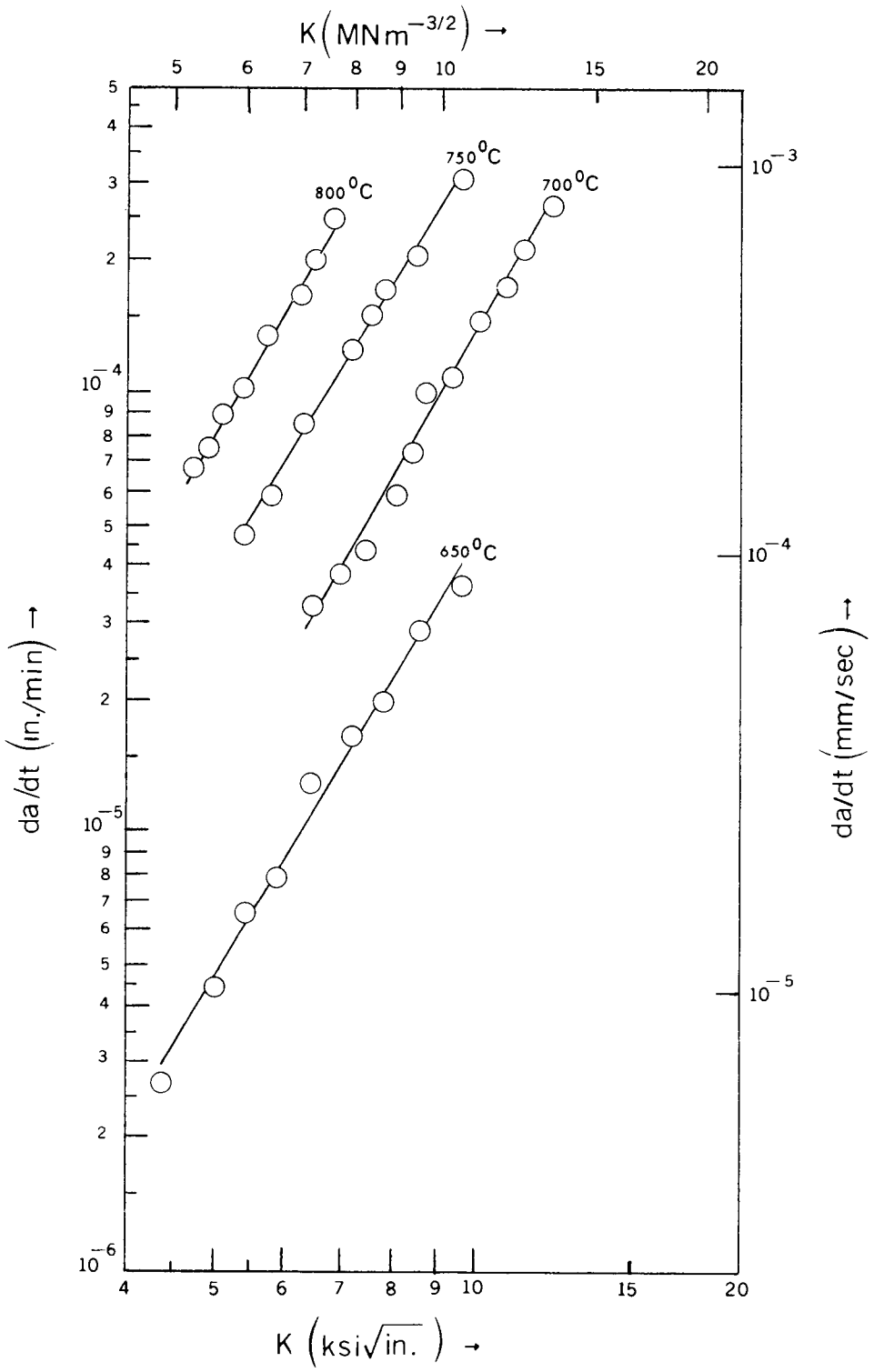

FIGURE 1 Crack Growth Rate as a Function of Stress Intensity Factor (He Atomsphere)

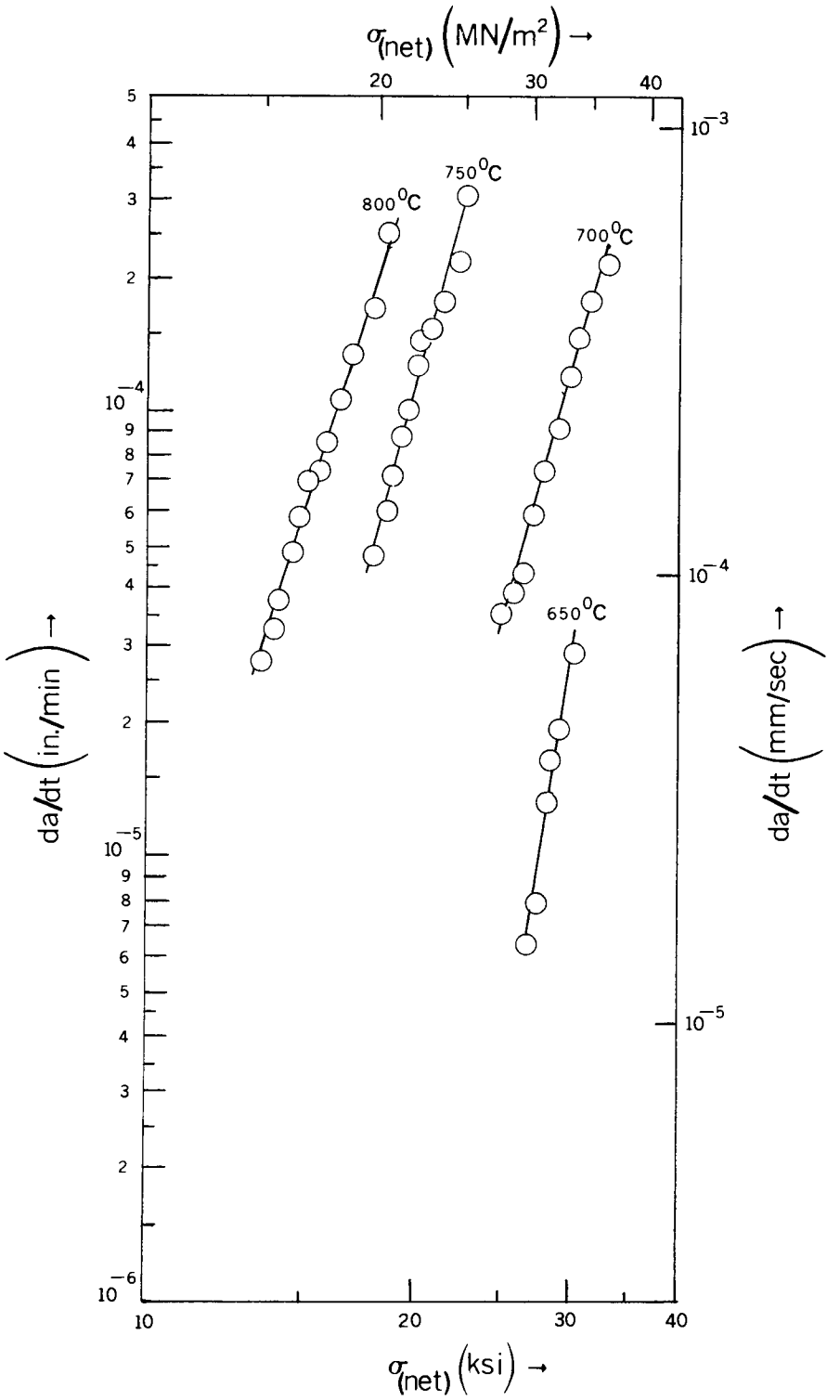

Figure 2 Crack Growth Rate as a Function of Net Section Stress (He Atmosphere)

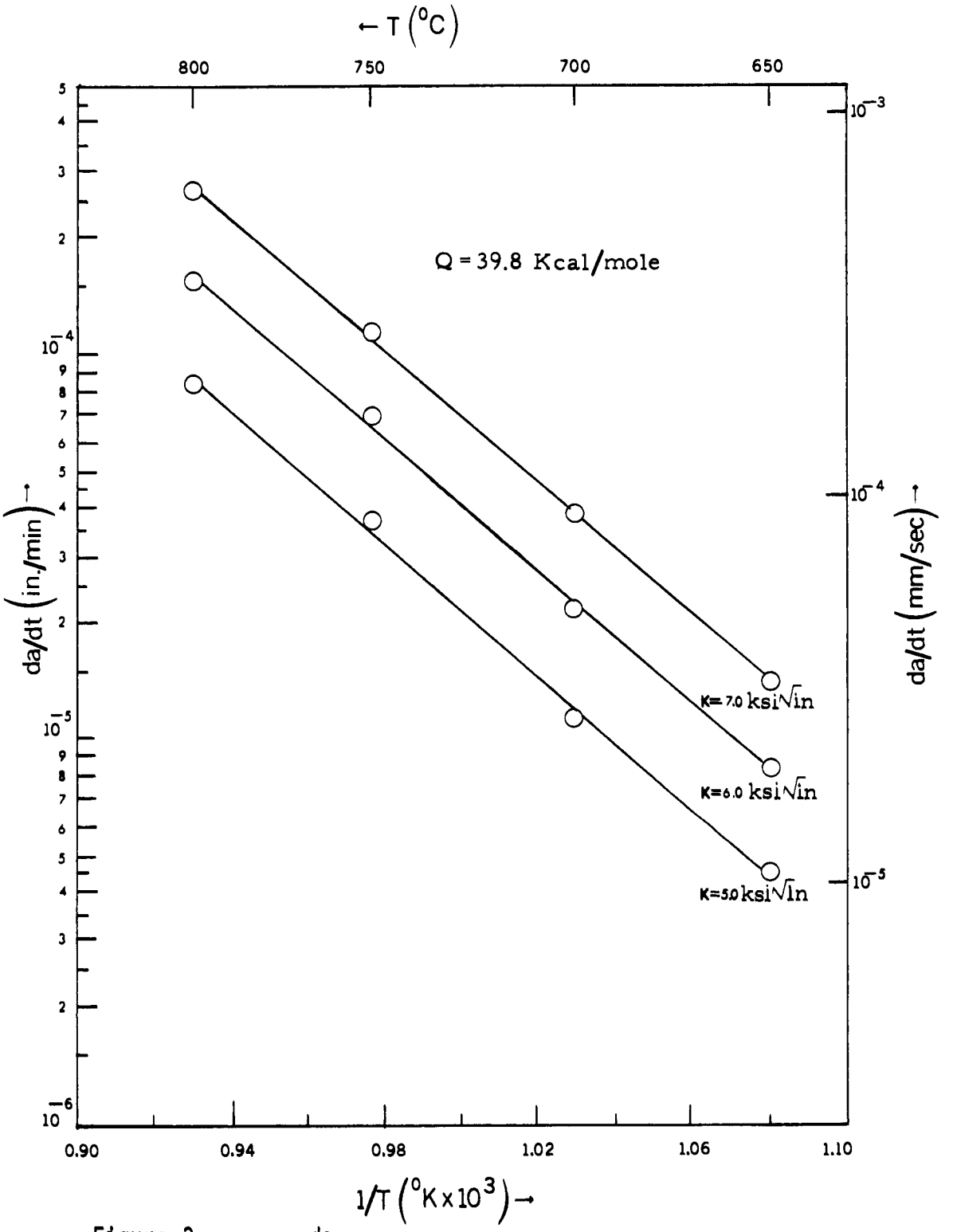

Figure 3 $\frac{da}{dt}$ vs. 1/T at constant values of K.

mechanistic point of view the stress intensity factor is the more meaningful correlating parameter, at least for the results obtained thus far. Future work will include obtaining creep crack growth rate data using compact tension specimens and comparing these results to those obtained using part-through surface flawed specimens. Hopefully, some insight will be gained as to why the stress intensity factor may be used to describe creep crack extension, even though creep rupture is a strain controlled time dependent mode of failure.

7.2.2 Creep Studies in Stainless Steels (O. Ajaja and A. J. Ardell)

7.2.2.1 Introduction

The effects of prior cold work on the various transient creep parameters and the secondary creep rates of Type 304 SS were presented in the last quarterly progress report[1]. Transmission electron microscopy has been performed on some specimens creep-tested at 704°C and 172.4 MN/m^2 in order to investigate the characteristic microstructures at various stages of the creep test. Figure 4 shows the creep curves for the annealed (curve A) and the (10%) prestrained (curve B) specimens. While the annealed specimen exhibits the normal type of creep curve, curve B shows a very brief transient creep stage, followed by an apparent steady state, beyond which prolonged accelerating creep leading to fracture is observed. We have observed this type of creep curve mainly at the lowest creep stresses investigated (137.9 and 172.4 MN/m^2 at 704°C).

As depicted in Fig. 4, each specimen was crept to a certain creep stage (designated 1, 2, 3, etc.) and later examined in the transmission

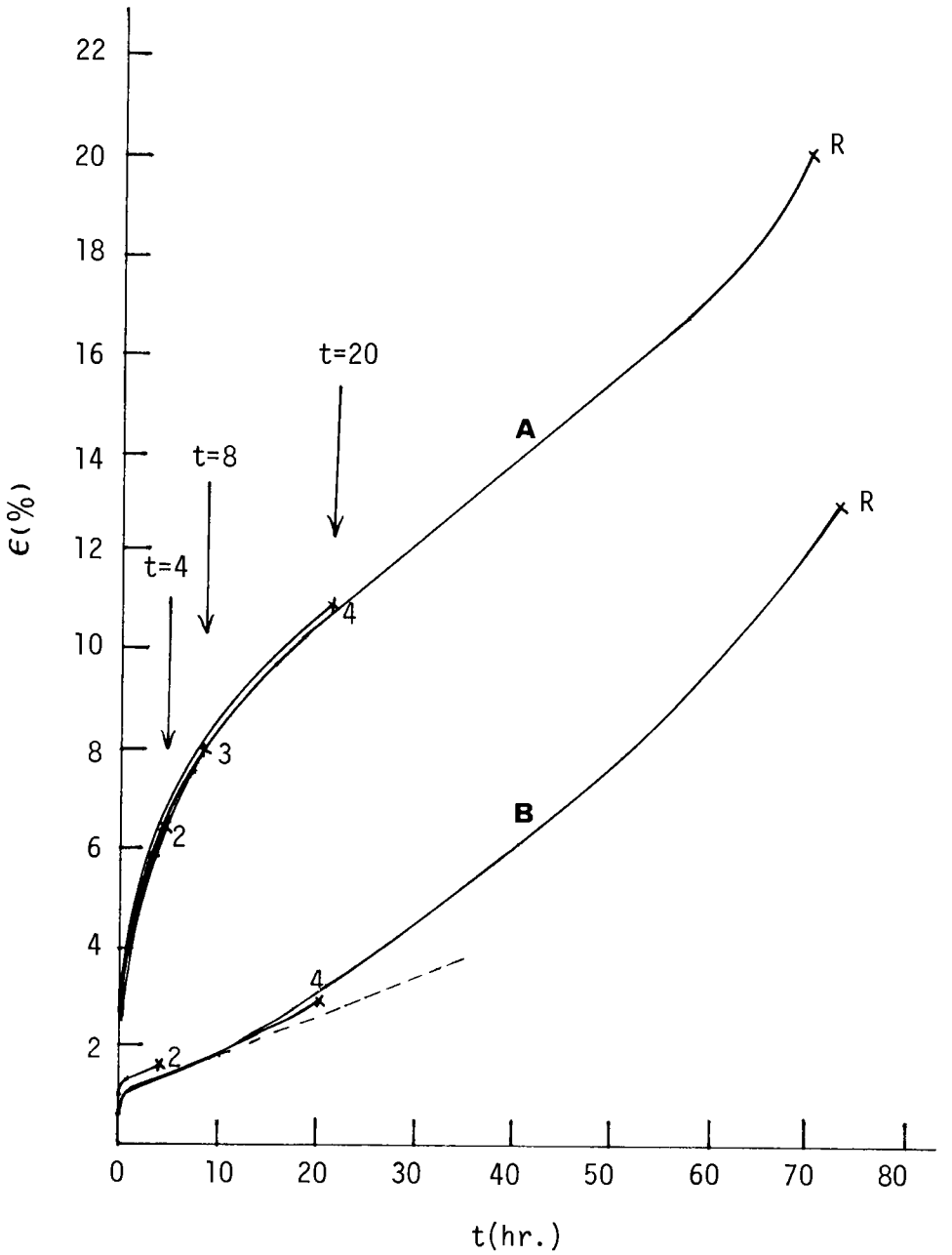

Fig. 4. Creep curves of the annealed (A) and (10%) pre-strained (B) 304 Stainless Steel creep tested at 704°C and 172.4 MN/m^2.

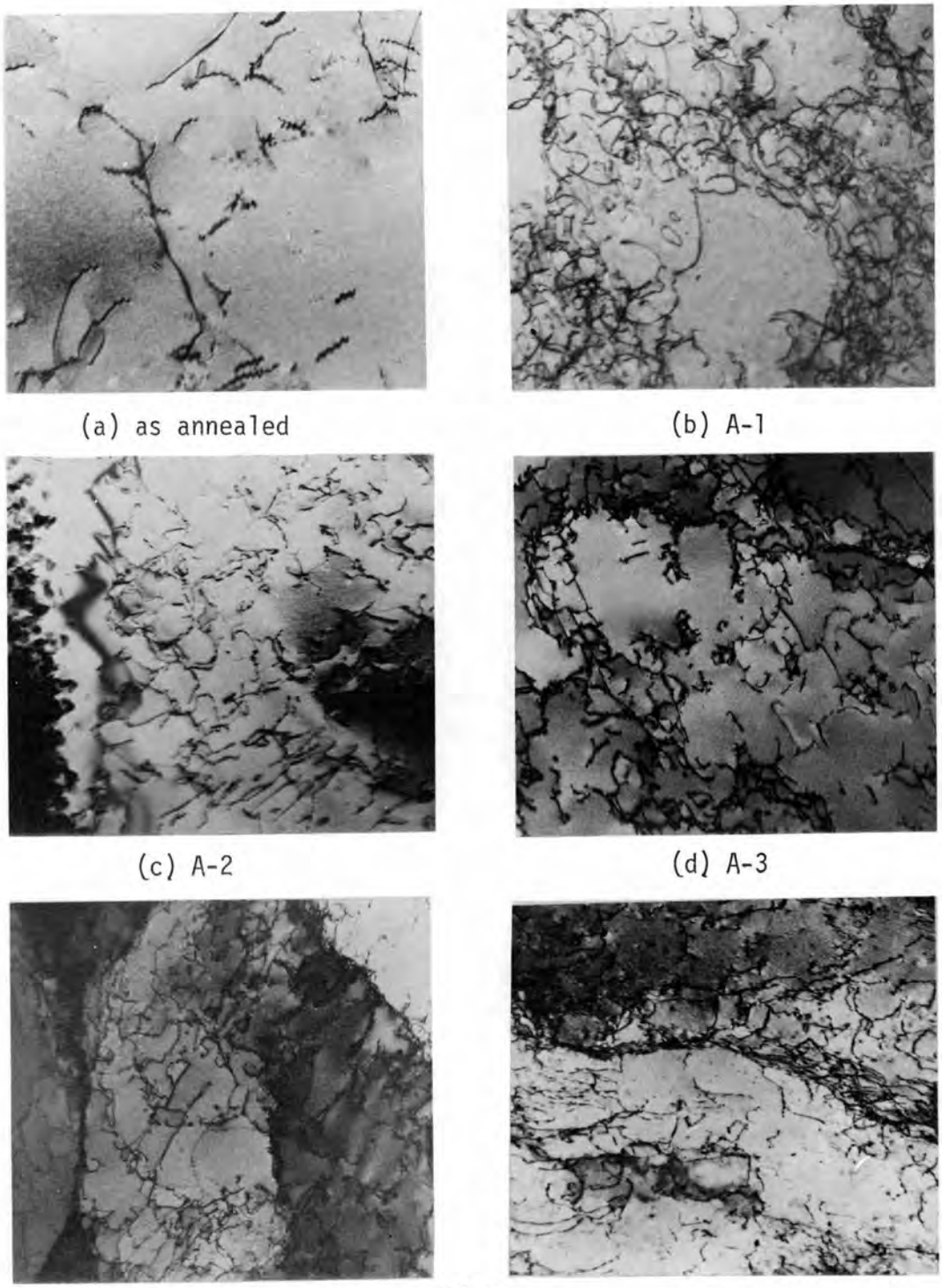

Fig. 5. Transmission Electron Micrographs of the microstructure at various creep stages (Fig. 1, curve A) of an annealed 304 SS tested at 704°C and 172.4 MN/m^2.

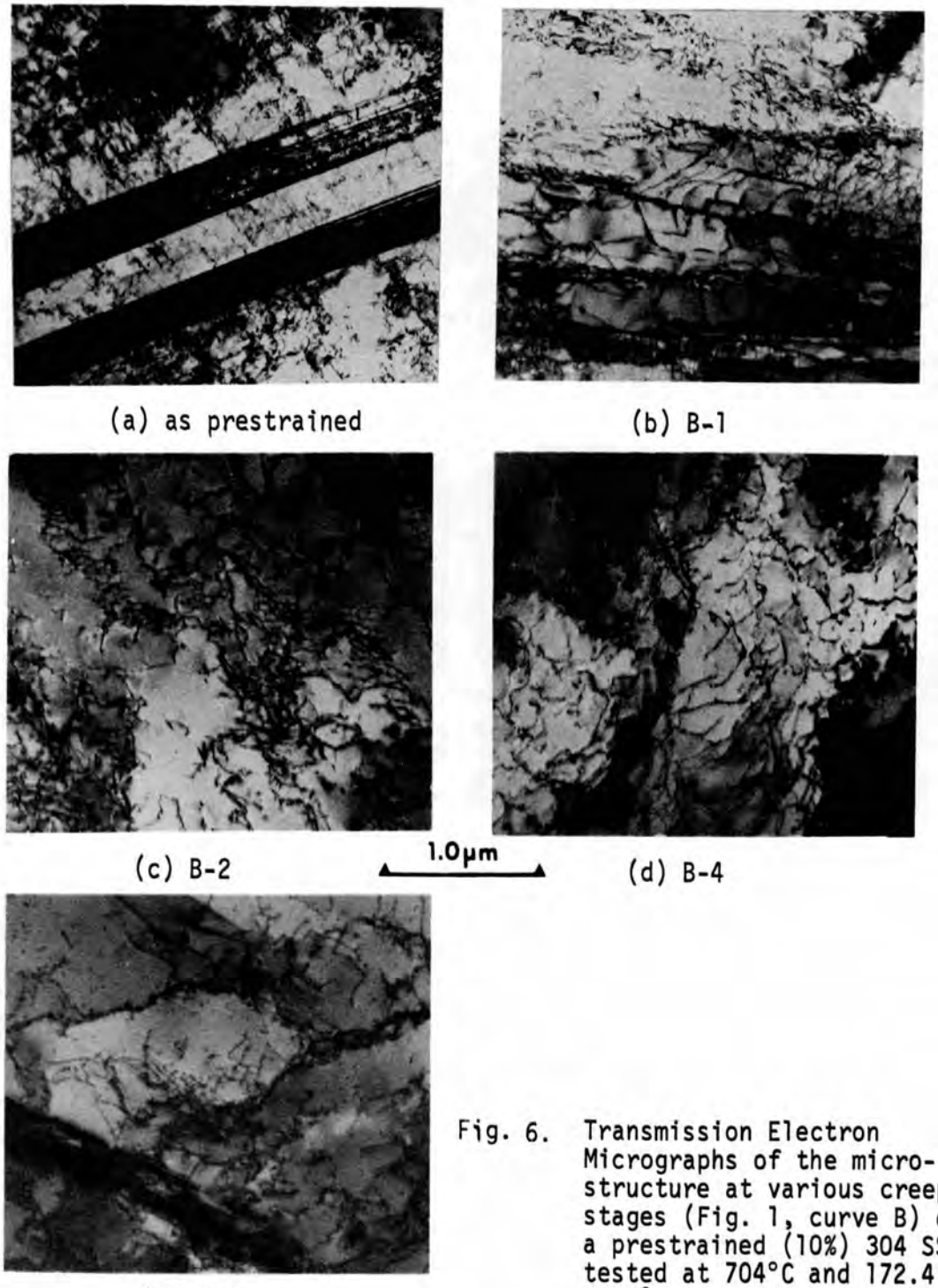

Fig. 6. Transmission Electron Micrographs of the microstructure at various creep stages (Fig. 1, curve B) of a prestrained (10%) 304 SS tested at 704°C and 172.4 MN/m^2

electron microscope using the techniques reported in the last progress report. For example, A-1 represents the annealed specimen immediately after creep loading (the loading duration is approximately 10-15 sec.). The numbers 2 to 4 next to each curve stand for the creep stages corresponding to the times indicated and R is the rupture point.

7.2.2.2 Results

The microstructures investigated by TEM so far are presented in Figs. 5 and 6. Referring to Fig. 5, the annealed specimen has a characteristic low density of dislocations and is precipitate-free (Fig. 5a). Immediately upon loading (Fig. 5b), a cellular dislocation structure is developed whose boundaries are made up of dislocation tangles and loops. After 4 hours of creep, which lies well within the transient stage (Fig. 5c), a uniform dislocation structure is observed and extensive grain boundary carbide precipitation has occurred. This structure is not significantly altered until after 8 hours of creep (Fig. 5d) which is closer to the end of the transient stage. However, isolated instances are observed where dislocations are beginning to cluster into walls that might later become well-defined dislocation sub-boundaries. At stage A-4 of creep which is well into the steady state (Fig. 5e), a few well-developed dislocation sub-boundaries are evident, but the microstructure is still dominated by ill-defined boundaries or uniform distribution of dislocations. This microstructure remains essentially unaltered until rupture (Fig. 5f) save for the appearance of some fine black spots (see micrograph) presumed to be some sort of precipitates, but yet unidentified.

The microstructures of the prestrained specimen at various stages

of the creep curve (Fig. 4, curve B) are presented in Fig. 6. Prior to creep, a rough cellular dislocation structure plus an extensive array of deformation bands are commonly observed (Fig. 6a). Immediately after creep loading (B-1), most dislocations are clustered in tangles whose walls lie parallel to the {111} slip traces (Fig. 6b). The dislocation structures after 4 hours and after 20 hours of creep (B-2 and B-4 respectively) are essentially the same. The microstructure has relaxed into a more uniform dislocation distribution and extensive precipitation has occurred at the grain boundaries after 4 hours of creep (not shown on the micrograph, Fig. 6c). After 20 hours, (Fig. 6d) carbide particles are observed occasionally in an otherwise precipitate-free matrix. The microstructure after rupture (B-R) is quite different from B-4, as expected from the creep behavior (Fig. 4). This consists essentially of subgrains with well defined boundaries. The dislocation density within the subgrains is quite low and there is an extensive array of carbide platelets precipitated on deformation bands (Fig. 6e). The small (unidentified) intragranular precipitates are also observed in this specimen.

7.2.2.3. Discussion

The microstructural observations in the annealed specimen show that the cellular dislocation structure that results immediately after loading gives way to a uniform structure during transient creep. At steady state the dislocation distribution is still predominantly uniform with occasional instances of well-defined dislocation sub-boundaries. This stable steady-state substructure develops over the transient stage of creep and remains essentially unaltered until fracture. This is consistent with

reported observations of the dislocation kinetics during the creep of various materials[5-7]. As previously mentioned, the type "B" creep curve has been observed in all the specimens (annealed and prestrained) tested at 704°C and 137.9 MN/m^2. The values of the secondary creep rates reported for all such tests in the last progress report (Fig. 3b of Ref. 1) are the observed creep rates in the "apparent" steady state region (such as the creep rate represented by the slope of the dashed line in Fig. 4).

The fact that the substructure of the prestrained specimen is not significantly modified until after about 20 hours of creep is consistent with the "apparent" steady state observed. The minimum creep rate is significantly less than the steady state creep rate observed for the annealed specimen. The accelerating creep that follows is an indication of an unstable substructure and this is clearly evident from a comparison of Fig. 6d and 6e. The subgrain formation that has occurred prior to rupture is a result of an appreciable climb-recovery process that occurs subsequent to the virtual steady-state and has significantly contributed to the observed accelerating creep. The microstructures at various stages of the accelerating creep are still being investigated in order to delineate the various characteristics associated with the transition from the "steady state" to the "rupture" substructure.

7.2.3 Microstructures and Mechanical Properties of Cr-Mo Steels (S. L. Hsu and K. Ono)

During this report period, the tensile properties of three heats of 2-1/4 Cr-1Mo steels that had been normalized (N), tempered (T) and addi-

tionally subjected to long time tempering (LTT) were determined at 454°C (850°F). The carbon contents of Alloys H, I and L were 0.12, 0.03 and 0.009%, respectively. The nominal strain rate was 2.7×10^{-4} sec^{-1}. Results are presented in Table II and in Figs. 7-9. Room temperature tensile properties and creep behavior of 454° to 566°C (1050°F) of these alloys that had received identical heat treatments were reported previously[8]. The tensile properties of N&T specimens were in good agreement with those reported by Klueh[9] on the same starting stocks.

The yield strength data of Alloys H, I and L tested at 454°C is plotted in Figure 7. In comparison to the room temperature tensile data of Alloy H specimens, the corresponding high temperature yield strength was consistently reduced by 55-70 MPa (8 to 10 ksi) and its dependence on the tempering conditions was essentially unchanged. In Alloys I and L, the yield strength values of the N&T specimens of these two alloys showed a varied response. In both alloys, LTT specimens showed only minor changes in the yield strength as a function of tempering time. The increase of test temperature affected the LTT specimens tempered at 454°C most and those tempered at 510°C (950°F) least. Consequently, the elevated temperature yield strengths of the latter were higher than those of the former (tempered at 454°C). It is also noted that the elevated temperature yield strengths of Alloy I specimens tempered at 454°C or at 560°C (1050°F) were the lowest among the present tests.

Neither initial discontinuous yielding nor serrated yielding were observed in Alloy H under all the heat treatment conditions. The N&T specimen of Alloy I showed a yield drop of 7 MPa (1 ksi) followed by a Lüders strain of 0.4%. Specimens tempered at 454°C for 4 and 8 months

TABLE II. Tensile Properties of 2-1/4 Cr-1Mo Steel
Test Temperature: 454°C
Strain Rate: 2.67×10^{-4}/Sec.

Alloy	Heat Treatment After Normalized and Tempered (N&T)	Strength (MPa) 0.2% Yield	Ultimate Tensile	Elongation (%) Uniform	Total
H	N&T Only	446	586	8.2	11.1
	2880 hr at 454°C	422	517	5.64	8.9
	5760 hr at 454°C	418	501	6.4	10
	8640 hr at 454°C	411	506	6.52	12.4
	2880 hr at 510°C	409	489	4.0	6.7
	5760 hr at 510°C	419	503	7.4	8.9
	8640 hr at 510°C	402	480	6.36	13.8
	2880 hr at 566°C	369	455	6.64	11.5
	5760 hr at 566°C	354	439	7.08	10.6
	8640 hr at 566°C	353	431	7.04	16
I	N&T Only	227*	468	11.2	13.5
	2880 hr at 454°C	145*	370	18.04	21.9
	5760 hr at 454°C	140*	371	18.4	23.3
	8640 hr at 454°C	147	354	17.8	22.2
	2880 hr at 510°C	184	324	16.0	20.8
	5760 hr at 510°C	184	327	16.3	23.1
	8640 hr at 510°C	164	330	17.2	23.2
	2880 hr at 566°C	156	298	16.5	20.7
	5760 hr at 566°C	132	294	19.2	24
	8640 hr at 566°C	137	305	15.16	21.5
L	N&T Only	204	414	12.2	15.9
	2880 hr at 454°C	175	378	19.2	22.8
	5760 hr at 454°C	176	371	19.1	23.9
	8640 hr at 454°C	162	372	20.0	24.2
	2880 hr at 510°C	189	325	17.1	24
	5760 hr at 510°C	182	326	18.2	24.1
	8640 hr at 510°C	188	335	18.8	24.1
	2880 hr at 566°C	142	308	17.6	22.8
	5760 hr at 566°C	154	302	18.8	21.6
	8640 hr at 566°C	167	312	16.7	24.2

*Lower Yield Strength

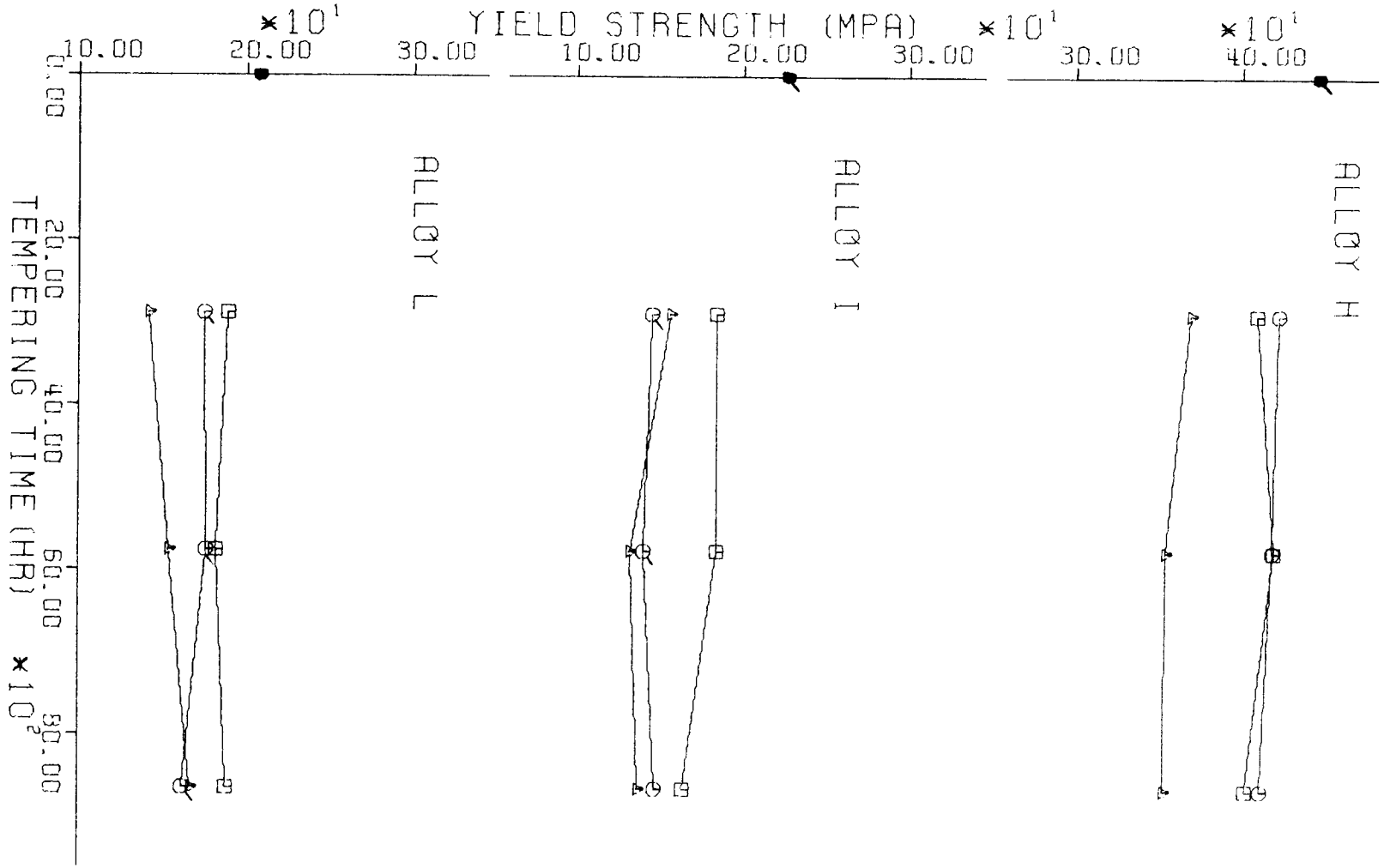

Figure 7. Yield Strength vs. Tempering Time
● N&T only, ○ 454°C temper
□ 510°C temper, △ 565°C temper

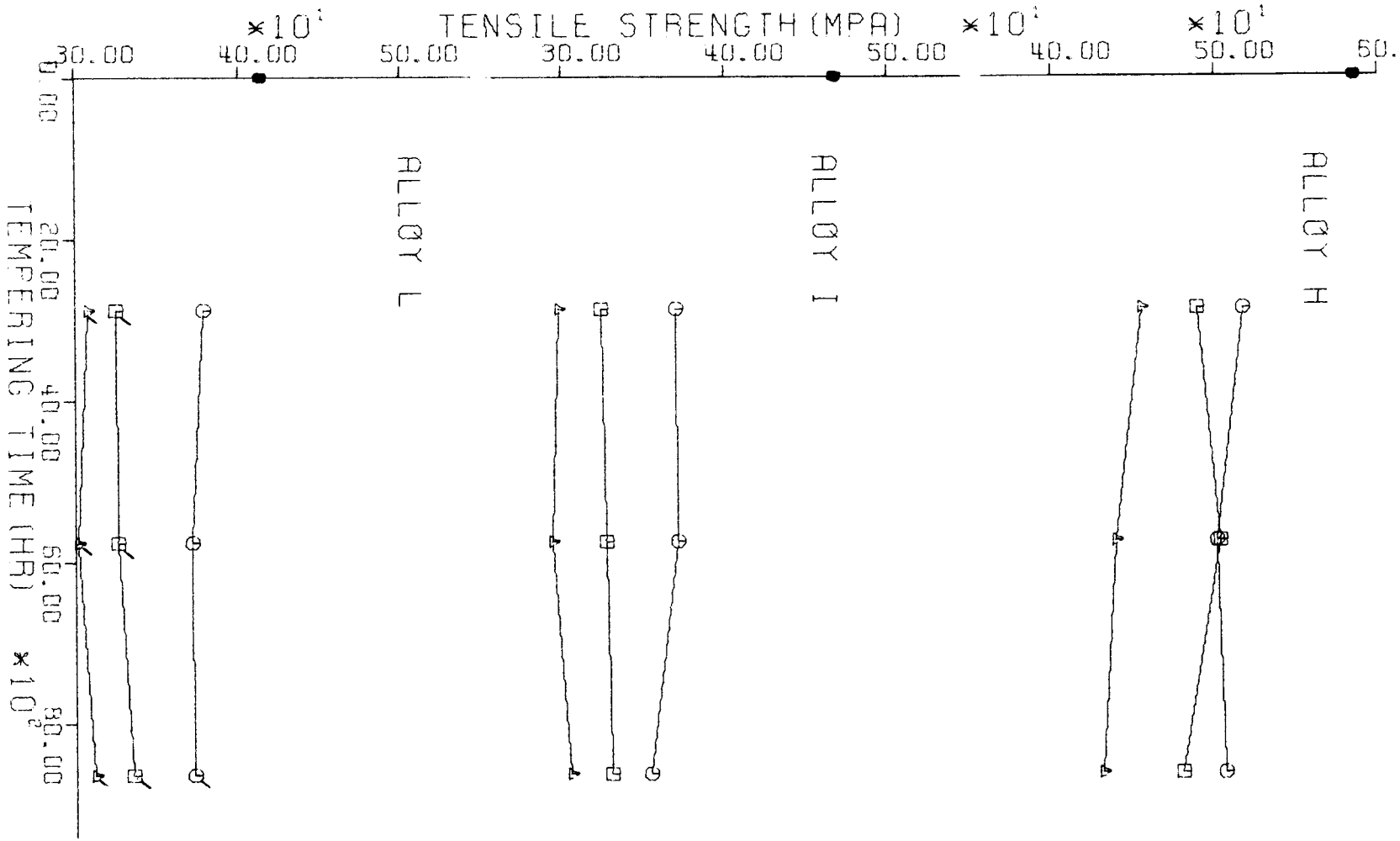

Figure 8. Tensile strength vs. tempering time
●N&T only, ○ 454°C temper
□510°C temper, △ 565°C temper

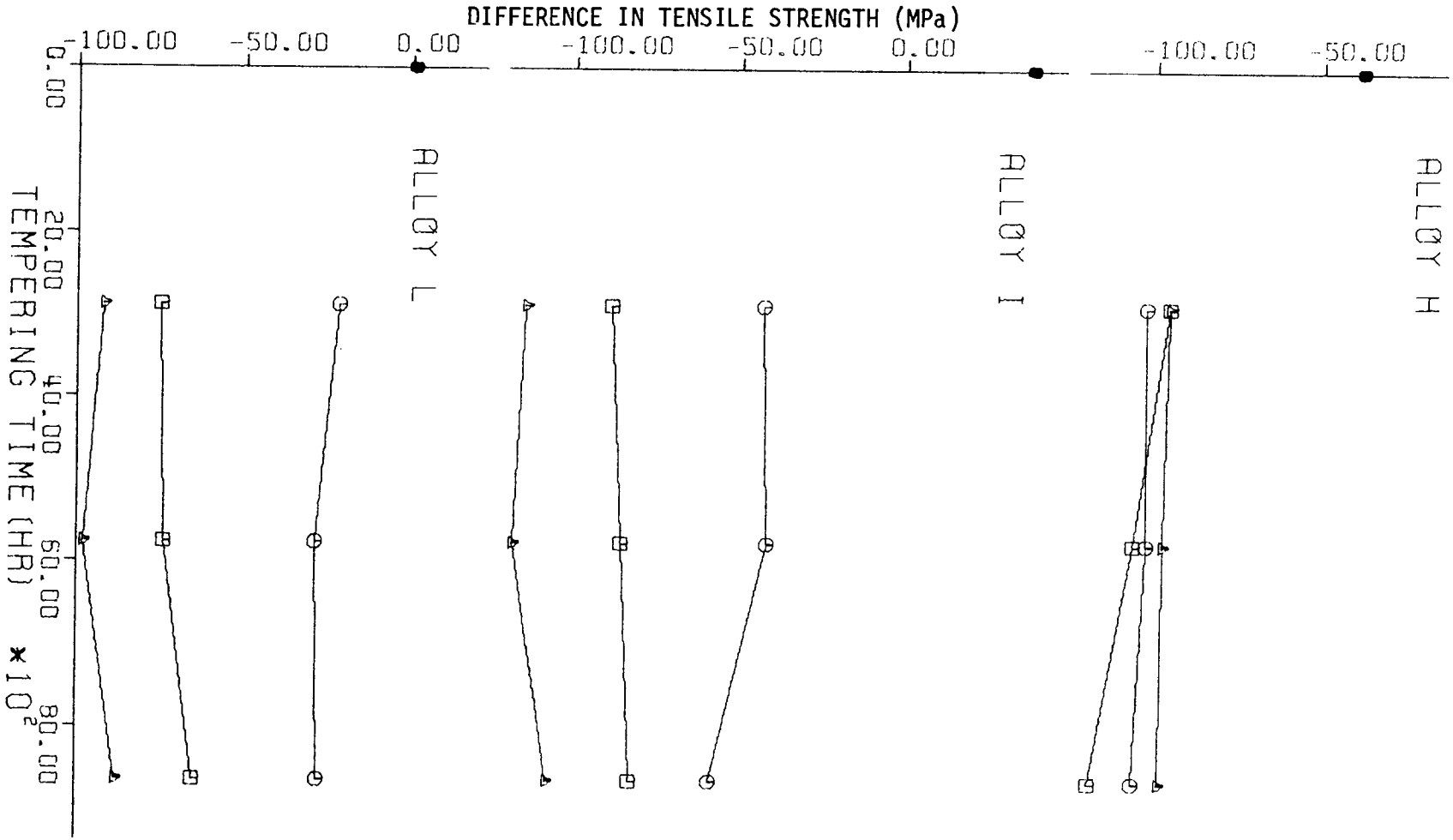

FIGURE 9. Tensile strength difference as a function of tempering conditions.
● N & T only, ○ 454°C temper.
□ 510°C temper, 565°C temper.

also showed initial discontinuous yielding, but the yield drop and Lüders strain were much smaller. Initial discontinuous yielding was absent in other specimens of Alloy I tested at 454°C. Initial discontinuous yielding was observed in Alloy L specimens in the N&T and LTT (at 454°C) conditions, but no measurable yield drop occurred. Lüders strain was in the range of 0.1 to 0.4%.

Tensile strength data at 454°C is given as a function of tempering time in Fig. 8. For the tempering times of 4 to 12 months, the tensile strength of LTT specimens was nearly unchanged. In Alloy H, the tensile strength of the N&T specimen was 140MPa (20 ksi) above the yield strength level. This difference decreased to 83-97MPa (12 to 14 ksi) in the LTT specimens. In Alloys I and L, differences between the tensile and yield strengths were in excess of 207 MPa (30 ksi) in the N&T and LTT (at 454°C) condictions, but were 140 to 172 MPa (20 to 25 ksi) in the other LTT conditions.

Effects of test temperature on the tensile strength of these alloys are shown in Fig. 9. The difference between the tensile strengths measured at 454°C and at room temperature is plotted as a function of tempering time. In the N&T conditions, the observed difference was small or non-existent. In Alloy H, a decrease in the tensil strength of 97 to 118MPa (14 to 17 ksi) was observed regardless of tempering temperature. The decrease became greater with a longer tempering time. In Alloys I and L, the tensile strength decrease was observed with LTT, but the magnitude was dependent on tempering conditions. Tempering temperature had a significant effect with a greater decrease resulting from a higher tempering temperature.

Serrated stress-strain curves were observed in some test of Alloy L specimens, as marked in Fig. 8. Critical plastic strain was 3 to 6% in specimens tempered at 566°C, but the serration did not start until after the ultimate tensile strength was reached in the specimens tempered at lower temperatures.

Substantial contributions of dynamic strain aging (DSA) are indicated by these finding in 454°C tests of Alloys I and L. In addition to the serrated flow, large differences between the yield and tensile strength levels at 454°C and small or negligible changes in the tensile strengths between 454°C and room temperature tests are characteristic of DSA. It is also significant to note that the yield strength at 454°C is 20 to 40% lower than the creep stresses for the strain rates of 10^{-5} - 10^{-4} hr^{-1}. Such a negative strain rate dependence (although the two types of experiments are not directly comparable) is again a consequence of DSA. It appears that the strain burst phenomenon, which we have reported previously for 2-1/4 Cr-1Mo steels, is closely related to DSA. This concept is under continual study.

These findings point up the importance of DSA in imparting the creep resistance of Cr-Mo steels. It is uncertain, however, whether long time creep resistance can be increased through the presence of DSA. Effects of DSA on the creep properties of these steels will be examined further in this investigation.

7.3 References

1. K. Ono, A. J. Ardell and A. S. Tetelman, ORNL Quarterly Progress Report for period ending July 31, 1976; ORNL-5200, p. 381-415.
2. P. L. Jones and A. S. Tetelman, ORNL-5107, December, 1975, p. 289.
3. R. W. K. Honeycombe, The Plastic Deformation of Metals, Edward Arnold, London, 1971, p. 368.
4. P. G. Shewmon, Physical Metallurgy (R. W. Cahn, Ed.), North-Holland Publishing Co., London-Amsterdam, 1970, 398.
5. F. Garofalo, O. Richmond, W. F. Domis and F. von Gemmingen, "Joint International Conference on Creep", Inst. of Mech. Engrs. (London), 1963, p. 1-31.
6. A. Ahmadieh and A. K. Mukherjee, Material Sci. and Engr., 21 (1975) 115.
7. A. Ahmadieh and A. K. Mukherjee, Scripta Met., 9 (1975) 1299.
8. P. A. Chaleo, Ph.D. Dissertation, Univ. of Calif., Los Angeles, 1974.
9. R. L. Kleuh, J. Nucl. Mat. 54 (1975) 41.

8. GENERAL ELECTRIC COMPANY

K. D. Challenger

8.1 INTRODUCTION

The principal objective of mechanical properties testing at the General Electric Company is to characterize the behavior of 2¼Cr-1Mo and austenitic stainless steels in sodium environments relevent to LMFBR steam generators and intermediate heat transport systems. Under conditions predicted for the intermediate sodium system of the CRBRP, 2¼Cr-1Mo will lose carbon to the system and be weakened. The carbon will tend to carburize and embrittle stainless steel components in other portions of the system. The effects of a carburizing environment on creep rupture properties of Type 316 stainless steel will be evaluated along with an assessment of creep-fatigue interactions. In addition, studies of fatigue crack propagation rates in carburizing sodium will be performed in order to assess environmental effects under pertinent intermediate sodium loop loading conditions. The loss of carbon from 2¼Cr-1Mo steel components can result in increased creep rates of the decarburized surface layer with the possibility of ratchetting under cyclic straining. These effects will be evaluated for base metal and weld metal in a decarburizing sodium environment. Elastic-plastic fracture mechanics methods, including J-Integral and Crack Opening Displacement (COD) are being employed to determine the toughness (K_{Ic}) of 2¼Cr-1Mo steel at relevant temperatures and to compute the critical flaw sizes for the onset of rapid fracture. The effects of welding procedure, flaw location and thermal aging are being evaluated. The effect of melting practice and heat treatment on the mechanical behavior of 2¼Cr-1Mo is being evaluated to confirm that the properties of consumable remelted 2¼Cr-1Mo meet the appropriate requirements of the ASME B&PV Code for LMFBR steam generators.

8.2 MECHANICAL PROPERTIES OF STAINLESS STEEL IN CARBURIZING SODIUM

8.2.1. Fatigue Crack Growth Studies - J. F. Copeland/J. L. Yuen

8.2.1.1 Background

The objective of this program is to determine the environmental influence of liquid sodium on the fatigue crack propagation rates for annealed Type 316 stainless steel and weldments. To be prototypic of expected LMFBR Intermediate Heat Transport System (IHTS) piping conditions, this testing is being done at low frequency (about 0.5 cycles per minute (cpm) and at 510°C [950°F]). Additionally, the existence of a high carburizing potential in the liquid sodium environment is a distinct possibility.[1] Since the exact carburizing potential of the IHTS sodium has not been determined, this experiment is being run under the most severe conditions, of carbon-saturated sodium. The use of carbon-saturated sodium also allows the acceleration of carburization in order to represent design life conditions with a relatively short-term test. Control tests in air are also being performed under the same loading conditions, in order to truly discern environmental effects. These results will show whether or not penalties or allowances for crack growth in secondary system sodium are required or warranted.

ASTM E399, 12.7 mm. (0.5 in.) thick, 3-point bend specimens were machined from annealed 15.9 mm. (5/8 in.) Type 316 plate[1] and fatigue precracked. Specimens to be tested in air were aged at 510°C (950°F) for 1000 hrs. in air. Those to be fatigued in high carbon sodium were pre-exposed in Loop A sodium with a Grade 1050 carbon steel source at 510°C (950°F) for 1000 hrs. The carburization incurred by these specimens during sodium pre-exposure is shown in Figure 8.1, and is typical of that anticipated[1] for a 30-year LMFBR design life with a 2¼Cr-1Mo steel carbon source.

Fatigue crack growth tests were performed in air and flowing, high carbon sodium in two specially designed fatigue test facilities.[1] Three tests could be run concurrently in each facility. After loading for an estimated number of cycles, the specimens were withdrawn and examined for crack growth. When the crack growth approximated 0.76 mm. (30 mils) the

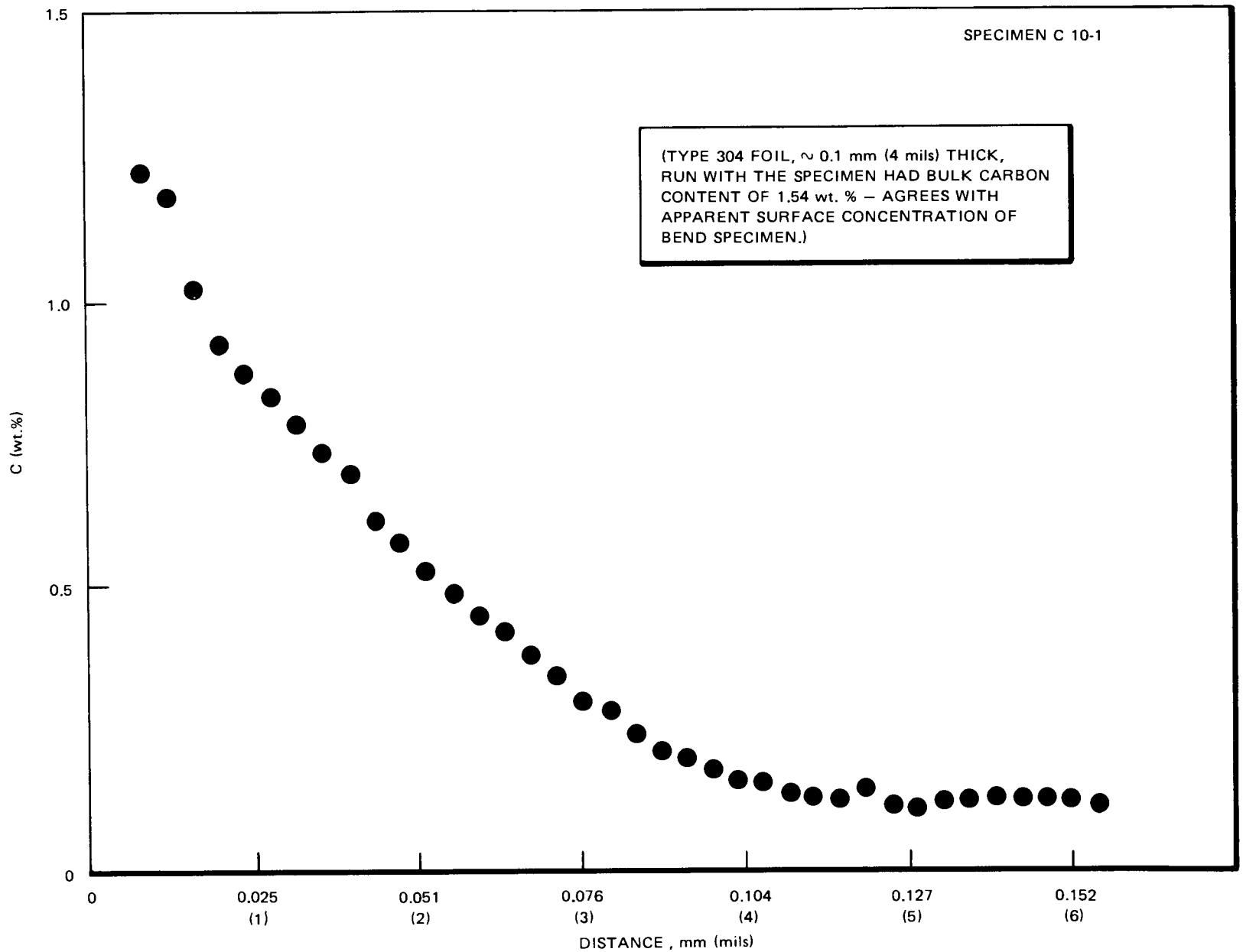

Figure 8.1 Carbon Profile (Electron Microprobe) on Annealed Type 316 12.7 mm (0.5 in.) Bend Specimen Aged in Loop A for 1000 hr. at 510°C (950°F). 1050 Carbon Steel Source (Carbon - Saturated Sodium)

specimen was fractured to accurately measure crack growth. A binocular microscope was used to measure the crack extension. The crack growth rate was computed from the ratio of crack extension to cycles.

8.2.1.2 Current Progress

Two control air runs were completed this quarter. The first run evaluated the effects of zero hold time at low frequency (0.033 cpm). The crack growth rates are in agreement with the results of earlier runs and are in good agreement with the air data of HEDL[2] and NRL.[3] In the second run, two effects were evaluated at a frequency of 0.33 cpm. Two specimens were run with a 1 minute hold at the peak stress and R = 0.05 (where R = minimum stress/maximum stress). The crack growth rates are slower than any of the previous air results, and are comparable to the sodium results.[4,5] The hold time may have blunted the crack tip, thereby retarding the crack growth, even though the effective time at the high stress intensity was greater. The third specimen was run at R=0.4 with no hold time. The growth rate was not significantly different from the earlier control air growth rates with $R \sim 0$. The above results are shown in Figure 8.2. Additional runs at high R values are planned for the next quarter. Gas Tungsten Arc (GTA) weld specimens, with 16-8-2 filler metal, have been prepared and pre-exposed for testing during the next quarter, also.

The 1000 hr. pre-exposure in sodium of these GTAW crack growth specimens has been completed along with air exposure control specimens. Crack growth tests with these specimens were initiated during the past quarter. A 1000 hr. pre-exposure in sodium of the special crevice carburization experiment was also completed. The crevice exposure specimen consisted of flat, annealed Type 316 stainless steel bars 25 mm (1 in.) X 100 mm (4 in.) stacked at different openings shown in Figure 8.3. The crevice openings were set by placing two thin foil shims 25 mm (1 in.) long across the width of the bar, spaced approximately 75 mm (3 in.) apart. The uncleaned crevice exposure specimen was dissassembled in an inert environmental chamber. All the crevice openings which ranged from 0.0175 mm (0.0007 in.) to 0.125 mm (0.005 in.) were found to be filled with sodium. From the examination of the dissassembled crevice surfaces,

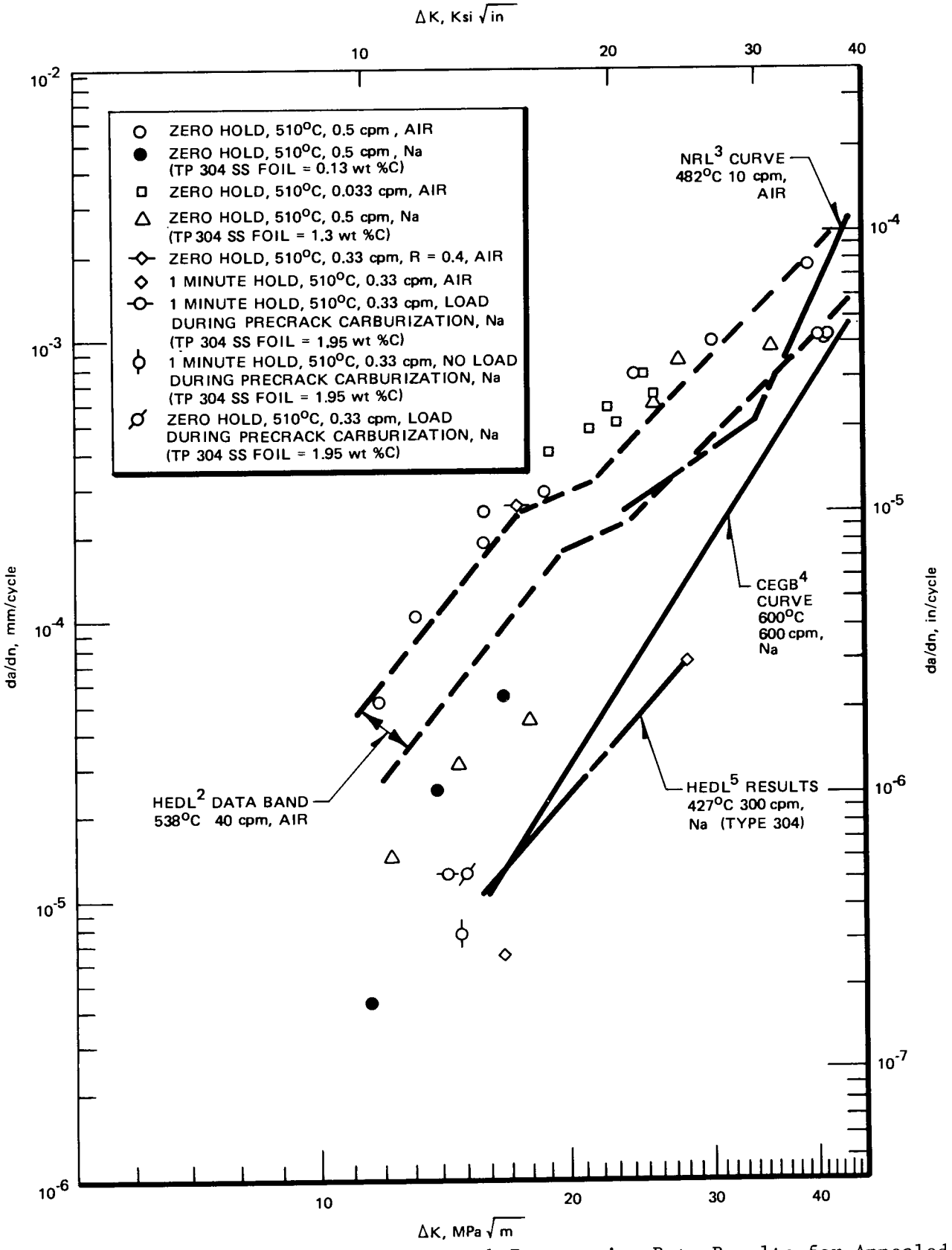

Fiugre 8.2 Comparison of Fatigue Crack Propagation Rate Results for Annealed Type 316 Stainless Steel at Elevated Temperatures.

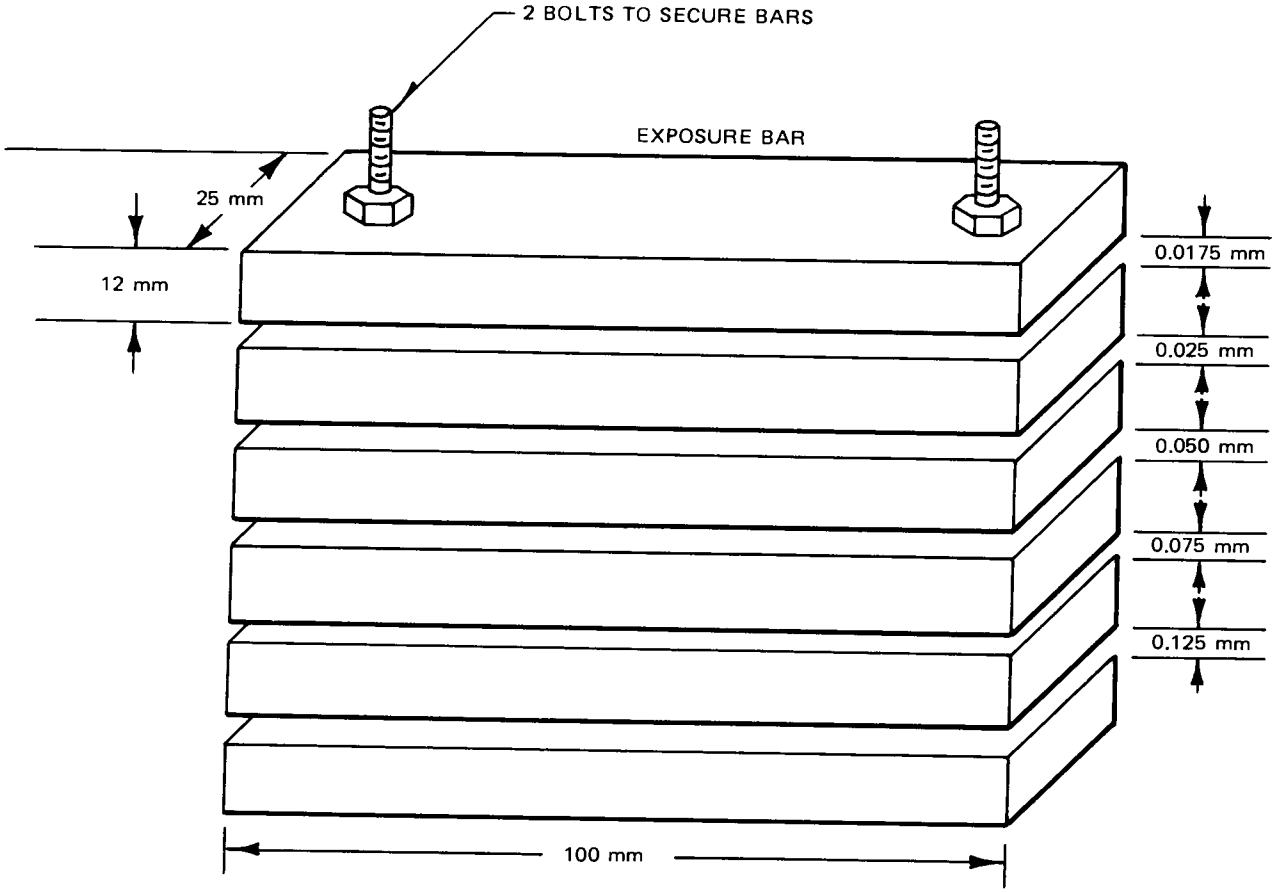

Figure 8.3 Flat Type 316 Stainless Steel Exposure Bars Spaced at Different Openings

small isolated voids were observed appearing mostly toward the mid-plane of the surface. Since the crevice openings were formed from two stacked bars, each crevice opening had essentially two mouths for sodium to enter. It is hypothesized that as the sodium entered from either side, pockets of gas were entrapped near the mid-plane of the crevice opening.

From optical metallography, the greatest amount of carburization was found adjacent to the mouth of the crevice opening, as expected. The amount of carburization decreased with increasing distance away from the mouth of the crevice opening. Electron microprobe analyses are planned for next quarter to quantitatively assess the depth of carburization as a function of crack opening. These preliminary results are particularly important in that we are assured that sodium is indeed able to flow into small crevice openings. A possible experimental problem gleaned from the crevice carburization experiment was the tendency of the flowing sodium to trap small pockets of cover gas in the crevice openings. If such an event occurs at the crack tip, sodium will be prevented from making contact with the crack tip, thus creating an essentially inert environment around the crack tip. Experimental techniques attempting to alleviate this problem will be pursued next quarter. Analysis of the carburization occurring in this crevice specimen is continuing, and appears to be of great value. The results will be related to test specimen crack opening displacements and crack growth rates in terms of a carburization process zone size expected at the crack tip. These results also give considerable insight into the relationship of relatively high frequency laboratory tests to lower frequency plant transient cycling. This analysis will be presented in the next quarterly report.

8.2.2 Creep Investigation - P. P. Pizzo

The second phase of creep testing carburized 316 H stainless steel was begun during the current reporting period. These tests are designed to investigate the influence of carburization on the creep behavior of specimens with different strain histories. A description of the specimens and the respective test matrices for this program were presented in the last quarterly report.[6]

Six tests have been completed. The results of these tests are presented in Table 8.1. The following comparisons are available in these data:

1. Tests 1 and 2 provide a comparison of control versus carburized conditions for a stress of 445.8 MPa (64.7 Ksi). The strain history of specimens C-28 and C-36 is determined by the applied test stress.

2. Tests 3 and 4 provide a comparison of control versus carburized conditions for specimens prestrained approximately 9% prior to testing at 425.2 MPa (61.7 Ksi).

3. Tests 5 and 6 compare control versus carburized conditions for specimens prestrained approximately 16% prior to testing at 425.2 MPa (61.7 Ksi).

The following trends are indicated in this data:

1. The creep rate of carburized specimens is lower than that of control specimens tested under equivalent conditions. The ratio for the minimum creep rate (control: carburized) is about 3:1 for the conventional creep test (Test 1 versus Test 2), and this ratio increases to about 18:1 for the specimens pre-strained to 16% prior to testing.

2. The creep strain-to-failure is lower for the carburized specimens. The average strain-to-failure is about 1.3% for carburized specimens while the control specimens exhibit about three times this fracture strain.

3. For the conventional creep tests (1 versus 2) the rupture life for the control specimen is greater than that of the carburized specimen. However, for the pre-strained specimens, the carburized specimens exhibit a longer rupture life than the control.

The above trends can be understood in terms of the inter-relationship between rupture life, strain-to-failure, and the minimum creep rate. The rupture life is proportional to the critical strain that can be accumulated

TABLE 8.1

Creep Test Results - 316H Stainless Steel Program

Test	Spec Design	Type	Prestrain Conditions σ_o (MPa)	Prestrain Conditions e_o (%)	σ_t (MPa)	e_f (%)	$\dot{e}_{mcr}$ (s^{-1})	t_r (Hours)
1	C-28	Argon	452	14.3	445.8	5.4	1.5×10^{-8}	768.5
2	C-36	Na/C	452	7.1	445.8	1.5	5.4×10^{-9}	435
3	C-27	Argon	429.3	9.7	425.2	2.4	7.7×10^{-9}	613
4	C-33	Na/C	466.4	8.5	425.2	1.1	1.9×10^{-9}	816
5	C-30	Argon	452	15.8	425.2	4.0	1.5×10^{-8}	631
6	C-32	Na/C	500.7	16.7	425.2	1.3	8.7×10^{-10}	983

Notes:
(1) All tests performed at 510°C (950°F)
(2) Specimens prestrained at 510°C (950°F) at $\dot{e}_o = 10^{-3} s^{-1}$
(3) σ_o is the engineering stress selected to prestrain the specimens and e_o is the corresponding engineering strain
(4) σ_t is the engineering test stress
(5) e_f is the total creep strain-to-failure

during creep prior to gross specimen instability. But the rupture life is also inversly proportional to the creep rate of the controlling deformation processes. The balance between these competing forces will determine the net rupture life exhibited by the specimen.

In tests 1 and 2 the ratio of creep rates, $\dot{e}$ control/$\dot{e}$ carburized, is low. The creep ductility of the carburized specimen is about 1/3 that of the control. As a result, the carburized specimen attains instability early, and a low rupture time is exhibited. In the pre-strained tests however, tests 3 through 6, the difference in ductility remains about the same, but the creep rate ratio increases. The carburized specimens creep at a progressively slower rate. The increased creep rate ratio is associated with the flow strength differential at constant strain demonstrated in the hot tensile strength data reported in the last quarterly report.[6] As a consequence, the time-to-failure of the carburized specimen increases, and the trend in rupture life is reversed.

The results presented in this report suggest that the rupture strength of carburized components is dependent on the stress/strain history of the material. The rupture strength is determined by a balance between creep ductilities and the rate of deformation. Consideration of creep behavior under equivalent strain conditions can be important in the design of components for service at elevated temperature. Temperature excursions for example will result in strain perturbations. Under such conditions, the rupture strength of the uncarburized condition may be limiting, and thus base metal data would serve as a conservative estimate for design.

The above results are preliminary. Tests are currently underway to further assess the creep behavior of 316 H at 510°C (950°F). Specifically, specimens C-29 and C-35 (reference Table 8.2 of the last quarterly report[6]) are being tested. Specimens C-29 and C-35 will provide a comparison for specimens tested at a stress of 425.2 MPa (61.7 Ksi). This applied stress is different than that originally intended. The stress has been altered to provide a direct comparison of the pre-strain test data of Table 8.1 with conventional creep data. The two government owned creep machines obtained from Atomics International last year have been rebuilt and are now being employed for these studies.

TABLE 8.2

Analysis of Foil Samples Removed After DP-9

1500 hours, 510°C (950°F)

Carbon (ppm)

Sample*	Co**	C	ΔC	ΔC/Co	$K(X10^8)\ \frac{gm^C}{cm^2 - sec^{\frac{1}{2}}}$
E19	950	406	544	0.57	2.34
E13	↑	753	197	0.21	0.85
E28		837	113	0.12	0.49
E56		858	92	0.10	0.40
E47		923	27	0.03	0.12
E38		812	138	0.15	0.60
E65		854	96	0.10	0.41
E8		330	620	0.65	2.67
E44		775	175	0.18	0.75
E76	↓	858	92	0.10	0.40
E83	950	887	63	0.07	0.27
V20	1100	575	525	0.48	2.26
V11	↑	815	285	0.26	1.23
V31		857	243	0.22	1.05
V56		734	366	0.33	1.58
V48		811	289	0.26	1.24
V65		849	251	0.23	1.08
V9		388	712	0.65	3.06
V35		875	225	0.20	1.00
V68	↓	894	206	0.19	0.90
V83	1100	910	190	0.17	0.82
L4	290	211	79	0.27	0.32
L12	↑	262	28	0.10	0.10
L22		239	51	0.18	0.20
L34		269	21	0.07	0.09
L40		71	219	0.76	0.93
L50		223	67	0.23	0.27
L56	↓	272	18	0.06	0.12
L65	290	273	17	0.06	0.05

* Note: L ≡ ELC (Extra Low Carbon)
E ≡ ESR (Electro-Slag Remelt)
V ≡ VAR (Vacuum-Arc Remelt)

** Compositions reported in 7th Quarterly Report - Steam Generator Materials Engineering, January-March 1976, GEAP-14029-7, Table 6-4.

8.3 DECARBURIZATION KINETICS AND DESIGN METHODS VERIFICATION TESTING

P. P. Pizzo/L. V. Hampton/J. L. Krankota

8.3.1 Background

The selection of 2¼Cr-1Mo steel as the reference alloy for sodium-heated steam generators was based primarily upon its immunity to stress corrosion cracking in chloride or caustic contaminated environments, and its proven fabricability. One of the major concerns with the use of this material for sodium applications is its susceptibility to decarburization during service. Early analyses assumed that relatively thin sections, such as steam generator tubing, would completely decarburize during the LMFBR lifetime, with concomitant design stress penalties necessarily imposed. In addition to the assumed carbon losses, the potential for carburization of stainless steel components in the loop was also recognized as a potential difficulty.

In the absence of an acceptable theoretical model for decarburization of 2¼Cr-1Mo steel, an approach introduced by Armijo and Krankota[7] was used to analyze the results obtained from many different experiments. This technique treats carbon loss data as if it were corrosion data; that is, the loss of carbon per unit area is described as a function of time. A parabolic time dependence has been observed which suggests that the decarburization process is diffusion controlled. The decarburization rate constants, K*, from all available data were fit to an Arrhenius type expression for design use. The resulting correlation provides estimates of carbon loss as a function of time at temperature. This is information essential toward establishing decarburization-associated design stress penalties for the steam generator. Preliminary data indicate that steam

---

*Where K is defined by:

$$K = \frac{gm^c}{cm^2 - sec^{\frac{1}{2}}}$$

$$M = \left(\frac{gm^c}{cm^2}\right) = Kt^{\frac{1}{2}}$$

generator tubes would not be expected to lose more than 300 ppm carbon in the design life of the CRBRP. Only a small design stress penalty (<10%) is associated with this loss.

The current assessment of the design stress penalty associated with decarburization is based on limited data available in the literature.[8,9,10] Much of these data are for steel melted to a low carbon content. Therefore, mechanical properties data are needed as a function of carbon content for 2¼Cr-1Mo steel decarburized to a particular carbon level. Such data can be combined with the results of the kinetics study and a knowledge of the decarburization profile to more accurately assess the strength degradation associated with the depletion of carbon from the steel matrix. In this program, elevated temperature mechanical properties data are being generated to meet this need. Uniaxial tests are being performed on sodium-filled and control pipe specimens in order to characterize the effect of decarburization on creep and hot tensile properties. Prototypic tubing and all-weld-metal tubes are being internally pressurized in sodium and control environments to assess the effects of the decarburizing environment on stress rupture properties. Description of the specimens test facilities, and test matrix has been included in earlier reports.[11,12,13]

8.3.2 Decarburization Kinetics of 2¼Cr-1Mo

8.3.2.1 Current Progress

Initial decarburization rate constant data for ESR, VAR and ELC (extra-low carbon) 2¼Cr-1Mo are now available with the completion of run DP-9 in Decarburization Pot #1 after 1500 hours at 510°C (950°F). The variation in decarburization rate constants with heat treatments is shown in Table 8.2 and Figure 8.4. The thin (0.25 X 10 X 80 mm [0.010 X 0.4 X 3.1 in.]) foils had been given the range of heat treatments listed in Table 8.3. The rate constants are calculated on the basis of one time point (1500 hours); that is, by assuming that M (grams C) vs. $t^{\frac{1}{2}}$ ($sec^{\frac{1}{2}}$) passed through the origin. These rates will be confirmed by data from samples with planned exposures of 4,000 and 10,000 hours at the same temperature.

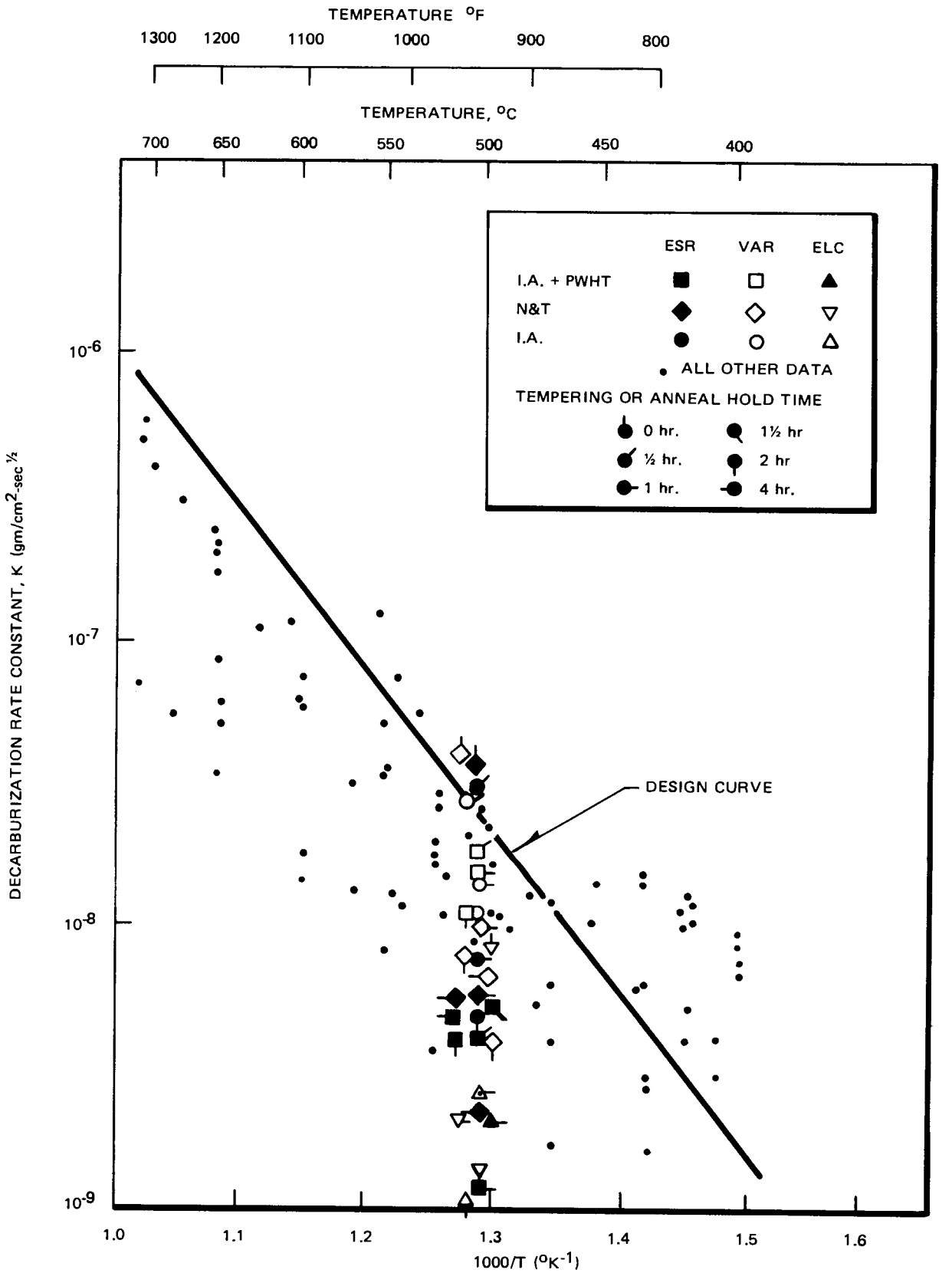

Figure 8.4 Decarburization Rate Constants for 2¼Cr-1Mo in Sodium, Data From Decarb Pot #1 (Run DP-9) With All Other Investigations

TABLE 8.3

Heat Treatment/Sodium Exposure Matrix

A) Isothermal Anneal

	HOLD TIME (hr) at 716°C (1320°F) after cooling from 927°C (1700°F)			
	½	1	1½	2
ESR	E19 E56*	E13 E47*	- E38*	E28 E65*
VAR	V20 V56*	V11 V48*	- -	V31 V65*
ELC	- -	L4 L22*	- -	L12 L34*

B) Normalize & Temper**

	TEMPERING TIME (hr) after normalizing at 927°C (1700°F) for 1 hr.			
	0	1	2	4
ESR	E8	E44	E76	E83
VAR	V9	V35	V68	V83
ELC	L40	L50	L56	L65

---

* These specimens were isothermally annealed as specified and also given a 4 hr. 727 ± 19°C (1340 ± 35°F) PWHT

** Temper ≡ 727 ± 19°C (1340 ± 35°F)

The data in Table 8.2 and Figure 8.4 clearly indicate that those materials with relatively unstable microstructures (either short tempering or anneal [transformation] hold times or none at all) decarburized the fastest. For example samples which were only normalized (one hour at 927°C [1700°F] air cool) lost 65%, 65% and 76% of initial carbon content for ESR, VAR and ELC materials respectively. The amount of carbon loss decreased with increasing tempering or anneal hold time in all materials, but less for the VAR material. It still lost almost 20% of the original amount, even after being tempered for 2-4 hours. Carbon losses in the ESR samples could be reduced to 5-10% carbon loss by the longer temper times.

Samples of all materials which were given the longest initial anneal hold time (2 hr.) were not further stabilized (with respect to decarburizing potential) by an additional tempering of 4 hours (which simulated the Post Weld Heat Treatment, PWHT). The PWHT significantly stabilized the samples with shorter initial anneal hold times (½ and 1 hour).

In general, the VAR material decarburized faster than the ESR material for similar heat treatments. These results confirm earlier observations in the Intermediate System Mockup Loop (ISML) on the same VAR and ESR materials.[14]

The ELC material decarburized for all material treatments. Earlier studies of the decarburization behavior of this material in a flowing loop situation ISML at hot leg temperature of 520°C (968°F) revealed that it tended to carburize in the isothermally annealed condition.[14] As with the ESR and VAR materials, the normalized ELC foil decarburized more rapidly and to the greatest extent. Tempering of the normalized foils lowered the decarburization rate significantly. Post weld heat treatment of isothermally annealed foils had negligible additional effect on the decarburization of this material.

8.3.2.2 Future Work

With the data obtained from run DP-9, it is apparent that the more unstable heat treatments are decarburizing at such high rates as to result in over-lapping of the carbon profiles at the center of the foils. Such an event would tend to lower the driving force for decarburization by decreasing the carbon activity at the center of the foil. Therefore,

at the beginning of fiscal year 1977, thicker foils (0.38 to 1.27 mm [0.015 to 0.050 in.]) will be made from the ESR, VAR and ELC 2¼Cr-1Mo heats and heat treated for exposure in run DP-11 (6000 hours long, with some samples receiving up to 10,000 hours total exosure).

8.3.3 Mechanical Properties of 2¼Cr-1Mo Steel in Decarburizing Sodium

Progress in this mechanical properties investigation during the current reporting period was limited by the non-availability of a suitable sodium filling source. Such a source is required for exposure capsule and test specimen filling. The requirement is for a source of clean (<10 ppm Oxygen) and low carbon activity sodium. Loop 6R, previously used for carburization studies, was modified for capsule filling; decarburization conditions were established in this loop through hot trapping techniques using titanium sponge as a gettering agent. The attainment of a decarburization potential was monitored using 2¼Cr-1Mo and/or 316 stainless steel surveillance coupons. Data obtained in reducing the carbon potential of Loop 6R is being ananlyzed, and the results of this program will be presented in the next quarterly report. Capsule filling was initiated in September, and an approximate delay of sixty days was incurred in the acqusiition of mechanical properties data for the decarburized condition.

The uniaxial creep testing of control ESR specimens was initiated during this reporting period. Specimens A-16 through A-19 are currently on-line. These four tests are being conducted at 510°C (950°F). The respective test stresses are: 130, 172, 150 and 150 MPa (18.9, 25.0, 21.7 and 21.7 Ksi). Rupture times from 500 to 5000 hours are expected. Specimens A-16 thru A-18 have been thermally aged 1000 hours prior to testing. Specimen A-19 has not been thermally aged prior to testing. A detailed description of the specimens and the pertinent test conditions can be obtained from Table 8.8, presented in the previous quarterly report. Mechanical properties data will be reported as it becomes available.

The testing of biaxial pressure pin specimens was also delayed during this period. An isolation valve failure and modification of the pressure control system were responsible for the delay. Repairs have been completed,

and the testing of 4 each pressure pin specimens is being initiated. The respective specimens are TØ1, TØ4, TØ6 and TØ8. These specimens represent four different test conditions represented in Table 8.9 of the last quarterly report.[6] Details of the test conditions will be specified as test data becomes available. All four tests are being conducted at an equivalent stress of 172 MPa (25.0 Ksi). Approximate 1000 hour rupture life is expected.

The capability for sodium filling of exposure capsules makes possible progress for the hot tensile properties program outlined in Table 8.7 of the last quarterly report.[6] Exposure chambers have been filled and sealed, and the control thermal aging treatment is being performed. The results of this study will be reported in the next quarterly.

8.4 FRACTURE TOUGHNESS OF LMFBR STEAM GENERATOR MATERIALS

J. F. Copeland/J. L. Yuen

8.4.1 Background

The objective of this program is to determine fracture toughness values (K_{Ic}) at 24°C (75°F) and higher temperatures, for potential LMFBR steam generator shell and tubesheet materials. These results will be combined with Charpy V-notch and drop-weight tests values (RT_{NDT} determinations) and tensile test results to evaluate resistence to fracture. The essence of this approach to prevent fracture is set forth in the K_{IR} curve of Appendix G to Section III of the ASME Boiler and Pressure Vessel Code. No toughness data on 2¼Cr-1Mo steel was included in the derivation of the Code K_{IR} curve. Therefore, testing is required at hydrostatic test and at service temperatures to assure that the present K_{IR} curve approach is adequate for this material. In order to evaluate the fracture toughness of 2¼Cr-1Mo above the Nil Ductility Transition Temperature (NDTT), it is necessary to employ elastic-plastic fracture toughness testing methods, such as the J-Integral approach.

Thick section 2¼Cr-1Mo steel plates were procured for this program and heat treated to represent potential LMFBR material conditions. The emphasis is on air melted (AM) material, although some testing has been

done on Vacuum Arc Remelted (VAR) steel. Information on test material chemical composition has been reported previously.[15] The air melted material is in the form of 89 mm. (3.5 in.) thick plate, while the VAR steel is 51 mm. (2 in.) thick plate. Two 122 cm. (48 in.) long, 8.9 cm. (3.5 in.) thick SMAW weldments were prepared from the AM plates as described previously.[15] These weldments passed the nondestructive examination and appear to be excellent test welds. The "K"-shaped joint was specified to provide a relatively straight edged fusion line for heat affected zone (HAZ) tests.

Initial tensile, Charpy V-notch (CVN), drop weight NDT, and fracture toughness (J_{Ic}, K_{Ic}) test results on base material are reported in Reference 15. Summaries of these results, along with the recent results, are presented again in this report in order to give a complete story to date.

8.4.2 Current Progress

Test material conditions are described in Table 8.4 These conditions include SMAW weld metal and HAZ tests. Specimen notch and gage length locations relative to these weldment zones are shown in Reference 15. Tensile test results are presented in Table 8.5 for material conditions A-H. A large number of these tensile results were discussed previously.[15] Tensile tests from room temperature to 510°C (950°F) were performed during this quarter on annealed base metal with a 24 hr. PWHT (at 727°C [1340°F]), on annealed base metal aged at 510°C (950°F) for 1000 hr. subsequent to a 4 hr. PWHT at 727°C (1340°F), and on specimens containing SMAW weld metal (E 9018-B3 electrodes) and HAZ regions in the center of the specimen gage length. It is concluded that the 24 hr. PWHT causes no significant further decrease in yield or ultimate tensile strength beyond that induced by a 4 hr. PWHT at 727°C (1340°F). However, thermal aging at 510°C (950°F) for 1000 hr. after a 4 hr. PWHT decreased the yield strength by about 13.8 to 34.5 MPa (2 to 5 Ksi.) from the base condition, but had no significant effect on ultimate tensile strength. The weld zone in the weld specimens was too small to cover the complete 24.5 mm. (1 in.) gage length of these tensile tests. Therefore, the option existed for failure to occur in

TABLE 8.4

MATERIAL CONDITION OF 2¼Cr-1Mo STEEL PLATES FOR FRACTURE TOUGHNESS TESTING

A. Anneal (AM Heat 86693)

927°C (1700°F) for 3 hr., furnace cool at max. rate of
55.5°C (100°F) per hr. to less than 482°C (900°F)

B. Anneal + Post Weld Heat Treatment (PWHT) (AM Heat 86693)

927°C (1700°F) for 3 hr., furnace cool at max. rate of
55.5°C (100°F) per hr. to less than 482°C (900°F)
+727°C (1340°F) for 4 hrs., air cool or furnace cool

C. Anneal + PWHT (VAR Heat 55262)

927°C (1700°F) for 3 hr., furnace cool at max. rate of
55.5°C (100°F) per hr. to less than 482°C (900°F)
+727°C (1340°F) for 4 hr., air cool

D. Anneal + PWHT + Embrittlement Treatment (AM Heat 86693)

927°C (1700°F) for 3 hr., furnace cool at max. rate of
55.5°C (100°F) per hr. to less than 482°C (900°F)
+727°C (1340°F) for 4 hr., air cool or furnace cool
+510°C (950°F) for 1000 hr., air cool

E. Normalize + Temper (AM Heat 86693)

927°C (1700°F) for 3 hr., air cool
+727°C (1340°F) for 4 hr., air cool

F. SMAW Weld Metal (AM Heat 86693)

915°C (1680°F) for 3.5 hr., furnace cool at max. rate of
55.5°C (100°F) per hour to less than 482°C (900°F)
+SMAW (see weld procedure, Ref. 14)
+727°C (1340°F) for 12 hr., furnace cool at max. rate of
55.5°C (100°F) per hour

G. SMAW Heat Affected Zone (HAZ) (AM Heat 86693)

915°C (1680°F) for 3.5 hr., furnace cool at max. rate of
55.5°C (100°F) per hour to less than 482°C (900°F)
+SMAW (see weld procedure, Ref. 14)
+727°C (1340°F) for 12 hr., furnace cool at max. rate of
55.5°C (100°F) per hour

H. Anneal + PWHT (24 hr., AM Heat 86693)

927°C (1700°F) for 3 hr., furnace cool at max. rate of
55.5°C (100°F) per hr. to less than 482°C (900°F)
+727°C (1340°F) for 24 hr., furnace cool at max. rate of
55.5°C (100°F) per hour

TABLE 8.5

Tensile Test Properties for 2¼Cr-1Mo Heat 86693.
Air-Melt 89 mm. (3.5 in.) Thick Plate, Properties at ¼ T Location.
Strain Rate = 0.04 min.$^{-1}$. Also, results for VAR Heat 55262.

Treatment	Test Temperature °C (°F)	Yield Point MPa (Ksi)	0.2% Y.S. MPa (Ksi)	U.T.S. MPa (Ksi)	%El. (25.4 mm)	% R.A.
A (Anneal)	24 (75)	270 (39.2)	243 (35.2)	472 (68.5)	39.6	65.3
		262 (38.0)	243 (35.2)	466 (67.6)	38.2	66.1
		260 (37.7)	235 (34.1)	470 (68.2)	41.5	66.9
	371 (700)	169 (24.5)	168 (24.3)	450 (65.3)	23.5	50.7
	454 (850)	- -	160 (23.2)	449 (65.1)	23.8	49.5
	510 (950)	- -	156 (22.6)	410 (59.5)	26.5	60.3
	566(1050)	- -	154 (22.4)	363 (52.7)	36.4	72.5
B (Anneal + PWHT)	24 (75)	295 (42.8)	261 (37.9)	466 (67.6)	33.3	65.9
		297 (43.1)	267 (38.7)	467 (67.7)	34.6	65.1
		- -	- -	453 (65.7)	32.7	69.5
		243 (35.2)	231 (33.5)	448 (65.0)	41.3	68.7
	177 (350)	196 (28.4)	192 (27.8)	374 (54.2)	36.5	68.3
		209 (30.3)	198 (28.7)	372 (53.9)	38.0	70.4
	288 (550)	194 (28.2)	181 (26.2)	298 (57.7)	24.9	59.7
	399 (750)	- -	146 (21.2)	399 (57.9)	24.0	54.3
	454 (850)	- -	152 (22.0)	386 (56.0)	27.8	56.2
	510 (950)	- -	143 (20.7)	340 (49.3)	33.2	65.1
	566(1050)	- -	133 (19.3)	292 (42.3)	43.6	76.6
C VAR* (Anneal + PWHT)	24 (75)	- -	275 (39.9)	439 (63.7)	36.1	51.6
D (Anneal + PWHT + 510°C, 1000 hr.)	24 (75)	234 (33.9)	221 (32.1)	459 (66.6)	34.8	64.4
		223 (32.4)	220 (31.9)	465 (67.4)	38.1	67.2
		- -	- -	478 (69.4)	31	69
		- -	218 (31.6)	475 (68.9)	31	65
	177 (350)	- -	165 (24.0)	387 (56.1)	27	35
		- -	154 (22.4)	385 (55.9)	32	35
	288 (550)	- -	150 (21.8)	388 (56.3)	25	42
	399 (750)	- -	148 (21.4)	381 (55.3)	23	50
		- -	177 (25.7)	394 (57.1)	22	45
	510 (950)	- -	148 (21.4)	334 (48.5)	30	35
		- -	- -	320 (46.4)	37	39

*Results by H. P. Offer (GE) on same VAR Heat No. (55262) - different plate, funded under 189a-SG029.

TABLE 8.5

(Continued)

Treatment	Test Temperature °C (°F)	Yield Point MPa (Ksi)	0.2% Y.S. MPa (Ksi)	U.T.S. MPa Ksi)	%El. (25.4 mm)	% R.A.
E (Norm. + Temp.)	24 (75)	298 (43.2)	285 (41.4)	462 (67.0)	38.4	68.7
		285 (41.4)	264 (38.3)	460 (66.7)	40.0	68.8
F (SMAW Weld Metal)	24 (75)	- -	281 (40.8)	461 (66.8)	23	69*
		- -	253 (36.7)	499 (77.4)	22	65*
	177 (350)	- -	208 (30.1)	376 (54.6)	22	35*
	288 (550)	- -	204 (29.6)	380 (55.1)	19	40*
	288 (550)	- -	200 (29.0)	370 (53.6)	21	37*
	399 (750)	- -	189 (27.4)	387 (56.1)	16	49*
	510 (950)	- -	186 (27.0)	331 (48.0)	27	25*
		- -	204 (29.6)	338 (49.0)	12	37*
G (SMAW HAZ)	24 (75)	- -	256 (37.2)	464 (67.3)	25	69**
		- -	263 (38.2)	478 (69.4)	22	71**
	177 (350)	- -	227 (32.9)	379 (54.9)	23	36**
	288 (550)	- -	211 (30.6)	403 (58.4)	20	41**
		- -	193 (28.0)	403 (58.4)	20	38**
	399 (750)	- -	232 (33.7)	422 (61.2)	19	43**
	510 (950)	- -	204 (29.6)	348 (50.5)	22	39**
		- -	208 (30.1)	348 (50.5)	21	37**
H (Anneal + PWHT [24 hr.])	24 (75)	- -	230 (33.3)	457 (66.3)	29	65
	177 (350)	- -	184 (26.7)	383 (55.5)	39	37
	399 (750)	- -	154 (22.4)	380 (55.1)	23	46

* Failure occurred outside the weld metal in the base metal.

** Failure occurred outside the weld metal and HAZ in the base metal.

the base metal, indicating that, at all test temperatures, the weld metal and HAZ are stronger than the base metal, even after a 12 hr. PWHT at 727°C (1340°F). Constraint of plasticity in these tests to a localized region caused a significant reduction in total uniform elongation and a 20.7 to 55.2 MPa. (3 to 8 Ksi.) increase in the base metal yield strength. Localized hardness readings will be made to complete this interpretation.

The CVN transition temperature criteria and the CVN upper shelf energies were reported and discussed previously.[15]

J-Integral fracture toughness test results are tabulated in Table 8.6. A large percentage of these results have been discussed previously.[15] New results, from tests performed during the last quarter, are shown for specimens II-3, II-7, II-4, G27, G34, G35 and G36 in Table 8.6. The method of determining the onset of crack extension (to evaluate Δpc, the critical load point displacement at the onset of crack extension) by perturbations in the crack opening rate was unsuccessful for these specimens. Therefore, the fallback method of analysing for J_{Ic} and K_{Ic} was employed: the multiple specimen R-curve method.[15] Results for material conditions D and G at 24°C (75°F) are illustrated in Figures 8.5 and 8.6 for the R-curve analysis. These new results, when combined with prior values, give a completed R-curve for condition D at 24°C (75°F). The value of J_{Ic} is, thus, well defined as 24.5 J./cm^2 (1400 in-lb./in^2) to give a K_{Ic} value of 236 MPa$\sqrt{m.}$ (215 Ksi$\sqrt{in.}$). The next tests to be run for this temper embrittled condition will be at 510°C (950°F). The result of J_{Ic} = 41.3 J./cm^2 (2360 in-lb./in^2) determined from Figure 8.6 must still be considered preliminary because of the scarcity of data in the vicinity of the Crack Opening Stretch (COS) line, at Δa less than 2 mm. (0.08 in.). This situation will be corrected, before the end of September, by performing more condition G (HAZ) tests at 24°C (75°F). The preliminary value of K_{Ic}, derived from J_{Ic}, is 307 MPa$\sqrt{m.}$ (279 Ksi$\sqrt{in.}$). This value is higher than the predicted HAZ toughnes[15] based on early pop-in's in weld metal tests. However, it is in agreement with the relatively good room temperature Charpy V-notch (CVN) toughness of the HAZ.[15] J-Integral HAZ testing is currently underway at 510°C (950°F) where CVN results[15] have shown that the HAZ toughness is quite poor (57 J. [42 ft-lb.]). The new

Table 8.6

COMPACT TENSION SPECIMEN (50.8 mm. [2 in.] THICK) FRACTURE TOUGHNESS RESULTS FOR 2¼Cr-1Mo HEAT 86693. AIR MELT 89 mm. (3.5 in.) THICK WELDMENTS AND PLATE WITH ROLLING RATIO OF 1.0. ALSO, TRANSVERSE RESULTS FOR VAR HEAT 55262, 50.8 mm. (2 in.) THICK PLATE. SPECIMEN LOAD POINT DISPLACEMENT RATE OF 1.52 mm./min. (0.06 in./min.)

Spec.* No.	Material Condition	Test Temperature °C	(°F)	Ductile Crack Extension, Δa, at Unload. mm.	(in.)	Remarks	Δpc mm.	(in.)	J at COS** or Δpc, J_{Ic} J/cm²	(in-lb/in.²)	K_{Ic} MPa√m.	(Ksi√in.)
G1				0.25	(0.0099)	COS* only.						
G2	A	24	(75)	3.00	(0.1180)	Stable Δa.	-	-	18.4	(1050)	206	(187)
G3				0.76	(0.030)	Δa, Pop-in.						
G6				0.70	(0.0276)	Δa, Pop-in.						
G7	B	24	(75)	3.00	(0.1180)	Stable Δa.	-	-	20.3	(1160)	216	(196)
G8				2.90	(0.1140)	Stable Δa.						
GV1				-	-	Pop-in.			9.3	(530)	145	(132)
GV2	C (VAR)	24	(75)	-	-	Pop-in.	-	-	11.7	(670)	164	(149)
GV3				-	-	Pop-in.			6.5	(370)	121	(110)
G14				0.30	(0.0118)	Δa, Pop-in.						
G15	E	24	(75)	1.00	(0.0394)	Stable Δa.	-	-	22.9	(1310)	229	(208)
G16				3.50	(0.1380)	Stable Δa.						

* Specimens G1 - G16 were analysed by multiple specimen method (intersect J versus Δa curve with COS line for J_{Ic}) since Δpc was not determined.

** Crack Opening Stretch - no real crack extension.

TABLE 8.6 (Cont'd.)

Spec.* No.	Condition	Test Temperature °C	(°F)	Ductile Crack Extension, Δa, at Unload. mm.	(in.)	Remarks	Δpc mm.	(in.)	J at COS** or Δpc, J_{Ic} J/cm²	(in-lb/in.²)	K_{Ic} MPa√m.	(Ksi√in.)
G19	B	24	(75)	1.1	(0.043)	Stable Δa.	5.588	(0.2200)	44.5	(2544)	319	(290)
G20				1.5	(0.059)	↑	5.334	(0.2100)	44.4	(2536)	318	(289)
G22				0.6	(0.024)		5.207	(0.2050)	40.0	(2287)	303	(275)
G21		177	(350)	1.5	(0.059)		4.445	(0.1750)	28.7	(1639)	250	(227)
G26		288	(550)	0.6	(0.024)		2.985	(0.1175)	17.1	(975)	190	(173)
G23		399	(750)	1.3	(0.051)		2.972	(0.1170)	16.0	(914)	179	(163)
G24		510	(950)	0.3	(0.012)		2.794	(0.1100)	12.4	(708)	149	(135)
G25				0.6	(0.024)	↓	3.048	(0.1200)	15.7	(897)	167	(152)
I-3	F	24	(75)	Not Measurable		Ductile	1.803	(0.0710)	12.5	(713)	168	(153)***
						Crack	4.597	(0.1810)	39.7	(2267)	300	(273)****
I-5				Not Measurable		Extension	2.337	(0.0920)	15.1	(863)	185	(168)***
						with Small	3.912	(0.154)	30.8	(1758)	264	(240)****
						Pop-in's						

* Specimens C19 to I-5 were analysed based on Δpc (specimen load point displacement at the onset of crack extension) determined by a clip gage at crack tip.

** Crack Opening Stretch - no real crack extension.

*** Values based on Δpc at first pop-in (may have occurred in small amount of HAZ).

**** Values based on Δpc at onset of ductile crack extension (probably indicates weld metal toughness).

TABLE 8.6 (Cont'd.)

Spec.* No.	Condition	Test Temperature °C	(°F)	Ductile Crack Extension, Δa. at Unload. mm.	(in.)	Remarks	Δpc mm.	(in.)	J at COS** or Δpc, J_{Ic} J/cm²	(in-lb/in.²)	K_{Ic} MPa√m.	(Ksi√in.)
II-3				7.25	(0.285)	Stable Δa.						
II-7	G	24	(75)	1.75	(0.069)	Stable Δa.	-	-	41.3	(2360)	307	(279)***
II-4				0.18	(0.007)	Stable Δa.						
G27	B	399	(750)	3.105	(0.122)	Ductile	-	-	-	-	-	- ***
G23				1.30	(0.051)	Crack Extension						
G34				0.64	(0.025)	Δa, Pop-in.	-	-				
G35				0.45	(0.018)	Δa, Pop-in.	-	-				
G36	- D	24	(75)	1.75	(0.069)	Stable Δa.	-	-	24.5	(1400)	236	(215)
G10				0.30	(0.0118)	Δa, Pop-in.	-	-				
G11				0.90	(0.0355)	Δa, Pop-in.	-	-				
G12				1.30	(0.0510)	Stable Δa.	-	-				

* Analysed by multiple specimen method (intersect J versus Δa curve with COS line for J_{Ic}) since Δpc was not determined.

** Crack Opening Stretch - no real crack extension.

*** Additional specimens will be required for analysis by multiple specimen method. These results for J_{Ic} and K_{Ic} must be considered preliminary.

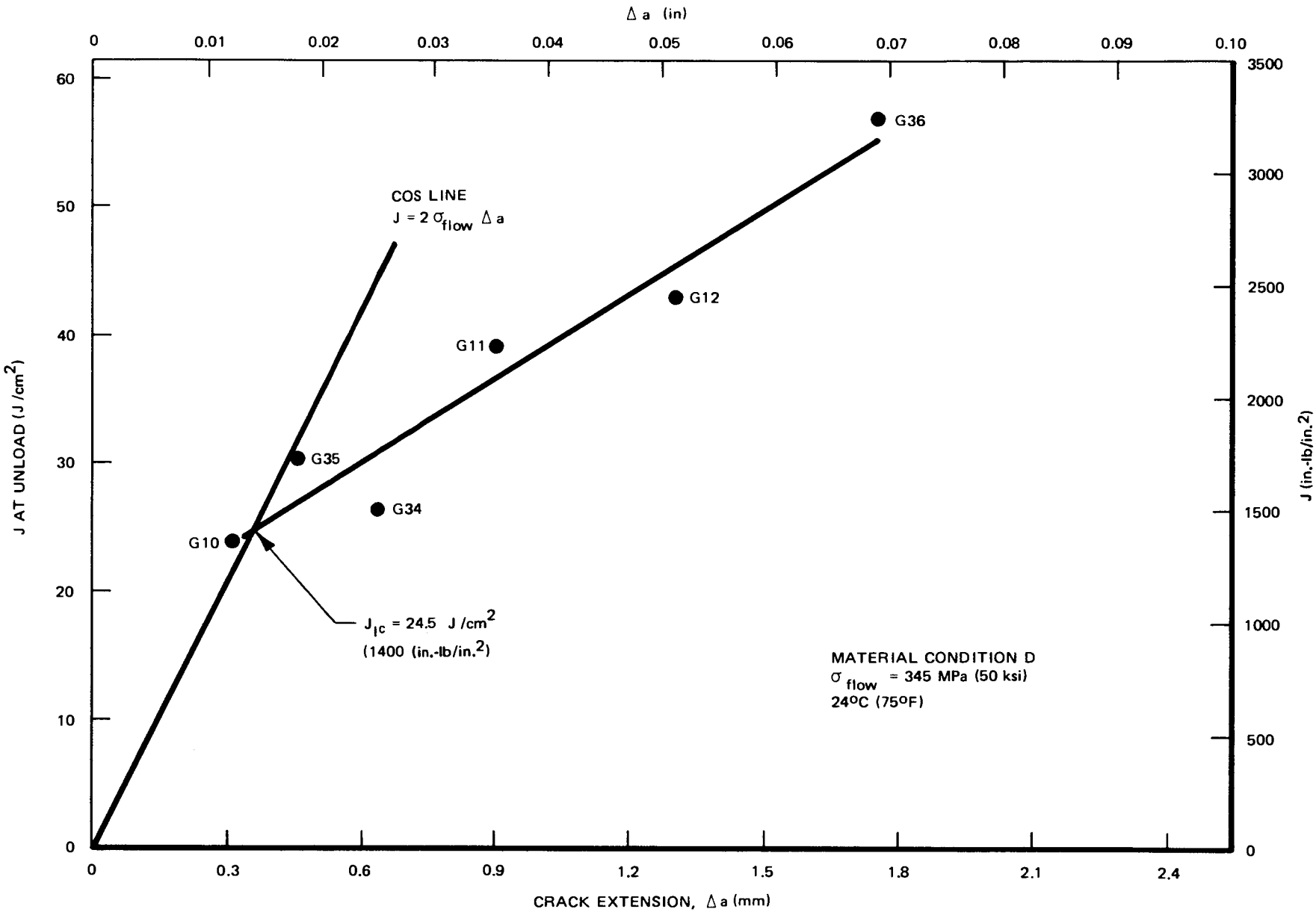

Figure 8.5 J-Integral "R-Curve" for Condition D at 24°C (75°F)

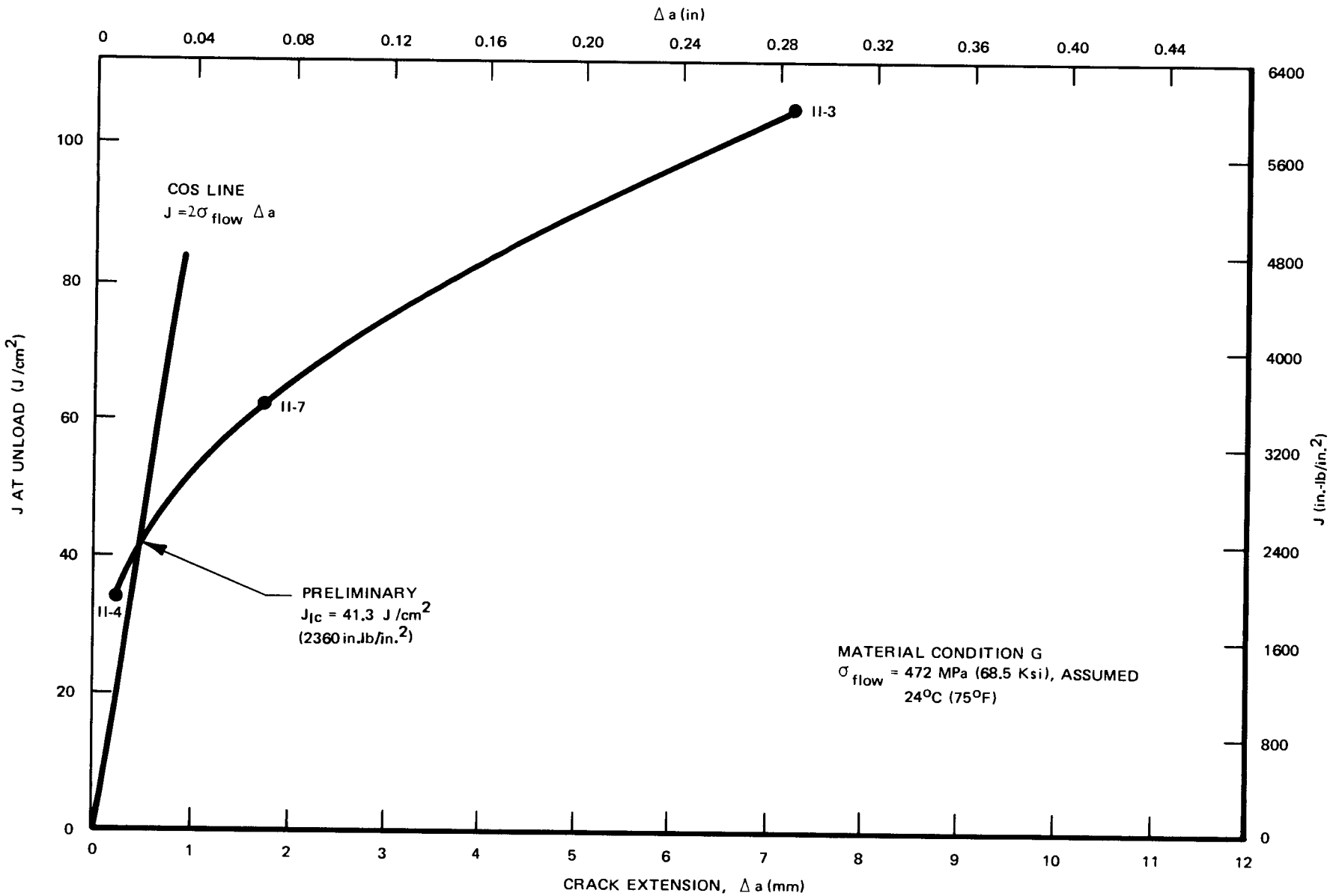

Figure 8.6 J-Integral "R-Curve" for Condition G at 24°C (75°F)

K_{Ic} data points at 24°C (75°F) are compared to the ASME Code K_{IR} curve in Figure 8.7, and are seen to be substantially above it. This indicates that hydrostatic testing of the steam generator at approximately 60F° above the material RT_{NDT} (ASME Code NB 2300 definition) should impose no fracture problems for the material conditions studied, provided that stress intensity factors are maintained at or below the K_{IR} curve. It still remains to verify this conclusion for temper embrittled welds, to be done on the new Shielded Metal Arc Weld (SMAW) which was just prepared. Also, there is a very large concern about the toughness of this material in the high temperature, operating regime. It can be seen from Figure 8.7 that base metal results[15] fall below the ASME K_{IR} curve. This indicates that a lowering of the K_{IR} curve for high temperature may be in order. The design implication here is that fracture toughness could become a limiting consideration for the steam generator shell, and very tight control of allowable flaw sizes, material conditions, and applied stresses would be required. This control can be quantified, based on a fracture mechanics analysis and the current results. Further high temperature tests, including welds, are now being performed to determine the lower limit of a modified K_{IR} curve at elevated temperatures.

8.5 REFERENCES

1. "Program for the Development of Design Data - LMFBR Steam Generator Materials" prepared for the ERDA under contract AT(04-3)-893 Task 10-G and Task 18, July 16 & 17, 1975.

2. L. A. James, "Effect of Thermal Aging Upon the Fatigue-Crack Propagation of Austenitic Stainless Steels", Met. Trans., Vol. 5, Apr. 1974, pp. 831-838.

3. P. Shahinian, et al, "Fatigue Crack Growth in Type 316 Stainless Steel at High Temperature", Trans. ASME, Nov. 1971, pp. 976-980.

4. P. Marshall, "The Fatigue Behavior of Annealed AISI 316 Stainless Steel in Air and High Temperature Sodium: Review and Preliminary Results", Central Electricity Generating Board, Report RD/B/N 3236, Nov. 1974.

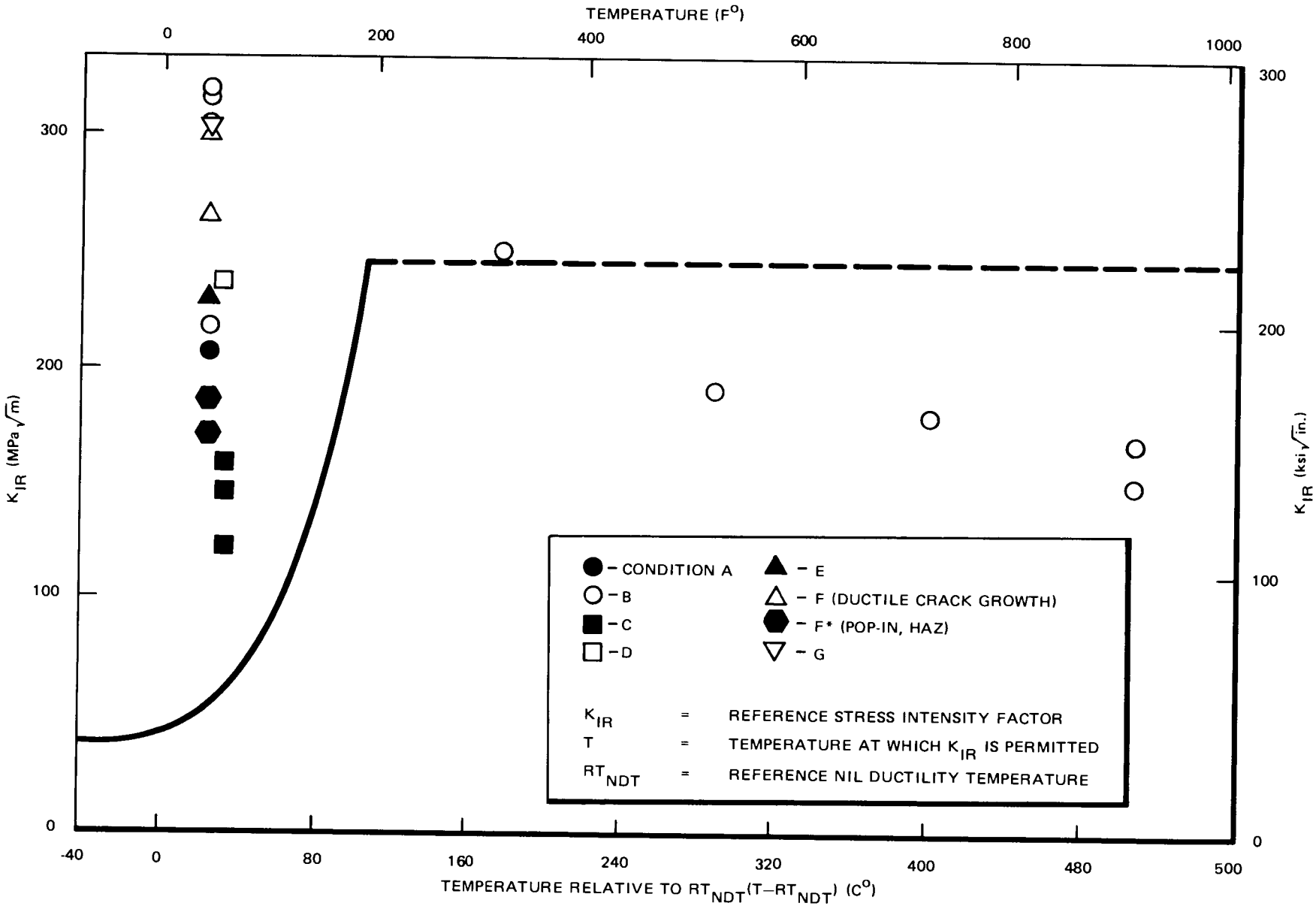

Figure 8.7 Comparison of Fracture Toughness Data with ASME Code Section III K_{IR} Curve

5. L. A. James and R. L. Knecht, "Fatigue-Crack Propagation Behavior of Type 304 Stainless Steel in a Liquid Sodium Environment", Met. Trans., Vol. 6A, Jan. 1975, pp. 109-116.

6. Mechanical Properties Test Data for Structural Materials, Quarterly Progress Report for Period Ending Aug. 31, 1976, ORNL Compilation by M. R. Hill.

7. J. L. Krankota and J. S. Armijo, "Decarburization Kinetics of Low Alloy Ferritic Steels in Sodium", Met. Trans., 3, pp. 2515-2523, Sept. 1972.

8. Low Carbon and Stabilized 2¼% Chromium 1% Molybdenum Steels, American Society of Metals, Metals Park, Ohio (1970).

9. R. L. Klueh, "Effect of Carbon on the Mechanical Properties of 2¼Cr-1Mo Steel", ORNL-4922, Nov. 1973.

10. R. L. Klueh and D. A. Canonico, "Carbon Effects on the Mechanical Properties of 2¼Cr-1Mo Steel Weldments", ORNL-5033, July 1975.

11. Steam Generator Materials Engineering - First Quarterly Report, GEAP-14029-1, (Oct. 1974).

12. Steam Generator Materials Engineering - Second Quarterly Report, GEAP-14029-2, (Jan. 1975).

13. Seventh Quarterly Report, Steam Generator Materials Engineering, Jan-Mar 1976, GEAP-14029-7, ERDA Contract E(04-3)-893, Task 18, (Apr. 1976).

14. J. L. Krankota, K. D. Challenger and L. V. Hampton, "Carbon Transport and Material Property Degradation in a Model of the Clinch River Breeder Reactor Secondary Sodium System", paper VIII B-2, International Conference on Liquid Metal Technology in Energy Production, May 3-6, 1976, Champion, Pennsylvania.

15. Steam Generator Materials Engineering - 8th Quarterly Report, GEAP-14029-8, (Aug. 1976).

INDEX

Test	Material	Page
Chemical Analysis Data		
	alloy 718	117
	type 316 SS	108–109
	2 1/4 Cr-1 Mo	180
Creep Test Data		
Base-Line Data		
	alloy 718	2–3, 146–149
	2 1/4 Cr-1 Mo weld metal	364–370
	2 1/4 Cr-1 Mo steel	364–370
	16-8-2 weld metal	150–152, 156–157
	Inconel 82 weld metal	212–213
	type 304 SS welded plate	292–293
	type 304 SS plate	293
	type 304 SS tube	294
	type 316 SS	133–134
	type 316 SS plate	293
	type 316 SS bar	294
	type 316 SS tube	295, 359–363
	type 316 SS weld metal	150–157
	type 330 SS	313, 319–330
Correlations		
	2 1/4 Cr-1 Mo steel	163–178
	type 304 SS	89–104, 137
	type 316 SS	134–138
Crack Growth Rate		
	type 304 SS	331–337
Effect of Aging		
	2 1/4 Cr-1 Mo steel	197–198
	Inconel 600	263–268
Effect of Environment		
	2 1/4 Cr-1 Mo steel	214–219
	Hastelloy X	214–218

Test	Material	Page
Creep Test Data (Continued)		
Effect of Prestrain		
	type 316 SS	359–363
Effect of Sodium Exposure		
	2 1/4 Cr-1 Mo	197–198
	2 1/4 Cr-1 Mo weld metal . .	364–370
	2 1/4 Cr-1 Mo steel tube . .	364–370
	type 316 SS	43–52
	type 316 SS tube (carburizing).	359–363
Microstructure Evaluation		
	type 304 SS	337–343
	type 330 SS	313, 319–330
Elastic Constants		
Dynamic Measurements		
	Inconel 617	142–145
Fatigue Test Data		
Base-Line Data		
	alloy 718	2–11
	2 1/4 Cr-1 Mo	253–257
Crack Growth Rate		
Base-Line Data		
	type 304 SS	317–319
	type 316 SS plate, weld . . .	353–359
	type AISI 316 SS weld	233–248
Effect of Aging		
	2 1/4 Cr-1 Mo steel	210
	type AISI 316 weld	238–241
Effect of Carbon Content		
	2 1/4 Cr-1 Mo steel	209
Effect of Frequency		
	2 1/4 Cr-1 Mo steel	206–208
	type 316 SS plate, weld . . .	353–359

Test	Material	Page
Fatigue Test Data (Continued		
Effect of Hold Time		
	type 316 SS plate, weld . . .	353–359
	type AISI SS weld	241–242
Effect of Stress Intensity Factor		
	type 316 SS plate, weld . . .	353–359
Effect of Sodium Exposure		
	type 316 SS plate, weld . . .	353–359
Effect of Temperature		
	2 1/4 Cr-1 Mo	205
Effect of Welding Variables		
	type AISI 316 SS weld	241–246
Observations vs ASME Code, Sect. XI		
	type AISI SS weld	246–247
Crack Initiation Observations		
	type 304 SS	38–43
Cyclic Stress Strain		
	alloy 718	2–5
Creep-Fatigue Interaction		
	2 1/4 Cr-1 Mo steel	219–220
Effect of Environment		
	2 1/4 Cr-1 Mo steel	254–256
Effect of Frequency		
	2 1/4 Cr-1 Mo steel	254–256
Effect of Heat Treatment		
	type 304 SS	69–85
	type 316 SS	69–85
Effect of Notches		
	type 304 SS	13–23
Effect of Sodium Exposure		
	type 304 SS	52–69
	type 316 SS	69–85, 297–306

Test	Material	Page
Fatigue Test Data (Continued)		
Load Control Tests		
	CDA 182 (Cu–1% Cr)	222–225
Prototypic Part Test		
	CDA 182 (Cu–1% Cr)	222–225
Specimen Geometry Effects		
	2 1/4 Cr-1 Mo steel	199–204
Hardness Data		
	2 1/4 Cr-1 Mo steel	182
	Inconel 718	308–310
	type 310 SS	308–310
	type 316 SS bar	108–120
Microstructure		
Product Form Variation		
	type 316 SS	108–119
Heat-to-Heat Variation		
	2 1/4 Cr-1 Mo	180–186
Tensile Test Data		
Base-Line		
	2 1/4 Cr-1 Mo steel, weld	370–381
	Inconel 82 transition joints	211
	Inconel 600	268–287
Effect of Aging		
	2 1/4 Cr-1 Mo steel	194–197, 343–350
Effect of Sodium Exposure		
	type 304 SS	52–69
Effect of Strain Rate		
	Inconel 600	268–287
	type 304 SS	89–104
Heat-to-Heat Variation		
	2 1/4 Cr-1 Mo	186–197
Product Form Variation		
	type 316 SS	121–133

Test	Material	Page
Tensile Test Data (Continued)		
Voce Equation Representation		
	type 304 SS	52–69
Weldment Variations		
	type 16-8-2 in 316 SS . . .	150–151
Toughness		
Charpy V-Notch Ductility		
	2 1/4 Cr-1 Mo steel, weld . .	370–381
	16-8-2 weld metal	153–155
Base-Line Data		
	alloy 718 plate, weld forging	248–252
Effect of Heat Treatment		
	alloy 718 plate, weld forging	250–252
Drop Weight NDT		
	2 1/4 Cr-1 Mo steel, weld . .	370–381
J-Integral		
	2 1/4 Cr-1 Mo steel, weld . .	370–381
	Inconel 718	259–263

ORNL-5237
Distribution
Category UC-79b, -h, -k

INTERNAL DISTRIBUTION

1–2. Central Research Library
3. Document Reference Section
4–6. Laboratory Records Department
7. Laboratory Records, ORNL RC
8. ORNL Patent Office
9. R. J. Beaver
10. R. G. Berggren
11. J. J. Blass
12. M. K. Booker
13. C. R. Brinkman
14. D. A. Canonico
15. J. Corum
16. W. R. Corwin
17. F. L. Culler
18. J. E. Cunningham
19. J. H. DeVan
20. R. G. Donnelly
21. D. P. Edmonds
22. G. Fee
23. M. H. Fontana
24. W. R. Gall
25. B. L. Greenstreet
26. J. C. Griess, Jr.
27. J. P. Hammond
28. W. O. Harms
29. R. L. Heestand
30. R. F. Hibbs
31–33. M. R. Hill
34. D. O. Hobson
35. H. Inouye
36. P. R. Kasten
37. J. F. King
38. R. T. King
39. R. L. Klueh
40. K. C. Liu
41. C. T. Liu
42. A. L. Lotts
43–63. W. R. Martin
64. W. J. McAfee
65. H. E. McCoy
66. H. C. McCurdy
67. C. J. McHargue
68. J. Merkle
69. P. Patriarca
70. S. Peterson
71. H. Postma
72. C. E. Pugh
73. P. L. Rittenhouse
74. D. N. Robinson
75. T. Roche
76. J. L. Scott
77. Myrtleen Sheldon
78. V. K. Sikka
79. G. M. Slaughter
80. W. J. Stelzman
81. J. P. Strizak
82. R. W. Swindeman
83. D. B. Trauger
84. J. R. Weir, Jr.
85. G. D. Whitman
86. T. Yahr
87. Paul M. Brister (consultant)
88. John Moteff (consultant)
89. Hayne Palmour III (consultant)
90. J. W. Prados (consultant)
91. N. E. Promisel (consultant)
92. D. F. Stein (consultant)

EXTERNAL DISTRIBUTION

93–94. ERDA DIVISION OF NUCLEAR FUEL CYCLE AND PRODUCTION, Washington, DC 20545
Director

95–96. ERDA DIVISION OF NUCLEAR RESEARCH AND APPLICATIONS, Washington, DC 20545
Director

97–98. ERDA DIVISION OF REACTOR DEVELOPMENT AND DEMONSTRATION, WASHINGTON, DC 20545
Director

99–100. ERDA OAK RIDGE OPERATIONS OFFICE, P.O. Box E, Oak Ridge, TN 37830
Director, Research and Technical Support Division
Director, Reactor Division

101–386. ERDA TECHNICAL INFORMATION CENTER, Office of Information Services, P.O. Box 62, Oak Ridge, TN 37830

For distribution as shown in TID-4500 Distribution Category, UC-79b (Fuels and Materials Engineering Development); UC-79h (Structural Materials Design Engineering); UC-79k (Components)

☆ U.S. GOVERNMENT PRINTING OFFICE: 1976-748-189/79